UNIVERSITÀ
DEGLI STUDI
FIRENZE

DOTTORATO DI RICERCA IN SCIENZE CHIMICHE

CICLO XXXII

COORDINATORE Prof. PIERO BAGLIONI

Biologically relevant phosphate-based nanostructures: interactions with soft matter and biomedical applications

Settore Scientifico Disciplinare CHIM/02

Dottorando
Dott. Rita Gelli

Tutore
Dr. Francesca Ridi

Coordinatore
Prof. Piero Baglioni

Anni 2016/2019

Abstract

This work of thesis deals with the physico-chemical investigation of biologically-relevant calcium and magnesium phosphate-based nanostructures. The motivation of this work relies on the evidence that these materials constitute the main inorganic components of human body, where they are present in several locations and fulfill a great number of functions. The study of their formation in bio-relevant conditions is thus noteworthy, as it could contribute both to unravel the *in vivo* formation mechanisms, as well as to guide in the design of tailored materials for biomedical applications. In this thesis, we mainly focused on two recently-discovered systems, which are amorphous magnesium-calcium phosphate nanoparticles (AMCPs) present in mammalians' gut and magnesium phosphate-based bone cements (MPCs). As far as the first topic is concerned, we aimed at studying the formation of synthetic analogs of AMCPs in conditions mimicking to a certain extent the *in vivo* milieu, with the ultimate goal of connecting the physico-chemical findings with the physiological and pathological role of AMCPs, given their involvement at the immune level. We inspected the effect of pH and Mg^{2+} on the lifetime of the amorphous phase, and we investigated how representative molecules belonging to soft matter, present in the gut and in simulated intestinal fluids, affect the formation and the features of AMCPs. We also investigated the possibility of including bio-relevant proteins within the inorganic structure. In all these case studies, the particles were characterized by means of a multi-technique approach, which allowed us to obtain a complete physico-chemical overview of the system. Aiming at assessing the potentialities of phosphate-based nanostructures for biomedical applications, we chose to focus our attention on MPCs, which are a new category of bone cements whose features still need to be completely established. These materials, which are obtained upon the mixing of a powder component and an aqueous-based solution, were assessed in terms of cohesion, setting time, crystallinity, microstructure and mechanical properties. We characterized how these properties change according to formulation parameters and due to the inclusion of citrate and polymeric additives. These investigations demonstrate our ability to tune the features of these cements, making them effective candidates for orthopedic applications.

Table of Contents

Preface

This work of thesis deals with the physico-chemical investigation of biologically-relevant calcium and magnesium phosphate-based nanostructures. The motivation of this work relies on the evidence that these materials are the main inorganic components of human body, where they are present in several locations and fulfill a great number of functions. The study of their formation in bio-relevant conditions is thus noteworthy, as it could both contribute to unravel the *in vivo* formation mechanisms, as well as to guide in the design of tailored materials for biomedical applications. In this thesis, we mainly focused on two recently-discovered systems, which are amorphous magnesium-calcium phosphate nanoparticles present in the mammalians' gut and magnesium phosphate-based bone cements.

In Chapter 1, the state of the art and the concepts necessary to contextualize the conducted work are presented. Chapter 2 and Chapter 3 describe the results attained in the investigation of, respectively, amorphous magnesium-calcium phosphate nanoparticles and magnesium phosphate-based bone cements: each chapter is divided in sub-sections, which give an overview of the different aspects explored throughout this PhD. Chapter 4 presents the conclusions and the future perspectives of the conducted work.

The experimental details about the techniques used in the experiments are reported in Appendix I, while in Appendix II the papers published during my PhD are reprinted with permission from the publisher; papers from I to V are related to this PhD research project, whereas papers VI and VII pertain to works not directly related to the PhD project, but were published within the same period. In Appendix III, the abstracts of the manuscripts currently in preparation are reported.

- **Paper I**: Gelli, R., Scudero, M., Gigli, L., Severi, M., Bonini, M., Ridi, F. & Baglioni, P., Effect of pH and Mg^{2+} on Amorphous Magnesium-Calcium Phosphate (AMCP) stability. *Journal of Colloid and Interface Science* 531, 681–692 (2018).
- **Paper II:** Gelli, R., Salvestrini, S., Ridi, F., Effect of biologically-relevant molecules on the physico-chemical properties of amorphous magnesium-calcium phosphate nanoparticles. *Journal of Nanoscience and Nanotechnology,* accepted for publication (2019).
- **Paper III:** Gelli, R., Tempesti, P., Ridi, F. & Baglioni, P. Formation and properties of amorphous magnesium-calcium phosphate particles in a simulated intestinal fluid. *Journal of Colloid and Interface Science* 546, 130–138 (2019).
- **Paper VI:** Gelli, R., Ridi, F. & Baglioni, P. The importance of being amorphous: calcium and magnesium phosphates in the human body. *Advances in Colloid and Interface Science* 269, 219-235 (2019).
- **Paper V:** Gelli, R., Mati, L., Ridi, F. & Baglioni, P. Tuning the properties of magnesium phosphate-based bone cements: Effect of powder to liquid ratio and aqueous solution concentration. *Materials Science and Engineering: C* 95, 248–255 (2019).
- **Paper VI**: Gelli, R., Del Buffa, S., Tempesti, P., Bonini, M., Ridi, F. & Baglioni, P., Multi-scale investigation of gelatin/poly(vinyl alcohol) interactions in water. *Colloids and Surfaces A: Physicochemical and Engineering Aspects* 532, 18–25 (2017). -master thesis-
- **Paper VII**: Gelli, R. Del Buffa, S., Tempesti, P., Bonini, M., Ridi, F. & Baglioni, P., Enhanced formation of hydroxyapatites in gelatin/imogolite macroporous hydrogels. *Journal of Colloid and Interface Science* 511, 145–154 (2018). -bachelor thesis-

List of abbreviations

in alphabetical order

ACP: Amorphous Calcium Phosphate

AMCP: Amorphous Magnesium-Calcium Phosphate

AMP: Amorphous Magnesium Phosphate

ATP: Adenosine Triphosphate

BET: Brunauer-Emmett-Teller

BJH: Barrett-Joyner-Halenda

CaP: Calcium Phosphate

CDHA: Calcium-Deficient Hydroxyapatite

CHA: Carbonated Hydroxyapatite

CPCs: Calcium Phosphate Cements

CPPs: Calciprotein Particles

CSCs: Calcium Sulfate Cements

CSH: Calcium Silicate Hydrate

DAC: Dibasic Ammonium Citrate monohydrate

DAHP: Di-Ammonium Hydrogen Phosphate

DCPD: Di-Calcium Phosphate Dihydrated

DLS: Dynamic Light Scattering

DTG: Differential Thermogravimetry

Fet-A: Fetuin-A

FT-IR: Fourier Transform-Infrared Spectroscopy

FWI: Free Water Index

GI: Gastro-Intestinal

HA: Hydroxyapatite

LT-DSC: Low Temperature-Differential Scanning Calorimetry

MEM: Minimum Essential Medium Eagle

MgP: Magnesium Phosphate

MPCs: Magnesium Phosphate Cements

MSH: Magnesium Silicate Hydrate

OCP: Octa-Calcium Phosphate

P/L: Powder to Liquid ratio

PAA: Poly(acylic acid)

PEG: Poly(ethylene glycol)

PMMA: Poly(methyl) methacrylate

RH: Relative Humidity

SEM: Scanning Electron Microscopy

SF: Splitting Factor

TCP: Tri-Calcium Phosphate

TEM: Transmission Electron Microscopy

TGA: Thermogravimetry

TMP: Tri-Magnesium Phosphate

SAXS: Small Angle X-Rays Scattering

SIF: Simulated Intestinal Fluids

XRD: X-Rays Diffraction

1 Introduction

1.1 Calcium and Magnesium Phosphates

Inorganic nanostructured phosphates, especially calcium and magnesium-based, are essential components of living organisms, since they contribute to maintain their structure and guarantee the correct functioning [1]. The (ortho)phosphate group (PO_4^{3-}), which is structurally different from meta (PO_3^-), pyro ($P_2O_7^{4-}$) and poly $(PO_3)_n^{n-}$, comprises PO_4^{3-}, $H_2PO_4^{2-}$ and HPO_4^{2-} [2]. The speciation of these anions in water depends on the pH of the solution, as it is shown in Figure 1.1 (K_{aI}=7.50·10^{-3}, K_{aII}=6.20·10^{-8}, K_{aIII}=1.70·10^{-12}) [3].

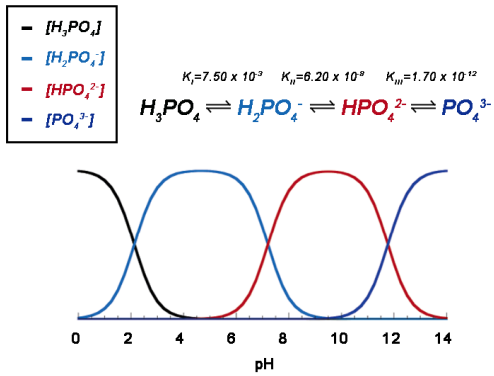

Figure 1.1: Triprotic equilibrium for orthophosphoric acid solutions as a function of pH, reprinted with permission from [3].

Due to this triprotic equilibrium, the typologies of calcium phosphates (CaPs) and magnesium phosphates (MgPs) that can crystallize are various; moreover, the two cations can be simultaneously combined with phosphate in mixed Ca-Mg phases. The array of compounds which results from these interactions is listed in Table 1.1.

Table 1.1: Main CaP, CaMgP and MgP crystalline phases [1, 4, 5]; the bold formulas refer to the phases which will be encountered in this thesis.

Chemical formula	Mineral name	Chemical name	Acronym
$Ca(H_2PO_4)_2$	-	Monocalcium phosphate anhydrous	MCPA
$Ca(H_2PO_4)_2 \cdot H_2O$	-	Monocalcium phosphate monohydrate	MCPM
$CaHPO_4$	Monetite	Dicalcium phosphate	DCPA
$CaHPO_4 \cdot 2H_2O$	Brushite	Dicalcium phosphate dihydrate	DCPD
α-/β-$Ca_3(PO_4)_2$	-	α-/β-Tricalcium phosphate	TCP
$Ca_{10}(PO_4)_6(OH)_2$	Hydroxyapatite	Pentacalcium hydroxide tris(phosphate)	HA
$Ca_{10}(PO_4)_6Cl_2$	Chloroapatite	Pentacalcium chloride tris(phosphate)	ClAP
$Ca_{10}(PO_4)_6F_2$	Fluorapatite	Pentacalcium fluoride tris(phosphate)	FAP
$Ca_{10}(PO_4)_6O$	Voelckerite	Oxyapatite	OA
$Ca_4(PO_4)_2O$	Hilgenstockite	Tetracalcium phosphate	TTCP
$Ca_{10}(PO_4,CO_3)_6(OH, CO_3)_2$	Dahlite	Carbonated hydroxyapatite	CHA
$Ca_8(HPO_4)_2(PO_4)_4 \cdot 5H_2O$	-	Octacalcium phosphate	OCP
$Ca_9MgHPO_4(PO_4)_6$	Whitlockite	Nonacalcium magnesium hydrogenphosphate hexaphosphate	TCMP
$Ca_4Mg_5(PO_4)_6$	Stanfieldite	Tetracalcium pentamagnesium hexaphosphate	TPHP
$MgHPO_4$	-	Magnesium hydrogen phosphate	MHP
$MgHPO_4 \cdot 3H_2O$	Newberyite	Magnesium hydrogen phosphate trihydrate	DMPT
$Mg_3(PO_4)_2$	Farringtonite	Trimagnesium bis(phosphate)	TMP
$Mg_3(PO_4)_2 \cdot 8H_2O$	Bobierrite	Trimagnesium bis(phosphate) octahydrate	TMPO
$Mg_3(PO_4)_2 \cdot 22H_2O$	Caattite	Trimagnesium bis(phosphate) docosahydrate	TMPD
$Mg_2PO_4OH \cdot 4H_2O$	Holtedahlite	Dimagnesium hydroxyphosphate tetrahydrate	DHPT
$MgNH_4PO_4 \cdot H_2O$	Dittmarite	Ammonium magnesium phosphate monohydrate	AMPM
$MgNH_4PO_4 \cdot 6H_2O$	Struvite	Ammonium magnesium phosphate hexaydrate	AMPH
$Mg(NH_4HPO_4)_2 \cdot 4H_2O$	Schertelite	Diammonium magnesium dihydrogen phosphate tetrahydrate	AMDT
$Mg_3(NH_4)_2(HPO_4)_4 \cdot 8H_2O$	Hannayite	Trimagnesium diammonium hydrogen phosphate octahydrate	TDHO

Each phase is endowed with a specific solubility and stability, in relation to temperature and pH [1, 4, 6]. For CaPs, the Ca/P ratio varies from 0.5 to 2.0, while Mg/P ratio ranges from 1.0 to 2.0 for MgPs. CaP is often regarded as the most important example of inorganic biomineral, constituting the majority of hard tissues of human body (see section 1.2). Given its relevance, it has been employed in a wide range of applications: apart from the biomedical ones, which are detailed in section 1.4, it has been used for water treatment, as fertilizer, for solid nuclear waste and as source of phosphorous [7]. Many synthesis methods have been developed to obtain CaPs with tailored size, shape and crystallinity [8], and several reviews address the features of each specific CaP phase [2, 4, 6]. MgP has, in general, received less attention than CaP. The use of MgP-based materials for biomedical applications is an emerging research area (see section 1.4), whereas they have been mainly employed in agricultural, environmental and civil engineering fields [9–12]. Before discussing the bio-relevant forms of CaPs and MgPs, which are the focus of this work of thesis, it is important to highlight that a complex equilibrium between these two classes of minerals exists in solution, due to their different stability and solubility. As a proof of that, the stability field diagrams reported in the literature (see Figure 1.2) clearly show that when both Mg^{2+} and Ca^{2+} are present in solution (together with phosphate and ammonium), the formation of a certain phase over another one depends on the ions' activity and pH; the simultaneous crystallization in solution of different phases can also occur [1]. As *in vivo* the interplay of these two ions plays a pivotal role [13], the fate of CaPs and MgPs is inevitably connected.

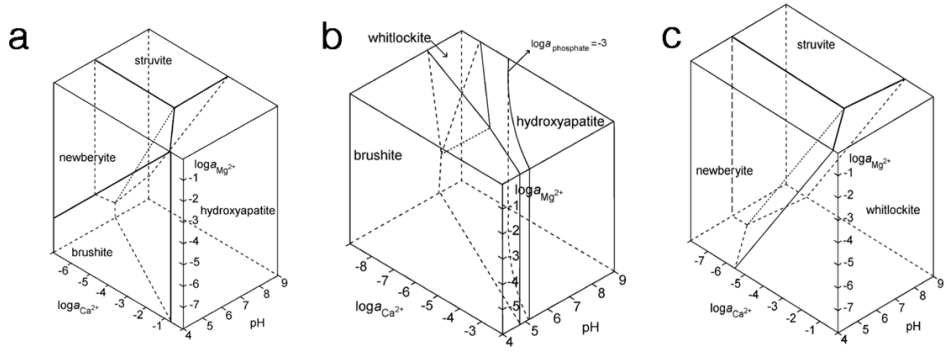

Figure 1.2: Stability fields diagrams for CaPs and MgPs in solution at 298.15 K. The axes refer to Ca^{2+} and Mg^{2+} activity in solution and pH. Each surface corresponds to a three-phase equilibrium, two adjacent solid phases and aqueous solution. In (a) and (b), the boundary between newberyite and struvite corresponds to loga_{NH4+}=-1.5. Reproduced from [1].

1.2 Relevance of CaP and MgP in human body

Among the different forms of CaP and MgP listed in Table 1.1, a significant number of them can be found in human body as physiological or pathological calcifications. Normal mineralized tissues contain mainly CaPs with an apatitic structure, whereas magnesium ions exist, in normal calcifications, at trace levels inside the calcium-containing solid phase structures [1]. Table 1.2 summarizes the distribution of these phases in the human body, further discussed in the sections below.

Table 1.2: Distribution of calcium and magnesium phosphate-based crystalline phases in human body. The phase constituting normal calcifications is referred to as "Carbonated calcium-deficient HA", even if some compositional differences among the three locations exist (see Table 1.3).

	Location	Phase	References
Normal calcifications	Bone	Carbonated calcium-deficient HA	[4, 14]
	Enamel	Carbonated calcium-deficient HA	[4, 15, 16]
	Dentin	Carbonated calcium-deficient HA	[4, 16]
Pathological calcifications	Dental calculi	Whitlockite, Brushite, OCP, CHA	[17]
	Salivary stones	Whitlockite, HA	[18]
	Kidney-Urinary stones	Struvite, Newberyite, CHA	[18, 19]
	Gallstones	HA	[1]
	Pseudo-gout	Calcium pyrophosphate dihydrate	[20, 21]
	Atherosclerotic plaques	CaP-based (non-specified)	[22, 23]

1.2.1 Bone

The most notable example of phosphate-based deposits in human body is constituted by non-stoichiometric apatite-based crystals, which comprise the inorganic matrix of bone and teeth. In bone, the inorganic phase is composed by nanometric platelets (~50 x 25 x 4 nm) of calcium-deficient hydroxyapatite (CDHA), whose growth is templated by soft collagen fibers (typical bone composition: 65 %wt inorganic, 25 %wt organic, 10 %wt water, see Table 1.3) [4]. Several impurities (carbonate, sodium, fluoride, chloride) are embedded in the apatitic structure, resulting in a poorly crystalline material [4, 24]. Magnesium is also present in bone (0.72 %wt) and resides either on the

surface of HA or in the hydration shell around the crystal [25]. The amount of Mg^{2+} in bone mineral is reported to decrease with increasing calcification, leading to a growth in crystallinity and stability [26, 27]. Another minor but important component is citrate, which bridges between mineral HA platelets and is involved in the control of their crystallinity [28]. The general formula for biological apatites can be indicated as $(Ca,Na,Mg,X)_{10}(PO_4, HPO_4, CO_3)_6(OH,Y)_2$ where X can be any other cation substituting for Ca and Y can be Cl^- or F^- substituting for (OH) [17].

Table 1.3: Typical composition of the inorganic phase of human calcified tissues [29].

Composition [%wt]	Bone	Enamel	Dentin
Calcium	34.8	36.5	35.1
Phosphorus	15.2	17.7	16.9
Ca/P (molar ratio)	1.71	1.63	1.61
Sodium	0.9	0.5	0.6
Magnesium	0.72	0.44	1.26
Potassium	0.03	0.08	0.05
Carbonate	7.4	3.5	5.6
Fluoride	0.03	0.01	0.06
Chloride	0.13	0.30	0.01
Pyrophosphate	0.07	0.022	0.10
Total inorganic	65	97	70
Total organic	25	1.5	20
Water	10	1.5	10

The mineralized matrix made of HA and collagen constitutes a complex and organized framework that provides mechanical support and exerts an essential role in the bone homeostasis; moreover, it hosts different types of cells involved in the dynamics of bone formation and remodeling, namely osteoclasts, osteoblasts and osteocytes [30, 31]. Osteoblasts and osteoclasts located at the outer and inner surfaces of bone are responsible for the renewal of bone tissues, so called remodeling, given by the simultaneous resorption of old bone by osteoclasts and the formation of new one by osteoblasts; osteocytes contribute to the maintenance of bone structure. The continuous remodeling process is presumably facilitated by the small size and/or non-

stoichiometry of the crystals, which endows the mineral phase with the solubility needed for bone's resorption by osteoclasts [14].

The hierarchical structure of bone is depicted in Figure 1.3: the combination at the atomic scale of the stiff HA-based platelets with the flexibility of a protein-based matrix results in a material with remarkable mechanical properties, *i.e.* a light-weight material able to carry large loads [32].

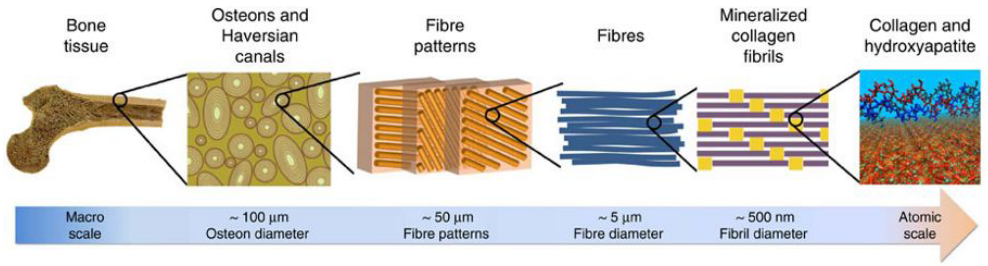

Figure 1.3: Hierarchical structure of bone, ranging from the macroscale skeleton to nanoscale collagen and HA. Reproduced with permission from [32].

1.2.2 Teeth

Teeth is constituted by three main parts, namely enamel (outer surface), dentin (bulk of the teeth) and cementum (layer around the root). The former is a rigid, inert and acellular layer, composed by 97 %wt of a dense array of needle-shaped carbonate-substituted apatite crystals (diameter ~50 nm and length of tens of µm). The *c*-axes of these crystals are aligned and form micrometric rods, resulting in an intricate 3D network that constitutes the bulk of enamel [15]; this peculiar arrangement reduces cracks propagation and enhances its mechanical strength and fatigue resistance [33], making it the hardest substance of our body [4]. In contrast to enamel, dentin and cementum are mineralized connective tissues with an organic matrix made of collagenous proteins and an inorganic phase with a crystallinity similar to bone (typical crystal size 35 x 25 x 4 nm). From a compositional viewpoint, bone, enamel and dentin differ in the concentration of important minor constituents (namely, Mg^{2+} and CO_3^{2-}, see Table 1.3) and in dissolution properties: the extent of *in vitro* dissolution in acidic buffer was shown to decrease in the order: bone=dentine >> enamel, consistently with the higher crystallinity of the latter [17].

1.2.3 Pathological calcifications

In normal situations, CaP calcifications are restricted to bone and teeth; ageing and diseases (atherosclerosis, arthritis, diabetes, cancer...) can cause the alteration of regular biological pathways, resulting in ectopic crystal depositions (inappropriate biomineralization occurring in soft tissues [34]) which may lead to diseases and mortality. The composition of pathological calcifications differs from that of normal CaP depositions in bone and teeth. For instance, calculi (concretions of material, usually mineral salts, that form in an organ or duct of the body) can be composed by different forms of CaP and MgP. Dental calculi consist of mixed phases of brushite, OCP, whitlockite and CHA. The relative abundance of the different phases depends on age (of the person and of the calculus itself) and location (sub- or supra-gingival) [35–39]. Salivary gland stones are also constituted by HA and whitlockite as major components, while OCP and brushite are rarely detected [40]. Kidney and urinary stones are typically composed by several phases including struvite, dittmarite, newberyite and CHA [19, 41–43]. Despite being mainly formed by cholesterol, stones formed in the gallbladder (gallstones) can include HA as a significant component, in particular in the black-pigment ones [1]. A peculiar pathology linked to undesired calcifications is pseudo-gout, a form of arthritis caused by the crystallization of calcium pyrophosphate dehydrate in the synovial fluid of the joints [20, 21]. Another disease in which CaP-based calcifications are involved is atherosclerosis, in which the formation of plaques containing cholesterol, cholesterol esters, phospholipids and calcium phosphate form within artery walls [16, 22, 23]. Such plaques result in a narrowing of major arteries, which cause the restriction of blood flow to tissue, potentially leading to heart attacks and strokes. A complete overview of all the pathological phosphate-based calcifications can be found in the literature [4].

1.3 Amorphous calcium and magnesium phosphates

Besides crystalline CaP and MgP deposits discussed in the previous section, amorphous calcium phosphates (ACP) and amorphous magnesium-calcium

phosphates (AMCP) are very frequent forms of CaP in biological organisms and play a fundamental role in their structure and functioning [44]. Amorphous materials, defined as highly disordered structures which lack of the long-range order at the atomic level characteristic of crystals [45], are significant to various aspects of evolution and life of biological organisms: Nature often takes advantage of this type of structures in opposition to more energetically-defined and ordered crystals, as their flexibility is useful to interface with the versatility of living organisms [46]. As a proof of that, amorphous materials represent ~ 20 % of approximately 60 different inorganic compounds and minerals formed by living organisms [47] and, in many biomineralization processes, the amorphous material is often the precursor to the formation of the crystalline counterpart [48]. The most notable example is calcium carbonate, which is produced in amorphous form by organisms such as crustaceans, sea urchins and certain mollusks [49–51]. As we outlined in a recent review, some specific structures in human body are made of CaP in its amorphous state [52]. The fact that such a thermodynamically unstable phase [53] is preserved in different sites of our body is intriguing, suggesting that the amorphous nature is crucial for the material to perform specific biological functions. Before reviewing the endogenous forms of ACP and Mg-substituted ACP, its main features are presented in section 1.3.1. We do not focus on amorphous magnesium phosphate (AMP) as this phase is not naturally-present in human body.

1.3.1 Features of ACP

The first report about ACP dates back to 1953, when Watson and Robinson described the formation of a “finely granular” precipitate resulting from the mixing of concentrated solutions of $CaCl_2$ and Na_2HPO_4, which displayed no electron diffraction pattern [54]. It is nowadays agreed that when mixing two solutions containing calcium and phosphate ions at sufficiently high supersaturation and pH, ACP with a molar Ca/P ratio between 1.18 and 2.50 forms [2]. The formation of non-crystalline calcium phosphate is a kinetic phenomenon [55]: the mixing of highly concentrated solutions creates sufficiently strong stochastic interactions among calcium and phosphate ions

so that they can form highly hydrated clusters that separate from the solution in a gel-like state [53]. The formed ACP is very unstable: being its precipitation kinetically-driven, hydrolysis and crystallization proceed by a sequential process which involves structural and compositional modifications of the amorphous precursors and crystalline intermediates (such as OCP), rather than a single-step pathway (see Figure 1.4a) [53, 56]. This precipitation mechanism is known as "Ostwald-Lussac Law of Stages": a disordered and highly soluble phase first forms and, through a series of phase transformations, eventually converts into a poorly soluble and more ordered crystalline phase [57, 58].

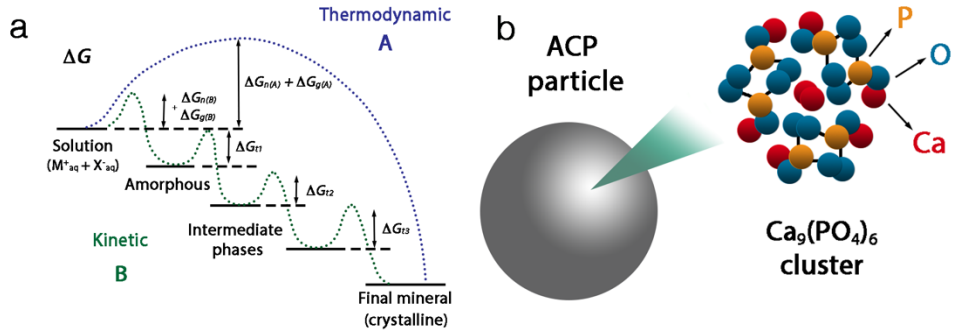

Figure 1.4: (a) Crystallization pathways under thermodynamic (A) and kinetic (B) control. A system follows a one-step route to the final mineral phase (pathway A) or proceeds by sequential precipitation (pathway B), depending on the free energy of activation (ΔG) associated with nucleation (n), growth (g), and phase transformation (t); (b) Model of ACP structure (Posner's cluster). Reproduced with permission from [52].

For ACP, the final step of the crystallization process is HA at neutral and alkaline pH or brushite at acidic pH [59]. It is important to note that ACP is not a mandatory precursor to crystalline CaP, as when sufficiently diluted solutions are used, apatite formation can occur without the detection of an amorphous precursor (A pathway in Figure 1.4a) [60, 61].

Though ACP is an amorphous material, a short-range order corresponding to $Ca_9(PO_4)_6$ units ("Posner's clusters") was proposed by Posner and Betts in 1974 [62]; the structural unit, whose size is about 9.5 Å, is depicted in Figure 1.4b. According to the Posner's model, the clusters randomly aggregate into spherical objects with a diameter of 30-100 nm, generating the typical morphology of ACP [63]. In ACP's structure, water plays a role, too: the freeze-dried material contains a relevant amount (15-20 %) of bound water,

which is located on the surface and in the interstices between the $Ca_9(PO_4)_6$ clusters [64]. While the validity of Posner's model has been corroborated by recent studies [65], much effort has been pursued in the last decade in the investigation of the first stages of ACP formation. In 2010 Dey *et al*. showed that surface-induced crystal nucleation of CaP is initiated by the generation of pre-nucleation clusters that densify at a templating surface, leading to the formation of an amorphous precursor phase which eventually transforms into crystalline apatite [66]. Later, a work from Habraken *et al*. unveiled the chemical nature of the process, showing that pre-nucleation clusters preceding ACP formation consist of soluble ion-association complexes $[Ca(HPO_4)_3]^{4-}$ that form 3D polymeric networks in solution [67]. Above the solubility limit of ACP, these aggregated pre-nucleation complexes collect Ca^{2+} from the solution and form insoluble post-nucleation clusters of $[Ca_2(HPO_4)_3]^{2-}$, which then precipitate as ACP; the continuous Ca^{2+} uptake converts ACP into OCP and subsequently into apatite. For further details about the pre-nucleation clusters theory and crystallization, the reader is referred elsewhere [68].

1.3.2 Stabilization strategies

Unless stabilizing agents are present in solution, when ACP forms or when it is dispersed in an aqueous medium it rapidly hydrolyses and subsequently converts into a more stable crystalline form of CaP. Several works have addressed the effect of factors such as temperature, pH or presence of ions/molecules in solution on the crystallization kinetic of ACP. A decrease in temperature [69, 70] and an increase in pH [70] delay the conversion of ACP to HA. In addition, it was recently reported that the formation of CaP in confined environments can lead to the stabilization of the amorphous precursor [71, 72].

The most effective strategy to enhance the lifetime of the amorphous phase in solution is the addition of foreign ions or molecules/macromolecules. The effect of Mg^{2+} has been extensively investigated in the literature, and several stabilization mechanisms have been proposed. A seminal work by Boskey and Posner addressed the conversion of ACP to HA at different Mg^{2+}

concentrations [73]. The authors report that an increase in Mg/Ca ratio from 0 to 0.04 results in a ~ 9 times extension of the amorphous phase lifetime at 26 °C, ~ 4 times at 37.5 °C and ~ 7 at 48 °C, concluding that the presence of Mg^{2+} decreases the solubility of ACP. In contrast, Bachra *et al.* attributed the stabilization effect to Mg^{2+} ability to form stronger complexes than Ca^{2+} with phosphate [74]. The group of Christoffersen *et al*. suggested that Mg^{2+} slows the transformation of ACP1 to ACP2, being ACP1 the initial fast-precipitating spherular amorphous form of CaP, which converts into a floccular form called ACP2 [75, 76]. Abbona and Baronnet proposed that the stabilizing action of Mg^{2+} is ascribable to the initial substitution for Ca^{2+} in Posner's clusters, which induces mechanical strains and hinders HA nucleation [77]. In some conditions, ACP prepared in the presence of magnesium can reach impressive stabilities: for instance, the amorphous phase can last up to 145 days when ACP is prepared at pH 10, 32.5 °C and with Mg/Ca ratio 0.25 [78]. Despite the large number of investigations conducted from the sixties, the precise role of Mg^{2+} on HA formation is still considerably debated, as shown by the several papers published on this topic in the last decade [79–83]. According to Yang *et al*., the formation of magnesium-phosphate ion pairs may reduce the thermodynamic driving force for ACP nucleation and phase transformation to HA [80], while the role of Mg^{2+} ions at the surface was elucidated by Ding *et al*. [81]. From the literature data reported so far, we can infer that precise pathway through which Mg^{2+} stabilizes the amorphous phase, which possibly results from the combination of multiple mechanisms, is only partly established, and requires further investigations. Besides Mg^{2+}, other cations which have shown a stabilizing action are Ga^{3+}[84], Cd^{2+}[85], Sr^{2+} and Zn^{2+}[86]. Some anions also exert an effect on ACP stability, including F^- [74, 87, 88], $P_2O_7^{4-}$ [86, 88, 89], CO_3^{2-} [90–92] and citrate ($C_6H_5O_7^{3-}$) [93, 94].

Biologically-relevant molecules can also act as stabilizing agents for ACP. Early studies showed that ATP (adenosine triphosphate, the molecule which provides energy to cells) is able to stabilize ACP [95–97], sometimes in combination with Mg^{2+}[98, 99]. The influence of some naturally-occurring biomacromolecules which can be found in human body has been explored: to cite some examples, casein phosphopeptide (derived from the milk protein casein by tryptic digestion) binds calcium and phosphate ions in an amorphous state, through the formation of complexes [100]. Proteoglycans,

heavily glycosylated proteins which play a role in regulating mineralization processes, are potent inhibitors of HA formation [101, 102]. Phosphatidylserine (PS), an acidic phospholipid which is concentrated in matrix vesicles (organelles believed to be the site of initial bone, dentine and cartilage calcification [103]), has a variable effect on *in vitro* HA proliferation [104, 105]. The effect of bile acids was also investigated, given the fact that HA can comprise up to 30 % of the total mass of black pigment stones [106]. Taurocholic acid does not influence the stability of the amorphous phase, while glycochenodeoxycholic acid prevents transformation of amorphous calcium phosphate to crystalline HA by competitively inhibiting the accumulation of phosphate on the crystal embryo surface [107].

In addition to the naturally-existing macromolecules, some synthetic polymers display the ability to slow down the conversion of ACP to crystalline CaP. Despite their synthetic nature, the study of their interaction with amorphous phosphates is relevant in view of their inclusion in ACP-based biomaterials, such as in the field of bone and teeth remineralization. Some examples include PEG (poly(ethylene glycol)) [108, 109], PAA (poly(acylic acid)) [110, 111], polyelectrolytes [112], poly(amino acids) [88, 113].

1.3.3 Endogenous forms of ACP and AMCP

The locations in which amorphous calcium phosphate is present in human body are bone, enamel, calciprotein particles in blood, casein micelles in milk and the small intestine (see the sketch in Figure 1.5).

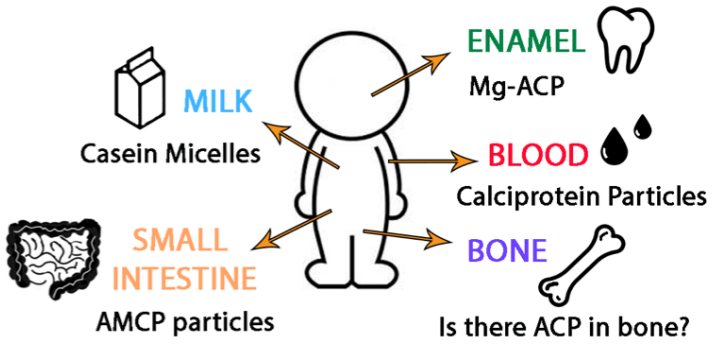

Figure 1.5: Cartoon summarizing the locations of human body in which ACP and Mg-substituted ACP is present. Reproduced with permission from [52].

In this section, we briefly outline the features of the first four classes, whereas we give a detailed overview of AMCP particles in the small intestine, which have been specifically addressed in this work of thesis.

1.3.3.1 Bone

The controversy of ACP in bone was considerably debated for a long time, and it is presented in this section in an historical perspective. Early investigations suggested that a significant portion of mammalian bone mineral could be constituted by ACP, its amount decreasing with aging [114–117]. In the seventies, Posner questioned these conclusions, stating that the amount of ACP in bone mineral could not be higher than 10 % [118] (early estimates suggested ~40 % [117]). A successive work by Grynpas *et al*. ruled out the existence of ACP in young bone mineral of embryonic chicks [119]. In 1997, Boskey reported that at the beginning of the '90s this controversy was overcome by the application of high resolution techniques that succeeded in revealing that 99 % of bone mineral consists of poorly crystalline hydroxyapatite [60]. However, it should be kept in mind that the characterization of the newly formed mineral deposits in a tissue without their alteration during sample preparation and/or analysis is challenging: the use of wet and/or poorly preserved samples can trigger the conversion of ACP into more stable apatite or OCP; moreover, water removal can affect ACP stability, as its dehydration can lead to premature crystallization [44]. Another potential reason for the inability to detect biogenic ACP in bone tissue is the hypothesis that this phase does not exist as separate particles but, instead, as a layer on apatite crystals [120, 121]. All these considerations highlight that the presence of ACP in mature bone mineral is not conclusively demonstrated.

An issue which is closely related is the involvement of ACP as a precursor of apatite formation in the biomineralization process, especially considering that Nature often takes advantage of a transient precursor amorphous phase for crystals formation [122]. Despite being serum concentrations of calcium and phosphate much lower than it would be necessary for triggering the precipitation of ACP [61, 123], the *in vivo* bone formation process is significantly more complicated than what simple thermodynamic

considerations about mineral precipitation would predict. In the last decade, some studies were published supporting the theory of bone mineral formation through ACP; even if these publications do not address specifically the human bone, the findings are of outmost importance to make some speculations of what may happen in our body. In 2006, Crane *et al.* studied early mineral deposits in mice calvaria by means of micro-Raman spectroscopy, showing that OCP is a precursor phase of bone apatite, and suggesting that ACP may form before OCP [124]. The theory of OCP as a precursor to bone mineral had been proposed in the past by Brown [125–127], and the report by Crane *et al.* is a significant step towards its demonstration. Despite some distinguished opinions considered this paper a strong evidence of the transient precursor strategy in vertebrates [128], others confuted the conclusions of the work [129]. Later, Mahamid *et al.* showed that in the continuously forming fin rays of a zebrafish the newly formed bone contains large amounts of ACP [130, 131]. The mineral formation in larval zebrafish caudal fin bone was successively studied *in vivo* by Weiner and Addadi, who demonstrated the presence of intracellular mineral particles consisting of a disordered calcium phosphate phase with characteristic features of OCP, located both between bones and away from the mineralized bone, in close association with blood vessels [132]. The presence of large amounts of mineral particles bound to membranes in the mitochondria of osteoclasts and osteoblasts was detected by the same group in the rapidly forming embryonic chicken bone, suggesting new pathways of bone formation [133].

In conclusion, the presence and the role of the amorphous mineral phase at the nanoscale in bone has garnered much attention in biomineralization research community. It appears that ACP acts as the precursor for the formation of bone mineral phase, and some evidences in animal experiments suggest that it may be found as a component of mature bone; nevertheless, in 2016 Addadi *et al.* reported that "there is no direct evidence that crystals form *de novo* inside the collagen fibril from a saturated solution or from an amorphous precursor phase" [134]. Therefore, as the topic is highly controversial and is currently the subject of active research from many different groups, we believe that in the future new findings on the biomineralization process will probably reshape these statements, further clarifying the role of ACP on bone formation.

1.3.3.2 Enamel

The features of the crystalline mineral composing tooth enamel have been outlined in section 1.2.2. Dental enamel formation (*i.e.* amelogenesis) is a complex process, which is the result of combined cellular and extracellular processes that control growth, shape, location and arrangement of the forming crystals [135, 136]. The presence of an amorphous transient mineral phases in developing enamel has been suggested in several studies starting from the eighties; in 2009, it was proved that the mineral nascent enamel consists of a transient ribbon-shaped ACP, which in time transforms into the final apatitic crystalline mineral [15]. The authors hypothesize that this transformation may be triggered by proteolytic degradation of the enamel matrix proteins (amelogenin and enamelin), which directly control the shape and organization of the mineral particles. The crucial role of these proteins in ACP stabilization was demonstrated in successive studies [137–139], as well as the importance of their self-assembly in the stabilization of pre-nucleation clusters [140].

In addition to its role as a transient precursor of crystalline apatite, it was recently reported that a Mg-substituted amorphous calcium phosphate (Mg-ACP) is present in mature enamel [141, 142]. It was first shown by atom probe tomography that in regular rodent enamel, the Mg^{2+} present (0.2-0.5 %wt) segregates at grain boundaries; the analyses by means of X-ray absorption techniques revealed that the environment of most Mg^{2+} in enamel exhibits short- to medium-range order, showing the same spectrum of Mg-ACP [141]. This enduring amorphous phase has a dramatic influence on the physico-chemical properties of enamel. In 2016, La Fontaine *et al.* reported a direct observation of an intergranular Mg-rich ACP phase between apatite nanowires in human mature enamel, by means of laser-assisted atom probe tomography [142]. This amorphous layer is ~2 nm wide, and it is homogeneously distributed along all sides of apatite nanowires. This Mg-ACP phase is more soluble than crystalline apatite, making thus enamel rod boundaries the most susceptible area to decay.

1.3.3.3 Calciprotein particles in blood

The concentration of calcium and phosphate ions in blood is supersaturated with respect to apatite: the ion activity product of [Ca^{2+}], [PO_4^{3-}] and [OH^-], together with the solubility product (K_{sp}) of HA, results in a degree of supersaturation ~ 12 for this mineral [143]. This would imply that any nucleation event (contusions, injections, fractures etc…) would result in a dramatic calcification of muscles, blood, skin and brain. This does not happen because serum contains many substances, such as proteins, that are able to bind the cited ions and modulate biomineralization processes. Among serum proteins, albumin and fetuin-A (Fet-A, in humans known as α_2-Heremans Schmidt glycoprotein) are particularly relevant. Albumin is the most abundant blood protein in mammals and acts by binding free Ca^{2+} to its acidic residues, thus reducing its supersaturation in serum [144]; nevertheless, in spite of its low concentration, the most efficient protein in inhibiting serum calcifications is Fet-A, which binds to nascent clusters of calcium and phosphate ions, forming the so-called calciproteins particles (CPPs) [145]. CPPs can be regarded as a defense mechanism against the precipitation of CaP in the blood, urine and soft tissues, as mice lacking Fet-A suffer from severe ectopic calcifications [146]. CPPs have diameters of the order of 25–150 nm and are initially constituted of ACP [145]. In time, the initial CPPs (denoted as CPP1) transform into mature secondary CPPs (CPP2), consisting of a needle-shaped core of OCP covered by a shell of Fet-A [147, 148]. All the factors that enhance ACP lifetime (alkaline pH, concentration of Fet-A, albumin, Mg^{2+}, pyrophosphate…) cause a delay in the conversion of CPP1 to CPP2 [149]. A high concentration of CPPs [148] or the presence of CPP2 over CPP1 [150] have been connected to pathological situations [52].

1.3.3.4 Casein micelles in breast milk

Another location in which ACP can be found in human body is within casein micelles in breast milk. The term "casein" refers to a family of phosphoproteins, *i.e.* proteins which are modified by the attachment of a phosphate group after their biosynthesis. According to the amino-acidic sequence and to the characteristics, they can be divided into 4 categories

(α_{s1}-, α_{s2}-, β- and κ-casein) which differ in the amount of phosphate groups and in the ability to interact with Ca^{2+}[151]. Casein is able to form micelles that embed ACP clusters: a typical micelle of 100 nm radius contains about 10^4 casein molecules and 800 nanoclusters of amorphous calcium phosphate [152]. The ability of casein to interact with CaP relies on its phosphorylation, which allows the interaction with Ca^{2+} and the subsequent binding of phosphate to generate ACP. Cryo-TEM investigation on casein micelles revealed that ACP nanoclusters are ~2.5 nm-sized and uniformly distributed in a homogeneous protein network [153]. Small angle scattering investigations reveal a similar cluster size (2 nm) and a correlation length of 0.35 nm^{-1}, which indicates that each ACP nanocluster is, on average, 18.6 nm apart from the other [154]. The binding action of casein slows down the rate of maturation of the amorphous state, preventing its crystallization and thus facilitating the infant assimilation of calcium and phosphorous, which are essential elements for the formation and growth of its bone tissue [155].

1.3.3.5 Small intestine

A peculiar location in which Mg-substituted ACP (AMCP) was recently detected is the small intestine. It is known since a long time that Ca^{2+} and phosphate ions are actively secreted from the intestinal mucosa into the lumen (in particular, the former ion in the jejunum and the ileum, while the latter in the ileum) [156]. These secretions, known as "endogenous losses", are maintained even under calcium and phosphorous-poor dietary regimes, suggesting that their biological function is of uppermost importance [156, 157]. In 1967 Schedl *et al.*, while studying calcium and phosphate concentrations in dogs' intestine, first suggested that a portion of these ions could form a precipitate [158], which comprises about one-third of the secreted Ca^{2+} [159]. The group by Powell, which pioneers the study of these endogenous particles, showed in 1999 that, in rats, this precipitate consists of particles of 2 μm, with a Ca:P ratio of ~5:3 [160]. The same group then hypothesized that these particles could bind lumen biomolecules (toxins and antigens) and then be scavenged by the M-cells-rich mucosa overlying intestinal lymphoid aggregates, thus promoting immune tolerance [156, 161]. Without entering in biological details, it is important to mention that M-cells

are able to capture and transport microparticles and nanoparticles from one side of the cell and release them to the opposite site (transcytosis) [162]. Tolerance can be defined as the prevention of an immune response against a specific antigen; for instance, the immune system is tolerant of self-antigens, thus avoiding the attack of the body's own cells, tissues, and organs. However, when tolerance is lost, disorders like autoimmune diseases or food allergies may occur. The conclusive evidence of the existence and the role of these endogenous particles was given in 2015, when Powell *et al.* isolated and characterized them, showing their precise function in our body [157]. By collecting the particles from the distal small bowel contents of both humans and mice, the authors found out that the endogenous particles are: *i.* constituted by calcium, magnesium and phosphate; *ii.* porous; *iii.* amorphous; *iv.* able to incorporate molecules present in the gut lumen. The amorphous nature of AMCP particles in the intestinal juice is certainly favored by the presence of Mg^{2+} and by the relatively high pH of the ileum [163]. AMCPs are abundant in the gut (Powell and co-workers estimate the presence of ~2×10^{14} luminal particles/day) and they chaperone antigens and peptidoglycans from the lumen to the immune cells of the intestinal tissue (*i.e.* antigens presenting cells, APCs, located in the Peyer's patches) via M-cells. This process induces the expression of programmed death-ligand 1 (PD-L1) on the surface of APCs, promoting immune tolerance. This mechanism (see Figure 1.6), hypothesized by the same group, was demonstrated by means of specific investigations. First, mice fed with a diet low in Ca and P showed, in Peyer's patches, phosphorous-deficient AMCPs (if compared to the ones found in mice fed with diets replete in Ca and P); this evidence supports a lumen-to-Peyer's patch route for the particles. Then, the nanomineral was almost absent from the Peyer's patches of mice lacking M-cells, proving their essential role for the transit of AMCPs from the lumen to the intestinal tissue. AMCPs were successively shown to have implications in pathological conditions, such as Crohn's disease [164], and biological pathways, as the reduction of T-Helper cell responses to recall antigens [165]. The group of Powell also prepared synthetic analogs of AMCPs and reported that, *in vitro*, the particles have a marked capacity to trap macromolecules during formation and deliver them to APCs, without regulating any gene or modifying any gene regulation [166].

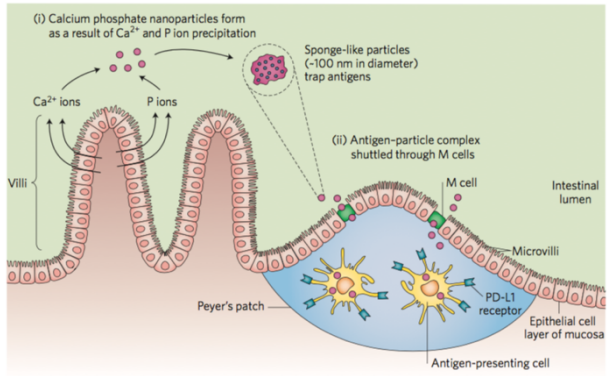

Figure 1.6: Action mechanism of AMCPs: *(i)* formation of the nanoparticles, which trap antigens; *(ii)* AMCP-antigen complex is transported to APCs through M-cells (reproduced with permission from [167]).

1.4 Calcium and magnesium phosphates for biomedical applications

Given the significance of CaPs, CaMgPs and MgPs as natural components of human body, their application as biomaterials is widespread, particularly in the field of bone substitute materials.

Bone is one of the few tissues which can self-heal and remodel, being able to recover its initial shape and its mechanical and biological functions; nevertheless, there is a limit to the size of fractures that it can heal by itself. For larger defects (also known as "critical-sized defects" [168], such as bone tumor resections and severe nonunion fractures [169]) bone grafting solutions are required to ensure bone growth and repair [30]. Bone grafting is defined as the procedure of replacing missing or damaged bone with natural or synthetic materials [170]; of the 5 million grafting procedures conducted yearly worldwide, 91 % is taken up by osteoinductive materials, such as autograft (*i.e.* bone from the patient), allografts (*i.e.* bone from a human cadaver) and xenografts (*i.e.* bone from an animal source) [30, 169]. The best outcomes are obtained from the transplanting of autologous bone, which nonetheless suffers of several drawbacks, namely the short supply and the considerable donor site morbidity associated with the harvest. The quest for new bone regeneration strategies is therefore a major challenge for our society.

In general, the ideal bone graft should satisfy a series of requirements [171]: *i.* biocompatibility, to avoid rejection or undesirable effects; *ii.* bioactivity, to ensure bonding to the surrounding bone tissue; *iii.* osteoinductivity, to promote bone cell recruitment and differentiation; *iv.* biodegradability or bioresorbability, being mandatory that degradation products are non-cytotoxic; *v.* presence of a highly interconnected porous network, formed by a combination of macro- and micropores (necessary to cellular colonization and vascularization, as well as to the diffusion of nutrients); *vi.* suitable mechanical strength and stiffness, which are typically detrimental to porosity.

Among the synthetic materials which have been exploited for orthopedic applications (metals, ceramics, polymers and composites) CaP holds an important position [172]. The main driving force behind its use as bone substitute is the chemical similarity to the mineral component of mammalian bones and teeth, namely poorly crystalline calcium-deficient HA (see section 1.2). CaPs were first proposed as bone graft substitutes in the 1970s [173] and, since then, they have been used for the healing of bone defects, fracture treatment, total joint replacement, bone augmentation, orthopedics, cranio-maxillofacial reconstruction, spinal surgery, otolaryngology, ophthalmology and percutaneous devices, dental fillings and periodontal treatments [172]. This variety of applications relies on the versatility of this material, which allows to prepare nanoparticles (used for gene delivery [174, 175]), coatings [176], scaffolds for tissue engineering [177] and self-setting cements [178]. Before focusing our attention on this latter category, which has been investigated in this work of thesis, it is important to point out that despite the chemical similarity with natural bone, CaP displays several limitations as a biomaterial. For instance, sintered CaPs commonly result in a low resorption kinetics and they often remain over years at the implantation site [168]. An attempt to overcome this issue is the use of protonated calcium phosphates (brushite or monetite), which should degrade faster because of their higher solubility. However, phase changes can occur *in vivo* because of dissolution/reprecipitation reactions, which result in CaPs with lower solubility. Magnesium phosphate materials are being currently investigated as alternatives to the above described CaPs. The rationale behind this idea is the higher solubility of MgP phases under *in vivo* conditions, which should

enhance resorbability, and the fact that Mg^{2+} is a potent inhibitor of HA crystal growth, thereby suppressing unwanted crystallization *in vivo*. In contrast to the in vivo dissolution of Mg-alloys, which produces large amounts of hydrogen gas and an alkaline environment, the dissolution of magnesium phosphates only results in the release of biocompatible Mg^{2+} and phosphate ions [168].

1.4.1 Bone cements

According to IUPAC, a bone cement is defined as a "synthetic, self-curing organic or inorganic material used to fill up a cavity or to create a mechanical fixation" [179]. While the "organic" term is related to poly(methyl methacrylate) (PMMA)-type cements, commonly used in dentistry, the "inorganic" materials commonly comprise calcium phosphate cements (CPCs) and calcium sulfate cements (CSCs) [180]. These systems are used as bone defect fillers in maxillofacial surgeries and in orthopedic fracture treatments, in order to augment weakened bone due to osteoporosis. They consist of a powder and a liquid component which when reacting form a paste that in time sets and forms a hardened material. In the case of CPCs, the reaction is a chemical dissolution/precipitation in which the entanglement of the newly-formed crystals generates the solid mass. Despite the numerous formulations investigated over the years, the final setting product of CPCs consists either of brushite or apatite. The advantage of having a moldable and sometimes even injectable material that sets at body temperature provides a unique advantage over bioceramics, as it allows to perform minimally invasive surgeries (with benefits for the patient itself and for the hospitalization costs) and to have an intimate adaption to the surrounding bone, even for irregularly-shaped cavities [170]. There are many important properties that one should consider in the design of a bone cements for orthopedic applications, and the most meaningful ones are listed below [170].

Setting time: according to the ASTM C266-13 definition [181], the first (or initial) and second (or final) setting times are the times at which the cement can withstand 113 g and 454 g of weight without observing an appreciable indentation. This parameter is measured by means of the

Gillmore method, using an apparatus endowed with two needles (light and thick - heavy and thin). Ideally, a paste should set slowly enough to provide sufficient time to the surgeon to mix, handle and adjust the material in the site of interest, but fast enough to ensure fast completion of the surgery and to provide initial support and rigidity. This concept is schematized in Figure 1.7a, where I and F are the initial and final setting time, and CT the cohesion time [178], defined as the time from which a cement no longer disintegrates when immersed in Ringer's solution [182]. The clinical meaning is that the cement paste should be implanted before time *I* and that the wound could be closed after time *F*. The handling requirements are 3′ ≤ I ≤ 8′ (3′ for dental, 8′ for orthopaedic applications), F ≤ 15′ and I-CT ≥ 1 [178].

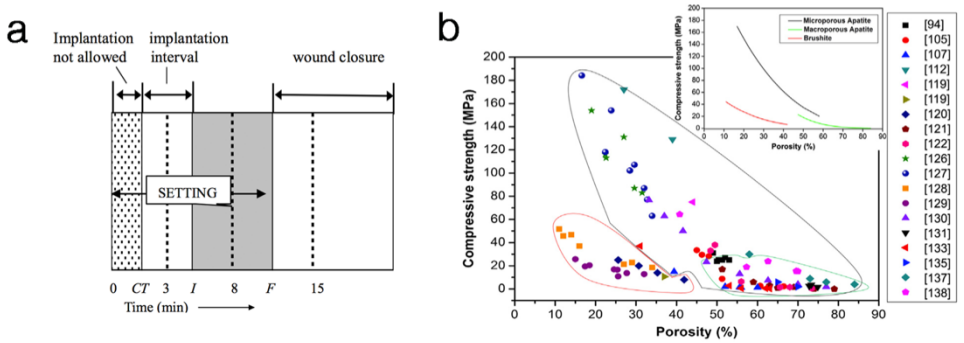

Figure 1.7: (a) Diagram of the setting parameters relevant for self-setting cements: *CT* – cohesion time; *I* – initial setting time; *F* – final setting time; reproduced from [178]; (b) Compressive strength of CPCs compiled from different studies (see the references in the original paper) as a function of total porosity. The circles refer to brushite CPCs (red), apatite CPCs (black) and macroporous apatite CPCs (green). The inset shows the power law fittings of all the data points of compressive strength of brushite (red), microporous apatite (black) and macroporous apatite (green); reproduced with permission from [170].

Cohesion and anti-washout ability: cohesion is defined as the ability of the paste to harden in a static aqueous environment without disintegrating, whereas the anti-washout ability is evaluated in a dynamic aqueous environment [170]. As the cement is designed to be applied *in vivo*, it is important that upon contact with biological fluids the paste does not disintegrate into small particles. As the cohesion is the result of the competition between forces acting on the cement's particles and forces acting between the paste and the surrounding fluid, factors enhancing van der

Waals forces (attractive) and decreasing electrostatic forces (repulsive) can be used to improve the cohesion of the paste [178].

Injectability: one of the main advantages of bone cements is the possibility to inject them directly in the site of interest. This property depends on the time between mixing and testing, the force and the speed applied to the syringe and the size of the needle. A major issue is the occurrence of phase separation (also known as "filter pressing") during injection, which leads to an extrudate with a liquid content higher than desired; this may cause extravasation from the surgical site and be detrimental to the final properties of the cement [183]. Phase-separation is so crucial that injectability was re-defined as the ability of the paste to stay homogeneous during injection [170]. Strategies to improve injectability include: *i.* increasing the viscosity of the liquid phase by adding rheology-modifying additives such as chitosan, gelatin, hyaluronic acid, methylcellulose, and others; *ii.* optimizing the powder in terms of the particle size, distribution, shape and particle-particle interactions; *iii.* regulating the setting reaction; *iv.* modifying the extrusion parameters such as mixing and sizes of the syringes and/or needles [184].

Mechanical properties and porosity: as the mechanical properties of a material are determined by its microstructure (porosity and amount, size, morphology and distribution of the crystals formed during setting), the two features are presented together. Natural bone displays impressive compressive strengths ranging from 130-190 MPa for cortical bone and 3.6-9.3 MPa for cancellous bone, due to the hierarchical structure of HA and collagen [5]. The mechanical properties of a material for bone substitution/integration must therefore be taken into account, as the required compressive strength varies according to the site of application [183]. At present, bone cements are mainly used in low-semiload or non-load bearing applications [5], due to their considerable porosity which weakens the mechanical properties of the material (see the relationship between compressive strength and porosity in Figure 1.7b). Despite being detrimental to the strength of the cement, porosity is important to ensure cells' permeation, nutrient transport and ossointegration [180]. CPCs are intrinsically endowed with porosities in the nano-sub micro range, while the macroporosities necessary for cells' ingrowth (> 100 μm) are obtained with the addition of porogenic or foaming agents [183]. As the increase in porosity

results in a weakening of the mechanical properties, the design of a bone cement is always a delicate and challenging balance of the two parameters.

Biocompatibility and bioresorbability: biocompatibility is an obvious requirement for every biomaterial and bioresorbability, defined as the removal of material by cellular activity and/or dissolution in a biological environment [185], also plays a crucial role in the efficacy of a bone cement. Cements should be resorbed and replaced over time by new bone; the resorption process relies on passive (driven by solubility) and active (driven by cells) dissolution [168]. The limited resorbability is one of the aspects that hinders the use of CPCs, especially of the apatite-based ones. Brushite is, in principle, two orders of magnitude more soluble than apatite, and this is beneficial in terms of resorbability; nevertheless, the setting of brushite occurs in acidic conditions and, given its metastability at physiological pH, *in vivo* transformations to apatite may occur.

Among the properties listed above, CPCs meet many of the requirements for clinical applications: they are biocompatible, able to set in physiological conditions and microporous. Despite several commercial products based on CPCs are available on the market [178], some crucial issues still hamper their use, in particular the phase-separation upon injection, the poor mechanical properties and the limited resorbability and cohesion [170]. Recently, Magnesium Phosphate Cements (MPCs) have been proposed as alternative materials to overcome some of the CPCs' limitations.

1.4.1.1 Magnesium phosphate-based bone cements

The field of MPCs for orthopedic applications is relatively unexplored with respect to CPCs. Figure 1.8 shows the results obtained from a query of the terms "calcium phosphate cements" and "magnesium phosphate cements" on Web of Science, which clearly shows that the interest in the latter category is growing exponentially. MPCs were used in the past for structural engineering and waste remediation, and in the last decade their application in the biomedical field gained significant attention.

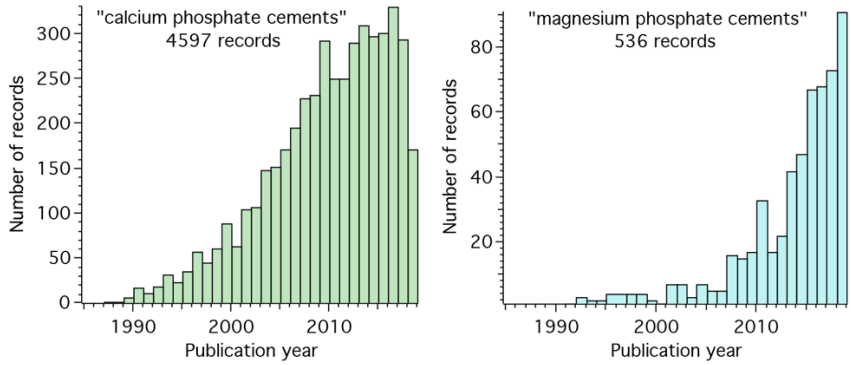

Figure 1.8: Histograms showing the number of papers as a function of publication year obtained with the query "calcium phosphate cements" (left) and "magnesium phosphate cements" (right) on Web of Science (updated in September 2019).

MPCs are typically obtained from the reaction of MgO or, less frequently [5], $Mg_3(PO_4)_2$ (Tri-Magnesium Phosphate, TMP) with an aqueous solution of a phosphate salt, such as $NH_4H_2PO_4$, $(NH_4)_2HPO_4$, Na_2HPO_4 or K_2HPO_4 (for a complete overview, the reader is referred to [5]). The reaction mechanism for MgO according to Wagh [186] is depicted in Figure 1.9: the dissolved oxide combines with water, forming an aquosol, which further reacts with the dissolved phosphate salts generating an amorphous gel.

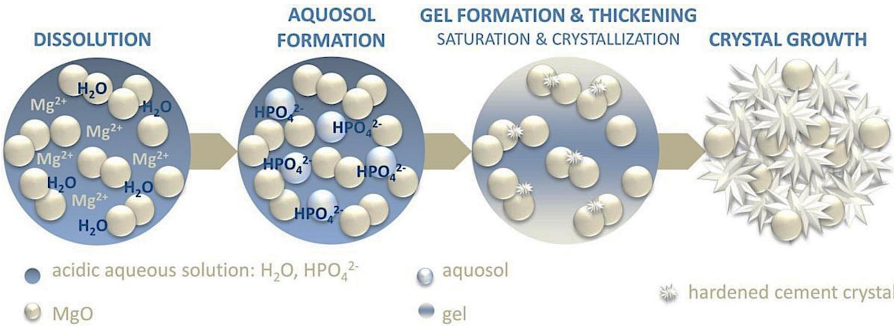

Figure 1.9: Scheme of the acid-base reaction which underlies the setting mechanism of MPC systems on the basis of MgO and contains intermediate aquosol and gel formation, reproduced with permission from [168].

In time, the cement reaction causes a thickening of the mixture, which leads to a crystallization process around undissolved MgO grains. The type of phases obtained upon crystallization depends on the used phosphate salt, and includes struvite, dittmarite, schertelite or hannayite (see Table 1.1 for their formula) [168].

As we mentioned in the previous paragraph, the interest in MPCs as bone cements is due to their attractive characteristics, which allow to overcome some of the limitations of CPCs [5, 168]. In addition to the increased mechanical strength [187], which is still not sufficient for load-bearing applications [5], MPCs have shown a more rapid dissolution rate in aqueous media, which results in an enhanced *in vivo* resorbability and favors bone growth [188]; moreover, MPCs have shown intrinsic adhesive capabilities, which are not reported for CPCs [5, 189, 190]. Another advantage of using MPCs over CPCs is that, *in vivo,* the release of Mg^{2+} was shown to stimulate osteoblast differentiation and to inhibit osteoclast formation, therefore favoring bone regeneration [191, 192]. Some MPCs were even reported to be naturally antibiotic [187, 193], while retaining good biocompatibility both *in vitro* and *in vivo* [168]. All these properties reveal the great potentialities of MPCs, which are still underexplored in comparison to the well-established CPCs.

1.5 Aim of this work

The research described in this thesis aims at the preparation and physico-chemical characterization of biologically relevant calcium and magnesium-phosphate-based nanostructures. In this framework, the definition "biologically relevant" includes both the structures naturally-present in the organism as well as those prepared for biomedical applications. Among the different endogenous forms of ACP described in paragraph 1.3, during my PhD I focused my attention on the investigation of synthetic analogs of the immunologically-relevant AMCP nanoparticles present in the small intestine (see section 1.3.3.5). The results concerning this topic are described in Chapter 2, and are divided in sub-sections corresponding to the different aspects investigated. The choice of this type of nanostructures over the other endogenous forms of ACP is motivated by the fact that, given the relatively recent discovery, their features and physiological role are currently not fully understood [166], and several interesting aspects about their physico-chemical characteristics emerge. Given the instability of amorphous calcium phosphates, it is indeed relevant to understand which are the factors that

affect the stability and the lifetime of the amorphous phase and that, at the same time, are relevant at the gut level. To this purpose, we investigated the effect of pH, Mg^{2+} and dilution factor on the stability and the crystallization pathway of AMCPs (section 2.1). As a next step, the formation of AMCPs in the presence of biologically relevant additives (section 2.2), in simulated intestinal fluids (section 2.3) and in the presence of the protein mucin (section 2.4) was explored, aiming at mimicking with different degrees of complexity the *in vivo* environment in which AMCPs form. A significant part of the experimental work was devoted to the characterization of the different features of the particles by means of a multi-technique approach, so to unravel the crystallinity, the morphology, and structural features of the amorphous particles and their crystallization products. The performed characterization allowed us to clarify the features of the endogenous-like particles formed in bio-relevant scenarios, and to speculate on their biological role. Besides the physico-chemical investigation of these particles, a potential application of AMCPs could be in the field of nutraceutics and delivery, given the potential biocompatibility and the amorphous nature which favors the loading with molecules. As a case study, the loading of AMCP with proteins extracted from *Moringa Oleifera* is described in section 2.5. Section 2.6 is devoted to preliminary biological experiments, directed to future investigations of AMCPs' interplay with cells and bacteria.

As far as calcium-magnesium phosphates to be used for orthopedic applications are concerned, we focused our attention on magnesium phosphate-based bone cements, and the pertaining results are reported in Chapter 3. Among the diverse formulations which have been described in the literature, we decided to use as starting component $Mg_3(PO_4)_2$ over MgO, given the limited reports present in the literature [5]. The liquid component used throughout this study is an aqueous solution of $(NH_4)_2HPO_4$. After a brief characterization of the powder component used to prepare the cements (section 3.1), the effect of simple formulation parameters, namely the powder to liquid ratio and the concentration of phosphate salt used, is addressed in section 3.2. Several properties relevant to the applications of these materials were addressed, such as cohesion, handling, microstructure, porosity and crystallinity. A relevant portion of this work of thesis deals with citrate-containing MPCs, which are detailed in section 3.3. The rationale behind the

inclusion of citrate in the formulation is that this ion, in addition to being a natural component of bone, was recently found to have beneficial effect when included in biomaterials for bone regeneration [194]. This investigation is the result of an on-going collaboration with the group of Professor Baldini from the Istituto Ortopedico Rizzoli, where cytotoxicity experiments on our materials were conducted. The properties relevant to the application of the cements were investigated, as well as citrate release profiles. Finally, section 3.4 deals with the inclusion of cellulose ethers as additives to improve the rheological properties of MPCs.

All the papers (published and in preparation) related to the presented work, as well as the experimental details about the characterization of the materials described in this thesis, are finally given in the Appendices. Two papers not specifically pertaining to this PhD project, but published within the same period, are also attached.

2 Amorphous Magnesium-Calcium Phosphate particles

A significant part of this work of thesis is devoted to the study of endogenous-like Amorphous Magnesium-Calcium Phosphate particles, whose role and features have been outlined in section 1.3.3.5. The formation of AMCPs in the small intestine is a very interesting phenomenon from a physico-chemical perspective, as the components and the conditions of such a complex milieu can affect the features and the stability of these amorphous phases. As the presence of AMCP in the gut only recently emerged, literature reports on the effect of complex media representative of the intestine on phosphate-based amorphous phases are lacking. During my PhD, several aspects concerning the formation and the stability of endogenous-like particles in biologically-relevant conditions have been addressed, and are described in this Chapter. In all the presented scenarios, AMCPs were synthesized using an aqueous-based process, and characterized in terms of crystallinity, morphology, chemical nature and thermal behavior, to attain a complete physico-chemical overview of the system. As a first step, we investigated the effect of pH and magnesium concentration on the stability and crystallization pathway of AMCP, which is described in section 2.1 and lead to the publication of paper I (attached in Appendix II). This investigation allowed us to understand how slight variations in these two bio-relevant parameters affect the lifetime and the features of the amorphous phase. Following this investigation, we shifted our attention towards the characterization of the effect of biologically-relevant molecules which can be naturally-present in the intestinal lumen and which AMCP can encounter during its endogenous formation. The synthesis of AMCP in the presence of

butyric acid, lactose, gluten and peptidoglycan is described in section 2.2, and can be found in paper II in the Appendix. After the analysis of the effect of single molecules/macromolecules, we kept on increasing the complexity of our synthetic medium, preparing AMCPs in a commercial simulated intestinal fluid, which contains bile salts and phospholipids. Results concerning this study are detailed in section 2.3 and in paper III (see Appendix II), and show that the presence of these components in the synthetic medium deeply affect AMCP's stability and morphology. Still focusing on the *in vivo* environment in which AMCPs form, we attempted to conduct the synthesis of the particles in mucin-based media. Mucin is a large glycoprotein constituting the mucus, a hydrogel-like layer which covers the intestinal epithelium and which AMCPs encounter during their formation process. The effect of this protein, both in dispersion and in form of hydrogel, are outlined in section 2.4.

Given that the conducted experiments highlighted the ability of AMCP to form in the presence of organic molecules while partially incorporating them, we decided to investigate the formation and the features of these particles in the presence of proteins extracted from *Moringa Oleifera*, a plant endowed with many beneficial effects from a nutritional and medical viewpoint. The protein was shown to influence the crystallization pathway of AMCP while being incorporated in it, therefore paving the way towards a potential application of the system in nutraceutics and as food supplement.

As a last aspect, section 2.6 briefly describes some preliminary experiments dealing with AMCP stability in culture medium, that we conducted in preparation of a study on interaction of AMCP with cells and microbioma.

2.1 Effect of pH, Mg^{2+} concentration and particles' dilution on the amorphous phase stability

The intestinal lumen is a complex and variable environment, and a multitude of factors can affect the formation and stability of AMCP which spontaneously self-assemble in such a mutable milieu. For this reason, in order to get familiar with the features and the stability of synthetic analogs of endogenous AMCPs, we began by investigating the effect of simple

physico-chemical parameters, namely pH, Mg^{2+} concentration and dilution factor. The reason behind the choice of these parameters relies on the fact that these factors can, in principle, affect the lifetime of the amorphous phase and undergo variations in the gastrointestinal tract, due to physiological or pathological situations. pH is particularly relevant, as it experiences great variations in the gastrointestinal (GI) tract: the pH of the stomach is 1–2, but as the acidic gastric content enters the proximal small bowel, the pH rises of several units, up to 5.7–6.4 (duodenum, jejunum) [195, 196]. Mucosal bicarbonate secretions result in a further rise of luminal pH, which goes up to 7.3–7.7 in the ileum. Finally, in the large intestine, colonic bacteria produce short chain fatty acids, which cause a decrease in luminal pH (5.7). These molecules are then absorbed by the colonic epithelium, and a slight rise in the pH along the distal colon occurs (6.8). A variation in the pH of a specific region of the GI tract may also be the consequence of a pathological condition, as it is reported that alterations in the gut pH are associated to illnesses such as ulcerative colitis, Crohn's disease and irritable bowel syndrome [196]. It is important to remark that endogenous AMCPs have been detected in the distal small intestine [157], which interestingly is the region of the GI tract that displays the highest pH value. This correlation becomes significantly relevant if we consider that ACP spontaneous crystallization is much slower at high pH values [70]. In addition to pH variations, modifications in the concentration of ions and molecules are obviously possible. The effect of Mg^{2+} is potentially relevant, as its absorption takes place in the distal small intestine [197], which is the site where AMCPs have been detected. Magnesium concentration in the organism is critical for humans' health [13]: its role in the gut is highly relevant, as some studies indicate that an increase in magnesium intake may help against irritable bowel syndrome and constipation [198], and its presence in the intestinal lumen may explain why the endogenous nanoparticles are Mg-rich. In fact, Mg^{2+} can co-precipitate with calcium and phosphate ions (secreted because of ''endogenous losses'') to form stable AMCP phases [73]. As outlined in section 1.3.2 in the Introduction, Mg^{2+} likely contributes to enhance the lifetime of the amorphous phase. We may reasonably infer that alterations in the luminal pH and Mg^{2+} concentration in the ileum region could alter the stability of the particles, perhaps compromising their biological function in the organism.

The aim of this study is thus to unravel the effect of pH and Mg^{2+} concentration on the stability of synthetic analogs of endogenous AMCPs.

2.1.1 Experimental protocols

2.1.1.1 Synthesis of AMCPs at different pHs

The synthesis of AMCPs was conducted using a protocol readapted from the literature [199], which involves the mixing at 37 °C of equal volumes of two aqueous solutions, namely solution A (containing NaCl, $MgCl_2$ and $CaCl_2$) and solution B (NaH_2PO_4 and Na_2HPO_4); the amounts and concentrations are reported in Table 2.1. NaCl (purity ≥ 99 %), $MgCl_2 \cdot 6H_2O$ (purity ≥ 99 %), $CaCl_2$ (purity ≥ 93 %) and NaOH pellets were purchased form Sigma-Aldrich, while $NaH_2PO_4 \cdot H_2O$ and $Na_2HPO_4 \cdot 12H_2O$ (purity ≥ 99 %) were obtained from Carlo Erba Reagents. The reaction temperature was monitored throughout the entire reaction and it was stable within 0.5 °C. The synthesis was conducted at four different pH values, attained by mixing different amounts of the monobasic and the dibasic sodium phosphate salts (solutions B_0, B_1, B_2, B_3, total concentration of the two phosphates 200 mM, see Table 2.1). This strategy was pursued to keep the amount of total phosphates constant in the four experiments.

Table 2.1: Amounts of reactants and concentrations used for AMCP synthesis at different pHs.

Solution	Salt	Amount [g]	NaH_2PO_4: Na_2HPO_4	Concentration [mM]	Reaction pH
A	NaCl	0.79	-	135	-
	$CaCl_2$	0.04		4	
	$MgCl_2 \cdot 6H_2O$	0.20		10	
B_0	$NaH_2PO_4 \cdot H_2O$	1.38	1:1	100	7.06 ± 0.03
	$Na_2HPO_4 \cdot 12H_2O$	3.58		100	
B_1	$NaH_2PO_4 \cdot H_2O$	0.69	1:3	50	7.23 ± 0.05
	$Na_2HPO_4 \cdot 12H_2O$	5.37		150	
B_2	$NaH_2PO_4 \cdot H_2O$	0.55	1:4	40	7.30 ± 0.04
	$Na_2HPO_4 \cdot 12H_2O$	5.73		160	
B_3	$NaH_2PO_4 \cdot H_2O$	0.45	1:5	33	7.40 ± 0.02
	$Na_2HPO_4 \cdot 12H_2O$	5.97		167	

100 mL of solution A and 100 mL of solution B (heated at 37 °C) were mixed in an Erlenmeyer flask using magnetic stirring, in a water bath at 37 °C. Immediately after the addition of A to B, the reacting solution became turbid. The pH was monitored throughout the reaction; only in the case of solution B_0, it was necessary to adjust the initial pH to 7.00 by adding few drops of NaOH 2 M solution. The average measured pH values are reported in the last column of Table 2.1, while Figure 2.1 shows the pH profile vs time.

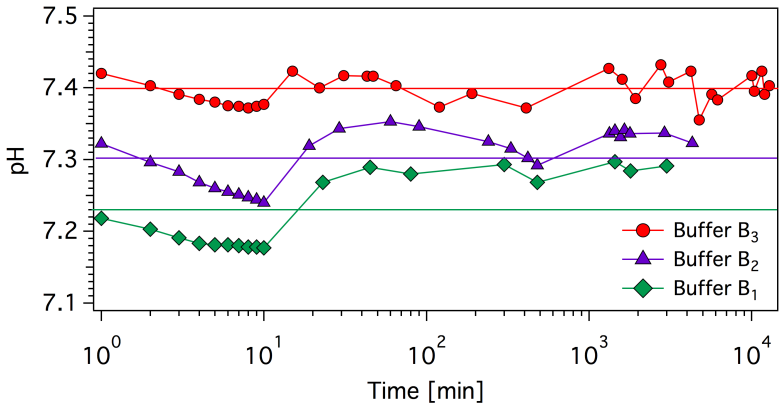

Figure 2.1: Trend of measured pH vs reaction time.

Aliquots (~ 20 mL) of the solution were withdrawn at different reaction times and filtered using a Millipore vacuum filtration system equipped with mixed cellulose esters filters (Millipore, pore size 0.22 μm). Immediately after filtration, the filters were placed in plastic test tubes and frozen in liquid nitrogen. The powders were then freeze-dried for 24 h, at -55 °C and ~ 30 mTorr (VirTis BenchTop freeze-dryer, NY, USA) and stored in the freezer (-18 °C), tightly closed to prevent any influence from environmental humidity [44]. The described procedure of filtration, freeze-drying and storage of AMCPs was applied to all the syntheses, unless differently specified.

2.1.1.2 Dispersion of AMCPs - effect of Mg^{2+} concentration

In order to evaluate how the presence of Mg^{2+} in the solution in which AMCP particles are dispersed affects their transformation to crystalline calcium phosphates, we performed experiments by dispersing dried AMCPs in solutions containing different concentrations of Mg^{2+} (0, 1, 3 and 5 mM), at pH 7.40, T=37 °C and particles' concentration 0.36 g/L. 140 mL of buffer B_1 (see Table 2.1 for the composition) were heated at 37 °C. The pH was adjusted to 7.40 by dropwise addition of NaOH 2 M, and $MgCl_2 \cdot 6H_2O$ was added to the solution under magnetic stirring (28.5 mg for $[Mg^{2+}]$=1 mM, 85.4 mg for $[Mg^{2+}]$=3 mM and 142.3 mg for $[Mg^{2+}]$=5 mM). When the salt was completely dissolved (*i.e.* after about 2 min), 50 mg of dried AMCPs (previously prepared at pH 7.40 and collected after 15 reaction minutes) were added to the buffer under magnetic stirring. Aliquots of the solution were withdrawn at different reaction times, filtered and freeze-dried (same procedure as in paragraph 2.1.1.1).

2.1.1.3 Dispersion of AMCPs - effect of solution pH (6.90- 7.40)

The effect of the solution pH on the stability of dispersed AMCP particles was investigated by re-dispersing freeze-dried AMCPs (using the same batch employed for the experiments with Mg^{2+}) in phosphate buffers at different pHs. The experiments were performed by equilibrating the solution at 37 °C, at pH 6.90 and 7.40, using buffer B_0 and B_1, respectively (see the composition in Table 1). In both cases, the pH was adjusted to the exact value by means of dropwise additions of NaOH 2 M. The amount of dried AMCPs necessary to reach the concentration of 0.36 g/L was then added to the buffer under magnetic stirring, and the solid material was filtered after 15 min of reaction (same procedure as in paragraph 2.1.1.1).

2.1.1.4 Effect of concentration

The aim of this experiment was to investigate how the concentration of particles dispersed in buffer solution affects the stability of the amorphous phase and the type of crystalline phase to which it converts. Two different concentrations were studied, at two different pHs. All the experiments were conducted using the following protocol: the phosphate buffer (B_0 for pH 6.90, B_1 for 7.40, composition reported in Table 1) was equilibrated at 37 °C and the pH was adjusted to the desired value by dropwise addition of NaOH 2 M. Then, the amount of AMCPs necessary to reach the desired concentration was added to the buffer under magnetic stirring. Aliquots of the solution were withdrawn at different reaction times and filtered (same procedure as in paragraph 2.1.1.1).

2.1.2 Results

2.1.2.1 Stability as a function of synthesis pH

We conducted the synthesis of AMCPs at four different pH values, to investigate its effect on the stability of the amorphous phase (synthetic protocol described in section 2.1.1.1). The transition from amorphous to crystalline CaP was monitored by means of FT-IR spectroscopy, which is a well-suited technique to investigate the transition from amorphous to crystalline CaP: in fact, ACP displays broad bands in its spectrum due to P-O stretching vibration, while sharp and distinctive signals appear when it converts into crystalline phases, such as HA, DCPD or OCP [200]. The spectra relevant to the detection of amorphous to crystalline transition at different synthesis pH are shown in Figure 2.2.

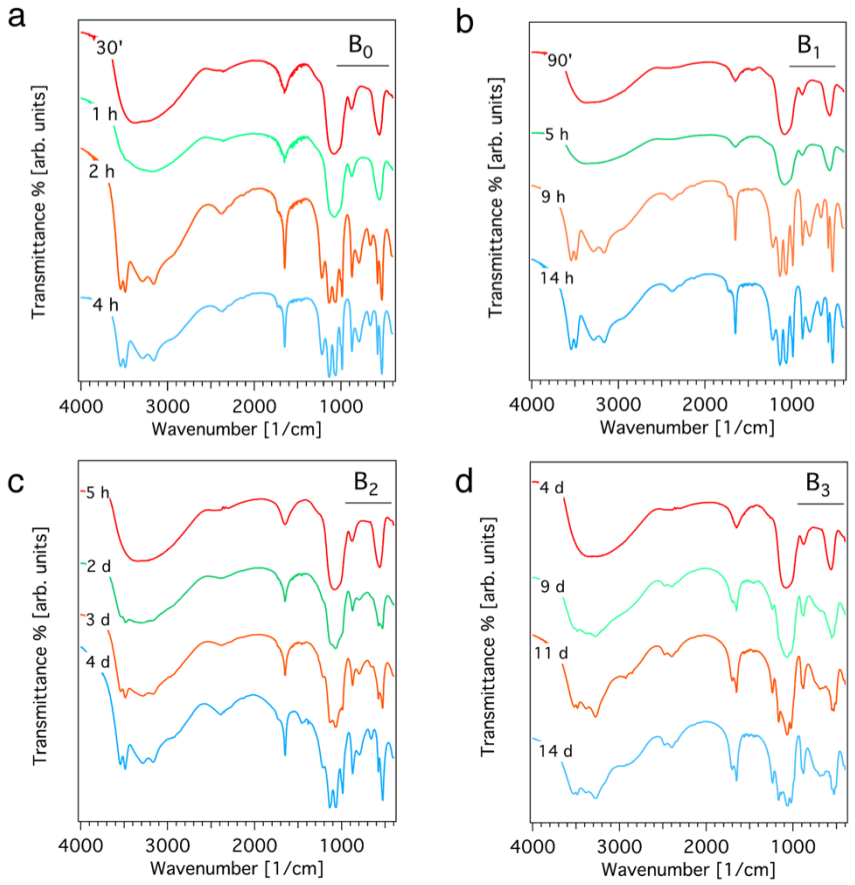

Figure 2.2: FT-IR spectra of AMCPs synthesized at (a) pH 7.06 ± 0.03 (buffer B_0); (b) pH 7.23 ± 0.05 (buffer B_1); (c) pH 7.30 ± 0.04 (buffer B_2); (d) pH 7.40 ± 0.02 (buffer B_3). The time after which each aliquot was withdrawn from the solution is reported on the left of each curve. The spectra are offset for display purpose.

The spectra detected in the early stages of the reaction (red curves in Figure 2.2) are compatible with amorphous calcium phosphate, as they show broad and featureless bands associated with phosphate stretching and bending vibrations (for peaks' assignment, see Table 2.2) [44, 199, 201, 202]. When the synthesis is conducted at pH 7.06 (Figure 2.2a), 7.23 (Figure 2.2b) and 7.30 (Figure 2.2c), AMCP converts in time to brushite ($CaHPO_4{\cdot}2H_2O$, detailed peaks' assignment in Table 2.3) [203, 204], while at pH 7.40 (Figure 2.2d) the crystalline phase first formed is newberyite ($MgHPO_4{\cdot}3H_2O$, see Table 2.4) [205–208]. As both brushite and newberyite contain crystallographically non-equivalent water molecules, several peaks arising from water stretching, bending and librational modes appear in the FT-IR spectrum, making it significantly different from that of AMCP.

Table 2.2: FT-IR peaks' assignment of AMCP.

AMCP		
Peak [cm^{-1}]	Assignment	Reference
561	ν_4 bending phosphate*	[44]
881	P-O(H) stretching mode of protonated phosphate species	[201]
1084	ν_3 stretching phosphate*	[44]
1653	Water bending	[44, 202]
2300	H-O(P) stretching of HPO_4^{2-} ions	[209]
3280	Water (O-H stretching)	[44, 202]

*Symmetric stretching (ν_1), Symmetric bending (ν_2), Antisymmetric stretching (ν_3), Antisymmetric bending (ν_4).

Table 2.3: FT-IR peaks' assignment of Brushite.

Brushite - $CaHPO_4 \cdot 2H_2O$		
Peak [cm^{-1}]	Assignment	Reference
528	O-P-O(H) bending mode	[203]
577	O-P-O(H) bending mode	[203]
660	Water libration mode/	[203]
	P-O bending	[204]
795	P-O-H out of plane bending/	[203]
	Water libration mode	[204]
874	P-O(H) stretching	[203]
988	P-O stretching	[203]
1065	P-O stretching	[204]
1136	P-O stretching	[203]
1218	P-O-H in plane bending	[203]
1653	H-O-H bending of lattice water molecules	[203]
2370	Combination of H-O-H bending and rotation of free water/	[203]
	O–H stretching of the hydrogen phosphate anions	[204]
2930	(P)O-H stretching (H_1*)	[203]
3164	O-H stretching of lattice water molecules (H_3*)	[203]
3285	O-H stretching of lattice water molecules (H_2*)	[203]
3490	O-H stretching of lattice water molecules (H_4*)	[203]
3540	O-H stretching of lattice water molecules (H_5*)	[203]

*H_1, H_2, H_3, H_4, H_5 refer to the five different H atoms of brushite, for details see ref. [203].

Table 2.4: FT-IR peaks' assignment of Newberyite.

Newberyite - $MgHPO_4 \cdot 3H_2O$		
Peak [cm^{-1}]	Assignment	Reference
528	ν_4 bending phosphate	[205]
881	P-O-H out-of-plane bending	[205]
	ν_1 stretching HPO_4^{2-}	[207]
1022	ν_3 stretching phosphate	[205, 208]
1061	ν_3 stretching phosphate	[205, 208]
1166	ν_3 stretching phosphate	[205, 208]
1237	P-O-H bending HPO_4^{2-}	[205]
1653	ν_2 water bending	[205, 208]
1700	Water bending	[205]
2479	PO-H stretching	[206]
3278	Water O-H stretching	[206]
3382	Water O-H stretching	[206]
3486	Water O-H stretching	[206]
3528	Water O-H stretching	[206]

When comparing the syntheses of AMCP at different pHs, it is evident that the crystallization process occurs on different time-scales: the amorphous phase is retained only for few hours when buffer B_0 is used, while the increase in 0.4 pH units enhances the lifetime of the amorphous phase up to about 10 days. To get a more quantitative information, we can calculate the Splitting Factor (SF): this parameter reflects the entity of the splitting of the P-O antisymmetric bending mode at 550-600 cm^{-1}, which is proportional to the crystallinity of the sample [210] (see the inset in Figure 2.3a for the calculation). Despite the SF is typically used to study the conversion of ACP to HA, we can extend it to the investigation of AMCP conversion to brushite, as also in this case the phosphate bending peak splits in two distinct signals; we consider SF=1 for the amorphous samples, and we report in Figure 2.3a the SF as a function of reaction time (the calculation was not performed for buffer B_3, as in newberyite the peak does not properly split in two distinct signals). This plot clearly shows an enhancement of the lifetime of the amorphous phase with the pH of the synthesis. The same conclusion can be drawn by plotting the amorphous phase stability (*i.e.* the time corresponding

to the appearance of the first crystalline peaks) as a function of reaction pH (see Figure 2.3b): we observe that the experimental data are consistent with an exponential trend. This suggests the possibility to prepare synthetic analogs of endogenous AMCP particles with predictable stability.

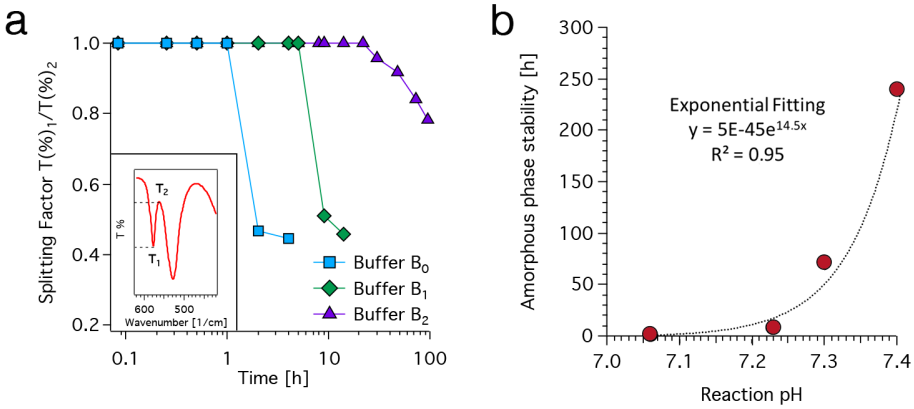

Figure 2.3: (a) Splitting Factors $(T(\%)_1/T(\%)_2)$ as a function of reaction time; the inset shows an example of a peak used to calculate the SF; (b) amorphous phase stability as a function of reaction pH. The dashed line represents the exponential fitting of the experimental data (equation and R^2 reported on the graph).

2.1.2.2 AMCP characterization

We characterized AMCPs prepared in buffer B_3 and collected after 15 min of reaction, analyzing the sample in terms of morphology, size, crystallinity and chemical nature, so to understand if we managed to obtain particles with features matching the endogenous ones. A representative FE-SEM micrograph is reported in Figure 2.4a: AMCPs display a porous and interconnected structure, which results from the aggregation of spherical nanoparticles. The average dimension of each object is about 30 nm (see the inset in Figure 2.4a). Given this aggregated structure, we investigated the size distribution in solution by means of laser granulometry, in order to understand if the aggregation of the spherical objects occurs already in the reacting medium. An aliquot of the reaction solution was collected before filtration and analyzed, obtaining the most representative population centered around 4 μm, with a smaller population centered around 700 nm (red curve in Figure 2.4b). On the other hand, when we analyze with the same

method the dried powder instead of the aliquot withdrawn from the reaction medium, we observe one single population centered around 100 μm (green curve in Figure 2.4b).

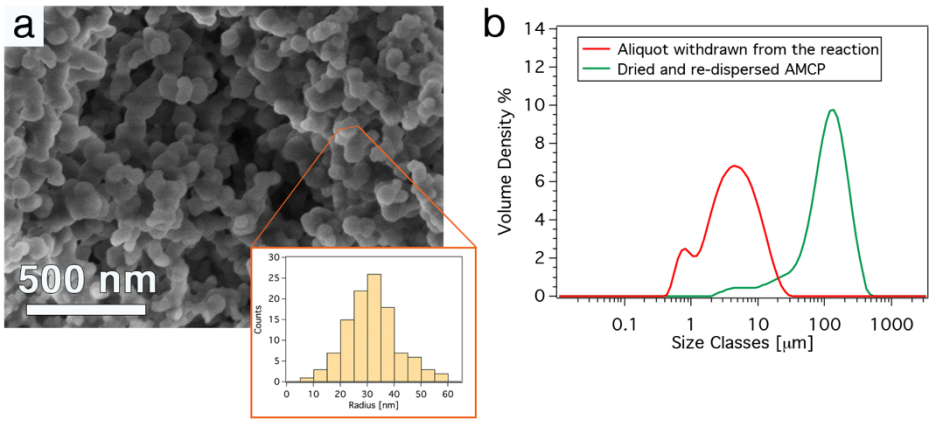

Figure 2.4: (a) FE-SEM micrograph of AMCPs. The inset shows the size distribution obtained averaging the measured sphere radii of 5 different SEM micrographs, using the software ImageJ; the average radius is (32 ± 10) nm; (b) Size distribution curves of AMCP obtained with laser granulometry. The red curve represents an aliquot of AMCP in solution withdrawn from the reaction medium, while the green curve corresponds to the freeze-dried powder dispersed in ethanol.

The elemental composition of the sample was qualitatively investigated by means of EDX spectroscopy in combination with SEM analysis (a representative spectrum is reported in Figure 2.5), showing that the sample is mainly constituted by Ca, Mg, P, O and Na. The semi-quantitative Ca/Mg atomic % ratio is 2.7 ± 0.4, while Ca/P ratio is 0.69 ± 0.05, consistently with the endogenous particles [157].

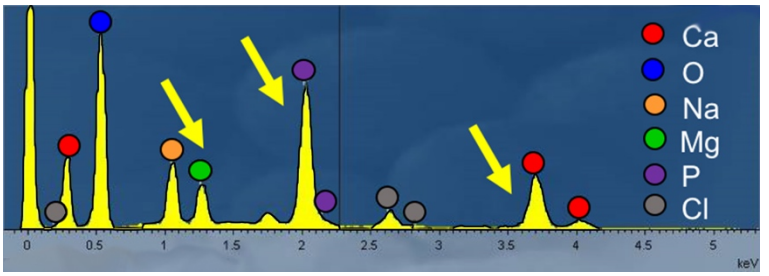

Figure 2.5: Representative EDX spectrum of AMCPs, which reveals the presence of Ca (red dots), Mg (green dots) and P (purple dots) in the particles.

The amorphous nature of AMCP emerges from both FT-IR and XRD analyses. The FT-IR spectrum (Figure 2.6a) shows the characteristic featureless peaks of amorphous calcium phosphate, which have been described in the previous paragraph (see Table 2.2). The collected XRD pattern (Figure 2.6b) is consistent with previous reports on ACP [53, 202], and displays the characteristic broad peak centered around 2θ=30° diagnostic for amorphous CaP phases.

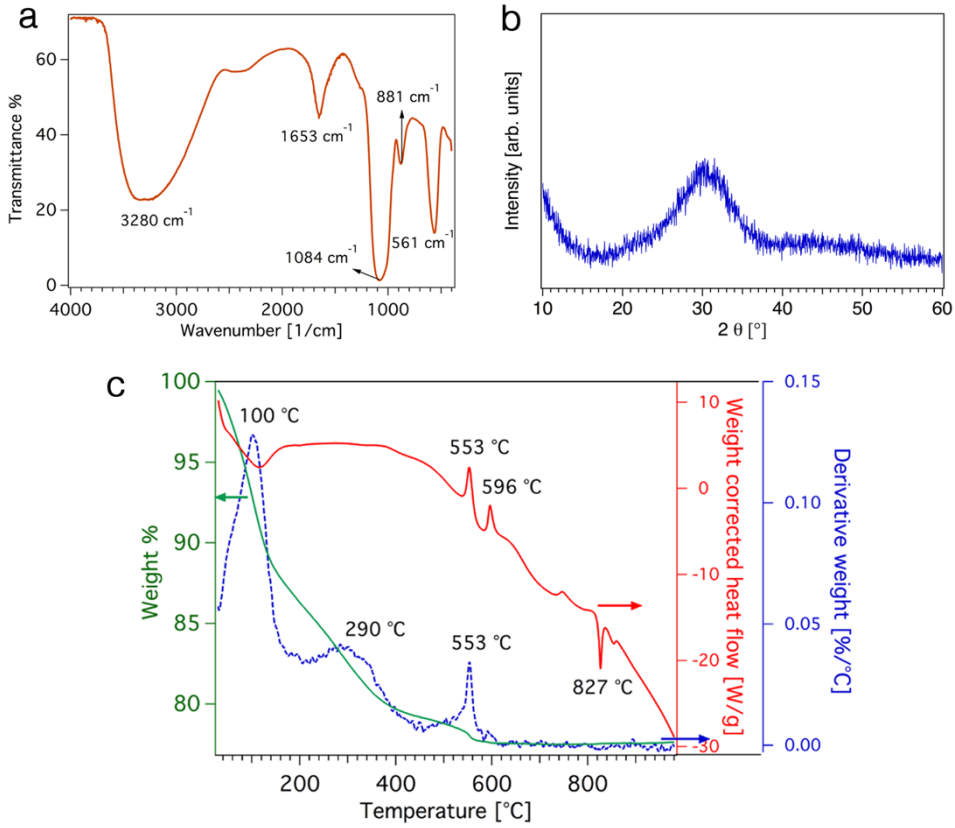

Figure 2.6: (a) FT-IR spectrum of AMCP; (b) XRD diffractogram of AMCP; (c) SDT data: thermogravimetry (green curve, left axis), differential thermogravimetry (dashed blue curve, right axis) and heat flow profile (red curve, right axis).

The thermal degradation profile of AMCP, together with the associated heat flow curve, is reported in Figure 2.6c. The sample displays three distinct weight loss events in TGA curve, when heated up to 1000 °C (green curve): the first one, taking place around 100 °C, is associated to the loss of loosely bound water molecules, while the second one can be assigned to the more strongly bound internal water molecules [53, 211]. The weight loss at 553 °C

occurs simultaneously with the first crystallization peak observed in the heat flow profile, and the total weight loss is 22 %. The DSC thermogram (red curve) displays three distinct peaks: the first two exothermic events, at 553 °C and 596 °C, are associated to crystallization events, whereas at 827 °C, we observe the endothermic melting of the crystalline phases formed while heating. In order to understand the nature of the phase transformations that occur while heating AMCPs, we performed two thermal treatments, by heating them up to 580 °C and 630 °C and analyzing the obtained powders by means of XRD. The diffraction patterns are reported in Figure 2.7. We found that the first peak in the heat flow profile is associated to the formation of a crystalline sodium calcium magnesium phosphate with a whitlockite-like structure ($Ca_9MgNa\cdot(PO_4)_7$, PDF (Powder Diffraction File from the International Centre for Diffraction Data database) n° 45-0136; the experimental pattern displays a good match also with PDF n° 70-2064 – $Ca_{18}Mg_2H_2(PO_4)_{14}$, Whitlockite magnesian).

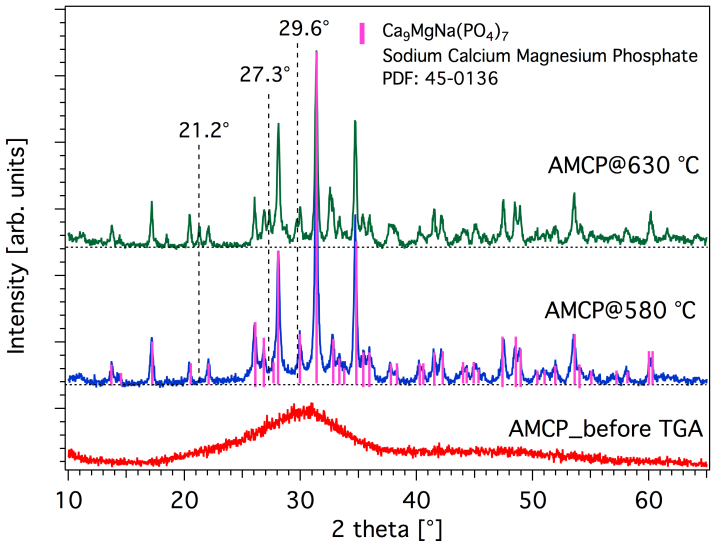

Figure 2.7: XRD patterns of (from the bottom) AMCP before TGA (red curve), AMCP heated at 580 °C (blue curve) and AMCP heated at 630 °C (green curve). The pink bars correspond to the PDF n° 45-0136 (crystalline sodium calcium magnesium phosphate). The black dashed lines highlight the peaks which are only present in the sample heated at 630 °C. The diffractograms are offset for display purpose.

According to literature reports, amorphous calcium phosphate converts to α-TCP or β-TCP above 600 °C, depending on the preparation conditions [53, 212–215]. When Mg^{2+} ions are present in the lattice, the formation of β -TMCP

(Mg-substituted TCP), which has a similar diffraction pattern to the phase that we detected, is observed [216]. The second peak detected in the heat flow profile (at 596 °C) can be associated to the conversion of the residual AMCP to very small amounts of sodium phosphate (PDF: 76-1112) and magnesium phosphate (PDF: 48- 11687).

The specific surface area (SSA) of the material and the pore size distribution were investigated by means of nitrogen sorption measurements: AMCPs are characterized by a reversible type II isotherm (see Figure 2.8a), typical of non-porous or macroporous solids [217], and a SSA of (38.3 ± 1.2) m^2/g (average ± standard deviation of three distinct measurements). The obtained SSA value is slightly lower than the values reported in the literature for amorphous calcium phosphates, which are in any case strongly dependent on the preparation conditions [216, 218, 219]. The pore volume distribution analysis, reported in Figure 2.8b, confirms that the majority of pores is in the macropores range (*i.e.* > 50 nm). The internal porosities of the particles, observed in high-magnification FE-SEM micrographs (see Figure 2.8c), are not accessible through nitrogen sorption measurements.

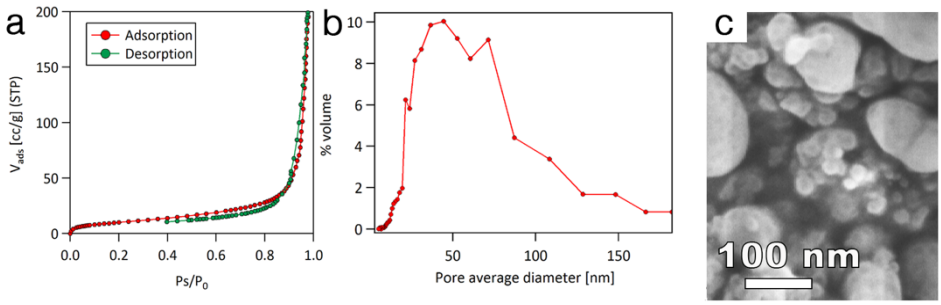

Figure 2.8: (a) adsorption (red) and desorption (green) nitrogen curves of AMCP, corresponding to a type II isotherm; (b) pore size distribution; (c) high-magnification SEM micrograph, which shows the internal porosities of the particles.

To sum up, the characterization performed on AMCPs shows that we managed to obtain particles which have features that match the ones that form *in vivo* [157]: in fact, our particles are composed by nanometric spheres which form larger aggregates, they are internally porous and mainly composed by Ca, Mg, P and, most importantly, they are amorphous. All the discussed characteristics are consistent with the biogenic particles.

2.1.2.3 *Effect of Mg^{2+} concentration*

The effect of Mg^{2+} on AMCP stability was investigated by dispersing dried particles (characterized in the previous paragraph) in fresh phosphate buffer containing 0, 1, 3 and 5 mM of Mg^{2+}, as described in section 2.1.1.2. The crystallization kinetic was monitored by means of FT-IR spectroscopy, and the spectra relevant to the amorphous-to-crystalline transition are shown in Figure 2.9.

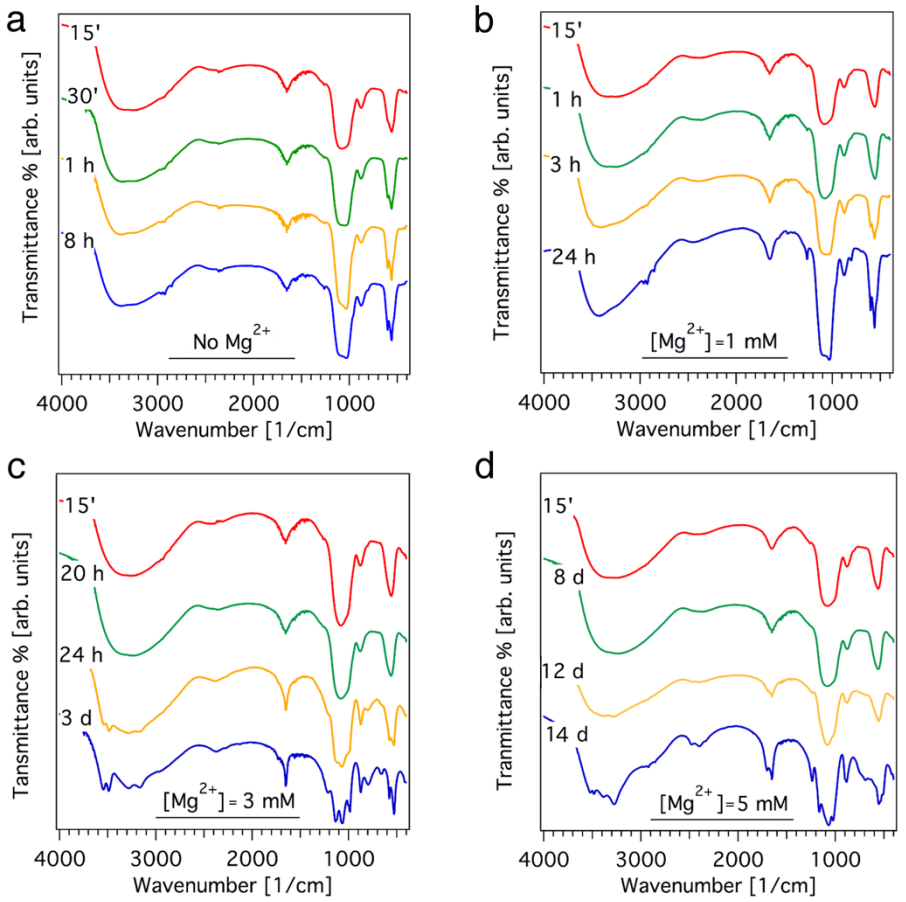

Figure 2.9: FT-IR spectra of AMCP particles dispersed in different buffer solutions at pH 7.40 and with (a) No Mg^{2+}; (b) $[Mg^{2+}]$ = 1 mM; (c) $[Mg^{2+}]$ = 3 mM; (d) $[Mg^{2+}]$ = 5 mM. The reaction time at which each aliquot was collected is indicated on the left of each curve. The spectra are offset for display purposes.

It is evident that the concentration of Mg^{2+} in solution has a huge impact on the lifetime of AMCP in solution: when AMCPs are dispersed in a fresh

phosphate buffer at pH 7.40, without the addition of Mg^{2+}, the amorphous phase is preserved for about 30 min; afterwards, the peak at ~ 550 cm^{-1} starts to split (see Figure 2.9a). At [Mg^{2+}] = 1 mM, the crystallization process is slightly delayed, since the cited peak splits after about 3 h (Figure 2.9b). In the case of [Mg^{2+}] = 3mM (Figure 2.9c) and [Mg^{2+}] = 5 mM (Figure 2.9d), crystallization begins after about 24 h and 14 days, respectively.

Figure 2.10a shows the Splitting Factors vs reaction time, calculated as described in section 2.1.2.1 considering the peak around 550 cm^{-1} which, we recall, is reported to be the most sensitive to the crystallinity of the material [210]. Results highlight the enhancement of the lifetime of the amorphous phase as a function of Mg^{2+} concentration in solution. The plot of the stability of the amorphous phase against Mg^{2+} concentration in solution, shown in Figure 2.10a, reveals a good exponential relationship between the two parameters, similarly to the effect of the synthesis pH (see paragraph 2.1.2.1).

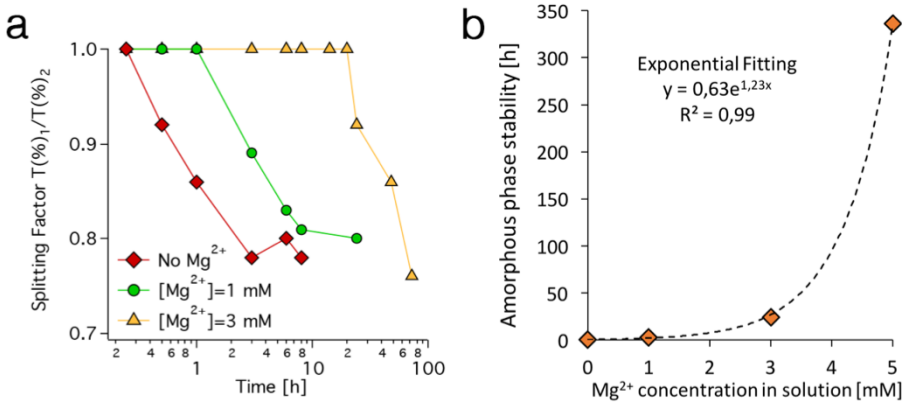

Figure 2.10: (a) Splitting Factors ($T(\%)_1/T(\%)_2$) as a function of reaction time. The SF of the system [Mg^{2+}]=5 mM was not calculated as the peak at ~550 cm^{-1} does not properly splits; (b) amorphous phase stability as a function Mg^{2+} added in solution. The dashed line represents the exponential fitting of the experimental data (equation and R^2 reported on the graph).

Together with the lifetime of the amorphous phase, FT-IR spectra also give important information about the nature of the formed crystalline phases, especially focusing on the shape of the peak between 700 and 1400 cm^{-1} (see the zoom of this region in Figure 2.11). From the analysis of the peak's position and shape, we observe that if Mg^{2+} is absent from the solution, or its concentration is very low (=1 mM), AMCP converts to poorly crystalline HA [200, 220, 221].

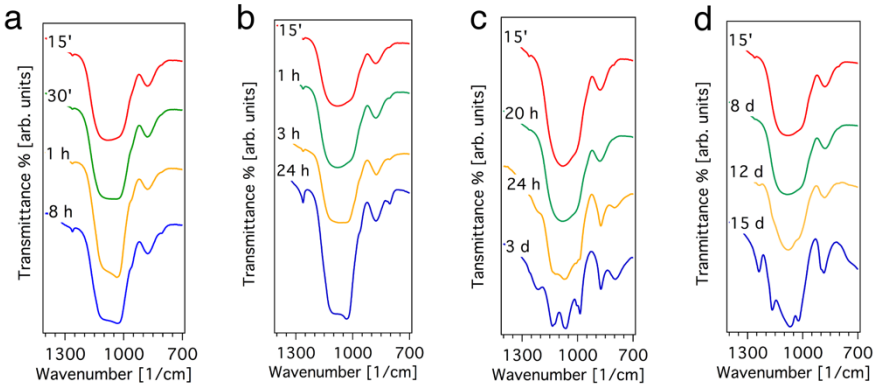

Figure 2.11: Zoom of the region 700-1400 cm^{-1} of the FT-IR spectra of AMCP dispersed at pH 7.40 and (a) without Mg^{2+}, (b) with $[Mg^{2+}]$=1 mM, (c) $[Mg^{2+}]$= 3 mM, (d) $[Mg^{2+}]$=5 mM.

The peak assignment is analogous to the one of AMCP (see Table 2.2), except for the splitting of the peak at 550 cm^{-1} and the slightly different shape of the peak at ~ 1100 cm^{-1}. As in FT-IR the bandwidths of the peaks are related to both the crystalline domain size and the degree of ion ordering into the unit cell, the spectra observed here differ from that of well-crystallized HA, which displays well-defined bands [221]. The rapid conversion of AMCP to poorly-crystalline HA is not surprising, as amorphous calcium phosphates are known to convert to apatitic phases in physiologic-like conditions [44]. The increase in the concentration of Mg^{2+} modifies the phase transformation of AMCP, since at $[Mg^{2+}]$ = 3 mM, the peaks typical of brushite appear after about 24 h (see Figure 2.9c) [222]. In the case of $[Mg^{2+}]$ = 5 mM (Figure 2.9d), the spectrum of the material collected after 14 days is compatible with the presence of newberyite [205–208]. The formation of this crystalline form of magnesium phosphate is due to the large amount of Mg^{2+} in solution. To further deepen the understanding of the nature of the formed crystalline phases and to confirm the hypotheses conducted over FT-IR results, FE-SEM and XRD analyses were performed on the crystalline samples, and the results are reported in Figure 2.12; since the nature of the crystalline material formed when AMCPs are dispersed without Mg^{2+} or at $[Mg^{2+}]$ = 1 mM coincide, we report here only the FE-SEM and XRD results for AMCPs dispersed without Mg^{2+}.

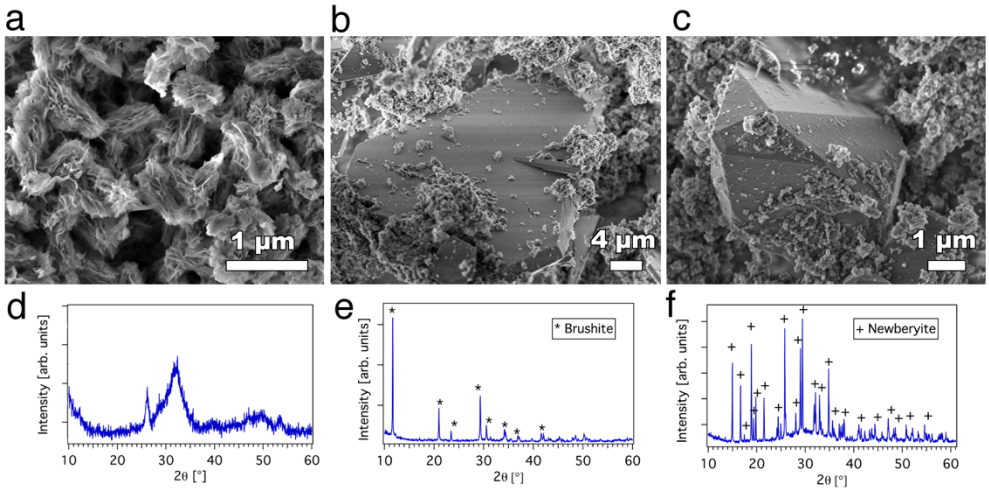

Figure 2.12: FE-SEM micrographs (a, b, c) and XRD patterns (d, e, f) of AMCPs dispersed at pH 7.40 without Mg^{2+} after 8 h (a, d), AMCPs dispersed at pH 7.40 at [Mg^{2+}] = 3 mM after 3 days, (b, e) AMCPs dispersed at pH 7.40 at [Mg^{2+}] = 5 mM after 14 days (c, f). The PDF used for XRD peaks' assignments are PDF: 09-0077 for brushite and PDF: 70-2345 for newberyite.

The morphology of poorly crystalline HA (see Figure 2.12a) is significantly different from that of AMCPs, as the sample consists of flake-like particles, hundreds of nm-sized. On the other hand, in the case of [Mg^{2+}] = 3 mM (Figure 2.12b), we observe brushite typical platelets [223], while some crystals with defined geometric shapes consistent with the presence of newberyite are visible for [Mg^{2+}] = 5 mM [18] (see Figure 2.12c); in the last two cases, we also observe a large portion of amorphous particles that surrounds the formed crystals, suggesting that the crystallization process is not complete yet. XRD results confirm the conducted observations: the diffractogram collected for AMCPs dispersed at pH 7.40 without Mg^{2+} and withdrawn after 8 h shows very broad and low-intensity peaks, which are diagnostic of a poorly-crystalline sample. The pattern, which displays peaks at 26°, 32°, 40° and 53°, is consistent with poorly-crystalline HA, which in the literature is often referred to as Calcium-Deficient HA (CDHA) [53, 224] or cryptocrystalline/poorly crystallized apatite [225]. In the case of [Mg^{2+}] = 3 mM (Figure 2.12e) and 5 mM (Figure 2.12f), the diffraction peaks can be assigned to brushite (PDF: 09–0077) and newberyite (PDF: 70– 2345), respectively. In Figure 2.12f, the peaks are superimposed to the large hump

at ~ 30° characteristic of AMCP (see Figure 2.6b), confirming that a considerable portion of amorphous material is not crystallized yet.

To sum up, our results show that the concentration of Mg^{2+} in the solution in which AMCPs are dispersed affects both the lifetime of the amorphous phase and the nature of the crystalline calcium phosphates which form upon AMCP conversion (see the Discussion section for a detailed explanation).

2.1.2.4 Effect of pH on re-dispersed particles

The effect of the synthesis pH on AMCP stability has been discussed in paragraph 2.1.2.1; here, we focus on the effect of the pH of the solution in which already synthesized AMCP particles are re-dispersed. This investigation aims at simulating different acid-base conditions that endogenous AMCP particles could encounter in physiological (like change of diet) or pathological conditions at the ileum level [226, 227], eventually leading to alterations of the immune-surveillance mechanisms. AMCP particles were dispersed in phosphate buffers at pH 6.90 and 7.40, at concentration 0.36 g/L (for the experimental details, see paragraph 2.1.1.3). Results for different samples are compared in Figure 2.13. The FT-IR spectra, and in particular the shape of the peaks at ~ 1100 and 550 cm^{-1} (see the highlighted region in Figure 2.13a), show that when AMCPs are dispersed at pH 6.90, the crystallization process is faster than at pH 7.40, and that the formed product is poorly-crystalline HA. The morphology of the samples confirms this observation, as at pH 6.90 FE-SEM micrographs (Figure 2.13b and c) show HA typical flake-like morphology (see Figure 2.12a for comparison), while at pH 7.40 this phase coexists with a large amount of amorphous phase, highlighted in Figure 2.13c. EDX analyses were performed to obtain semi-quantitative elemental ratios; Ca/Mg ratio is of outmost importance, as it gives insights about the crystallinity of the samples. As AMCPs displays Ca/Mg ratio of about 2.7, while crystalline CaPs such as HA and brushite are Mg-free, the crystallinity of the samples is directly proportional to Ca/Mg ratio (*i.e.* high crystallinity means low Mg amount, which implies high Ca/Mg ratio). Atomic ratios are reported in Figure 2.13d (the inset shows a zoom that highlights the low atomic % region). On the one

hand, Mg/Na, Ca/Na and Ca/P ratios are not significantly affected by the pH of the solution; on the other hand, Ca/Mg ratio is much higher for the sample at 6.90, confirming the more crystalline nature of the material. The high standard deviations associated to these ratios could be related to inhomogeneities in roughness and composition of different samples (*i.e.* the amorphous portions are not homogeneously distributed all over the specimen). These results suggest that, in addition to the concentration of Mg^{2+} in solution, the pH has a critical impact on the solubility of AMCPs and the subsequent crystallization to calcium phosphates.

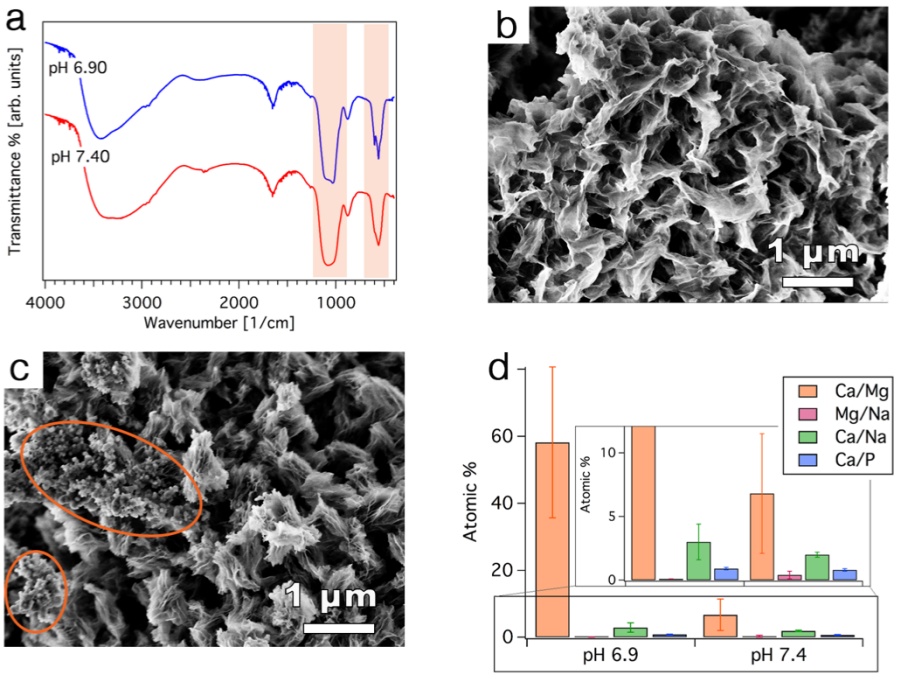

Figure 2.13: (a) FT-IR spectra of AMCPs dispersed at pH 6.90 (top blue curve) and 7.40 (bottom red curve) and collected after 15 min; (b) and (c) FE-SEM micrographs at the same magnification of AMCPs dispersed in phosphate buffer and withdrawn after 15 min at (b) pH 6.90, (c) pH 7.40. The orange ellipses in c highlight the amorphous portions of the samples; (d) Atomic % ratios calculated with EDX analysis, averaging 3 different sites for each sample (the error bars correspond to the standard deviations). In the inset, the zoom of the selected region is reported.

2.1.2.5 Effect of dispersion concentration

Together with the presence of Mg^{2+} ions and the pH of the solution, we observed that the concentration of dispersed particles also affects the crystallization rate of AMCP and the type of formed phase. At pH 6.90,

particles crystallize after few minutes, as discussed in the previous section, and convert to poorly crystalline HA (see FT-IR spectra as a function of time in Figure 2.14a and FE-SEM micrograph of the product collected after 15 min in Figure 2.13b); however, when we increase the amount of particles that we disperse in the buffer (here, 3 g/mL), AMCPs evolve to brushite instead of HA, as shown by FT-IR spectra (Figure 2.14b) and FE-SEM micrographs (Figure 2.14c). The crystallization kinetic is also different at the two pHs, as it is evident from EDX results (Figure 2.14d): in the diluted regime, a much higher Ca/Mg ratio is obtained, highlighting that the critical factor for the stability of the amorphous phase is the amount of Mg^{2+} in solution (see later in the Discussion section).

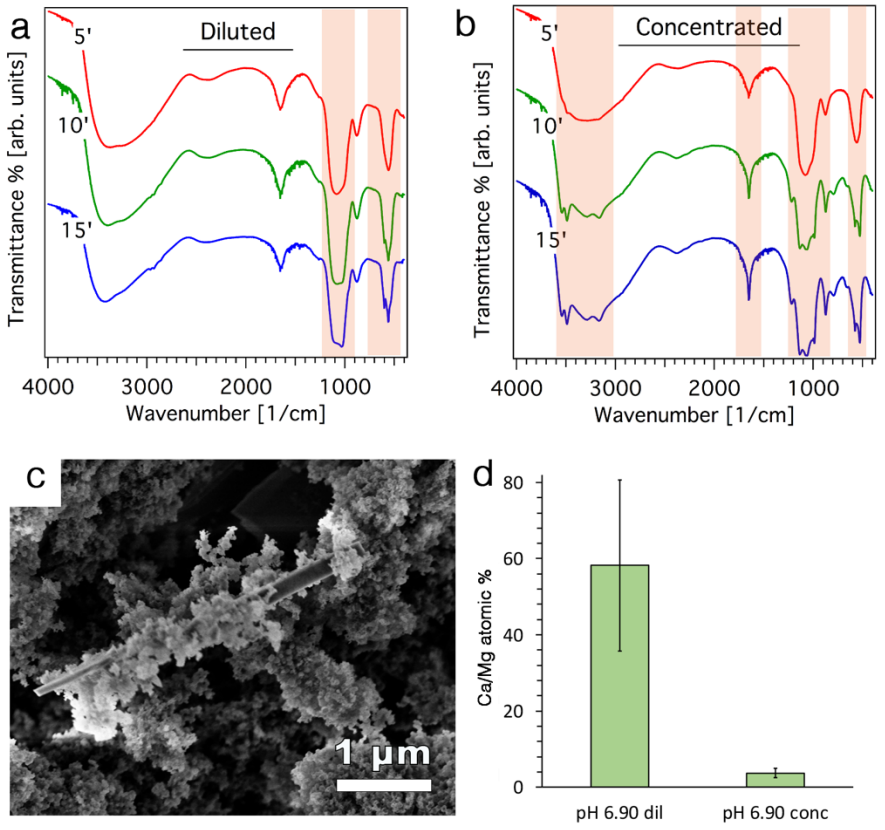

Figure 2.14: (a,b) FT-IR spectra of AMCPs dispersed at pH 6.90 and withdrawn after 5, 10 and 15 min (a) in the diluted regime (0.36 g/L) and (b) the concentrated regime (3 g/L); (c) FE-SEM micrograph of AMCPs dispersed at pH 6.90 in the concentrated regime and withdrawn after 15 min, where brushite platelets surrounded by amorphous particles are visible; (d) Ca/Mg ratio of the products collected after 15 min as obtained by means of EDX analysis.

The same observations were conducted by dispersing AMCPs at pH 7.40: in this system too, the particles convert to poorly crystalline HA in the diluted system, while in the concentrated one brushite forms (compare the series of FT-IR spectra in Figure 2.9a, which refer to the diluted regime, with those in Figure 2.15a for the concentrated system). The nature of the samples withdrawn after 8 h was investigated by means of XRD (Figure 2.15b) and FE-SEM (Figure 2.15c and d), and the findings are consistent with FT-IR results.

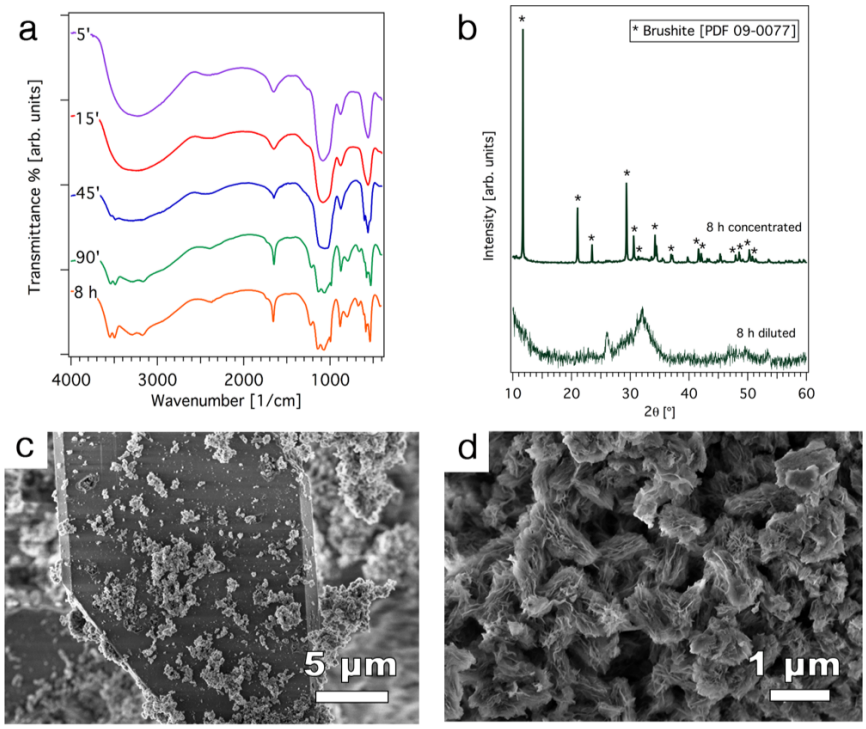

Figure 2.15: (a) FT-IR spectra of AMCPs dispersed at pH 7.40 in the concentrated regime, and withdrawn after (from the top to the bottom) 5, 15, 45, 90 min and 8 h; (b) XRD pattern of AMCPs dispersed at pH 7.40 and withdrawn after 8 h in the diluted (bottom curve) and concentrated (top curve) system; (c,d) FE-SEM micrographs of the samples AMCPs dispersed at pH 7.40 after 8 h, concentrated (c) and diluted (d) systems.

The kinetics of the crystallization process was estimated by comparing the trends of Ca/Mg ratios vs incubation time (see Figure 2.16). In both systems, Ca/Mg ratio increases with the increase of incubation time (*i.e.* the crystallinity increases), and the ratios for the concentrated system are significantly lower than the ones of the diluted regime, suggesting that also at pH 7.40 the crystallization is faster when the particles are diluted.

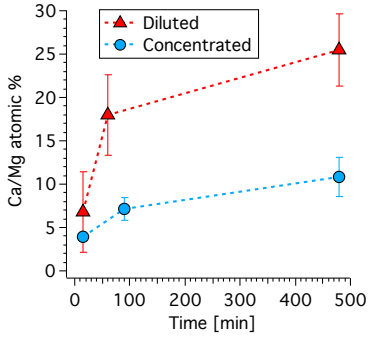

Figure 2.16: Ca/Mg atomic % ratio, calculated by means of EDX, as a function of reaction time (red triangles: diluted system, blue dots: concentrated system) for the pH 7.40 experiments.

2.1.3 Discussion

The data presented so far clearly show that endogenous-like AMCP is an unstable material, given its spontaneous crystallization into CaP or MgP-based phases: amorphous calcium phosphates are indeed known to exist due to kinetic reasons, as they thermodynamically tend to convert into stable crystalline phases [53, 209]. The kinetics of this transformation depends on several factors, as we outlined in the Introduction; among the stabilization strategies which can be employed to enhance the lifetime of the amorphous phase, it is known that Mg^{2+} ions contribute to the stabilization of the amorphous phase, kinetically hindering the nucleation and growth of hydroxyapatite by competing for lattice sites with calcium ions [73, 77, 228]. The evidence that the endogenous nanoparticles which are found in human intestine contain both Ca^{2+} and Mg^{2+} is intriguing: in fact, the presence of the latter ion may contribute to preserve their amorphous nature and potentially their functional role in the organism. To mimic the effect of Mg^{2+} concentration in intestinal fluids on endogenous AMCP particles, we prepared synthetic analogues. Our results confirm the stabilization of ACP through the inclusion of Mg^{2+}; moreover, we were able to establish an exponential relationship between the lifetime of the amorphous phase and Mg^{2+} concentration added in solution, allowing for the possibility of predicting the stability of AMCPs. Very interestingly, we observed that the concentration of this ion affects not only the lifetime of the amorphous phase,

but also the type of crystalline phase to which AMCP converts. These results can be explained in terms of CaP solubility and of the effect of Mg^{2+} on CaP crystallization rate. At 37 °C and ionic strength of 0.1 M, HA is the thermodynamically more stable phase in an extended range of pH, while at pH < 4, brushite (DCPD) is favored (see Figure 2.17a) [59]. Therefore, the conversion of AMCP to poorly crystalline HA that we observe at low Mg^{2+} concentration (paragraph 2.1.2.3) is not surprising, and the poor crystallinity of the material is likely due to Mg^{2+} that limit the re-arranging ability of Ca^{2+} and phosphate ions. Moreover, we know from the literature that Mg^{2+} hinders the crystallization of the various CaPs to a different extent, as it mostly hampers HA formation, while brushite crystallization is un-affected by the presence of Mg^{2+} (see Figure 2.17b) [228].

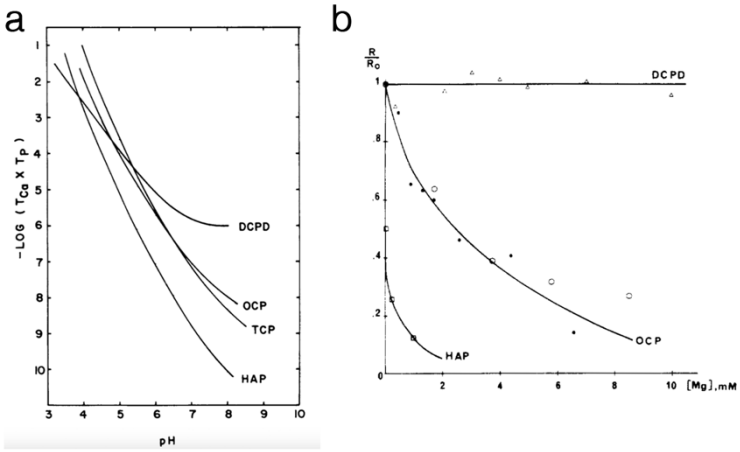

Figure 2.17: (a) Solubility isotherms of CaPs at 37 °C and 0.1 M ionic strength (reproduced with permission from [59]; (b) Normalized rates of growth of DCPD, OCP and HA in the presence of magnesium ions. R and R_0 are the rates of growth in the presence and absence of magnesium, respectively (reproduced with permission from [228]).

This is consistent with our observations, as when Mg^{2+} concentration in solution increases (3 mM), the amorphous phase is more stable and brushite is the phase that finally precipitates, because of the large amount of Mg^{2+} that does not allow for HA formation. When [Mg^{2+}] = 5 mM, AMCP particles are extremely stable and Mg^{2+} is so abundant in solution that a magnesium phosphate, $MgHPO_4 \cdot 3H_2O$, is the first crystalline phase that precipitates. This explanation is also compatible with the results that we achieved in the

experiments at different AMCP concentration (paragraph 2.1.2.5): here, Mg^{2+} was not added on purpose in the solution, but it was released due to AMCPs dissolution that occurs when they get in contact with the aqueous medium. When a small amount of particles is dispersed in solution, a low concentration of Mg^{2+} is released and AMCP rapidly converts to poorly crystalline HA; when a larger quantity of particles is dispersed in solution, dissolution occurs to a larger extent, and the significant amount of Mg^{2+} released stabilizes the remaining solid amorphous phase, allowing for the formation of brushite over HA, both at pH 6.90 (see Figure 2.14) and 7.40 (Figure 2.15 and Figure 2.16). It is therefore clear that Mg^{2+} concentration has a paramount importance in determining AMCPs behavior and fate. The levels of this ion in the gut lumen are tightly controlled, as its absorption takes place in the intestine [13]. Intestinal levels of Mg^{2+} have important implications for the health: experiments on rats show that magnesium deficiency induces inflammation in the small intestine [229] and magnesium supplements are often therapeutically effective against the symptoms of irritable bowel disease [230]. For the moment, the direct connection between Mg^{2+} concentration in the intestine and the stability/amount of AMCPs formed is not demonstrated. However, we may speculate that a Mg^{2+} deficiency in the gut could hamper the stability of the particles, thus affecting the biological pathway in which they are involved.

As far as the pH effect is concerned, the observed stabilization of AMCP with the increase of pH (both during the synthesis –paragraph 2.1.2.1- and when dispersed in solution –paragraph 2.1.2.4) is consistent with the data reported in the literature [70]. Our results clearly show a dramatic sensitivity to pH variations, as a difference of few tenths of pH unit induces an enhancement of the stability of about 10 days. We found an exponential relationship between the amorphous phase stability in the reaction medium and the pH during the synthesis (similarly to $[Mg^{2+}]$), allowing for the prediction of the lifetime of AMCPs for a given pH value. The stability that the particles display in their reaction medium at pH 7.40 is remarkable. Very interestingly, we observed that the nature of the crystalline product formed as a consequence of AMCP conversion changes by modifying the pH, as brushite forms at pH in the range 7.06–7.30, while at pH 7.40 we detect the presence

of newberyite. The precipitation of brushite can be easily justified considering the effect of Mg^{2+} ions in solution that hinder HA precipitation. The formation of newberyite could be explained considering that AMCP dissolution is slowed down at pH 7.40, and that the combined presence of Mg^{2+} ions in solution hampers the ability of forming new crystals; in these conditions, the concentration of calcium in solution needed for the formation of brushite could not be attained, and the first crystalline phase that would precipitate is newberyite. The pH of the solution which AMCPs get in contact with has also a crucial role in the crystallization kinetic (paragraph 2.1.2.4): being ACP less stable in acidic conditions [70], the particles dissolve more rapidly at pH 6.90 than at pH 7.40, causing an increase in solution of all the ions constituting the particles (Ca^{2+}, Mg^{2+}, phosphate). This results in the rapid conversion to poorly-crystalline HA, while at pH 7.40 the solid material which precipitates is richer in the amorphous component, being the dissolution of AMCPs slower in these conditions. To sum up, pH has a deep impact of the stability of the amorphous phase. It is important to recall that, as highlighted at the beginning of section 2.1, alterations in the gut pH are associated to pathologies, such as inflammatory bowel disease [226], chronic pancreatitis and cystic fibrosis, which seem to decrease pH of the proximal small intestine [227]. In general, inflammatory conditions are related to acidic pH and, interestingly, AMCPs are less stable in that environment; all the factors which contribute to raise the pH of the small intestine could potentially increase the stability of the particles, leading to the correct achievement of their biological function. As far as diet is concerned, it is not easy to relate our eating habits to variations of the parameters crucial to AMCPs stability; it is generally recognized that food has no significant influence on intestinal and colonic pH [231]; nevertheless, it was also shown that, in rodents, a high fiber diet (which is known to have beneficial effects for gut health) caused an increase in the pH of the small intestine by 0.35–0.75 pH units [232].

All our data taken together demonstrate that slight variations in factors which are biologically relevant deeply affect the stability and the fate of AMCPs. We believe that these results have a two-fold relevance, as they contribute to the topic of amorphous-to-crystalline transition of CaPs and may help in clarifying the role of the endogenous particles.

2.2 Effect of additives

While forming in the distal small intestine, AMCPs can encounter a variety of molecules and macromolecules that can be absorbed and even shape their structure and their stability. With this scenario in mind, we selected some biologically-relevant and representative molecules of the intestinal milieu as case studies (butyric acid, lactose, gluten and peptidoglycan, see Figure 2.18) to investigate how their presence in the reaction medium can affect the physico-chemical features of AMCPs.

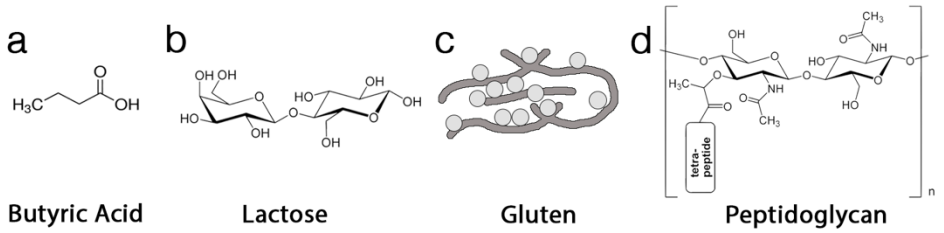

Figure 2.18: Formula of the additives employed in this study: (a) butyric acid; (b) lactose; (c) gluten; (d) peptidoglycan.

Butyric acid (see Figure 2.18a) is a short-chain fatty acid and, together with acetic and propionic acid, is produced within the intestinal lumen by bacterial fermentation of undigested dietary carbohydrates and dietary and endogenous proteins [233]. Butyrate is the preferred energy source for colonocytes and serves as cellular mediator regulating multiple functions of gut cells [233, 234]; it also has an anti-inflammatory effect and has potential benefit in irritable bowel syndrome [235–237].

Lactose (see Figure 2.18b) is a disaccharide composed of galactose and glucose; it enters the intestine upon milk intake, where the glycosidic bond is cleaved by the enzyme lactase. The resulting monosaccharides can then be absorbed and used as energy source by our organism. Individuals which have a deficiency in lactase production are not able to digest lactose: in this case, the disaccharide passes intact in the colon, where it is fermented by bacteria. The resulting production of gas may cause various abdominal symptoms.

Gluten (see Figure 2.18c) can be defined as the rubbery mass that remains when wheat dough is washed to remove starch granules and water-soluble

constituents [238, 239]. It contains hundreds of protein components, which are typically divided into two fractions, *i.e.* gliadins (soluble in alcohol-water solutions) and glutenins (insoluble). In a small part of the population, gluten can trigger adverse autoimmune reactions responsible for a broad spectrum of gluten-related disorders, such as coeliac disease [240].
Peptidoglycan (see Figure 2.18d) is a polymer composed of sugars (N-acetylglucosamine and N-acetylmuramic acid) and amino acids, and is the component of most bacteria's cell wall; being the gut flora so abundant, it is expected that peptidoglycans are representative components of the intestinal environment.

2.2.1 Synthesis of AMCPs in the presence of additives

AMCPs were prepared following the same procedure described in paragraph 2.1.1.1, by mixing 50 mL of solution A ([NaCl]=135 mM, [$CaCl_2$]=40 mM, [$MgCl_2$]=13.3 mM) with 50 mL of solution B_1 (see Table 2.1), and adjusting the pH at 7.7 before collecting them after 15 min. The modifications in the concentrations with respect to the synthesis in paragraph 2.1.1.1 were adopted to maximize AMCP yield, while maintaining all the particles in the amorphous phase.
For the synthesis in the presence of additives, each molecule was dissolved/dispersed in solution A at 1 mg/mL before mixing with solution B_1 [166]. The particles synthesized with butyric acid (purity ≥ 99 %, Sigma-Aldrich) are coded as sample "AMCP_B", with lactose (D(+)-lactose monohydrate ≥ 98 %, Fluka) "AMCP_L", with gluten (crude, ≥ 80 % protein, Sigma-Aldrich) "AMCP_G" and with peptidoglycan (from *Bacillus Subtilis,* Sigma-Aldirch*)* "AMCP_P". The only difference among the four syntheses was conducted in the preparation with gluten, as, being this protein composed by glutenin (soluble in water) and gliadin (insoluble in water) [238], it was not possible to readily dissolve it in solution A. The sonication of the dispersion for 10 min lead to the partial agglomeration of the protein; therefore, we tried to improve the dispersion by stirring the sample at 70 °C for 36 h, and then we filtered the solution (0.45 μm filters) to remove the

insoluble portion. The synthesis was then conducted analogously to the other systems.

2.2.2 Results and discussion

AMCPs prepared in the absence of additives are analogous to those described in section 2.1.2.2: the particles are amorphous, and electron microscopy investigation shows aggregated nanometric particles endowed with internal porosities (see Figure 2.19). The only noteworthy difference with respect to the particles described in the previous paragraph is the Ca/Mg atomic % ratio as calculated by means of EDX analysis, which in this case is higher (6.8 ± 0.5), given the greater Ca^{2+} concentration with respect to Mg^{2+} used in the synthesis.

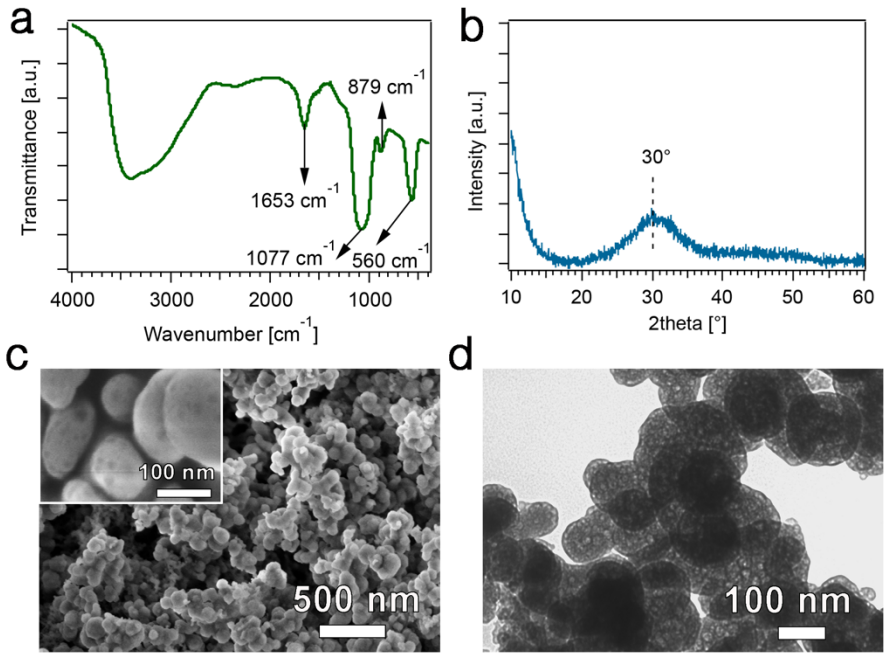

Figure 2.19: AMCP characterization: (a) FT-IR spectra; (b) XRD pattern; (c) FE-SEM micrographs (inset: high magnification); (d) TEM micrograph.

The incorporation of the additives in the particles was investigated by means of FT-IR spectroscopy and thermogravimetry, and the results are shown in Figure 2.20.

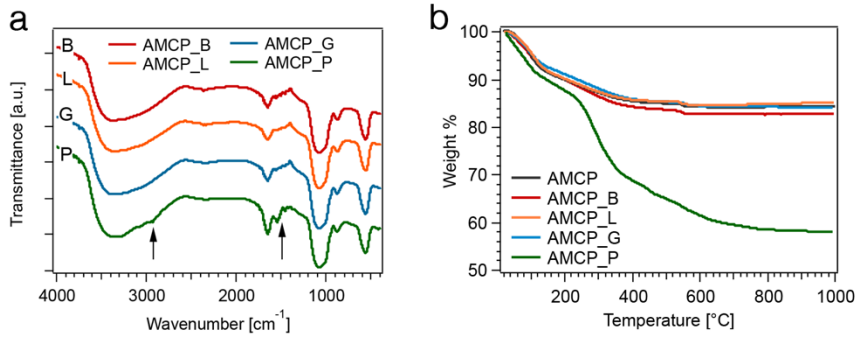

Figure 2.20: (a) FT-IR spectra and (b) thermogravimetric curves of AMCP synthesized in the presence of: butyric acid (AMCP_B, red curve), lactose (AMCP_L, orange curve), gluten (AMCP_G, blue curve) and peptidoglycan (AMCP_P, green curve). The arrows in (a) highlight the additional signals present in the spectrum of AMCP_P, due to the incorporated peptidoglycan.

The FT-IR spectra (Figure 2.20a) of the particles prepared in the presence of butyric acid (red curve), lactose (orange curve) and gluten (blue curve) do not show any additional signal with respect to AMCP (see Figure 2.19a for comparison). On the contrary, sample AMCP_P displays further signals, at 1545 cm^{-1}, 2929 cm^{-1} and 2965 cm^{-1}, which are compatible with peptidoglycan vibrations [241]. This evidence suggests that, similarly to the *in vivo* process, this polymer is partially incorporated in AMCPs, unlike butyric acid, lactose and gluten. In order to quantitatively assess the incorporation of organic material in AMCPs, samples were analyzed by means of thermogravimetry, and the results are shown in Figure 2.20b. From the comparison of the weight losses % at 1000 °C, we can clearly observe that samples AMCP_B, AMCP_L and AMCP_G lose about 16 % of their initial weight (±1 %), similarly to AMCP (15 %); on the other hand, AMCP_P display a weight loss % of 42 %, thus indicating that the particles prepared in the presence of peptidoglycan can incorporate ~ 27 % by weight of the polymer.

The morphology of the particles was investigated by means of FE-SEM, and the micrographs are reported in Figure 2.21.

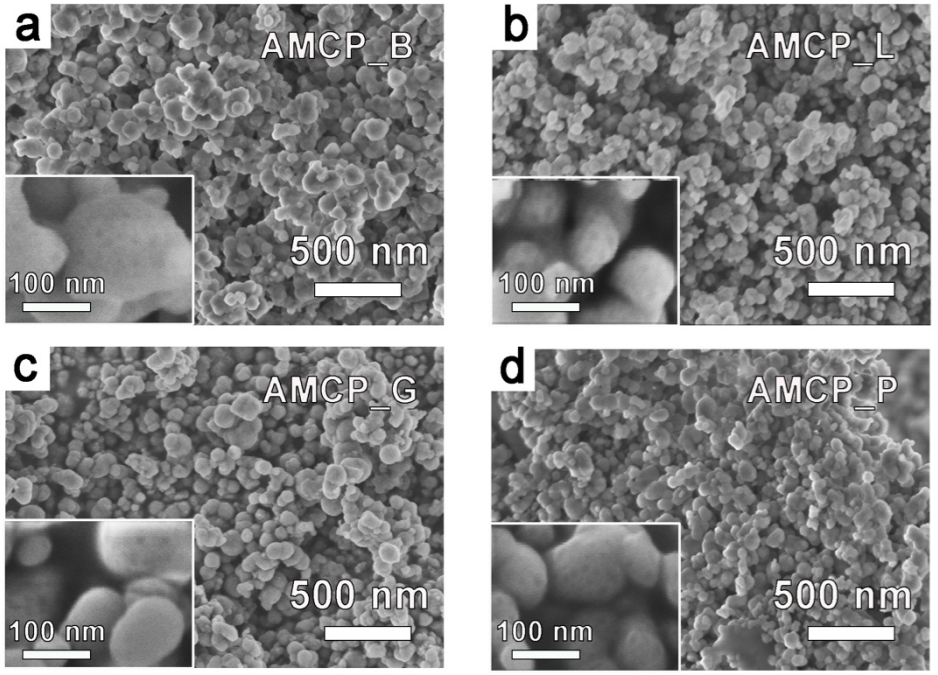

Figure 2.21: FE-SEM micrographs of (a) AMCP_B; (b) AMCP_L; (c) AMCP_G; (d) AMCP_P. In the insets, high magnification images are shown.

The type of additive used in the synthesis does not influence the morphology of the particles, as in all samples we observe the presence of aggregated nanospheres, similarly to AMCP (see Figure 2.19c for comparison). At high magnification, the internally porous nature of the single particles is detectable in all samples (see the insets in Figure 2.21). We can therefore conclude that the presence in solution of the additives does not result in a modification of AMCP's morphology. Moreover, as no peptidoglycan-rich domains are detectable in SEM micrographs, we can conclude that this macromolecule is incorporated in AMCP structure. In terms of chemical composition, the semi-quantitative Ca/Mg ratio measured by means of EDX analysis does not reveal any significant difference among the samples, as we obtain 7.2 ± 1.3 for AMCP_B, 7.2 ± 1 for AMCP_L, 7.4 ± 0.9 for AMCP_G and 6.2 ± 0.6 for AMCP_P: this suggests that the additives do not affect the relative amount of magnesium included in the structure of the particles.

The morphology of AMCP was also assessed by means of TEM microscopy, so to gain some insights into the internal structure of the particles (see Figure 2.22). All the samples display a morphology which is similar to AMCP

prepared without additives (see Figure 2.19d), as the aggregated nanometric particles appear polydisperse and intrinsically porous. As already discussed over SEM results, we do not detect any marked difference among the four samples.

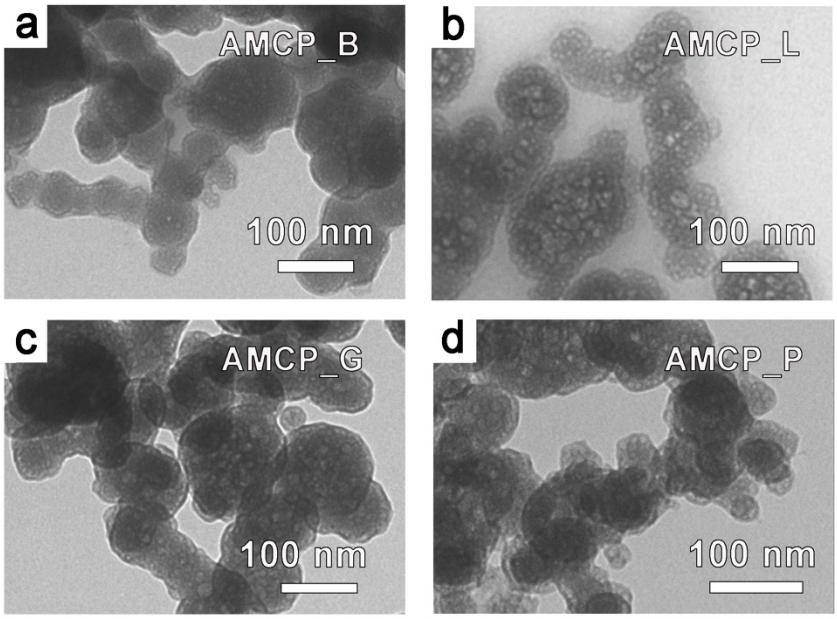

Figure 2.22: TEM micrographs of (a) AMCP_B; (b) AMCP_L; (c) AMCP_G; (d) AMCP_P.

To sum up, the presence in solution of butyric acid, lactose and gluten does not affect the physico-chemical features of endogenous-like AMCPs; peptidoglycan is the only additive which is incorporated in AMCP, despite not affecting the morphology and the Ca/Mg ratio of the particles. This is of outmost importance, as one of the roles that AMCPs is thought to fulfil *in vivo* is the incorporation of bacterial peptidoglycans in the lumen, with the subsequent transport to the immune cells of the intestinal tissue [157].

2.3 Formation in Simulated Intestinal Fluids

As AMCPs form in the distal region of the small intestine, it is of outmost importance to understand which are the conditions of the lumen and try to mimic them, so to reproduce the *in vivo* formation of the particles and gain useful insights in their formation mechanism and features.
The characterization of the intestinal juice composition is challenging, as this medium is typically prone to a large variability in its composition [242]. A possibility to partially mimic the environment in which AMCP form in a standardized condition is to use commercial Simulated Intestinal Fluids (SIF). These media typically consist of aqueous solutions of bile salts (anionic natural steroidal surfactants, typically sodium taurocholate, formula shown in Figure 2.23a) and phospholipids (such as lecithin, formula shown in Figure 2.23b), in addition to other components that allow the fluid to mimic the pH, the osmolality and the buffer capacity of each specific tract of the gut [243, 244]. These media have been developed to assess the dissolution and solubility of drugs, but can be regarded as valuable tools to mimic the gastrointestinal environment. As AMCP form in the ileum, we chose for our investigation the SIF which mimic specifically this region of the gut [243].

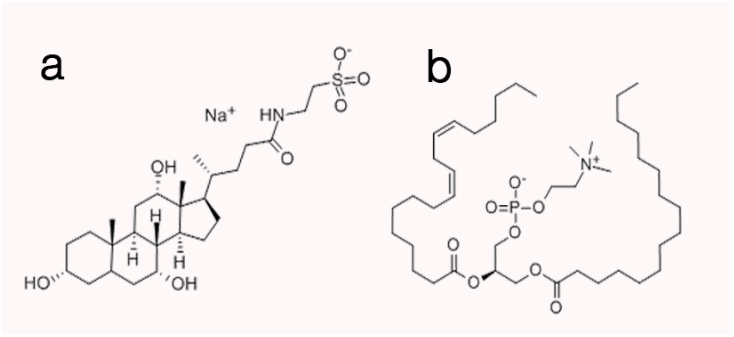

Figure 2.23: Formula of (a) sodium taurocholate and (b) lecithin.

2.3.1 Experimental protocols

2.3.1.1 Preparation of SIF

The SIF specifically mimicking the ileum region of the gut was prepared according to the instructions given by the supplier (Biorelevant.com Ltd).

500 mL of the fluid were prepared by dissolving 0.880 g of NaCl, 3.065 g of maleic acid (≥ 99 %, Sigma-Aldrich) and 2.115 g of NaOH in deionized water (450 mL). A solution of NaOH 2 M was used to adjust the pH at 7.5, then we made up to the final volume with water. 0.3 g of powder ("FaSSIF/FeSSIF/FaSSGF") were dissolved in the prepared buffer, and the fluid was let stand for at least 2 h before use. The medium was used within 24 h from the preparation. The final concentrations of the components are reported in the table below.

Table 2.5: SIF composition, according to the producer [243].

SIF composition	
Sodium taurocholate	0.8 mM
Lecithin	0.2 mM
Maleic acid	52.8 mM
Sodium hydroxide	105 mM
Sodium chloride	30.1 mM
pH	7.5
Osmolality	190 mOsm/Kg
Buffer capacity	10 (mmol/L)/ΔpH

2.3.1.2 Synthesis of AMCP in SIF and in water

AMCP was obtained by mixing equal volumes (200 mL) of two solutions, namely solution A and solution B_1 (same concentrations as in Table 2.1). Two syntheses were conducted using the same procedure, except for the fact that the salts were dissolved either in SIF or water. Solution A and B_1 were separately heated at 37 °C in a water bath. Solution A was added to solution B_1 and the pH was adjusted to 7.50 by dropwise addition of NaOH 2 M. Aliquots of the solution (~20 mL) were periodically withdrawn from the reaction flask and filtered using a Millipore vacuum filtration system equipped with mixed cellulose esters filters (Millipore, pore size 0.22 μm). Filters were immediately placed in plastic test tubes and frozen in liquid nitrogen, prior to lyophilization for 24 h.

2.3.1.3 Dispersion of AMCP in SIF

The stability of AMCP in SIF was also evaluated by dispersing dried particles (prepared as described in paragraph 2.1.1.1 at pH 7.40 and collected after 15 min) in SIF, at pH 7.50. 50 mg of AMCP were dispersed in 140 mL of SIF at pH 7.510, at 37 °C under stirring. Aliquots of the solution were collected after 15 min, 1 h, 3 h, 6 h, 8 h, 14 h, 20 h, 24 h and 48 h. The separation of the particles from the solution was performed as described in the previous paragraph.

2.3.2 Results and discussion

2.3.2.1 SIF characterization

The prepared SIF was characterized in order to investigate the presence of self-assembled structures. Literature reports on similar systems show that the simultaneous presence in solution of bile salts and lecithin often results in the formation of self-assembled structures, such as mixed micelles, depending on their molar ratio, concentration, pH, ionic strength and temperature [244–250]. DLS analysis, performed at 37 °C, revealed the presence of nanosized objects with a mean hydrodynamic radius of 17 nm and high polydispersity (0.28), in good accordance with previously synthesized taurocholate-lecithin colloids [244] (see Figure 2.24a).

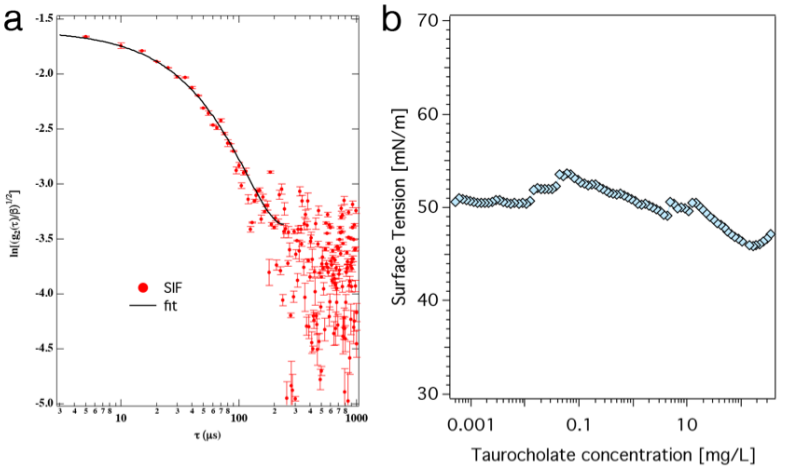

Figure 2.24: (a) DLS autocorrelation function of SIF (red full circles) together with cumulant analysis fit (black solid line) (b) Surface tension vs taurocholate concentration in the SIF, which does not reveal a defined CMC.

The interfacial properties of the medium were examined by means of force tensiometry. We found that the SIF does not show a CMC, as the surface tension does not display a steep decrease at a given concentration value (see Figure 2.24b). Again, this is in agreement with the literature, as many data suggest that for bile salts the transition from monomeric to micellar solution occurs stepwise over a broad range of concentrations [245, 251].

2.3.2.2 AMCP stability

We assessed the stability of AMCPs prepared in SIF and in water, to evaluate the effect of the taurocholate and lecithin on their crystallization process. The kinetic was monitored by means of FT-IR spectroscopy, and the results are shown in Figure 2.25.

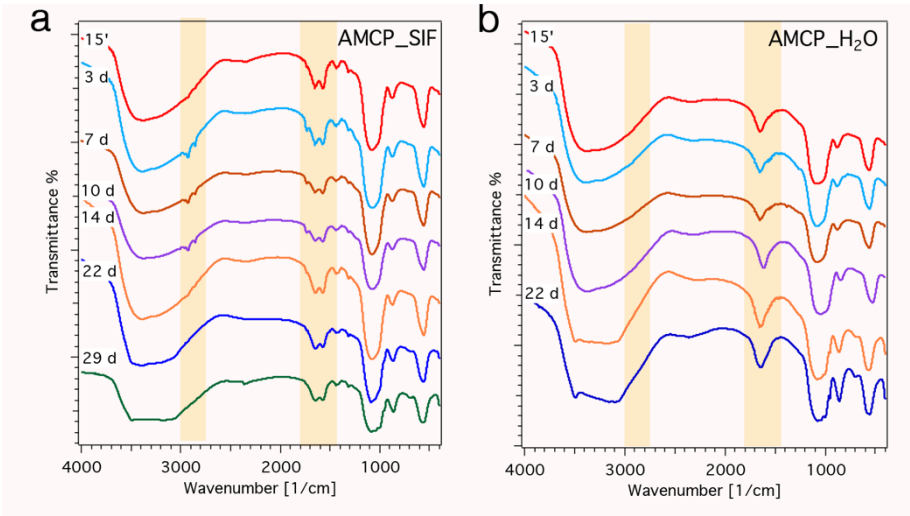

Figure 2.25: FT-IR spectra of AMCPs synthesized in (a) SIF and (b) water; the spectra are offset for display purposes. The highlighted regions emphasize the areas where diagnostic signals of the molecules in the SIF are present.

As described for the synthesis at different pHs (paragraph 2.1.2.1), we observe in both systems the transition from amorphous to crystalline phosphate in time. Interestingly, the lifetime of the amorphous phase in the two media is different, as in SIF the first signatures of crystallinity in the spectrum appear after 29 days, while in water the spectrum of the 14 days-product shows a small peak at 3489 cm^{-1}, together with the initial splitting of the ν_3 phosphate stretching peak around 1000 cm^{-1}. This stabilizing action is

likely due to the effect of taurocholate, which is known to inhibit the precipitation of crystalline calcium phosphates [251]. The spectra of the crystalline products (blue curves) are different from those discussed in the previous paragraph, and are compatible with bobierrite ($Mg_3(PO_4)_2 \cdot 8H_2O$, see peaks' assignment in Table 2.6) [252].

Table 2.6: FT-IR peaks' assignment of bobierrite [252].

Bobierrite ($Mg_3(PO_4)_2 \cdot 8H_2O$)	
Peak [cm^{-1}]	Assignment
3490	Water
3110	Water
1645	Water
1080	ν_3 stretching phosphate
1044	ν_3 stretching phosphate
1001	ν_3 stretching phosphate
953	ν_1 stretching phosphate
859	Not assigned
555	ν_4 bending phosphate

It is worth highlighting that here, when we synthesize AMCP at pH 7.5, the observed crystalline phase is bobierrite, while at pH 7.4 (see paragraph 2.1.2.1) we observe the transition towards newberyite ($MgHPO_4 \cdot 3H_2O$). This difference is ascribable to the slightly more alkaline conditions [1], which may shift the equilibrium of HPO_4^{2-} towards PO_4^{3-}.

In order to gain more insights into the crystallinity of these materials, selected samples were analyzed by means of XRD, and the diffractograms are reported in Figure 2.26. The analysis of the XRD patterns confirms the observations conducted over FT-IR results, as it reveals the amorphous nature of the particles collected after 15 min and the formation of bobierrite with aging (PDF: 33-0878). The stabilization effect of the SIF is evident from the comparison of the diffractograms of the products collected after 22 days (blue patterns in Figure 2.26), which clearly show higher crystallinity of the sample prepared in water.

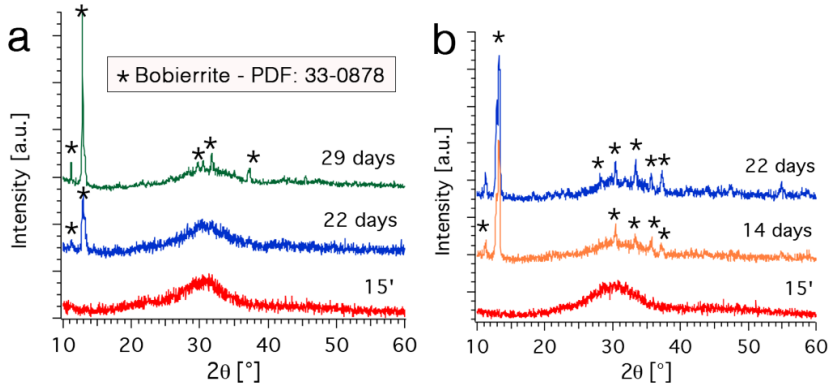

Figure 2.26: (a) XRD patterns of AMCPs_SIF collected after 15 min, 22 and 29 days of reaction; (b) XRD patterns of AMCPs_H_2O collected after 15 min, 14 and 22 days of reaction. The diffractograms are offset for display purposes.

The morphology of the amorphous and crystalline particles as obtained by means of FE-SEM is reported in Figure 2.27.

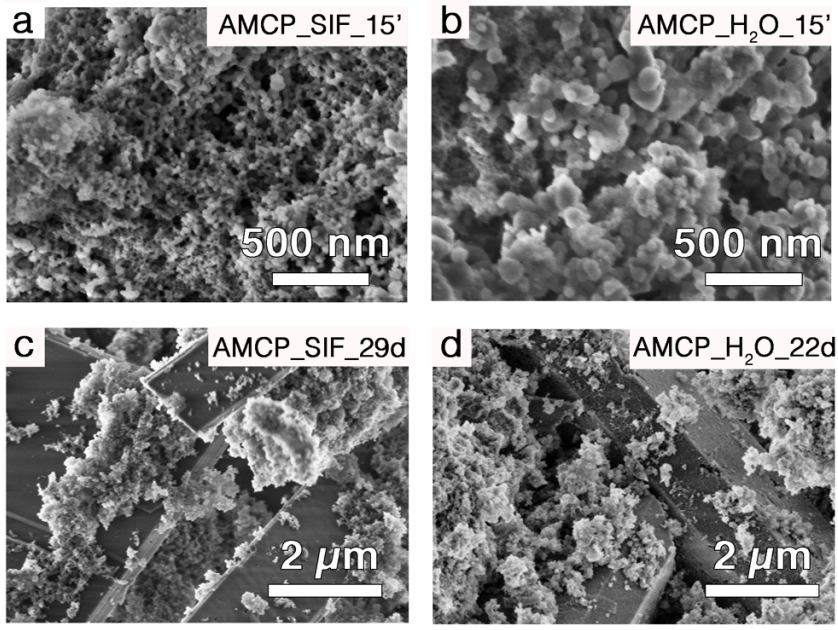

Figure 2.27: FE-SEM micrographs of (a) AMCP_SIF_15min; (b) AMCP_H_2O_15min; (c) AMCP_SIF_29d; (d) AMCP_H_2O_22d.

When comparing AMCPs collected after 15 min prepared in SIF (Figure 2.27a) and water (Figure 2.27b), we observe that the presence of the organic molecules in the SIF affects the morphology of the particles: AMCPs synthesized in this medium appear much smaller and interconnected than those obtained from the analogous procedure in water. On the other hand,

bobierrite crystals formed upon conversion of AMCPs show the same morphology in both syntheses, namely parallelepiped-like objects surrounded by amorphous particles (Figure 2.27c and d).

2.3.2.3 *Incorporation of organic molecules*

A peculiar feature of endogenous AMCPs is their ability to trap antigens and peptidoglycans in the lumen, acting like a shuttle for the delivery of the organic cargo to the immune cells in the intestinal wall lining [157, 167]. The ability of AMCP-like nanoparticles to trap macromolecules during formation was investigated *in vitro* by Pele *et al.*, who found macromolecule-incorporation properties similar to the *in vivo* counterpart [166]. Our experiments described in section 2.2.2 also confirmed the ability of AMCP to incorporate peptidoglycan. As we observed that the organic molecules present in the SIF affect the stability and the morphology of the synthesized particles, we inspected their incorporation/adsorption on AMCPs. The comparison of FT-IR spectra synthesized in SIF and in water gives a hint in this direction, as an additional peak at 1576 cm^{-1} is present in all samples prepared in SIF (see the highlighted regions in Figure 2.25). Moreover, samples collected from 3 to 10 synthesis days also present absorptions at 1733 cm^{-1}, 2855 cm^{-1} and 2927 cm^{-1}. These signals are compatible with the stretching vibrations of C-C and C-H bonds in lecithin and taurocholate, as it is shown in Figure 2.28.

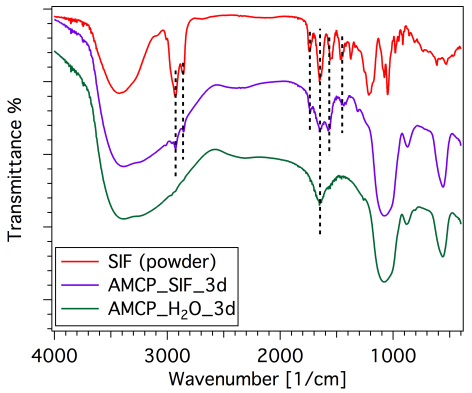

Figure 2.28: Comparison of the FT-IR spectra of AMCPs after 3 synthesis days (purple curve in SIF, green curve in water) with the powder used to prepare the SIF, which contains sodium taurocholate and lecithin. The spectra are offset for display purposes.

The red spectrum in the Figure refers to the powder used to prepare SIF (as received), which only contains sodium taurocholate and lecithin; the incorporation of these organic molecules in AMCPs is therefore demonstrated. The different number of peaks among the samples prepared in SIF may be due to a different amount of organic material incorporated in the particles. This parameter was estimated by means of thermogravimetry, comparing the extent of the weight losses % at 1000 °C. The analysis of the thermograms given in Figure 2.29a reveals that AMCP_SIF samples show a time-dependent weight loss, which is in all cases higher than that of AMCP_H_2O_15min, consistently with the thermal degradation of some organic material incorporated in the particles: in fact, the TGA profiles of the analyzed samples differ in the extent of the weight losses in the range 200-450 °C, due to the degradation of organic molecules (see the derivative thermogravimetric curves in Figure 2.29b).

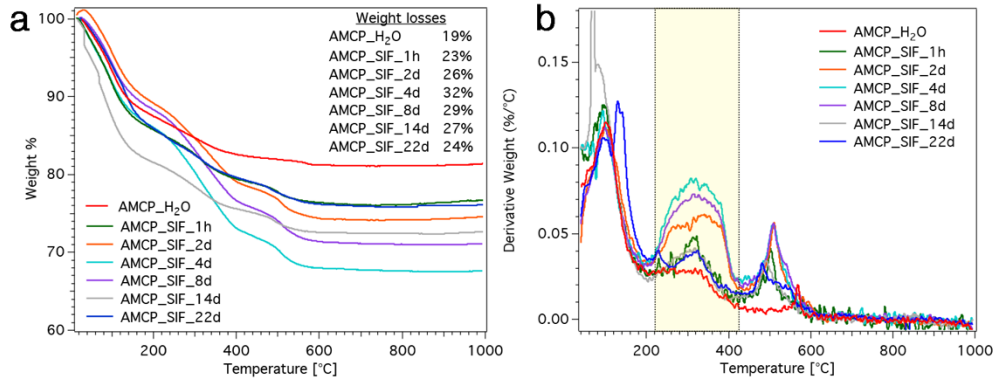

Figure 2.29: Thermogravimetric analysis of AMCP_SIF: (a) weight % as a function of T and (b) derivative weight % as a function of T. The highlighted area shows the region in which the curves display major variations.

The weight loss % as a function of time, reported in Figure 2.30 (red diamonds), reveals that the amount of organic material in AMCP_SIF samples increases during the early stages of the synthesis, reaches a maximum after ~4 days and then decreases. The samples showing the highest weight losses are the ones displaying, in the FT-IR spectra, the peaks at 1733 cm^{-1}, 2855 cm^{-1} and 2927 cm^{-1} (see Figure 2.25a), confirming that these additional infrared features are due to the higher relative amount of organic

material in the samples. We sought to understand the reason for this phenomenon, and we hypothesized that different specific surface areas of the samples and/or different particles' size could lead to a dissimilar behavior in terms of organic molecules' extent of adsorption. The analysis of the samples by means of nitrogen sorption measurements did not reveal any peculiar trend of the BET specific surface area as a function of time (see Figure 2.30, blue triangles). The analysis of the size distribution of the particles was conducted by means of laser granulometry on aliquots withdrawn from the reaction medium, which were analyzed using as dispersant medium absolute ethanol (we chose not to use water to prevent potential dissolution/crystallization phenomena of AMCPs). The plot of D_{10}, D_{50} and D_{90} as a function of reaction time is shown in Figure 2.30b: no significant variations in the size distribution of the particles is observed, except for a slight increase in D_{50} and D_{90} after 22 reaction days. We can conclude that the reason why the amount of organic material in AMCP synthesized in SIF reaches a maximum after about 4 days is still unclear, as it does not depend on variations in specific surface area or particles' size.

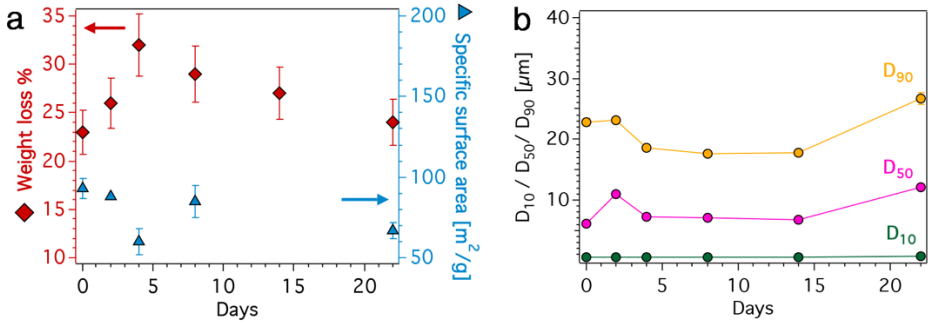

Figure 2.30: (a) Weight loss % (red diamonds) and BET specific surface area (blue triangles) as a function of reaction days for AMCP_SIF. The error bars associated to the weight losses, which are 5 % of the value, account for the discrepancies arising from different measurements on samples from two analogous syntheses; (b) D_{10}, D_{50} and D_{90} (μm) obtained by means of laser granulometry on aliquots withdrawn from the reaction medium.

Interesting information on the effect of the organic molecules embedded in AMCP can be obtained from the heat flow profile acquired simultaneously to the thermogravimetry experiments (see Figure 2.31a): as discussed in paragraph 2.1.2.2, while heating AMCP, two exothermic events appear in the heat flow profile, corresponding to the crystallization towards a whitlockite-

like sodium calcium magnesium phosphate (PDF: 45-0136, see the red curve in Figure 2.31a).

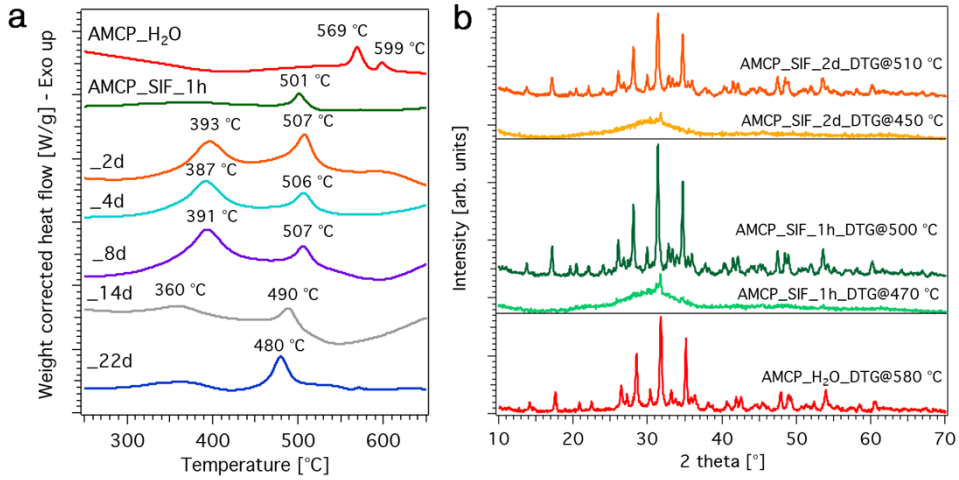

Figure 2.31: (a) Heat flow profiles of AMCP_SIF at different reaction days, compared with AMCP_H_2O (red curve). The curves are offset for display purposes. The baselines were subtracted using a 3rd order polynomial function; (b) XRD patterns of AMCP_SIF analyzed by means of thermogravimetry before and after the crystallization peak.

Interestingly, the amorphous particles prepared in SIF also crystallize when heated, but the exothermic peaks are shifted towards lower temperatures. To understand the nature of these phases, selected samples were recovered after the TGA experiment, interrupting the measurement after the first and the second exothermic peak. XRD analyses (Figure 2.31b) reveal that crystallization occurs in correspondence of the second exothermic peak, and the obtained phase is the same that forms when AMCP are prepared in water (red pattern in Figure 2.31b). As exothermic transitions occur from a less ordered to a more ordered state, the shift to lower temperatures of the peaks indicates that less energy is required for the crystallization to occur for AMCP_SIF samples, suggesting that the amorphous phase is even more disordered than when prepared in water, *i.e.* it is easier for the structural units composing AMCP to re-arrange into a crystalline form.

2.3.2.4 AMCP structure at the nanoscale

The structure at the nanoscale of AMCPs prepared in SIF was compared to their counterpart obtained in water, to investigate if lecithin and taurocholate

affect the nanostructure of the amorphous particles. As the endogenous self-assembly of AMCPs constantly occurs in mammalian gut, we inspected the structure of AMCPs obtained after few minutes from the beginning of the reaction, as we expect the *in vivo* formation process to be relatively fast. TEM micrographs of AMCP_SIF_15min and AMCP_H_2O_15min are compared in Figure 2.32.

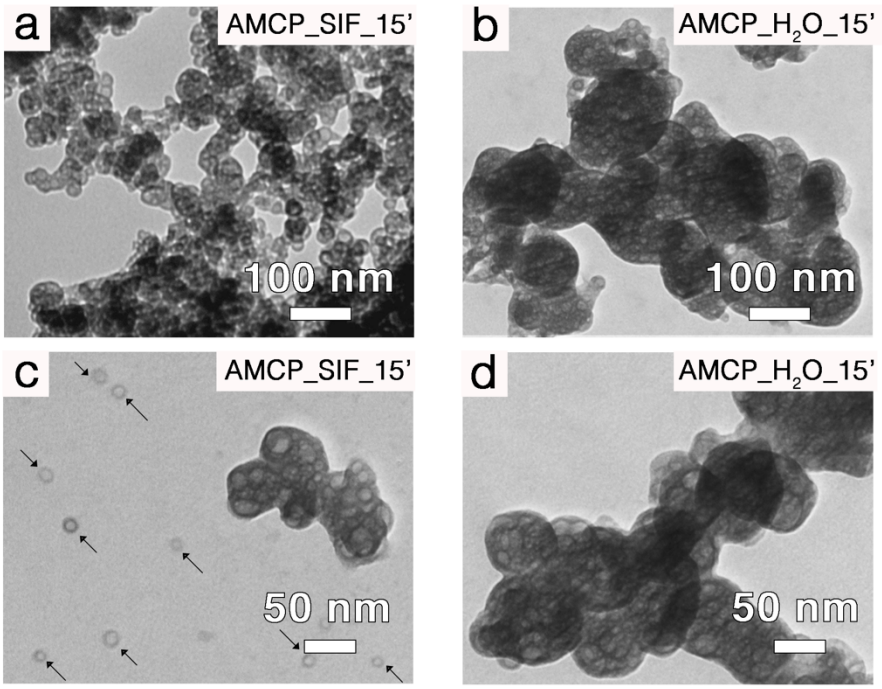

Figure 2.32: TEM micrographs of (a + c) AMCP_SIF_15min and (b + d) AMCP_H_2O_15min at low (a+b) and high (c+d) magnification. The black arrows in (c) highlight the core-shell-like structures.

The images at lower magnification (Figure 2.32a and b) confirm the observations conducted over SEM results, *i.e.* the amorphous particles obtained in SIF are smaller than those synthesized in water; moreover, in both cases, the nanometric objects are clustered and endowed with nanometric porosities, similarly to the endogenous ones [157]. The high magnification micrographs (Figure 2.32c and d) reveal a very peculiar feature of AMCPs prepared in SIF: together with clustered structures analogous to the ones obtained from the synthesis in water, we can observe isolated core-shell structures (highlighted by the black arrows in (Figure 2.32c). These objects have a core diameter of (10 ± 3) nm and a shell thickness of (3 ± 1) nm. As the

shell is more electron-dense than the core, we hypothesize that when AMCP self-assemble in the SIF, a portion of the inorganic material forms a shell on the micelles that are present in the fluid (see paragraph 2.3.2.1) resulting in core-shell structures. Therefore, our findings suggest that at least a part of the organic material detected by means of FT-IR spectroscopy and TGA is incorporated in AMCPs thanks to the self-assembled taurocholate/lecithin structures present in solution. Hollow nanospheres made of calcium phosphate have already been reported in the literature in the presence of several templating agents, such as block copolymers [253, 254], lecithin [255], polystyrene [256], phenol-formaldehyde resin spheres [257], polyelectrolytes [258], amino acids and dipeptides [259], and surfactants [260]; nevertheless, our finding is the first example of CaP-based shells driven by taurocholate-lecithin micelles.

AMCP structure at the nanoscale was further explored by means of SAXS analysis. The curves of both AMCP_SIF_15min and AMCP_H_2O_15min, reported in Figure 2.33, display a very low scattering intensity at high q values ($q > 0.1$ Å^{-1}) followed by an upturn in the mid- and low-q regions due to the presence of AMCP aggregates.

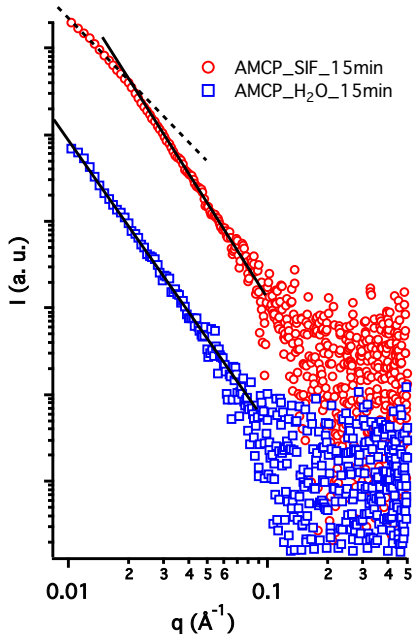

Figure 2.33: Log-log representation of SAXS curves of AMCP_SIF_15min (red circles) and AMCP_H_2O_15min (blue squares) samples. Black solid and dashed lines represent curve fittings according to Eq. 2.1.

The presence of core-shell particles as revealed by TEM micrographs on AMCP_SIF_15min sample is not found in the SAXS curve, thus suggesting that the overall scattering intensity is mainly dominated by the aggregates. The fractality of the system was investigated by fitting the experimental curves in the $0.01 > q > 0.1$ Å^{-1} range with the equation:

$$I(q) = A\, q^{-p} \tag{2.1}$$

where A is a scale factor and p is the slope of the linear fitting. When $1 \leq p \leq 3$, p represents the mass-fractal dimension (D_m) that is 3 for full solid materials [261]. When $3 \leq p \leq 4$, one can calculate the surface-fractal dimension (D_s) from the equation:

$$D_s = 6 - p \tag{2.2}$$

Typically, D_s is 2 for smooth surfaces, and goes towards 3 as the roughness increases [262]. Fitting the AMCP_H_2O_15min results in $p = 3.37 \pm 0.01$ (black solid line in Figure 2.33). According to Eq. 2.2, this corresponds to a surface-fractal dimension $D_s = 2.63$. For AMCP_SIF_15min, a similar pattern is found in the mid-q region with $p = 3.45 \pm 0.01$ and $D_s = 2.55$, which indicates that, in this dimensional range, the surface of AMCP particles in water is slightly rougher than that in SIF. A second power law dominates the scattering in the low-q region of AMCP_SIF, with $p = D_m = 2.37 \pm 0.01$ (black dashed line). The cause of this surface (primary domain) to mass (secondary domain) fractal crossover can be found in the micelles present in SIF structuring the AMCP aggregates into less compact domains. This behavior has been previously reported for particles assembling in solutions and gels when the environment surrounding the particles is changed [263, 264], which in our case can be referred to the use of water or SIF as the reaction medium.

2.3.2.5 Dispersion of AMCP in SIF

In order to gain more insights into the stabilizing effect given by taurocholate and lecithin, we performed an additional experiment by dispersing dried AMCPs in SIF, as described in section 2.3.1.3. We monitored the

crystallization kinetic by means of FT-IR spectroscopy, and the results are shown in Figure 2.34a.

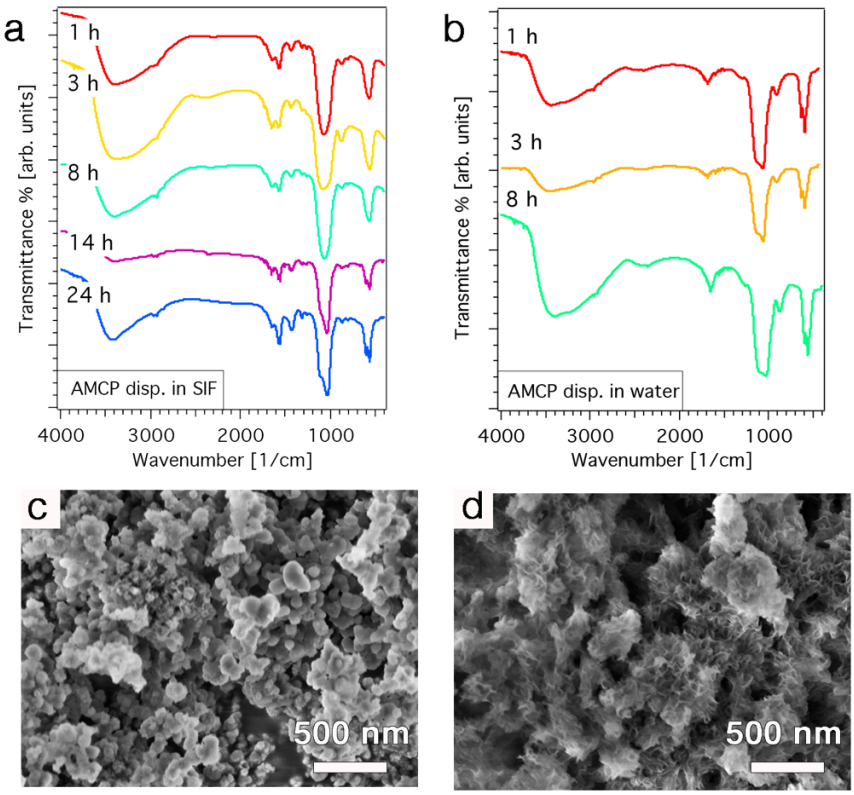

Figure 2.34: (a,b) FT-IR spectra of AMCP dispersed in (a) SIF and (b) water as a function of incubation time; (c,d) FE-SEM micrographs of AMCP dispersed in SIF and collected after (c) 1 h and (d) 24 h.

Comparing the results with the spectra of AMCPs dispersed in phosphate buffer at the same pH and concentration (Figure 2.34b), we can observe that the stabilizing effect of the organic molecules is retained even when AMCPs are dispersed in the medium instead of being synthesized in it: crystallization in SIF occurs after ~14 h, while in water the particles are crystalline after 1 h. The crystalline phase formed in this context is poorly crystalline HA, as it is shown by the shape of the FT-IR peaks (see section 2.1.2.3 for the discussion of FT-IR features) and FE-SEM micrographs (Figure 2.34d). Interestingly, also in this experiment, the signals characteristic of taurocholate and lecithin (region 1300-1800 cm^{-1}) are visible in the spectrum, indicating an incorporation of the organic molecules within AMCP. This suggests a

dissolution/reprecipitation mechanism: when the particles get in contact with the aqueous medium, dissolution begins and the created oversaturation leads to a precipitation process. When precipitating, the particles (both AMCP and poorly crystalline HA) incorporate the organic molecules in the SIF, thus making the results similar to those about the synthesis of AMCPs in SIF.

To sum up, we found out that the presence of lecithin and taurocholate in the medium in which AMCPs form prolongs the lifetime of the amorphous phase; this effect is observed even when dried AMCPs are dispersed in the SIF. Moreover, the presence of the biorelevant molecules in the synthetic medium affects the morphology of the amorphous particles as, at the same time, produces the formation of smaller particles and core-shell like structures templated by the self-assembled structures present in the medium.

2.4 Formation of AMCP in mucin-based systems

In addition to the molecules present in the intestinal juice, AMCPs will likely get in contact with the components of the intestinal epithelium during their formation process, possibly affecting their formation and features. In the small intestine, the epithelium is covered by a single and easily removable mucus hydrogel layer, which forms a diffusion barrier and acts as a protection against hazardous and infective agents [265] (see Figure 2.35a). Alterations in the mucus characteristics can result in pathological situations, such as cystic fibrosis, ulcerative colitis, inflammatory bowel syndrome and Crohn's disease [266, 267]. Among the different molecules composing mucus, mucins form the main skeleton: these large glycoproteins, whose basic structure is shown in Figure 2.35b, are extensively decorated by *O*-linked glycans, which bind water and give to mucus gel-like properties. To date, 21 mucin-type glycoproteins, which collectively belong to the *MUC* gene family, have been identified in the human body [268], and are divided in two main categories, *i.e.* secreted [269] and cell bound [270].

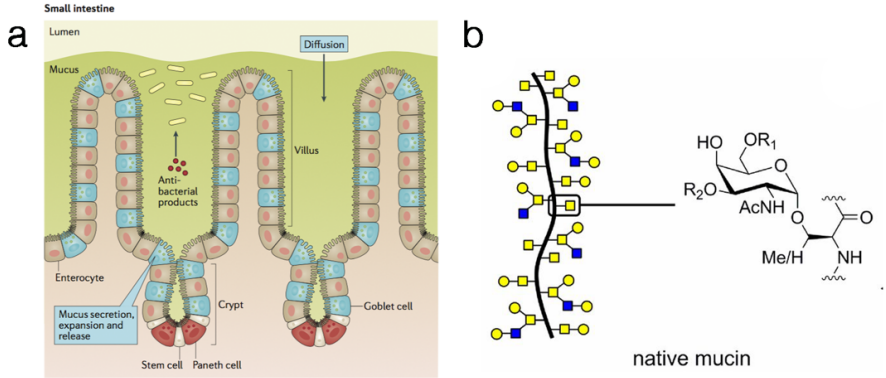

Figure 2.35: (a) Sketch of the mucus layer in the small intestine, reproduced with permission from [265]; (b) structure of native mucin (reprinted with permission from [271]).

Though the interaction of mucin with different types of nanoparticles has been explored in the literature [267, 272–275], its interplay with calcium phosphate-based nanoparticles was never addressed so far. Nevertheless, this topic assumes great relevance in the framework of AMCPs formation in the intestine, as the understanding of the effect of mucin on the formation and features of AMCPs could contribute to unravel their largely unexplored *in vivo* formation mechanism. In this section, we describe AMCPs synthesis

in different mucin-based systems: as the layer of mucin in the small intestine is defined as "loose and unattached" [266], mucin's hydrogels and dispersions were chosen as simple models to mimic the intestinal layer.

2.4.1 Experimental protocols

2.4.1.1 Synthesis of AMCP in mucin hydrogels

As previous experiments showed that AMCPs can be effectively obtained by mixing two aqueous solutions containing calcium, magnesium and phosphates, our initial idea for synthesizing AMCP in mucin hydrogels involved two steps, *i*. dissolution of mucin in solution A (see the composition in Table 2.7) to form a hydrogel, and *ii.* addition of solution B on the top of the hydrogel. For step *i*, 0.250 g of mucin (Mucin from porcine stomach type II, Sigma-Aldrich) were dissolved in 0.50 mL of water (sample B_0) or of solution A_1-A_5 (see Table 2.7). The pH of the solutions A and B was separately adjusted at 7.50 by dropwise addition of NaOH 2 M. After mixing, samples were equilibrated in plastic vials at room temperature for 24 h; afterwords, 0.50 mL of solution B_1 (see Table 2.1, pH adjusted at 7.50) were added on the top of the hydrogel, and equilibrated for 24 h. After the removal of the supernatant, samples were freeze-dried for 24 h.
Another set of samples was prepared using a more diluted hydrogel (0.100 g of mucin with 0.50 mL of solution) with water and solution A_3.

Table 2.7: composition of the solutions used to prepare mucin hydrogels.

Salt	A_1	A_2	A_3	A_4	A_5	A_M
$CaCl_2$	4 mM	10 mM	15 mM	40 mM	100 mM	37.5 mM
$MgCl_2{\cdot}6H_2O$	10 mM	10 mM	10 mM	100 mM	250 mM	25 mM
NaCl	135 mM	135 mM	135 mM	135 mM	135 mM	135 mM

2.4.1.2 Synthesis of AMCP in mucin dispersions

For the synthesis of AMCP in mucin dispersions, 5, 50 and 500 mg of mucin were dispersed using magnetic stirring in 5 mL of solution A_M at 37 °C (see

Table 2.1), to obtain dispersion at 1, 10 and 100 mg/mL (samples "AMCP_1", "AMCP_10" and "AMCP_100"). The different concentrations of salts in solution A used in this synthesis were adopted to increase AMCP yield, while obtaining amorphous particles with a Ca/Mg ratio compatible with that of the endogenous ones (data not shown). 5 mL of solution B (see Table 2.1) were added to mucin dispersion at 37 °C, and the pH was adjusted to 7.50 by dropwise addition of NaOH 2 M. After 15', the solution was centrifuged at 6000 rcf for 3', and the supernatant discarded. The solid was washed 3 times with denatured ethanol (5 mL of ethanol for the initial 10 mL of reacting solution) and dried with N_2 flux and in desiccator using vacuum for 30'.

2.4.2 Results and discussion

2.4.2.1 AMCP in mucin hydrogels

We first characterized the freeze-dried mucin hydrogels B_0, B_A_1, B_A_2 and B_A_3, aiming at understanding if we obtained the formation of AMCPs within the gel matrix. The top portion of the xerogel was analyzed, as we expected a higher amount of particles in the region of contact of solution B with the hydrogel. Results are shown in Figure 2.36. We were not able to detect AMCP formation in any of the prepared samples: both the FT-IR spectra (Figure 2.36a) and XRD patterns (Figure 2.36b) are not significantly different from those of mucin hydrogel prepared with water (red curves in the figure). The only peaks present in XRD pattern of B_A_1 and B_A_3 are due to NaCl crystals. Thermogravimetry was carried out to estimate the amount of inorganic material formed in the hydrogel matrix (Figure 2.36c) but, again, no clear evidence of AMCP formation was found (weight loss for B_0: 97.5 %, B_A_1: 91 %, B_A_2: 80 %, B_A_3: 89 %). The morphology of the xerogels, analyzed by means of FE-SEM, showed only the presence of structures compatible with organic material. We hypothesized two explanations for the lack of AMCP formation within mucin matrix: *i.* the gel network is too thick and does not allow for the diffusion of solution B, preventing the interaction of phosphate with Ca^{2+} and Mg^{2+}; *ii.* the amount of calcium and magnesium ions is too low.

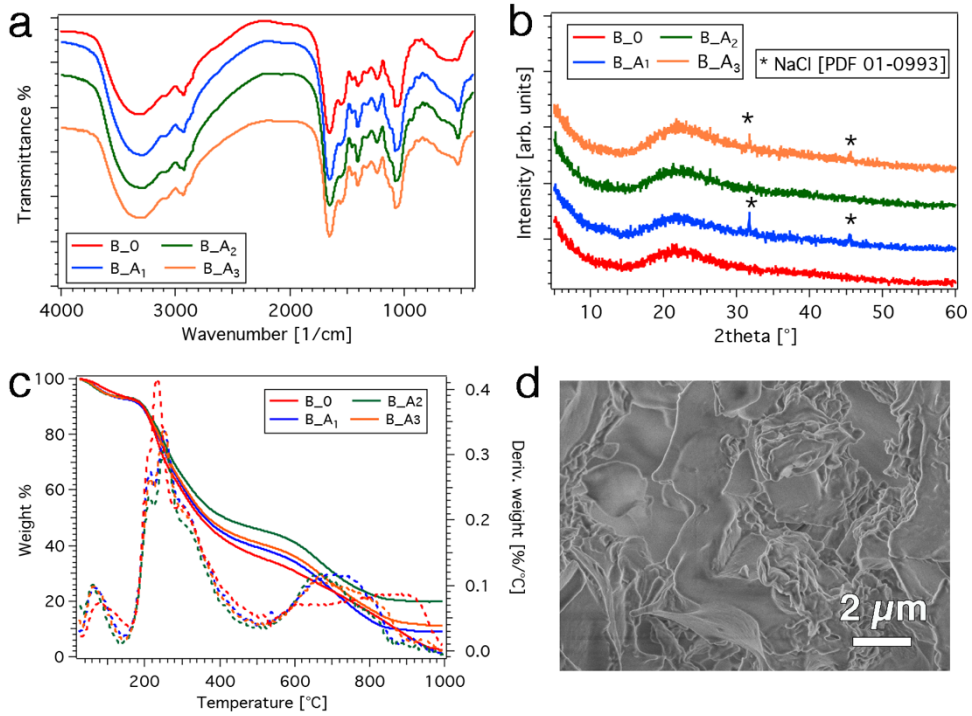

Figure 2.36: Characterization of samples B_0, B_A1, B_A2, B_A3: (a) FT-IR spectra, (b) XRD diffractograms, (c) thermal analysis; (d) representative FE-SEM of the samples' morphology.

In order to assess these two hypotheses, we prepared samples B_A4 and B_A5, at higher Ca^{2+} and Mg^{2+} concentrations, and a more diluted gel (see the preparation in section 2.4.1.1). The FT-IR spectra displayed in Figure 2.37 show that, again, AMCP formation did not occur in the prepared samples, as the curves do not show any difference with respect to mucin (B_0, red spectra).

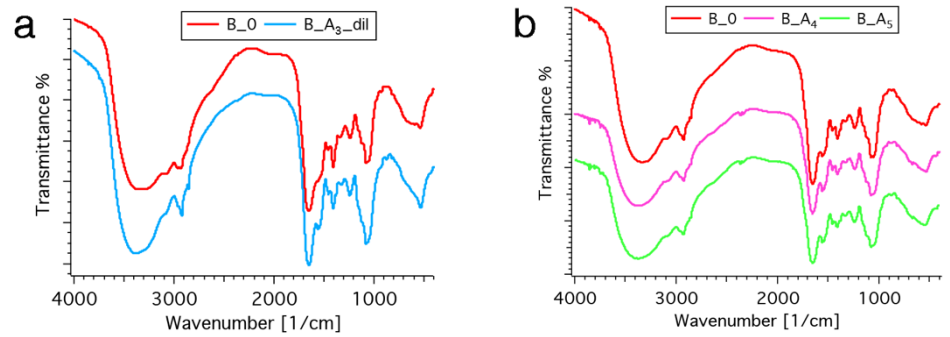

Figure 2.37: FT-IR spectra of (a) diluted gel (light blue) vs mucin (red) and (b) sample B_A4 and B_A5 (concentrated solutions). The spectra are offset for display purposes.

We can therefore conclude that we were not able to obtain the formation of AMCP in mucin hydrogels or, at least, not in detectable amounts. In fact, to understand if a small amount of AMCPs in mucin hydrogels could be detected, we performed an additional test by preparing hydrogels mixing mucin powder with a dispersion of dried AMCPs (0.250 g of mucin with 0.5 mL of AMCP dispersion at 50 mg/mL). Even in this case, AMCP signals were not detectable in the FT-IR spectra (data not shown), suggesting that, at a particle to mucin ratio of 0.1 by weight, AMCPs are not detectable by FT-IR. We hypothesize that the absence of formation of a detectable amount of AMCP within gel matrix might be due to a poor diffusion of solution B in mucin hydrogel and/or to the fact that the ions are bound to the hydrogel and are not free to interact with each other to form the particles.

2.4.2.2 AMCP in mucin dispersions

As a second scenario, we addressed the synthesis of the particles in mucin dispersions, as described in section 2.4.1.2, preparing AMCPs in the presence of 1, 10 and 100 mg/mL of mucin. XRD and FT-IR characterization is reported in Figure 2.38.

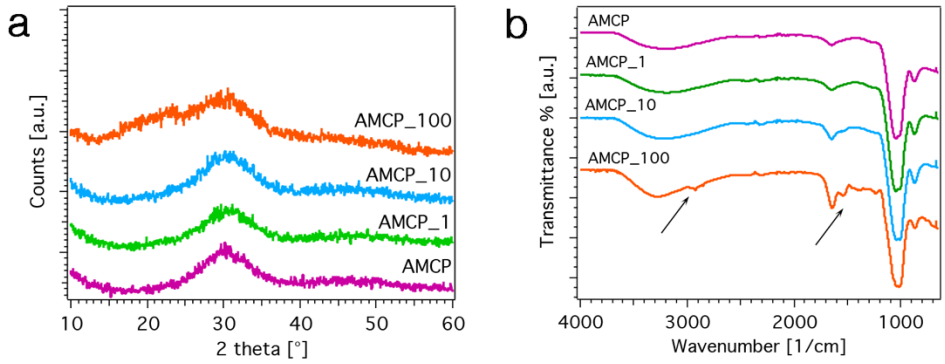

Figure 2.38: (a) XRD patterns and (b) FT-IR spectra of AMCP synthesized in the presence of different mucin concentrations. The curves are offset for display purposes.

Results show that in all systems we successfully obtained the formation of amorphous particles, as it is revealed by the broad hump around 30° in the XRD pattern. In sample AMCP_100, the shoulder in the 2θ range 15-25° is due to mucin (see the patterns in Figure 2.36b). FT-IR spectra are consistent with these considerations, showing the signals distinctive of the amorphous

phase (see Table 2.2) and of mucin in sample AMCP_100 (see the arrows in Figure 2.38b). The amount of mucin incorporated within AMCP was estimated by means of thermogravimetry, and the curves are reported in Figure 2.39a. While sample AMCP_1 displays a weight loss comparable to AMCP (22 %), AMCP_10 and AMCP_100 lose respectively 30 % and 60 % of their initial weight, revealing that a significant amount of mucin is incorporated in the particles.

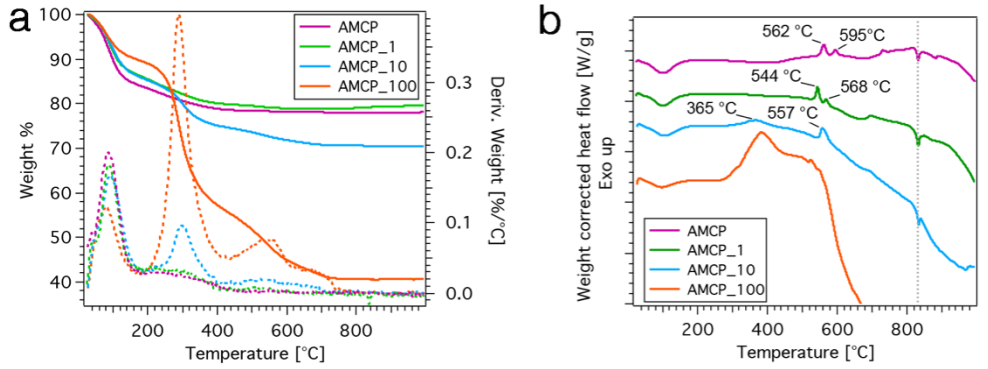

Figure 2.39: Thermal analysis of AMCP prepared in mucin dispersions: (a) TGA curves and (b) heat flow profiles. The heat flow profiles are offset for display purposes.

The heat flow profiles collected simultaneously to the thermogravimetry measurement (Figure 2.39b) show that the thermally-induced crystallization of the amorphous phase is shifted when AMCPs are prepared in mucin dispersions. Interestingly, even for sample AMCP_1, in which no mucin could be detected, the peaks are shifted towards lower temperature. As discussed in section 2.3.2.3, this difference suggests that the presence of mucin during the synthesis and/or its incorporation in AMCP provokes some structural differences in the amorphous phase, which crystallizes at a different temperature.

The morphology of the particles was inspected by means of scanning electron microscopy, and the results are shown in Figure 2.40. No significant difference in the appearance and size of the amorphous particles is detected when mucin is present in the synthetic medium, as in all cases we observe nanometric particles with a heterogeneous size distribution. Sample AMCP_100 (Figure 2.40d) shows that a portion of the amorphous particles has a rough and irregular surface, suggesting a superficial adsorption of

mucin. EDX analysis does not reveal any difference in the Ca/Mg ratio of the particles (AMCP: 2.3 ± 0.1, AMCP_1: 2.4 ± 0.3, AMCP_10: 2.5 ± 0.2, AMCP_100: 3.9 ± 1.5).

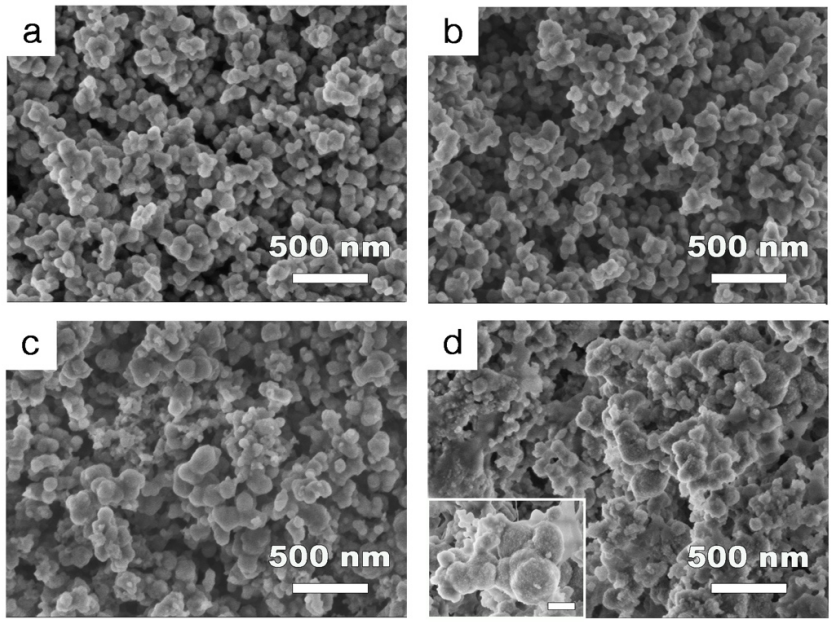

Figure 2.40: FE-SEM micrographs of AMCPs synthesized in the presence of mucin dispersions: (a) AMCP; (b) AMCP_1; (c) AMCP_10; (d) AMCP_100.

To sum up, results show that the presence of mucin in the synthetic medium where AMCPs form does not significantly affect the morphological and chemical features of the amorphous particles. Further studies are necessary to establish if a specific interaction between mucin and AMCP exist. A technique suitable to this purpose would be solid state NMR, as the analysis of the shift of the ^{31}P peaks may indicate an interaction at the atomic level between the organic and the inorganic components.

2.5 AMCP and proteins extracted from *Moringa Oleifera*

We discussed in the Introduction the biological function of AMCP, able to load organic macromolecules (antigens and peptidoglycans) and to release them in the site of interest. Taking inspiration from their endogenous role, we decided to test a potential application of this material as a platform for the loading of actives, for use in the field of drug delivery and nutraceutics. Among the plethora of molecules and macromolecules that could be selected for this case study, we chose to investigate the effect of proteins extracted from *Moringa Oleifera* seeds. *Moringa Oleifera* is a tree native to tropical and subtropical regions of South Asia, which has an impressive range of medicinal uses and high nutritional values. Different parts of this plant contain a profile of important minerals, and are a good source of protein, vitamins, β-carotene, aminoacids and various phenols [276]. Its seeds are largely employed for the treatment of water and wastewater [277] and are reported to have antimicrobial activity [276]. As *Moringa*-based dietary supplements are commonly used, we aimed at exploring AMCP capability to incorporate this protein, for a potential application in nutraceutics. Nanocarriers are frequently used to load food products, in order to improve their bioavailability and protect valuable nutraceuticals at food processing or digestion [278]. The potentiality of calcium phosphate for the loading and release of proteins has been reported for bovine serum albumin [279–281] and bone morphogenetic protein [282]. In principle, the amorphous and porous nature of AMCP should improve the loading capability of the inorganic structure. Moreover, as the effect of proteins from *Moringa Oleifera* on amorphous calcium phosphate was never addressed in the literature, we also aimed at understanding if they display a stabilizing action on the lifetime of the amorphous phase.

2.5.1 Experimental protocol

AMCP was prepared by mixing 20 mL of solution A with 20 mL of solution B at 37 °C, under magnetic stirring (see Table 2.8 for the composition). 50 mL

of each solution were prepared by dissolving salts in MilliQ water, and flasks were separately heated at 37 °C. Immediately after mixing the two solutions, the pH was adjusted at 7.30 by dropwise addition of NaOH 2 M; the pH was monitored throughout the synthesis, and maintained at 7.30 ± 0.02 by means of small additions of NaOH 1 M or HCl 0.1 M. Aliquots of 5 mL were collected after 15', 30', 60', 90', 2 h, 6 h, 24 h and 48 h. Each dispersion was centrifuged at 6000 rpm for 3', and the supernatant was discarded. Particles were washed with 5 mL of absolute ethanol, and centrifuged at 6000 rpm for 3'; the process was repeated 3 times, and particles were dried by means of a nitrogen flux and kept 30' under vacuum. Samples were stored at -18 °C. The syntheses in the presence of 1 mg/mL (AMCP_1MO) and 10 mg/mL (AMCP_10MO) of protein extracted from the seeds of *Moringa Oleifera* (referred to as "Moringa protein", extraction and features reported elsewhere [283–285]) were conducted by dispersing, respectively, 40 mg and 400 mg of Moringa in 2 mL of water, and simultaneously adding 19 mL of A and 19 mL of B. The synthesis and the separation were conducted at the same pH (7.30 ± 0.02) and with an equivalent procedure than described for the blank sample (AMCP without Moringa protein).

Table 2.8: Composition of the solutions used to prepare AMCP (grams referred to 50 mL of solutions).

	Salts	Concentration [mM]	Amount [g]
A	$NaH_2PO_4 \cdot H_2O$	50	0.345
	$Na_2HPO_4 \cdot 12H_2O$	150	2.686
B	NaCl	135	0.395
	$CaCl_2$	40	0.222
	$MgCl_2 \cdot 6H_2O$	100	1.017

2.5.2 Results and discussion

The lifetime of the amorphous phase was monitored by means of FT-IR spectroscopy, and the curves are shown in Figure 2.41. When Moringa protein is not present, we observe that AMCP crystallization occurs within 30'. The spectra of the phases formed upon crystallization are compatible

with the simultaneous presence of newberyite ($MgHPO_4 \cdot 3H_2O$, see Table 2.4) and bobierrite ($Mg_3(PO_4)_2 \cdot 8H_2O$, see Table 2.6), as confirmed by XRD analysis (see the discussion of Figure 2.43 later in this paragraph).

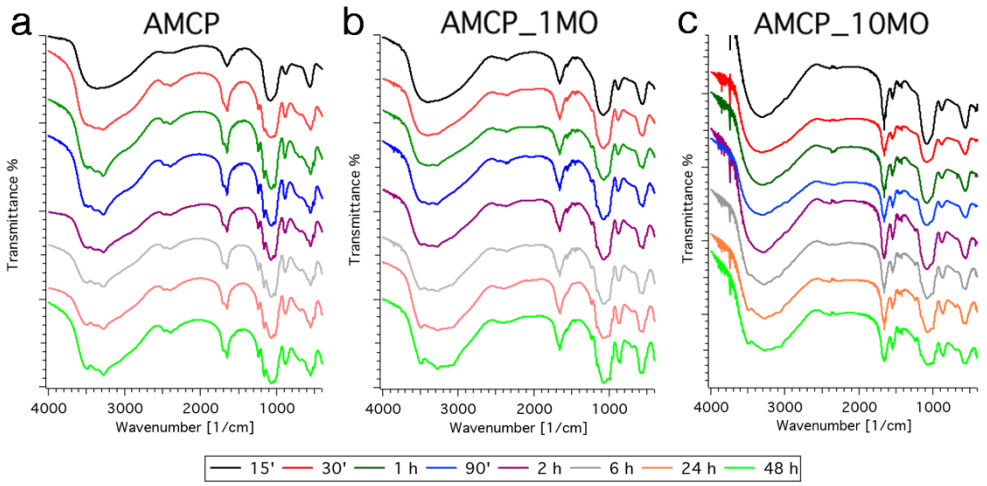

Figure 2.41: FT-IR spectra at different reaction times for (a) AMCP; (b) AMCP prepared with 1 mg/mL of Moringa protein; (c) AMCP prepared with 10 mg/mL of Moringa protein. The curves are offset for display purposes.

The presence of Moringa protein dispersions increases the lifetime of the amorphous phase and the more protein was added, the more the transition from amorphous to crystalline phases was retarded. In particular, in the case of AMCP_10MO, the first signatures of crystallinity appear after 6 h. If we compare the spectra of the particles prepared with 10 mg/mL of Moringa protein with those of the other two systems, we observe an additional peak at around 1540 cm^{-1}, which is consistent with the incorporation of a portion of protein in the samples (see the spectra of Moringa protein in Figure 2.42a as a reference). The comparison of the spectra of the most crystalline systems, *i.e.* 48 h, reveals some differences in the spectra (see the highlighted regions in Figure 2.42b), suggesting that the relative ratio between newberyite and bobierrite might be different

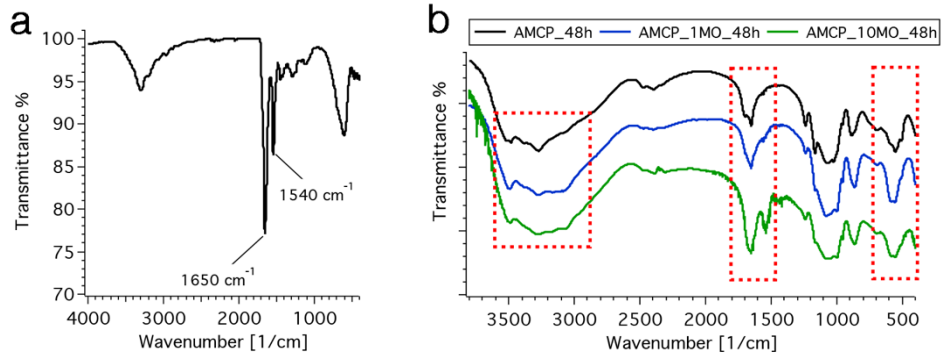

Figure 2.42: (a) ATR-FT-IR spectra of Moringa protein; (b) Comparison between the FT-IR spectra of the three samples after 48 h. The highlighted areas show the regions where the most significant differences among the spectra are visible.

This aspect was further clarified by means of XRD analysis on samples collected after 15', 30', 6 h and 48 h, and the results are displayed in Figure 2.43.

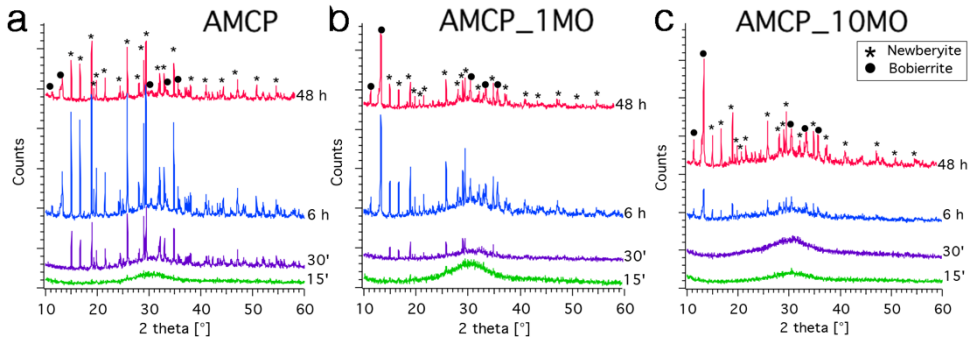

Figure 2.43: XRD diffractograms of AMCPs synthesized without protein (left), in the presence of 1 mg/mL of Moringa protein (center) and in the presence of 10 mg/mL of Moringa protein (right). The time after which each aliquot was withdrawn from the solution is reported on the right of each curve. PDF for bobierrite: 33-0878, for newberyite: 70-2345. The diffractograms are offset for display purposes.

All the patterns at 15' display a broad peak centered around 30°, consistently with previous reports on AMCP. At longer times, the transition from amorphous to crystalline phosphates occurs and some differences were observed when Moringa protein is present. In AMCP sample, the evolution of the amorphous particles to newberyite and bobierrite crystalline phases occurs already after 30', consistently with FT-IR results. On the other hand, when 1 mg/mL of Moringa protein is used, the crystallization occurs slightly slower and the bobierrite/newberyite ratio increases. This effect is even more

evident in AMCP_10MO samples, in which at 6 h very poor amounts of crystalline phases seem to be present and, even in this case, the bobierrite/newberyite ratio is higher than in the blank sample. The results suggest that the addition of Moringa protein to AMCP particles not only affects the stability of the amorphous phase, but also the type of crystalline phases to which it converts. The precipitation of newberyite or bobierrite upon AMCP crystallization was already observed in different systems described in this chapter: as highlighted in section 2.3.2.2, bobierrite was detected when synthesizing AMCP at pH 7.5 (paragraph 2.3), while newberyite at pH 7.4 (paragraph 2.1). Here, AMCP preparation was conducted at different Ca^{2+} and Mg^{2+} concentrations and pH with respect to the syntheses carried on in the cited paragraphs (so to improve the yield of the reaction), thus explaining the observed different stability and crystallization pathway. The different bobierrite/newberyite ratio detected can only be ascribed to the effect of Moringa protein, which may interact with Ca^{2+}, Mg^{2+} and phosphate ions, thus modifying the supersaturation and, as a consequence, the conditions necessary to drive the formation of a phase over another.

Thermogravimetry was used to estimate the amount of organic material incorporated in the particles. We chose to analyze only samples collected after 15', which are constituted by one single and amorphous phase: this allows to ascribe differences in the weight loss solely to the presence of organic material. The same consideration does not apply for samples also containing crystalline material, as the different amount of bobierrite/newberyite would result in a different weight loss profile, making not possible to estimate the amount of protein in the samples. Thermograms are reported in Figure 2.44. AMCP lose 24 % of their initial weight, whereas AMCP_1MO 27 % and AMCP_10MO 35 %. Assuming a complete degradation of the protein at 1000 °C, 3 % and 11 % of Moringa protein are incorporated in sample AMCP_1MO and AMCP_10MO, respectively. Peaks due to protein degradation are visible in the derivative curve, centered at ~300 °C and ~560 °C.

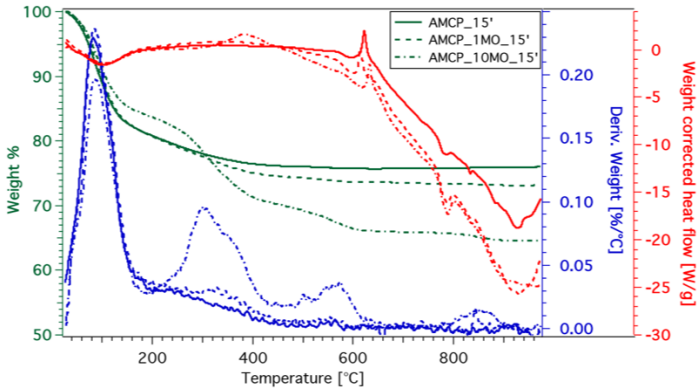

Figure 2.44: Thermogravimetric data of AMCPs collected after 15 min and synthesized without protein (full line), in the presence of 1 mg/mL of protein (dashed line) and 10 mg/mL (dots and lines). Green curves refer to the weight %, the blue ones are the derivative signals and the red ones show the heat flow profile.

The morphology of the samples was observed by means of FE-SEM (see Figure 2.45). Amorphous samples (figure a, b and c) consist of the characteristic spherical aggregated particles typical of AMCP, which in time evolve into more ordered structures, compatible with newberyite and bobierrite. Comparing the morphology of samples collected after the same amount of time, the number of crystalline objects decreases with the increase of protein, consistently with FT-IR and XRD analyses. The presence of Moringa protein does not affect the morphology of the amorphous particles precipitated after 15 min, whereas it influences that of samples at longer times. When 1 mg/mL or 10 mg/mL of protein are used, flake-like objects replace part of the spherical AMCPs (see Figure 2.45 e, f, h, i): this effect is concentration-dependent, as the amount of these structures increases with the increase of protein in the reacting medium. These "new" structures are very abundant in the sample, and cannot be ascribed to domains of organic molecules. Their aspect rather resembles that of poorly-crystalline hydroxyapatite crystals, which were observed as a product of AMCP crystallization previously in this chapter (section 2.1, Figure 2.12 a and Figure 2.13 b and c). This phase was not detected by means of FT-IR and XRD analyses; nevertheless, as its pattern is very broad and has a reduced intensity, its signals might be covered by those of the well-crystalline bobierrite and newberyite structures. We cannot therefore rule out the

possibility that this phase forms in the presence of Moringa protein. The analysis of the semi-quantitative Ca/Mg atomic ratio of the samples by means of EDX analysis (see Figure 2.46) does not give useful insights in this direction, as no significant differences are observed among samples with and without Moringa protein.

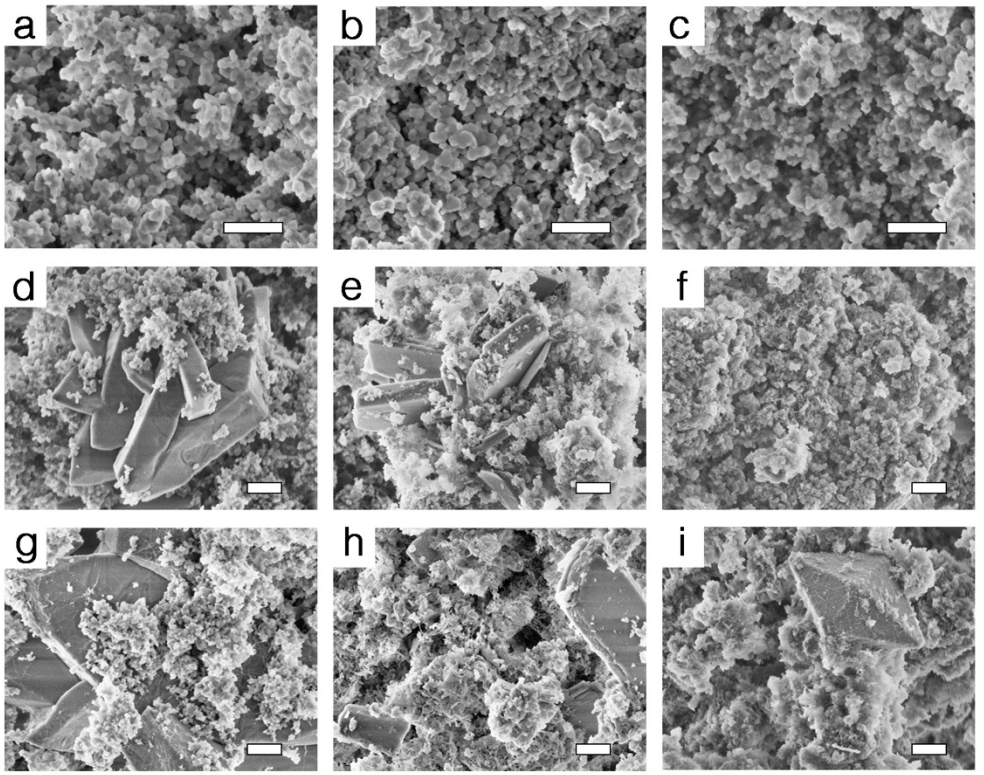

Figure 2.45: Representative FE-SEM micrographs of AMCP (first column), AMCP_1MO (second column) and AMCP_10MO (third column) of samples collected after 15′ (first row), 6 h (second row) and 48 h (third row). The scale bar corresponds to 500 nm.

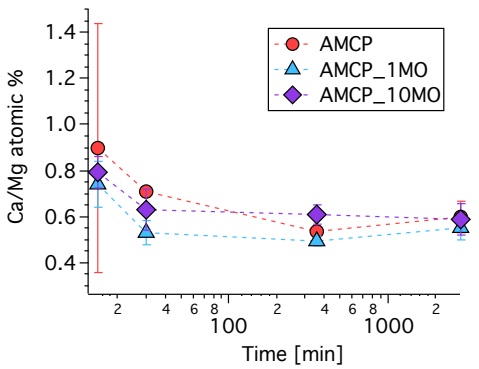

Figure 2.46: Ca/Mg % atomic ratio, as obtained by means of EDX analysis.

Further experiments are necessary to assess the nature and the relative amount of phases formed when AMCPs self-assemble in the presence of proteins extracted from *Moringa Oleifera*; nevertheless, results obtained so far clearly highlight that this protein has an effect in shaping the stability and the crystallization pathway of AMCP. These macromolecules can also be loaded within AMCP in a concentration-dependent fashion, paving the way for a potential application of this material in nutraceutics and drug delivery.

2.6 Preparatory tests for biological experiments

As we outlined in the Introduction, the investigation of the interplay between AMCPs and biological systems would be of outmost importance to clarify the role of the endogenous nanoparticles. In this framework, we tried to establish a collaboration with researchers of the gastroenterology unit of our university: among the different topics we believed were worth studying, the interaction of the amorphous particles with gut myco-biota was selected as starting point.

Since AMCPs present a low stability when dispersed in solution, as a first step we were requested to test the stability of our particles in culture media which are commonly used for *in vitro* experiments. We were provided with 20 mL of three different yeast media containing different saccharides, *i.e.* one with galactose (YPG), one with glucose (YPD) and one with lactose (YPL).

A literature research showed that in experiments dealing with the interaction between nanoparticles and gut microbiota, the most widely used range of concentration is 0-1000 μg/mL [286]; therefore, we decided to start by dispersing 10 mg of AMCP in 10 mL of medium (=1000 μg/mL), at 37 °C, collecting two aliquots after 1 and 2 reaction days. The measured pH of YPD before dispersing the particles was 5.94 at 37 °C (6.10 at 15 °C). After 1 and 2 reaction days, we filtered aliquots of the solution, and a very low amount of solid material was retained above the filter. The analysis by means of FT-IR spectroscopy (see Figure 2.47a) showed some peaks similar to AMCP; however, a careful comparison of the spectra of AMCP (green curve) with the one of the product collected after 2 days (red curve) reveals that they do not correspond to the same material. As a further evidence, the XRD analysis of the medium reveals a flat pattern and does not present the hump at $2\theta=30°$ characteristic of AMCP (data not shown). Our hypothesis is that the low pH of the medium causes the dissolution of AMCP, which in these conditions are not able to re-precipitate (we recall that the solubility of CaP is higher at acidic pH).

In order to circumvent this issue, we slightly modified the YPD medium by increasing its pH to 7.40 (by dropwise addition of NaOH 2M) and adding 5 mM of Mg^{2+}, with the purpose of increasing AMCP stability. We replicated

the previous experiment by dispersing 10 mg of AMCP in 10 mL of the modified YPD, and collected aliquots after 1, 2 and 5 synthesis days. FT-IR analyses reported in Figure 2.47b show that, in the modified medium, AMCP can retain their amorphous structure for 5 days, which is the typical duration of experiments with gut flora. The shape of the peak at 1450-1800 cm^{-1} reveals that, together with amorphous particles, the components of the YPD are also present in the sample (features similar to the spectrum of AMCP_YPD_2d, red curve in Figure 2.47a).

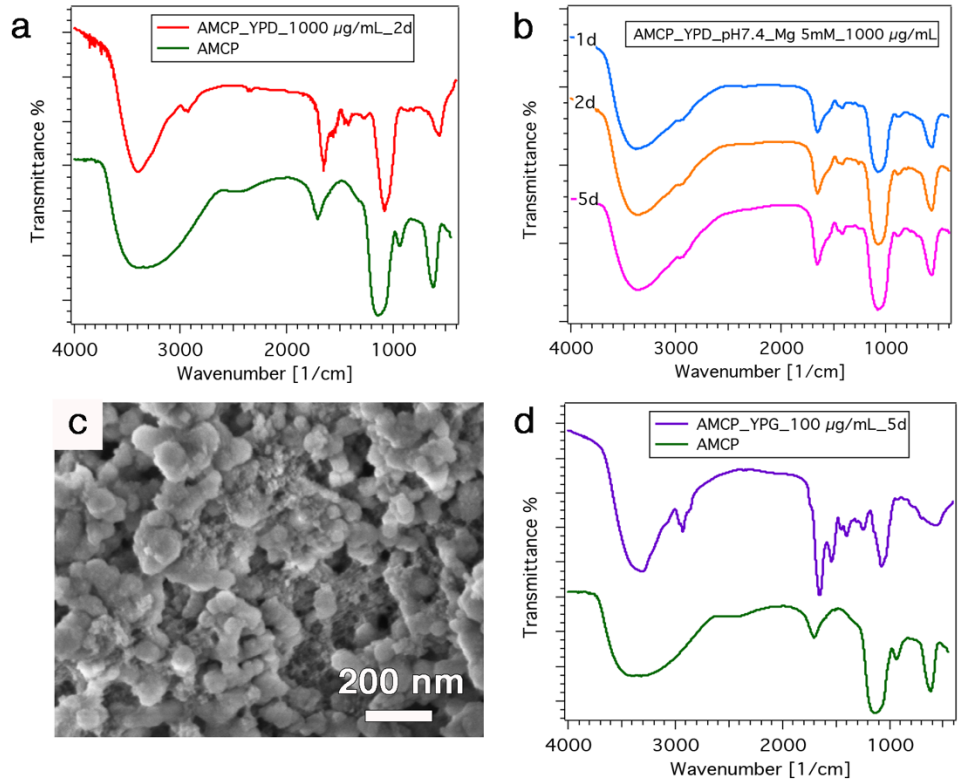

Figure 2.47: (a) FT-IR spectrum of AMCP dispersed in YPD at 1000 µg/mL and collected after 2 days (red curve), in comparison with AMCP as a reference (green curve); (b) FT-IR spectra of AMCP dispersed in YPD (pH 7.40 and $[Mg^{2+}]$=5 mM) at 1000 µg/mL and collected after 1, 2 and 5 days (c) FE-SEM micrograph of AMCP dispersed in YPD (pH 7.40 and $[Mg^{2+}]$=5 mM) at 1000 µg/mL and collected after 5 days (d) FT-IR spectrum of AMCP dispersed in YPG at 1000 µg/mL and collected after 5 days (purple curve), in comparison with AMCP as a reference (green curve). All the FT-IR spectra in the figure are offset for display purposes.

SEM micrographs confirm the presence of AMCPs, as their typical morphology is observed in samples collected after 1, 2 and 5 days

(representative micrograph in Figure 2.47c). Together with the amorphous spherical particles, smaller interconnected structures that "connect" the inorganic particles are also visible, compatibly with the organic components present in the YPD and detected by means of FT-IR spectroscopy. To sum up, we could demonstrate that AMCPs are able to preserve their amorphous phase in the modified culture medium for 5 days.

We tested the stability of the particles at lower concentration (100 μg/mL) in the YPG medium modified at pH 7.40 with $[Mg^{2+}]$ = 5 mM, collecting AMCPs after 5 days of incubation. The reason for the use of YPG over YPD is related to the low amount of medium available, as YPD was terminated in the 1000 μg/mL experiments; besides, we did not expect an effect due the presence of galactose over glucose on the stability of AMCP. FT-IR results displayed in Figure 2.47d show that at 100 μg/mL, AMCPs are not present after 5 incubation days, despite the use of the modified medium which was supposed to enhance the stability: the spectrum is in fact analogous to that of the organic material constituting the medium.

Summarizing, these preliminary tests show that when planning experiments that foresee the dispersion of AMCPs in culture media, several precautions must be taken to prevent the dissolution (and in some cases, presumably crystallization) of the amorphous particles. It is essential to control and prevent these phenomena, as the goal is to study the interaction of amorphous particles with bacteria/fungi. It would be indeed interesting to investigate the different response of these micro-organisms towards different forms of CaP, *i.e.* amorphous or crystalline.

3 Magnesium Phosphate-based cements

In addition to the physico-chemical investigation of calcium and magnesium phosphates naturally-present in human bodies, among which AMCP was chosen as case study (Chapter 2), this work of thesis also deals with the study of CaMgP-based materials for biomedical applications. This is a very broad area, as we outlined in the Introduction, and we chose to focus our attention on Magnesium Phosphate-based bone cements (MPCs). Bone cements constitute a very interesting category of biomaterials, as the preparation of systems endowed with the right characteristics to be used for real orthopedic applications presents many challenges which can be approached from a physico-chemical perspective. We decided to address the study of magnesium-based cements over their counterpart containing calcium as MPCs were only very recently proposed for use in the biomedical field, and the knowledge about their formation mechanism and full potentialities is still limited. In this chapter, cements prepared by means of tri-magnesium phosphate and aqueous solutions of di-ammonium hydrogen phosphate are described and characterized by means of a multi-technique approach, aiming at exploring the systems from a both fundamental point of view and in terms of properties relevant to orthopedic applications (cohesion, porosity, mechanical properties, injectability…). We initially illustrate the features of the tri-magnesium phosphate powder used to prepare cements, and in particular its evolution in time; this study, presented in section 3.1, is of paramount importance to prepare samples with reproducible properties. Section 3.2 deals with the investigation of the effect of powder-to-liquid ratio and concentration of di-ammonium hydrogen phosphate on the most

important features of the cements, which lead to the publication of paper V. This study is motivated by the evidence that, in the literature, very diverse formulations are used to prepare such systems, making it difficult to understand how simple parameters such as type and concentration of phosphate salt used or the ratio between the components affect the properties of the cements. Our investigation lead to very useful results, as we could understand how to enhance a specific property of the material by simply adjusting formulation parameters.

Following this investigation, we shifted our attention towards the study of MPCs containing citrate (section 3.3). This project is the result of an on-going collaboration with researchers from the Istituto Ortopedico Rizzoli in Bologna, with the goal of preparing materials for orthopedic applications able to release citrate; this ion, which is a minor yet important component of bone organic matrix, was recently reported to have beneficial effects in bone regeneration processes, and we demonstrate its successful inclusion in MPCs. We describe both its effect on the most meaningful properties of the cements, as well as the release profile in physiologic solutions. Biological experiments with fibroblasts are also reported, highlighting the potentialities of citrate-MPCs in this field.

As a last topic, the effect of cellulose ethers on the properties of cements is described in section 3.4. These additives were included in MPCs to improve their cohesion, handling properties and injectability; moreover, reports on MPCs containing polymeric additives are very limited in the literature.

All the results reported in this chapter highlight the great potentialities of MPCs as bone cements and clarify their formation mechanism from a physico-chemical perspective.

3.1 Effect of aging on TMP

In this work of thesis, we focused our attention exclusively on MPCs prepared using tri-magnesium phosphate (TMP) as powder component. As outlined in the Introduction, this class of MPCs is less investigated than those prepared starting from MgO [5], and their effective exploitation requires the understanding of the features of the components used to prepare them. Given that our preliminary experiments dealing with cements preparation revealed

poor reproducibility in the consistency of the pastes obtained using batches of TMP at different aging time, we decided to investigate the features of TMP as a function of its aging.

3.1.1 Synthesis of TMP

TMP powder ($Mg_3(PO_4)_2$) was obtained by means of a calcination reaction, according to a method reported in the literature [287]. Briefly, 40 g of newberyite ($MgHPO_4 \cdot 3H_2O$, Sigma Aldrich) and 6.69 g of magnesium hydroxide ($Mg(OH)_2$, Fluka) were mixed (molar ratio 2:1) and placed in ceramic crucibles. The powder was heated in a muffle at 1000 °C for 5 h. The reaction which takes place is the following:

$$2MgHPO_4 \cdot 3H_2O + Mg(OH)_2 \rightarrow Mg_3(PO_4)_2 + 8H_2O \quad (3.1)$$

The sintered cake was collected when quenched at room temperature and grinded using ball milling: around 6 g of TMP were loaded in a ZrO_2 jar, together with ~ 40 g of ZrO_2 grinding balls (ø=1 mm), and processed for 10 min at 10 Hz (mixer mill MM 400, Retsch). These conditions were chosen following the work of Klammert *et al.* [288], who showed that no significant changes in the granulometry of the particles are obtained by grinding from 10 to 40 min, despite being longer grinding times often reported in the literature [287, 289, 290]. The powder was separated from the grinding balls with the help of a 355 μm sieve. The operation was repeated until grinding the ~ 30 g of TMP, and the obtained powder was equally distributed in 4 plastic bottles. Each aliquot was analyzed at 4 different aging, namely immediately after grinding, and after 1, 3 and 7 days.

3.1.2 Preparation of cements

Cements were prepared using TMP at the 4 different aging times, with a powder to liquid (P/L) ratio of 2 g/mL: 0.500 g of the powder were mixed with 250 μL of a 3.5 M aqueous solution of di-ammonium hydrogen phosphate ($(NH_4)_2HPO_4$, DAHP, Fluka). The obtained pastes were immediately

transferred onto a piece of millimeter graph paper for the evaluation of their cohesion.

3.1.3 Results

The consistency of the pastes prepared using differently-aged TMP is shown in Figure 3.1a: the evaluation of the spreading of the pastes clearly indicates that TMP aging has an effect, since the paste prepared with the powder immediately after grinding is significantly more liquid-like than those obtained with TMP aged for 1, 3 and 7 days, which have a similar toothpaste-like aspect. The initial and final setting time of these pastes was evaluated by means of the Gillmore method (see details in Appendix I), but no significant differences among the four samples were detected (see Figure 3.1b).

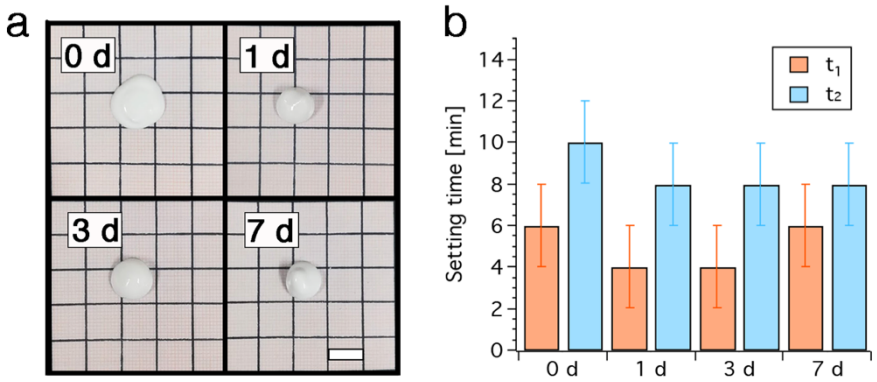

Figure 3.1: (a) Photos of the pastes after 1' from the beginning of mixing, prepared using TMP immediately after grinding (0 d) and after 1, 3 and 7 days from grinding (scale bar: 1 cm); (b) initial (orange) and final (blue) setting times obtained by means of the Gillmore method. The error bars are ± 2 min.

In the attempt of understanding the reason for the different consistency of the pastes, TMP was characterized in terms of crystallinity, chemical nature, granulometry and specific surface area (SSA). The results are reported in Figure 3.2. All the analyses reveal that TMP's features do not significantly change over time. XRD patterns (Figure 3.2a) show in all cases the signals diagnostic of well-crystalline farringtonite, the crystalline form of $Mg_3(PO_4)_2$. The FT-IR spectra (Figure 3.2b) do not change with aging and show the phosphate vibrations in the 1300-800 cm^{-1} and in the 700-500 cm^{-1} regions, consistently with the signals reported for $Mg_3(PO_4)_2$ calcined at high temperature [291].

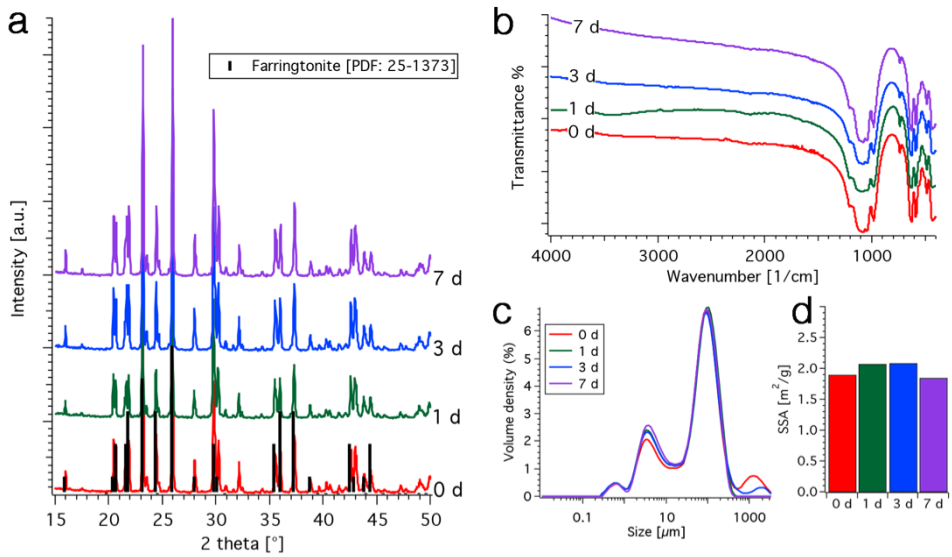

Figure 3.2: Characterization of the TMP powder: (a) XRD patterns as a function of TMP aging (the black bars correspond to the Farringtonite, PDF: 25-1373); (b) FT-IR spectra; (c) size distributions curves as obtained by means of laser granulometry; (d) BET SSA obtained from nitrogen sorption measurements.

The size distribution curves of the powder obtained by means of laser granulometry (dispersant: isopropanol, see Figure 3.2c) reveal a heterogeneous size distribution which ranges from 0.3 to 400 μm (the major population is centered at 90 μm). It is worth recalling that, after grinding, TMP was processed through a 355 μm sieve (paragraph 4.1.1); therefore, the small peak centered around 1 mm that is detected for sample "0 d" and "3 d" is likely due to aggregation processes occurring during the measurement. The specific surface area of the material, which is in general connected to its reactivity, was calculated with the BET method from the analysis of adsorption isotherms: the obtained values do not change over time, as in all samples SSA ranges from 1.8 to 2.0 m^2/g (Figure 3.2d).

In conclusion, despite we empirically observed that TMP aging affects the initial consistency of the pastes, we were not able to understand which is the parameter that provokes the observed effect. Further analyses are necessary to address this issue as, at this point, we can only rule out variations in TMP's crystallinity, size distribution, specific surface area and chemical nature.

As a general protocol, we decided to use TMP powder after at least 3 days from the grinding procedure for the preparation of all samples presented in this thesis, to obtain reproducible results in the consistencies.

3.2 Effect of P/L ratio and DAHP concentration

In order to get familiar with the formulation and the features of MPCs, we prepared a series of samples by varying simple parameters, namely DAHP concentration and powder to liquid ratio, and we analyzed the properties of the pastes and of the hardened cements. The understanding of the effect of these parameters on MPCs is of outmost importance, as it could help in the design of cements with tailored properties. The necessity of this investigation arises from the very diverse preparation conditions reported in the literature for this type of materials, which make it difficult to compare the obtained results and to choose the most suitable formulations. To cite some examples, Ewald *et al.* and Grossardt *et al.* prepared MPCs by mixing the powder component (TMP and struvite, 1:2 ratio by weight) with a 3.5 M solution of DAHP, using a powder to liquid ratio (P/L) of 2 g/mL [290, 292]. Kanter *et al.* employed as a liquid phase a solution containing both $(NH_4)_2HPO_4$ and $NH_4H_2PO_4$ and mixed it with TMP at P/L of 2.0 and 3.0 g/mL [289, 293]. A similar liquid composition was used by Klammert *et al.*, who reported an application of MPCs for 3D printing: TMP was blended with 20 % of $(NH_4)_2HPO_4$ powder and a solution 0.75 M $(NH_4)_2HPO_4$ and 0.75 M $(NH_4)H_2PO_4$ was used as liquid binder [288]. Remaining in the 3D printing field, Vorndran *et al.* combined TMP with 20 % H_3PO_4, K_2HPO_4 2 M or $(NH_4)_2HPO_4$ 0.5 M (P/L: 2 g/mL); the samples were then post-hardened in 20 % phosphoric acid, 2 M K_2HPO_4 or 3.5 M $(NH_4)_2HPO_4$ solution, respectively [294]. Kim *et al.* extruded a TMP paste prepared with hydroxypropyl methylcellulose and ethanol, which was then post-hardened in an aqueous solution of 3.5 M DAHP [295, 296]. Ostrowski *et al.* described the preparation of MPCs using amorphous, semi-crystalline and crystalline TMP mixed with a pH 7, 3.0 M solution of $NH_4H_2PO_4$ and $(NH_4)_2HPO_4$, and explored a variety of P/L (1:1, 1:2, 2:3, 3:2, 2:5) [291]. The P/L ratio was also varied by Moeske *et al.*, who prepared MPCs at P/L ratios from 1.0 to 3.3 g/mL using TMP and solutions of pure $(NH_4)_2HPO_4$ or mixtures of $(NH_4)_2HPO_4$ and di-ammonium citrate, with a total salt concentration of 3.5 M [287]. Recently, the group of Gbureck showed that by following high-energy ball milling of pure TMP, a nanocrystalline material forms, which reacts with water to form a cementitious material, without the addition of further reactants (in this case,

the final product is $Mg_3(PO_4)_2 \cdot 22H_2O$) [297]. Given the data reported above, we decided to prepare MPCs by mixing TMP and aqueous solutions of DAHP, systematically varying the powder to liquid ratio and the concentration of DAHP solution; both the pastes and the final cements were studied with a multi-technique approach, aiming at understanding how variations in these two parameters affect the most meaningful properties of the obtained materials.

3.2.1 Preparation of cements

TMP was synthesized as described in paragraph 3.1.1. The only difference in the synthetic protocol consists in the grinding procedure as, in these experiments, we chose to grind TMP with mortar and pestle over using ball milling. This decision was motivated by the fact that these cements are intended for biomedical applications, and we wanted to prevent a potential contamination of the powder from the materials of the grinding balls/jar. Therefore, the sintered cake was collected when quenched at room temperature, crushed by means of agate mortar and pestle and passed through a 150 μm sieve. Cement pastes were produced by mixing 0.500 g of TMP with aqueous solutions of DAHP. The amount and the concentration of the DAHP solution were varied so to obtain samples with P/L ratio of 1.0, 1.5 and 2.0 g/mL and DAHP concentration of 0.5, 2.0 and 3.5 M. The composition, together with the sample nomenclature and other useful parameters, is reported in Table 3.1.

Table 3.1: Composition of the prepared samples.

Sample	DAHP solution [μL]	DAHP [mmol]	Ratio mol TMP/ mol DAHP	DAHP solution* [g]	DAHP [g]	Water [g]
0.5M_P/L 1	500	0.25	7.6	0.53	0.03	0.49
2.0M_P/L 1	500	1.00	1.9	0.58	0.13	0.44
3.5M_P/L 1	500	1.75	1.1	0.60	0.23	0.36
0.5M_P/L 1.5	334	0.17	11.4	0.35	0.02	0.33
2.0M_P/L 1.5	334	0.67	2.9	0.38	0.09	0.29
3.5M_P/L 1.5	334	1.17	1.6	0.40	0.15	0.24
0.5M_P/L 2	250	0.13	15.2	0.26	0.02	0.25
2.0M_P/L 2	250	0.50	3.8	0.29	0.07	0.22
3.5M_P/L 2	250	0.88	2.2	0.30	0.12	0.18

*The densities of the solutions used in the calculation were: 1.05 g/mL for DAHP 0.5 M, 1.15 g/mL for DAHP 2.0 M, 1.19 g/mL for DAHP 3.5 M (data obtained by weighting a known volume of each DAHP solution).

The reaction which takes place, with the formation of struvite ($MgNH_4PO_4 \cdot 6H_2O$) as binging phase, is the following [287]:

$$Mg_3(PO_4)_2 + (NH_4)_2HPO_4 + 15H_2O \rightarrow 2MgNH_4PO_4 \cdot 6H_2O + MgHPO_4 \cdot 3H_2O \quad (3.2)$$

After mixing, the pastes were poured into cylindrical polyethylene molds (diameter 1 cm) and stored at 37 °C, relative humidity > 90 %, for at least 5 days.

3.2.2 Results and discussion

3.2.2.1 TMP characterization

We characterized the batch of TMP used to prepare the cements. The XRD pattern shows that we obtained a well-crystalline material (see Figure 3.3a), with a complete conversion to farringtonite (the crystalline form of TMP).

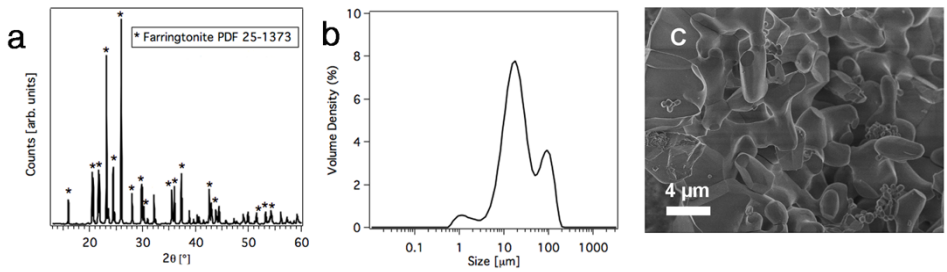

Figure 3.3: (a) XRD pattern of the calcined TMP powder; (b) Particle size distribution of TMP, measured using laser diffraction; (c) FE-SEM micrograph of TMP powder.

The analysis of the powder by means of laser granulometry conducted using isopropanol as dispersant shows a size distribution curve in the micrometric range, with a maximum around 20 µm (see Figure 3.3b). The grains have an irregular shape with a smooth surface, as it appears from FE-SEM micrographs (a representative example is displayed in Figure 3.3c). The specific surface area of the powder, as measured by means of nitrogen sorption, is 0.29 m^2/g. The comparison of these results with those referred to

TMP obtained by means of ball milling (Figure 3.2) reveals that the grinding through mortar and pestle produces smaller objects with a lower SSA.

3.2.2.2 Handling properties

The handling properties and the cohesion of the pastes were evaluated by mixing 0.50 g of TMP with the appropriate amount of aqueous solution (see Table 3.1) for 1 min; after 2 min from the beginning of mixing, the pastes were poured onto a piece of millimeter graph paper, and the cohesion degree was evaluated qualitatively according to the spreading of the paste. The results are shown in Figure 3.4.

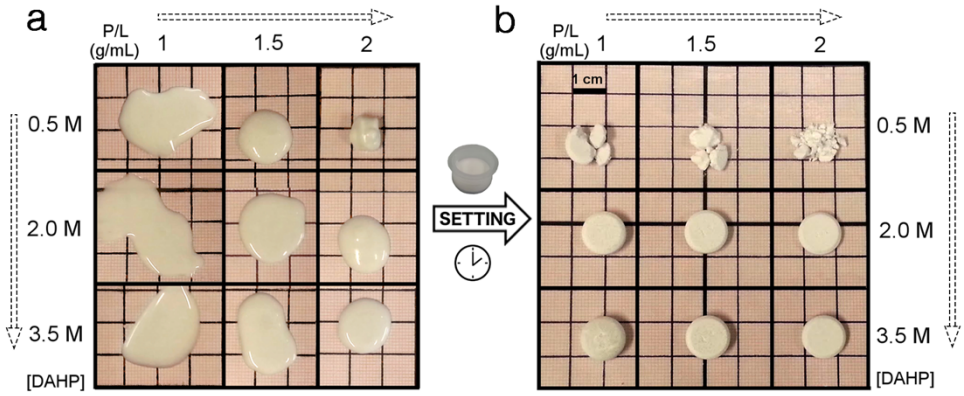

Figure 3.4: Photos of the samples (a) after 2 min from the mixing and (b) after setting in the mold for 5 days. In both pictures, the P/L ratio increases horizontally from the left to the right, while the concentration of DAHP increases from the top to the bottom.

When comparing the aspect and the consistency of the pastes (Figure 3.4a), it is evident that the cohesion degree increases while increasing the P/L ratio. This observation is consistent with data reported in the literature for CPCs [170, 178], and it was expected, considering the amount of water in the samples (see Table 3.1): in fact, immediately after mixing, a high water content makes the paste more viscous and less compact. Interestingly, we also noticed that the initial cohesion of the samples increases with the decrease of DAHP concentration. This effect may be due to the high wettability of the TMP powder, which in the 0.5M_samples is in large excess with respect to DAHP (see Table 3.1) [298]. We can hypothesize that, for a given P/L ratio, when the amount of TMP with respect to DAHP is large,

during mixing an immediate reaction between the two components occurs, and the small amount of formed struvite covers the large TMP grains; this results in an apparently more compact paste, in which the extent of the formed struvite network is limited. On the other hand, when more NH_4^+ and phosphate ions are available for the reaction (*i.e.* higher concentration of DAHP solution), a more homogeneous struvite precipitation occurs; consequently, the paste will appear more liquid-like, as DAHP can react with a larger amount of TMP and form a more interconnected and diffused struvite network which penetrates the whole sample in the early stages (see Figure 3.4a). The compactness of the dried cements was assessed by observing the samples' aspect after 5 days of setting in a mold (Figure 3.4b). The initial cohesion degree does not reflect on the compactness of the final cements: for example, the system which displays the highest cohesion degree after mixing (0.5M_P/L 2, top right in Figure 3.4a), is the one that after setting crumbles the most and is not able to maintain the shape of the mold, as for all the 0.5M_samples. On the other hand, the samples prepared with DAHP solution 2.0 M and 3.5 M allow for the formation of compact and hard cements. This observation is consistent with the significant and diffused formation of struvite in the 2.0M_ and 3.5M_samples, which finally percolates and hardens the whole specimens.

3.2.2.3 Crystallinity

The hardened cements were characterized in terms of crystallinity. According to the literature [287], TMP and DAHP react in a molar ratio 1:1 and form struvite ($MgNH_4PO_4 \cdot 6H_2O$), see Eq. 3.2. XRD patterns of the final cements are reported in Figure 3.5. In every analyzed sample, we observe the simultaneous presence of crystalline TMP (farringtonite) and struvite. The presence of unreacted TMP within the resulting cement structure is often observed in the literature [5]; it is worth stressing that in all the prepared samples TMP is in excess with respect to DAHP (see Table 3.1). When the ratio between TMP and DAHP is close to 1 (but again in a slight excess of TMP, sample 3.5M_P/L 1) we detect in its XRD pattern the signals characteristic of unreacted DAHP, despite the stoichiometry of the reaction would predict its complete consumption (see Figure 3.5c, pattern on the

bottom). This evidence indicates that it is not possible to entirely convert the reactants to the final product, suggesting that the formation of struvite occurs on the boundaries of the TMP grains and this mechanism hinders them from further reacting with DAHP.

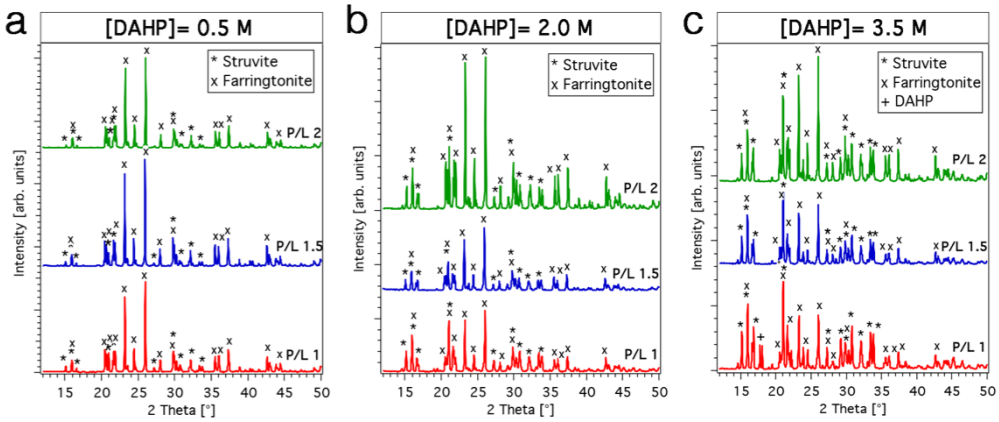

Figure 3.5: XRD patterns of the investigated samples (the diffractograms are offset for display purposes): (a) DAHP 0.5 M, (b) DAHP 2.0 M, (c) DAHP 3.5 M. The powder diffraction files used for the assignment are: PDF: 25-1373 for farringtonite (TMP) and PDF: 03-0240 for struvite; the diffractogram for pure DAHP was collected experimentally.

If we compare the intensities of the diffraction peaks, it is evident that a different composition of reactants leads to a different amount of struvite and farringtonite in the cement, since the relative intensities of the diagnostic peaks of the two phases are markedly different. In the 0.5M_samples, struvite peaks are very weak, while farringtonite signals predominate; in contrast, when we increase the concentration of DAHP, struvite's peaks become more intense compared to farringtonite's ones. In order to estimate the conversion degree to struvite, we performed a quantitative Rietveld analysis on the recorded diffractograms. The amount of formed struvite is reported in Figure 3.6a. Consistently with the qualitative observations of the intensities of the diffraction peaks, the amount of struvite in the cements increases with the increase of DAHP concentration and decreases as the P/L ratio raises. The obtained trend agrees with the theoretical conversion degree to struvite that we obtain considering the molar ratio between TMP and DAHP (see Table 3.1): as the powder/liquid ratio decreases, the composition gets closer to the stoichiometry of the reaction (1:1) and the conversion degree to struvite increases (we recall that all the investigated compositions display an excess

of TMP with respect to struvite). This observation is straightforward if we observe the plot of the amount of formed struvite (found by Rietveld method) against the ratio between the moles of TMP and DAHP (Figure 3.6b).

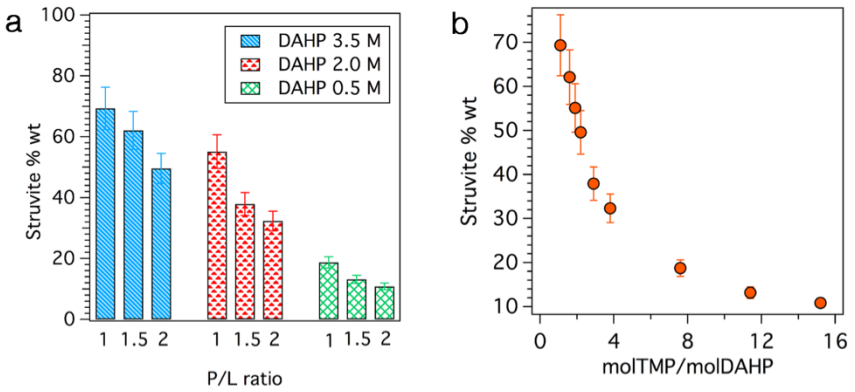

Figure 3.6: (a) Histogram reporting the amount of struvite obtained by means of a Rietveld fitting on the recorded diffractograms (error bars: 10 % of the obtained value). From the left: DAHP concentration of 3.5 M (blue), 2.0 M (red) and 0.5 M (green). For each set, the P/L ratio increases from the left to the right; (b) Plot of the amount of struvite (according to the Rietveld fitting) vs the ratio between the moles of TMP and DAHP, which reflects the theoretical conversion degree to struvite.

3.2.2.4 *Setting reaction*

We empirically observed that the hardening of the cements occurs on short time-scales: to obtain quantitative information, the setting time of the pastes was measured by means of the Gillmore method, and the results are reported in Figure 3.7.

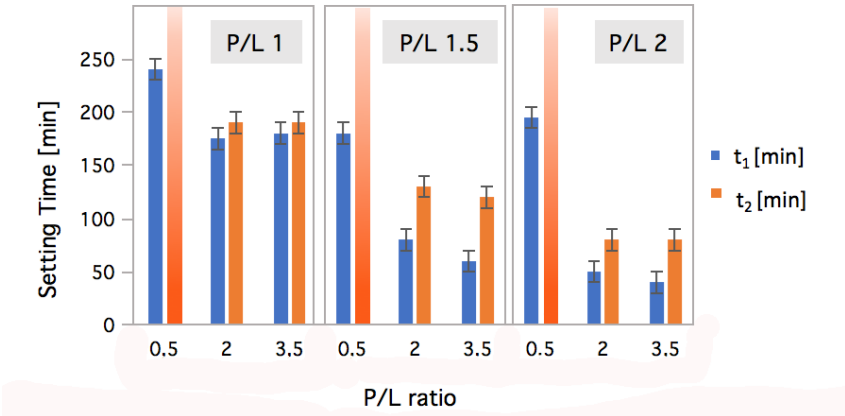

Figure 3.7: Initial (t_1, blue) and final (t_2, orange) setting times of the cements, measured by means of the Gillmore method.

All the samples display both initial and final setting times well above the ideal values for clinical applications (*i.e.* $t_1 \sim$ 8 min and $t_2 \sim$ 15 min [5]), and the 0.5M_samples do not reach the t_2, as the cements' surface crumbles upon indentation. Some trends can be identified: at a given DAHP concentration, t_1 and t_2 decrease with the increase of the P/L ratio, while at a given P/L ratio, a higher DAHP concentration reduces setting time.

On a selected specimen (3.5M_P/L 1.5) we investigated the kinetic of struvite formation by means of time-dependent XRD: we prepared the paste and we immediately deposited it on the sample holder. We recorded 15 diffraction patterns over 2 hours, and the results are shown in Figure 3.8.

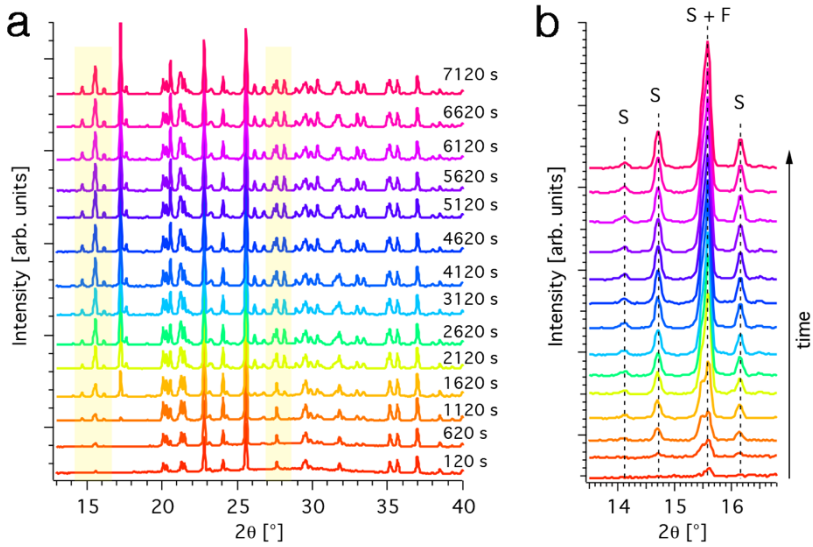

Figure 3.8: (a) Time-dependent XRD patterns recorded during the setting of the 3.5M_P/L 1.5 sample; the highlighted areas indicate the regions diagnostic for struvite formation, whereas time labels refer to the elapsed time from the beginning of the mixing; (b) zoom of the region 2θ=13°-17°. The patterns are offset for display purposes.

We observe that, after 120 s from the beginning of paste mixing, only farringtonite (TMP) signals are visible, indicating that crystalline struvite did not form yet. After about 10 min, signals diagnostic of struvite begin to appear, and they increase in intensity with the increase of reaction time (see the highlighted regions in Figure 3.8a). The kinetic of struvite formation can be easily followed by focusing on the 2θ region 13°-17°, where 4 diagnostic signals of this phase are present (see Figure 3.8b). No significant variations are detected after about 1 hour, revealing that the formation process of

struvite is relatively fast. One should also note the presence of two additional peaks (located at 17.2° and 17.6°), whose intensity increases as a function of time and which are not present in the pattern of the 3.5M_P/L 1.5 sample shown in Figure 3.5c: these signals are compatible with unreacted DAHP, which was already observed in sample 3.5M_P/L 1 (see the red pattern in Figure 3.5c). The presence of this component in the 3.5M_P/L 1.5 sample might be due to the different experimental set-up (diverse setting conditions, different sample holder, sample not grinded prior to analysis).

Results presented so far suggest that the hardening of the cement is mainly related to the formation of struvite crystals, as the time-scales in which the paste sets are compatible with the appearance of its signals in XRD pattern; despite that, we aimed at understanding if struvite formation and water consumption also take place on larger time-scales. This investigation was carried out having in mind the behavior of building cements, such as calcium silicate hydrate (CSH) or magnesium silicate hydrate (MSH) in which, despite a relatively short hardening time, the hydration process can last for over a month [299]. A very effective technique to follow this process relies on the calculation of the free water index (FWI) by means of low-temperature differential scanning calorimetry (LT-DSC), as the monitoring of the cooling and the melting of the water inside the pastes can give information on the hydration process [300]. By periodically freezing cement pastes at −60 °C and then melting them at a constant rate, the integration of the ice melting peak provides ΔH_{exp}, which is used in equation 3.3:

$$FWI\ \% = \frac{\Delta H_{exp}}{\phi \Delta H_{theo}} \cdot 100 \tag{3.3}$$

where ϕ is the original weight fraction of water in the paste and ΔH_{theor} is the theoretical melting enthalpy of water (333.4 J/g). The FWI is related to the water present in the sample which is able to freeze and then melt: if water is consumed during the formation of hydrated phases, or if it is confined in nanometric porosities, it will not behave as free water, not contributing to the ice melting peak. We chose to investigate our systems by preparing small amounts of pastes and analyzing them after 3 h, 24 h, 7 days and 28 days of setting, keeping them in hermetically-sealed steel pans at 37 °C. The FWI %

as a function of time is reported in Figure 3.9. The data collected after 3 h of setting show that the highest amount of free water is present in the 0.5M_samples, while cements prepared with DAHP 3.5 M display a low FWI, suggesting that the majority of water is consumed during struvite formation; nevertheless, there is not a direct correlation with the conversion degree to struvite (see Figure 3.6a). In samples prepared using the same DAHP concentration, the FWI % always decreases with the increasing of the P/L ratio, consistently with the inferior amount of water used in the formulation. We can therefore conclude that the FWI in the pastes likely results from the combination of the amount of struvite formed with the quantity of water used in the formulations. In the majority of samples, the FWI % as a function of setting time decreases very slowly, confirming that the formation of struvite mainly occurs on short time-scales. Some samples (in particular 0.5M_P/L 1, 2M_P/L 1.5, 2M_P/L 2) display a significant decrease of the FWI after 28 days, suggesting that in some cases struvite formation and/or water confinement slowly continues over time.

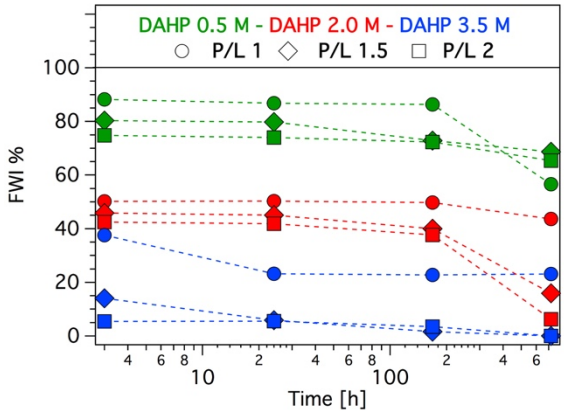

Figure 3.9: Free Water Index % vs time. Circles refer to P/L=1, diamonds to P/L=1.5 and squares at P/L=2. Green markers correspond to [DAHP]=0.5 M, red ones to [DAHP]=2.0 M and blue ones [DAHP]=3.5 M.

The difference in the hydration process among this type of cements and traditional CSH or MSH-based ones is likely related to their microstructure: if we consider a classical Portland cement, its porous microstructure allows for a slow diffusion of water, which leads to a hydration reaction that lasts over time and to the confinement of water in nanometric porosities [300]. Being MPCs composed by rapidly-forming and well-crystalline structures,

the diffusion of water within their matrix is likely inhibited, not allowing for struvite-formation reaction to proceed at longer time-scales. Being the microstructure and the porosity of these cements so important, they are discussed in the following paragraphs.

3.2.2.5 Morphology and microstructure

The morphology of the prepared MPCs was investigated by means of FE-SEM, and the micrographs are shown in Figure 3.10.

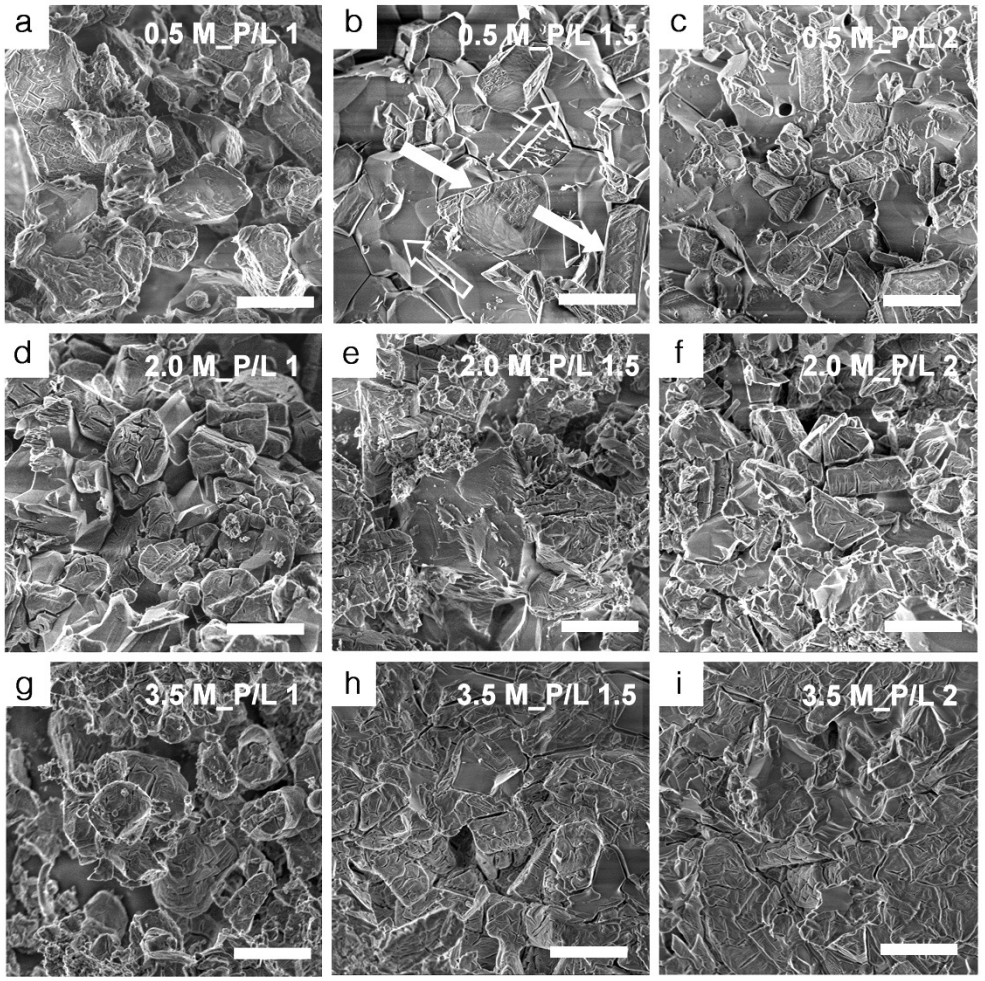

Figure 3.10: FE-SEM micrographs of the investigated MPCs. The identity of the samples is reported on each picture. Scale bar: 5 μm.

In the 0.5M_samples, we can clearly distinguish between two different types of structures, which are highlighted by the arrows in Figure 3.10b. The smooth objects indicated by the empty arrows are typical of TMP (see the morphology in Figure 3.3c for comparison), while the full arrows indicate the parallelepiped-like structures with a rough surface, characteristic of struvite [301]. High magnification images of struvite crystals, shown in Figure 3.11, reveal the very peculiar morphology of this mineral, which displays a typical hemimorphic character (*i.e.* the two ends of a crystallographic *c*-axis are not related by symmetry, see Figure 3.11a) [302]. The crystals thus show both tabular planes and rough surfaces, revealing cracks with regular shapes that carry an intrinsic porosity (see Figure 3.11b) [303].

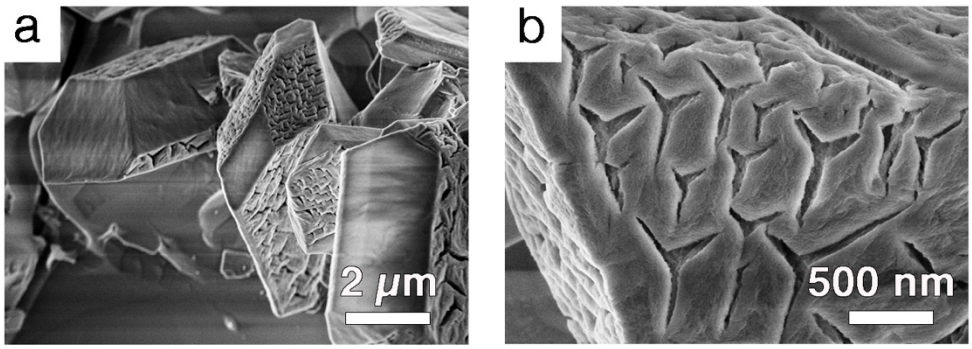

Figure 3.11: (a,b) High magnification SEM micrographs of struvite crystals in MCP samples.

It is interesting to observe that when we increase the concentration of DAHP in the formulations, the amount of struvite-like structures increases, and the number of TMP-rich domains diminishes. This observation agrees with the data obtained by means of XRD and discussed in section 3.2.2.3, which revealed that the conversion degree to struvite increases with increasing the concentration of DAHP (and decreasing the P/L ratio). Furthermore, when DAHP 3.5 M is used, we observe a more compact and uniform morphology produced by the network of the formed struvite.

3.2.2.6 Porosity and specific surface area

Porosity is one of the key parameters which should be taken into account in the design of a bone cement, as it affects both the biological activity and the mechanical properties of the material; cements should display a combination

of micro and macroporosity, so to allow for the impregnation of biological fluids, for cell ingrowth and for the replacement by new bone [170]. The total porosity of our cements was calculated according to Eq. 3.4 [304], by weighting and measuring (diameter and height) cylindrical samples at different composition, so to obtain the density of the cements (ρ_{cement}). The samples prepared with DAHP 0.5 M were not considered for this analysis, as we were not able to measure them since they did not maintain their shape after removal from the mold.

$$\text{Porosity} = \frac{\rho_{\text{fully dense material}} - \rho_{\text{cement}}}{\rho_{\text{fully dense material}}} \tag{3.4}$$

The density of the fully dense material was calculated considering the weight fraction of the two phases composing each sample (farringtonite and struvite), as obtained by means of the Rietveld method from the XRD results (see paragraph 3.2.2.3); the density of farringtonite is 2.74 g/cm^3 [305] and struvite 1.70 g/cm^3 [306]. The results are reported in Figure 3.12a.

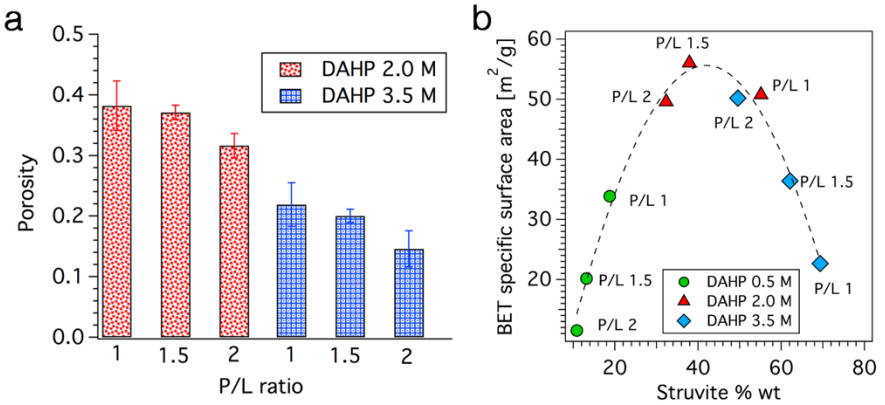

Figure 3.12: (a) Total porosity of the investigated samples, calculated according to Eq. 3.4 (average of 4 different measurements ± standard deviation); (b) Plot of specific surface area vs %wt of struvite (from Rietveld analysis). DAHP 0.5 M (circles), DAHP 2.0 M (triangles), DAHP 3.5 M (diamonds). P/L ratio is reported on the graph. The dashed curve is a guide to the eyes, not a fitting of the experimental data.

The obtained porosities range from 0.1 to 0.4 (being 0 a non-porous sample), and are higher for the 2.0M_samples than for the 3.5M_samples; moreover, at a given DAHP concentration, the porosity decreases when the P/L ratio increases. The latter trend is probably ascribable to the higher amount of

unreacted water that generates larger porosities while evaporating during setting [178]; furthermore, at fixed P/L ratio, the porosity is larger for the 2.0M_samples, consistently with the higher amount of water present (see Table 3.1).

We also studied the specific surface area (SSA) and the pore size distribution of the prepared cements. All the investigated samples display a reversible type II isotherm with a multi-layer adsorption (see Figure 3.13a). The BJH analysis reveals that the cements possess a quite heterogeneous pore size distribution, with a small population of micropores and most pores with a diameter over 30 nm (see Figure 3.13b for a significant example).

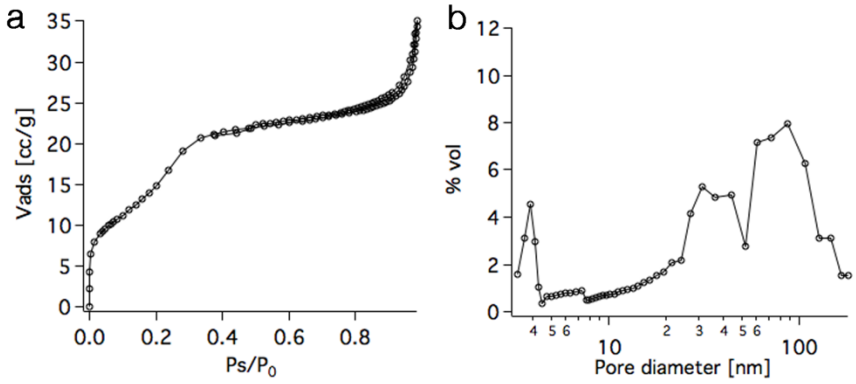

Figure 3.13: (a) Representative adsorption and desorption isotherm; (b) representative pore size distribution plot of the investigated cements. The curves refer to the sample 2.0M_P/L 1.5.

The SSA of the cements was calculated with the BET method. Given that unreacted TMP is characterized by a smooth morphology, while struvite is endowed with some intrinsic porosity on its surface, we plotted the SSA against the struvite content of each sample (see paragraph 3.2.2.3), to evaluate a possible connection between these two parameters (see Figure 3.12b). Interestingly we observe that, up to 40 %wt of struvite, the SSA increases with the increase of struvite content; however, when the amount of struvite exceeds 40 %wt, the trend inverses, and the SSA decreases as the quantity of struvite in the sample increases. We believe that this peculiar trend is strictly related to the morphology of the cements (see Figure 3.10): samples prepared with DAHP 3.5 M display a very compact microstructure, which becomes more "dense" as struvite content increases (see Figure 3.10 g, h and i). This type of structure possibly decreases the overall surface area of the samples, leading to the observed effect. It is worth commenting that the SSA trend does

not correspond to the total porosity of the cements previously discussed (see Figure 3.12a): in fact, nitrogen sorption technique gives access to porosities from few to hundreds of nm, while large macropores, which can increase the total porosity of the material, do not contribute to the BET specific surface area of the samples.

3.2.2.7 Mechanical properties

The mechanical properties of bone cements are of outmost importance for surgical applications: as these materials should set directly within the bone defect/fracture where they are applied, it is important to understand which is the load they are able to withstand after setting. In the literature, compressive or tensile loadings are often evaluated [170]. In our case, we assessed the compressive strength of the cements in order to understand if different formulations lead to a diverse behavior in terms of load withstanding, trying to relate this property to the microstructure and to the struvite conversion degree. The 0.5M_samples could not be analyzed, as they crumbled once removed from the mold and could not retain their shape. The measured compressive strengths for the other samples are reported in Figure 3.14a. Our samples display a compressive strength which ranges from about 10 to 30 MPa, in agreement with literature data for similar materials [5] and, on average, higher than CPCs [170]. Moreover, considering the error bars, the measurements show that the compressive strengths increase with the P/L ratio and with the concentration of DAHP (at fixed P/L ratio).

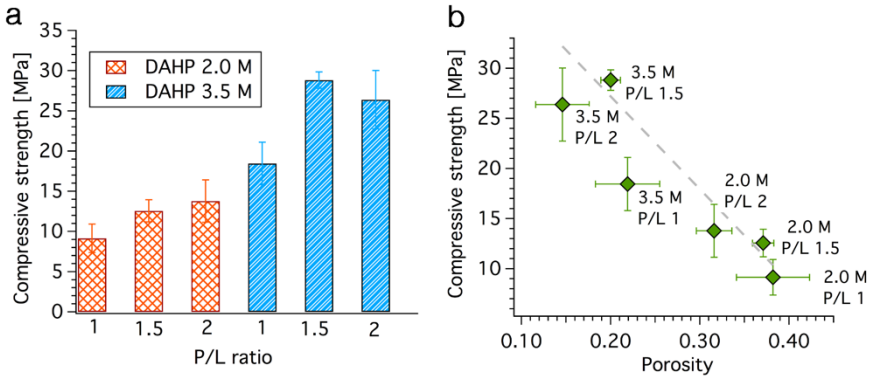

Figure 3.14: (a) Compressive strength of the analyzed cements (average of 4 different measurements ± standard deviation); (b) Plot of compressive strength vs porosity of the cements. The dashed line represents a linear fitting of the experimental data.

From these results, we can infer that the compressive strength is not directly correlated with the amount of struvite in the samples (see section 3.2.2.3), which increases with the concentration of DAHP but decreases with the P/L ratio. Interestingly, samples which display the highest compressive strength (3.5M_P/L 1.5 and 3.5M_P/L 2) are those whose morphology appears more compact and uniform. Since for CPCs mechanical properties are dependent on the microstructure and on the total porosity of the material [170], we plotted the compressive strength against the porosity of the samples (data shown in Figure 3.12a), and the results are shown in Figure 3.14b. We can observe that the compressive strength increases as the porosity decreases; this trend well matches the data reported in the literature for CPCs [170] and for calcium-magnesium mixed cements [307]. To sum up, we can state that there is not a direct correlation between the amount of struvite and the mechanical properties; we can though hypothesize that a specific conversion degree to struvite is necessary to obtain an interconnected network that binds together the unreacted TMP grains and to produce a very compact microstructure of the material.

In conclusion, we succeeded in understanding how the modification in the P/L ratio and the DAHP concentration affects the most meaningful properties of TMP-based cements. All the final materials are constituted by variable amounts of struvite and unreacted TMP, as shown by XRD analysis. SEM micrographs reveal that when the amount of struvite is low, the morphology of the two components is detectable, whereas when the concentration of struvite increases, only its typical morphology can be observed, despite XRD measurements still indicate the presence of a significant amount of unreacted TMP. This suggest that the formation of struvite occurs on TMP grains, and the network which is generated prevents a further reaction between TMP and DAHP. The use of DAHP solution 2.0 M and 3.5 M allows for the formation of compact and hard cements, whose compressive strengths significantly vary with the formulation: this mechanical property grows with the P/L ratio and with the concentration of DAHP solution, being inversely proportional to the total porosity of the material. The results here presented can be used as useful guidelines in the design and realization of this kind of bone cements, representing a step forward in the preparation and use of MPCs in the biomedical field.

3.3 Citrate-containing MPCs

The idea of preparing MPCs able to release citrate came from a collaboration with researchers from the "Istituto Ortopedico Rizzoli" in Bologna (Italy). This collaboration allows us to assess the biocompatibility of MPCs; since we learned how to prepare cements whose properties can be tuned by the variation of simple formulation parameters, we aimed at understanding which are the key features that one should focus on in the design of a bone cement for a real application. The profitable discussion with researchers at Istituto Rizzoli moved our interest towards the study of citrate-based biomaterials. Citrate ($C_6H_5O_7^{3-}$) is a tricarboxylic acid which comprises 5 %wt of bone [308], where it bridges between mineral HA-based platelets [28] and controls their size and crystallinity [309], acting as a key mineralization regulator. Being its pKa 2.9, 4.3 and 5.6, in most human tissues it is present as citrate: ~ 90 %wt is accumulated in human bone, while the rest is included in physiological and pathological calcifications (dentin, kidney stones and atherosclerotic plaques) and soft tissues (brain, prostate, kidneys) [310]. The natural existence of citrate and its importance in bone physiology suggest that this ion should be considered in orthopedic biomaterials and scaffolds design [311]. Many studies were recently devoted to the synthesis of citrate-based polymers, taking advantage of the ester bond formation occurring between citrate's carboxylic moieties and diols (HO-R-OH) [310, 312]; citrate-based polymers are often used as fluorescent biomaterials [313] or combined with inorganic components to prepare composites [311, 314–316]. The inclusion of citrate in bone biomaterials has demonstrated many interesting outcomes: a recent study has shown that this ion, whether present on a biomaterial surface or supplemented into cell culture media, has unique effects on gene expression: it upregulates osterix (a transcription factor which essential for osteoblast differentiation and bone formation), alkaline phosphatase (an enzyme which is among the first functional genes expressed in the process of calcification), and osteopontin, downregulating osteocalcin in myoblasts and human mesenchymal stem cells [311]. Citrate also has implications in treatments for osteopenia and osteoporosis, pathological situations due to aging which result in decreased bone mineral density,

deterioration of bone architecture and, ultimately, enhanced susceptibility to fractures [317]. As these pathologies can be enhanced by acidosis conditions, which favor bone resorption processes and inhibit osteogenic functions [318], treatments with substances able to neutralize acidosis (a metabolic condition in which high acid load exceeds physiological neutralization capacity) represent effective strategies for preventing osteopenia progression. A study from 2013 reports that in a group of healthy elderly persons without osteoporosis, treatment with K-citrate for 24 months resulted in a significant increase in bone mineral density at several sites tested, while also improving bone microarchitecture [319]. A meta-analysis also confirmed the reduction in bone resorption due to treatments with K-citrate [320], while recent findings from Rizzoli's colleagues showed that K-citrate supplementations induced positive effects on bone turnover in a group of osteopenic women showing low-grade acidosis [321]. Moreover, further elucidations on the implications of citrate ions in bone loss processes revealed that K-citrate supplemented in culture media inhibits osteoclastogenesis and enhances the anti-osteoclastogenesis activity of alendronate (a bisphosphonate commonly used in the treatment of osteoporosis) in a way that does not exclusively depend on the alkalinizing properties [322]. In light of these studies, the integration of citrate in MPCs could represent an innovative and unexplored field. In the literature, we only find one example of TMP-based MPC prepared using a combination of DAHP and a citrate salt [287]: the study is manly focused on the rheological and mechanical properties of the material, and reveals that the higher the citrate content in the formulation, the lower is the compressive strength and the better the injectability of the material. In contrast, citrate was often included in CPCs, with the main purpose of enhancing setting time and injectability of the pastes [323–330].

Our idea was to prepare a material which could be molded or even injected in a bone defect, able to set in few minutes and form a hardened cement which, upon contact with biological fluids, could gradually release citrate. In principle, the released citrate could favor the formation of new bone, while the MPC matrix could provide the mechanical stability to the bone while resorbing.

3.3.1 Preparation of citrate-containing MPCs

Cements containing citrate were prepared by mixing TMP (obtained as in section 3.1.1) with an aqueous solution of DAHP and/or DAC (dibasic ammonium citrate monohydrate, Riedel de Haën, structure in Figure 3.15).

DAHP DAC

Figure 3.15: Formulas of the two salts used to prepare the aqueous solutions.

Several systems were investigated by combining different ratios of DAC and DAHP, maintaining a total salt concentration of 3.5 M; all the prepared solutions and their composition are listed in Table 3.2.

Table 3.2: Sample identity and amount of DAHP and DAC used to prepare 1 mL of solution.

Sample	DAC [M]	DAHP [M]	DAC [g]	DAHP [g]	Molar ratio DAC/DAHP
Cit_0M	-	3.500	-	0.4620	-
Cit_0.5M	0.500	3.000	0.1221	0.3962	0.167
Cit_1.0M	1.000	2.500	0.2442	0.3302	0.400
Cit_1.5M	1.500	2.000	0.3663	0.2641	0.750
Cit_2.0M	2.000	1.500	0.4884	0.1981	1.330
Cit_2.5M	2.500	1.000	0.6105	0.1321	2.500
Cit_3.0M	3.000	0.500	0.7326	0.0660	6.000
Cit_3.5M	3.500	-	0.8547	-	-
Cit_0.025M	0.025	3.475	0.0061	0.4589	0.007
Cit_0.05M	0.050	3.450	0.0122	0.4556	0.014
Cit_0.1M	0.100	3.400	0.0244	0.4490	0.029

The powder and the liquid components were mixed for ~ 1 min and, in all cases, a paste-like consistency was immediately obtained. Samples described in section 3.3.2 were prepared using a P/L ratio of 3 g/mL (0.500 g of TMP with 166 μL of solution), while those analyzed in 3.3.4 and 3.3.5 with a P/L ratio of 2 g/mL (0.500 g of TMP with 250 μL of solution). In the second set of

experiments, a higher amount of solution was necessary to achieve a paste-like consistency, as with 166 μL crumbled samples were obtained, possibly because of different batches of TMP employed in the two set of samples. The pastes were placed into plastic cylindrical molds (⌀=1 cm) and set at 37 °C and relative humidity (RH) > 96 % for 3 days. Cement samples were named after the solution used to prepare them (for instance, Cit_0M is the sample prepared with solution Cit_0M).

3.3.2 Investigation of citrate effect on MPCs

Among the list of prepared samples (see Table 3.2), we started from the characterization of the samples with the largest differences in the composition, namely Cit_0M and Cit_3.5M, together with two intermediate compositions (Cit_1.5M and Cit_2.5M), in order to better highlight the effect of citrate on the cements' properties.

3.3.2.1 Handling properties, cohesion and setting time

When mixing TMP with the aqueous solutions Cit_0M, Cit_1.5M, Cit_2.5M and Cit_3.5M, we observe the formation of a paste with a very viscous and "rubbery" consistence, which can be easily molded and shaped (see Figure 3.16a). The use of a solution with a high citrate content produces slightly less compact pastes.

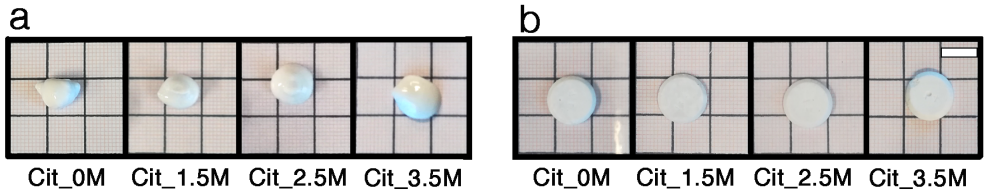

Figure 3.16: Photos of the cements (a) immediately after mixing and (b) after setting in the molds. Scale bar: 1 cm. Cit_0M=DAC 0 M, DAHP 3.5 M; Cit_1.5M=DAC 1.5 M, DAHP 2.0 M. Cit_2.5M=DAC 2.5 M, DAHP 1.0 M. Cit_3.5M=DAC 3.5 M, DAHP 0 M.

The liquefying effect observed in citrate-containing samples was already reported in the literature in the work by Moseke *et al.* [287]; while for CPCs this effect is ascribed to an increased dispersibility of the initial agglomerates due to the greater electrostatic repulsion given by citrate adsorption [323], for MPCs this effect is rather caused by the adsorption of citrate ions on the

particles during the setting reaction [287]. After setting in the molds, in all cases we obtain the formation of a compact and hard cement (see Figure 3.16b).

In addition to the compactness of the paste in a "dry" environment, its ability to harden in a static aqueous environment without disintegrating (*i.e.* cohesion) [331] is a parameter of crucial importance in the field of bone cements. Cohesion was evaluated by readapting a protocol from the literature [332]: after 2 min from the beginning of the mixing, the pastes were put in contact with 9.7 mL of water, and stored at 37 °C. After 4 h of soaking, the mold containing the cements was removed from the water and dried (3 days at 37 °C). The cohesion % was calculated using equation 3.5:

$$Cohesion\ (\%) = \frac{weight\ of\ the\ sediment}{original\ weight\ of\ the\ cement} \times 100 \qquad (3.5)$$

In the equation, the *original weight of the cement* is the weight of cement samples prepared using the same procedure and set for 3 days at 37 °C and RH > 96 %, without putting them in contact with water. Results reported in Figure 3.17a show that an increase in citrate content in the formulation corresponds to a decrease in the cohesion of the cement.

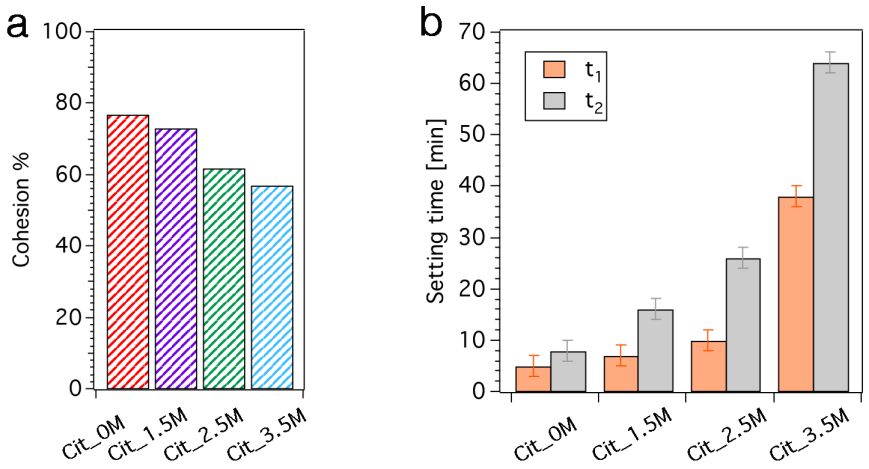

Figure 3.17: (a) Cohesion % of the 4 investigated samples; (b) initial (t_1) and final (t_2) setting time of the investigated formulations, obtained by means of the GIllmore test. Cit_0M=DAC 0 M, DAHP 3.5 M; Cit_1.5M=DAC 1.5 M, DAHP 2.0 M. Cit_2.5M=DAC 2.5 M, DAHP 1.0 M. Cit_3.5M=DAC 3.5 M, DAHP 0 M.

We highlight that the obtained results were acquired by putting the cements in contact with water after 2 min from the beginning of the mixing; we believe that delaying the addition of water would result in a higher cohesion % of the samples. The cohesion results are consistent with the setting times (see Figure 3.17b), which reveal that a higher citrate content delays the setting time of the cement, in agreement with a previous study [287].
According to the literature, t_1 should be $3 < t_1 < 8$ min, while $t_2 < 15$ min [178]; therefore, the formulations Cit_0M and Cit_1.5M display excellent setting times, while samples containing a higher citrate amount should be modified with additives able to decrease the setting time (such as cellulose ethers, see section 3.4) in order to become good candidates for surgical applications.

3.3.2.2 Characterization of the set cements

The nature of the crystalline phases formed upon setting was investigated by means of XRD, and the collected diffractograms are reported in Figure 3.18a.

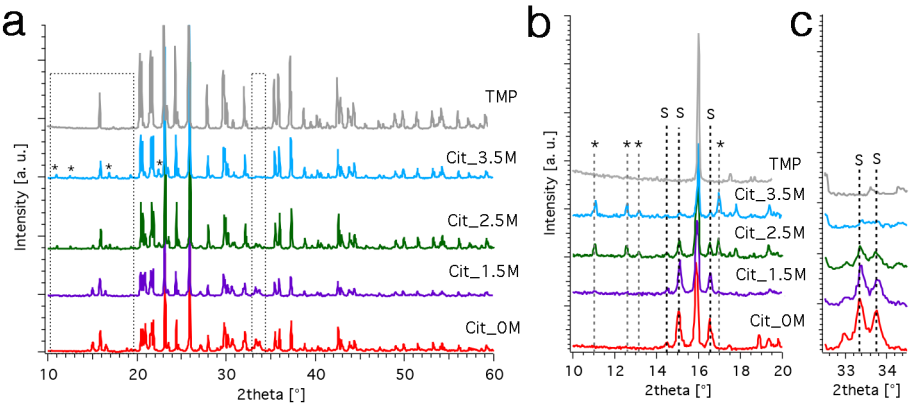

Figure 3.18: (a) XRD patterns of the four samples, together with that of TMP as a reference. The * marks the peaks which are present only in sample Cit_3.5M and, to a lesser extent, in Cit_2.5M; (b) zoom of the region 10-20° and (c) 32.5-34.5°, which show the regions diagnostic for struvite ("S" peaks, see the PDF: 03-0240). The patterns are offset for display purposes.

The pattern of sample Cit_0M (*i.e.* without citrate, red curve in Figure 3.18) reveals the presence of a large amount of unreacted TMP (see the grey pattern, which matches the PDF: 25-1373, farringtonite) together with some struvite, as it is revealed by the additional peaks in the areas highlighted by the rectangles in Figure 3.18a and the zooms of the diagnostic regions in

Figure 3.18b and c. In citrate-containing samples, we observe that the peaks diagnostic of struvite decrease while increasing citrate content, and they are nearly absent in sample Cit_3.5M. Moreover, in sample Cit_3.5M (and, to a lesser extent, also in sample Cit_2.5M), we observe the appearance of some small new peaks, marked with a * in Figure 3.18. We can therefore conclude that when we increase the amount of DAC with respect to DAHP, the amount of formed struvite decreases. However, as we obtain in all cases compact and hard cements, a binding phase which forms a network around TMP grains must be present also in samples containing only DAC (note that mixing water and TMP does not result in the formation of a compact cement). This binding phase can be either an amorphous phase (non-detectable by means of XRD) or a new crystalline phase giving rise to the new peaks marked with * in the blue pattern. In order to understand the nature of this new binding phase, never discussed in the literature, samples were analyzed in terms of morphology and thermal behavior.

The microstructure of the cross-sections as observed by means of FE-SEM is reported in Figure 3.19, while the insets show the morphologies of the surfaces.

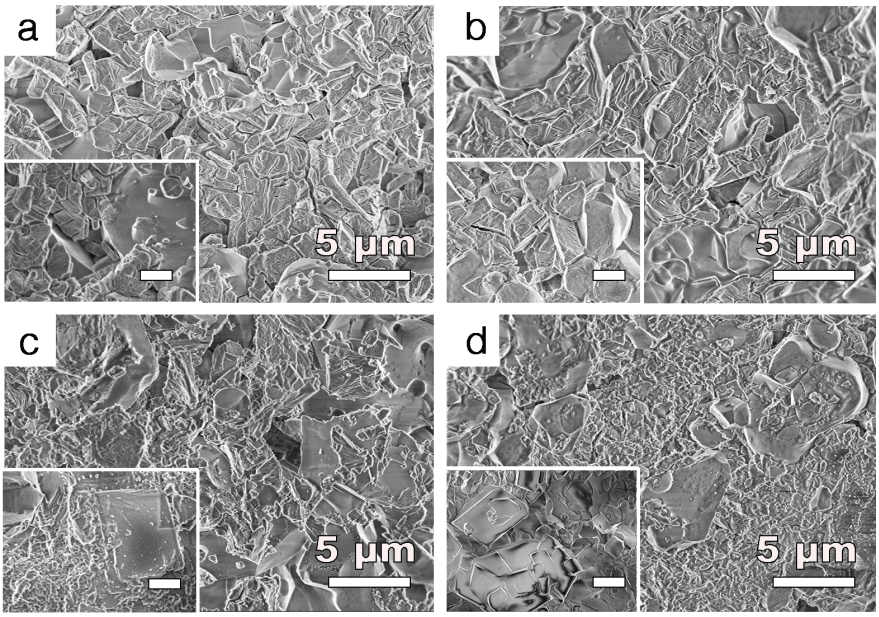

Figure 3.19: FE-SEM micrographs of sample (a) Cit_0M (DAC 0 M, DAHP 3.5 M), (b) Cit_1.5M (DAC 1.5 M, DAHP 2.0 M), (c) Cit_2.5M (DAC 2.5 M, DAHP 1.0 M), (d) Cit_3.5M (DAC 3.5 M, DAHP 0 M); the insets show the morphology of the surfaces.

Sample Cit_0M displays the typical morphology of MPCs, which results from the combination between TMP smooth grains and struvite characteristic network, consisting of Y-shaped cracks and pores on parallelepiped-like structures (see Figure 3.10 for comparison). With the decrease of DAHP content in the sample, we observe that the number of domains typical of struvite decreases, while TMP is visible in all the samples, consistently with XRD results. Interestingly, in samples Cit_2.5M and Cit_3.5M, which have a high citrate content, we observe many small and irregular objects with a non-defined shape, which surround TMP grains. The morphology of the surfaces (see the insets in Figure 3.19) well matches the internal structure of the cements, except for sample Cit_3.5M which shows objects with a geometric shape, compatible with crystalline material. EDX analysis in this area reveals high carbon content, whereas Mg is nearly absent (data not shown). We can infer that, on the surface of this cement, a citrate-based ammonium salt crystallizes because of an excess of DAC in the formulation. These crystals could be the responsible of the additional diffraction peaks detected in the XRD pattern of sample Cit_3.5M (blue pattern in Figure 3.18). The surface of the cements was also assessed in terms of roughness, as this parameter is of outmost importance for biomaterials and their interaction with cells: for CaP-based systems, it is demonstrated that the roughness, both at the nano- and micro-scale, affects cellular adhesion, proliferation and differentiation [333, 334]. The technique chosen for this investigation was confocal microscopy, as it allows to access the roughness profile on the micrometric scale. The morphologies of the surfaces and the corresponding Ra values are reported in Figure 3.20 (see the calculation details in Appendix I).

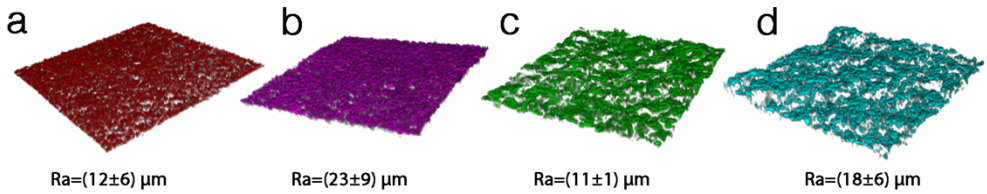

Figure 3.20: Cements surfaces as obtained by means of confocal microscopy on sample (a) Cit_0M (DAC 0 M, DAHP 3.5 M), (b) Cit_1.5M (DAC 1.5 M, DAHP 2.0 M), (c) Cit_2.5M (DAC 2.5 M, DAHP 1.0 M), (d) Cit_3.5M (DAC 3.5 M, DAHP 0 M). Each area corresponds to 310 µm x 310 µm. Ra values for each sample are reported below (average ± standard deviation over 8 measurements) and were calculated by means of the software "Fiji": two plugins were used, "Extended depth of field" and "SurfCharJ" (see the details in Appendix I).

Results show that all samples are endowed with roughness in the micrometric scale, which are not significantly different according to the composition. The high standard deviations associated to the average values are due to the heterogeneous microstructure, which is consistent with the observations conducted over SEM micrographs and with the fact that different phases with a very diverse morphology (*i.e.* smooth TMP grains and rough struvite crystals/citrate-based objects) are simultaneously present.

The nature of the phases present in the cements was further investigated by means of simultaneous TGA/DSC, allowing for the simultaneous determination of the degradation profile and the phase transitions occurring in samples upon heating (see Figure 3.21). Sample Cit_0M (red curve in Figure 3.21a) displays a weight loss at 1000 °C of 19.7 %, which mainly occurs below 100 °C (14.4 %). The degradation profile is entirely ascribable to the thermal decomposition of struvite (TMP, when heated up to 1000 °C, loses about 0.2 % of its weight) and is compatible with data reported in the literature [335–337].

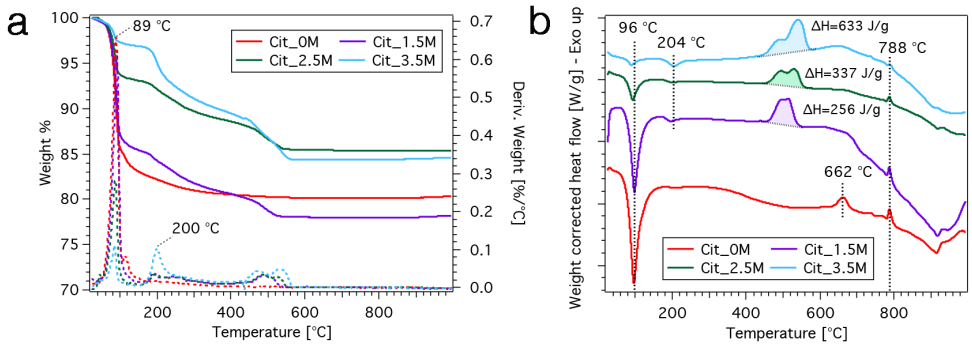

Figure 3.21: (a) TGA (left axis, solid lines) and derivative TGA (right axis, dashed curves) of the four investigated samples; (b) heat flow profiles associated to the TGA measurements. Red curve: Cit_0M (DAC 0 M, DAHP 3.5 M). Purple curve: Cit_1.5M (DAC 1.5 M, DAHP 2.0 M). Green curve: Cit_2.5M (DAC 2.5 M, DAHP 1.0 M). Blue curve: Cit_3.5M (DAC 3.5 M, DAHP 0 M). The enthalpy associated to the highlighted peak is reported on the graph. The curves are offset for display purposes.

The first weight loss event (peak in the derivative curve centered around 90 °C) corresponds to the loss of 5 moles of crystallization water, with the formation of dittmarite, $MgNH_4PO_4 \cdot H_2O$ (reaction 3.6). The residual weight loss, related to the simultaneous loss of 1 mole of crystallization water and ammonia with the formation of amorphous $MgHPO_4$ (reaction 3.7), likely

occurs gradually as a function of temperature, rather than as a distinct step, as we do not observe peaks in the corresponding DTG curve [338]. Considering that, at 1000 °C, a pure struvite sample would lose ~ 55 % of its initial weight [339], while sample Cit_0M displays a weight loss of 19.7 %, we can roughly estimate the composition of our cement (~ 35 % of struvite and ~ 65 % of TMP). In the heat flow profile, the exothermic peak above 600 °C is attributed to a general high temperature phase transition [340] or to the polymerization of $MgHPO_4$ [336, 339] (see reaction 3.8). The exothermic transition at 788 °C is not assigned.

$$MgNH_4PO_4{\cdot}6H_2O \rightarrow MgNH_4PO_4{\cdot}H_2O + 5H_2O \uparrow \quad 3.6$$

$$MgNH_4PO_4{\cdot}H_2O \rightarrow MgHPO_4 + NH_3 \uparrow + H_2O \uparrow \quad 3.7$$

$$2MgHPO_4 \rightarrow Mg_2P_2O_7 + H_2O \uparrow \quad 3.8$$

As we increase the citrate content in the samples, we observe several effects: *i*: the extent of the weight loss before 100 °C decreases (12.8 % in sample Cit_1.5M, 6.2 % in sample Cit_2.5M and 2.7 % in sample Cit_3.5M); *ii:* a weight loss between 400 and 600 °C takes place; *iii*: a large exothermic peak, whose enthalpy is proportional to citrate content, appears in the heat flow profile between 450 and 600 °C; *iv*: in sample Cit_3.5M, a large weight loss at ~200 °C is present. Collectively, these data suggest that from sample Cit_0M to Cit_3.5M struvite content decreases, being the weight loss before 100 °C due to the loss of its crystallization water; this evidence is consistent with XRD and SEM results. The exothermic peak in the heat flow profile suggests that the binding phase formed in samples containing citrate is amorphous, as it crystallizes upon heating. The weight loss observed in sample Cit_3.5M at ~200 °C is ascribable to the degradation of a citrate salt (the major weight loss of DAC occurs between 150 and 250 °C, data not shown), whose presence on Cit_3.5M surface was observed in SEM micrographs. Samples Cit_0M and Cit_3.5M, recovered after the TGA measurements, were analyzed by means of XRD, to investigate the nature of the phases formed upon the thermal treatment. The patterns, reported in Figure 3.22, show that in both cases the only detected phase is TMP (grey pattern as a reference in the figure).

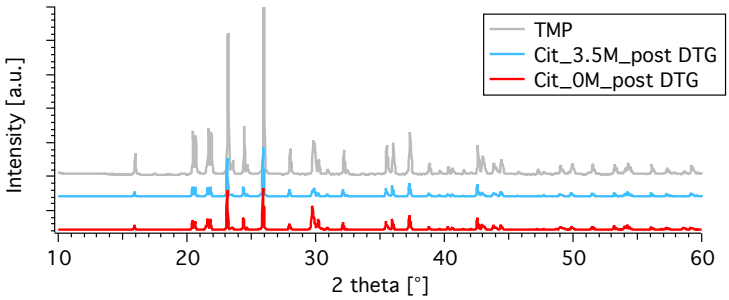

Figure 3.22: XRD patterns of samples Cit_0M (DAC 0 M, DAHP 3.5 M) and Cit_3.5M (DAC 0 M, DAHP 3.5 M) after TGA measurement (for sample Cit_3.5M, TGA measurement was interrupted at 600 °C, in the attempt of identifying the phase formed after the exothermic event). The grey pattern refers to TMP, as a reference.

3.3.2.3 Release experiments

As these materials were designed to release citrate, we investigated this property by means of two separate experiments, coded as "Experiment 1" and "Experiment 2". The experimental details are reported in Appendix I. As far as release experiment 1 is concerned, we recall that 5 replicas for each formulation (Cit_1.5M, Cit_2.5M and Cit_3.5M) were prepared, and each was immersed in 10 mL of physiological solution; one specimen for every composition was removed from the physiological solution after 1, 3, 7, 14 and 28 days. The pH of the incubating solution (NaCl 0.9 % w/v) was monitored within the 28 days of incubation. Measurements were conducted at 37 °C, by daily immersing the electrode in the solutions. The obtained profile, reported in Figure 3.23a, shows that the pH slightly increases in time: the solution in which sample Cit_2.5M and Cit_3.5M were incubated shows an analogous trend, starting from pH ~ 9.0 after 1 day from the beginning of the incubation and gradually reaching ~9.5 after 28 days. Sample Cit_1.5M, which has the lowest citrate content, produces in the solution an initial pH of 7.0, which reaches ~9.0 in 15 days. These data suggest that citrate content influences the pH of the solution in which the cements are incubated. As a general comment, the fact that these cements lead to an alkalization of the medium with which they get in contact is an attractive feature in view of their application as bone cements, since inflammatory conditions in bones are related to acidification of the surroundings, which results in bone loss [321, 322]. Having a material

that when in contact with a bone defect is able to reverse this process is potentially useful.

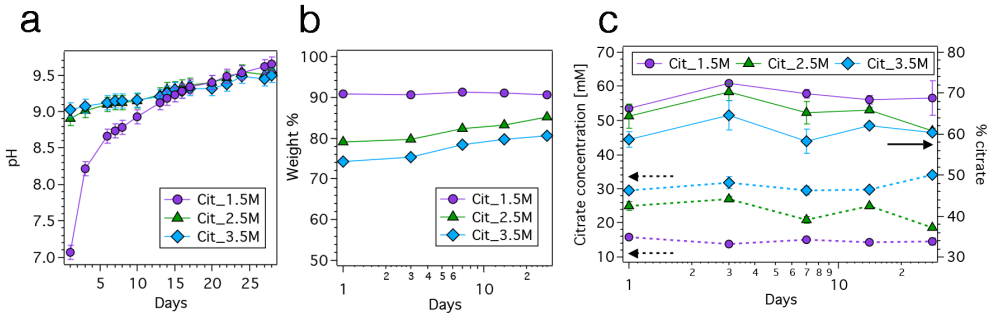

Figure 3.23: Release experiment 1: (a) pH of the physiologic solution in which the cements were incubated as a function of time; (b) weight % of the cements as a function of incubation time: each point refers to a different specimen withdrawn from the incubating solution after 1, 3, 7, 14 and 28 days; (c) quantification of citrate release: on the y-left axis, citrate concentration (dashed lines) and, on the y-right axis (solid lines), the % of released citrate (referred to the maximum amount they could release).

The five replicas of each sample were removed from the physiological solution after 1, 3, 7, 14 and 28 days. The incubated cements were dried in the oven at 37 °C, and weighted up to constant value. The residual weights % as a function of time are reported in Figure 3.23b. The results obtained for the weight % after 1 day are consistent with the cohesion experiments (see Figure 3.17a), as the weight loss increases with the increase of citrate content in the formulations. However, in contrast with our expectations, the cements do not lose weight during their incubation up to 28 days: sample Cit_1.5M maintains its weight constant, while Cit_2.5M and Cit_3.5M slightly increase their weight. A possible explanation for this result could be due to the static environment in which the cements were incubated: in these conditions, an equilibrium between the initially-dissolved material and the cements might occur, hindering a further dissolution of the cement. In samples Cit_2.5M and Cit_3.5M, the increase in weight with incubation time could be explained by the re-crystallization from the solution to the surface of the cement of some salts/hydrated phases. We believe that, in an *in vivo* dynamic environment, the continuous replacement of fresh biological fluids and the action of the cells would probably modify this scenario, enhancing the dissolution process. The concentration of citrate released in solution was assessed by means of UV-spectroscopy [341] by reading the absorbance value at 209 nm (average

results of 5 measurements ± standard deviation, see the experimental details in Appendix I), and it is reported as a function of time in Figure 3.23c (y-left axis). It is important to underline that each point of the graph corresponds to a different specimen (5 replicas for each type of formulation, each one related to a different incubation time). Each sample, when prepared, had a slightly different weight (differences in the tens of mg), but was incubated in the same amount of physiological solution (10 mL). For this reason, to quantitatively compare the obtained concentrations, it is necessary to multiply the concentration value for a weight normalization factor. From the obtained data, we observe that the concentration of citrate released in solution increases with the increase of citrate content in the cements. For sample Cit_1.5M, the concentration of citrate over time is constant (*i.e.* the cement does not release after 28 days a different citrate amount than that already released after 1 day), meaning that an equilibrium situation is reached within 24 h. The trend of sample Cit_2.5M and Cit_3.5M is similar to Cit_1.5M, as the concentrations oscillate, eventually slightly decreasing for Cit_2.5M and increasing for Cit_3.5M. We also calculated the % of released citrate as a function of time (Figure 3.23, y-right axis), which reflects the quantity of citrate released in solution compared with the amount present in the samples: this parameter was in fact calculated as the ratio between the mg of citrate released in the incubating solution and the mg of citrate present in the cement. We observe that the sample which is more prone to losing citrate is Cit_1.5M, despite being the one that contains the lowest amount of it. Moreover, this is also the sample that when in contact with the physiological solution loses the least amount of weight (Figure 3.23b); we cannot therefore ascribe the highest % citrate to a major massive dissolution of the sample. We can hypothesize that, being the network of sample Cit_1.5M mainly composed by struvite, the citrate which is embedded in the final matrix is less "bound" to it and more prone to being released. On the other hand, the cement matrix of Cit_3.5M is composed by an amorphous phase which contains citrate; this ion is therefore a structural component of the cement matrix, as it tends to be less released than it does in Cit_1.5M. The trend of % citrate in time shows an initial slight increase in the % of citrate released, while after 3 days we can consider it being constant, given the large error bars associated to the results. At 28 days, the % citrate of sample Cit_2.5M appears

to diminish, potentially correlating with a decrease in citrate content in solution because of its re-precipitation on the cement (consistently with the slight increase in the residual weight %, see Figure 3.23b). All these data taken together suggest that the release of citrate in solution is a fast phenomenon, as it mainly occurs within the first day and the concentration is roughly constant from 1 to 28 days of incubation.

In the attempt of simulating a more dynamic environment, we performed release experiment 2, in which 1 mL of physiological solution was daily collected and replaced with fresh solution (see the experimental details in Appendix I). The pH profile as a function of time is reported in Figure 3.24a. The obtained trend is similar to that of release experiment 1 (see Figure 3.23a), in which sample Cit_1.5M initially displays a neutral pH that rapidly increases and reaches that of the other two samples after ~ 7 days (this rise is quicker in this experiment, as in 1 the curves cross after ~ 15 days). All the solutions eventually reach a pH ~ 9.5. The concentration of citrate was measured by means of UV-spectroscopy, and it is reported as a function of time in Figure 3.24b. Consistently with release experiment 1, we observe that the concentration of released citrate is directly proportional to the amount used for the preparation of the cements. The majority of the release occurs within the early stages of the incubation for all the samples.

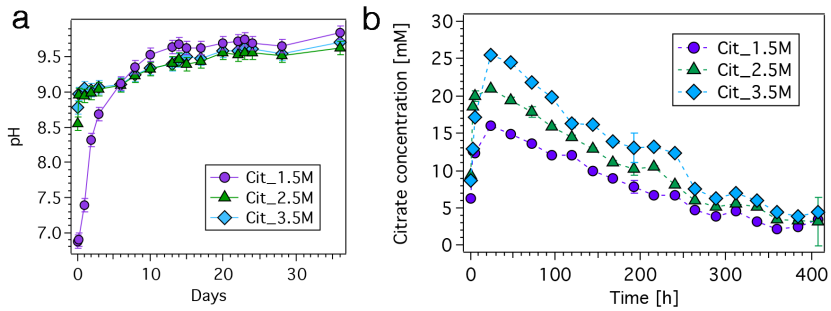

Figure 3.24: Release experiment 2: (a) pH profile and (b) concentration of citrate measured by means of UV-spectroscopy in the aliquot withdrawn from the solution, after equilibration of at least 24 h.

The cumulative release profile was fitted according to different models, so to gain insights into the kinetic and mechanism of citrate release. Following a procedure commonly reported in the literature [342–344], we fitted our experimental data using different models (see Figure 3.25, equations reported on the graph) by means of least-square nonlinear regressions [345, 346], and

the goodness of each fit was evaluated in terms of the correlation coefficients (r^2), reported in Table 3.3.

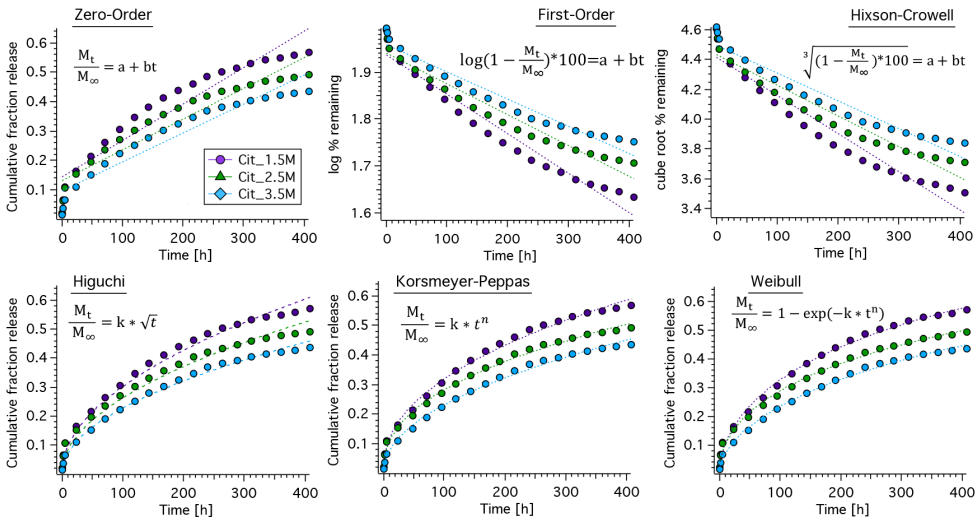

Figure 3.25: Fitting of the release experiments data (dashed lines). The equation associated to each model is reported on the graph. The cumulative fraction release was evaluated from the ratio between the moles of citrate release at time t (M_t) and that contained in the cement (M_∞).

Table 3.3: Correlation coefficients (r^2) corresponding to each fitting in Figure 3.25.

	Zero-order	First-order	Hixson-Crowell	Higuchi	Korsmeyer-Peppas	Weibull
Cit_1.5M	0.903	0.954	0.939	0.987	0.994	0.996
Cit_2.5M	0.899	0.943	0.930	0.981	0.995	0.996
Cit_3.5M	0.918	0.952	0.941	0.994	0.995	0.997

The best results (r^2 closer to 1) are attained using the Weibull model [347], which leads to n values of 0.56 ± 0.01 for Cit_1.5M, 0.51 ± 0.01 for Cit_2.5M and 0.57 ± 0.01 for Cit_3.5M. Being these values close to 0.5, and considering that good fittings are also obtained with Higuchi and Korsmeyer-Peppas models (see Figure 3.25 and Table 3.3) we can conclude that the release of citrate from the cements occurs with Fickian diffusion mechanism [344].

In conclusion, we demonstrated that citrate can be effectively included in TMP-based MPCs. The use of DAC over DAHP produces pastes with a lower cohesion and longer setting time, eventually resulting in an amorphous

network as a binding phase. Citrate can be effectively released in the incubating medium, and the % release can be tuned according to the initial amount of citrate used in the formulation.

3.3.3 Stability and release of MPCs in culture medium

As a preliminary test for the cytotoxicity experiments, we were asked to assess the stability of the set cements against dissolution in the culture medium at 37 °C. In the perspective of seeding cells on MPCs, it is important for the material not to macroscopically dissolve, as the presence of particulate may be detrimental to cell viability. Set cements at different citrate content (see the composition in Table 3.2) were incubated in a 24-well plate with 1 mL of culture medium (MEM, Minimum Essential Medium Eagle, Sigma-Aldrich) at 37 °C for four days (the duration of the experiment was chosen basing on the requisites for cells' experiments). The aspect of the cements as a function of time is reported in Figure 3.26.

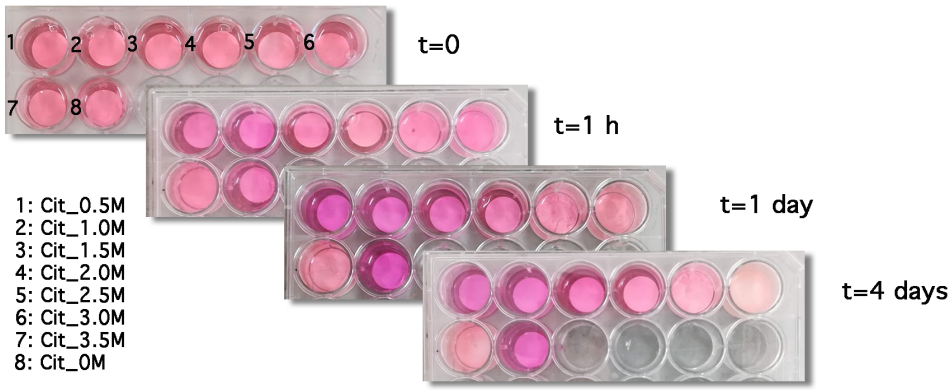

Figure 3.26: Photos of the cements incubated in 1 mL of culture medium at 37 °C at time=0, 1 h, 1 day and 4 days. The identity of each well is reported in the picture.

After only 1 h of incubation we observe that samples Cit_2.5M, Cit_3.0M and Cit_3.5M, which are the ones at highest citrate content, begin to dissolve: this is evident as the edges of the discs are not visible anymore. On the other hand, samples Cit_0M, Cit_0.5M, Cit_1.0M, Cit_1.5M and Cit_2.0M are integer at the end of the incubation period: the comparison of the weight of the cements before and after incubation reveals that sample Cit_0M retains 100 % of its

weight, while Cit_0.5M: 96 %, Cit_1.0M: 91 %, Cit_1.5M: 89 % and Cit_2.0M: 88 %. The extent of cements' dissolution is therefore related to citrate content in the samples, consistently with cohesion experiments (see Figure 3.17a). At this point, it is important to clarify some aspects. The outcome of this experiment appears in contrast with results reported in Figure 3.23b, which did not reveal a macroscopic dissolution of samples Cit_1.5M, Cit_2.5M and Cit_3.5M when incubated in physiological solution during release experiment 1. The reason for the different behavior of samples with the same composition is likely related to the different area of contact between the cements and the aqueous medium: in the release experiments, the pastes were poured in the molds, which were subsequently immersed in the solution. Only the surface of the cements was therefore in contact with the aqueous medium; on the other hand, the experiments described in this section were conducted by immersing the discs of the set cements (removed from the mold) in the MEM: all the surfaces of the discs were therefore in contact with the medium, and this could have enhanced the dissolution of the material. Formulations Cit_2.5M, Cit_3.0M and Cit_3.5M were thus discarded, and we tried to quantify the released citrate in the culture medium by means of UV-vis spectroscopy. This method, which demonstrated its effectiveness in the study of the release in physiological solution (see section 3.3.2.3) was, as expected, much more complicated in MEM. According to its datasheet, this medium contains many organic components, amino acids, vitamins and glucose, which make the detection of small amounts of citrate very challenging. As from the calibration curve we attained quite a good relationship between the absorbance at 230 nm and citrate concentration in the medium (see Appendix I), we analyzed by means of UV spectroscopy the solution in which Cit_0M, Cit_0.5M, Cit_1.0M, Cit_1.5M and Cit_2.0M were immersed for 4 days. The spectra are reported in Figure 3.27a. If we compare this series of spectra with that reported in the Appendix for the calibration curve, we observe some differences: *i.* the baseline of the spectra is higher; *ii.* a broad signal at 260-300 nm appears; *iii.* the spectrum of sample Cit_0M, which does not contain citrate, displays a peak at 230 nm. The intensity of this peak is nevertheless citrate-dependent, as absorbance increases with the increase of citrate content in the sample. We were quite puzzled by these observations, and we conducted further experiments. In order to be sure that

the observed signals were ascribable only to citrate and not to the presence of some phosphate or Mg^{2+} ions released by the cements, we dissolved some DAHP and a magnesium salt in fresh MEM, and obtained in both cases a flat spectrum (green and orange dashed curves in Figure 3.27a).

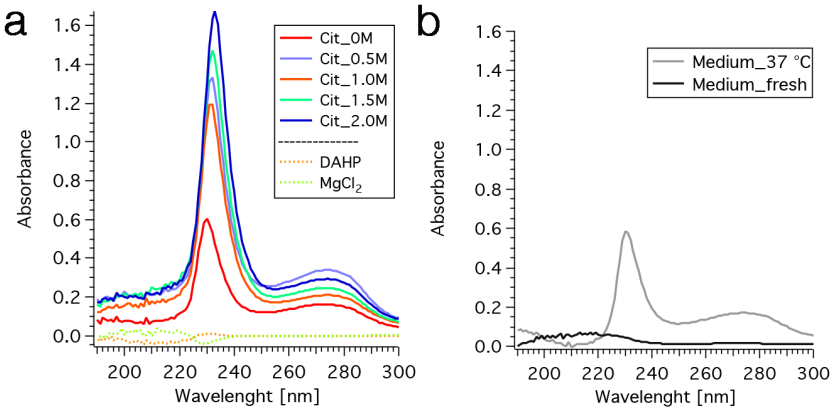

Figure 3.27: (a) UV absorption spectra of the MEM in which cements were incubated at 37 °C for 4 days; as a reference, the spectra of DAHP and $MgCl_2$ dissolved in fresh MEM are reported (dashed lines); (b) UV absorption spectra of pure MEM incubated at 37 °C for 4 days (grey curve) and fresh medium (black curve). In both systems, fresh MEM was used as a blank for the subtraction.

The only hypothesis to explain the obtained data is that the medium itself, when incubated at 37 °C, experienced some variations which resulted in the appearance of new peaks (we recall that, as a blank, fresh medium was employed). This guess was assessed by incubating 1 mL of MEM at 37 °C for four days, and then analyzing it by using fresh medium as blank for the subtraction. Results shown in Figure 3.27b confirm the validity of our hypothesis, as the spectrum of the MEM incubated at 37 °C is comparable to the one of sample Cit_0M in Figure 3.27a; on the other hand, the analysis of the fresh MEM results in a flat spectrum, consistently with the use of the same solution as blank.

In conclusion, the accurate quantification of citrate released in the MEM by means of UV-spectroscopy is challenging, given that the medium itself shows an important absorption superimposed to citrate diagnostic peaks. We can only observe that, given that the intensity of citrate peak increases from sample Cit_0.5M to Cit_2.0M (only Cit_0.5M and Cit_1.0M do not agree to this trend), the amount of released citrate is proportional to its content in the cements.

3.3.4 MPCs with intermediate citrate content

The experiments reported in the previous section revealed that MPCs formulated with a high citrate content rapidly dissolve in aqueous media, thus not being suitable to perform cytotoxicity experiments. Based on these findings, samples Cit_0M, Cit_0.5M, Cit_1.0M and Cit_2.0M (see the composition in Table 3.2), which demonstrated a good stability against dissolution, were selected to be tested with cells. Samples were prepared as described in section 3.3.1, and their properties were investigated by means of the same techniques used for formulations Cit_0M, Cit_1.5M, Cit_2.5M and Cit_3.5M. Given that citrate effect on MPCs was extensively discussed in section 3.3.2, here we will only give a quick overview of the main characterization results, prior to discussing cytotoxicity experiments.

3.3.4.1 Characterization of the cements

Consistently with the comments presented in section 3.3.2.1, we notice that citrate ions have a liquefying effect on the pastes, as observed from their consistencies after 1 min of mixing (see Figure 3.28a). The setting time of the pastes, reported in Figure 3.28b, shows that samples Cit_0M, Cit_0.5M and Cit_1.0M set in few minutes, whereas the t_2 of Cit_2.0M is around 20 min, because of the high citrate content. The nature of the crystalline phases formed upon setting was analyzed by means of XRD, and the obtained results are reported Figure 3.28c. All the samples display signals which are compatible with the simultaneous presence of farringtonite and struvite, as already discussed in this chapter. Also in this set of samples, the relative amount of struvite in the cements decreases as DAC content increases (*i.e.* DAHP content decreases). It also appears that the use of DAC over DAHP does not lead to the formation of a new crystalline phase, as no new peak can be detected in sample Cit_2.0M; citrate ions could therefore be included in the final cements as unreacted material or as components of an amorphous phase.

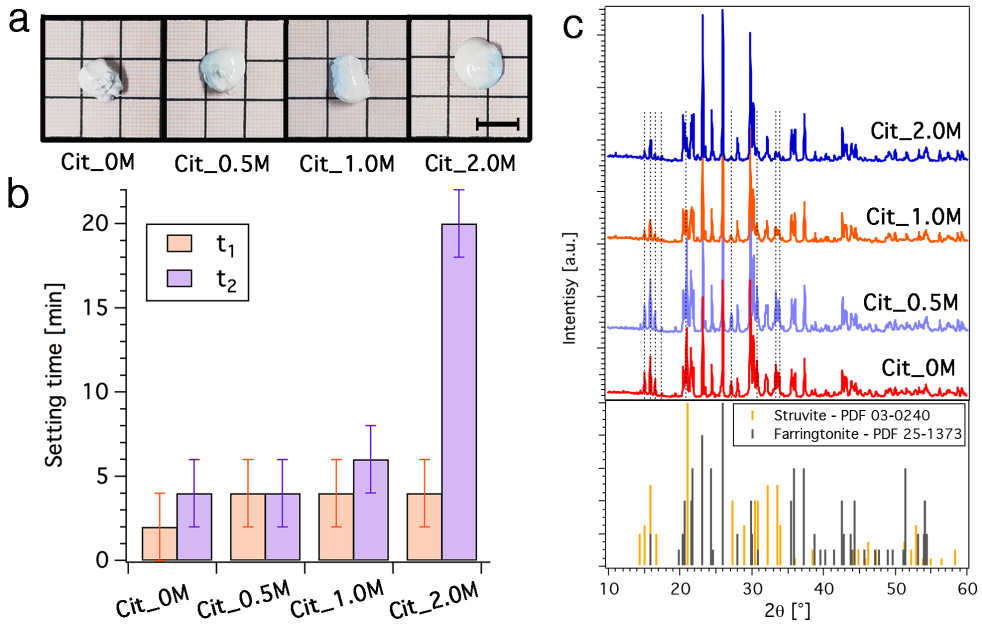

Figure 3.28: a) Photos of the samples after 1 min from the beginning of the mixing (scale bar: 1 cm); (b) Initial (t_1, orange bars) and final (t_2, purple bars) setting times of the cements, according to the Gillmore test; (c) On the top, XRD patterns of the four cements: Cit_0M (DAC 0 M, DAHP 3.5 M), red; Cit_0.5M (DAC 0.5 M, DAHP 3.0 M), lilac; Cit_1.0M (DAC 1.0 M, DAHP 2.5 M), orange; Cit_2.0M (DAC 2.0 M, DAHP 1.5 M), blue. The diffractograms are offset for display purposes. The dashed lines identify struvite diagnostic peaks, whose intensity decreases from Cit_0M to Cit_2.0M. On the bottom, PDF of struvite (n° 03-0240, yellow bars) and farringtonite (n° 25-1373, grey bars).

The morphology and microstructure of the cements were investigated by means of FE-SEM (see representative micrographs in Figure 3.29). Sample Cit_0M (Figure 3.29a) and Cit_0.5M (Figure 3.29b) are rich in struvite crystals, which are characterized by a rough surface with inner cracks and porosities. A limited number of TMP grains with a smooth surface can also be detected. On the other hand, the extent of struvite network in sample Cit_1.0M (Figure 3.29c) and Cit_2.0M (Figure 3.29d) is scarce, as a large amount of TMP grains is visible, consistently with XRD results. We can also detect some very small objects with an irregular shape (see the black circles in Figure 3.29c and Cit_1.0M), which are analogous to those observed in sample Cit_2.5M and Cit_3.5M (see Figure 3.19c and d) and represent the citrate-based binding phase.

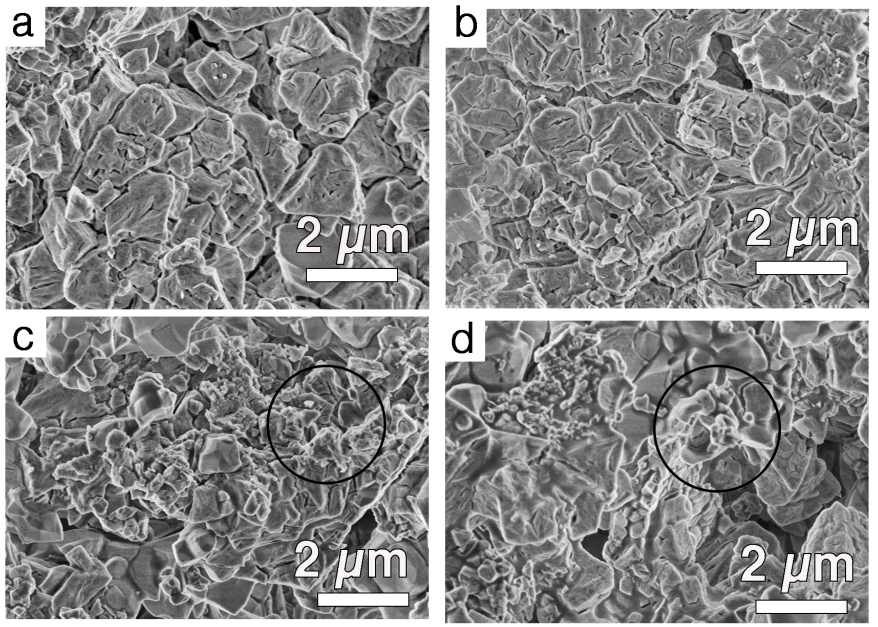

Figure 3.29: Representative FE-SEM micrographs of a cross-section of the cements; (a) sample Cit_0M; (b) sample Cit_0.5M; (c) sample Cit_1.0M; (d) sample Cit_2.0M.

In order to gain more insights into the phases formed in the cements and their features, the samples were analyzed by means of thermogravimetry coupled with differential scanning calorimetry (see Figure 3.30).

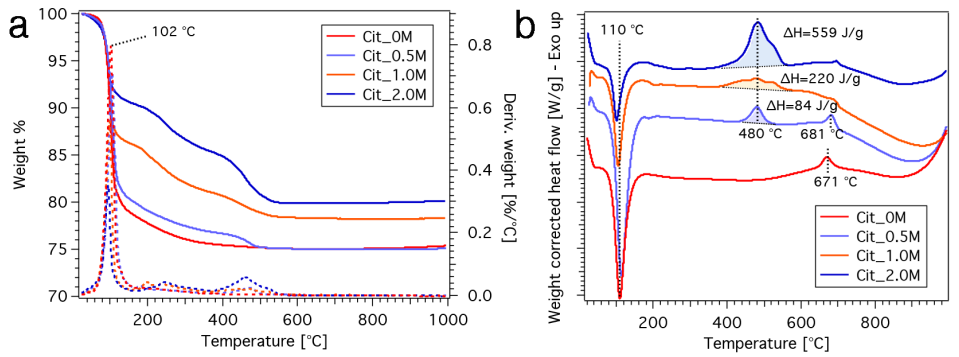

Figure 3.30: (a) Thermogravimetric curves (solid lines, left axis) and derivative curves (dashed lines, right axis) of the four cements (Cit_0M, red; Cit_0.5M, lilac; Cit_1.0M, orange; Cit_2.0M, blue). (b) Heat flow curves acquired simultaneously with the TGA measurements, together with the linear integration of the exothermic peak centered at ~ 480 °C. The curves are offset for display purposes.

In analogy to the discussion reported in section 3.3.2.2, the thermogram of sample Cit_0M (red curve in Figure 3.30a) is compatible with thermal

behavior of struvite; the weight loss at 1000 °C is 24.9 %, suggesting a composition of our sample ~ 45 % of struvite and ~ 55 % of TMP (pure struvite would lose 55 % of its initial weight [339]). The lower conversion degree to struvite when comparing this result with the one obtained for sample Cit_0M in section 3.3.2.2 is consistent with the lower P/L ratio used in this series of samples (*i.e.*, 2 g/L vs 3 g/L, see section 3.2.2.3 for the analysis of the P/L ratio on the conversion degree to struvite). The thermograms of citrate-containing-samples show that, as the amount of DAC in the formulation increases, the extent of the weight loss below 150 °C diminishes (20 % for sample Cit_0.5M, 14 % for sample Cit_1.0M and 9 % for sample Cit_2.0M), in agreement with the decrease in struvite observed by means of both XRD and SEM analyses. Moreover, in the DTG profiles, we detect the presence of new small peaks in the region 200-300 °C and 350-550 °C, whose intensity increases consistently with the amount of citrate in the formulation: these signals could be due to the new amorphous phase that forms by the reaction of TMP and DAC. The heat flow profiles (Figure 3.30b) show, in sample Cit_0M and Cit_0.5M, a small exothermic peak at 670 °C, due to the conversion of $MgHPO_4$ to $Mg_2P_2O_7$ (see reaction 3.8) [335, 339]. The intensity of this peak decreases accordingly to struvite content in the samples. Citrate-containing cements also display an exothermic peak with a maximum at ~ 480 °C, whose area grows from sample Cit_0.5M to Cit_2.0M (ΔH=84 J/g for Cit_0.5M, 220 J/g for Cit_1.0M, 559 J/g for Cit_2.0M), which is likely due to the crystallization of the amorphous binding phase formed in the citrate-containing samples, as previously discussed.

3.3.4.2 Cytotoxicity experiments

Cytotoxicity of the extracts (*i.e.* culture medium incubated with cements for 4 days) towards human fibroblasts was tested, in collaboration with researchers from "Istituto Ortopedico Rizzoli" in Bologna. The vitality % of cells as a function of time is reported in Figure 3.31. Results show that citrate-containing samples are cytotoxic after only 24 h of incubation, whereas sample Cit_0M does not display a marked toxicity towards cells, except for a mild decrease in the vitality after 48 h. Even if the response of MPCs towards cell is a relatively unexplored field, these materials are generally recognized

as biocompatible [5, 168]. Even if no report about MPC and fibroblasts was found, in the work of Klammert *et al.* a cement with composition similar to ours showed a suitable biocompatibility for human osteoblastic cells [288], while the group of Bhaduri reported that extracts obtained from the incubation of amorphous MgP did not show cytotoxicity towards osteoblastic cells from mouse calvaria [348]. Osteoblast-like cells growth and cell activity on struvite was reported to be even higher than the one on brushite and HA [290]. *In vivo* experiments also demonstrated the potentialities of MPCs [289, 293].

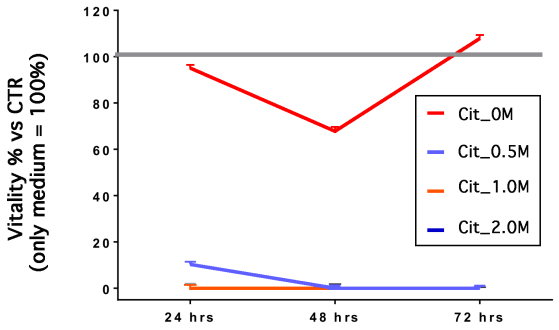

Figure 3.31: Vitality % of cells vs medium, monitored over 3 days. Cements containing citrate are cytotoxic.

As our study is the first that addresses the cytotoxicity of MPCs containing citrate, no direct comparison with previous studies can be done; nevertheless, citrate is naturally abundant in bone tissue, and citrate-based biomaterials play an important role in regenerative medicine [312]. Recently, a cement prepared with MgO, $Ca(H_2PO_4)_2{\cdot}H_2O$ and citric acid was shown to exhibit a good cytocompatibility for the culture of mBMSCs (mouse bone marrow stromal cells) on its surface, independent on the amount of citric acid in the formulation [349]. We believe that the reason for the observed drop in cells' vitality in our system is likely due to the significant citrate concentration released in the medium. A previous study from our collaborators [322] showed that, for K-citrate, the IC_{50} (half maximal inhibitory concentration) was 25.7 mM for RAW 264.7 cells (macrophages from blood) and 4.7 mM for human osteoblasts.

The data necessary to estimate the concentration of citrate released in the medium are those reported in Figure 3.27. As already discussed in section

3.3.3, the problem in quantifying citrate by means of UV-spectroscopy is due to the change of the spectrum of the MEM which, when incubated at 37 °C, modifies its absorption. However, even if a precise quantification was not possible, we tried to roughly estimate the concentration of citrate from those data, to have an idea of the order of magnitude of the released citrate. If we consider that the absorption at 230 nm of sample Cit_0M, which does not contain citrate, is 0.60, the subtraction of this value from the absorbance at the same wavelength of sample Cit_0.5M, Cit_1.0M and Cit_2.0M results in a concentration of ~150 mM for Cit_0.5M, ~130 mM for Cit_1.0M and ~240 mM for Cit_2.0M (dilution factor used 1:10, see the calibration curve in the Appendix). Even if the obtained data are very broad estimates, we can conclude that all the cements release a high concentration of citrate, thus explaining the low cells' survival rate.
In light of these results, we shifted our attention towards formulations containing a lower citrate amount, which are presented in the section below.

3.3.5 MPCs with low citrate content

The composition of this new set of samples is reported in Table 3.1. Cements were incubated in 1 mL of water at 37 °C for 4 days, in order to estimate the amount of released citrate. The obtained UV absorption curves are reported in Figure 3.32a. We observe that the intensity of the peak at 209 nm increases with the increase of the amount of citrate used in the formulation. Since also sample Cit_0M (without citrate) gives a small absorption in the spectral region of interest (likely due to an unsatisfactory subtraction of the baseline) we subtracted its spectrum from the ones of citrate-containing cements, so to only account for the signals due to this ion (see Figure 3.32b). Based on the calibration curve (see Appendix I) and considering the dilution factor 1:1 at which these experiments were conducted, we obtain that the concentration of released citrate is 1.1 mM for Cit_0.025M, 2.8 mM for Cit_0.05M and 10.2 mM for Cit_0.1M. As samples were prepared by mixing 0.300 g of TMP with 150 μL of solution, each disc respectively contains 0.00375 mmoles, 0.0075 mmoles and 0.015 mmoles, corresponding to a % of released citrate of 29 % for Cit_0.025M, 37 % of Cit_0.05M and 68 % for Cit_0.1M.

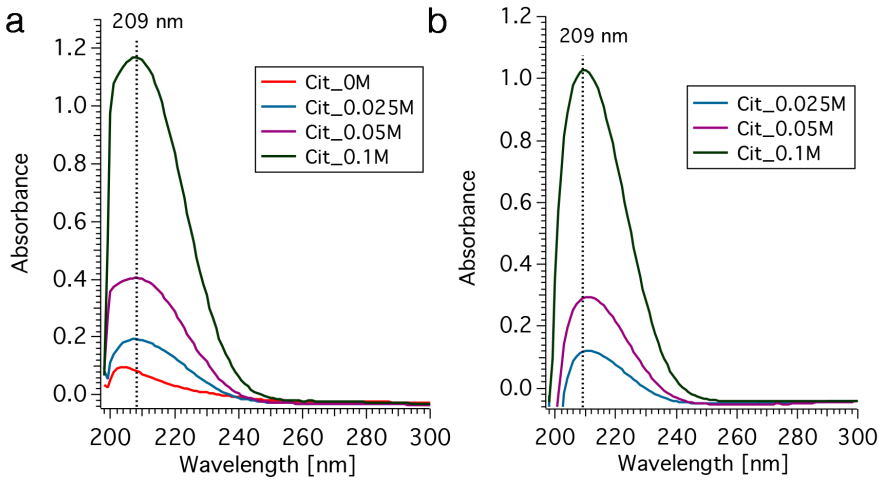

Figure 3.32: (a) UV absorption spectra of water incubated with cements Cit_0M (DAC 0 M, DAHP 3.5 M), Cit_0.025M (DAC 0.025 M, DAHP 3.475 M), Cit_0.05M (DAC 0.05 M, DAHP 3.45 M) and Cit_0.1M (DAC 0.1 M, DAHP 3.4 M) for 4 days (Cit_0M: red, Cit_0.025M: blue, Cit_0.05M: purple, Cit_0.1M: green); (b) curves in which the spectrum of sample Cit_0M (without citrate) was subtracted, so to consider only signals due to citrate.

Given these results, the cytotoxicity of the formulations was tested, and the results are reported in Figure 3.33. As it is shown in figure a, all cements display a good cell viability after 24 h of incubation, which slightly decreases over time. The different amount of citrate released by formulations Cit_0.025M, Cit_0.05M and Cit_0.1M does not affect fibroblasts' vitality, as it is evident when comparing data in Figure 3.33b.

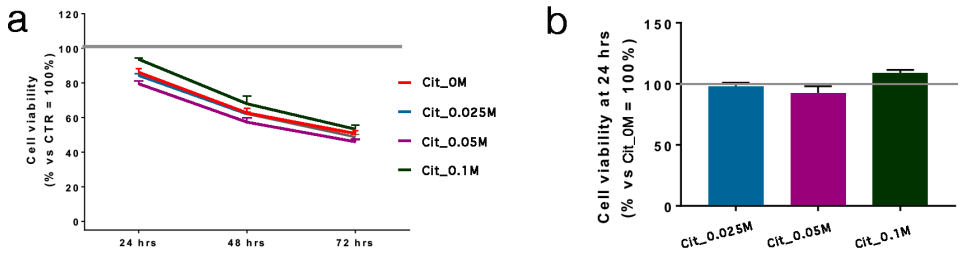

Figure 3.33: (a) Cell viability % vs medium, monitored over 3 days; red: Cit_0M (DAC 0M, DAHP 3.5M), blue: Cit_0.025M (DAC 0.025M, DAHP 3.475M), purple: Cit_0.5M (DAC 0.05M, DAHP 3.45M), green: Cit_0.1M (DAC 0.1M, DAHP 3.4M); (b) Cell viability % with respect to formulation Cit_0M (without citrate) at 24 h.

It was not possible to determine citrate concentration released in the extracts because of the issues due to the absorption of the medium incubated at 37 °C already discussed in section 3.3.3. Even if we tried to use as a blank the MEM incubated at 37 °C instead of the fresh one, we were not able to obtain an

acceptable subtraction of the baseline, likely because of the low concentration of released citrate (data not shown); nevertheless, we can reasonably suppose that the amount released is similar to that calculated from measurements in water.

To sum up, we developed a new category of biomaterials with promising characteristics: MPCs containing citrate display many of the recommended features of bone cements (moldability, adequate setting time and cohesion, good biocompatibility) and their ability to release citrate can, in principle, be beneficial in bone regeneration processes. Further experiments are necessary to clarify the nature of the amorphous phase that act as binder in cements containing citrate and to understand the reason for the mild cytotoxicity of these formulations; the biocompatibility of these cements will be therefore compared with that of CPCs already used in clinical applications, such as those based on TCP or HA.

3.4 Effect of cellulose ethers on MPCs

Results presented so far demonstrate that the properties of MPCs can be tuned by modifications in formulations parameters (section 3.2) and by the inclusion of citrate (section 3.3). CPCs are commonly modified by the addition of polymers (either included in the liquid phase or in solid state as additives to the powder phase), to enhance specific features of the material [350]. It is commonly acknowledged that the main properties affected by the addition of polymeric additives are setting time, cohesion, anti-washout ability and injectability, which are typically not-satisfactory in bare cements [350, 351]. The effect of polymeric additives on MPCs was far less investigated than on CPCs. In the literature, some reports describe the effect of gelatin [352], hydroxypropylmethyl cellulose [294, 353], chitosan [354] and polyvinyl alcohol [348], but the mechanism of interaction of these macromolecules with the inorganic phases constituting the cement is not clarified. The goal of this investigation was to include some cellulose ethers, namely CMC (carboxymethyl cellulose), HPC (hydroxypropyl cellulose) and HPMC (hydroxypropylmethyl cellulose), in TMP-based cements (see Figure 3.34). These macromolecules were selected as they are biocompatible, biodegradable, and commonly used as additives in the cosmetic, food and pharmaceutical field [355]; moreover, they are used as rheology modifiers for CPCs [304, 356–358]. We were interested in understanding how the features of MPCs are modified by the inclusion of these additives, and to unravel if their action is solely related to the interaction with water or to a specific interaction with MgP-based phases.

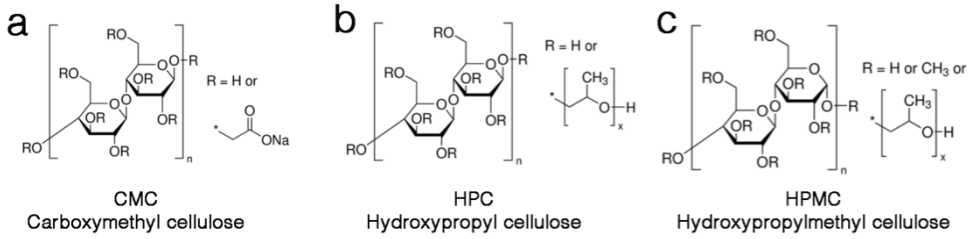

Figure 3.34: Formula of CMC (carboxymethyl cellulose), HPC (hydroxypropyl cellulose) and HPMC (hydroxypropylmethyl cellulose).

3.4.1 Samples preparation

Cements were prepared as described in section 3.2.1, using a P/L ratio of 1.5 g/mL and [DAHP]=3.5 M. Samples containing cellulose ethers (CMC and HPMC, Sigma-Aldrich, and HPC, Lamberti, formulas reported in Figure 3.34) were prepared by carefully mixing the polymers as powders with TMP, at 5 and 10 %wt (weight of the polymer with respect to the weight of TMP + DAHP solution). The amount of DAHP solution necessary to reach P/L ratio of 1.5 g/mL was then added and pastes were obtained upon mixing (typically 0.50 g of TMP with 333 μL of solution). Cements were set at 37 °C and RH > 96 % for at least 5 days.

3.4.2 Results and discussion

3.4.2.1 Handling properties and setting reaction

As polymeric additives are known to modify the cohesiveness of the pastes, we initially evaluated the appearance of the pastes immediately after mixing. As it is evident from the pictures in Figure 3.35, cellulose ethers dramatically affect the handling properties of the pastes in a concentration-dependent manner. While MPC without additives is very liquid-like, the addition of CMC, HPC and HPMC produces more compact and toothpaste-like formulations. Among the three polymers, CMC displays major effects, making the paste very thick.

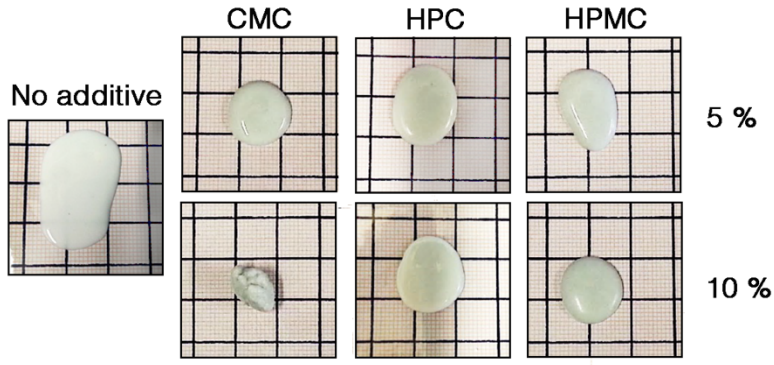

Figure 3.35: Photos of the pastes after 2 min from the beginning of mixing.

This very simple test already gives very useful information, as one can tune the initial cohesiveness of the cements by modulating the amount and type of cellulose. A more quantitative information on the effect of these additives on the setting reaction of the cements can be obtained from the analysis of the setting time, as measured by means of the Gillmore method (see Appendix I for the experimental details). Results reported in Figure 3.36 clearly highlight the impressive impact of the additives in the shortening of setting times, especially for t_1: the paste without additive reaches the initial setting time after 60 min, whereas with cellulose ethers this value can be lowered down to 15 min. Despite the amount of additive, in particular for CMC, has a deep impact on the initial cohesion of the paste, it does not have a marked effect on the setting time. Given that t_1 and t_2 should respectively be around 5 and 15 min for surgical applications [178], this investigation demonstrates that the inclusion of cellulose ethers in MPC-based formulation is an effective way to make these materials closer to the needs for a real application as bone cements.

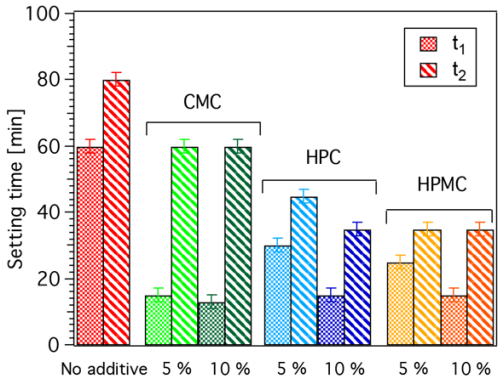

Figure 3.36: Initial (t_1) and final (t_2) setting times of the cement pastes prepared with cellulose ethers (green bars: CMC, blue bars: HPC, orange bars: HPMC). The setting time was assessed every 2 min.

The hydration reaction of the pastes was also investigated by means of low temperature (LT)-DSC. This technique, as already discussed in section 3.2.2.4, allows for the investigation of the amount and type of water in cementitious pastes, by monitoring the heat flow associated to the freezing and melting of water. We analyzed the pastes after 3 hours from the beginning of mixing, with the purpose of understanding if and how the inclusion of cellulose ethers in the formulation affects the formation of hydrated phases: water

used in the reaction can in fact follow three routes: *i.* become part of the binding phase, which is a hydrated salt (struvite, $NH_4MgPO_4 \cdot 6H_2O$); *ii.* be confined in the porosities of the cement; *iii.* evaporate. By means of LT-DSC we can estimate the amount of free (unreacted) and bound (*i.e.* confined in nanometric porosities) water, assuming that no evaporation occurs (samples stored and analyzed in hermetic steel pans). The cooling (blue) and heating (red) cycles are reported in Figure 3.37.

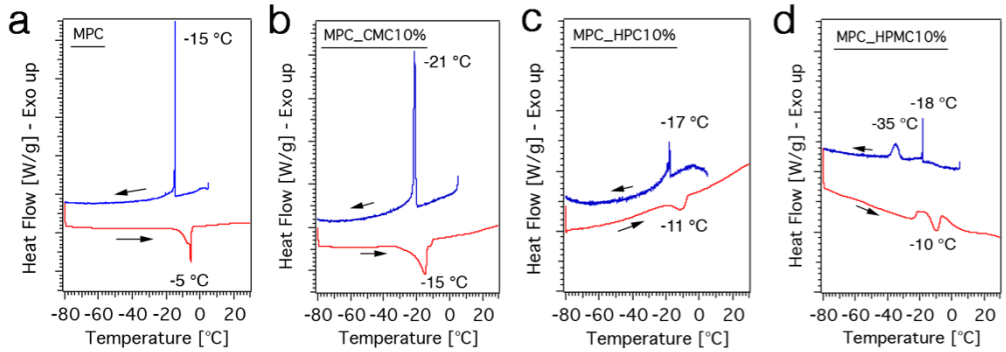

Figure 3.37: Cooling (blue) and heating (red) cycles measured by means of LT-DSC for (a) MPC, (b) MPC with CMC 10 %, (c) MPC with HPC 10 % and (d) MPC with HPMC 10 %.

Focusing our attention on the cooling cycle, we observe in all cases the sharp and intense crystallization peak of bulk water, at temperature ranging from - 15 to -21 °C; interestingly, when HPMC is present in the formulation (Figure 3.37), we also detect a small and broad peak at -35 °C, which is diagnostic of the presence of confined water [300]. This evidence suggests that this cellulose ether affects the microstructure of the cement matrix, generating nanometric porosities in which water can penetrate. The enthalpy of the melting peaks (see the red curves) reveals that the FWI % (see equation 3.3) is 7 % for MPC, 19 % for MPC_CMC10%, 3 % for MPC_HPC10% and 4 % for MPC_HPMC10%; therefore, in all samples, the majority of water is not freezable, being likely included as crystallization water in struvite crystals or not being able to freeze because strongly bound to the polymer. The fact that when using CMC the amount of free water increases suggests that this polymer may hinder struvite formation, due to its strong interaction with water (proven by the shift of the melting peak at lower temperature, -15 °C). Measurements were repeated after 7 days on the same specimens, revealing that freezable water is no longer present in samples with additives, whereas

for MPC the FWI is 4 % (curves not shown). These data can be explained hypothesizing that, in time, cellulose ethers *i.* contribute to accelerate water confinement within the cement matrix; *ii.* strongly bind water molecules, making them not able to freeze; *iii.* favor the formation of hydrated phases.

3.4.2.2 Crystallinity and microstructure

The nature of the formed phases was assessed by means of XRD measurements (see Figure 3.38a). The patterns show that no difference occurs when the polymer is included in the formulation, as in all cases we observe the presence of peaks compatible with struvite (reaction product) and farringtonite (TMP, see reaction 3.2). The extent of conversion from TMP to struvite was estimated by means of the Rietveld analysis on the recorded diffractograms, and the results are shown in Figure 3.38b: the presence of cellulose ethers in the formulation hinders struvite formation, particularly when 10 % of CMC is used (~ 33 %wt vs ~ 60 %wt for the blank). This conclusion is consistent with LT-DSC data discussed in the previous section, further highlighting the impact of these polymers on the formation of struvite binding-phase.

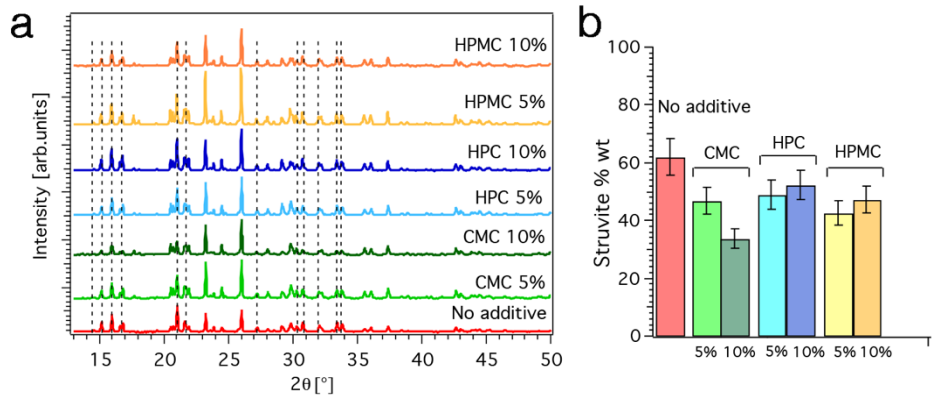

Figure 3.38: (a) XRD patterns of cements prepared with and without cellulose ethers; the dashed lines indicate the peaks corresponding to struvite (PDF: 03-0240), while all the others are compatible with farringtonite (PDF: 25-1373). (b) Quantification of struvite content in the samples, as calculated by means of the Rietveld method.

The morphology of the cements was analyzed observing cross-sections of the cements by means of FE-SEM. The micrographs of samples prepared with 10 % of cellulose are reported in Figure 3.39.

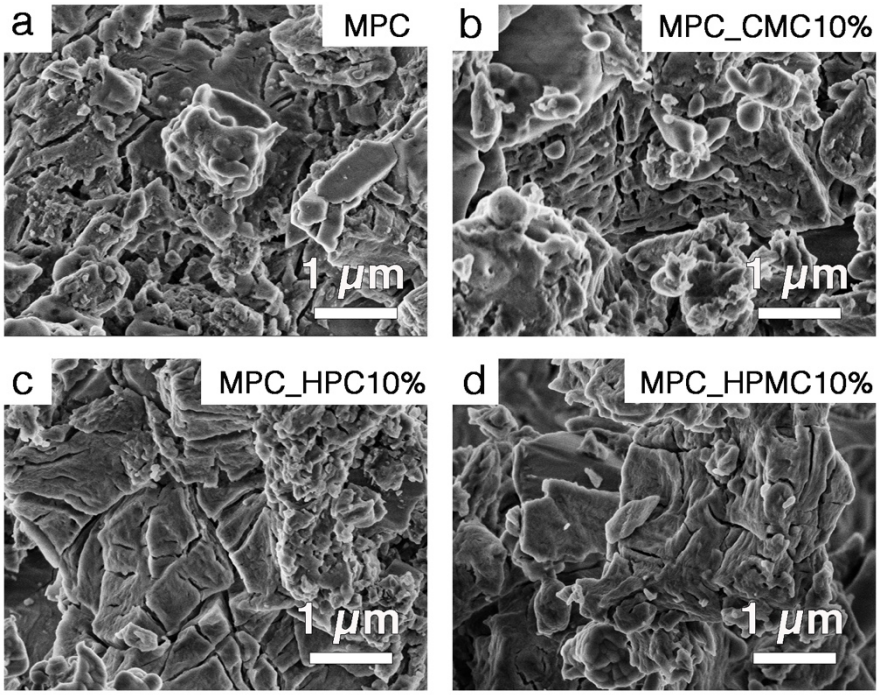

Figure 3.39: FE-SEM micrographs of (a) MPC without cellulose ethers; (b) MPC with 10 % of CMC; (c) MPC with 10 % of HPC; (d) MPC with 10 % of HPMC.

In every sample, we recognize struvite typical domains (objects with inner cracks and porosities) and smooth TMP grains, resulting in a very heterogeneous morphology. No marked difference is observed when cellulose ethers are included in the matrix, possibly because of the homogeneous distribution of the polymer within the inorganic phase.

The porosity and specific surface area of the cements was investigated by means of nitrogen sorption measurements. As it is shown in Figure 3.40, MPC (figure a) and MPC_HPC10% (figure c) display a type II isotherm, typical of non-porous or macroporous (> 50 nm) solids, whereas MPC_CMC10% (figure b) and MPC_HPMC10% (figure d) exhibit a combination of type II + type IV isotherms, suggesting the simultaneous presence of macropores (> 50 nm) and mesopores (2-50 nm) [217]. The analysis of the isotherms by means of BJH (Barrett-Joyner-Halenda) model was used to calculate the pore size distributions, and confirms the observations conducted over the isotherms about samples' porosity (see Figure 3.40 e-h). The calculation performed on the isotherms with BET model for the specific surface area indicates that MPC without additive and with HPC have a low SSA (3.5 m^2/g

and 2.6 m^2/g, respectively), while the inclusion of CMC and HPMC leads to an enhancement of this property (27.0 m^2/g for MPC_CMC10% and 79.1 m^2/g for MPC_HPMC10%).

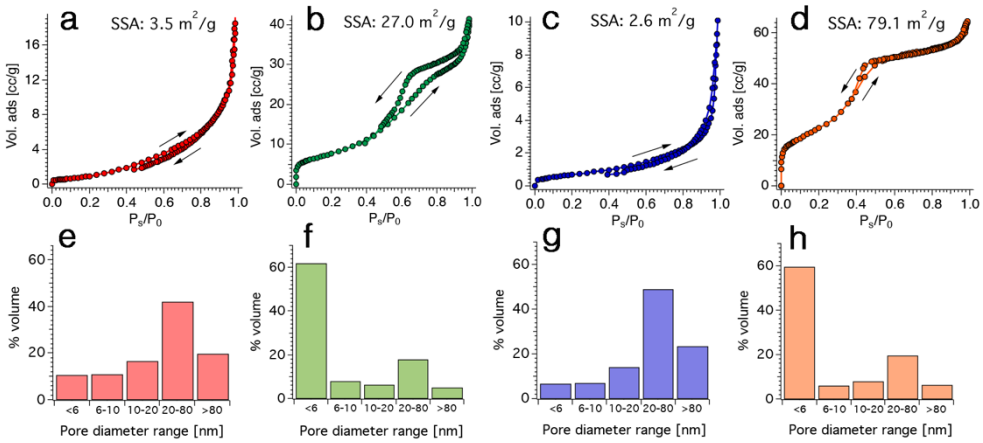

Figure 3.40: (a-d) Nitrogen sorption and desorption isotherms and (e-f) pore size distribution calculated with BJH model for MPC (red, a and e), MCP_CMC10% (green, e and f), MPC_HPC10% (blue, c and g) and MPC_HPMC10% (orange, d and h). The SSA calculated with BET model is reported above each isotherm.

3.4.2.3 Injectability and dissolution behavior

Considering the potential applications of MPCs, we tested the injectability and the dissolution behavior of MPCs in physiologic solution. The experimental conditions of the injectability test are detailed in Appendix I, and the results are shown in Figure 3.41: cellulose ethers have a great impact in the injectability of the pastes, after both 3 and 7 min from the mixing. As expected, injectability decreases as we increase the time that the paste sets in the syringe. CMC displays the greatest effect, as when present at 10 %wt makes the pastes non-injectable, whereas the other additives contribute to the reduction of the injectability. One could think that the inclusion of these polymers in the formulation is detrimental to injectability, as the bare cement displays 100 % of injectability. It is though important to consider the nature of the extruded paste: when no additive is used, MPC is immediately extruded from the syringe upon application of the load, given its very liquid-like nature, and does not maintain a compact shape. On the other hand, the extruded pastes in systems containing cellulose ethers are much more

compact and do not spread, despite not being totally injectable. Further experiments are necessary to characterize the nature of the extruded paste, so to understand which is the additive that better allows to retain the features of the paste in the extruded phase or, in other words, that limit phase-separation phenomena (see section 1.4.1).

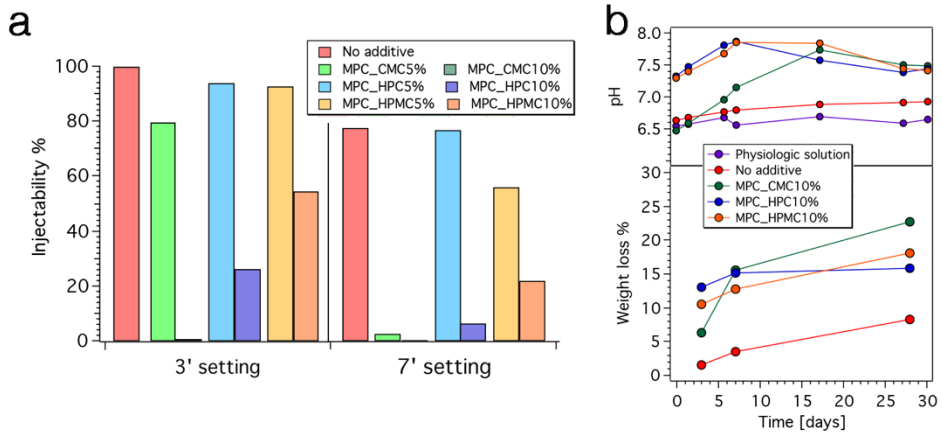

Figure 3.41: Injectability of the pastes after 3 min and 7 min of setting in the syringe; (b) incubation of cements in physiologic solution. On top: pH as a function of time; on the bottom: weight loss % as a function of time.

Set cements were incubated in physiological solution for 28 days (discs of diameter 12 mm and height 6 mm in 4 mL of solution), in order to understand how they affect the solution pH and to quantify the extent of the weight loss. Three replicas of each sample were prepared, and collected after 3, 7 and 28 days. pH results, reported in Figure 3.41b (top), show that MPC without additives does not cause significant variations in the pH of the physiological solution (6.5± 0.1), while formulations with cellulose ethers cause a slight increase in pH, which remains within the neutrality range. As far as the weight loss is concerned (see Figure 3.41b, bottom), all formulations slightly lose a certain amount of weight: this behavior is beneficial in view of the application of these materials, which in time should degrade and be replaced by new bone. The greater resorbability is indeed one of the advantages of MPCs over CPCs, as discussed in the Introduction. When cellulose ethers are included in the formulation, the extent of the weight loss is higher: this evidence may indicate that the polymer, when incubated in aqueous solution, slowly detaches from the inorganic matrix, being released in solution. This is

not necessarily detrimental for the application of these materials, as CMC, HPC and HPMC are considered biocompatible [355].

In conclusion, the addition of cellulose ethers to MPC-based formulations leads to a modification in many of the properties of the cements, such as consistency, setting time, porosity and injectability, making them more suitable for an application as bone cements. According to our preliminary results, it appears that the polymers have a direct effect in the setting reaction and mechanism of formation of the hydrated phases, being CMC the additive that most influence the formation of struvite. Further experiments are necessary to identify the additive that maximizes pastes injectability, by characterizing the features of the extruded paste.

4 Conclusions and future perspectives

This thesis describes the preparation and physico-chemical characterization of biologically-relevant forms of calcium and magnesium phosphate nanostructures (CaMgPs). These materials are of outmost importance for human beings since they constitute the main inorganic components of physiological and pathological calcifications in our body. Their formation in complex media and the interaction with biomolecules is therefore a relevant topic, as the unraveling of these mechanisms could contribute to both the understanding of their *in vivo* formation as well as to acquire knowledge to be exploited for the development of tailored materials for biomedical applications.

Among the variety of existing calcium and magnesium phosphates, during my PhD I mainly focused my attention on two categories, *i.e.* endogenous-like amorphous magnesium-calcium phosphate nanoparticles (AMCPs) and magnesium phosphate-based bone cements (MPCs). The reason for the choice of these two classes of materials is due to the fact that the attention of the scientific community toward their formation and features only recently emerged, and the understanding of their self-assembly and the interplay with bio-relevant molecules is still lacking in the literature.

AMCPs are naturally present in human ileum, where they self-assemble and trap antigens and peptidoglycans, transporting them to the immune cells of the intestinal tissue. During my PhD, we aimed at studying the formation of synthetic analogs of these particles in conditions mimicking to a certain extent the *in vivo* milieu, with the ultimate goal of connecting the physico-chemical findings with the physiological and pathological role of AMCPs. As

we were interested in determining how parameters relevant to gut's health affect the stability and the features of these particles, we started by investigating the effect of pH and Mg^{2+} concentration on the stability and crystallization pathway of AMCPs (section 2.1 and paper I). Interestingly, thanks to the combined use of infrared spectroscopy, X-rays diffraction and electron microscopy, we found out that the increase in both parameters exponentially enhances the lifetime of the amorphous phase and influences its crystallization pathway. We can therefore speculate that, *in vivo*, imbalances in pH and Mg^{2+} could lead to a destabilization of the amorphous phase, possibly resulting in alterations of the physiological functions of AMCPs. In this framework, it would be interesting to understand if cells present in intestinal epithelium show a different response towards amorphous and crystalline phosphates, so to clarify if the amorphous nature of AMCP is essential to fulfill their biological role of it is simply the inevitable consequence of the environment in which they form.

As a next step, we focused on the study of the effect of biologically-relevant molecules and macromolecules which AMCP could encounter while forming in the intestine, in the attempt of unraveling if they display an effect on AMCP features and stability. As we outlined in section 2.2 and paper II, we studied the formation of AMCP in the presence of butyric acid, lactose, gluten and peptidoglycan, finding that only the latter additive is incorporated in the inorganic structure, similarly to what happens *in vivo*. Following this investigation, we kept on increasing the complexity of our synthetic medium and we studied the formation of AMCPs in a simulated intestinal fluid (section 2.3 and paper III). Results demonstrate that the presence of sodium taurocholate and lecithin (a bile salt and a phospholipid, respectively) in the synthetic medium significantly enhances the lifetime of the amorphous phase; moreover, these organic molecules are incorporated in the particles in a time-dependent fashion, further highlighting the *in vivo* role of AMCP which traps antigens and peptidoglycans and transport them to the immune cells of the intestinal tissue. We also observed that the supramolecular aggregates present in the fluid (mixed micelles based on taurocholate and lecithin) template the formation of a shell of inorganic material around them, revealing a new strategy to prepare core-shell like structures based on calcium phosphate.

The interaction of proteins with AMCP was also addressed in two different case-studies: in the first one, again focusing on the environment in which endogenous AMCP form, we addressed the study of the AMCP interplay with mucins, large glycoproteins that are the main components of intestinal mucus (see section 2.4). We studied the formation of the amorphous particles in both mucin hydrogels and dispersions, finding that only in the latter case the formation of particles can be achieved. The obtained AMCPs are able, to some extent, to incorporate the protein, which does not affect the morphology or the Ca/Mg ratio of the particles. Further studies are necessary to establish if there is a specific interaction between particles and mucins, for instance taking advantage of solid state NMR or small angle X-rays scattering investigations.

The second case-study dealing with AMCP and proteins, described in section 2.5, was designed to assess the potentialities of AMCP for the loading of bio-relevant macromolecules, in view of their application as vehicles for nutraceutics or drug delivery. The protein selected for this investigation was an extract from the seeds of *Moringa Oleifera*, which is a tree endowed with a number of beneficial aspects from nutritional and medical point of view, and which is commonly taken as a supplement. Our study shows that not only this extract of proteins can be incorporated within AMCPs, but it also acts as stabilizer for the amorphous phase and affects its crystallization pathway. These results pave the way for the use of AMCPs in the field of loading and release of actives, following an accurate assessment of the biocompatibility of the hybrids and of the release profile in bio-relevant conditions.

The findings summarized so far have certainly contributed to shed light on the features and the stability of AMCP from a physico-chemical perspective: the attempts of mimicking the intestinal milieu are inevitably only partially representative of the real situation, and it would be interesting to investigate AMCP formation in real matrixes. Moreover, the study of AMCP interaction with cell cultures representative of the intestinal epithelium could contribute to clarify the *in vivo* formation and role of the particles. In the framework of a collaboration with gastroenterologists and biotechnologists, it would be interesting to compare the features of patients-derived AMCPs with synthetic ones, and to understand if patients' age, gender, diet or pathologies affect the feature of the particles.

As AMCPs are involved in the regulation of the immune system, it would be also intriguing to address their interplay with gut myco- and micro-biota, which is ubiquitously present in our intestine and has important implications at the immunity level. This type of studies would require extensive collaborations with biologists and biotechnologists, whose competences in the field could effectively combine with our expertise in the preparation and characterization of these inorganic structures.

In my PhD, the study of CaMgPs was not limited to structures naturally-present in our body: materials based on these inorganic phases can in fact be designed with tailored characteristics and be exploited in the biomedical field, mainly in orthopedics. In this work, we focused our attention on magnesium phosphate-based formulations as bone cements since, unlike analogous materials based on calcium phosphate, they are so far poorly explored in the literature. After an initial characterization of the features of the powder component (tri-magnesium phosphate) used to prepare them (section 3.1), we analyzed the effect of simple formulation parameters, namely P/L ratio and DAHP concentration, on the features of the pastes and of the set cements (section 3.2 and paper V). Several properties were addressed, namely cohesion, setting time, morphology, crystallinity, microstructure, porosity and mechanical properties. Thanks to this investigation, we were able to understand how these features vary according to the two formulation parameters, allowing one to design a material with tailored properties; furthermore, we clarified the setting mechanism of the pastes, showing that the formation of the binding phase (struvite) occurs on the grains of the initial reacting powder (TMP), and demonstrating that the amount of formed struvite does not always correspond to an improvement of the features of the material.

A significant part of the work was then devoted to the development of MPCs able to release citrate (section 3.3). This work is the result of an on-going collaboration with researches from the Istituto Ortopedico Rizzoli in Bologna, who suggested us that the inclusion of citrate in a material for orthopedic applications could display beneficial effects in bone regeneration processes. We partially replaced di-ammonium hydrogen phosphate with di-ammonium citrate as starting solution to prepare the cements, and we investigated how the inclusion of citrate impacts the most meaningful

properties of the material. We observed that this ion displays a liquefying effect on the pastes, prolongs the setting time and it is included within the cement matrix as an amorphous binding phase. Cements were then incubated in a physiological solution, and we could observe that they display and alkalinizing effect and that they release an amount of citrate which is proportional to that included in the initial formulation. In addition, the cytotoxicity of the formulations was tested in Bologna, and results showed that only cements releasing an amount of citrate < 10 mM are compatible with cells' vitality. MPCs containing citrate are therefore promising candidates for orthopedic applications, and further experiments are necessary to test their injectability and to assess their biological response.

As a last part, we included some cellulose ethers in MPCs, aiming at improving their handling properties and injectability (section 3.4). The additives investigated were carboxymethyl cellulose, hydroxypropyl cellulose and hydroxypropylmethyl cellulose. The use of these polymers in MPCs, which was never reported in the literature on such systems, allowed us to shorten the setting times, making them closer to clinical needs, and to modulate the consistency of the pastes and their injectability.

To sum up, the results presented in this thesis contribute to extend the knowledge about biologically-relevant CaMgPs, both when prepared to mimic the endogenous forms and when designed for biomedical applications. The relevance of these nanostructures supports the study of their formation mechanisms and their effective application in the biomedical field. Many questions still need to be answered, and future studies are necessary to achieve the full understanding of their potentialities.

5 Bibliography

[1]E. Königsberger and L. Königsberger, Biomineralization: medical aspects of solubility, J. Wiley, **2006**.
[2]L. Wang and G. H. Nancollas, *Chem. Rev.*, 108, 4628–4669, **2008**.
[3]A. K. Lynn and W. Bonfield, *Acc. Chem. Res.*, 38, 202–207, **2005**.
[4]S. V. Dorozhkin, *Progress in Biomaterials*, 5, 9–70, **2016**.
[5]N. Ostrowski et al., *ACS Biomater. Sci. Eng.*, 2, 1067–1083, **2016**.
[6]N. Eliaz and N. Metoki, *Materials*, 10, 334, **2017**.
[7]J. F. Rakovan and J. D. Pasteris, *Elements*, 11, 195–200, **2015**.
[8]K. Lin et al., *Acta Biomater*, 10, 4071–4102, **2014**.
[9]I. L. Shashkova et al., *Inorg Mater*, 36, 826–829, **2000**.
[10]M. A. Aramendía et al., *Journal of Coll and Int Sci*, 217, 288–298, **1999**.
[11]J. W. Park et al., *Adv in Mat Sci and Eng*, 2016, e7179403, **2016**.
[12]Q. Yang et al., *Mat. Struct.*, 33, 229–234, **2000**.
[13]W. Jahnen-Dechent and M. Ketteler, *Clin Kidney J*, 5, i3–i14, **2012**.
[14]M. J. Olszta et al., *Mat Sci and Eng: R: Reports*, 58, 77–116, **2007**.
[15]E. Beniash et al., *Journal of Structural Biology*, 166, 133–143, **2009**.
[16]L. N. Poloni and M. D. Ward, *Chem. Mater.*, 26, 477–495, **2014**.
[17]R. Z. LeGeros, *Z Kardiol*, 90, 116–124, **2001**.
[18]F. Tamimi et al., *Acta Biomaterialia*, 7, 2678–2685, **2011**.
[19]R. Miano et al., *Urol. Int.*, 79 Suppl 1, 32–36, **2007**.
[20]D. J. McCarty, *Arthritis & Rheumatism*, 19, 275–285, **1976**.
[21]L. S. Steinbach and D. Resnick, *Curr Probl Diagn Rad*, 29, 206–229, **2000**.
[22]S. V. Dorozhkin, M. Epple, *Angewandte Chemie Int Ed*, 41, 3130–3146, **2002**.
[23]C. M. Giachelli, *Kidney Int.*, 75, 890–897, **2009**.
[24]N. Reznikov et al., *Acta Biomaterialia*, 10, 3815–3826, **2014**.
[25]S. Castiglioni et al., *Nutrients*, 5, 3022–3033, **2013**.

[26]J. M. Burnell et al., *Calcif Tissue Int*, 31, 13–19, **1980**.

[27]A. Bigi et al., *Calcif Tissue Int*, 50, 439–444, **1992**.

[28]E. Davies et al., *PNAS*, 111, E1354–E1363, **2014**.

[29]J. Jeong et al., *Biomater Res*, 23:4, **2019**.

[30]F. Barrère-de Groot et al., *Mat Today: Proceedings*, 5, 15501–15505, **2018**.

[31]R. Florencio-Silva et al., *Biomed Res Int*, 2015, **2015**.

[32]A. K. Nair et al., *Nat Commun*, 4, 1724, **2013**.

[33]S. Bechtle et al., *Biomaterials*, 31, 375–384, **2010**.

[34]C. M. Giachelli, *Am J Pathol*, 154, 671–675, **1999**.

[35]H. E. Schroeder, *J. Periodontol.*, 40, 643–646, **1969**.

[36]R. Zapanta Le Geros, *J Dent Res*, 53, 45–50, **1974**.

[37]R. Z. LeGeros, *Monogr Oral Sci*, 15, 1–201, **1991**.

[38]D. J. White, *European Journal of Oral Sciences*, 105, 508–522, **1997**.

[39]R. A. Barrea et al., *X-Ray Spectrometry*, 32, 387–395, **2003**.

[40]L. S. Burnstein et al., *J. Oral Pathol.*, 8, 284–291, **1979**.

[41]S. Materazzi et al., *Thermochimica Acta*, 264, 75–93, **1995**.

[42]R. Selvaraju et al., *Spectrochimica Acta Part A,* 137, 1397–1402, **2015**.

[43]A. K. Mukherjee, *Journal of the Indian Institute of Science*, 94, 35-44–44, **2014**.

[44]C. Combes and C. Rey, *Acta Biomaterialia*, 6, 3362–3378, **2010**.

[45]A. D. McNaught and A. Wilkinson, Blackwell Scientific Publications, Oxford, **1997**.

[46]V. Uskoković, *Crystal Growth & Design*, 19, 4340–4357, **2019**.

[47]H. A. Lowenstam and S. Weiner, *On Biomineralization,* Oxford University Press, **1989**.

[48]L. B. Gower, *Chem. Rev.*, 108, 4551–4627, **2008**.

[49]Y. Politi et al., *Science*, 306, 1161–1164, **2004**.

[50]I. M. Weiss et al., *Journal of Experimental Zoology*, 293, 478–491, **2002**.

[51]L. Addadi et al., *Adv. Mater.*, 15, 959–970, **2003**.

[52]R. Gelli et al., *Advances in Colloid and Interface Science*, 269, 219–235, **2019**.

[53]S. V. Dorozhkin, *Int Journal of Materials and Chemistry*, 2, 19–46, **2012**.

[54]M. L. Watson and R. A. Robinson, *Am. J. Anat.*, 93, 25–59, **1953**.

[55]E. D. Eanes et al., *Nature*, 208, 365–367, **1965**.

[56]H. Cölfen and S. Mann, *Angewandte Chemie Int Ed*, 42, 2350–2365, **2003**.

[57]J. J. De Yoreo, *Reviews in Mineralogy and Geochemistry*, 54, 57–93, **2003**.

[58]H. C. Margolis et al., *Front. Physiol.*, 5, **2014**.

[59]M. Johnsson, G. H. Nancollas, *Crit Rev in Oral Bio & Med*, 3, 61–82, **1992**.
[60]A. L. Boskey, *J Dent Res*, 76, 1433–1436, **1997**.
[61]A. L. Boskey and A. S. Posner, *J. Phys. Chem.*, 80, 40–45, **1976**.
[62]F. Betts and A. S. Posner, *Materials Research Bulletin*, 9, 353–360, **1974**.
[63]J. Zhao et al., *Journal of Dental Sciences*, 7, 316–323, **2012**.
[64]A. S. Posner et al., *Prog in Crystal Growth and Character*, 3, 49–64, **1980**.
[65]G. Mancardi et al., *Journal of Materials Chemistry B*, 5, 7274–7284, **2017**.
[66]A. Dey et al., *Nat Mater*, 9, 1010–1014, **2010**.
[67]W. J. E. M. Habraken et al., *Nature Communications*, 4, 1507, **2013**.
[68]D. Gebauer et al., *Chemical Society Reviews*, 43, 2348–2371, **2014**.
[69]E. D. Eanes and J. L. Meyer, *Calc. Tis Res.*, 23, 259–269, **1977**.
[70]A. L. Boskey and A. S. Posner, *J. Phys. Chem.*, 77, 2313–2317, **1973**.
[71]Y.-W. Wang et al., *Chem. Mater.*, 26, 5830–5838, **2014**.
[72]A. Rajasekharan, M. Andersson, *Cryst Growth & Des*, 15, 2775–2780, **2015**.
[73]A. L. Boskey and A. S. Posner, *Materials Research Bulletin*, 9, 907–916, **1974**.
[74]B. N. Bachra and H. R. A. Fischer, *Calc. Tis Res.*, 3, 348–357, **1969**.
[75]W. Kibalczyc et al., *Journal of Crystal Growth*, 106, 355–366, **1990**.
[76]J. Christoffersen et al., *Journal of Crystal Growth*, 94, 767–777, **1989**.
[77]F. Abbona and A. Baronnet, *Journal of Crystal Growth*, 165, 98–105, **1996**.
[78]E. D. Eanes and A. S. Posner, *Calc. Tis Res.*, 2, 38–48, **1968**.
[79]O. Bertran et al., *Chemistry - A European Journal*, 21, 2537–2546, **2015**.
[80]X. Yang et al., *CrystEngComm*, 13, 1153–1158, **2011**.
[81]H. Ding et al., *Crystal Growth & Design*, 14, 763–769, **2014**.
[82]Q. Liu et al., *Eur. J. Inorg. Chem.*, 2016, 5623–5629, **2016**.
[83]I. Buljan Meić et al., *Crystal Growth & Design*, 17, 1103–1117, **2017**.
[84]N. C. Blumenthal et al., *Calcif. Tissue Int.*, 45, 81–87, **1989**.
[85]N. C. Blumenthal et al., *Calcif Tissue Int*, 56, 316–322, **1995**.
[86]M. J. Root, *Calcif Tissue Int*, 47, 112–116, **1990**.
[87]E. D. Eanes and J. L. Meyer, *J Dent Res*, 57, 617–624, **1978**.
[88]J. D. Termine et al., *Archives of Biochem and Biophys*, 140, 318–325, **1970**.
[89]H. Fleisch et al., *Calc. Tis Res.*, 2, 49–59, **1968**.
[90]R. Z. LeGeros et al., *Key Engineering Materials*, 284–286, 7–10, **2005**.
[91]N. C. Blumenthal et al., *Calc. Tis Res.*, 18, 81–90, **1975**.
[92]D. J. Greenfield and E. D. Eanes, *Calc. Tis Res.*, 9, 152–162, **1972**.
[93]L. Brecević and H. Füredi-Milhofer, *Calcif Tissue Int*, 28, 131–136, **1979**.

[94] Y. Chen et al., *CrystEngComm*, 16, 1864–1867, **2014**.
[95] G. L. Becker et al., *J Cell Biol*, 61, 316–326, **1974**.
[96] F. Betts et al., *Proc. Natl. Acad. Sci. U.S.A.*, 72, 2088–2090, **1975**.
[97] R. E. Wuthier et al., *Calcif Tissue Int*, 37, 401–410, **1985**.
[98] A. S. Posner et al., *Calc. Tis Res.*, 22, 208–212, **1976**.
[99] N. C. Blumenthal et al., *Calc. Tis Res.*, 23, 245–250, **1977**.
[100] K. J. Cross et al., *J. Biol. Chem.*, 280, 15362–15369, **2005**.
[101] N. C. Blumenthal et al., *Calcif Tissue Int*, 27, 75–82, **1979**.
[102] N. C. Blumenthal, *Clin. Orthop. Relat. Res.*, 279–289, **1989**.
[103] E. E. Golub, *Biochim Biophys Acta*, 1790, 1592–1598, **2009**.
[104] A. L. Boskey and A. S. Posner, *Calc. Tis Res.*, 23, 251–258, **1977**.
[105] E. D. Eanes et al., *Calcified tissue international*, 36, 421–430, **1984**.
[106] R. S. Crowther and R. D. Soloway, *Semin. Liver Dis.*, 10, 171–180, **1990**.
[107] S. M. Qiu et al., *J. Clin. Invest.*, 88, 1265–1271, **1991**.
[108] Y. Li et al., *Journal of Materials Science Letters*, 22, 1015–1016, **2003**.
[109] Y. Li and W. Weng, *J Mater Sci Mater Med*, 18, 2303–2308, **2007**.
[110] J. Wang et al., *CrystEngComm*, 15, 6151–6158, **2013**.
[111] Z. Amjad, *Phosphorus Research Bulletin*, 7, 45–54, **1997**.
[112] Z. Amjad, *Colloids and Surfaces*, 48, 95–106, **1990**.
[113] B. Cantaert et al., *Journal of Materials Chemistry B*, 1, 6586–6595, **2013**.
[114] R. A. Robinson and M. L. Watson, *Annals of the NY Academy of Sciences*, 60, 596–630, **1955**.
[115] R. A. Harper, A. S. Posner, *Proc. Soc. Exp. Biol. Med.*, 122, 137–142, **1966**.
[116] J. D. Termine and A. S. Posner, *Calc. Tis Res.*, 1, 8–23, **1967**.
[117] J. D. Termine and A. S. Posner, *Science*, 153, 1523–1525, **1966**.
[118] A. S. Posner and F. Betts, *Acc. Chem. Res.*, 8, 273–281, **1975**.
[119] M. D. Grynpas et al., *Calcif Tissue Int*, 36, 291–301, **1984**.
[120] E. D. Eanes, in *Monographs in oral science: Octacalcium Phosphate*, 18, 130–147, **2001**.
[121] Y. Wang et al., *Nature Materials*, 12, 1144–1153, **2013**.
[122] S. Weiner et al., *Science*, 309, 1027–1028, **2005**.
[123] J. D. Termine and E. D. Eanes, *Calc. Tis Res.*, 15, 81–84, **1974**.
[124] N. J. Crane et al., *Bone*, 39, 434–442, **2006**.
[125] W. E. Brown, *Clin. Orthop. Relat. Res.*, 44, 205–220, **1966**.
[126] W. E. Brown et al., *Adv Dent Res.*, 1, 306–313, **1987**.

[127] W. E. Brown and L. C. Chow, *Annual Rev of Mat Sci*, 6, 213–236, **1976**.
[128] S. Weiner, *Bone*, 39, 431–433, **2006**.
[129] M. D. Grynpas and S. Omelon, *Bone*, 41, 162–164, **2007**.
[130] J. Mahamid et al., *Proc. Natl. Acad. Sci. U.S.A.*, 105, 12748–12753, **2008**.
[131] J. Mahamid et al., *PNAS*, 107, 6316–6321, **2010**.
[132] A. Akiva et al., *Bone*, 75, 192–200, **2015**.
[133] M. Kerschnitzki et al., *Journal of Structural Biology*, 195, 82–92, **2016**.
[134] L. Addadi et al., *Isr. J. Chem.*, 56, 227–241, **2016**.
[135] J. P. Simmer et al., *J Dent Res*, 89, 1024–1038, **2010**.
[136] S. Weiner and H. Lowenstam, *Critical Rev in Biochem*, 20, 365–408, **1986**.
[137] S.-Y. Kwak et al., *J Biol Chem*, 284, 18972–18979, **2009**.
[138] M. Iijima et al., *Cryst Growth Des*, 10, 4815–4822, **2010**.
[139] X. Yang et al., *J. Phys. Chem. B*, 114, 2293–2300, **2010**.
[140] P.-A. Fang et al., *PNAS*, 108, 14097–14102, **2011**.
[141] L. M. Gordon et al., *Science*, 347, 746–750, **2015**.
[142] A. L. Fontaine et al., *Science Advances*, 2, e1601145, **2016**.
[143] H. Pan et al., *Acta Biomaterialia*, 6, 4181–4188, **2010**.
[144] M. M. X. Cai et al., *Bonekey Rep*, 4, 672, **2015**.
[145] A. Heiss et al., *J. Biol. Chem.*, 278, 13333–13341, **2003**.
[146] C. Schäfer et al., *J Clin Invest*, 112, 357–366, **2003**.
[147] A. Heiss et al., *Biointerphases*, 2, 16–20, **2007**.
[148] E. R. Smith et al., *PLOS ONE*, 8, e60904, **2013**.
[149] C. N. Rochette et al., *ChemBioChem*, 10, 735–740, **2009**.
[150] P. Aghagolzadeh et al., *Atherosclerosis*, 251, 404–414, **2016**.
[151] M. Van Kemenade, P. L. de Bruyn, *J Coll and Int Sci*, 129, 1–14, **1989**.
[152] C. Holt, *Current Opinion in Structural Biology*, 23, 420–425, **2013**.
[153] S. Marchin et al., *The Journal of Chemical Physics*, 126, 045101, **2007**.
[154] C. G. de Kruif et al., *Adv in Coll and Int Sci*, 171–172, 36–52, **2012**.
[155] S. Lenton et al., *Dairy Sci. & Technol.*, 95, 3–14, **2015**.
[156] M. C. E. Lomer et al., *Proceedings of the Nutrition Soc*, 61, 123–130, **2002**.
[157] J. J. Powell et al., *Nat Nano*, 10, 361–369, **2015**.
[158] H. P. Schedl et al., *Nature*, 215, 198–199, **1967**.
[159] H. Schedl et al., *American Journal of Physiology*, 214, 814–819, **1968**.
[160] J. J. Powell et al., *Journal of Inorganic Biochemistry*, 75, 167–180, **1999**.
[161] J. J. Powell et al., *Br J Nutr*, 98, S59–S63, **2007**.

[162] J. J. Powell et al., *Journal of Autoimmunity*, 34, J226–J233, **2010**.
[163] R. Gelli et al., *Journal of Colloid and Interface Science*, 531, 681–692, **2018**.
[164] J. Robertson et al., *Sci Rep*, 6, **2016**.
[165] R. E. Hewitt et al., *Frontiers in Immunology*, 8, **2017**.
[166] L. C. Pele et al., *Nanomedicine: Nanotech, Biol and Med*, 13, 619–630, **2017**.
[167] J. D. Söderholm, *Nat Nano*, 10, 298–299, **2015**.
[168] M. Nabiyouni et al., *Acta Biomaterialia*, 66, 23–43, **2018**.
[169] M. M. Stevens, *Materials Today*, 11, 18–25, **2008**.
[170] J. Zhang et al., *Acta Biomaterialia*, 10, 1035–1049, **2014**.
[171] M. Canillas et al., *Boletín de la Sociedad Española de Cerámica y Vidrio*, 56, 91–112, **2017**.
[172] S. V. Dorozhkin, *Ceramics International*, 41, 13913–13966, **2015**.
[173] S. N. Bhaskar et al., *Oral Surgery, Medicine, Pathology*, 32, 336–346, **1971**.
[174] W. Habraken et al., *Materials Today*, 19, 69–87, **2016**.
[175] V. Uskoković, D. P. Uskoković, *J. Biomed. Mater. Res.*, 96B, 152–191, **2011**.
[176] R. A. Surmenev et al., *Acta Biomaterialia*, 10, 557–579, **2014**.
[177] S. Samavedi et al., *Acta Biomaterialia*, 9, 8037–8045, **2013**.
[178] S. V. Dorozhkin, *Int Journal of Materials and Chemistry*, 1, 1–48, **2012**.
[179] M. Vert et al., IUPAC Recommendations 2012, 84, 377–410, **2012**.
[180] Y. J. No et al., *Nanomedicine*, 9, 1745–1764, **2014**.
[181] C01 Committee, ASTM C266 - 13, ASTM International.
[182] I. Khairoun et al., *Journal of Mat Science: Mat in Med*, 9, 667–671, **1998**.
[183] R. O'Neill et al., *Acta Biomaterialia*, 50, 1–19, **2017**.
[184] H. H. Xu et al., *Bone Research*, 5, 17056, **2017**.
[185] D. F. Williams, *The Williams Dictionary of Biomaterials*, Liverpool University Press, **1999**.
[186] A. S. Wagh and S. Y. Jeong, *J. Amer. Ceramic Society*, 86, 1838–1844, **2003**.
[187] G. Mestres and M.-P. Ginebra, *Acta Biomaterialia*, 7, 1853–1861, **2011**.
[188] F. Wu et al., *Acta Biomaterialia*, 4, 1873–1884, **2008**.
[189] L. V. Gulotta et al., *Am J Sports Med*, 36, 1290–1297, **2008**.
[190] L. J. M. Hirvinen et al., *American Journal of Vet Research*, 70, 964–972, **2009**.
[191] S. Yoshizawa et al., *Acta Biomaterialia*, 10, 2834–2842, **2014**.
[192] L. Wu et al., *Acta Biomaterialia*, 27, 294–304, **2015**.
[193] G. Mestres et al., *Acta Biomaterialia*, 9, 8384–8393, **2013**.
[194] C. Ma et al., *Biomaterials*, 178, 383–400, **2018**.

[195] J. Aron-Wisnewsky et al., *Nature Rev. Gastroent. and Hepat.*, 9, 590, **2012**.
[196] S. G. Nugent et al., *Gut*, 48, 571–577, **2001**.
[197] L. L. Hardwick et al., *Miner Electrolyte Metab*, 16, 174–180, **1990**.
[198] K. Murakami et al., *Eur J Clin Nutr*, 61, 616–622, **2007**.
[199] C. Holt et al., *Journal of Crystal Growth*, 92, 239–252, **1988**.
[200] C. Drouet, *BioMed Research International*, 2013, 490946, **2013**.
[201] C. Holt et al., *Materials Research Bulletin*, 24, 55–62, **1989**.
[202] A. C. Tas, *Journal of Materials Chemistry B*, 1, 4511-4520, **2013**.
[203] L. Tortet et al., *Journal of Solid State Chemistry*, 132, 6–16, **1997**.
[204] M. P. Gashti et al., *J. Mater. Chem. B*, 1, 1501–1508, **2013**.
[205] B. Šoptrajanov et al., *Spectroscopy Letters*, 32, 703–717, **1999**.
[206] B. Šoptrajanov et al., *Spectroscopy Letters*, 31, 1191–1205, **1998**.
[207] D. Liu et al., *Materials Letters*, 240, 169–171, **2019**.
[208] P. Sikder and S. B. Bhaduri, *J. Amer. Ceram. Society*, 101, 2537–2544, **2018**.
[209] S. V. Dorozhkin, *Acta Biomaterialia*, 6, 4457–4475, **2010**.
[210] N. C. Blumenthal et al., *Materials Research Bulletin*, 7, 1181–1189, **1972**.
[211] Y. Kojima et al., *Phosphorus Research Bulletin*, 4, 47–52, **1994**.
[212] S. Somrani et al., *J. Mater. Chem.*, 13, 888–892, **2003**.
[213] T. Kanazawa et al., *J. Chem. Technol. Biotechnol.*, 32, 399–406, **1982**.
[214] J. Vecstaudza et al., *J. of the European Ceramic Society*, 39, 1642–1649, **2019**.
[215] V. M. Wu et al., *ACS Appl. Mater. Interfaces*, 10, 34013–34028, **2018**.
[216] D. Lee and P. N. Kumta, *Mat. Sci. Eng.: C*, 30, 1313–1317, **2010**.
[217] M. Thommes et al., *Pure and Applied Chemistry*, 87, 1051–1069, **2015**.
[218] J. M. Holmes and R. A. Beebe, *Calcified Tissue Research*, 7, 163–174, **1971**.
[219] J. Vecstaudza and J. Locs, *Key Engineering Materials*, 721, 172–176, **2016**.
[220] S. Cazalbou et al., *J. Phys. Chem. B*, 119, 3014–3024, **2015**.
[221] J. Gómez-Morales et al., *Prog. in Cryst. Grow. Charac. Mat.*, 59, 1–46, **2013**.
[222] A. Hirsch et al., *Chem. Mater.*, 26, 2934–2942, **2014**.
[223] A. Betke and G. Kickelbick, *Inorganics*, 2, 1–15, **2014**.
[224] L.-Y. Huang et al., *Nanoscale Research Letters*, 8, 417, **2013**.
[225] A. C. Tas, *Materials Science and Engineering: C*, 32, 1097–1106, **2012**.
[226] A. Press et al., *Alimentary Pharmacology & Therapeutics*, 12, 673–678, **1998**.
[227] J. Fallingborg, *Dan Med Bull*, 46, 183–196, **1999**.
[228] M. H. Salimi et al., *Langmuir*, 1, 119–122, **1985**.
[229] B. J. Scanlan et al., *Mol. Cell. Biochem.*, 306, 59–69, **2007**.

[230] B. E. Lacy et al., *Therap Adv Gastroenterol*, 2, 221–238, **2009**.
[231] A. Y. Abuhelwa et al., *Europ. J. of Pharm. Biopharm.*, 112, 234–248, **2017**.
[232] K. D. Kohl et al., *Journal of Exp. Zoology Part A,* 319, 225–229, **2013**.
[233] A. Bedford and J. Gong, *Animal Nutrition*, 4, 151–159, **2018**.
[234] S. E. Pryde et al., *FEMS Microbiology Letters*, 217, 133–139, **2002**.
[235] J.-P. Segain et al., *Gut*, 47, 397–403, **2000**.
[236] A. Załęski et al., *Prz Gastroenterol*, 8, 350–353, **2013**.
[237] K. Borycka-Kiciak et al., *Prz Gastroenterol*, 12, 83–89, **2017**.
[238] H. Wieser, *Food Microbiology*, 24, 115–119, **2007**.
[239] P. R. Shewry et al., *Philos Trans R Soc Lond B Biol Sci*, 357, 133–142, **2002**.
[240] J. F. Ludvigsson et al., *Gut*, 62, 43–52, **2013**.
[241] J. A. Leenheer and C. E. Rostad, US Geological Survey, Scientific Investigations Report 2004-5217, **2004**.
[242] D. Riethorst et al., *Journal of Pharmaceutical Sciences*, 105, 673–681, **2016**.
[243] C. Markopoulos et al., *Europ. J. Pharm. and Biopharm.*, 93, 173–182, **2015**.
[244] B. Kloefer et al., *Dissolution Technologies*, 17, 6–13, **2010**.
[245] M. C. di Gregorio et al., *Langmuir*, 35, 21, 6803-6821, **2018**.
[246] R. Holm et al., *International Journal of Pharmaceutics*, 453, 44–55, **2013**.
[247] C.-Y. Cheng et al., *Langmuir*, 30, 10221–10230, **2014**.
[248] J. Cautela et al., *Colloids and Surfaces A*, 532, 411–419, **2017**.
[249] K. Kleberg et al., *Journal of Pharmaceutical Sciences*, 99, 3522–3532, **2010**.
[250] G. A. Kossena et al., *Journal of Pharmaceutical Sciences*, 92, 634–648, **2003**.
[251] E. W. Moore et al., *Gastroenterology*, 83, 1079–1089, **1982**.
[252] M. A. Rivadeneyra et al., *Mineralogical Journal*, 13, 443–447, **1987**.
[253] B. P. Bastakoti et al., *Chem. Comm.*, 48, 6532–6534, **2012**.
[254] W. Tjandra et al., *Nanotechnology*, 17, 5988–5994, **2006**.
[255] G.-J. Ding et al., *Journal of Materials Chemistry B*, 3, 1823–1830, **2015**.
[256] C. Wu et al., *Int J Nanomedicine*, 12, 7979–7992, **2017**.
[257] S. Huang et al., *Materials Letters*, 197, 1–4, **2017**.
[258] A. Bigi et al., *Angewandte Chemie*, 114, 2267–2270, **2002**.
[259] D. Hagmeyer et al., *Journal of Materials Chemistry*, 21, 9219–9223, **2011**.
[260] Y. Cai et al., *Chem. Mater.*, 19, 3081–3083, **2007**.
[261] B. Hammouda, The SANS toolbox, **2012**.
[262] D. W. Schaefer, *MRS Bulletin*, 13, 22–27, **1988**.
[263] A. P. Perissinotto et al., *Langmuir*, 31, 562–568, **2015**.

[264] P. Wong and Q. Cao, *Phys. Rev. B*, 45, 7627–7632, **1992**.
[265] M. E. V. Johansson and G. C. Hansson, *Nat. Rev. Imm.*, 16, 639–649, **2016**.
[266] M. E. V. Johansson et al., *Nat Rev Gastroenterol Hepatol*, 10, 352–361, **2013**.
[267] V. N. Boya et al., *Journal of Colloid and Interface Science*, 488, 258–268, **2017**.
[268] C. e. Wagner et al., *Annu. Rev. Cell Dev. Biol.*, 34, 189–215, **2018**.
[269] D. J. Thornton et al., *Annu. Rev. Physiol.*, 70, 459–486, **2008**.
[270] C. L. Hattrup and S. J. Gendler, *Annu. Rev. Physiol.*, 70, 431–457, **2008**.
[271] J. R. Kramer et al., *PNAS*, 112, 12574–12579, **2015**.
[272] N. Hendler et al., *Chem. Commun.*, 47, 7419–7421, **2011**.
[273] B. Belgorodsky et al., *Small*, 6, 262–269, **2010**.
[274] N. Barbero et al., *Int. Journal of Pharmaceutics*, 535, 438–443, **2018**.
[275] P. C. Griffiths et al., *Europ. J. of Pharm. and Biopharm.*, 97, 218–222, **2015**.
[276] F. Anwar et al., *Phytotherapy Research*, 21, 17–25, **2007**.
[277] S. K. Kansal and A. Kumari, *Chem. Rev.*, 114, 4993–5010, **2014**.
[278] J. Jampilek et al., *Nanomaterials*, 9, 296, **2019**.
[279] V. O. Kollath et al., *RSC Adv.*, 5, 55625–55632, **2015**.
[280] P. J. T. Reardon et al., *Advanced Healthcare Materials*, 2, 682–686, **2013**.
[281] C. Ching Lau et al., *ACS Biomater. Sci. Eng.*, 1, 947–954, **2015**.
[282] R. Rohanizadeh and K. Chung, *J. Oral Implantology*, 37, 659–672, **2011**.
[283] H. M. Kwaambwa and A. R. Rennie, *Biopolymers*, 97, 209–218, **2012**.
[284] H. M. Kwaambwa et al., *Langmuir*, 26, 3902–3910, **2010**.
[285] M. S. Hellsing et al., *Coll and Surf A:*, 460, 460–467, **2014**.
[286] A. Pietroiusti et al., *Toxicology and Applied Pharmacology*, 299, 90–95, **2016**.
[287] C. Moseke et al., *J Mater Sci Mater Med*, 22, 2591–2598, **2011**.
[288] U. Klammert et al., *J Mater Sci: Mater Med*, 21, 2947–2953, **2010**.
[289] B. Kanter et al., *Acta Biomaterialia*, 10, 3279–3287, **2014**.
[290] A. Ewald et al., *J. Biomed. Mater. Res. Part B*, 96, 326–332, **2011**.
[291] N. Ostrowski et al., *J. Materials Science & Technology*, 31, 437–444, **2015**.
[292] C. Großardt et al., *Tissue Engineering Part A*, 16, 3687–3695, **2010**.
[293] B. Kanter et al., *Acta Biomaterialia*, 69, 352–361, **2018**.
[294] E. Vorndran et al., *Advances in Applied Ceramics*, 110, 476–481, **2011**.
[295] J. A. Kim et al., *Biomaterials*, 157, 51–61, **2018**.
[296] J.-A. Kim et al., *Acta Biomaterialia*, 44, 155–167, **2016**.
[297] T. Brückner et al., *J. American Ceramic Society*, 101, 1830–1834, **2018**.
[298] G. Buckton, *Powder Technology*, 61, 237–249, **1990**.

[299] F. Ridi et al., *Journal of Colloid and Interface Science*, 357, 255–264, **2011**.
[300] F. Ridi et al., *Langmuir*, 34, 2205–2218, **2018**.
[301] H. Li et al., *RSC Adv.*, 5, 91601–91608, **2015**.
[302] J. Rakovan, *Rocks & Minerals*, 82, 329–337, **2007**.
[303] F. Abbona and R. Boistelle, *Journal of Crystal Growth*, 46, 339–354, **1979**.
[304] W. Liu et al., *Acta Biomaterialia*, 9, 5740–5750, **2013**.
[305] http://webmineral.com/data/Farringtonite.shtml#.WoG8zZM-eCf.
[306] http://webmineral.com/data/Struvite.shtml#.WoG88pM-eCf.
[307] E. Vorndran et al., *J Mater Sci Mater Med*, 22, 429–436, **2011**.
[308] R. L. Hartles, in *Advances in Oral Biology*, Ed. Elsevier, 225–253, **1964**.
[309] Y.-Y. Hu et al., *Chem. Mater.*, 23, 2481–2490, **2011**.
[310] C. Ma et al., *Biomaterials*, 178, 383–400, **2018**.
[311] R. T. Tran et al., *J. Biomed. Materials Research Part A*, 102, 2521–2532, **2014**.
[312] R. T. Tran et al., *Annu Rev Mater Res*, 45, 277–310, **2015**.
[313] D. Shan et al., *Advanced Healthcare Materials*, 7, 1800532, **2018**.
[314] Y. Jiao et al., *Soft Matter*, 8, 1499–1507, **2012**.
[315] H. Qiu et al., *Biomaterials*, 27, 5845–5854, **2006**.
[316] D. Xie et al., *J Mater Chem B Mater Biol Med*, 3, 387–398, **2015**.
[317] P. Kwan, *Mech. Ageing Dev.*, 145, 26–38, **2015**.
[318] T. R. Arnett, *Arch. Biochem. Biophys.*, 503, 103–109, **2010**.
[319] S. Jehle et al., *J. Clin. Endocrinol. Metab.*, 98, 207–217, **2013**.
[320] H. Lambert et al., *Osteoporos Int*, 26, 1311–1318, **2015**.
[321] D. Granchi et al., *Nutrients*, 10, **2018**.
[322] D. Granchi et al., *PLOS ONE*, 12, e0181230, **2017**.
[323] U. Gbureck et al., *Biomaterials*, 25, 2187–2195, **2004**.
[324] J. E. Barralet et al., *Biomaterials*, 25, 2197–2203, **2004**.
[325] X. P. Qi, *Advanced Materials Research*, 197–198, 151–155, **2011**.
[326] S. Sarda et al., *J. Biomed. Mater. Res.*, 61, 653–659, **2002**.
[327] N. Fukuda et al., *Biomed. Mater.*, 12, 015027, **2017**.
[328] K. Kiminami et al., *Materials*, 10, 941, **2017**.
[329] M. Bohner et al., *J. Mat. Sci: Materials in Medicine*, 11, 111–116, **2000**.
[330] A. Yokoyama et al., *Biomaterials*, 23, 1091–1101, **2002**.
[331] I. Khairoun et al., *Biomaterials*, 20, 393–398, **1999**.
[332] J. An et al., *J Mater Sci: Mater Med*, 27:58, **2016**.
[333] W.-K. Lee et al., *J. Industrial and Engineering Chemistry*, 15, 677–682, **2009**.

[334] D. D. Deligianni et al., *Biomaterials*, 22, 87-96, **2001**.
[335] G. Liptay, *Atlas of Thermoanalytical Curves*, **1975**.
[336] J. Shu et al., *Journal of Cleaner Production*, 135, 468–475, **2016**.
[337] B. Tansel et al., *Chemosphere*, 194, 504–514, **2018**.
[338] M. I. H. Bhuiyan et al., *Chemosphere*, 70, 1347–1356, **2008**.
[339] B. E. I. Abdelrazig, J. H. Sharp, *Thermochimica Acta*, 129, 197–215, **1988**.
[340] C. K. Chauhan and M. J. Joshi, *J. of Crystal Growth*, 362, 330–337, **2013**.
[341] S. Krukowski et al., *Journal of Food and Drug Analysis*, 25, 717–722, **2017**.
[342] J. Xu et al., *Polymers*, 7, 1850–1870, **2015**.
[343] N. Panda et al., *Int. J. of Pharmacy and Pharmaceutical Sciences*, 7, 10, **2015**.
[344] D. Tatini et al., *Colloids Surf B Biointerfaces*, 135, 400–407, **2015**.
[345] S. Dash et al., *Acta Pol Pharm*, 67, 217–223, **2010**.
[346] G. Singhvi and M. Singh, *Int. J. of Pharm. Studies and Research*, 8, **2011**.
[347] V. Papadopoulou et al., *Int. Journal of Pharmaceutics*, 309, 44–50, **2006**.
[348] E. Babaie et al., *Biomed. Mater.*, 11, 055010, **2016**.
[349] S. Yu et al., *J. of Mechanical Behavior of Biomed. Mater.*, 91, 229-236, **2018**.
[350] R. A. Perez et al., *J Tissue Eng*, 3, **2012**.
[351] Low Kah Ling et al., *J. Biomed. Mat. Research Part B,* 94B, 273–286, **2010**.
[352] M. M. Farag and H. Yun, *Materials Letters*, 132, 111–115, **2014**.
[353] J. Lee et al., *Materials Science and Engineering: C*, 36, 252–260, **2014**.
[354] J. Liao et al., *Int. J. Appl. Ceram. Technol.*, 15, 514–521, **2018**.
[355] H. C. Arca et al., *Biomacromolecules*, 19, 2351–2376, **2018**.
[356] A. Cherng et al., *J. Biomed. Mater. Res.*, 35, 273–277, **1997**.
[357] M. A. Jyoti et al., *Applied Surface Science*, 257, 1533–1539, **2010**.
[358] S. Dorozhkin, *Journal of biomedical materials research*, 54, 247–55, **2001**.

Appendix I

Experimental details

Fourier-Transform Infrared Spectroscopy FT-IR

FT-IR spectra of powder samples were collected using a Bio-Rad FTS-40 spectrophotometer (Hercules, CA, USA). The samples were analyzed in KBr pellets, which were prepared with 1.00 ± 0.05 mg of sample and 100 ± 1 mg of KBr (Sigma-Aldrich, FT-IR grade). Each spectrum was acquired with resolution of 2 cm^{-1}, 64 scans, in the range 4000-400 cm^{-1} and scan delay 600 s.

X-Rays Diffraction XRD

XRD patterns were collected with a D8 Advance with DAVINCI design (Bruker, Milan, Italy), using as X-rays source the Cu Kα radiation (wavelength λ=1.54 Å), at 40 kV and 40 mA, 2θ range of 5°-60°, step size of 0.03°, and a time/step of 0.3 s (slit: 0.6 mm). Prior to the measurement, the powders were grinded with agate mortar and pestle and flattened onto a Si zero-background sample holder. Only for the measurement of the kinetic of struvite formation (section 3.2.2.4), plastic sample-holder was used. Peaks were assigned using the Powder Diffraction Files (PDF) of the ICDD database (International Centre for Diffraction Data). Rietveld fittings were performed to estimate the relative amount of formed phases, using the software Topas (Bruker). The CIF (Crystallographic Information File) data used for the analysis were obtained from the American Mineralogist Crystal Structure Database (0011901 for farringtonite and 0009807 for struvite). The percentage error associated to the fitting is 10 %.

Simultaneous Thermogravimetry/Differential Scanning Calorimetry SDT

SDT analyses were performed using SDT Q600 from TA Instruments (New Castle, DE, USA). Each sample was placed in an alumina pan and measurements were conducted in N_2 atmosphere (flow rate 100 mL/min) from room temperature to 1000 °C, at 10 °C/min.

Differential Scanning Calorimetry DSC

DSC in the low temperature regime (LT-DSC) was used to investigate water freezing and melting in the cement matrix. The analyses were carried out on a Q2000 DSC (TA Instruments), in N_2 atmosphere (flow rate 50 mL/min). The pastes were lodged in steel hermetic pans, which were equilibrated at -80 °C and heated at 0.5 °C/min up to 30 °C. The measurements were performed on each sample after 3 h, 24 h, 7 days and 28 days from the preparation of the paste. The pans were stored at 37 °C.

Field Emission-Scanning Electron Microscopy FE-SEM

The morphology of AMCPs and MPCs was investigated by means of a Zeiss ΣIGMA FE-SEM (Carl Zeiss Microscopy GmbH, Jena, Germany). Samples were placed over aluminum stubs by means of conductive tape. The use of a Field Emission source, together with a low accelerating voltage (2 kV), a reduced sample-detector distance (~ 2 mm) and the In-Lens detector, allowed for the imaging of non-conductive samples at high magnification.

Energy Dispersive X-rays spectroscopy EDX

Energy dispersive X-rays spectroscopy (EDX) was carried out in combination with SEM measurements, using X-act Silicon Drift Detector (Oxford Instruments, England). To collect EDX spectra, the accelerating voltage used was 10 kV, while the working distance was ~ 8 mm.

Transmission Electron Microscopy TEM

TEM analysis of AMCPs was performed with a TEM Philips CM12 (Eindhoven, The Netherlands), working with an electron gun operating at 100 kV. Samples were prepared by depositing a droplet of a sonicated

AMCPs dispersion in ethanol onto a carbon-coated copper grid. After solvent evaporation, particles were imaged.

Laser Granulometry

Laser granulometry measurements were performed by means of a Mastersizer 3000 laser diffraction particle size analyzer (Malvern Panalytical, UK), equipped with HYDRO SM wet dispersion unit. For AMCPs, absolute ethanol was used as dispersant medium, whereas iso-propanol was employed for TMP characterization. Each curve reported in Chapter 2 and 3 represents the average of 20 measurements, each lasting 5 s with a delay of 5 s. For the calculation of the size, the parameters present in the instrumental database for tricalcium phosphate were used for AMCP (particle refractive index: 1.630, particle absorption index: 0.100), whereas for TMP those of magnesium phosphate were employed (particle refractive index: 1.540, particle absorption index: 0.010).

Surface Tension

The surface tension properties of the SIF were determined using a Force Tensiometer K100 (Krüss GmbH, Hamburg, Germany). Inverse critical micelle concentration (CMC) measurements were performed using a Pt plate, at T = 37 °C and diluting the sample with water up to $1 \cdot 10^{-5}$ mM sodium taurocholate concentration.

Dynamic Light Scattering DLS

DLS measurements of the SIF were performed on a Brookhaven Instruments apparatus (BI 9000AT correlator and BI 200 SM goniometer). The light source was a Torus laser, mpc3000, LaserQuantum, UK (λ = 532 nm) and the scattered intensity was detected by a BI-APD detector. The samples were placed in glass tubes and immersed in a thermostated cell at T = 37 °C filled with decahydronaphthalene to match the glass refractive index. The scattering intensity of pure toluene was used as a standard. The field autocorrelation functions reported in this work are the result of the averaging of five experiments for each sample. The averaged functions were analyzed through cumulant analysis.

Small Angle X-Rays Scattering SAXS

SAXS measurements of AMCPs were carried out using a HECUS SWAX-camera (Kratky) equipped with a position-sensitive detector (OED 50 M) containing 1024 channels of width 54 μm. Cu Kα radiation of wavelength λ = 1.542 Å was provided using a Seifert ID-3003 X-ray generator (sealed-tube type), operating at a maximum power of 2 kW. A 10-mm thick Ni-filter was used to remove Cu Kβ radiation. The sample-to-detector distance was 275 mm. The volume between the sample and the detector was kept under vacuum during the measurements to minimize scattering from the air. The Kratky camera was calibrated in the small angle region using silver behenate (d = 5.838 nm). Scattering curves were obtained in the Q-range, $Q = (4\pi/\lambda)\sin(\theta/2)$, between 0.009 and 0.54 $Å^{-1}$, with Q being the scattering vector, and θ the scattering angle. The samples were contained in 2 mm quartz capillaries. Standard measurement conditions were 40 kV, 20 mA, and 3 h (acquisition time) at 25 °C. All scattering curves were corrected for the solvent/empty cell contribution considering the relative transmission factor. SAXS curves were iteratively desmeared using the procedure reported by Lake [1].

Confocal Microscopy

The roughness of the cements' surfaces was analyzed using confocal microscopy in reflection mode. A z-series of data was collected, and Ra values were calculated by means of the software "Fiji": two plugins were used, "Extended depth of field" and "SurfCharJ" [2]. The first one generates a height profile image, in which all the pixels which occur in the same vertical plane have the same value, representing the height at that plane. The height maps are then processed by the "SurfCharJ" plugin, which gives as outputs the roughness values on the whole surface. Ra is the arithmetic average of the absolute values of the profile height deviations from the mean line, and is defined as:

$$Ra = \frac{1}{l}\int_0^l |y(x)|dx$$

where l is the length of the profile and $y(x)$ are the deviations from the mean line [3]. Measurements were carried out with a Leica TCS SP2 Confocal Microscope (Leica Microsystems). For each sample, 8 images (310 μm x 310 μm) collected on different areas of the surface were considered for Ra evaluation. The 20X objective was used, with a 0.69 μm step size for each image.

Compressive strength measurements

The compressive strength of MPCs was assessed on cylindrical specimens (ø=8 mm), prepared by mixing 1 g of TMP with the adequate amount of DAHP solution to achieve the desired composition. The surface of the specimens was polished so to obtain an aspect ratio of about 2 (height/diameter) and to make the two surfaces of the cylinders as flat as possible. Measurements were conducted using a 50 kN load cell (Controls, Milan) and 4 samples for each composition were tested. For these measurements, we gratefully acknowledge Dr. Enzo Barlacchi and Dr. Leonardo Bucci from the "Laboratorio Prove Strutture e Materiali" of the Department of Civil and Environmental Engineering (DICEA), University of Florence.

Setting time

The initial (t_1) and final (t_2) setting times were measured using a Gillmore apparatus (Matest) and performing the test according to the ASTM 266 standard. About 0.50 g of TMP were mixed with the appropriate amount of DAHP/DAC solution for about 30 s, and poured in cylindrical molds (diameter 1 cm). The cements were set at 37 °C and relative humidity > 96 %, and periodically tested (every 10 min for samples described in section 3.2, and every 2 min those in section 3.3). We consider the cement to have attained its initial or final setting time if its surface is able to withstand the pressure generated respectively by 113.4 g (ø=2.12 mm) and 453.6 g (ø=1.06 mm) needles without appreciable indentation.

Gas porosimetry

The specific surface area and the pore size distribution of AMCP and MCPs were assessed by means of gas sorption measurements. The experiments were conducted using a Coulter SA3100 (Beckman Coulter): nitrogen was used as adsorbate, while freespace was measured with helium. Prior to the measurement, samples were outgassed: for MPCs, the procedure was conducted at 50 °C for 3 h (low T prevents struvite transformation to dittmarite [4]). AMCPs were outgassed at 100 °C for 1 h, and we verified by means of FT-IR spectroscopy that the outgas procedure did not alter the amorphous nature of the particles. The specific surface area (SSA) was obtained using the Brunauer-Emmet-Teller (BET) method, while the pore size distribution was estimated using Barrett-Joyner-Halenda (BJH) analysis.

Cytotoxicity experiments

Biological experiments were conducted in collaboration with researchers from the "Istituto Ortopedico Rizzoli" in Bologna. Cements (previously sterilized by means of γ-radiation) were incubated with 1 mL of medium (MEM, Minimum Essential Medium Eagle, Sigma-Aldrich) for 4 days, thus obtaining the extracts. Cells (human fibroblasts, MRC-5 line) were seeded, and after 1 day the culture medium was replaced with the extracts. The vitality was evaluated after 24 h, 48 h and 72 h, by incubating cells with Alamar Blue for 4 hours and reading by means of a spectrophotometer the fluorescence signal.

Citrate release experiments

The two release experiments discussed in section 3.3.2.3 were conducted as it follows: release experiment 1 was performed by incubating the cements in physiological solution (NaCl 0.9% w/v) for different time intervals (1, 3, 7, 14, 28 days). Five replicas of each sample containing citrate (Cit_1.5M, Cit_2.5M and Cit_3.5M) were prepared by mixing TMP (0.50 g) and the aqueous solution (366 μL) for 1 min. Each paste was placed in a mold and set at 37 °C and RH > 96 % for 9 min. After 11 min from the beginning of the mixing, the mold was placed in a 20-mL glass vial, and 10 mL of physiological solution (1.8 g of NaCl in 200 mL of deionized water) were added (only the surface of

the cements was in contact with the solution). The closed vials were stored in the oven at 37 °C. The pH of the solutions (always the 28 days-samples) was daily monitored using a pH-meter (pH/ion 3310, WTW). After the selected incubation times, the molds containing the samples were removed from the solution and dried at 37 °C and RH > 96 %. Their weight was recorded after reaching a constant value, and the residual weight % was calculated according to the following equation:

$$Residual\ weight\ \% = \frac{final\ weight}{initial\ weight} \times 100$$

Release experiment 2 was carried out by preparing the samples as described for experiment A. Here, 1 mL of incubating solution was daily withdrawn and replaced with 1 mL of fresh physiological solution. Moreover, within the first 24 h, we also collected an aliquot after 1 h, 3 h and 6 h.

The release of citrate was monitored by means of a UV spectrophotometric determination, using a method recently reported in the literature [5]. The procedure takes advantage of the absorption peak of citric acid at 209 nm, which can be obtained in citrate-containing samples by addition of HCl 0.25 M. The addition of HCl makes the pH of the solution < 1 and, in these conditions, we can consider only un-dissociated citric acid being present in solution: this leads to the presence in the UV spectrum of a peak centered at 209 nm rather than a broad absorption band. The calibration curve was obtained analyzing solutions with a known citrate concentration (prepared using serial dilutions with DAC 10 mM, 8 mM, 6 mM, 4 mM, 2mM and 1 mM), and diluting them with HCl 0.25 M v/v 1:1. The spectra and the calibration line ($y=0.201x+0.005$, $r^2=0.9995$) are reported in Figure A.1.

Quartz cuvettes were used for the experiments (1 cm path length), and the spectra were collected in the range 300-190 nm using an UV-visible spectrophotometer (Cary 1000 Bio, Varian). The solutions withdrawn during the release experiments were diluted 1:10 with HCl 0.25 M directly in the cuvette (0.2 mL sample + 1.8 mL HCl 0.25 M). The baseline was collected using 0.2 mL of NaCl 0.9 %wt physiological solution + 1.8 mL HCl 0.25 M. Each measurement was repeated 5 times (release experiment 1) or 3 times (release experiment 2), and the average value ± the standard deviation is reported.

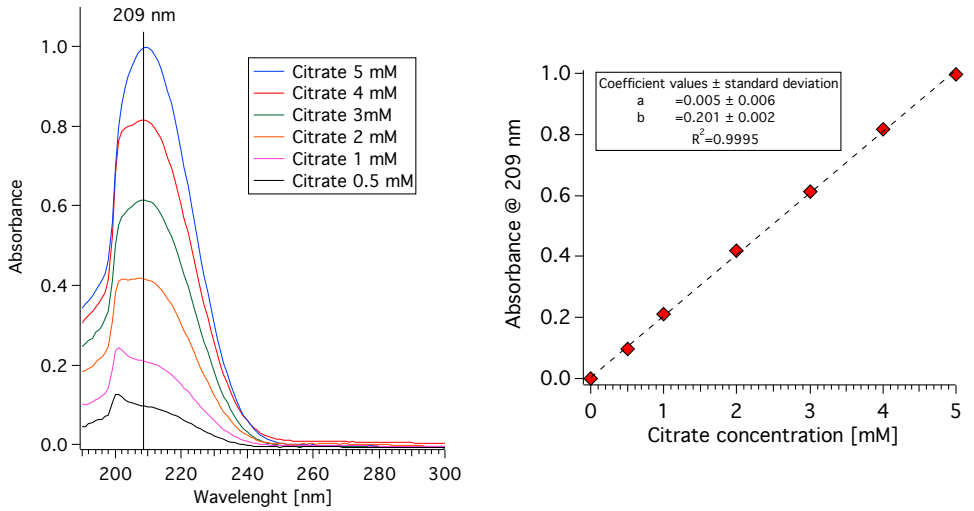

(a) (b)

Figure A.1: (a) UV spectra of DAC standard solutions; (b) calibration line (y=0.201x+0.005).

For the quantification of released citrate in the culture medium, known amounts of DAC were dissolved in the culture medium, and the spectra were collected (see Figure A.2a). Here, we observe that the absorption maximum is shifted at 230 nm. The absorbance at this value was used to calculate the calibration line (Figure A.2b)

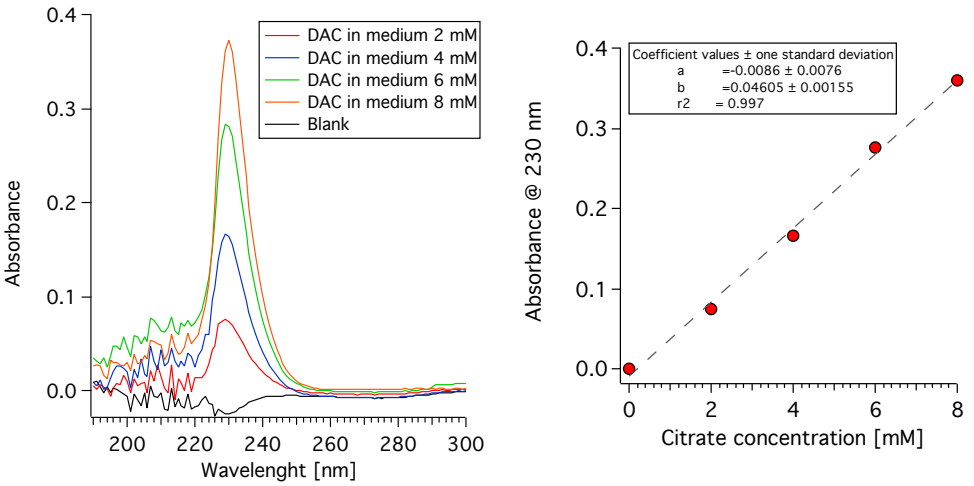

(a) (b)

Figure A.2: (a) UV spectra of DAC standard solutions in MEM; (b) calibration line (y=0.046x+0.0086).

Injectability

The injectability of the pastes was measured by means of a custom-made apparatus in which controlled loads are applied to commercial syringes. The used syringes have a diameter of 9 mm and capacity 2 mL; the metallic needle was removed, and pastes were extruded through the plastic small needle endowed with the syringe (diameter 2 mm, length 9 mm). A load of 794 g (7.8 N) was applied, and the injectability % was calculated according to equation:

$$Injectability\ \% = \frac{extruded\ mass}{loaded\ mass} \times 100$$

where extruded mass is the amount of paste extruded within a minute from the application of the load. Experiments were typically conducted preparing pastes with 1 g of TMP, and analyzing the injectability after 3 and 7 min of setting.

References

[1] J. A. Lake, *Acta Crystallogr*, 23, 2, 191–194, **1967**.
[2] G. Chinga et al., *J Microsc*, 227, 3, 254–265, **2007**.
[3] E. S. Gadelmawla et al., *J. Mat. Processing Technology*, 123, 1, 133–145, **2002**.
[4] M. V. Ramlogan, A. A. Rouff, *J Therm Anal Calorim*, 123, 1, 145–152, **2016**.
[5] S. Krukowski et al., *Journal of Food and Drug Analysis*, 25, 3, 717–722, **2017**.

Appendix II

Publications

- **Paper I**: Gelli, R. *et al.* Effect of pH and Mg^{2+} on Amorphous Magnesium-Calcium Phosphate (AMCP) stability. *Journal of Colloid and Interface Science* 531, 681–692 (2018).
- **Paper II:** Gelli, R. *et al.* Effect of biologically-relevant molecules on the physico-chemical properties of amorphous magnesium-calcium phosphate nanoparticles. *Journal of Nanoscience and Nanotechnology,* accepted (2019).
- **Paper III:** Gelli, R. *et al.* Formation and properties of amorphous magnesium-calcium phosphate particles in a simulated intestinal fluid. *Journal of Colloid and Interface Science* 546, 130–138 (2019).
- **Paper VI:** Gelli, R. *et al.* The importance of being amorphous: calcium and magnesium phosphates in the human body. *Advances in Colloid and Interface Science* 269, 219-235 (2019).
- **Paper V:** Gelli, R. *et al.* Tuning the properties of magnesium phosphate-based bone cements: Effect of powder to liquid ratio and aqueous solution concentration. *Materials Science and Engineering: C* 95, 248–255 (2019).
- **Paper VI**: Gelli, R. *et al.* Multi-scale investigation of gelatin/poly(vinyl alcohol) interactions in water. *Colloids and Surfaces A: Physicochemical and Engineering Aspects* 532, 18–25 (2017). –topic related to master thesis-
- **Paper VII**: Gelli, R. *et al.* Enhanced formation of hydroxyapatites in gelatin/imogolite macroporous hydrogels. *Journal of Colloid and Interface Science* 511, 145–154 (2018). - topic related to bachelor thesis-

In the following pages, reprints of all the manuscripts published during the period of my PhD are reported. All the papers are reprinted with permission from the publisher.

Paper I

Journal of Colloid and Interface Science 531 (2018) 681–692

Contents lists available at ScienceDirect

Journal of Colloid and Interface Science

journal homepage: www.elsevier.com/locate/jcis

Regular Article

Effect of pH and Mg^{2+} on Amorphous Magnesium-Calcium Phosphate (AMCP) stability

Rita Gelli [a,b], Martino Scudero [a,b], Lucia Gigli [a,b], Mirko Severi [a], Massimo Bonini [a,b], Francesca Ridi [a,b,*], Piero Baglioni [a,b]

[a] Department of Chemistry "Ugo Schiff", University of Florence, via della Lastruccia 3, Sesto Fiorentino, 50019 Florence, Italy
[b] CSGI Consortium, via della Lastruccia 3, Sesto Fiorentino, 50019 Florence, Italy

GRAPHICAL ABSTRACT

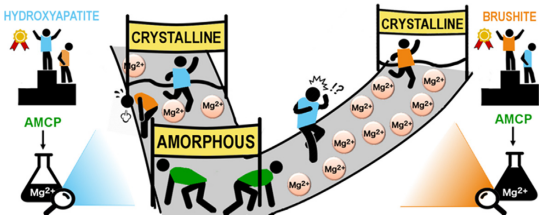

ARTICLE INFO

Article history:
Received 5 June 2018
Revised 23 July 2018
Accepted 23 July 2018
Available online 24 July 2018

Keywords:
Calcium phosphates
Amorphous Magnesium Calcium Phosphate
Endogenous particles
pH
Magnesium
Stability
Crystallization
Gut

ABSTRACT

Hypothesis: Amorphous Magnesium-Calcium Phosphate (AMCP) particles in the distal small intestine have been shown to have a fundamental role in mammals' immune-surveillance mechanisms. Their formation in the gut lumen and their stability against crystallization are expected to depend upon physiological conditions such as pH and [Mg^{2+}]. Knowing the influence of these parameters on AMCP stability would allow to predict the presence and the activity of the particles in physiological or pathological conditions.

Experiments: We performed the synthesis of AMCP particles at physiological temperature, in phosphate buffer at variable pH from ~7.0 to 7.4. The stability of the particles was then tested by dispersing them in different conditions of [Mg^{2+}], pH and concentration, so to mimic different biological conditions. The particles were characterized in terms of morphology, crystallinity, chemical composition and porosity.

Findings: The characterization showed that we managed to prepare AMCPs with features matching those of the endogenous particles. Both the lifetime of the amorphous phase and the nature of the formed crystalline material were found to depend upon [Mg^{2+}], pH and concentration. This article paves the way for the comprehension of possible dysfunctions of the gut immune-surveillance mechanisms due to imbalances of these physico-chemical parameters.

Abbreviations: AMCP, Amorphous Magnesium-Calcium Phosphate; ACP, Amorphous Calcium Phosphate; GI, Gastrointestinal tract; FT-IR, Fourier Transform Infrared Spectroscopy; ICP-AES, Inductively Coupled Plasma-Atomic Emission Spectrometry; FE-SEM, Field Emission Scanning Electron Microscopy; EDX, Energy Dispersive X-rays Spectroscopy; XRD, X-rays Diffraction; PDF, Powder Diffraction File; SDT, Simultaneous Thermogravimetry/Differential Scanning Calorimetry; TGA, Thermogravimetry; DSC, Differential Scanning Calorimetry; BET, Brunauer-Emmet-Teller; BJH, Barrett-Joyner-Halenda; DCPD, Dicalcium Phosphate Dihydrate; TCP, Tri-Calcium Phosphate; CDHA, Calcium-Deficient Hydroxyapatite.

* Corresponding author at: Department of Chemistry "Ugo Schiff" and CSGI, University of Florence, via della Lastruccia 3, Sesto Fiorentino, 50019 Florence, Italy.
E-mail address: francesca.ridi@unifi.it (F. Ridi).

https://doi.org/10.1016/j.jcis.2018.07.102
0021-9797/

1. Introduction

Calcium and magnesium phosphate-based nanostructures represent essential components of the human body. Together with crystalline deposits, such as the hydroxyapatite-based inorganic matrix of bones and teeth [1], amorphous calcium and magnesium phosphates have recently attracted great attention in view of their biological relevance: in fact, their presence has been detected in dental enamel [2,3] and, most intriguingly, in the intestine of mammals [4]. The role of these amorphous nanoparticles is still under investigation [4–7]. It is proposed that calcium and phosphate ions which are secreted in the distal small intestine of humans and other mammals co-precipitate with magnesium ions into the lumen and form amorphous magnesium-substituted calcium phosphate (AMCP) nanostructures, which are able to upload macromolecules such as bacterial peptidoglycans and antigens and transport them to the immune cells of the intestinal tissue [4]. This process likely promotes immune-surveillance of luminal antigens in our body. Beside the biomedical aspects, the full understanding of this process opens up to a series of intriguing aspects also from a physico-chemical perspective. Endogenous AMCP particles are reported to possess a porous and amorphous structure, with a size of 75–150 nm, and are composed by Ca, Mg, Na, O and P [4,6]. Compared to AMCP, amorphous calcium phosphates (ACP) are well-known to be highly unstable, as they spontaneously evolve into a more thermodynamically stable form of crystalline calcium phosphate [8]. This is a solution-mediated process, which involves nucleation and crystal proliferation: ACP first dissolves until the critical supersaturation concentration is reached, taking to the formation of stable primary crystalline nuclei. The growth of these nuclei (together with the formation of new ones) then produces crystalline particles [9]. The kinetics of this process is dramatically affected by several aspects, such as pH, temperature, ionic strength, molecules and ions in solution (Mg^{2+}, Al^{3+}, carbonate, pyrophosphates…) [10]. Among these factors, the pH and the presence/concentration of ions and molecules in the lumen are of outmost importance in the gastrointestinal (GI) tract. The pH value displays a great variation in different GI tracts, as it is the result of a dynamic interplay between motion, secretion and metabolism [11]: the pH of the stomach is 1–2, but as the acidic gastric content enters the proximal small bowel, the pH rises of several units, up to 5.7–6.4 (duodenum, jejunum) [12,13]. Mucosal bicarbonate secretions result in a further rise of luminal pH, which goes up to 7.3–7.7 in the ileum. Finally, in the large intestine, colonic bacteria produce short chain fatty acids, which cause a decrease in luminal pH (5.7). These molecules are then absorbed by the colonic epithelium, and the decrease in their concentration, in combination with bicarbonate secretions, leads to a slight rise in the pH along the distal colon (6.8). A variation in the pH of a specific region of the GI tract may also be the consequence of a pathological condition, as it is reported that alterations in the gut pH are associated to illnesses such as ulcerative colitis, Crohn's disease and irritable bowel syndrome [13]. It is important to remark that the endogenous AMCP nanoparticles have been detected in the distal small intestine [4], which interestingly is the region of the GI tract that displays the highest pH value. This correlation becomes significantly relevant if we consider the deep impact of the pH on the stability of ACP, as its conversion to crystalline material is much slower at high pH values [9]. We may reasonably infer that an alteration in the luminal pH of the ileum region could alter the stability of the particles, perhaps compromising their biological function in the organism.

Together with the pH, another factor which could potentially alter the lifetime and the properties of the endogenous AMCPs is the presence of proteins, macromolecules and ions in the lumen. In this paper, we focus on the role of magnesium: in fact, similarly to Ca^{2+}, Mg^{2+} is absorbed in the gut, stored in bone in the form of phosphates, and the excess is excreted by the kidneys [14]. Intriguingly, it is reported that the majority of Mg^{2+} absorption takes place in the distal small intestine [15], which is the site where AMCPs have been detected. Magnesium concentration in the organism is critical for humans' health [14]: its role in the gut is highly relevant, as some studies indicate that an increase in magnesium intake may help against irritable bowel syndrome and constipation [16], and its presence in the intestinal lumen may explain why the endogenous nanoparticles are Mg-rich. In fact, Mg^{2+} can co-precipitate with calcium and phosphate ions (secreted because of "endogenous losses") to form stable AMCP phases [17].

This paper aims at elucidating the role of pH and Mg^{2+} concentration on the structural properties and the stability of synthetic analogues of endogenous AMCP particles, so to investigate how an alteration in these parameters may affect the fate of the nanostructures, and potentially their role in the organism. We performed the synthesis of the particles at physiological temperature by readapting a protocol from the literature [18], consisting in the co-precipitation of Ca^{2+} and Mg^{2+} from phosphate buffers, using an excess of magnesium and phosphorous with respect to calcium to favor the formation of AMCP. The effect of subtle pH differences (in the physiological range) was explored, by using different $H_2PO_4^-/HPO_4^{2-}$ molar ratios, but keeping constant the total phosphate concentration. Precipitates were characterized with a multi-technique approach in terms of morphology, crystallinity, chemical composition and porosity, obtaining AMCPs with features matching those found in the gut. The stability of the prepared particles was then tested by re-dispersing them in aqueous phosphate buffers at different concentrations, pHs, and at different Mg^{2+} concentrations. We found that subtle differences in these three parameters strongly affect the lifetime of the amorphous phase and the nature of the newly-formed crystalline material. The results are discussed in the attempt of correlating the obtained physico-chemical information with the biologically relevant aspects.

2. Materials and methods

2.1. Materials

Sodium chloride (NaCl, ≥99%), magnesium chloride ($MgCl_2{\cdot}6H_2O$, ≥99%) calcium chloride ($CaCl_2$, ≥93%) and NaOH pellets were purchased form Sigma-Aldrich (Milan, Italy). Sodium phosphate monobasic ($NaH_2PO_4{\cdot}H_2O$, ≥99%), and sodium phosphate dibasic ($Na_2HPO_4{\cdot}12H_2O$, ≥99%) were obtained from Carlo Erba Reagents (Milan, Italy). Deionized water was used during all the experiments.

2.2. Synthesis of AMCP particles at different pH

The synthesis of AMCPs was conducted using a protocol readapted from the literature [18], which involves the mixing at 37 °C of equal volumes of two aqueous solutions, namely solution A (which contains NaCl, $MgCl_2$ and $CaCl_2$, amounts and concentrations are given in Table 1) and solution B (NaH_2PO_4 and Na_2HPO_4, see Table 1). The reaction temperature was monitored throughout the entire reaction and it was stable within 0.5 °C. In order to investigate the effect of the pH on the stability of AMCP, the synthesis was conducted at four different pH values, obtained by mixing different amounts of the monobasic and the dibasic sodium phosphate salts (solutions B_0, B_1, B_2, B_3, total concentration of the two phosphates is fixed at 200 mM, see Table 1). This strategy was pursued to keep the amount of total phosphates constant in all the four different experiments.

In a typical experiment, 100 mL of solution A and 100 mL of solution B (already heated at 37 °C) are mixed in an Erlenmeyer

Table 1
Amounts of reactants and concentrations used for the synthesis of AMCP particles at different pH.

Solution	Salt	Amount [g]	Millimoles	Molar ratio NaH_2PO_4: Na_2HPO_4	Concentration [mM]	Reaction pH*
A	NaCl	0.79	13.5		135	
	$CaCl_2$	0.04	0.4	/	4	/
	$MgCl_2{\cdot}6H_2O$	0.20	1.0		10	
B_0	$NaH_2PO_4{\cdot}H_2O$	1.38	10.0	1:1	100	7.06 ± 0.03
	$Na_2HPO_4{\cdot}12H_2O$	3.58	10.0		100	
B_1	$NaH_2PO_4{\cdot}H_2O$	0.69	5.0	1:3	50	7.23 ± 0.05
	$Na_2HPO_4{\cdot}12H_2O$	5.37	15.0		150	
B_2	$NaH_2PO_4{\cdot}H_2O$	0.55	4.0	1:4	40	7.30 ± 0.04
	$Na_2HPO_4{\cdot}12H_2O$	5.73	16.0		160	
B_3	$NaH_2PO_4{\cdot}H_2O$	0.45	3.3	1:5	33	7.40 ± 0.02
	$Na_2HPO_4{\cdot}12H_2O$	5.97	16.7		167	

* The pH values were monitored throughout the entire reaction by means of a pH-meter pH/ION 3310 (WTW, Weilheim, Germany). Values reported in the table are the average values throughout the entire reaction and the associated standard deviations. The pH accuracy as indicated by the manufacturer is ±0.005. According to buffer calibration curve vs T, temperature oscillations (within 0.5 °C, as stated before) would result in maximal pH variations in the order of ±0.002. Note that the standard deviations are about one order of magnitude larger than the instrumental accuracy, reasonably accounting for pH oscillations generated by the reaction.

flask using magnetic stirring, in a water bath at 37 °C. Immediately after the addition of A to B, the solution becomes turbid. The pH was monitored throughout the reaction. Only in the case of solution B_0, it was necessary to adjust the initial pH to 7.00 by adding few drops of NaOH 2 M solution. The average measured values are reported in the last column of Table 1. Aliquots (∼20 mL) of the solution were withdrawn at different reaction times and filtered using a Millipore vacuum filtration system equipped with mixed cellulose esters filters (Millipore, pore size 0.22 μm). Immediately after filtration, the filters were placed in plastic test tubes and frozen in liquid nitrogen. The powders were then freeze-dried for 24 h, at −55 °C and ∼30 mTorr (VirTis BenchTop freeze-dryer, NY, USA) and stored in freezer (−18 °C), tightly closed to prevent any influence from environmental humidity [10].

2.3. Dispersion of AMCP particles in solution

2.3.1. Effect of Mg^{2+} concentration

In order to evaluate how the presence of Mg^{2+} in the solution in which AMCP particles are dispersed affects their transformation to crystalline calcium phosphates, we performed experiments by dispersing AMCPs in solutions containing different concentrations of Mg^{2+} (0, 1, 3 and 5 mM), at pH 7.40, T = 37 °C and particles' concentration 0.36 g/L. For these experiments, we used sample AMCP_B_3_15 min. 140 mL of buffer B_1 (see Table 1 for the composition) were heated at 37 °C. The pH was adjusted to 7.40 by dropwise addition of NaOH 2 M, and $MgCl_2{\cdot}6H_2O$ was added to the solution under magnetic stirring (28.5 mg for $[Mg^{2+}]$ = 1 mM, 85.4 mg for $[Mg^{2+}]$ = 3 mM and 142.3 mg for $[Mg^{2+}]$ = 5 mM). When the salt was completely dissolved (*i.e.* after about 2 min), 50 mg of AMCPs were added to the buffer under magnetic stirring. Aliquots of the solution were withdrawn at different reaction times and filtered using Millipore vacuum filtration system with mixed cellulose esters 0.22 μm pore size filters (Millipore). Immediately after the filtration, the filters were placed in plastic test tubes, frozen in liquid nitrogen and freeze-dried. After the lyophilization was completed (∼24 h), the samples were stored in freezer (−18 °C).

2.3.2. Effect of the pH of the solution (6.90 vs 7.40)

The effect of the pH of the solution on the stability of dispersed AMCP particles was investigated by re-dispersing freeze-dried AMCPs (using the same batch employed for the experiments with Mg^{2+}) in phosphate buffers at different pHs. The experiments were performed by equilibrating the solution at 37 °C, at pH 6.90 and 7.40, using buffer B_0 and B_1, respectively (see the composition in Table 1). In both cases the pH was adjusted to the exact value by means of dropwise NaOH 2 M additions. The amount of dried AMCPs necessary to reach the concentration of 0.36 g/L was then added to the buffer under magnetic stirring, and the solid material was filtered after 15 min of reaction using Millipore vacuum filtration system with mixed cellulose esters 0.22 μm pore size filters (Millipore). The filters were immediately placed in plastic test tubes and frozen in liquid nitrogen. Freeze-drying was performed during ∼24 h and the particles were stored in freezer (−18 °C).

2.3.3. Effect of concentration

The aim of this experiment was to investigate how the concentration of particles dispersed in buffer solution affects the stability of the amorphous phase and the type of crystalline phase to which it converts. Two different concentrations were studied, at two different pHs. All the experiments were conducted using the following protocol: the phosphate buffer (B_0 for pH 6.90, B_1 for 7.40, composition reported in Table 1) was equilibrated at 37 °C and the pH was adjusted to the desired value by dropwise addition of NaOH 2 M. Then, the amount of AMCPs necessary to reach the desired concentration was added to the buffer under magnetic stirring. Aliquots of the solution were withdrawn at different reaction times and filtered using Millipore vacuum filtration system equipped with mixed cellulose esters 0.22 μm pore size filters (Millipore). Immediately after filtration, the filters were put in plastic test tubes, frozen in liquid nitrogen and lyophilized for about 1 day. The powders were stored in freezer (−18 °C).

2.4. Characterization techniques

2.4.1. Fourier Transform Infrared Spectroscopy (FT-IR)

FT-IR spectra were collected using a Bio-Rad FTS-40 spectrophotometer (Hercules, CA, USA). The samples were analyzed in KBr pellets, which were prepared with 1.00 ± 0.05 mg of sample and 100 ± 1 mg of KBr (Sigma-Aldrich, FT-IR grade). Each spectrum was acquired with resolution of 2 cm^{-1}, 64 scans, in the range 4000–400 cm^{-1} and with scan delay 600 s.

2.4.2. Inductively Coupled Plasma-Atomic Emission Spectrometry (ICP-AES).

The amount of calcium, magnesium and phosphorous in the samples was determined by means of a Varian 720-ES Inductively Coupled Plasma Atomic Emission Spectrometer (ICP-AES). 10 mg of each sample were dissolved in 1 mL of nitric acid, spiked with 1 ppm of Ge used as an internal standard, and analysed. The wavelength used for Ca determination was 317.933 nm, for Mg

analysis was 279.800 nm whereas for P the line at 213.618 nm was used.

2.4.3. Field Emission Scanning Electron Microscopy (FE-SEM) coupled with Energy Dispersive X-rays spectroscopy (EDX)

The morphology of AMCP particles was investigated by means of Field Emission Scanning Electron Microscopy (FE-SEM), using a Zeiss ΣIGMA FE-SEM (Carl Zeiss Microscopy GmbH, Jena, Germany). The powders were placed over aluminum stubs by means of conductive tape. The use of a Field Emission source, together with a low accelerating voltage (2 kV), a reduced sample-detector distance (~2 mm) and the In-Lens detector, allowed for the imaging of non-conductive samples at high magnification. Energy dispersive X-rays spectroscopy (EDX) was carried out using X-act Silicon Drift Detector (Oxford Instruments, England). To collect EDX spectra, the accelerating voltage used was 10 kV, while the working distance was ~8 mm.

2.4.4. X-rays Diffraction (XRD)

The crystallinity was investigated on powder samples by means of X-rays Diffraction (XRD). The diffractograms were collected with a D8 Advance with DAVINCI design (Bruker, Milan, Italy), using as X-rays source the Cu Kα radiation (wavelength λ = 1.54 Å), at 40 kV and 40 mA, a 2θ range of 5–70°, a step size of 0.03°, and a time/step of 0.3 s. Prior to the measurement, the powder was grinded with agate mortar and pestle and flattened onto a Si zero-background sample holder. Peaks were assigned using the Powder Diffraction Files (PDF) of the ICDD database (International Centre for Diffraction Data).

2.4.5. Thermal analysis

Thermal analysis on AMCP sample was performed with a Simultaneous Thermogravimetry/Differential Scanning Calorimetry SDT Q600 from TA Instruments (New Castle, DE, USA). The sample was placed in an alumina pan and measurements were conducted in N_2 atmosphere (flow rate 100 mL/min) from room temperature to 1000 °C, at 10 °C/min.

2.4.6. Gas porosimetry

The specific surface area and the pore size distribution of AMCP particles were assessed by means of gas sorption measurements. The experiments were conducted using a Coulter SA3100 (Beckman Coulter, Brea, CA, USA): nitrogen was used as adsorbate gas, while the free space was measured with helium. Prior to the measurement, samples were outgassed at 100 °C for 1 h. We verified with FT-IR spectroscopy that the outgas procedure did not alter the amorphous nature of the particles. The specific surface area (SSA) was calculated using the Brunauer-Emmet-Teller (BET) method, while the pore size distribution was estimated using Barrett-Joyner-Halenda (BJH) analysis.

3. Results

3.1. AMCP stability as a function of pH during the synthesis

We conducted the synthesis of AMCP particles at four different pH values to investigate its effect on the stability of AMCPs, using the protocol described in Section 2.2. The transition from amorphous to crystalline calcium phosphate was monitored by means of FT-IR spectroscopy. It is known from the literature that ACP (amorphous calcium phosphate) displays broad bands in its spectrum due to P-O stretching vibration, while sharp and distinctive signals appear when it converts into a crystalline phase, such as hydroxyapatite, brushite or octacalcium phosphate [19]. Thus, FT-IR is a well-suited technique to monitor the transition from amorphous to crystalline phase. The spectra relevant to the detection of amorphous to crystalline transition are reported in Fig. 1.

We can easily observe that the lifetime of the amorphous phase dramatically depends on the solution pH: at pH 7.06, AMCP is very unstable, as after about 1 h its featureless peaks begin to split, meaning that the spontaneous crystallization process started. In this case, the formed phase is brushite ($CaHPO_4{\cdot}2H_2O$, dicalcium phosphate dihydrate, DCPD), as it is evident from the spectra of the samples collected after 2 h and 4 h [20]. Peak assignments for AMCP and brushite are reported in Table 2.

As the pH of the synthesis is increased, the stability is markedly modified: when solution B_1 is used (*i.e.* pH ~ 7.2), the amorphous phase is stable up to 5 h, while after 9 h brushite forms. The use of solution B_2 (pH ~ 7.3) further hinders the crystallization, as the amorphous peaks start to split after about 2 days. We can observe that in the latter case brushite peaks are not as sharp and well-defined as the ones of the crystallized phases formed with solution B_0 and B_1, indicating that after 4 days the conversion process is not complete and a portion of amorphous material may still exist. At pH 7.40 (solution B_3) peaks' splitting begins around 9 days, but a distinctive spectrum appears only after 11 days. In this case, the spectrum indicates that the crystalline product formed does not correspond to a calcium phosphate phase, but rather to a magnesium phosphate phase, namely newberyite ($MgHPO_4{\cdot}3H_2O$, XRD and SEM features of this phase will be discussed in Section 3.3.1) [26,27]. If we plot the stability of the amorphous phase as a function of the solution pH, we observe that the experimental data are fairly consistent with an exponential trend (see Fig. 2a). This suggests the possibility to prepare synthetic analogs of endogenous AMCP particles with predictable stability.

The initially-formed AMCPs precipitated at different pHs were characterized by means of ICP-AES, in order to obtain the Ca/Mg and (Ca + Mg)/P ratios of the different products. All the amorphous particles are endowed with a Ca/Mg ratio of about 4, irrespectively of the synthesis pH; the obtained (Ca + Mg)/P ratios are, in all cases, around 1.6, and do not show significant differences within the experimental error. This result suggests that in all the investigated AMCP samples, the phosphate ions do not entirely consist of HPO_4^{2-} species [1].

3.2. Characterization of AMCP particles

We characterized sample AMCP_B_3_15 min, analyzing the sample in terms of morphology and size, crystallinity and chemical nature (see Fig. 3).

A representative SEM micrograph is reported in Fig. 3a: AMCPs displays a porous and interconnected structure which results from the aggregation of spherical nanoparticles. The average dimension of each object is about 30 nm (size distribution in Fig. S1a). At very high magnification, some inner porosities of the material are visible (see Fig. S1b); this evidence suggests that, together with the porosity given by the aggregation of the single particles, AMCPs are endowed with very small porosities in the nanometric range.

Supplementary data associated with this article can be found, in the online version, at https://doi.org/10.1016/j.jcis.2018.07.102.

The particle size analysis was carried out using laser granulometer (see the experimental details in the SI). An aliquot of the reaction solution was collected before filtration and analyzed, obtaining the most representative population centered around 4 μm, with a smaller population centered around 700 nm (curves shown in Fig. S1c). On the other hand, when we analyze with the same method the dried powder instead of the aliquot withdrawn from the reaction medium, we observe one single population centered around 100 μm. The elemental composition of the sample was qualitatively investigated by means of EDX spectroscopy in combination with SEM analysis (a representative spectrum is

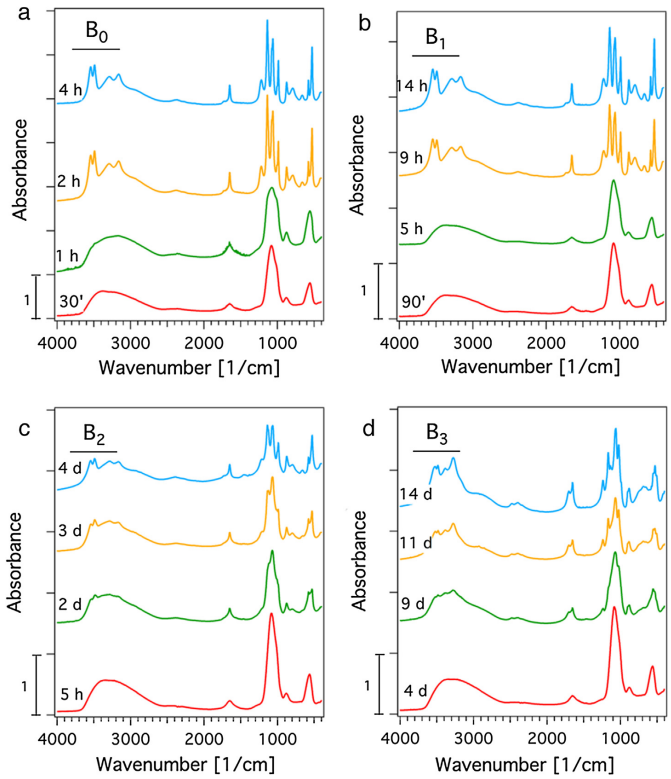

Fig. 1. FT-IR spectra of AMCPs synthesized at (a) pH 7.06 (buffer B_0); (b) pH 7.23 (buffer B_1); (c) pH 7.30 (buffer B_2); (d) pH 7.40 (buffer B_3). The time after which each aliquot was withdrawn from the solution is reported on the left of each curve. The spectra are offset for display purposes.

reported in Fig. S1d), showing that the sample is mainly constituted by Ca, Mg, P, O and Na. The amorphous nature of AMCP emerges from both XRD and FT-IR analyses. The collected XRD pattern (Fig. 3b) is consistent with previous reports on amorphous calcium phosphate [8,22], and displays the characteristic broad peak centered around 30°. The FT-IR spectrum (Fig. 3c) also shows the characteristic featureless peaks of amorphous calcium phosphate, which have been described in the previous paragraph (see Table 2). The specific surface area (SSA) of the material and the pore size distribution were investigated by means of nitrogen sorption measurements: AMCPs are characterized by a reversible type II isotherm, typical of non-porous or macroporous solids [28], (see Fig. S1e), and a SSA of (38.3 ± 1.2) m^2/g (this result is the average ± standard deviation of three different measurements). The obtained SSA value are slightly lower than the values reported in the literature for amorphous calcium phosphates, which are in any case strongly dependent on the preparation conditions [29–31]. The pore volume distribution analysis, reported in Fig. S1f, confirms that the majority of pores is in the macropores range (*i.e.* > 50 nm). Fig. 3d shows the thermal degradation profile of AMCP, together with the associated heat flow curve. The sample displays three distinct weight loss events in TGA curve, when heated up to 1000 °C (green curve in Fig. 3d): the first one, taking place around 100 °C, is associated to the loss of loosely bound water molecules, while the second one can be assigned to the more strongly bound internal water molecules [8,32]. The weight loss at 553 °C occurs simultaneously with the first crystallization peak observed in the heat flow profile, and the total weight loss is 22%. The DSC thermogram (red curve in Fig. 3d) displays three distinct peaks: the first two exothermic events, at 553 °C and 596 °C, are associated to crystallization events; at 827 °C, we observe the endothermic melting of the crystalline phases formed while heating. In order to understand the nature of the phase transformations that occur while heating AMCPs, we performed two thermal treatments, by heating them up to 580 °C and 630 °C and analyzing the obtained samples by means of XRD. The diffraction patterns and peak assignments are reported in Fig. S2a and b. We found that the first peak in the heat flow profile is associated to the formation of a crystalline sodium calcium magnesium phosphate ($Ca_9MgNa(PO_4)_7$, PDF 45-0136). In the literature it is reported that, depending on the preparation conditions, amorphous calcium phosphate converts to α-TCP (tricalcium phosphate) or β-TCP above 600 °C [8,33,34]. When Mg^{2+} ions are present in the lattice, the formation of β-TMCP (Mg-substituted TCP), which has a similar diffraction pattern to the phase that we detected, is observed [31]. The second peak in the heat flow profile (at 596 °C) is associated with the

Table 2
FT-IR peaks assignment for AMCP and brushite, according to the literature.

Peak [cm^{-1}]	Assignment	References
	AMCP	
561	ν_4 phosphate	[10]
881	P-O(H) stretching mode of protonated phosphate species	[21]
1084	ν_3 phosphate	[10]
1653	Water bending	[10,22]
2300	H-O(P) stretching of HPO_4^{2-} ions	[23]
3280	Water (O-H stretching)	[10,22]
	Brushite $CaHPO_4{\cdot}2H_2O$	
528	O-P-O(H) bending mode	[24]
577	O-P-O(H) bending mode	[24]
660	Water libration mode	[24]
	P-O bending	[25]
795	P-O-H out of plane bending	[24]
	Water libration mode	[25]
874	P-O(H) stretching	[24]
988	P-O stretching	[24]
1065	P-O stretching	[25]
1136	P-O stretching	[24]
1218	P-O-H in plane bending	[24]
1653	H-O-H bending of lattice water molecules	[24]
2370	Combination of H-O-H bending and rotation of residual free water	[24]
	O–H stretching of the hydrogen phosphate anions	[25]
2930	(P)O-H stretching (H_1*)	[24]
3164	O-H stretching of lattice water molecules (H_3*)	[24]
3285	O-H stretching of lattice water molecules (H_2*)	[24]
3490	O-H stretching of lattice water molecules (H_4*)	[24]
3540	O-H stretching of lattice water molecules (H_5*)	[24]

* H_1, H_2, H_3, H_4 and H_5 refer to the five different H atoms of brushite, see the details in Ref. [24].

conversion of the residual AMCP to very small amounts of sodium phosphate (PDF 76-1112) and magnesium phosphate (PDF 48-11687).

To sum up, the characterization performed on AMCPs shows that we managed to obtain particles which have features that match the ones that form *in vivo* [4]: in fact, our particles are composed by nanometric spheres which form larger aggregates, they are porous and mainly composed by Ca, Mg, P and, most importantly, they are amorphous. All the discussed characteristics are consistent with the biogenic particles.

3.3. Dispersion of AMCP

Once verified that the obtained AMCP particles are similar to their endogenous counterpart in terms of morphology, porosity, chemical nature and composition, we investigated how parameters relevant to the functioning of the gastrointestinal tract affect the stability of the amorphous phase and the fate of the particles. To this purpose, sample AMCP_B3_15 min was dispersed in fresh phosphate buffer solutions, as described in Section 2.3; three different factors were examined: Mg^{2+} concentration, pH and dispersion concentration.

3.3.1. Effect of Mg^{2+} concentration

The lifetime of AMCP's amorphous phase in solutions containing different amounts of Mg^{2+}, conducted as described in paragraph 2.3.1, was monitored by means of FT-IR spectroscopy. The most significant spectra are reported in Fig. 4.

Focusing on the crystallization process, it is already evident at a first glance that the presence of Mg^{2+} in solution dramatically affects the stability of the amorphous phase. When AMCPs are dispersed in a fresh phosphate buffer solution at pH 7.40, without the addition of Mg^{2+}, the amorphous phase is preserved for about 30 min; afterwards, the peak at ~550 cm^{-1} starts to split (see Fig. 4a). It is worth recalling that, for calcium phosphates, the peak around 550 cm^{-1} is reported to be the most sensitive to the crystallinity of the material [35]. At $[Mg^{2+}]$ = 1 mM, the crystallization process is slightly delayed, since the cited peak splits after about 3 h (see Fig. 4b). In the case of $[Mg^{2+}]$ = 3 mM (Fig. 4c) and $[Mg^{2+}]$ = 5 mM (Fig. 4d), crystallization begins after about 24 h and 14 days, respectively. The plot of the stability of the amorphous phase against Mg^{2+} concentration in solution, shown in Fig. 2b, reveals a good exponential relationship between the two parameters, as observed in paragraph 3.1 for the pH of the synthesis.

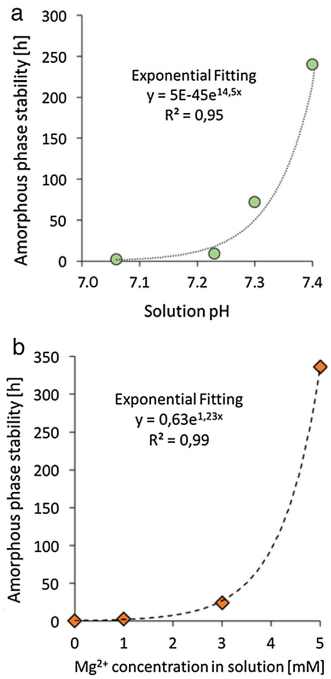

Fig. 2. (a) Plot of the stability of the amorphous phase vs pH during the synthesis. (b) Plot of the stability of the amorphous phase vs concentration of Mg^{2+} in the solution in which the particles are dispersed. In both figures, the dashed lines represent the exponential fitting of the experimental data (equation and correlation coefficient reported on the graph).

Together with the lifetime of the amorphous phase, FT-IR spectra also give important information about the nature of the formed crystalline phases, especially looking at the shape of the peak between 700 and 1400 cm^{-1} (see the zoom of this region in Fig. S3). If Mg^{2+} is absent from the solution or its concentration is very low, the spectrum of the obtained material reveals the presence of poorly crystalline hydroxyapatite [19,36,37]. The peak assignment is analogous to AMCP (see Table 2), the only difference between the two phases is the splitting of the peak at 550 cm^{-1} and the slightly different shape of the peak at ~1100 cm^{-1}. As in FT-IR the bandwidths of the peaks are related to both the crystalline domain size and the degree of ion ordering into the unit cell, the spectra observed here differs from the one of well-crystallized

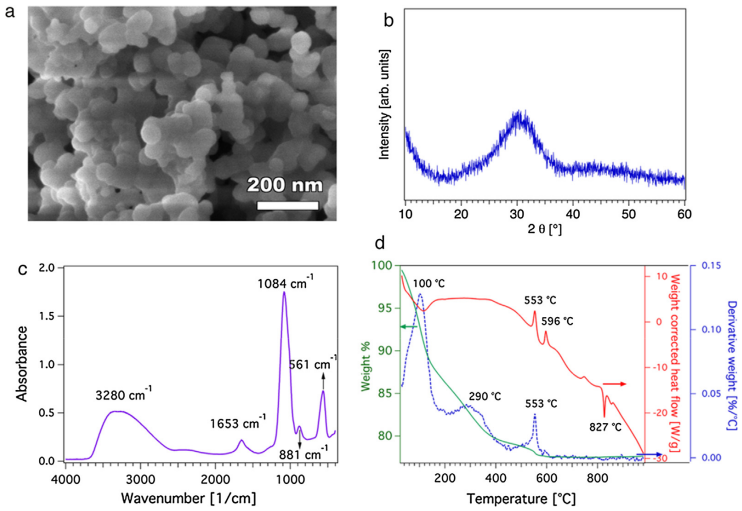

Fig. 3. (a) SEM micrograph of AMCP, magnification 250.00 KX; (b) XRD diffractogram of AMCP; (c) FT-IR spectrum of AMCP; (d) SDT data: thermogravimetry (green curve, left axis), differential thermogravimetry (dashed blue curve, right axis) and heat flow profile (red curve, right axis). (For interpretation of the references to colour in this figure legend, the reader is referred to the web version of this article.)

hydroxyapatite, which displays well-defined bands [37]. The rapid conversion of AMCP to poorly-crystalline hydroxyapatite is not surprising, as amorphous calcium phosphates are known to convert to apatitic phases in physiologic-like conditions [10]. Increasing the concentration of Mg^{2+} modifies the phase transformation of AMCP, since at $[Mg^{2+}] = 3$ mM, the peaks typical of brushite ($CaHPO_4{\cdot}2H_2O$, [20]) form after about 24 h (see Fig. 4c). In the case of $[Mg^{2+}] = 5$ mM (Fig. 4d), the spectrum of the material collected after 14 days is compatible with the presence of newberyite ($MgHPO_4{\cdot}3H_2O$) [26,27]. The formation of this crystalline form of magnesium phosphate is due to the large amount of Mg^{2+} in solution, which makes the dispersing medium supersaturated with respect to newberyite (calculation performed with the software Visual MINTEQ). We point out that the dispersing medium is stable against precipitation within the investigated time range, most reasonably because of the nucleation kinetics. This suggests that AMCP particles act as nucleation seeds for the formation of newberyite. To further deepen the understanding of the nature of the formed crystalline phases and to confirm the hypotheses conducted over FT-IR results, SEM and XRD analyses were performed on the crystalline samples obtained in the different conditions, and the results are reported in Fig. 5; since the nature of the crystalline material formed when AMCPs are dispersed without Mg^{2+} or at $[Mg^{2+}] = 1$ mM coincide, we report here only the SEM and XRD results for AMCPs dispersed without Mg^{2+}.

The morphology of poorly crystalline hydroxyapatite (see Fig. 5a) is significantly different from the one of AMCPs, as the sample consists of flake-like particles, hundreds of nm-sized. On the other hand, in the case of $[Mg^{2+}] = 3$ mM (Fig. 5b), we observe brushite typical platelets [38], while some crystals with defined geometric shapes consistent with the presence of newberyite are visible for $[Mg^{2+}] = 5$ mM [39] (see Fig. 5c); in the last two cases, we also observe a large portion of amorphous particles that surround the formed crystals, suggesting that the crystallization process is not complete. XRD results confirm the conducted observations: the diffractogram collected for AMCPs dispersed at pH 7.40 without Mg^{2+} and withdrawn after 8 h shows very broad and low-intensity peaks, which are diagnostic of a poorly-crystalline sample. The pattern, which displays peaks at 26°, 32°, 40° and 53°, is consistent with poorly-crystalline hydroxyapatite, which in the literature is often referred to as calcium-deficient hydroxyapatite (CDHA) [8,40] or cryptocrystalline/poorly crystallized apatite [41]. In the case of $[Mg^{2+}] = 3$ mM (Fig. 5e) and 5 mM (Fig. 5f), all the diffraction peaks can be respectively assigned to brushite (PDF 09–0077) and newberyite (PDF 70–2345). In Fig. 5f, the peaks are superimposed to the large hump at ~30° characteristic of AMCP (see Fig. 2b), revealing that a considerable portion of amorphous material is not crystallized yet.

To sum up, our results show that the concentration of Mg^{2+} in the solution in which AMCPs are dispersed affects both the lifetime of the amorphous phase and the nature of the crystalline calcium phosphates which form upon AMCP conversion; the reasons why these phenomena occur will be addressed in detail in the Discussion section.

3.3.2. Effect of the pH of the dispersion

The effect of different pHs during the synthesis of AMCPs has been discussed in Section 3.1; here we focus on the effect of the pH of the solution where already synthesized AMCP particles are re-dispersed. This investigation aims at simulating the different acid-base conditions which endogenous AMCP particles could encounter in physiological (like change of diet) or pathological conditions at the level of ileum [42,43] eventually leading to alterations of the immune-surveillance mechanisms. As described in Section 2.3.2, AMCP particles were dispersed in phosphate buffers at pH 6.90 and 7.40, at concentration 0.36 g/L. Results for different samples are compared in Fig. S4. FT-IR spectra, and in particular the splitting of the peak at ~550 cm^{-1}, reveal that when AMCPs are dispersed at pH 6.90, the crystallization process is faster than at pH 7.40, and that the formed product is poorly crystalline hydroxyapatite (see Fig. S4a, for the discussion of the spectrum the reader is referred to the previous section). The morphology of

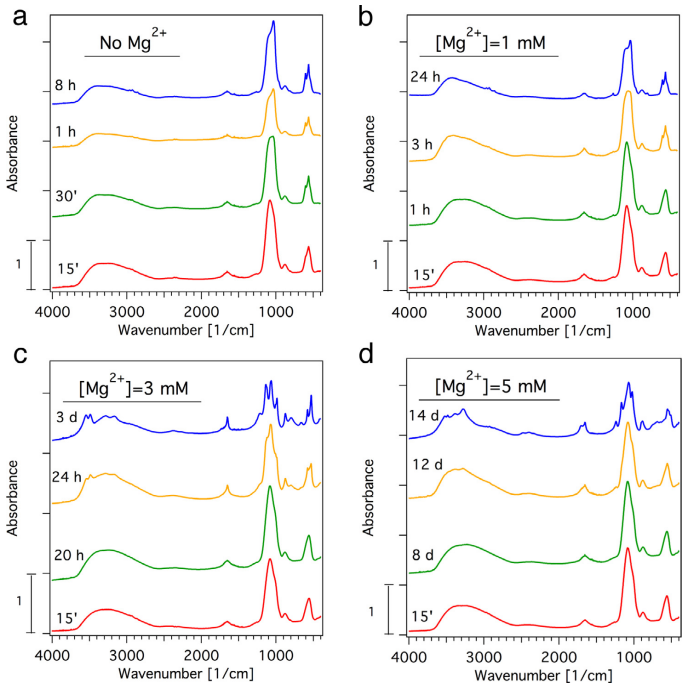

Fig. 4. FT-IR spectra of AMCP particles dispersed in different buffer solutions at pH 7.40 and with (a) No Mg^{2+}; (b) Mg^{2+} 1 mM; (c) Mg^{2+} 3 mM; (d) Mg^{2+} 5 mM. The reaction time at which each aliquot was withdrawn is indicated on the left of each curve. The spectra are offset for display purposes.

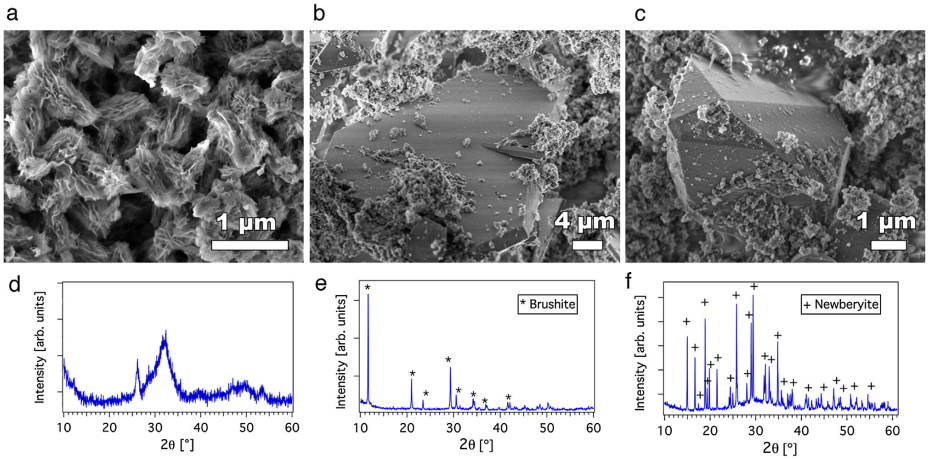

Fig. 5. SEM micrographs (a, b, c) and XRD patterns (d, e, f) of AMCPs dispersed at pH 7.40 without Mg^{2+} after 8 h (a, d), AMCPs dispersed at pH 7.40 at $[Mg^{2+}]$ = 3 mM after 3 days, (b, e) AMCPs dispersed at pH 7.40 at $[Mg^{2+}]$ = 5 mM after 14 days (c, f). The PDF used for XRD peaks' assignments are PDF 09-0077 for brushite and PDF 70-2345 for newberyite.

the samples confirms this observation, as at pH 6.90 we observe the flake-like morphology typical of hydroxyapatite, while at pH 7.40 this phase coexists with a large amount of amorphous phase (see SEM micrographs in Fig. S4b and c). EDX analysis was performed to obtain information about the elemental composition; Ca/Mg ratio is of outmost importance, as it gives insights about the crystallinity of the samples. As AMCPs displays Ca/Mg ratio of about 2.7, while crystalline calcium phosphates such as hydroxyapatite and brushite are Mg-free, the crystallinity of the samples is directly proportional to Ca/Mg ratio (*i.e.* high crystallinity means low Mg amount, which implies high Ca/Mg ratio). Atomic ratios are reported in Fig. S4d (the inset shows a zoom that highlights the low atomic % region, see Table S1 for the specific values). On the one hand, Mg/Na, Ca/Na and Ca/P ratios are not significantly affected by the pH of the solution; on the other hand, Ca/Mg ratio is much higher for the sample at 6.90, confirming the more crystalline nature of the material. The high standard deviations associated to these ratios could be related to inhomogeneities in roughness and composition of different samples (*i.e.* the amorphous portions are not homogeneously distributed all over the specimen), as the data were obtained averaging the elemental composition of 3 different sites for each sample. The results suggest that, in addition to the concentration of Mg^{2+} in solution, the pH has a critical impact on the solubility of AMCPs and the subsequent crystallization to calcium phosphates, as it will be analyzed in the Discussion section.

3.3.3. Effect of dispersion concentration

Together with the presence of Mg^{2+} ions and the pH of the solution, we observed that also the concentration of dispersed particles affects both the crystallization rate of AMCP and the type of formed phase. At pH 6.90, the particles crystallize after few minutes, as discussed in the previous section, and convert to poorly crystalline hydroxyapatite (see FT-IR spectra in Fig.S5a and SEM micrograph in Fig. S5b); however, when we increase the amount of particles that we disperse in the buffer, AMCPs evolve to brushite instead of hydroxyapatite (see Fig. S5c and S5d). EDX results (see Fig. S6) suggest that the crystallization process is faster in the diluted regime (given the higher Ca/Mg ratio obtained), highlighting that the critical factor is the amount of Mg^{2+} in solution (see later in the Discussion section).

The effect of the concentration was also investigated at pH 7.40, and the results we found are consistent with the observations conducted at pH 6.90. Also in this case, AMCPs convert to poorly crystalline hydroxyapatite in the diluted system, while in the concentrated one brushite forms (compare the series of FT-IR spectra in Fig. 4a, which refer to the diluted regime, with the ones in Fig. S7a for the concentrated system). The nature of the samples withdrawn after 8 h was investigated by means of XRD (Fig. S7b) and SEM (Fig. S7c and S7d) and the findings agree with FT-IR results. The kinetics of the crystallization process was estimated by comparing the trends of Ca/Mg ratios vs incubation time (see Fig. 6 and Table S2). Both in the diluted (Fig. 6a) and in the concentrated (Fig. 6b) experiments, Ca/Mg ratio increases with the increasing of incubation time (*i.e.* the crystallinity increases), while Mg/Na, Ca/Na and Ca/P ratio are rather constant. Moreover, Ca/Mg ratios for the concentrated system are significantly lower than the ones on the diluted regime, suggesting that also at pH 7.40 the crystallization is faster when the particles are diluted.

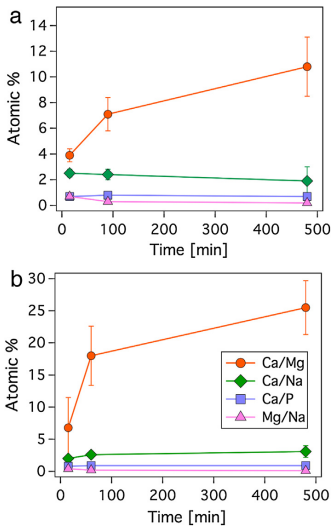

Fig. 6. Elemental ratios (Ca/Mg (circles), Ca/Na (diamonds), Ca/P (squares) and Mg/Na (triangles)) calculated by means of EDX spectroscopy as a function of incubation time of AMCPs dispersed at pH 7.40 in the (a) concentrated (2 g/L) and (b) diluted (0.36 g/L) system.

4. Discussion

The existence of ACP is a kinetically driven condition: from a thermodynamic point of view, amorphous materials are unstable, and tend to convert into crystalline phases [8,23]. The kinetics of this transformation depends on several factors, such as temperature, pH, ions and molecules in solution; these are the key parameters that regulate both the dissolution of ACP and the formation of the preliminary crystalline nuclei [9]. "Good recipes" to obtain ACP typically require basic pH, rapid mixing, low temperature, high addition rate and freeze-drying of the precipitates [8]. All these conditions take to an extension of the induction period (*i.e.* when no formation of crystalline material is observed), as they decrease ACP solubility [9]. Among the stabilization strategies which can be employed, it is known that Mg^{2+} ions contribute to the stabilization of the amorphous phase, kinetically hindering the nucleation and growth of hydroxyapatite by competing for lattice sites with calcium ions [44]. The evidence that the endogenous nanoparticles which are found in human intestine contain both calcium and magnesium is intriguing: in fact, the presence of the latter ion may contribute to preserve their amorphous nature and potentially their functional role in the organism. To mimic the effect of Mg^{2+} concentration in intestinal fluids on endogenous AMCP particles, we prepared synthetic analogues. Our results confirm the stabilization of ACP through the inclusion of Mg^{2+}, as documented in the literature [17,44,45], showing an exponential relationship between the lifetime of the amorphous phase and Mg^{2+} concentration added in solution. This paves the way towards predicting the stability of AMCP particles. Very interestingly, we observed that the concentration of this ion affects not only the lifetime of the amorphous phase, but also the type of crystalline phase to which AMCP converts. These results can be explained in terms of the calcium phosphates solubility and of the effect of magnesium ions on the calcium phosphates crystallization rate. At 37 °C and ionic strength of 0.1 M, hydroxyapatite is the thermodynamically stable phase in an extended range of pH, while at pH < 4, brushite (DCPD) is favored [46]. Therefore, the conversion of AMCP to poorly crystalline hydroxyapatite that we observe at low Mg^{2+} concentration

is not surprising, and the poor crystallinity of the material is probably due to Mg^{2+} that limit the re-arranging ability of Ca^{2+} and phosphate ions. Moreover, Mg^{2+} hinders the crystallization of the various calcium phosphate phases to a different extent: in particular, it mostly hampers hydroxyapatite formation, while brushite crystallization is un-affected by the presence of Mg^{2+} [44]. Consequently, when Mg^{2+} concentration in solution increases ($\geq$3 mM), the amorphous phase is more stable and brushite is the phase that finally precipitates, as the large amount of Mg^{2+} does not allow for hydroxyapatite formation. When $[Mg^{2+}] = 5$ mM, AMCP particles are extremely stable and Mg^{2+} is so abundant in solution that a magnesium phosphate, $MgHPO_4{\cdot}3H_2O$, is the first crystalline phase that precipitates. This explanation is also compatible with the results that we achieved in the experiments at different AMCP particles concentration: here, Mg^{2+} was not added on purpose in the solution, but it is worth recalling that AMCP particles contain a significant portion of Mg^{2+} ions in their lattice; therefore, when the particles get in contact with an aqueous solution, their dissolution begins and some Mg^{2+} ions are released in the solution. When a small amount of particles is dispersed in solution, a low concentration of Mg^{2+} is released and AMCP rapidly converts to poorly crystalline hydroxyapatite; when a larger quantity of particles is dispersed in solution, dissolution occurs to a larger extent, and the significant amount of Mg^{2+} released stabilizes the remaining solid amorphous phase, allowing for the formation of brushite over hydroxyapatite. It is therefore clear that Mg^{2+} concentration has a paramount importance in determining AMCPs behavior and fate. The levels of this ion in the gut lumen are tightly controlled, as its absorption takes place in the intestine [14]. Intestinal levels of Mg^{2+} have important implications for the health: experiments on rats show that magnesium deficiency induces inflammation in the small intestine [47] and magnesium supplements are often therapeutically effective against the symptoms of irritable bowel disease [48]. For the moment, the direct connection between Mg^{2+} concentration in the intestine and the stability/amount of AMCPs formed is not demonstrated. However, we may speculate that a Mg^{2+} deficiency in the gut could hamper the stability of the particles, thus affecting the biological pathway in which they are involved.

As far as the pH effect is concerned, the observed stabilization of AMCP with the increase of pH (both during the synthesis and when dispersed in solution) is consistent with the data reported in the literature [9]. Our results clearly show a dramatic sensitivity to pH variations, as a difference of few tenths of pH unit induce an enhancement of the stability of about 10 days. We found an exponential relationship between the amorphous phase stability in the reaction medium and the pH during the synthesis (similarly to $[Mg^{2+}]$), allowing for the prediction of the lifetime of AMCPs for a given pH value. The stability that the particles display in their reaction medium at pH 7.40 is remarkable. Very interestingly, we observed that the nature of the crystalline product formed as a consequence of AMCP conversion changes by modifying the pH, as brushite forms at pH in the range 7.06–7.30, while at pH 7.40 we detect the presence of newberyite. The precipitation of brushite can be easily justified considering the effect of Mg^{2+} ions in solution that hinder hydroxyapatite formation. The formation of newberyite could be explained considering that AMCP dissolution is slowed down at pH 7.4, and that the combined presence of Mg^{2+} ions in solution hampers the ability of forming new crystals; in these conditions, the concentration of calcium in solution needed for the formation of brushite could not be attained, and the first crystalline phase that would precipitate is newberyite. The pH of the solution which AMCPs get in contact with has also a crucial role in the crystallization kinetic: being ACP less stable in acidic conditions [9], the particles dissolve more rapidly at pH 6.90 than at pH 7.40, causing an increase in solution of all the ions constituting the particles (Ca^{2+}, Mg^{2+}, phosphate). This results in the spontaneous conversion to poorly-crystalline hydroxyapatite, while at pH 7.40 the solid material which precipitates is richer in the amorphous component, being the dissolution of AMCPs slower in these conditions.

Summarizing, pH has a deep impact of the stability of the amorphous phase. It is important to recall that, as highlighted in the Introduction, alterations in the gut pH are associated to pathologies, such as inflammatory bowel disease [42], chronic pancreatitis and cystic fibrosis, which seem to decrease pH of the proximal small intestine [43]. Air pollution can also be indirectly related to pH variations in the intestine, as it is reported that this factor may exacerbate systemic inflammation and cause oxidative damage of colonic mucosa, contributing to the occurrence of inflammatory bowel syndrome's symptoms [49]. In general, inflammatory conditions are related to acidic pH and, interestingly, AMCPs are less stable in that environment; all the factors which contribute to raise the pH of the small intestine could potentially increase the stability of the particles, leading to the correct achievement of their biological function. As far as diet is concerned, it is not easy to relate our eating habits (apart from reaching the calcium and magnesium Recommended Daily Allowance) to variations of the parameters crucial to AMCPs stability; it is generally recognized that food has no significant influence on intestinal and colonic pH [50]; nevertheless, it was also shown that, in rodents, a high fiber diet (which is known to have beneficial effects for gut health) caused an increase in the pH of the small intestine by 0.35–0.75 pH units [51].

All our data taken together demonstrate that slight variations in factors which are biologically relevant deeply affect the stability and the fate of AMCPs. We believe that these results have a two-fold relevance, as they contribute to the topic of amorphous-to-crystalline transition of calcium phosphates and may help in clarifying the role of the endogenous particles.

5. Conclusions

In this work, we describe the preparation and we investigate the stability of Amorphous Magnesium-Calcium Phosphate (AMCP) particles analogous to those present in the distal small intestine of humans and other mammals. These metastable structures have a fundamental role in the immune-surveillance mechanisms at the gut level [4]: for this reason, we investigated their stability as a function of the pH, of the $[Mg^{2+}]$ and of the particles' concentration. These parameters are susceptible to alterations in vivo in some physiological and in pathological conditions and, therefore, knowing their influence on AMCP stability would allow to predict possible immunological dysfunctions.

We found that the stability against crystallization of the amorphous phase dramatically depends on subtle pH variations: at pH $\sim$7.06, AMCP is very unstable, and after about 1 h it spontaneously crystallizes to brushite. The higher the pH of the synthesis, the longer the stability of the particles, following an exponential trend. The effect of the pH was also dramatic in the case of preparation and re-dispersion of the particles in a fresh phosphate buffered solution: the crystallization process is faster at pH 6.90 than at pH 7.40. In this case, where no Mg^{2+} was present in solution, the product of the crystallization was poorly-crystalline hydroxyapatite. By increasing $[Mg^{2+}]$ in the solution, we found an exponential relationship between the lifetime of the amorphous phase and this parameter. We observed that $[Mg^{2+}]$ also affects the crystalline phase to which AMCP converts: up to $[Mg^{2+}] = 1$ mM, AMCP crystallizes to poorly-crystalline hydroxyapatite, at $[Mg^{2+}] = 3$ mM the crystalline phase becomes brushite, and finally at $[Mg^{2+}] = 5$

mM the product of the crystallization is a magnesium phosphate (newberyite).

This paper advances the knowledge in the field of stabilization of amorphous calcium phosphate [8,17,44] by focusing on parameters relevant in the distal small intestine environment and highlighting the physico-chemical changes that could result in dysfunctions of the gut immune-surveillance mechanisms, due to the decreasing of AMCP stability.

As a next step, it is necessary to transfer what we learned by this physico-chemical approach, expanding our investigation to biologically relevant samples: in this view, we are already studying both *in vitro* and *ex vivo* samples to verify the fate of AMCP in real biological matrix, in the presence of complex molecules and of the gut micro- and mycobiota.

Acknowledgments

CSGI is acknowledged for financial support. Prof. Antonio Calabrò is acknowledged for fruitful discussion.

References

[1] S.V. Dorozhkin, Calcium orthophosphates ($CaPO_4$): occurrence and properties, Prog. Biomater. 5 (2016) 9–70, https://doi.org/10.1007/s40204-015-0045-z.
[2] L.M. Gordon, M.J. Cohen, K.W. MacRenaris, J.D. Pasteris, T. Seda, D. Joester, Amorphous intergranular phases control the properties of rodent tooth enamel, Science 347 (2015) 746–750, https://doi.org/10.1126/science.1258950.
[3] A.L. Fontaine, A. Zavgorodniy, H. Liu, R. Zheng, M. Swain, J. Cairney, Atomic-scale compositional mapping reveals Mg-rich amorphous calcium phosphate in human dental enamel, Sci. Adv. 2 (2016), https://doi.org/10.1126/sciadv.1601145 e1601145.
[4] J.J. Powell, E. Thomas-McKay, V. Thoree, J. Robertson, R.E. Hewitt, J.N. Skepper, A. Brown, J.C. Hernandez-Garrido, P.A. Midgley, I. Gomez-Morilla, G.W. Grime, K.J. Kirkby, N.A. Mabbott, D.S. Donaldson, I.R. Williams, D. Rios, S.E. Girardin, C. T. Haas, S.F.A. Bruggraber, J.D. Laman, Y. Tanriver, G. Lombardi, R. Lechler, R.P. H. Thompson, L.C. Pele, An endogenous nanomineral chaperones luminal antigen and peptidoglycan to intestinal immune cells, Nat. Nanotechnol. 10 (2015) 361–369, https://doi.org/10.1038/nnano.2015.19.
[5] J. Robertson, C.T. Haas, L.C. Pele, T.P. Monie, C. Charalambos, M. Parkes, R.E. Hewitt, J.J. Powell, Intestinal APCs of the endogenous nanomineral pathway fail to express PD-L1 in Crohn's disease, Sci. Rep. 6 (2016), https://doi.org/10.1038/srep26747.
[6] L.C. Pele, C.T. Haas, R.E. Hewitt, J. Robertson, J. Skepper, A. Brown, J.C. Hernandez-Garrido, P.A. Midgley, N. Faria, H. Chappell, J.J. Powell, Synthetic mimetics of the endogenous gastrointestinal nanomineral: silent constructs that trap macromolecules for intracellular delivery, Nanomed. Nanotechnol. Biol. Med. 13 (2017) 619–630, https://doi.org/10.1016/j.nano.2016.07.008.
[7] R.E. Hewitt, J. Robertson, C.T. Haas, L.C. Pele, J.J. Powell, Reduction of T-helper cell responses to recall antigen mediated by codelivery with peptidoglycan via the intestinal nanomineral-antigen pathway, Front. Immunol. 8 (2017), https://doi.org/10.3389/fimmu.2017.00284.
[8] S.V. Dorozhkin, Amorphous calcium orthophosphates: nature, chemistry and biomedical applications, Int. J. Mater. Chem. 2 (2012) 19–46, https://doi.org/10.5923/j.ijmc.20120201.04.
[9] A.L. Boskey, A.S. Posner, Conversion of amorphous calcium phosphate to microcrystalline hydroxyapatite. A pH-dependent, solution-mediated, solid-solid conversion, J. Phys. Chem. 77 (1973) 2313–2317, https://doi.org/10.1021/j100638a011.
[10] C. Combes, C. Rey, Amorphous calcium phosphates: synthesis, properties and uses in biomaterials, Acta Biomater. 6 (2010) 3362–3378, https://doi.org/10.1016/j.actbio.2010.02.017.
[11] M. Koziolek, M. Grimm, D. Becker, V. Iordanov, H. Zou, J. Shimizu, C. Wanke, G. Garbacz, W. Weitschies, Investigation of pH and temperature profiles in the GI tract of fasted human subjects using the Intellicap® system, J. Pharm. Sci. 104 (2015) 2855–2863, https://doi.org/10.1002/jps.24274.
[12] J. Aron-Wisnewsky, J. Doré, K. Clement, The importance of the gut microbiota after bariatric surgery, Nat. Rev.Gastroenterol. Hepatol. 9 (2012) 590, https://doi.org/10.1038/nrgastro.2012.161.
[13] S.G. Nugent, D. Kumar, D.S. Rampton, D.F. Evans, Intestinal luminal pH in inflammatory bowel disease: possible determinants and implications for therapy with aminosalicylates and other drugs, Gut 48 (2001) 571–577, https://doi.org/10.1136/gut.48.4.571.
[14] W. Jahnen-Dechent, M. Ketteler, Magnesium basics, Clin. Kidney J. 5 (2012) i3–i14, https://doi.org/10.1093/ndtplus/sfr163.
[15] L.L. Hardwick, M.R. Jones, N. Brautbar, D.B. Lee, Site and mechanism of intestinal magnesium absorption, Miner. Electrolyte Metab. 16 (1990) 174–180.
[16] K. Murakami, S. Sasaki, H. Okubo, Y. Takahashi, Y. Hosoi, M. Itabashi, Freshmen in Dietetic Courses Study II Group, Association between dietary fiber, water and magnesium intake and functional constipation among young Japanese women, Eur. J. Clin. Nutr. 61 (2007) 616–622, https://doi.org/10.1038/sj.ejcn.1602573.
[17] A.L. Boskey, A.S. Posner, Magnesium stabilization of amorphous calcium phosphate: a kinetic study, Mater. Res. Bull. 9 (1974) 907–916, https://doi.org/10.1016/0025-5408(74)90169-X.
[18] C. Holt, M. Van Kemenade, J.E. Harries, L.S. Nelson, R.T. Bailey, D.W.L. Hukins, S. S. Hasnain, P.L. De Bruyn, Preparation of amorphous calcium-magnesium phosphates at pH 7 and characterization by x-ray absorption and fourier transform infrared spectroscopy, J. Cryst. Growth. 92 (1988) 239–252, https://doi.org/10.1016/0022-0248(88)90455-1.
[19] C. Drouet, Apatite formation: why it may not work as planned, and how to conclusively identify apatite compounds, BioMed Res. Int. 2013 (2013) 490946, https://doi.org/10.1155/2013/490946.
[20] A. Hirsch, I. Azuri, L. Addadi, S. Weiner, K. Yang, S. Curtarolo, L. Kronik, Infrared absorption spectrum of brushite from first principles, Chem. Mater. 26 (2014) 2934–2942, https://doi.org/10.1021/cm500650t.
[21] C. Holt, M.J.J.M. Van Kemenade, L.S. Nelson, D.W.L. Hukins, R.T. Bailey, J.E. Harries, S.S. Hasnain, P.L. De Bruyn, Amorphous calcium phosphates prepared at pH 6.5 and 6.0, Mater. Res. Bull. 24 (1989) 55–62, https://doi.org/10.1016/0025-5408(89)90008-1.
[22] A.C. Tas, X-ray-amorphous calcium phosphate (ACP) synthesis in a simple biomineralization medium, J. Mater. Chem. B 1 (2013) 4511, https://doi.org/10.1039/c3tb20854k.
[23] S.V. Dorozhkin, Amorphous calcium (ortho)phosphates, Acta Biomater. 6 (2010) 4457–4475, https://doi.org/10.1016/j.actbio.2010.06.031.
[24] L. Tortet, J.R. Gavarri, G. Nihoul, A.J. Dianoux, Study of protonic mobility in CaHPO4·2H2O (Brushite) and CaHPO4 (Monetite) by infrared spectroscopy and neutron scattering, J. Solid State Chem. 132 (1997) 6–16, https://doi.org/10.1006/jssc.1997.7383.
[25] M.P. Gashti, M. Bourquin, M. Stir, J. Hulliger, Glutamic acid inducing kidney stone biomimicry by a brushite/gelatin composite, J. Mater. Chem. B 1 (2013) 1501–1508, https://doi.org/10.1039/C3TB00088E.
[26] B. Šoptrajanov, G. Jovanovski, I. Kuzmanovski, V. Stefov, Fourier transform vibrational spectra of magnesium hydrogenphosphate trihydrate. I. The O-H stretching region, Spectrosc. Lett. 31 (1998) 1191–1205, https://doi.org/10.1080/00387019808003295.
[27] Newberyite – RRUFF Database: Raman, X-ray, Infrared, and Chemistry, n.d. http://rruff.info/Newberyite.
[28] M. Thommes, K. Kaneko, A.V. Neimark, J.P. Olivier, F. Rodriguez-Reinoso, J. Rouquerol, K.S.W. Sing, Physisorption of gases, with special reference to the evaluation of surface area and pore size distribution (IUPAC Technical Report), Pure Appl. Chem. 87 (2015) 1051–1069, https://doi.org/10.1515/pac-2014-1117.
[29] J.M. Holmes, R.A. Beebe, Surface areas by gas adsorption on amorphous calcium phosphate and crystalline hydroxyapatite, Calcif. Tissue Res. 7 (1971) 163–174, https://doi.org/10.1007/BF02062604.
[30] J. Vecstaudza, J. Locs, Effect of synthesis temperature and Ca/P ratios on specific surface area of amorphous calcium phosphate, Key Eng. Mater. 721 (2016) 172–176, https://doi.org/10.4028/www.scientific.net/KEM.721.172.
[31] D. Lee, P.N. Kumta, Chemical synthesis and characterization of magnesium substituted amorphous calcium phosphate (Mg-ACP), Mater. Sci. Eng., C 30 (2010) 1313–1317, https://doi.org/10.1016/j.msec.2010.05.009.
[32] Y. Kojima, K. Sakama, T. Toyama, T. Yasue, Y. Arai, Dehydration of water molecule in amorphous calcium phosphate, Phosphorus Res. Bull. 4 (1994) 47–52, https://doi.org/10.3363/prb1992.4.0_47.
[33] S. Somrani, C. Rey, M. Jemal, Thermal evolution of amorphous tricalcium phosphate, J. Mater. Chem. 13 (2003) 888–892, https://doi.org/10.1039/B210900J.
[34] T. Kanazawa, T. Umegaki, N. Uchiyama, Thermal crystallisation of amorphous calcium phosphate to α-tricalcium phosphate, J. Chem. Technol. Biotechnol. 32 (1982) 399–406, https://doi.org/10.1002/jctb.5030320206.
[35] N.C. Blumenthal, A.S. Posner, J.M. Holmes, Effect of preparation conditions on the properties and transformation of amorphous calcium phosphate, Mater. Res. Bull. 7 (1972) 1181–1189, https://doi.org/10.1016/0025-5408(72)90097-9.
[36] S. Cazalbou, G. Bertrand, C. Drouet, Tetracycline-loaded biomimetic apatite: an adsorption study, J. Phys. Chem. B 119 (2015) 3014–3024, https://doi.org/10.1021/jp5116756.
[37] J. Gómez-Morales, M. Iafisco, J.M. Delgado-López, S. Sarda, C. Drouet, Progress on the preparation of nanocrystalline apatites and surface characterization: Overview of fundamental and applied aspects, Prog. Cryst. Growth Charact. Mater. 59 (2013) 1–46, https://doi.org/10.1016/j.pcrysgrow.2012.11.001.
[38] A. Betke, G. Kickelbick, Bottom-up, wet chemical technique for the continuous synthesis of inorganic nanoparticles, Inorganics 2 (2014) 1–15, https://doi.org/10.3390/inorganics2010001.
[39] F. Tamimi, D.L. Nihouannen, D.C. Bassett, S. Ibasco, U. Gbureck, J. Knowles, A. Wright, A. Flynn, S.V. Komarova, J.E. Barralet, Biocompatibility of magnesium phosphate minerals and their stability under physiological conditions, Acta Biomater. 7 (2011) 2678–2685, https://doi.org/10.1016/j.actbio.2011.02.007.
[40] L.-Y. Huang, T.-Y. Liu, T.-Y. Liu, A. Mevold, A. Hardiansyah, H.-C. Liao, C.-C. Lin, M.-C. Yang, Nanohybrid structure analysis and biomolecule release behavior of polysaccharide-CDHA drug carriers, Nanoscale Res. Lett. 8 (2013) 417, https://doi.org/10.1186/1556-276X-8-417.

[41] A.C. Tas, Calcium metal to synthesize amorphous or cryptocrystalline calcium phosphates, Mater. Sci. Eng. C 32 (2012) 1097–1106, https://doi.org/10.1016/j.msec.2012.01.024.
[42] A. Press, I. Hauptmann, L. Hauptmann, B. Fuchs, M. Fuchs, K. Ewe, G. Ramadori, Gastrointestinal pH profiles in patients with inflammatory bowel disease, Aliment. Pharmacol. Ther. 12 (1998) 673–678, https://doi.org/10.1046/j.1365-2036.1998.00358.x.
[43] J. Fallingborg, Intraluminal pH of the human gastrointestinal tract, Dan. Med. Bull. 46 (1999) 183–196.
[44] M.H. Salimi, J.C. Heughebaert, G.H. Nancollas, Crystal growth of calcium phosphates in the presence of magnesium ions, Langmuir 1 (1985) 119–122, https://doi.org/10.1021/la00061a019.
[45] F. Abbona, A. Baronnet, A XRD and TEM study on the transformation of amorphous calcium phosphate in the presence of magnesium, J. Cryst. Growth. 165 (1996) 98–105, https://doi.org/10.1016/0022-0248(96)00156-X.
[46] M.S.-A. Johnsson, G.H. Nancollas, The role of brushite and octacalcium phosphate in apatite formation, Crit. Rev. Oral Biol. Med. 3 (1992) 61–82, https://doi.org/10.1177/10454411920030010601.
[47] B.J. Scanlan, B. Tuft, J.E. Elfrey, A. Smith, A. Zhao, M. Morimoto, J.J. Chmielinska, M.I. Tejero-Taldo, I.T. Mak, W.B. Weglicki, T. Shea-Donohue, Intestinal inflammation caused by magnesium deficiency alters basal and oxidative stress-induced intestinal function, Mol. CellBiochem. 306 (2007) 59–69, https://doi.org/10.1007/s11010-007-9554-y.
[48] B.E. Lacy, K. Weiser, R. De Lee, The treatment of irritable bowel syndrome, Therap Adv Gastroenterol. 2 (2009) 221–238, https://doi.org/10.1177/1756283X09104794.
[49] M. Marynowski, A. Likońska, H. Zatorski, J. Fichna, Role of environmental pollution in irritable bowel syndrome, World J. Gastroenterol. 21 (2015) 11371–11378, https://doi.org/10.3748/wjg.v21.i40.11371.
[50] A.Y. Abuhelwa, D.B. Williams, R.N. Upton, D.J.R. Foster, Food, gastrointestinal pH, and models of oral drug absorption, Eur. J. Pharm. Biopharm. 112 (2017) 234–248, https://doi.org/10.1016/j.ejpb.2016.11.034.
[51] K.D. Kohl, A. Stengel, M. Samuni-Blank, M.D. Dearing, Effects of anatomy and diet on gastrointestinal pH in rodents, J. Exp. Zool. Part A: Ecol. Genet. Physiol. 319 (2013) 225–229, https://doi.org/10.1002/jez.1786.

Supplementary Material

Effect of pH and Mg^{2+} on Amorphous Magnesium-Calcium Phosphate (AMCP) stability

Rita Gelli[a,b], Martino Scudero[a,b], Lucia Gigli[a,b], Mirko Severi[a], Massimo Bonini[a,b], Francesca Ridi[a,b,*], Piero Baglioni[a,b]

[a] *Department of Chemistry "Ugo Schiff", University of Florence, via della Lastruccia 3, Sesto Fiorentino, 50019 Florence, Italy*
[b] *CSGI Consortium, via della Lastruccia 3, Sesto Fiorentino, 50019 Florence, Italy*

Corresponding author at: Department of Chemistry "Ugo Schiff" and CSGI, University of Florence, via della Lastruccia 3, Sesto Fiorentino, 50019 Florence, Italy.
E-mail: francesca.ridi@unifi.it (F. Ridi).

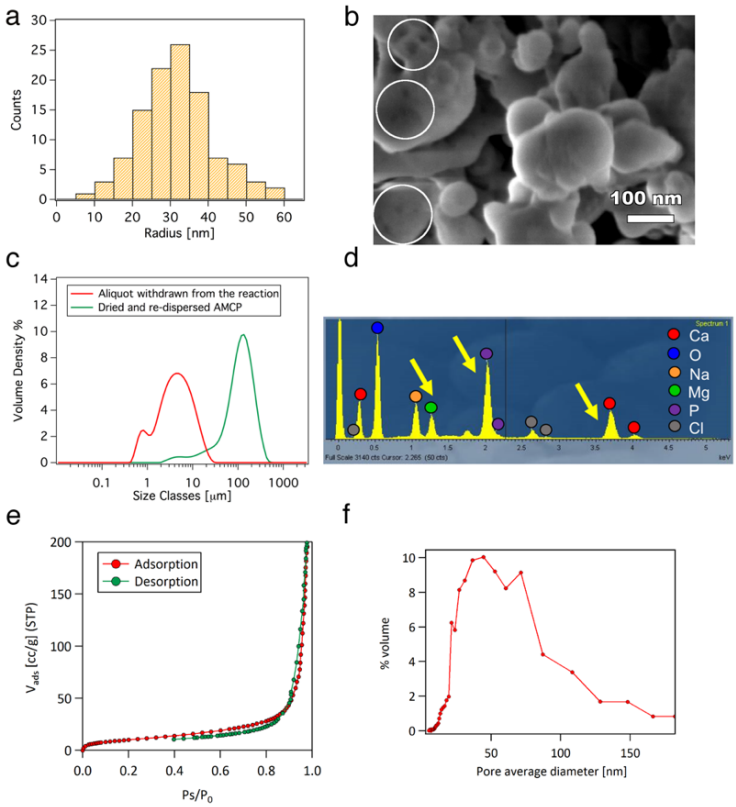

Fig. S1: (a) Size distribution obtained averaging the measured sphere radii of 5 different SEM micrographs, using the software ImageJ; the average radius is (31.6±9.9) nm (b) High magnification SEM micrograph, magnification 400.00 KX. The white circles highlight the internal porosities of the particles; (c) Size distribution curves of AMCP obtained with laser granulometry. The red curve represents an aliquot of AMCP in solution withdrawn from the reaction medium, while the green curve is the freeze-dried powder dispersed in ethanol. The measurements were performed by means of a Mastersizer 3000 laser diffraction particle size analyser, equipped with HYDRO SM wet dispersion unit. Absolute ethanol was used as a solvent to prevent particles crystallization. Each curve is the average of 10 measurements of 5 s each; (d) Representative EDX spectrum of AMCP particles, where the presence of Ca, Mg, Na and P shows the chemical composition of the particles; (e) Adsorption (red) and desorption (green) isotherm of AMCP sample; (f) Pore size distribution curve of AMCP, obtained from the desorption branch using BJH method.

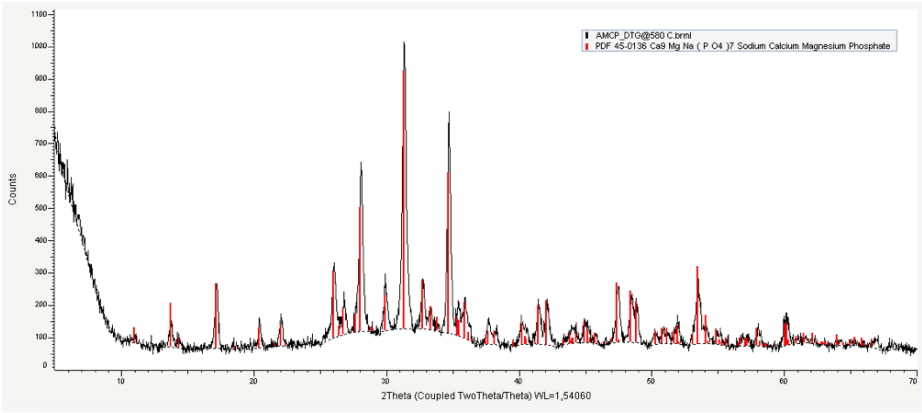

(a)

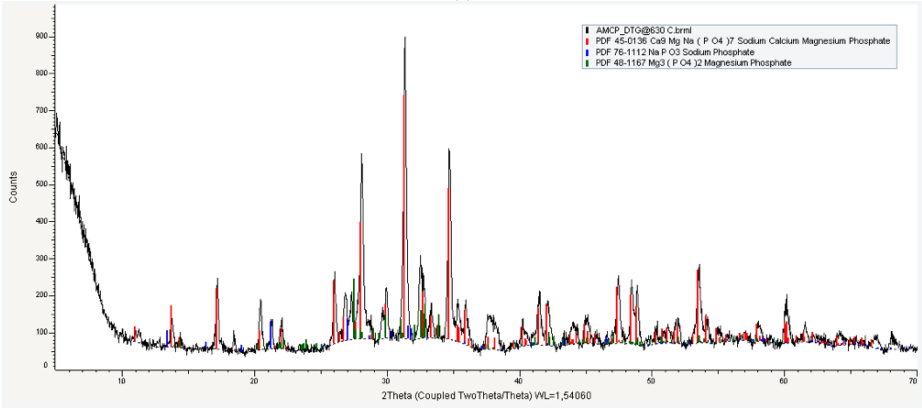

(b)

Fig. S2: XRD patterns of AMCP samples recovered after TGA measurement up to 580 °C (a) and 630 °C (b). The red sticks correspond to the PDF file of sodium calcium magnesium phosphate ($Ca_9MgNa(PO_4)_7$, PDF 45-0136), while in (b) the blue and green sticks are associated to sodium phosphate (PDF 76-1112) and magnesium phosphate (PDF 48-1167). These two phases take into account for the two additional peaks (21.4° and 27.4°) which are not present in (a) pattern.

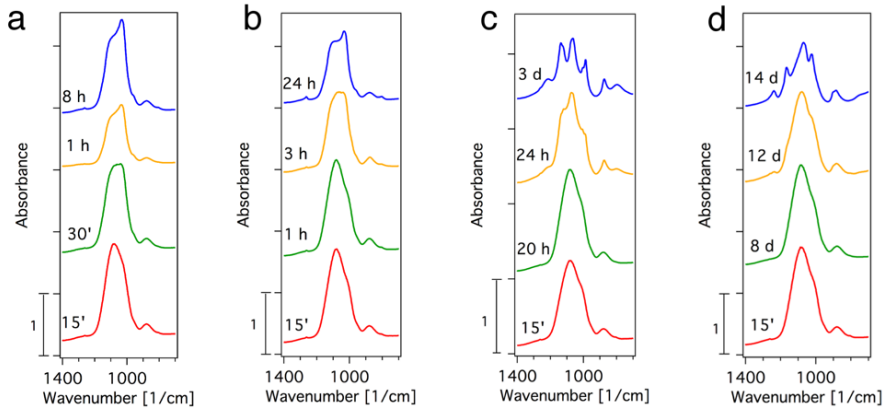

Fig. S1: Zoom of the region 700-1400 cm^{-1} of the FT-IR spectra of AMCP dispersed at pH 7.40 and (a) without Mg^{2+}, (b) with Mg^{2+}1 mM, (c) with Mg^{2+} 3 mM, (d) with Mg^{2+}5 mM.

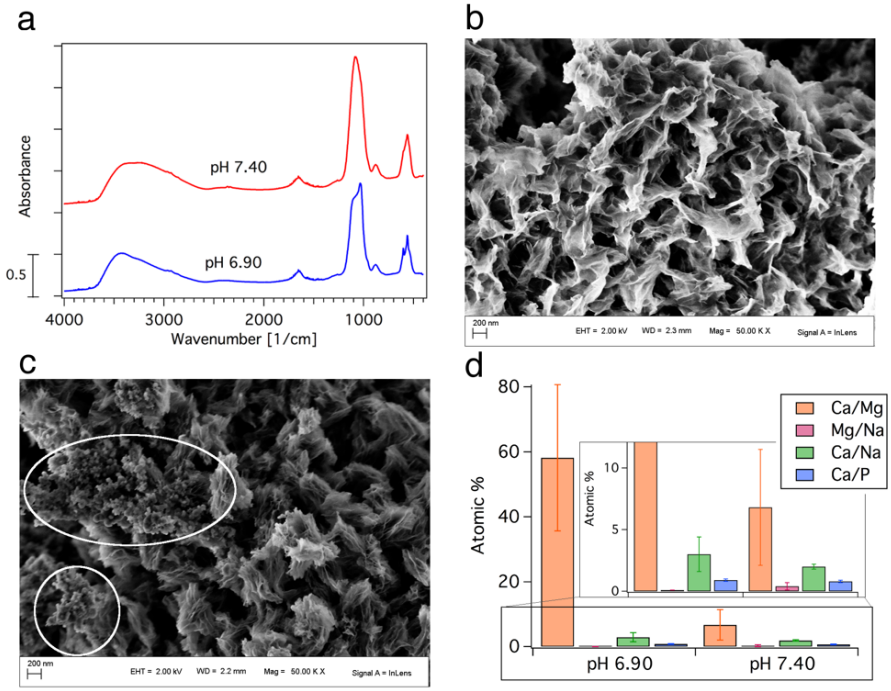

Fig. S4: (a) FT-IR spectra of AMCPs dispersed at pH 6.90 (top curve) and 7.40 (bottom curve); (b) and (c) SEM micrographs at the same magnification of AMCPs dispersed in phosphate buffer and withdrawn after 15 min at (b) pH 6.90, (c) pH 7.40. The white circles highlight the portions of the samples which are still amorphous; (d) Atomic % ratios calculated with EDX analysis, averaging 3 different sites for each sample. The error bars associated to each ratio represent the standard deviations. In the inset, the zoom of the selected region is reported, to highlight the data at low atomic %.

Table S1: Semi-quantitative elemental ratios obtained by means of EDX analysis on AMCPs dispersed at pH 6.90 vs 7.40 (histogram shown in Fig. S4d). The average value ± the standard deviation is reported (values obtained on 3 different sites for each sample).

pH	Ca/Mg	Ca/Na	Ca/P	Mg/Na
6.90	58±22	3±1	0.9±0.1	0.1±0.0
7.40	7±5	2.0±0.2	0.8±0.1	0.4±0.3

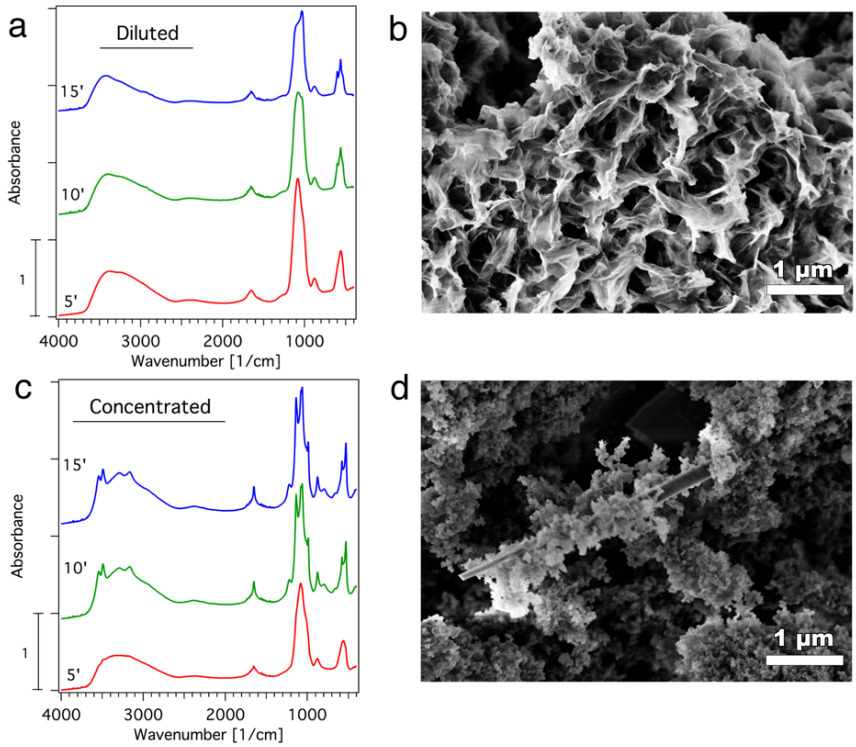

Fig. S5: (a) FT-IR spectra of AMCPs dispersed at pH 6.90 in the diluted regime (0.36 g/L) and withdrawn after 5, 10 and 15 min; (b) SEM micrograph of AMCPs dispersed at pH 6.90 in the diluted regime and withdrawn after 15 min; (c) FT-IR spectra of AMCPs dispersed at pH 6.90 in the concentrated regime (3 g/L) and withdrawn after 5, 10 and 15 min; (d) SEM micrograph of AMCPs dispersed at pH 6.90 in the concentrated regime and withdrawn after 15 min, where brushite platelets surrounded by the amorphous product are visible.

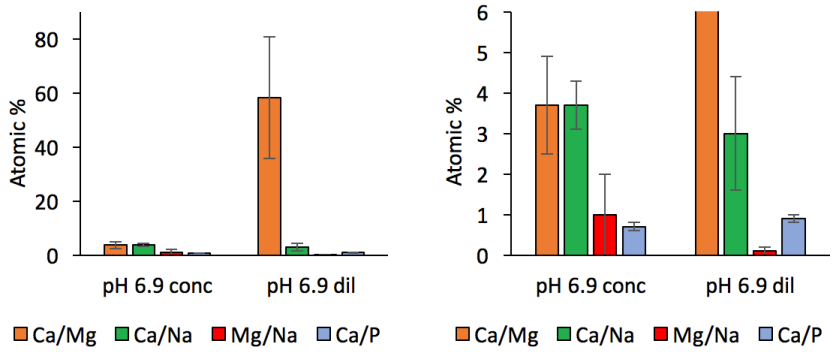

Fig. S6: Atomic % ratios obtained from EDX analysis on AMCPs dispersed at pH 6.90 at the two different dilutions. On the right, the Y-axis range is reduced to highlight Ca/Na, Mg/Na and Ca/P ratios. The data reported are the average of the ratios calculated in 3 different sites for each sample, while the error bars represent the standard deviations.

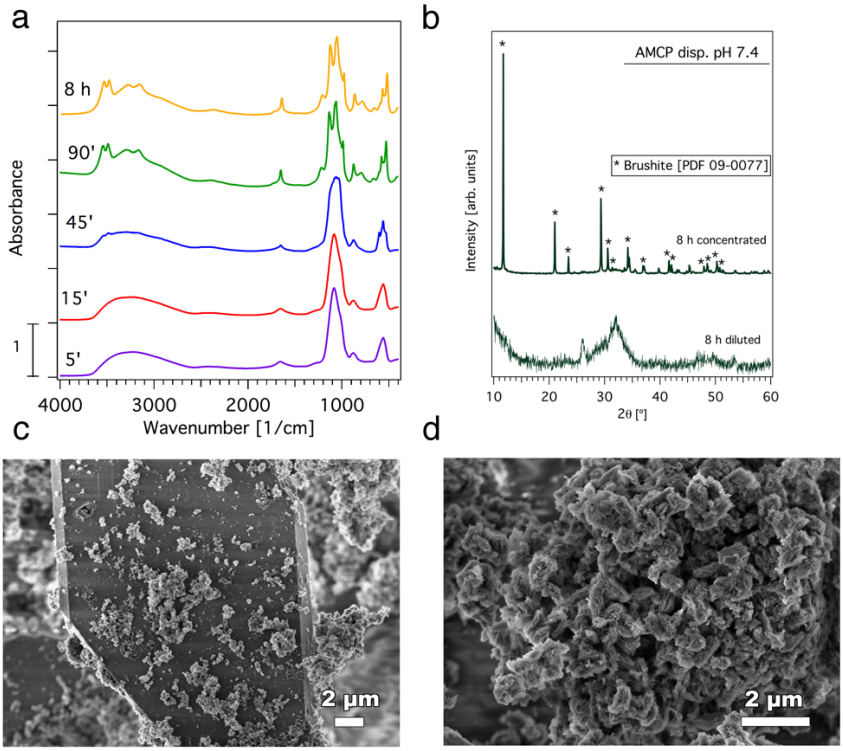

Fig. S7: (a) FT-IR spectra of AMCPs dispersed at pH 7.40 in the concentrated regime, and withdrawn after (from the top to the bottom) 5, 15, 45, 90 min and 8 h; (b) XRD pattern of AMCPs dispersed at pH 7.40 and withdrawn after 8 h in the diluted (bottom curve) and concentrated (top curve) system; (c) and (d) SEM micrographs of the samples AMCPs dispersed at pH 7.40 after 8 h, concentrated (c) and diluted (d) systems.

Table S2: Semi-quantitative elemental ratios obtained by means of EDX analysis on AMCPs dispersed at pH 7.40 in the concentrated and diluted regimes (trend shown in Fig. 6). The average value ± the standard deviation is reported (values obtained on 3 different sites for each sample).

pH 7.40 concentrated				
Time [min]	Ca/Mg	Ca/Na	Ca/P	Mg/Na
15	3.9±0.5	2.5±0.3	0.7±0.0	0.7±0.2
90	7.1±1.3	2.4±0.4	0.8±0.0	0.3±0.0
480	10.8±2.3	1.9±1.1	0.7±0.2	0.2±0.1
pH 7.40 diluted				
15	6.8±4.7	2.0±0.2	0.8±0.1	0.4±0.3
60	18.0±4.6	2.6±0.5	0.9±0.0	0.2±0.1
480	25.5±4.2	3.1±0.9	0.9±0.1	0.1±0.0

Paper II

Effect of biologically-relevant molecules on the physico-chemical properties of amorphous magnesium-calcium phosphate nanoparticles

Rita Gelli, Serena Salvestrini, Francesca Ridi*

Department of Chemistry "Ugo Schiff" and CSGI, University of Florence,

Via della Lastruccia 3, 50019 Sesto Fiorentino, Florence, Italy

*Corresponding author: Francesca Ridi, Email: francesca.ridi@unifi.it

Abstract

The recently-discovered endogenous formation of amorphous magnesium-calcium phosphate nanoparticles (AMCPs) in human distal small intestine occurs in a complex environment, which is rich in biologically-relevant molecules and macromolecules that can shape the properties and the stability of these inorganic particles. In this work, we selected as case studies four diverse molecules, which have different properties and are representative of intestinal luminal components, namely butyric acid, lactose, gluten and peptidoglycan. We prepared AMCPs in the presence of these four additives and we investigated their effect on the features of the particles in terms of morphology, porosity, chemical nature and incorporation/adsorption. The combined use of electron microscopy, infrared spectroscopy and thermal analysis showed that while the morphology and microstructure of the particles do not depend on the type of additive present during the synthesis, AMCPs are able to incorporate a significant amount of peptidoglycan, similarly to the process in which they are involved *in vivo*.

Keywords Amorphous Magnesium-Calcium Phosphate Particles; Nanostructure; Gut; Intestinal Luminal Components.

1. Introduction

The formation of calcium phosphate-based nanostructures is a phenomenon which consistently occurs in the human body and is essential for its correct functioning. Besides the notable examples of poorly-crystalline hydroxyapatite nanocrystals in bone [1] and the needle-shaped carbonated apatite crystals which form enamel [2], it was recently found that amorphous magnesium-calcium phosphate (AMCP) nanoparticles spontaneously form in the distal region of human small intestine [3–6]. While forming in the lumen, AMCPs trap soluble molecules, such as orally fed protein antigens and bacterial peptidoglycans, and transport them through the microfold-cells (M-cells) of the intestinal tissue, shaping intestinal immune homeostasis. Endogenous AMCPs are constituted by nanometric spheres which form larger agglomerates, they are porous and do not possess a long-range order [3]. The formation of amorphous calcium phosphates (ACP) in such a complex environment, *i.e.* the intestinal fluids, is an intriguing phenomenon, as the lumen contains molecules, proteins, biopolymers and bacteria, which may affect to a diverse extent the stability and the features of these inorganic particles. *In vitro*, the precipitation of ACP and AMCP is very sensitive to the conditions of the reaction medium: pH, foreign ions and molecules, temperature and ionic strength deeply affect the lifetime of the amorphous phase and the features of the particles [7–15]. The intestinal fluid contains several components, such as proteins, enzymes, sugars, lipids and bile salts; meal intake also influences its composition, as nutrient absorption takes place in the intestine. Being this medium prone to such a large variability, the accurate determination of its composition is challenging [16,17]. In addition, our gastrointestinal tract is home to more than 10^{14} microorganisms, *i.e.* gut microbiota and mycobiota, and their nutrients and metabolites affect the composition of the intestinal fluid [18,19].

In this framework, it is evident that, while forming, AMCP can encounter a variety of molecules/macromolecules that can be absorbed and can even shape their structure and stability [20]. In this work, we selected four different molecules/macromolecules as case studies, to investigate how their presence in the reaction medium can affect the physico-chemical features of AMCPs: butyric acid, lactose, gluten and peptidoglycan.

Butyric acid is a short-chain fatty acid and, together with acetic and propionic acid, is produced within the intestinal lumen by bacterial fermentation of undigested dietary carbohydrates, and to a lesser extent, dietary and endogenous proteins [21]. Butyrate is the preferred energy source for colonocytes and serves as cellular mediator regulating multiple functions of gut cells [21,22]; it also has an anti-inflammatory effect and has potential benefit in irritable bowel syndrome [23–25].

Lactose is a disaccharide composed of galactose and glucose; it enters the intestine upon milk intake, where the glycosidic bond is cleaved by the enzyme lactase. The resulting monosaccharides can then be absorbed and used as energy source by our organism. Individuals which have a deficiency in lactase production are not able to digest lactose: in this case, the disaccharide passes intact in the colon, where it is fermented by bacteria. The resulting production of gas may cause various abdominal symptoms.

Gluten can be defined as the rubbery mass that remains when wheat dough is washed to remove starch granules and water-soluble constituents [26,27]. It contains hundreds of protein components, which are typically divided into two fractions, *i.e.* gliadins (soluble in alcohol-water solutions) and glutenins (insoluble). In a small part of the population, gluten can trigger adverse autoimmune reactions responsible for a broad spectrum of gluten-related disorders, such as coeliac disease [28].

Peptidoglycan is a polymer composed of sugars (N-acetylglucosamine and N-acetylmuramic acid) and amino acids, and constitutes the cell wall of most bacteria; being the gut flora so

abundant, it is expected that peptidoglycans are a representative component of the intestinal environment.

The effect of these diverse molecules/macromolecules on the precipitation of endogenous-like AMCPs was addressed in this study. We compared the physico-chemical features of the particles obtained in the presence of these biologically-relevant additives, to simulate a possible scenario for the *in vivo* formation of the particles. In particular, we were interested in their effect on the crystallinity, morphology and internal porosity of AMCPs, as well as in estimating their incorporation in the inorganic phase.

2. Materials and methods

2.1 Materials

For the synthesis of AMCPs, calcium chloride ($CaCl_2$, ≥ 93%), magnesium chloride ($MgCl_2 \cdot 6H_2O$, ≥ 99 %), sodium chloride (NaCl, ≥ 99%) and NaOH pellets (purity ≥ 97%) were obtained from Sigma-Aldrich (Milan, Italy). Sodium phosphate monobasic ($NaH_2PO_4 \cdot H_2O$, ≥ 99%) and sodium phosphate dibasic ($Na_2HPO_4 \cdot 12H_2O$, ≥ 99%) were purchased from Carlo Erba Reagents (Milan, Italy). Butyric acid ($CH_3CH_2CH_2COOH$, ≥ 99 %), gluten from wheat (crude, ≥ 80 % protein), and peptidoglycan from *Bacillus Subtilis* were obtained from Sigma-Aldrich, while D(+)-lactose monohydrate ($C_{12}H_{22}O_{11} \cdot H_2O$, ≥ 98 %) from Fluka. Deionized water was used throughout all the experiments.

2.2 Synthesis of AMCPs

AMCPs were prepared by readapting a protocol from the literature [29], which involves the mixing of equal volumes of two aqueous solutions (see Table 1) at 37 °C. We increased Ca^{2+} concentration with respect to the literature to improve the yield of the reaction, and a Ca/Mg molar ratio of 5 was used so to obtain all the particles in amorphous phase (data not shown). 50 mL of solution A were added to 50 mL of solution B under magnetic stirring, and the pH was adjusted to 7.7 by dropwise addition of NaOH 2 M (the pH value was chosen to reproduce the

conditions in the ileum [30]). After 15 min, the solution was filtered using mixed cellulose esters filters (Millipore, pore size 0.45 μm). Filters were immediately placed in plastic test tubes, frozen in liquid nitrogen and lyophilized for 24 h. The obtained particles are referred to as sample "AMCP".

Table 1: Reactants used for the synthesis of AMCPs.

Solution	Salt	Amount [g]	Concentration [mM]
A	NaCl	0.395	135
	$CaCl_2$	0.222	40
	$MgCl_2 \cdot 6H_2O$	0.135	13.3
B	$NaH_2PO_4 \cdot H_2O$	0.345	50
	$Na_2HPO_4 \cdot 12H_2O$	2.686	150

2.3 Synthesis of AMCPs in the presence of additives

AMCPs prepared in the presence of additives were synthesized using the procedure described in paragraph 2.2, dissolving/dispersing each additive in solution A at 1 mg/mL before mixing with solution B [4]. The investigated additives are butyric acid (sample "AMCP_B"), lactose (sample "AMCP_L"), gluten (sample "AMCP_G") and peptidoglycan (sample "AMCP_P"). The only difference among the four syntheses was conducted in the preparation with gluten, as, being this protein composed by glutenin (soluble in water) and gliadin (insoluble in water) [26], it was not possible to readily dissolve it in solution A. The sonication of the dispersion for 10' lead to the partial agglomeration of the protein; therefore, we tried to improve the dispersion by stirring the sample at 70 °C for 36 h, and then we filtered the solution (0.45 μm filters) to remove the insoluble portion. The synthesis was then conducted analogously to the other systems.

2.4 Characterization techniques

2.4.1 Fourier Transform-Infrared Spectroscopy (FT-IR)

FT-IR spectra were acquired using a Bio-Rad FTS-40 spectrophotometer (Hercules, CA, USA). Freeze-dried AMCPs were analyzed in KBr pellets, obtained by mixing 1.00 ± 0.05 mg of sample with 100 ± 1 mg of KBr (Sigma-Aldrich, FT-IR grade). The spectra were collected using a resolution of 2 cm^{-1}, 64 scans and 600 s scan delay, in the range 4000-400 cm^{-1}.

2.4.2 X-Rays Powder Diffraction (XRPD)

The XRPD pattern of AMCPs was collected by means of a D8 Advance with DAVINCI design (Bruker, Milan, Italy). The X-rays source was the Cu Kα radiation (wavelength λ=1.54 Å), at 40 kV and 40 mA, in 2θ range from 10° to 60°, a step size of 0.03°, and a time/step of 0.3 s. The powder was grinded with mortar and pestle and flattened on a Si zero-background sample holder.

2.4.3 Field Emission-Scanning Electron Microscopy (FE-SEM) coupled with Energy Dispersive X-Rays (EDX) Spectroscopy

FE-SEM analyses were conducted using a Zeiss SIGMA FE-SEM (Carl Zeiss Microscopy GmbH, Jena, Germany). The powders were fixed on aluminum stubs using conductive tape. The micrographs were acquired with an accelerating voltage of 2 kV, sample-detector distance of about 2 mm and using the In-Lens detector. EDX spectroscopy was carried out using X-act Silicon Drift Detector (Oxford Instruments, England). To collect EDX spectra, the accelerating voltage used was 10 kV, while the working distance was around 8 mm.

2.4.4 Transmission Electron Microscopy (TEM)

TEM analysis was carried out by means of a TEM Philips CM12 (Eindhoven, The Netherlands), using an accelerating voltage of 100 kV. AMCPs were dispersed in absolute ethanol at 0.5 mg/mL and sonicated for 20 min at 59 kHz; a droplet of the dispersion was deposited on a carbon-coated copper grid and, after solvent evaporation, the particles were imaged.

2.4.5 Thermogravimetry (TGA)

Thermal analyses were performed with a Simultaneous Thermogravimetry/ Differential Scanning Calorimetry SDT Q600 from TA Instruments (New Castle, DE, USA). AMCPs were

placed in alumina pans and measurements were conducted in N_2 atmosphere (flow rate 100 mL/min) from room temperature to 1000 °C, at 10 °C/min.

3. Results and discussion

3.1 AMCP characterization

The characterization of AMCP synthesized in the absence of additives (see section 2.2) is reported in Figure 1. The FT-IR spectrum (Figure 1 a) shows that the obtained particles consist of amorphous calcium phosphate [7,8,31,32]. In particular, the peak at 560 and 1077 cm^{-1} are respectively referred to ν_4 and ν_3 phosphate vibrations [7], while the signal at 879 cm^{-1} is compatible with P-O(H) stretching mode of the protonated phosphate species present in the structure of AMCP [31]. The peak at 1653 cm^{-1} and the broad band at 2700-3700 cm^{-1} are due to water bending and stretching, respectively [7,32]; the latter signal is also ascribable to O-H stretching of HPO_4^{2-} groups [29]. The amorphous nature of AMCP was further confirmed by XRPD analysis (see Figure 1 b), as the pattern does not show any marked diffraction peak characteristic of crystalline calcium phosphates [33]; the broad hump centered at $2\theta \cong 30°$ is a distinctive feature of ACP, and reflects the short-range order due to Posner's clusters [32,34,35]. The morphology of AMCP was investigated by means of both scanning and transmission electron microscopy. SEM micrographs show that AMCP particles consist of nanometric heterogeneous spheres (radius: 58 ± 19 nm) which aggregate forming larger structures. EDX spectroscopy analysis, performed in combination with SEM measurements, proved that magnesium was successfully incorporated in the particles, as we found a Ca/Mg atomic ratio of 6.8±0.5. Similarly to the endogenous ones [3], our particles are endowed with inner porosities, as observed both in high magnification SEM micrographs (see the inset in Figure 1 c) and TEM images (see Figure 1 d).

From the reported characterization, we can conclude that the obtained AMCPs are good candidates to mimic the *in vivo* process, as they share many features with the endogenous ones (chemical nature, crystallinity, porosity, morphology) [3].

3.2 Characterization of AMCP in the presence of additives

The incorporation of the additives in the particles was investigated by means of FT-IR spectroscopy (Figure 2) and thermogravimetry (Figure 3). The FT-IR spectra of the particles prepared in the presence of butyric acid (red curve), lactose (orange curve) and gluten (blue curve) do not show any additional signal with respect to AMCP (see Figure 1 a for comparison). On the contrary, the sample AMCP_P displays further signals, at 1545, 2929, 2965 cm^{-1}, which are compatible with peptidoglycan vibrations [36]. This evidence suggests that, similarly to the *in vivo* process, this polymer is partially incorporated in AMCPs, unlike butyric acid, lactose and gluten.

In order to quantitatively assess the incorporation of organic material in AMCPs, the samples were analyzed by means of thermogravimetry, and the results are shown in Figure 3. From the comparison of the weight losses % at 1000 °C, we can clearly observe that samples AMCP_B, AMCP_L and AMCP_G lose about 16% of their initial weight (±1%), similarly to AMCP (15%); on the other hand, AMCP_P display a weight loss of 42%, thus indicating that the particles prepared in the presence of peptidoglycan can incorporate about 27% by weight of the polymer.

The morphology of the particles was investigated by means of SEM, and the micrographs are reported in Figure 4. The type of additive used in the synthesis does not influence the morphology of the particles, as in all samples we observe the presence of aggregated nanospheres, similarly to AMCP (see Figure 1 c for comparison). The size of the individual spherical units is not significantly different among the samples (radius for AMCP_B: 48 ± 21 nm, AMCP_L: 44 ± 14 nm, AMCP_G: 47 ± 19 nm and AMCP_P: 48 ± 18 nm). At high magnification, the porous nature of the single particles is detectable in all samples, which do

not show any difference from a qualitative perspective (see the insets in Figure 4). We can therefore conclude that neither the incorporation of peptidoglycan in the particles nor the presence in solution of the other additives result in a modification of AMCP's morphology; further studies are necessary to understand if quantitative modifications in the porosity occur because of the additives.

In terms of chemical composition, the semi-quantitative Ca/Mg atomic ratio measured by means of EDX analysis does not reveal any significant difference among the samples, as we can observe from the results in Figure 5: this suggests that the additives do not affect the relative amount of magnesium included in the structure of the particles.

The morphology of the particles was also assessed by means of TEM microscopy, so to gain some insights into the effect of the additives on the internal structure of the particles. The micrographs are reported in Figure 6. All the samples display a morphology which is similar to AMCP prepared without additives (see Figure 1 d), as the aggregated nanometric particles appear polydisperse and intrinsically porous. As already discussed over SEM results, we do not detect any marked difference among the four samples, further supporting the hypothesis that the inclusion of peptidoglycan does not affect the morphology of the particles.

4. Conclusions

In this paper, we described the effect of biologically-relevant molecules and macromolecules on the features of endogenous-like AMCPs. The self-assembly of amorphous phosphate-based nanoparticles in human intestinal lumen is an intriguing phenomenon that was recently shown to occur in our gut, being connected to immune surveillance mechanisms [3]. Intestinal fluids are complex systems which contain a great number of different molecules which can determine the properties and the stability of the amorphous particles. Here, we selected as case study four molecules/macromolecules which are representative of the intestinal environment, *i.e.* butyric acid, lactose, gluten and peptidoglycan, and we investigated, for the first time, how they affect the properties of AMCPs in terms of morphology, crystallinity, porosity. We took advantage of

a synthetic protocol that allowed us to obtain AMCPs which reproduce the features of their endogenous counterpart. Irrespectively of the presence and of the kind of additive, the obtained particles are endowed with inner porosities and form nanometric spheres that aggregate into micrometric objects. Interestingly, FT-IR spectroscopy and thermogravimetry revealed that peptidoglycan is the only additive which is incorporated in AMCP, despite not affecting the morphology and the Ca/Mg atomic ratio of the particles. This is of outmost importance, as one of the roles that AMCPs is thought to fulfill *in vivo* is the incorporation of bacterial peptidoglycans in the lumen, with the subsequent transport to the immune cells of the intestinal tissue [3]. We were therefore able to prove that the morphology and the microstructure of AMCP is preserved *in vitro*, suggesting also a preserved biological function of AMCP. The incorporation of this specific biopolymer in AMCPs may be due to its molecular weight and/or functional groups. On the other hand, butyric acid, lactose and gluten do not exert any effect on the investigated properties, suggesting that *in vivo* they do not affect the formation of AMCPs. The findings presented in this work contribute to shed light on the biological process in which these particles are involved; moreover, the ability of these novel particles to incorporate certain types of macromolecules suggest their potential use as drug delivery systems.

Acknowledgements

Fondazione CR Firenze (project 2017.0720), CSGI consortium and MIUR-Italy ("Progetto Dipartimenti di Eccellenza 2018-2022" allocated to Department of Chemistry "Ugo Schiff") are acknowledged for financial support.

References

[1] Olszta, M.J., Cheng, X., Jee, S.S., Kumar, R., Kim, Y.-Y., Kaufman, M.J., Douglas, E.P. and Gower, L.B., **2007.** Bone structure and formation: A new perspective. *Materials Science and Engineering: R: Reports*, *58(3-5)*, pp. 77–116.

[2] Beniash, E., Metzler, R.A., Lam, R.S.K. and Gilbert, P.U.P.A, **2009**. Transient amorphous calcium phosphate in forming enamel. *Journal of Structural Biology, 166(2)*, pp. 133–143.

[3] Powell, J.J., Thomas-McKay, E., Thoree, V., Robertson, J., Hewitt, R.E., Skepper, J.N., Brown, A., Hernandez-Garrido, J.C., Midgley, P.A., Gomez-Morilla, I., Grime, G.W., Kirkby, K.J., Mabbott, N.A., Donaldson, D.S., Williams, I.R., Rios, D., Girardin, S.E., Haas, C.T., Bruggraber, S.F.A., Laman, J.D., Tanriver, Y., Lombardi, G., Lechler, R., Thompson, R.P.H. and Pele, L.C., **2015**. An endogenous nanomineral chaperones luminal antigen and peptidoglycan to intestinal immune cells. *Nature Nanotechnology*, *10(4)*, pp. 361–369.

[4] Pele, L.C., Haas, C.T., Hewitt, R.E., Robertson, J., Skepper, J., Brown, A., Hernandez-Garrido, J.C., Midgley, P.A., Faria, N., Chappell, H. and Powell, J.J., **2017.** Synthetic mimetics of the endogenous gastrointestinal nanomineral: Silent constructs that trap macromolecules for intracellular delivery. *Nanomedicine: Nanotechnology, Biology and Medicine, 13(2)*, pp. 619–630.

[5] Robertson, J., Haas, C.T., Pele, L.C., Monie, T.P., Charalambos, C., Parkes, M., Hewitt, R.E. and Powell, J.J., **2016**. Intestinal APCs of the endogenous nanomineral pathway fail to express PD-L1 in Crohn's disease. Scientific Reports, *6*, 26747.

[6] Hewitt, R.E., Robertson, J., Haas, C.T., Pele, L.C. and Powell, J.J., **2017**. Reduction of T-Helper Cell Responses to Recall Antigen Mediated by Codelivery with Peptidoglycan via the Intestinal Nanomineral–Antigen Pathway. *Frontiers in Immunology, 8*, 284.

[7] Combes, C. and Rey, C., **2010**. Amorphous calcium phosphates: Synthesis, properties and uses in biomaterials. *Acta Biomaterialia*, 6, pp. 3362–3378.

[8] Dorozhkin, S.V., **2010**. Amorphous calcium (ortho)phosphates. *Acta Biomaterialia*. *6(9)*, pp. 4457–4475.

[9] Eanes, E.D. and Meyer, J.L., **1977**. The maturation of crystalline calcium phosphates in aqueous suspensions at physiologic pH. *Calcified Tissue Research*, *23(1)*, pp. 259–269.

[10] Boskey, A.L. and Posner, A.S., **1973**. Conversion of amorphous calcium phosphate to microcrystalline hydroxyapatite. A pH-dependent, solution-mediated, solid-solid conversion. *The Journal of Physical Chemistry, 77(19)*, pp. 2313–2317.

[11] Meyer, J.L. and Weatherall, C.C., **1982**. Amorphous to crystalline calcium phosphate phase transformation at elevated pH. *Journal of Colloid and Interface Science, 89(1)*, pp. 257–267.

[12] Gelli, R., Scudero, M., Gigli, L., Severi, M., Bonini, M., Ridi, F. and Baglioni, P., **2018**. Effect of pH and Mg^{2+} on Amorphous Magnesium-Calcium Phosphate (AMCP) stability. *Journal of Colloid and Interface Science*, *531*, pp. 681-692.

[13] Chen, Y., Gu, W., Pan, H., Jiang, S. and Tang, R., **2014**. Stabilizing amorphous calcium phosphate phase by citrate adsorption. *CrystEngComm*, *16(10)*, pp. 1864–1867.

[14] Bar-Yosef Ofir, P., Govrin-Lippman, R., Garti, N. and Füredi-Milhofer, H., **2004**. The Influence of Polyelectrolytes on the Formation and Phase Transformation of Amorphous Calcium Phosphate. *Crystal Growth & Design, 4(1)*, pp. 177–183.

[15] Gelli, R., Ridi, F. and Baglioni, P., **2019**. The importance of being amorphous: calcium and magnesium phosphates in the human body. *Advances in Colloid and Interface Science*, *269*, pp. 219–235.

[16] Riethorst, D., Mols, R., Duchateau, G., Tack, J., Brouwers, J. and Augustijns, P., **2016**. Characterization of Human Duodenal Fluids in Fasted and Fed State Conditions. *Journal of Pharmaceutical Sciences*, *105(2)*, pp. 673–681.

[17] Ulleberg, E.K., Comi, I., Holm, H., Herud, E.B., Jacobsen, M. and Vegarud G.E., **2011**. Human Gastrointestinal Juices Intended for Use in In Vitro Digestion Models. *Food Digestion*, *2(1-3),* pp. 52–61.

[18] Thursby, E. and Juge, N., **2017**. Introduction to the human gut microbiota. *Biochemical Journal, 474(11)*, pp. 1823–1836.

[19] Rowland, I., Gibson, G., Heinken, A., Scott, K., Swann, J., Thiele, I. and Tuohy, K., **2018**. Gut microbiota functions: metabolism of nutrients and other food components. *European Journal of Nutrition, 57(1),* pp. 1–24.

[20] Gelli, R. Tempesti, P., Ridi, F. and Baglioni, P., **2019**. Formation and properties of amorphous magnesium-calcium phosphate particles in a simulated intestinal fluid. *Journal of Colloid and Interface Science, 546*, pp. 130–138.

[21] Bedford, A. and Gong, J., **2018**. Implications of butyrate and its derivatives for gut health and animal production. *Animal Nutrition, 4(2)*, pp. 151–159.

[22] Pryde, S.E., Duncan, S.H., Hold, G.L., Stewart, C.S. and Flint, H.J., **2002**. The microbiology of butyrate formation in the human colon. *FEMS Microbiology Letters, 217(2)*, pp. 133–139.

[23] Segain, J.-P., de la Blétière, D.R., Bourreille, A., Leray, V., Gervois, N., Rosales, C., Ferrier, L., Bonnet, C., Blottière, H.M. and Galmiche, J.-P., **2000**. Butyrate inhibits inflammatory responses through NFκB inhibition: implications for Crohn's disease. *Gut, 47(3)*, pp. 397–403.

[24] Załęski, A., Banaszkiewicz, A. and Walkowiak, J., **2013**. Butyric acid in irritable bowel syndrome. *Przeglad Gastroenterology*, *8(6)*, pp. 350–353.

[25] Borycka-Kiciak, K., Banasiewicz, T. and Rydzewska, G., **2017**. Butyric acid – a well-known molecule revisited. *Przeglad Gastroenterology, 12(2)*, pp. 83–89.

[26] Wieser, H., **2007**. Chemistry of gluten proteins. *Food Microbiology, 24(2)*, pp. 115–119.

[27] Shewry, P.R., Halford, N.G., Belton, P.S. and Tatham, A.S., **2002**. The structure and properties of gluten: an elastic protein from wheat grain. *Philosophical Transactions R Soc Lond B Biol Sci*., *357(1418)*, pp.133–142.

[28] Ludvigsson, J.F., Leffler, D.A., Bai, J., Biagi, F., Fasano, A., Green, P.H., Hadjivassiliou, M., Kaukinen, K., Kelly, C., Leonard, J.N., Lundin, K.E., Murray, J.A., Sanders, D.S., Walker, M.M., Zingone, F. and Ciacci, C., **2013**. The Oslo definitions for coeliac disease and related terms. *Gut*, *62(1)*, pp. 43–52.

[29] Holt, C., Van Kemenade, M., Harries, J.E., Nelson, L.S., Bailey, R.T., Hukins, D.W.L., Hasnain, S.S. and De Bruyn, P.L., **1988.** Preparation of amorphous calcium-magnesium phosphates at pH 7 and characterization by x-ray absorption and Fourier transform infrared spectroscopy. *Journal of Crystal Growth, 92(1-2)*, pp. 239–252.

[30] Aron-Wisnewsky, J., Doré, J. and Clement, K., **2012**. The importance of the gut microbiota after bariatric surgery. *Nature Reviews Gastroenterology and Hepatology, 9(10)*, pp. 590-598.

[31] Holt, C., Van Kemenade, M.J.J.M., Nelson, L.S., Hukins, D.W.L., Bailey, R.T., Harries, J.E., Hasnain, S.S. and De Bruyn, P.L., **1989**. Amorphous calcium phosphates prepared at pH 6.5 and 6.0. *Materials Research Bulletin*, *24(1)*, pp. 55–62.

[32] Tas, A.C., **2013**. X-ray-amorphous calcium phosphate (ACP) synthesis in a simple biomineralization medium. *Journal of Materials Chemistry B, 1(35)*, pp. 4511-4520.

[33] Drouet, C., **2013**. Apatite Formation: Why It May Not Work as Planned, and How to Conclusively Identify Apatite Compounds. *BioMed Research International,* 490946.

[34] Li, Y., Wiliana, T. and Tam, K.C., **2007.** Synthesis of amorphous calcium phosphate using various types of cyclodextrins. *Materials Research Bulletin, 42(5)*, pp. 820–827.

[35] Lai, R.-H., Dong, P.-J., Wang, Y.-L. and Luo, J.-B., **2014**. Redispersible and stable amorphous calcium phosphate nanoparticles functionalized by an organic bisphosphate. *Chinese Chemical Letters, 25(2)*, pp. 295–298.

[36] Leenheer, J.A. and Rostad, C.E., **2004**. Fractionation and characterization of organic matter in wastewater from a Swine waste-retention basin. US Department of the Interior, US Geological Survey.

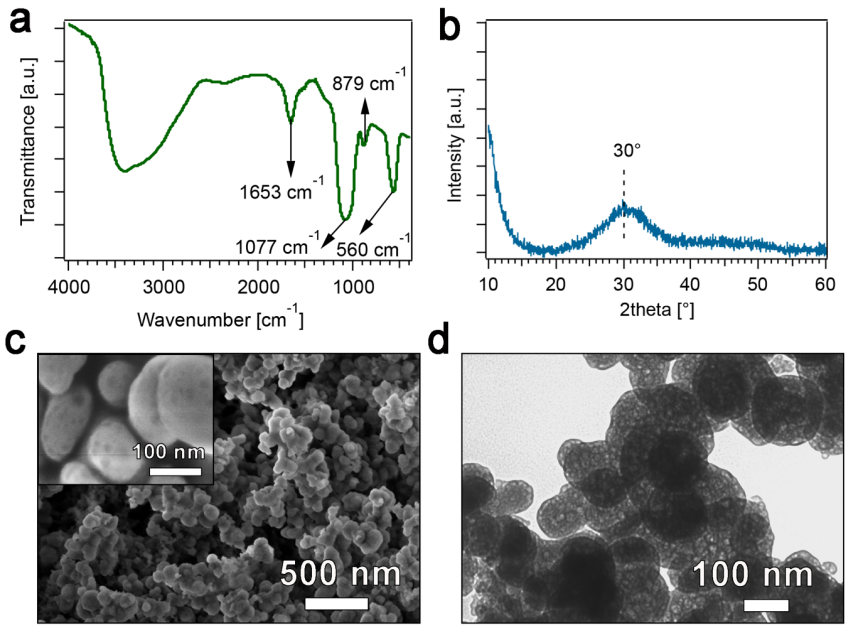

Figure 1: AMCP characterization: (a) FT-IR spectra; (b) XRPD pattern; (c) FE-SEM micrographs (inset: high magnification); (d) TEM micrograph.

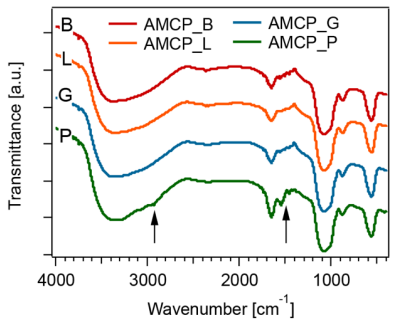

Figure 2: FT-IR spectra of AMCP synthesized in the presence of (from the top) butyric acid (AMCP_B), lactose (AMCP_L), gluten (AMCP_G) and peptidoglycan (AMCP_P). The arrows highlight the additional signals present in the spectrum of AMCP_P, due to the incorporated peptidoglycan.

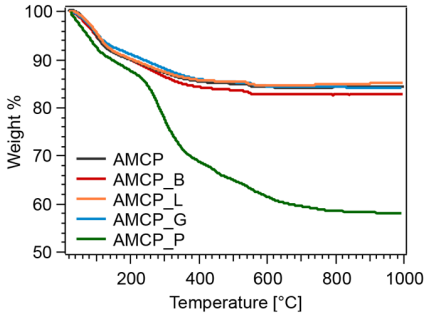

Figure 3: Thermograms of AMCP prepared in the presence of butyric acid (red curve), lactose (orange curve), gluten (blue curve) and peptidoglycan (green curve), compared to pure AMCP (black curve).

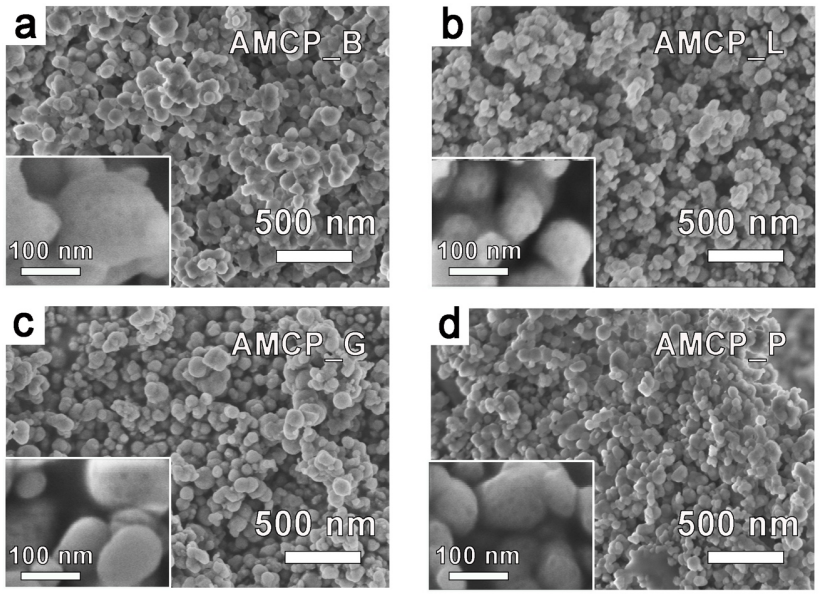

Figure 4: FE-SEM micrographs of (a) AMCP_B; (b) AMCP_L; (c) AMCP_G; (d) AMCP_P. In the insets, high magnification images are shown.

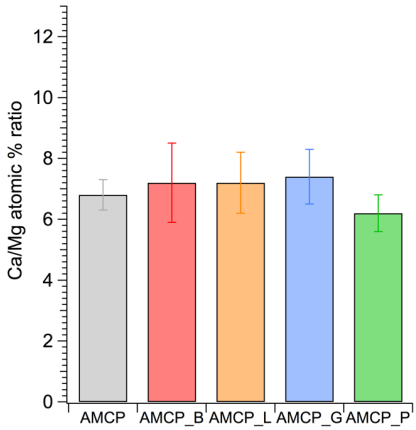

Figure 5: Ca/Mg semi-quantitative atomic ratios obtained by means of EDX spectroscopy; the reported data are the average values ± standard deviations of 5 different analysis on different sites of each sample.

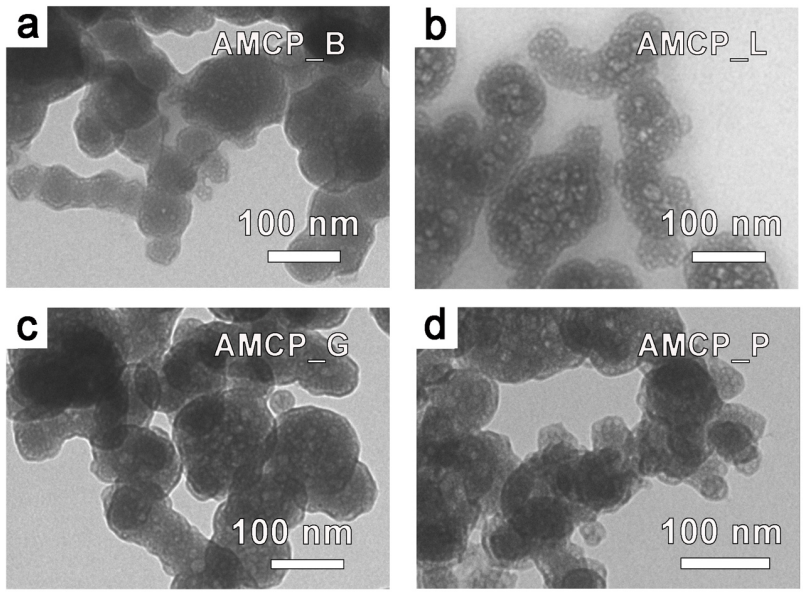

Figure 6: TEM micrographs of (a) AMCP_B; (b) AMCP_L; (c) AMCP_G; (d) AMCP_P.

Paper III

Journal of Colloid and Interface Science 546 (2019) 130–138

Contents lists available at ScienceDirect

Journal of Colloid and Interface Science

journal homepage: www.elsevier.com/locate/jcis

Regular Article

Formation and properties of amorphous magnesium-calcium phosphate particles in a simulated intestinal fluid

Rita Gelli, Paolo Tempesti, Francesca Ridi *, Piero Baglioni

Department of Chemistry "Ugo Schiff" and CSGI, University of Florence, via della Lastruccia 3, 50019 Sesto Fiorentino, Florence, Italy

GRAPHICAL ABSTRACT

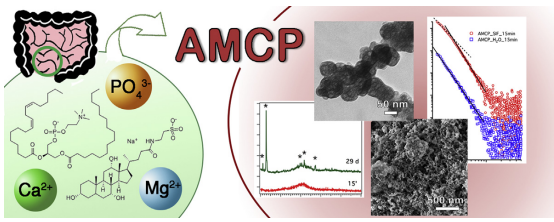

ARTICLE INFO

Article history:
Received 15 January 2019
Revised 12 March 2019
Accepted 18 March 2019
Available online 19 March 2019

Keywords:
Amorphous magnesium-calcium phosphate
Gut
Simulated intestinal fluids
Lecithin
Taurocholate
Self-assembly
Stability
Porosity
Nanostructure

ABSTRACT

Hypothesis: The endogenous self-assembly of amorphous magnesium-calcium phosphate (AMCP) nanoparticles in human small intestine is an intriguing and newly-discovered process involved in immune-surveillance mechanisms. The study of nano and microparticles formation in complex media mimicking *in vivo* conditions contributes to unravel the features of endogenous AMCPs and, from a physico-chemical perspective, to shed light on the effect of biorelevant molecules on the precipitation of AMCPs.

Experiments: Endogenous-like AMCPs have been synthesized in a commercial simulated intestinal fluid (SIF), which contains biorelevant molecules such as lecithin and taurocholate. The properties of these particles were compared to the features of AMCPs synthesized in water. The stability of the amorphous phase as a function of time, as well as AMCPs' morphology, have been investigated. In particular, the effect of the organic molecules present in the SIF was examined in terms of incorporation in the nano and micro particles and on their nanoscale structure.

Findings: Taurocholate and lecithin, present in the SIF, enhance stability of amorphous phase against particles crystallization, and lead to the formation of smaller AMCP aggregates with a rougher surface. They are also incorporated in the inorganic phase, and their self-assembled structure leads to the formation of core-shell nanoparticles.

Abbreviations: CaPs, Calcium Phosphates; AMCP, Amorphous Magnesium-Calcium Phosphate; AMP, Amorphous Magnesium Phosphate; ACP, Amorphous Calcium Phosphate; GI, Gastrointestinal; SIF, Simulated Intestinal Fluid; HA, Hydroxyapatite; PC, Phosphatidylcholine; DLS, Dynamic Light Scattering; CMC, Critical Micelle Concentration; FT-IR, Fourier Transform-Infrared Spectroscopy; XRD, X-Rays Diffraction; PDF, Powder Diffraction File; FE-SEM, Field Emission-Scanning Electron Microscopy; TEM, Transmission Electron Microscopy; SAXS, Small Angle X-Rays Scattering.

* Corresponding author at: Department of Chemistry "Ugo Schiff" and CSGI, University of Florence, via della Lastruccia 3, Sesto Fiorentino, 50019 Florence, Italy.
E-mail address: francesca.ridi@unifi.it (F. Ridi).

https://doi.org/10.1016/j.jcis.2019.03.060
0021-9797/

1. Introduction

The *in vivo* formation of biogenic calcium phosphates (CaPs) is regulated by relevant biomolecules controlling the self-assembly process typical of Soft Matter [1]. The most notable example is the process of bone biomineralization, in which the deposition of platelet-like apatitic nanocrystals is templated by the collagen I fibers' network formed through self-assembly [2]. Other examples include the role of amelogenin on the regulation of carbonated apatite crystalline 3D network in enamel [3] and the action of the protein fetuin-A in complexing amorphous calcium phosphate clusters in serum [4]. Another scenario where the formation of CaP-based minerals occurs in a complex biological environment is the small intestine. It has been recently shown that in the ileum region of the human gut, the endogenous secretions of calcium and phosphate ions from the distal small intestine into the lumen lead to the precipitation of amorphous magnesium-substituted calcium phosphate particles (AMCPs) [5]. These particles trap macromolecules, *i.e.* orally fed protein antigens and bacterial peptidoglycans, and transport them to the immune cells of the intestinal tissue, promoting the immuno-surveillance mechanisms. Endogenous AMCPs are porous and composed by agglomerates of small nanoparticulate structures; the amorphous nature allows for the effective incorporation of the organic cargo, as it was shown during *in vitro* experiments [6].

The study of amorphous magnesium and calcium phosphates is particularly relevant. On the one hand, amorphous magnesium phosphates (AMPs) constitute an emerging field of research: together with crystalline magnesium phosphates, these components represent relatively new biocompatible options for the preparation of nanostructured biomaterials [7–10]. On the other hand, amorphous calcium phosphates (ACPs) have been extensively investigated in the past for their interesting properties [11,12]; moreover, it is known that, both *in vivo* and *in vitro*, their structure and stability are sensitive to many physico-chemical properties (temperature, pH, viscosity, ionic strength, presence of foreign ions and molecules [11–14]) of the medium in which they form. The determination of these properties in human ileum is challenging, since intestinal fluids are prone to a large variability in their composition [15]. Moreover, the majority of literature studies are devoted to the duodenal and jejunal composition, and the features of the lower part of the gastrointestinal tract (GI), such as the ileum where AMCPs form, are often neglected [16,17].

The development of standardized simulated fluids that mimic the different regions of the GI tract is of outmost importance, especially in the assessment of the dissolution and solubility of drugs. Nowadays, some biorelevant simulated intestinal fluids (SIF) are commercially available. These media typically consist of aqueous solutions of bile salts (anionic natural steroidal surfactants, typically sodium taurocholate) and phospholipids (such as lecithin, a mixture of phosphatidylcholines), in addition to other components that allow the fluid to mimic the pH, the osmolality and the buffer capacity of each specific tract of the gut [18,19]. The simultaneous presence in solution of bile salts and lecithin often results in the formation of self-assembled structures, such as mixed micelles, depending on their molar ratio, concentration, pH, ionic strength and temperature [19,20]. In the mixed micelles, which are also present *in vivo* and allow for the solubilization and absorption of dietary fats [21], bile salts are located between polar head groups of phospholipids, with their hydrophilic sides exposed to the aqueous environment; this results in the formation of either spherical, cylindrical or worm-like micelles, with sizes ranging from 3.5 to 70 nm, depending on the phospholipid and bile salt amount and their ratio [19,21–25]. To the best of our knowledge, the detailed characterization of the fluid which mimics specifically the ileum region of the intestine [18] has never been reported.

Given the presence of endogenous AMCP nanoparticles in the distal small intestine, understanding the formation mechanism of CaPs in a complex fluid that simulates the *in vivo* conditions is particularly relevant. Even though AMCP formation in SIF has never been investigated so far, the literature reports some examples about the effect of the separate components, *i.e.* taurocholate and lecithin, on the formation of CaP-based materials. Bile can inhibit the formation of CaP, likely because of the action of bile salt/phospholipid micelles [26]. It was suggested that Ca^{2+} interaction with both free and micellar taurocholate anions is responsible for the inhibitory effect, as it limits Ca^{2+} concentration and potentially acts as buffer against the precipitation of calcium-containing gallstones [27]. Moreover, different bile salts have a different inhibitory effect [28]. The effect of mixed taurodeoxycholate/phosphatidylcholine (PC) micelles on hydroxyapatite (HA) binding and precipitation inhibition was also investigated, showing that the ability to delay HA formation/precipitation is dependent on the composition of the micelles [26,29].

The effect of lecithin on calcium phosphate formation was explored to a lesser extent. Recently, soybean lecithin was used as a template to prepare ACP porous hollow microspheres [30], while Michał et al. obtained HA nanoparticles using a lecithin-based wet chemical precipitation method [31].

In a previous work, we investigated the effect of pH and Mg^{2+} concentration on the amorphous phase stability of endogenous-like AMCPs [14]. We thoughtfully characterized the physico-chemical properties of the obtained particles, and we related the variations of the cited parameters (which are known to have implications in gut health) to the lifetime of the amorphous phase in solution. In the attempt of gaining new insights in the *in vivo* formation process and stability, the present work reports on the formation and the features of endogenous-like AMCPs prepared in a simulated intestinal fluid. We believe that these results have a two-fold relevance, as they shed light on the effect of sodium taurocholate and lecithin on the precipitation of amorphous calcium and magnesium phosphates, relevant for the *in vivo* formation and features of AMCPs.

2. Materials and methods

2.1. Materials

The powder "FaSSIF/FeSSIF/FaSSGF" used to prepare the Simulated Intestinal Fluid (SIF) was purchased from Biorelevant.com Ltd (London, UK). Sodium chloride (NaCl, ≥ 99%), maleic acid ($C_4H_4O_4$, ≥ 99%), magnesium chloride ($MgCl_2{\cdot}6H_2O$, ≥99%) calcium chloride ($CaCl_2$, ≥ 93%) and NaOH pellets were purchased from Sigma-Aldrich (Milan, Italy). Sodium phosphate monobasic ($NaH_2PO_4{\cdot}H_2O$, ≥ 99%), and sodium phosphate dibasic ($Na_2HPO_4{\cdot}12H_2O$, ≥ 99%) were obtained from Carlo Erba Reagents (Milan, Italy). Deionized water was used during all the experiments.

2.2. Preparation of the simulated intestinal fluid

The SIF specifically mimicking the ileum region of the gut was prepared according to the instructions given by the supplier. 500 mL of the fluid were prepared by dissolving 0.880 g of NaCl, 3.065 g of maleic acid and 2.115 g of NaOH in deionized water (450 mL). A solution of NaOH 2 M was used to adjust the pH at 7.5, then we made up to the final volume with water. 0.3 g of powder (FaSSIF/FeSSIF/FaSSGF) were dissolved in the prepared buffer, and the fluid was let stand for at least 2 h before use. The medium was used within 24 h from the preparation. The final concentrations of the components are: sodium taurocholate 0.8 mM, lecithin 0.2 mM and maleic acid 52.8 mM [18].

2.3. Synthesis of AMCP in water and in SIF

AMCP was obtained by mixing equal volumes (200 mL) of two solutions, namely solution A (which contains NaCl, $MgCl_2$ and $CaCl_2$, amounts and concentrations listed in Table S1 in the Supplementary Material) and solution B (NaH_2PO_4 and Na_2HPO_4, see Table S1) [32]. The ionic concentrations used are consistent with the ones typical of ileum [33]. Two syntheses were conducted using the same procedure, except for the fact that the salts were dissolved in SIF or water. Solution A and B were separately heated at 37 °C in a water bath. Solution A was added to solution B and the pH was adjusted to 7.50, which is representative of the ileum region [34], by dropwise addition of NaOH 2 M. Aliquots of the solution (~20 mL) were periodically withdrawn from the reaction flask and filtered using a Millipore vacuum filtration system equipped with mixed cellulose esters filters (Millipore, pore size 0.22 μm). Filters were immediately placed in plastic test tubes and frozen in liquid nitrogen, prior to lyophilization for 24 h. As a preventive measure, particles were stored at −18 °C, tightly closed to prevent any influence from environmental humidity which could lead to spontaneous crystallization.

2.4. Characterization techniques

2.4.1. Dynamic light scattering (DLS)

DLS measurements were performed on a Brookhaven Instruments apparatus (BI 9000AT correlator and BI 200 SM goniometer). The light source was a Torus laser, mpc3000, LaserQuantum, UK (λ = 532 nm) and the scattered intensity was detected by a BI-APD detector. The samples were placed in glass tubes and immersed in a thermostated cell at 37 °C filled with decahydronaphthalene to match the glass refractive index. The scattering intensity of pure toluene was used as a standard. The field autocorrelation functions reported in this work are the result of the averaging of five experiments for each sample. The averaged functions were analyzed through cumulant analysis (see Supplementary Material for details).

2.4.2. Surface tension

The surface tension properties of the SIF were determined using a Force Tensiometer K100 (Krüss GmbH, Hamburg, Germany). Inverse critical micelle concentration (CMC) measurements were performed using a Pt plate, at T = 37 °C and diluting the sample with water up to $1{\cdot}10^{-5}$ mM sodium taurocholate concentration.

2.4.3. Fourier transform infrared spectroscopy (FT-IR)

FT-IR spectra were collected using a Bio-Rad FTS-40 spectrophotometer (Hercules, CA, USA). The samples were analyzed in KBr pellets, prepared by mixing 1.00 ± 0.05 mg of sample with 100 ± 1 mg of KBr (Sigma-Aldrich, FT-IR grade). The spectra were acquired in the range 4000–400 cm^{-1} using a resolution of 2 cm^{-1}, 64 scans and scan delay of 600 s.

2.4.4. X-rays diffraction (XRD)

X-rays Diffraction (XRD) patterns were collected with a D8 Advance with DAVINCI design (Bruker, Milan, Italy), using as X-rays source the Cu Kα radiation (wavelength λ = 1.54 Å), at 40 kV and 40 mA, a 2θ range of 5–60°, a step size of 0.03°, and a time/step of 0.3 s. A Si zero-background sample holder was used, while peaks' assignment was based on the Powder Diffraction Files (PDF) of the ICDD database (International Centre for Diffraction Data).

2.4.5. Field emission-scanning electron microscopy (FE-SEM)

Field Emission-Scanning Electron Microscopy (FE-SEM) analysis was conducted using a Zeiss ΣIGMA FE-SEM (Carl Zeiss Microscopy GmbH, Jena, Germany). The powders were placed over aluminum stubs by means of conductive tape. The micrographs were acquired with an accelerating voltage of 2 kV, sample-detector distance ~2 mm and using the In-Lens detector.

2.4.6. Simultaneous thermogravimetry/differential scanning calorimetry

Simultaneous Thermogravimetry/Differential Scanning Calorimetry analyses were performed using SDT Q600 from TA Instruments (New Castle, DE, USA). Each sample was placed in an alumina pan and measurements were conducted in N_2 atmosphere (flow rate 100 mL/min) from room temperature to 1000 °C, at 10 °C/min.

2.4.7. Transmission electron microscopy (TEM)

Transmission Electron Microscopy (TEM) analysis of AMCPs was performed with a TEM Philips CM12 (Eindhoven, The Netherlands), working with an electron gun operating at 100 kV. Samples were prepared by depositing a droplet of a sonicated AMCPs dispersion in ethanol onto a carbon-coated copper grid.

2.4.8. Small angle X-rays scattering (SAXS)

SAXS measurements were carried out using a HECUS SWAX-camera (Kratky) equipped with a position-sensitive detector (OED 50 M) containing 1024 channels of width 54 μm. Cu K_α radiation of wavelength λ = 1.542 Å was provided using a Seifert ID-3003 X-ray generator (sealed-tube type), operating at a maximum power of 2 kW. A 10-mm thick Ni-filter was used to remove Cu K_β radiation. The sample-to-detector distance was 275 mm. The volume between the sample and the detector was kept under vacuum during the measurements to minimize scattering from the air. The Kratky camera was calibrated in the small angle region using silver behenate (d = 5.838 nm). Scattering curves were obtained in the Q-range, $Q = (4\pi/\lambda)\sin(\theta/2)$, between 0.009 and 0.54 $Å^{-1}$, with Q being the scattering vector, and θ the scattering angle. The samples were contained in 2 mm quartz capillaries. Standard measurement conditions were 40 kV, 20 mA, and 3 h (acquisition time) at 25 °C. SAXS curves reported in this work have been compared with those obtained on very short time scales and no differences were detectable between the two sets of measurements. All scattering curves were corrected for the solvent/empty cell contribution considering the relative transmission factor. SAXS curves were iteratively desmeared using the procedure reported by Lake [35]. The interpretation of the curves was carried out with a power law model associated to the linear regions in the double log representation (Eq. (1)):

$$I(q) = Aq^{-p} \tag{1}$$

where A is a scale factor and p is the slope of the linear fitting. When $1 \leq p \leq 3$, p represents the mass-fractal dimension (D_m) that is 3 for full solid materials [36]. When $3 \leq p \leq 4$ one can calculate the surface-fractal dimension (D_s) from the equation:

$$D_s = 6 - p \tag{2}$$

Typically, D_s is 2 for smooth surfaces, and goes towards 3 as the roughness increases [37].

3. Results and discussion

3.1. SIF characterization

DLS was employed to investigate the presence of self-assembled aggregates in the SIF. Cumulant analysis of the autocorrelation function (Fig. S1 in the Supplementary Material) revealed the presence of nanosized objects with a mean hydrodynamic

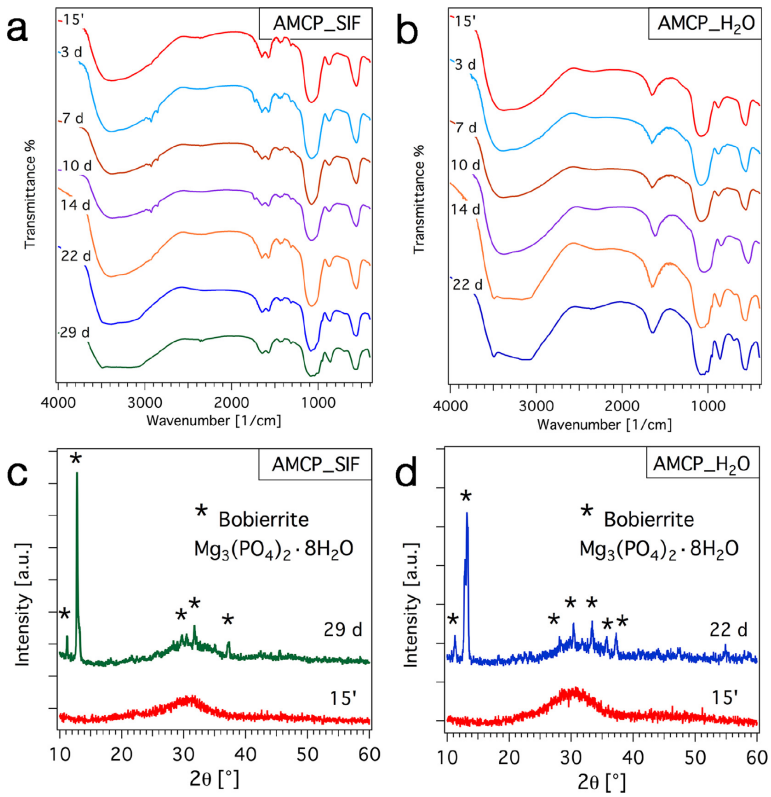

Fig. 1. (a,b) FT-IR spectra of AMCPs synthesized in (a) SIF and (b) water; the spectra are offset for display purposes; c) XRD patterns of AMCPs_SIF collected after 15 min and 29 days of reaction; d) XRD patterns of AMCPs_H_2O collected after 15 min and 22 days of reaction. The diffractograms are offset for display purposes. The PDF of Bobierrite is [33-0878].

radius of 17 nm and high polydispersity (0.28), in good accordance with previously synthesized taurocholate-lecithin colloids [19].

As DLS revealed the presence of nanosized objects in the fluid, the interfacial properties of the medium were examined by means of force tensiometry. We found that the SIF does not show a CMC, as the surface tension does not display a steep decrease at a given concentration value (data not shown). Again, this is in agreement with the literature, as many data suggest that for bile salts the transition from monomeric to micellar solution occurs stepwise over a broad range of concentrations [20,27].

3.2. AMCP stability

We assessed the stability of AMCPs prepared in the SIF and in water, to evaluate the effect of the taurocholate and lecithin on the nano/microparticles crystallization process. Given that amorphous calcium and magnesium phosphates are well-known to spontaneously crystallize in aqueous solution [11,38], the conversion kinetics of amorphous calcium phosphate to crystalline material was monitored through the analysis of the particles by means of FT-IR spectroscopy and XRD, see Fig. 1.

The shape and the position of the IR peaks reveal that, in both SIF and water syntheses, the initially formed precipitate is an amorphous phosphate [11,38–41] (for a more detailed peaks' assignment of AMCP, the reader is referred elsewhere [14]). The kinetic stability of the amorphous phase is different depending on the reaction medium: when AMCPs are prepared in the SIF (Fig. 1a), the ν_3 phosphate stretching peak (~1080 cm^{-1}) appears slightly split after 22 days, while AMCPs synthesized in water turn crystalline after 14 days (see Fig. 1b, [1]orange spectrum). The shape of the O—H stretching band (2700–3700 cm^{-1}) also evolves in time, and a sharp peak at 3488 cm^{-1} appears. The nature of the crystalline phase formed upon conversion of AMCPs was investigated by means of XRD analysis (see Fig. 1c and d). The XRD patterns of the 29-day product in SIF and the 22 day-product in water are displayed in Fig. 1c and d, respectively, as they represent the most aged samples collected during the syntheses. For both synthetic pathways, we can observe that the product collected after 15 min is amorphous (broad hump centered at ~32° [41]) and converts to crystalline bobierrite

[1] For interpretation of color in Fig. 1, the reader is referred to the web version of this article.

($Mg_3(PO_4)_2{\cdot}8H_2O$, PDF 33-0878). The lack of formation of crystalline CaP phases is likely due to the presence of Mg^{2+} in solution, which strongly hinders ACP crystallization [13,14,42]; moreover, the conversion of amorphous phosphates containing Mg to bobierrite was already reported in the literature [10,43]. The FT-IR spectra of the crystalline samples (green curve in Fig. 1a and blue curve in Fig. 1b) are also consistent with the presence of bobierrite [44]. From the difference in the crystallization temporal intervals in the two synthetic media, we can conclude that the lifetime of the amorphous phase of AMCPs is enhanced when they are prepared in the SIF, suggesting a stabilizing action of sodium taurocholate and/or lecithin. This effect is particularly evident when comparing the intensity of the diffraction peaks of the particles after 22 days of reaction (see Fig. S2 in the Supplementary Material), *i.e.* the particles prepared in water are more crystalline than the ones obtained in the SIF. Among the components present in the SIF, the stabilizing action is likely due to taurocholate, which is able to inhibit the precipitation of crystalline CaP [27].

The morphology of the amorphous and crystalline samples was studied with scanning electron microscopy (SEM), and the micrographs are reported in Fig. 2. When comparing AMCPs collected after 15 min prepared in SIF (Fig. 2a) and water (Fig. 2b), it is clear that the presence of the organic molecules in the SIF affects the morphology of the particles: AMCPs synthesized in this medium appear much smaller and interconnected than the ones obtained from the analogous procedure in water. On the other hand, bobierrite crystals formed upon conversion of AMCPs show the same morphology in both syntheses, namely parallelepiped-like objects surrounded by amorphous particles (see Fig. 2c and d).

3.3. Incorporation of organic molecules

A peculiar feature of the endogenous AMCPs is their ability to trap antigens and peptidoglycans in the lumen, acting like a shuttle for delivering the organic cargo to the immune cells in the intestinal wall lining [5,45]. The ability of AMCP-like nanoparticles to trap macromolecules during formation was investigated *in vitro* by Pele et al., who found macromolecule-incorporation properties similar to their *in vivo* counterpart [6]. As we observed that the organic molecules present in the SIF affect the morphology of the synthesized particles, we inspected their incorporation/adsorption on AMCPs as a function of time.

By comparing the series of FT-IR spectra of AMCP_SIF (see Fig. 1a) with that of AMCP_H_2O (see Fig. 1b), we found that AMCP_SIF shows an additional peak at 1576 cm^{-1} and, in samples from 3 to 10 synthesis days, also present absorptions at 1733 cm^{-1}, 2855 cm^{-1} and 2927 cm^{-1}. These signals can be ascribed to the stretching vibrations of C—C and C—H bonds in lecithin and taurocholate (see Fig. S3 in the Supplementary Material), suggesting the incorporation of these organic molecules in AMCPs. The reason for the different number of peaks in the infrared spectrum as a function of time is probably due to a different amount of organic material, which was estimated by means of thermogravimetry, comparing the weight losses % at 1000 °C. The thermograms are given in Fig. S4a (see the Supplementary Material), and the weight losses as a function of time are shown in Fig. 3a. AMCP_SIF samples show a time-dependent weight loss, which is in all cases higher than that of AMCP_H_2O (the weight loss of the particles prepared in water is 19 ± 1% and does not significantly change over time).

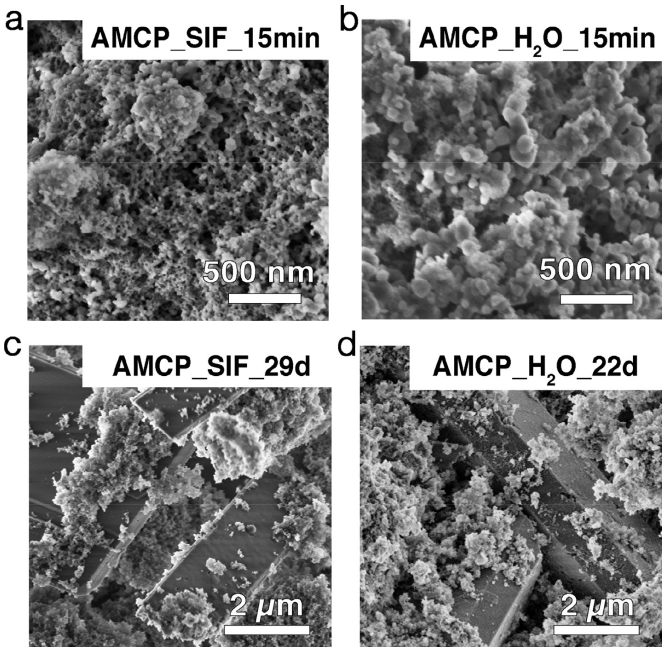

Fig. 2. FE-SEM micrographs of (a) AMCP_SIF_15min; (b) AMCP_H_2O_15min; (c) AMCP_SIF_29d; (d) AMCP_H_2O_22d.

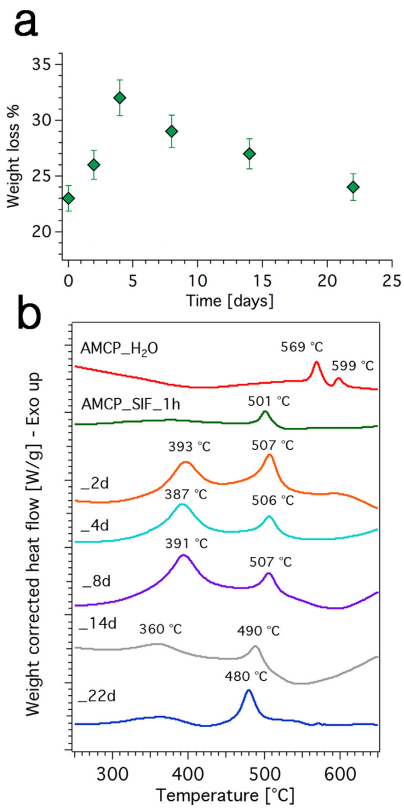

Fig. 3. (a) Weight losses % at 1000 °C of AMCP_SIF as a function of reaction time. The error bars associated to the experimental points, which are the 5% of the value, take into account the discrepancies arising from different measurements on samples obtained from two analogous syntheses. (b) Heat flow profiles of AMCP_SIF, compared with AMCP_H_2O (red curve). The curves are offset for display purposes. The baselines were subtracted using a 3rd order polynomial function. (For interpretation of the references to colour in this figure legend, the reader is referred to the web version of this article.)

The higher weight loss observed for AMCPs prepared in SIF is consistent with the thermal degradation of some organic material incorporated into particles: in fact, the TGA profiles of the analyzed samples differ in the extent of the weight losses in the range 200–450 °C, due to the degradation of organic molecules (see the derivative thermogravimetric curves in Fig. S4b).

The amount of organic material in AMCP_SIF samples increases during the early stages of the synthesis, reaches a maximum after ~4 days and then decreases. The samples showing the highest weight losses are the ones displaying, in the FT-IR spectra, the peaks at 1733 cm^{-1}, 2855 cm^{-1} and 2927 cm^{-1}, confirming that these additional infrared features are due to the higher relative amount of organic material in the samples. Some important information can also be obtained from the heat flow profile acquired simultaneously to the thermogravimetry experiments (see Fig. 3b): while heating, two exothermic events appear in the heat flow profile of AMCP_H_2O_15 min, which correspond to crystallization processes (conversion to a crystalline sodium calcium magnesium phosphate, see [14]). The amorphous particles prepared in SIF also crystallize when heated, but the exothermic peaks are shifted toward lower temperatures, despite converting to the same phase (see Fig. S5 in the Supplementary Material). As exothermic transitions occur from a less ordered to a more ordered state, the shift to lower temperatures of the peaks indicates that less energy is required for the crystallization to occur for AMCP-SIF samples, suggesting that the amorphous phase is even more disordered than when prepared in water, *i.e.* it is easier for the structural units composing AMCP to re-arrange into a crystalline form.

3.4. AMCP nanostructure

The structure at the nanoscale of AMCPs prepared in SIF was compared to their counterpart obtained in water to investigate if lecithin and taurocholate affect the nanostructure of the amorphous particles. As the endogenous self-assembly of AMCPs constantly occurs in mammalian gut, we inspected the structure of AMCPs obtained after few minutes from the beginning of the reaction, as we expect the *in vivo* formation process to be relatively fast.

TEM micrographs of AMCP_SIF_15min and AMCP_H_2O_15min are compared in Fig. 4. The images at lower magnification (Fig. 4a and b) confirm the observations conducted over SEM results, *i.e.* the amorphous particles obtained in SIF (Fig. 4a) are smaller than the ones synthesized in water (Fig. 4b); moreover, in both cases, the nanometric objects are clustered and endowed with nanometric porosities, similarly to the endogenous ones [5]. We verified that particles' agglomeration does not occur on TEM grid as a consequence of sample preparation by analyzing aliquots directly withdrawn from the reacting solution by means of granulometry; the obtained size distributions confirmed that particles' agglomeration occurs in solution (see Fig. S6 in the Supplementary Material).

The high magnification micrographs (Fig. 4c and d) reveal a very peculiar feature of AMCPs prepared in SIF. Together with clustered structures analogous to the ones obtained from the synthesis in water, we can observe isolated core-shell structures (highlighted by the black arrows in Fig. 4 c). These objects have a core diameter of (10 ± 3) nm and a shell thickness of (3 ± 1) nm (see the size distribution in Fig. S7 in the Supplementary Material). As the shell is more electron-dense than the core, we hypothesize that when AMCP self-assemble in the SIF, a portion of the inorganic material forms a shell on the micelles that are present in the fluid (see paragraph 3.1) resulting in core-shell structures. This hypothesis can be supported by the fact that the hydrodynamic diameter obtained by DLS and the core of the objects observed by means of TEM are compatible. In addition, the possibility that the cited objects consist of simple micelles can be excluded, considering that freeze-drying generally leads to the aggregation and/or disruption of self-assembled structures [46,47]; moreover, taurocholate-lecithin micelles are typically observed under cryo-TEM [19,24,48] showing mostly vesicular structures, while here the appearance of the shell suggests the presence of a homogeneous electron-dense material on the outer layer.

Therefore, our findings suggest that at least a part of the organic material, detected by means of FT-IR spectroscopy and TGA, is incorporated in AMCPs thanks to the self-assembled taurocholate/lecithin structures present in solution.

Hollow nanospheres made of calcium phosphate have already been reported in the literature in the presence of several templating agents, such as block copolymers [49,50], lecithin [30], polystyrene [51] and phenol-formaldehyde resin spheres [52], polyelectrolytes [53], amino acids and dipeptides [54], and surfactants [55].

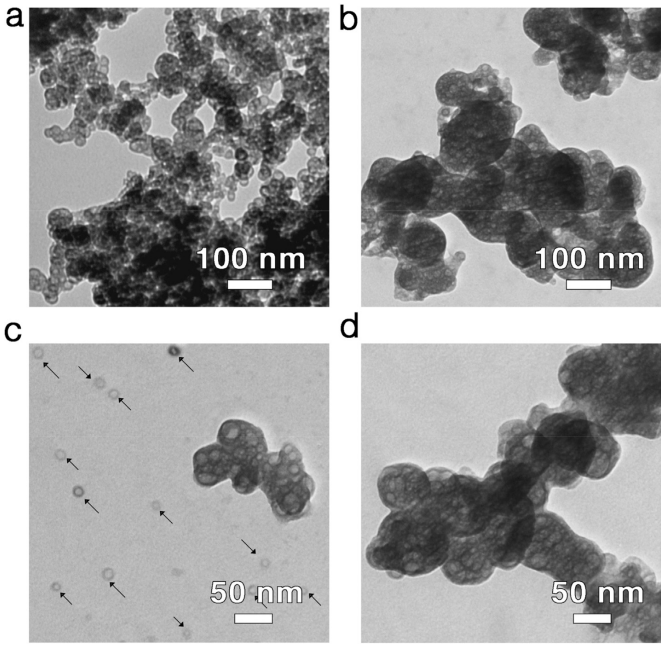

Fig. 4. TEM micrographs of (a + c) AMCP_SIF_15min and (b + d) AMCP_H_2O_15min at low (a + b) and high (c + d) magnification. The black arrows in c highlight the core-shell-like structures.

AMCP structure at the nanoscale was further explored by means of SAXS analysis. The curves of both AMCP_SIF_15min and AMCP_H_2O_15min, reported in Fig. 5, display a very low scattering intensity at high q values ($q > 0.1$ Å^{-1}) followed by an upturn in the mid- and low-q regions due to the presence of AMCP aggregates.

The presence of core-shell particles as revealed by TEM micrographs on AMCP_SIF_15min sample is not found in the SAXS curve, thus suggesting that the overall scattering intensity is mainly dominated by the aggregates. Filtering AMCP_SIF_15min sample with 0.22 μm filters resulted in a clearer solution, however the SAXS intensity was very low (not shown) and, again, a slight upturn was found at low q values. This indicates that the scattering from the single particle is extremely poor, probably due to low contrast between AMCP and the solvent.

Fitting the AMCP_H_2O_15min linear pattern in the $0.01 > q > 0.1$ Å^{-1} range with Eq. (1) (black solid line in Fig. 5) results in $p = 3.37 \pm 0.01$. According to Eq. (2), this corresponds to a surface-fractal dimension $D_s = 2.63$. For AMCP_SIF_15min, a similar pattern is found in the mid-q region with $p = 3.45 \pm 0.01$ and $D_s = 2.55$, which indicates that, in this dimensional range, the surface of AMCP particles in SIF is slightly rougher than that in water. More interestingly, a second power law dominates the scattering in the low-q region with $p = D_m = 2.37 \pm 0.01$ (black dashed line). The cause of this surface (primary domain) to mass (secondary domain) fractal crossover can be found in the micelles present in SIF structuring the AMCP aggregates into less compact domains. This behavior has been previously reported for particles assembling in solutions and gels when the environment surrounding the particles is changed [56–58], which in our case can be referred to the use of water or SIF as the reaction medium.

4. Conclusions

This work deals with the physico-chemical investigation of the formation and stability of amorphous magnesium-calcium phosphates in a simulated intestinal fluid. The relevance of AMCPs has recently emerged because of the discovery of their endogenous formation in human small intestine. This process, which has a role in the immune-surveillance mechanisms of our organism, is far from being completely understood [5]. As the formation of amorphous calcium phosphates in complex media mimicking intestinal fluids has never been investigated so far, in this study we synthesized AMCPs in a commercial SIF, which specifically reproduces the ileum region of the gut and contains sodium taurocholate and lecithin. The effect of the two separate components on the precipitation of CaPs was barely addressed in the literature [27,28,30,31]; here, we focused our attention on a system containing both molecules in biorelevant conditions, as the simultaneous presence of the two components well mimics the *in vivo* conditions of the ileum. By comparing the features of the obtained particles with the ones of AMCPs produced in water with an analogous method, we found out that the presence of lecithin and taurocholate prolongs the lifetime of the amorphous phase, delaying the conversion of AMCP to bobierrite. This stabilizing action is likely due to the effect of taurocholate, which is known to inhibit the precipitation of crystalline calcium phosphates [27]. The morphology of AMCPs

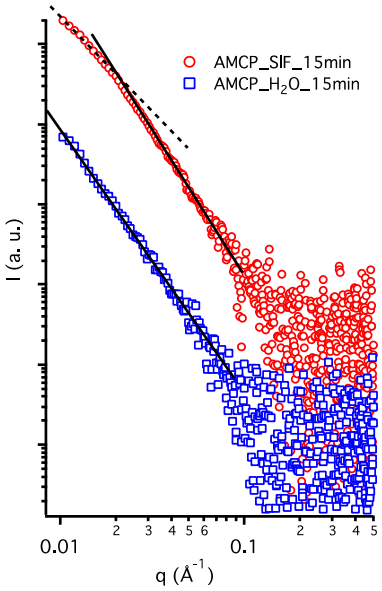

Fig. 5. Log-log representation of SAXS curves of AMCP_SIF_15min (red circles) and AMCP_H_2O_15min (blue squares) samples. Black solid and dashed lines represent curve fittings according to Eq. (1). (For interpretation of the references to colour in this figure legend, the reader is referred to the web version of this article.)

in the two synthetic media is also different, as the particles forming in the SIF are smaller and less aggregated than in water. We also observed that AMCPs are able to incorporate the organic molecules present in the fluid in a time-dependent manner, as shown by means of both FT-IR spectroscopy and thermal analysis. This feature, which is a characteristic of endogenous AMCPs [5], is retained *in vitro* in agreement with previous literature reports [6]. The nanoscale structure of the amorphous particles was further inspected, and TEM analysis revealed a very peculiar structure in AMCPs_SIF: together with clustered particles, it was possible to observe some core-shell structures, with a 10 nm-core and an electron-dense 3 nm-shell. The formation of these objects is likely driven by the presence of self-assembled structures in the SIF with a hydrodynamic radius of 17 nm that we detected by means of DLS. These self-assembled objects possibly are mixed micelles formed by lecithin and sodium taurocholate, which have been described in similar media [19–21,24,25]. Finally, SAXS analysis revealed a different fractal structure for AMCPs synthesized in water or in SIF. In particular, for the latter, a surface-to-mass fractal crossover is found at low scattering vectors, thus revealing distinct aggregation patterns for the two AMCPs in solution. This behavior could influence the crystallization process and consequently provide an explanation to the differences in the temporal stability of the amorphous phases in the two mediums.

As a next step, we aim at addressing the formation of AMCPs in progressively more complex media, exploiting interdisciplinary collaborations with biologists and medics: in fact, a fundamental part of the gut functioning is due to the mutualistic relationship with a huge number of species of microorganisms (both bacteria and fungi). The importance of this flora on the intestinal health is proved and is still an active field of research; the effect of the intestinal microbiota and micobiota on the process of AMCP formation, which is involved in the immunosurveillance mechanisms, is likely to be of great relevance.

Acknowledgements

Fondazione CR Firenze (project 2017.0720) and CSGI consortium are acknowledged for financial support.

Appendix A. Supplementary material

Supplementary data to this article can be found online at https://doi.org/10.1016/j.jcis.2019.03.060.

References

[1] F. Ridi, I. Meazzini, B. Castroflorio, M. Bonini, D. Berti, P. Baglioni, Functional calcium phosphate composites in nanomedicine, Adv. Coll. Interf. Sci. 244 (2017) 281–295, https://doi.org/10.1016/j.cis.2016.03.006.
[2] G. Tomoaia, R.-D. Pasca, On the collagen mineralization, A Rev. Clujul Med. 88 (2015) 15–22, https://doi.org/10.15386/cjmed-359.
[3] P.-A. Fang, J.F. Conway, H.C. Margolis, J.P. Simmer, E. Beniash, Hierarchical self-assembly of amelogenin and the regulation of biomineralization at the nanoscale, Proc. Natl. Acad. Sci. 108 (2011) 14097–14102, https://doi.org/10.1073/pnas.1106228108.
[4] C.N. Rochette, S. Rosenfeldt, A. Heiss, T. Narayanan, M. Ballauff, W. Jahnen-Dechent, A shielding topology stabilizes the early stage protein-mineral complexes of fetuin-a and calcium phosphate: a time-resolved small-angle X-ray study, ChemBioChem. 10 (2009) 735–740, https://doi.org/10.1002/cbic.200800719.
[5] J.J. Powell, E. Thomas-McKay, V. Thoree, J. Robertson, R.E. Hewitt, J.N. Skepper, A. Brown, J.C. Hernandez-Garrido, P.A. Midgley, I. Gomez-Morilla, G.W. Grime, K.J. Kirkby, N.A. Mabbott, D.S. Donaldson, I.R. Williams, D. Rios, S.E. Girardin, C. T. Haas, S.F.A. Bruggraber, J.D. Laman, Y. Tanriver, G. Lombardi, R. Lechler, R.P. H. Thompson, L.C. Pele, An endogenous nanomineral chaperones luminal antigen and peptidoglycan to intestinal immune cells, Nat. Nanotechnol. 10 (2015) 361–369, https://doi.org/10.1038/nnano.2015.19.
[6] L.C. Pele, C.T. Haas, R.E. Hewitt, J. Robertson, J. Skepper, A. Brown, J.C. Hernandez-Garrido, P.A. Midgley, N. Faria, H. Chappell, J.J. Powell, Synthetic mimetics of the endogenous gastrointestinal nanomineral: silent constructs that trap macromolecules for intracellular delivery, Nanomedicine Nanotechnol. Biol. Med. 13 (2017) 619–630, https://doi.org/10.1016/j.nano.2016.07.008.
[7] M. Nabiyouni, T. Brückner, H. Zhou, U. Gbureck, S.B. Bhaduri, Magnesium-based bioceramics in orthopedic applications, Acta Biomater. 66 (2018) 23–43, https://doi.org/10.1016/j.actbio.2017.11.033.
[8] U. Klammert, T. Reuther, M. Blank, I. Reske, J.E. Barralet, L.M. Grover, A.C. Kübler, U. Gbureck, Phase composition, mechanical performance and in vitro biocompatibility of hydraulic setting calcium magnesium phosphate cement, Acta Biomater. 6 (2010) 1529–1535, https://doi.org/10.1016/j.actbio.2009.10.021.
[9] F. Tamimi, D.L. Nihouannen, D.C. Bassett, S. Ibasco, U. Gbureck, J. Knowles, A. Wright, A. Flynn, S.V. Komarova, J.E. Barralet, Biocompatibility of magnesium phosphate minerals and their stability under physiological conditions, Acta Biomater. 7 (2011) 2678–2685, https://doi.org/10.1016/j.actbio.2011.02.007.
[10] E. Babaie, B. Lin, V.K. Goel, S.B. Bhaduri, Evaluation of amorphous magnesium phosphate (AMP) based non-exothermic orthopedic cements, Biomed. Mater. 11 (2016) 055010, https://doi.org/10.1088/1748-6041/11/5/055010.
[11] C. Combes, C. Rey, Amorphous calcium phosphates: synthesis, properties and uses in biomaterials, Acta Biomater. 6 (2010) 3362–3378, https://doi.org/10.1016/j.actbio.2010.02.017.
[12] S.V. Dorozhkin, Amorphous calcium (ortho)phosphates, Acta Biomater. 6 (2010) 4457–4475, https://doi.org/10.1016/j.actbio.2010.06.031.
[13] A.L. Boskey, A.S. Posner, Magnesium stabilization of amorphous calcium phosphate: a kinetic study, Mater. Res. Bull. 9 (1974) 907–916, https://doi.org/10.1016/0025-5408(74)90169-X.
[14] R. Gelli, M. Scudero, L. Gigli, M. Severi, M. Bonini, F. Ridi, P. Baglioni, Effect of pH and Mg^{2+} on amorphous magnesium-calcium phosphate (AMCP) stability, J. Coll. Interf. Sci. 531 (2018) 681–692, https://doi.org/10.1016/j.jcis.2018.07.102.
[15] D. Riethorst, R. Mols, G. Duchateau, J. Tack, J. Brouwers, P. Augustijns, Characterization of human duodenal fluids in fasted and fed state conditions, J. Pharm. Sci. 105 (2016) 673–681, https://doi.org/10.1002/jps.24603.
[16] K. Kleberg, J. Jacobsen, A. Müllertz, Characterising the behaviour of poorly water soluble drugs in the intestine: application of biorelevant media for solubility, dissolution and transport studies, J. Pharm. Pharmacol. 62 (2010) 1656–1668, https://doi.org/10.1111/j.2042-7158.2010.01023.x.
[17] C.A.S. Bergström, R. Holm, S.A. Jørgensen, S.B.E. Andersson, P. Artursson, S. Beato, A. Borde, K. Box, M. Brewster, J. Dressman, K.-I. Feng, G. Halbert, E. Kostewicz, M. McAllister, U. Muenster, J. Thinnes, R. Taylor, A. Mullertz, Early pharmaceutical profiling to predict oral drug absorption: current status and

unmet needs, Eur. J. Pharm. Sci. 57 (2014) 173–199, https://doi.org/10.1016/j.ejps.2013.10.015.
[18] C. Markopoulos, C.J. Andreas, M. Vertzoni, J. Dressman, C. Reppas, In-vitro simulation of luminal conditions for evaluation of performance of oral drug products: choosing the appropriate test media, Eur. J. Pharm. Biopharm. 93 (2015) 173–182, https://doi.org/10.1016/j.ejpb.2015.03.009.
[19] B. Kloefer, P. van Hoogevest, R. Moloney, M. Kuentz, M.L.S. Leigh, J. Dressman, Study of a standardized taurocholate– lecithin powder for preparing the biorelevant media FeSSIF and FaSSIF, Dissolution Technol. 17 (2010) 6–13, https://doi.org/10.14227/DT170310P6.
[20] M.C. di Gregorio, L. Travaglini, A. Del Giudice, J. Cautela, N.V. Pavel, L. Galantini, Bile salts: natural surfactants and precursors of a broad family of complex amphiphiles, Langmuir (2018), https://doi.org/10.1021/acs.langmuir.8b02657.
[21] R. Holm, A. Müllertz, H. Mu, Bile salts and their importance for drug absorption, Int. J. Pharm. 453 (2013) 44–55, https://doi.org/10.1016/j.ijpharm.2013.04.003.
[22] C.-Y. Cheng, H. Oh, T.-Y. Wang, S.R. Raghavan, S.-H. Tung, Mixtures of lecithin and bile salt can form highly viscous wormlike micellar solutions in water, Langmuir 30 (2014) 10221–10230, https://doi.org/10.1021/la502380q.
[23] J. Cautela, M. Giustini, N.V. Pavel, G. Palazzo, L. Galantini, Wormlike reverse micelles in lecithin/bile salt/water mixtures in oil, Coll. Surf. Physicochem. Eng. Asp. 532 (2017) 411–419, https://doi.org/10.1016/j.colsurfa.2017.04.052.
[24] K. Kleberg, F. Jacobsen, D.G. Fatouros, A. Müllertz, Biorelevant media simulating fed state intestinal fluids: colloid phase characterization and impact on solubilization capacity, J. Pharm. Sci. 99 (2010) 3522–3532, https://doi.org/10.1002/jps.22122.
[25] G.A. Kossena, B.J. Boyd, C.J.H. Porter, W.N. Charman, Separation and characterization of the colloidal phases produced on digestion of common formulation lipids and assessment of their impact on the apparent solubility of selected poorly water-soluble drugs, J. Pharm. Sci. 92 (2003) 634–648, https://doi.org/10.1002/jps.10329.
[26] D.J. Sutor, J.M. Percival, Presence or absence of inhibitors of crystal growth in bile. 1. effect of bile on the formation of calcium phosphate, a constituent of gallstones, Gut. 17 (1976) 506–510, https://doi.org/10.1136/gut.17.7.506.
[27] E.W. Moore, L. Celic, J.D. Ostrow, Interactions between ionized calcium and sodium taurocholate: bile salts are important buffers for prevention of calcium-containing gallstones, Gastroenterology 83 (1982) 1079–1089, https://doi.org/10.1016/S0016-5085(82)80077-2.
[28] R.S. Crowther, M. Okido, Inhibition of calcium phosphate precipitation by bile salts: a test of the Ca(2+)-buffering hypothesis, J. Lipid Res. 35 (1994) 279–290.
[29] M. Okido, R.D. Soloway, R.S. Crowther, Influence of phospholipid on bile salt binding to calcium hydroxyapatite and on the poisoning of nascent hydroxyapatite crystals, Liver 16 (1996) 321–325, https://doi.org/10.1111/j.1600-0676.1996.tb00753.x.
[30] G.-J. Ding, Y.-J. Zhu, C. Qi, B.-Q. Lu, F. Chen, J. Wu, Porous hollow microspheres of amorphous calcium phosphate: soybean lecithin templated microwave-assisted hydrothermal synthesis and application in drug delivery, J. Mater. Chem. B. 3 (2015) 1823–1830, https://doi.org/10.1039/C4TB01862A.
[31] W. Michał, D. Ewa, C. Tomasz, Lecithin-based wet chemical precipitation of hydroxyapatite nanoparticles, Colloid Polym. Sci. 293 (2015) 1561–1568, https://doi.org/10.1007/s00396-015-3557-0.
[32] C. Holt, M. Van Kemenade, J.E. Harries, L.S. Nelson, R.T. Bailey, D.W.L. Hukins, S. S. Hasnain, P.L. De Bruyn, Preparation of amorphous calcium-magnesium phosphates at pH 7 and characterization by x-ray absorption and fourier transform infrared spectroscopy, J. Cryst. Growth. 92 (1988) 239–252, https://doi.org/10.1016/0022-0248(88)90455-1.
[33] H.M. Fadda, A.W. Basit, Dissolution of pH responsive formulations in media resembling intestinal fluids: bicarbonate versus phosphate buffers, J. Drug Deliv. Sci. Technol. 15 (2005) 273–279, https://doi.org/10.1016/S1773-2247(05)50049-2.
[34] J. Aron-Wisnewsky, J. Doré, K. Clement, The importance of the gut microbiota after bariatric surgery, Nat. Rev. Gastroenterol. Hepatol. 9 (2012) 590, https://doi.org/10.1038/nrgastro.2012.161.
[35] J.A. Lake, An iterative method of slit-correcting small angle X-ray data, Acta Crystallogr. 23 (1967) 191–194, https://doi.org/10.1107/S0365110X67002440.
[36] B. Hammouda, Probing Nanoscale Structures - The SANS Toolbox, (2012) <https://Www.Ncnr.Nist.Gov/Staff/Hammouda/The_SANS_toolbox.Pdf>.
[37] D.W. Schaefer, Fractal models and the structure of materials, MRS Bull. 13 (1988) 22–27, https://doi.org/10.1557/S088376940006632X.
[38] S.V. Dorozhkin, Amorphous calcium orthophosphates: nature, chemistry and biomedical applications, Int. J. Mater. Chem. 2 (2012) 19–46, https://doi.org/10.5923/j.ijmc.20120201.04.
[39] C. Drouet, Apatite formation: why it may not work as planned, and how to conclusively identify apatite compounds, BioMed Res. Int. 2013 (2013) 490946, https://doi.org/10.1155/2013/490946.
[40] C. Holt, M.J.J.M. Van Kemenade, L.S. Nelson, D.W.L. Hukins, R.T. Bailey, J.E. Harries, S.S. Hasnain, P.L. De Bruyn, Amorphous calcium phosphates prepared at pH 6.5 and 6.0, Mater. Res. Bull. 24 (1989) 55–62, https://doi.org/10.1016/0025-5408(89)90008-1.
[41] A.C. Tas, X-ray-amorphous calcium phosphate (ACP) synthesis in a simple biomineralization medium, J. Mater. Chem. B. 1 (2013) 4511, https://doi.org/10.1039/c3tb20854k.
[42] M.H. Salimi, J.C. Heughebaert, G.H. Nancollas, Crystal growth of calcium phosphates in the presence of magnesium ions, Langmuir 1 (1985) 119–122, https://doi.org/10.1021/la00061a019.
[43] E. Babaie, B. Lin, S.B. Bhaduri, A new method to produce macroporous Mg-phosphate bone growth substitutes, Mater. Sci. Eng. C. 75 (2017) 602–609, https://doi.org/10.1016/j.msec.2017.02.111.
[44] M.A. Rivadeneyra, A. Ramos-Cormenzana, A. Garcia-Cervigon, Formation of bobierrite (magnesium phosphate) crystal aggregates by Acinetobacter sp, Mineral. J. 13 (1987) 443–447, https://doi.org/10.2465/minerj.13.443.
[45] J.D. Söderholm, Gut immunology: nanoparticles ferry gut antigens, Nat. Nanotechnol. 10 (2015) 298–299, https://doi.org/10.1038/nnano.2015.58.
[46] J. Logie, S.C. Owen, C.K. McLaughlin, M.S. Shoichet, PEG-graft density controls polymeric nanoparticle micelle stability, Chem. Mater. 26 (2014) 2847–2855, https://doi.org/10.1021/cm500448x.
[47] C. Di Tommaso, C. Como, R. Gurny, M. Möller, Investigations on the lyophilisation of MPEG–hexPLA micelle based pharmaceutical formulations, Eur. J. Pharm. Sci. 40 (2010) 38–47, https://doi.org/10.1016/j.ejps.2010.02.006.
[48] D.G. Fatouros, I. Walrand, B. Bergenstahl, A. Müllertz, Colloidal structures in media simulating intestinal fed state conditions with and without lipolysis products, Pharm. Res. 26 (2009) 361–374, https://doi.org/10.1007/s11095-008-9750-9.
[49] B.P. Bastakoti, M. Inuoe, S. Yusa, S.-H. Liao, K.C.-W. Wu, K. Nakashima, Y. Yamauchi, A block copolymer micelle template for synthesis of hollow calcium phosphate nanospheres with excellent biocompatibility, Chem. Commun. 48 (2012) 6532–6534, https://doi.org/10.1039/C2CC32279J.
[50] W. Tjandra, P. Ravi, J. Yao, K.C. Tam, Synthesis of hollow spherical calcium phosphate nanoparticles using polymeric nanotemplates, Nanotechnol. Print. 17 (2006) 5988–5994, https://doi.org/10.1088/0957-4484/17/24/014.
[51] C. Wu, J. Xu, Y. Hao, Y. Zhao, Y. Qiu, J. Jiang, T. Yu, P. Ji, Y. Liu, Application of a lipid-coated hollow calcium phosphate nanoparticle in synergistic co-delivery of doxorubicin and paclitaxel for the treatment of human lung cancer A549 cells, Int. J. Nanomedicine. 12 (2017) 7979–7992, https://doi.org/10.2147/IJN.S140957.
[52] S. Huang, C. Li, Q. Xiao, Tunable pore sizes of monodispersed amorphous calcium phosphate hollow nanospheres, Mater. Lett. 197 (2017) 1–4, https://doi.org/10.1016/j.matlet.2017.03.069.
[53] A. Bigi, E. Boanini, D. Walsh, S. Mann, Morphosynthesis of octacalcium phosphate hollow microspheres by polyelectrolyte-mediated crystallization, Angew. Chem. 114 (2002) 2267–2270, https://doi.org/10.1002/1521-3757(20020617)114:12<2267::AID-ANGE2267>3.0.CO;2-N.
[54] D. Hagmeyer, K. Ganesan, J. Ruesing, D. Schunk, C. Mayer, A. Dey, N.A.J.M. Sommerdijk, M. Epple, Self-assembly of calcium phosphate nanoparticles into hollow spheres induced by dissolved amino acids, J. Mater. Chem. 21 (2011) 9219–9223, https://doi.org/10.1039/C1JM11316J.
[55] Y. Cai, H. Pan, X. Xu, Q. Hu, L. Li, R. Tang, Ultrasonic controlled morphology transformation of hollow calcium phosphate nanospheres: a smart and biocompatible drug release system, Chem. Mater. 19 (2007) 3081–3083, https://doi.org/10.1021/cm070298t.
[56] A.P. Perissinotto, C.M. Awano, D.A. Donatti, F.S. de Vicente, D.R. Vollet, Mass and surface fractal in supercritical dried silica aerogels prepared with additions of sodium dodecyl sulfate, Langmuir 31 (2015) 562–568, https://doi.org/10.1021/la504272g.
[57] P. Wong, Q. Cao, Correlation function and structure factor for a mass fractal bounded by a surface fractal, Phys. Rev. B. 45 (1992) 7627–7632, https://doi.org/10.1103/PhysRevB.45.7627.
[58] P. Tempesti, G.S. Nicotera, M. Bonini, E. Fratini, P. Baglioni, Poly(N-isopropylacrylamide)-hydroxyapatite nanocomposites as thermoresponsive filling materials on dentinal surface and tubules, J. Coll. Interf. Sci. 509 (2018) 123–131, https://doi.org/10.1016/j.jcis.2017.09.001.

Supplementary Material

Formation and properties of amorphous magnesium-calcium phosphate particles in a simulated intestinal fluid

Rita Gelli, Paolo Tempesti, Francesca Ridi*, Piero Baglioni

Department of Chemistry "Ugo Schiff" and CSGI, University of Florence, via della Lastruccia 3, 50019 Sesto Fiorentino, Florence, Italy

Table of content

Fig. S7: Size distribution estimated from TEM images using the software Fiji of (a) core diameter and (b) shell thickness of the sample AMCP_SIF_15min.

Paragraph S1: DLS theory

Paragraph S2: Cumulant analysis

Table S1: Reactants used for the synthesis of AMCPs in water and SIF.

Solution	Salt	Amount [g]	Concentration [mM]
A	NaCl	1.578	135
	$CaCl_2$	0.089	4
	$MgCl_2 \cdot 6H_2O$	0.407	10
B	$NaH_2PO_4 \cdot H_2O$	1.380	50
	$Na_2HPO_4 \cdot 12H_2O$	10.744	150

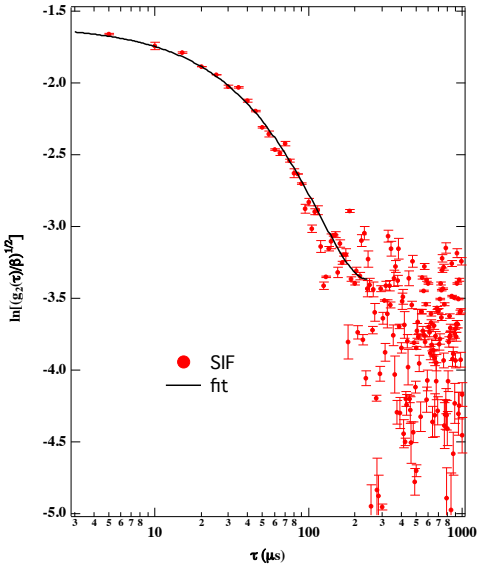

Fig. S1: DLS autocorrelation function of SIF (red full circles) together with cumulant analysis fit (black solid line).

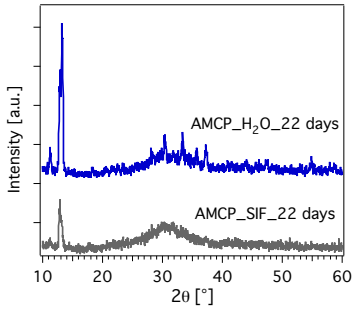

Fig. S2: Comparison of the XRD pattern of AMCPs after 22 days of reaction in SIF (blue curve) and in water (grey curve). The diffractograms are offset for display purposes.

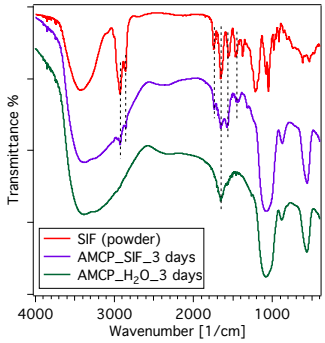

Fig. S3: Comparison of the FT-IR spectra of AMCPs after 3 synthesis days (purple curve in SIF, green curve in water) with the powder used to prepare the SIF, which contains sodium taurocholate, lecithin and maleic acid. The spectra are offset for display purposes.

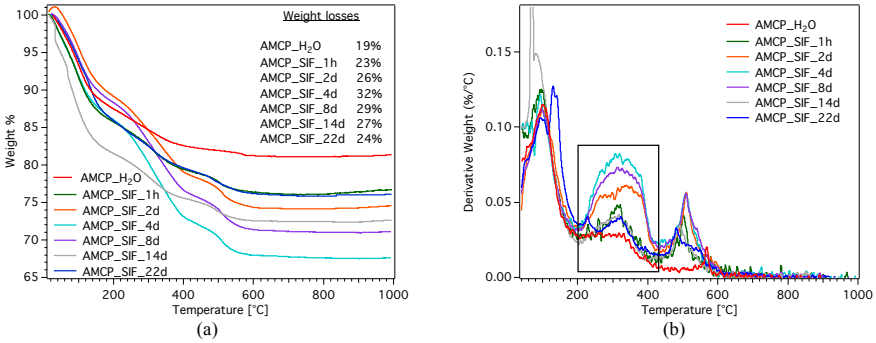

(a) (b)

Fig. S4: Thermogravimetric data of AMCP_SIF: (a) weight % as a function of T and (b) derivative weight % as a function of T.

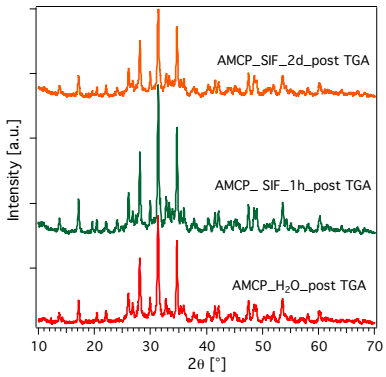

Fig. S5: XRD patterns of AMCP_H2O_15min (red curve), AMCP_SIF_1h (blue curve) and AMCP_SIF_2d (green curve) after the TGA experiments. The diffractograms are offset for display purposes.

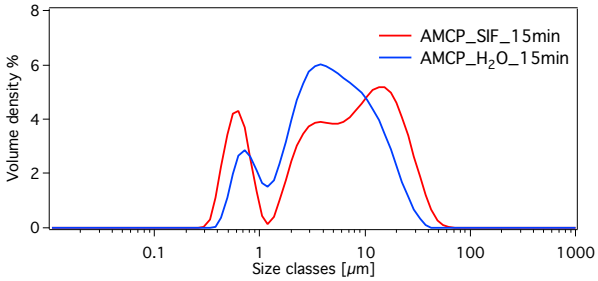

Fig. S6: Size distribution curves of AMCP in SIF (red curve) and water (blue curve) obtained by means of laser granulometry. Aliquots were withdrawn from the reaction medium after 15 min of aging. The measurements were performed by means of a Mastersizer 3000 laser diffraction particle size analyser, equipped with HYDRO SM wet dispersion unit. Absolute ethanol was used as a dispersant to prevent particles crystallization. Each curve is the average of 20 measurements of 5 s each.

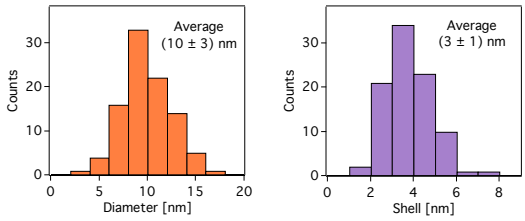

(a) (b)

Fig. S7: Size distribution estimated from TEM images using the software Fiji of (a) core diameter and (b) shell thickness of the sample AMCP_SIF_15min.

Paragraph S1: DLS theory

In DLS experiments at a fixed angle, the time correlation functions $G_2(\tau)$ of the scattered light were measured at different angles and the normalized intensity autocorrelation function ($g_2(,\tau)$) are obtained directly from the software during the measurement. $g_2(,\tau)$ is connected to the normalized electric field autocorrelation function $g_1(,\tau)$, by the Siegert relation (Eq. S1)

$$g_2(\tau) = 1 + \beta^2|g_1(\tau)|^2 \tag{S1}$$

with $\beta^2 \leq 1$ a coherence factor that depends on the experimental conditions.

For a suspension of polydisperse Brownian spheres, $g_1(\tau)$ decays exponentially

$$g_1(\tau) = \int_0^\infty P(D)\exp(-q^2 D\tau)\, dD \tag{S2}$$

where D is the diffusion coefficient and $P(D)$ is the intensity-weighted probability distribution function of the diffusion coefficient.

Particle sizing is performed by extracting D from $g_2(\tau)$ fitting and applying the Stokes-Einstein equation

$$D = \frac{k_B T}{6\pi\eta R_h} \tag{S3}$$

where k_B is the Boltzmann constant, T is the absolute temperature, η is the viscosity of the solvent, and R_h is the hydrodynamic radius of the spheres.

Paragraph S2: Cumulant analysis

In the classic cumulant method analysis, we have that ln[g1(q,τ)] is written as a Taylor series in the correlation time

$$\ln[(g_1(q,\tau)] = ln\beta^2 + 2[-\Gamma_1\tau + \frac{\Gamma_2\tau^2}{2!} + \cdots + \frac{(-1)\Gamma_n\tau^n}{n!}] \tag{S4}$$

and by stopping to the second order we have

$$\Gamma_1 = \bar{D}q^2 \tag{S5}$$

and

$$\Gamma_2 = \frac{\overline{D^2} - \bar{D}^2}{\bar{D}^2}\Gamma_1^2 \tag{S6}$$

where

$$\overline{D^n} = \int_0^\infty D^n P(D) dD \tag{S7}$$

is the *n*th order of the intensity-weighted probability distribution function of *D* (*P(D)*).

The polydispersity index (PDI) is defined as

$$\sigma^2 = \frac{\Gamma_2}{\Gamma_1^2} \tag{S8}$$

Paper IV

Advances in Colloid and Interface Science 269 (2019) 219–235

Contents lists available at ScienceDirect

Advances in Colloid and Interface Science

journal homepage: www.elsevier.com/locate/cis

Historical Perspective

The importance of being amorphous: calcium and magnesium phosphates in the human body

Rita Gelli [a,b], Francesca Ridi [a,*], Piero Baglioni [a,b,*]

[a] Department of Chemistry "Ugo Schiff", University of Florence, via della Lastruccia 3, 50019, Sesto Fiorentino, Florence, Italy
[b] CSGI, Center for Colloid and Surface Science, via della Lastruccia 3, 50019, Sesto Fiorentino, Florence, Italy

ARTICLE INFO

Article history:
24 April 2019
Available online 27 April 2019

Keywords:
Amorphous calcium phosphate
Stabilization
Human body
Nanostructure
Biomaterials

ABSTRACT

This article focuses on the relevance of amorphous calcium (and magnesium) phosphates in living organisms. Although crystalline calcium phosphate (CaP)-based materials are known to constitute the major inorganic constituents of human hard tissues, amorphous CaP-based structures, often in combination with magnesium, are frequently employed by Nature to build up components of our body and guarantee their proper functioning. After a brief description of amorphous calcium phosphate (ACP) formation mechanism and structure, this paper is focused on the stabilization strategies that can be used to enhance the lifetime of the poorly stable amorphous phase. The various locations of our body in which ACP (pure or in combination with Mg^{2+}) can be found (*i.e.* bone, enamel, small intestine, calciprotein particles and casein micelles) are highlighted, showing how the amorphous nature of ACP is often of paramount importance for the achievement of a specific physiological function. The last section is devoted to ACP-based biomaterials, focusing on how these materials differ from their crystalline counterparts in terms of biological response.

Contents

Abbreviations: CaP, Calcium phosphates; HA, Hydroxyapatite; ACP, Amorphous calcium phosphate; AMCP, Amorphous magnesium calcium phosphate; TEM, Transmission electron microscopy; OCP, Octacalcium phosphate; ATP, Adenosine triphosphate; DCPD, Dicalcium phosphate dihydrate; ADP, Adenosine diphosphate; AMP, Adenosine monophosphate; PS, Phosphatidylserine; PEG, Poly(ethylene glycol); TCP, Tri-calcium phosphate; PVA, Poly(vinyl alcohol); PVP, Polyvinylpyrrolidone; PEI, Polyethyleneimine; PEO, Polyethylene oxide; PAA, Poly(acrylic acid); PSS, Polystyrene sulfonate; PGA, Poly-L-glutamic acid; PLL, Poly-L-lysine; Mw, Molecular weight; XANES, X-ray absorption near-edge structure; EXAFS, Extended X-ray absorption fine structure; AMCP, Amorphous magnesium-calcium phosphate; APCs, Antigen presenting cells; Fet-A, Fetuin-A; CPPs, Calciprotein particles; DLS, Dynamic light scattering; SANS, Small angle neutron scattering; SAXS, Small Angle X-rays scattering; CKD, Chronic kidney disease; CasPP-ACP, Casein phosphopeptide-amorphous calcium phosphate; PCCP, Partially crystallized calcium phosphate; DCPA, Dicalcium phosphate anhydrous.

* Corresponding authors at: Department of Chemistry "Ugo Schiff", University of Florence, via della Lastruccia 3, Sesto Fiorentino, 50019, Florence, Italy.
E-mail addresses: francesca.ridi@unifi.it (F. Ridi), piero.baglioni@unifi.it (P. Baglioni).

https://doi.org/10.1016/j.cis.2019.04.011
0001-8686/

1. Introduction

Calcium phosphates (CaP) represent the main inorganic component present in human organisms, as they constitute the majority of the inorganic matrix of bones (~65% with respect to total bone weight) and teeth (~97% wt enamel, ~70% wt dentine) [1]. In bone, CaP is found as poorly crystalline, nano-sized platelets of non-stoichiometric, calcium-deficient and carbonate-rich hydroxyapatite, whose growth is templated by a soft matrix consisting of type I collagen fibrils [2]. Teeth composition is similar to that of bone, except for the outer surface (enamel), which has a higher inorganic content and is formed by strongly oriented prismatic crystals of larger dimensions. In addition to bone and teeth, which are the most notable sites of calcium phosphate in the body, this mineral can be found in crystalline forms in many other locations, such as pathologic calcifications (dental calculi, urinary and salivary stones, deposits in synovial fluids and heart calcifications) [3]. However, beside crystalline deposits, amorphous calcium phosphates (ACP) and amorphous magnesium calcium phosphates (AMCP) are very frequent forms of CaP in biological organisms [4,5] and play a fundamental role in their structure and functioning. Amorphous structures are significant to various aspects of evolution and life of biological organisms, as they represent ~ 20% of approximately 60 different inorganic compounds and minerals formed by living organisms [6]. Calcium phosphate is not the only mineral which has some relevance in the amorphous state. It is reported that, in many biomineralization processes, the amorphous material is often the precursor to the formation of the crystalline material [7]. The most notable example is calcium carbonate, which is produced in amorphous form by organisms such as crustaceans, sea urchins and certain mollusks [8–10]. Interestingly, some specific structures in our body are made of calcium phosphate in its amorphous state. The fact that such a thermodynamically unstable phase [11] is preserved in its state in different sites in our body is intriguing, suggesting that the amorphous nature is crucial for the material to perform some specific biological functions.

The purpose of this paper is to shed light on the relevance of amorphous calcium and magnesium phosphates to living organisms: we focus our attention on both naturally-occurring amorphous-based structures and amorphous-based biomaterials, in the attempt to unravel the importance of these fascinating structures to organisms' functioning. First, we will briefly present the main features of ACP from a chemical and structural perspective (section 2). In section 3, the stability of ACP and the stabilization strategies that preserve the amorphous state are illustrated, while section 4 explores the different locations where the amorphous material can be found in the human body. Finally, in section 5, the importance of ACP-based biomaterials (compared to their crystalline counterpart) is reviewed.

2. ACP first detection, formation and structure

The definition of "amorphous" refers to materials that are highly disordered and lack in the long-range order characteristic of crystals, which instead present three-dimensional order on the level of atomic dimensions [12]. As it is reported by Eanes [13], the first observation of amorphous calcium phosphate dates back to 1953, when Watson and Robinson described the formation of a "finely granular" precipitate resulting from the mixing of concentrated solutions of $CaCl_2$ and Na_2HPO_4, which displayed no electron diffraction pattern [14].

It is nowadays agreed that when mixing two solutions containing calcium and phosphate ions at sufficiently high supersaturation and pH, amorphous calcium phosphate with a molar Ca/P ratio between 1.18 and 2.50 is formed [15]. One of the first reports about ACP states that "the formation of non-crystalline calcium phosphate is a kinetic phenomenon" [16]: the mixing of highly concentrated solutions creates sufficiently strong stochastic interactions among calcium and phosphate ions so that they can form highly hydrated clusters that separate from the solution in a gel-like state [11]. The formed ACP is very unstable; therefore, being its precipitation a kinetically-driven process, ACP hydrolysis and crystallization proceed by a sequential process which involves structural and compositional modifications of the amorphous precursors and crystalline intermediates (such as OCP, octacalcium phosphate), rather than a single-step pathway (see Fig. 1A) [11,17]. This precipitation mechanism is known as "Ostwald-Lussac Law of Stages": a disordered and highly soluble phase first forms and, through a series of phase transformations, eventually converts into a poorly soluble and more ordered crystalline phase [18,19]. For ACP, the final step of the crystallization process is hydroxyapatite (HA, $Ca_{10}(PO_4)_6(OH)_2$) at neutral and alkaline pH or brushite ($CaHPO_4 \cdot 2H_2O$) at acidic pH [20]. It is important to note that ACP is not a mandatory precursor to crystalline CaP, as when sufficiently diluted solutions are used, apatite formation can occur without the detection of an amorphous precursor (A pathway in Fig. 1A) [21,22]. The stability of the amorphous phase is dramatically dependent on several factors, which will be discussed in detail in section 3.

Although ACP is an amorphous material, a short range order corresponding to $Ca_9(PO_4)_6$ units ("Posner's clusters") was proposed by Posner and Betts in 1974, on the basis of X-rays radial distribution function studies [23]. The validity of their model has been assessed in the following years, and it was found that also *ab initio* calculations support Posner's model [24]. These structural units, whose size is about 9.5 Å, are depicted in Fig. 1B. According to the Posner's model, the clusters randomly aggregate into spherical objects with a diameter of 30–100 nm, generating the typical morphology of ACP [25]. The hypothesis of cluster aggregation is supported by calculations, which show that the random packing of the clusters corresponds to a large stabilization energy [24]. It is important to specify that the curvilinear shape of ACP particles is referred to the dried sample, and that the solution pH, the reactants' concentration and the temperature affect the final size of the formed spherical particles (for instance, smaller particles are obtained using high supersaturations) [11].

While the validity of Posner's model has been corroborated by recent studies [26], much effort has been pursued in the last decade in the attempt of unravelling the first stages involved in ACP formation. In 2010, Dey et al. showed that, for calcium phosphates, surface-induced crystal nucleation is initiated by the generation of pre-nucleation clusters that densify at a templating surface, leading to the formation of an amorphous precursor phase which eventually transforms into crystalline apatite. Later, a work from Habraken et al. unveiled the chemical nature of the pre-nucleation clusters [27]: by combining cryo-TEM with *in situ* analysis techniques and ab initio calculations, it was reported that pre-nucleation clusters preceding ACP formation consist of soluble ion-association complexes $[Ca(HPO_4)_3]^{4-}$ that form 3D polymeric networks in solution. Above the solubility limit of ACP, these aggregated pre-nucleation complexes collect Ca^{2+} from the solution and form insoluble post-nucleation clusters of [Ca_2

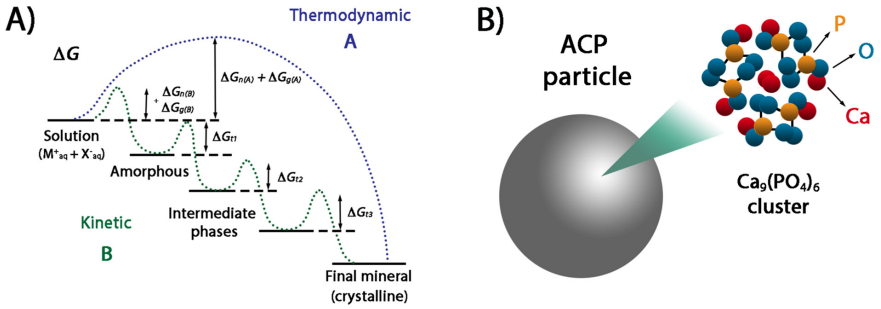

Fig. 1. (A) Crystallization pathways under thermodynamic (A) and kinetic (B) control. A system follows a one-step route to the final mineral phase (pathway A) or proceeds by sequential precipitation (pathway B), depending on the free energy of activation (ΔG) associated with nucleation (n), growth (g), and phase transformation (t) (readapted with permission from [17]). (B) Model of ACP structure (Posner's cluster), readapted with permission from [1] (license at: http://creativecommons.org/licenses/by/4.0/).

$(HPO_4)_3]^{2-}$, which then precipitate as ACP; the continuous Ca^{2+} uptake converts ACP into OCP and subsequently into apatite. For further details about the pre-nucleation clusters theory and crystallization, the reader is referred elsewhere [28].

In the structure of ACP, water plays a role, too: the freeze-dried material contains a relevant amount (15–20%) of bound water, which is located in the interstices between the $Ca_9(PO_4)_6$ clusters [29]. When heating ACP, water is removed from the cluster according to two different mechanisms depending on the interaction of water molecules within the cluster: loosely bound water molecules adsorbed on ACP surface and more strongly bound inter-cluster water molecules. The first step is reversible, while the second is not [4].

3. Stability of ACP and stabilization strategies

Unless stabilizing agents are present in solution, when ACP forms or when it is dispersed in an aqueous medium, it rapidly hydrolyses and subsequently converts into more stable crystalline forms of CaP. The highly instable nature of ACP was evident since its discovery, as Watson and Robinson detected the conversion of ACP to hydroxyapatite when in contact with the synthetic medium [14]. Since then, several works have addressed the effect of factors such as temperature, pH or presence of ions/molecules in solution on the crystallization kinetic of ACP. The conversion of ACP to HA was studied at pH 7.4 as a function of temperature (20 °C and 37 °C), finding that the ACP conversion to HA gets slower as the temperature decreases [30]. The same observation was reported by Boskey and Posner, who studied the conversion at pH 8 at 48 °C, 37 °C, 26 °C and 10 °C: the authors demonstrate that an increase in temperature results in both a shortening of the induction period and an increase in the rate of crystal proliferation [31]. The induction period is an important parameter related to ACP stability, and it is defined as the time after which the first crystalline material forms. It is typically evaluated from the analysis of the plot of ACP to HA conversion vs reaction time. The obtained sigmoidal curves can be divided into three regions: the "induction period" in which no change in the extent of reaction is observed, a "proliferation period," where the extent of reaction rapidly increases, and a "tapering off" period, when the rate of the transformation slows down.

In addition to the temperature effect, the influence of pH at a given temperature was also investigated with the same method, showing that the length of the induction period increases from pH 6.8 to 10 [31]. A successive investigation at higher pH (9.25–12.80) showed that the maximum stability of the amorphous phase is reached at pH 10.25, with a subsequent decrease in the lifetime of the amorphous phase, suggesting a different crystallization mechanism in highly alkaline media [32]. In addition to temperature and pH, it was recently reported that the formation of CaP in confined environments can lead to the stabilization of the amorphous precursor [33,34]. Besides the effect of the cited factors, the presence of ions, molecules and macromolecules in solution has a dramatic impact on the lifetime of ACP. In the following sub-sections, the three categories will be separately reviewed.

3.1. Ions

The interaction of calcium and phosphate ions leads to the formation of ACP, which quickly coalesces into clusters large enough to separate from the solution before having the possibility to rearrange into ordered nuclei [35]. It is not surprising that foreign ions in solution affect the formation and the subsequent crystallization of this mineral; for instance, the stabilizing role of magnesium is of paramount importance and has been explored since ACP discovery [36–50]. In the human body, magnesium is mainly located in the bone, muscles and non-muscular soft tissue (~24 g of magnesium in an average 70 kg adult, 42 times less abundant than calcium) [51]. Despite the low content in hard tissues (0.44% wt in enamel, 1.23% wt in dentine, 0.5–0.9% wt in cementum and 0.72% wt in bone [1]), Mg^{2+} plays an important role in the formation of hydroxyapatite and in the mineralization of hard tissues [52]. A seminal work on this topic is the kinetic study by Boskey and Posner, who investigated the conversion of ACP to HA at different Mg^{2+} concentrations [37]. The authors report that an increase in Mg/Ca ratio from 0 to 0.04 results in a ~9 times increase in the induction period at 26 °C, ~4 times at 37.5 °C and ~ 7 at 48 °C (experiments conducted at pH=8). They concluded that the presence of Mg^{2+} decreased the solubility of ACP, while Bachra et al. attributed the stabilization effect to Mg^{2+} ability to form stronger complex than Ca^{2+} with phosphate [36]. The group of Christoffersen et al. suggested that Mg^{2+} slows the transformation of ACP1 to ACP2, being ACP1 the initial fast-precipitating spherular amorphous form of CaP, which converts into a floccular form called ACP2 [42,46]. Abbona and Baronnet [45] reported that magnesium does not affect the formation of ACP1, but prolongs by at least four times the induction period of HA; moreover, it exerts strong effects on morphology, crystal perfection, nucleation and growth kinetics. According to the authors, the stabilizing action is ascribed to the initial Mg^{2+} substitution for Ca^{2+} in Posner's clusters, which induces mechanical strains and hinders HA nucleation; Mg^{2+} adsorption onto the surfaces of ACP and of HA crystallites has an effect, too. In some conditions, ACP prepared in the presence of magnesium can reach impressive stabilities: for instance, the amorphous phase can last up to 145 days when ACP is prepared at pH 10, 32.5 °C and with Mg/Ca ratio 0.25 [41]. Despite the large number of investigations conducted from the sixties, the precise role of Mg^{2+} on HA formation is still considerably debated, as shown by the several papers published on this topic in the last decade [52–56].

According to Yang et al., the formation of magnesium- phosphate ion pairs may reduce the thermodynamic driving force for ACP nucleation and phase transformation to HA [53], while the role of Mg^{2+} ions at the surface was elucidated by Ding et al. [54]. From the literature data reported so far, it is clear that the precise pathway through which Mg^{2+} stabilizes the amorphous phase, which possibly results from the combination of multiple mechanisms, is only partly established, and requires further investigations. The fact that magnesium is so effective in stabilizing the structure of ACP play an important role in preserving it *in vivo* [35], as it will be discussed in section 4.

In addition to Mg^{2+}, the effect of several other cations on ACP stability/HA formation has been examined in the past. For instance, Ga^{3+} is reported to slow down HA nucleation and/or growth kinetics [57]; similarly, Cd^{2+} has an inhibitory effect on HA nucleation and growth [58]. Sr^{2+} [36,59] and Zn^{2+} [60] have also shown to delay calcium phosphate crystallization, to a lesser extent than Mg^{2+} (inhibition efficiency $Zn^{2+} < Sr^{2+} < Mg^{2+}$ [59]). A synergistic effect of these ions has been observed by LeGeros et al. [61,62]. In addition to cations, also some anions influence the stability of ACP: according to Eanes et al., small amounts of fluoride (F^-) reduce the stability of OCP, which is often the intermediate phase in the ACP to apatite conversion [63], while other reports suggested its role as inhibitor in apatite formation [36,64]. The stabilizing role of pyrophosphate ($P_2O_7^{4-}$) [59,64,65] is significant from a biochemical perspective, as this ion is produced in cells as a consequence of ATP (adenosine triphosphate) hydrolysis. The effect of CO_3^{2-} is controversial: while some authors suggested that it is not involved in ACP stabilization, only reducing HA crystal size [66] or modifying the structure of the amorphous precipitate [67], LeGeros et al. reported an enhancement of ACP stability because of the action of carbonate ions [62]. Citrate ions ($C_6H_5O_7^{3-}$) also influence ACP formation and stability. This ion plays an important role in bone biomineralization, as it strongly interacts with apatite crystals; it has been recently shown that about one-sixth of bone-apatite crystallites are strongly bound with citrate [68]. The first reports indicated that its presence in calcium and phosphate solutions slows down OCP and HA crystal growth because of surface adsorption of negatively charged ions [69]. It has been recently shown that citrate takes active roles during the early amorphous stage, far before crystal nucleation, and that the association of citrate on the ACP surface has paramount effects in controlling HA crystal nucleation [70]. As carbonate and citrate ions are minor but essential components of human hard tissues, a deeper understanding of their effect on ACP formation, structure and stability is certainly worth of investigation.

3.2. Molecules and macromolecules

There is a great number of biologically-relevant molecules that somehow influence the amorphous stability and/or the pathway to form the crystalline calcium phosphates. Among them, ATP has been investigated, as it was found to stabilize ACP in the mitochondria of cells from the hepatopancreas of the blue crab [71,72]. Wuthier et al. studied the kinetics and nature of mineral formation that occurs when small amounts of Ca^{2+} are added to a buffer which mimics the cytosol of epiphyseal chondrocytes, with and without ATP [73]. In the presence of ATP, ACP was the only solid phase detected, being stable for at least 24 h; however, in its absence, ACP rapidly converts to DCPD (Dicalcium Phosphate Dihydrate). Interestingly, both ATP and ADP (adenosine diphosphate) act as stabilizing agents, while AMP (adenosine monophosphate) is ineffective [74,75]. The mechanism of ATP stabilization was investigated by Posner et al., who proposed that ATP prevents HA formation by (a) poisoning heterogeneous nucleation sites in the transformation system and/or (b) binding to embryonic HA nuclei preventing their growth to the critical nucleus size [44]. The effect of ATP is often studied in combination with Mg^{2+}, and the two species synergistically act to delay the conversion of a slurry of ACP to crystalline HA [43]. In some cases, the conversion is delayed more than 10 times with respect to either ATP or Mg^{2+} alone; this effect is due to the fact that crystallization begins only when ATP in solution has decreased through hydrolysis to an undetectable level, and Mg^{2+} is able to reduce substantially the rate of the ATP hydrolysis.

The influence of some naturally-occurring biomacromolecules which can be found in human body has been explored: to cite some examples, casein phosphopeptide (derived from the milk protein casein by tryptic digestion [76]) binds calcium and phosphate ions in an amorphous state, through the formation of complexes (see section 5.1 for further discussion) [77]. Proteoglycans, heavily glycosylated proteins which play a role in regulating mineralization processes, are potent inhibitors of HA formation [78,79]. Phosphatidylserine (PS), an acidic phospholipid which is concentrated in matrix vesicles (organelles believed to be the site of initial bone, dentine and cartilage calcification [80]), has a variable effect on *in vitro* HA proliferation: PS promotes *in vitro* mineralization in systems in which calcium-PS-phosphate complexes are allowed to form [81], while it inhibits *in vitro* mineralization when incorporated into liposomes [82]. Other studies highlighted that when PS is added before the precipitation of ACP, the effects are quite different from those obtained when the lipid was added after ACP was already formed [83]; in the first case, ACP transforms relatively quickly into HA, while in the second scenario ACP only partially converts to apatite by 23 h. Successive studies indicated that PS binds to HA crystals and therefore retards the proliferation of these mineral crystals [84]. The effect of bile acids was also investigated, given the fact that HA can comprise up to 30% of the total mass of black pigment stones [85]. Taurocholic acid does not influence the stability of the amorphous phase, while glycochenodeoxycholic acid prevents transformation of amorphous calcium phosphate to crystalline HA by competitively inhibiting the accumulation of phosphate on the crystal embryo surface [86].

3.3. Synthetic polymers

In addition to the naturally-existing macromolecules, whose effect on ACP has been described in the previous paragraph, some synthetic polymers display the ability to slow down the conversion of ACP to crystalline calcium phosphates. Despite their synthetic nature, the study of their interaction with amorphous phosphates is relevant in view of their inclusion in ACP-based biomaterials, such as in the field of bone and teeth remineralization. For instance, the presence of poly(ethylene glycol) (PEG) in ACP-forming solutions enhances the lifetime of the synthesized amorphous phase [87,88]; moreover, it was observed that ACP prepared with different PEG content shows structural differences, which lead to crystallization of α-TCP (tri-calcium phosphate), biphasic α/β -TCP or β-TCP after heat-treatment at 800 °C [89]. Li et al. compared the effect of PEG, PVA (poly(vinyl alcohol)), and PVP (polyvinylpyrrolidone), by preparing Ca^{2+}-polymer complexes and reacting them with a phosphate solution to obtain ACP [90]; they showed that ACP precipitates could be formed in the presence of PVA or PEG while only crystalline HA was formed in the presence of PVP. Recently, the functionalization with PEG chains was exploited to produce stable ACP nanoparticles [91]: the grafting with the polymeric chains allowed for an extended stability of the ACP powder (1 year) and for a better redispersibility (narrow particle size distributions in methanol without any sedimentation after 3 months) because of the formation of PEG brushes onto the individual ACP nanoparticles. Urch et al. studied the effect of PVP and PEI (polyethyleneimine) on the formation of CaP particles with adjustable dispersibility and crystallinity [92]. The influence of PEO (polyethylene oxide) was studied by Antonucci et al., in combination with some nonionic and anionic surfactants [93]: while the introduction of amphiphilic molecules during the spontaneous precipitation of ACP stabilized the amorphous solid phase against the conversion to HA, the presence of PEO resulted in a more pronounced ACP particles' agglomeration. Cationic surfactants also exert an effect on ACP: Selmani et al. recently showed that, depending on their aggregation state (monomers or micelles) and on the geometry of the aggregate of the investigated

surfactant (dodecyltrimethylammonium bromide), different outcomes on the rate of ACP transformation were obtained, as well as effects on the morphology of the amorphous and crystalline phases [94]. Poly (acrylic acid) (PAA) was used to produce ACP precursors to be studied in the remineralization of dentin collagen [95]. In the experimental conditions employed, when no PAA was present, ACP converted to HA in few minutes. The addition of PAA in the medium, at a concentration of 100 μg/ml, inhibited the transformation kinetics, as such amorphous–crystalline transition was not completed until 8 hours. PAA effect was dose-dependent, as 500 μg/ml resulted in a stable ACP phase up to 10 days, while with 1000 μg/ml no crystalline HA was observed after 30 days. The PAA effect had been previously reported by Amjad [48]. Ofir et al. studied the effect of some polyelectrolytes (polystyrene sulfonate, PSS, poly-L-glutamic acid, PGA, and poly-L-lysine, PLL) at different molecular weights (M_w) on the kinetics of ACP to HA transformation, finding a concentration-dependent mechanism: all polymers induced nucleation of HA when at low concentrations, while they inhibited it at high concentrations [96]. The authors hypothesized that, at low concentrations, polymers' chains adsorb on the surfaces of ACP particles in random conformation and, as a consequence, a large number of small and highly charged particles are created, which concentrate Ca^{2+} or HPO_4^{2-} ions, providing effective sites for secondary nucleation (see Fig. 2A). On the other hand, in the concentrated system, the polyelectrolytes spread on ACP surface and cover it, inhibiting the transport of ions to the template surface (see Fig. 2B). The investigated polyelectrolytes displayed a different inhibition efficiency, following the trend $PLL_{Low\ Mw} = PLL_{HighMw} < PSS < PGA_{LowMw} < PGA_{HighMW}$.

Poly(amino acids), such as poly-glutamic acid and poly-aspartic acid, are often investigated as they represent simple systems which mimic the non-collagenous acidic proteins involved in bone formation [97]. Many studies have been devoted to the analysis of their interaction with HA or OCP [98–101], but these polymers also display an action on ACP lifetime. Termine et al. showed that ACP is 60 times more stable when prepared in the presence of poly-L-glutamic acid, suggesting that acidic amino acid side chains may represent crucial sites for any given macromolecule-mineral interaction in biomineralization processes [64]. Recently, poly-aspartic acid was shown to exert a different effect on ACP when in solution or in a confined environment: ACP crystallization was reported to occur faster in membrane pores than in bulk solution in the presence of this polymer, which apparently promotes nucleation when located on a substrate, while behaving as an inhibitor in solution [102].

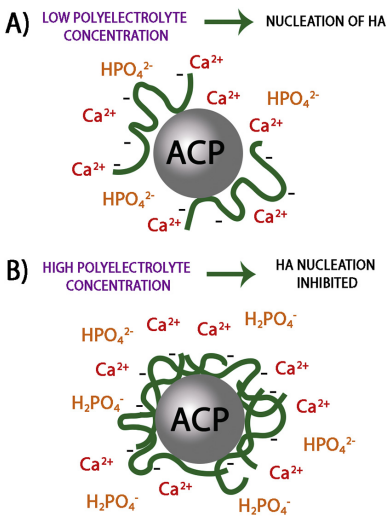

Fig. 2. Drawing of ACP particles formed in the presence of a negatively charged polyelectrolyte: (A) low polyelectrolyte concentration – induction of HA nucleation and (B) high polyelectrolyte concentration – inhibition of HA nucleation (readapted with permission from [96]).

In conclusion, many strategies for the stabilization of amorphous CaP have been investigated; it is important to highlight that the present paper is focused on amorphous calcium phosphate, therefore only the most significant examples relative to this specific category of CaP have been discussed. For a comprehensive overview of the effect of various polymers and complex fluids on the formation of different forms of calcium phosphates, the reader is referred to other comprehensive reviews [103–105].

4. Occurrence of ACP in human body

4.1. Bone

The issue of the presence of ACP in the skeletal tissue of mammalians is highly controversial. In 1955 Robinson and Watson, while studying the crystal-collagen relationship in bone by means of electron microscopy, first hypothesized that "the less distinct electron diffraction pattern obtained on recently calcified bone matrix suggests that […] some of the observed inorganic components in newly formed bone may not be in a crystalline form" [106]. About a decade later, Harper and Posner [107] and Termine and Posner [108] tried to quantify ACP in bone mineral. Their early X-rays diffraction estimates detected the presence of ~40% of amorphous mineral in bones of different animal species, its amount decreasing with the increasing age of the animal [109]. The theory of ACP as a bone component was supported by the evidence that the inorganic matrix of bone displays a very broad X-rays diffraction pattern, which is not compatible with the exclusive presence of crystalline hydroxyapatite [107]. However, some years later, Posner himself reevaluated his own conclusions [110]: by examining the X-ray radial distribution function of mature mammalian bone (being radial distribution function a plot of atomic density vs atomic separation, which gives information about the atomic structure of a material), he concluded that "it is probable that fully developed bone mineral cannot contain over 10% of a phase which is a close analog of the synthetic amorphous calcium phosphate". He proposed that the substitution of carbonate in the hydroxyapatite structure and the internal structural disorder that it provokes are responsible for the experimental broad diffraction pattern. Later, Grynpas et al. [111] studied the young bone mineral of embryonic chicks which, according to the age-dependence of ACP content in bone [108], should be rich in amorphous material; nevertheless, by using the radial distribution function method, they found no evidence of the presence of ACP in any of the samples studied. They concluded that "the widely promulgated and held "ACP theory", which has proposed that the initial solid mineral phase deposited in bone is an ACP, and that the progressive conversion of this ACP to poorly crystalline hydroxyapatite accounts for the compositional and X-ray diffraction changes accompanying aging and maturation of the mineral phase, is no longer tenable". This conclusion does not imply that the crystallinity of bone is age-independent, as a large body of literature data supports the evidence that crystallinity increases as mammalian bone gets older [112–114]; however, this observation is not related to a different content of ACP, but rather to an increase in crystallite size and/or a decrease in lattice imperfections [115]. Besides X-rays diffraction or infrared spectroscopy, morphological investigations have been useful in the detection of amorphous-rich zones in bone [35]. A limited number of early transmission electron microscopy (TEM) studies, avoiding aqueous processing of bone specimens, reported the presence of spheroidal particles near to crystal-rich areas of bone tissues, which displayed hazy and diffuse electron diffraction patterns [116–118].

Nevertheless, at that time, the majority of TEM studies did not mention the presence of ACP-like structures [35].

From these literature data, it is evident that the controversy of ACP in bone was a topic of considerable debate for a long time. In 1997, Boskey reported that at the beginning of the '90s this discussion was overcome by the application of high resolution techniques that succeeded in revealing that 99% of bone mineral consists of poorly crystalline hydroxyapatite [21]. However, some issues still need to be addressed: first, it should be kept in mind that the characterization of the newly formed mineral deposits in a tissue without their alteration during sample preparation and/or analysis is challenging: the use of wet and/or poorly preserved samples can trigger the conversion of ACP into more stable apatite or OCP; moreover, water removal can affect ACP stability, as its dehydration can lead to premature crystallization [4]. Another potential reason for the inability to detect biogenic ACP in bone tissue is the hypothesis that ACP does not exist as separate particles but, instead, as a layer on apatite crystals [35]. When Eanes proposed this theory, there was no experimental evidence to support it, even if the formation of an amorphous coating on apatite crystals had already been observed in *in vitro* experiments in physiological-like solutions [119]. About ten years later, thanks to the great advances in the sampling and characterization techniques, his hypothesis was validated by experimental analysis: solid-state nuclear magnetic resonance experiments, in combination with wide-angle X-ray scattering and cryogenic transmission electron microscopy, allowed for the detection of an amorphous calcium phosphate layer that coats the crystalline core of bone apatite [120]. It is proposed that the surface ACP layer would allow the binding of a significant amount of water molecules, able to mediate the orientation of the apatite crystals.

An issue which is closely related to the presence of ACP in mature bone is the involvement of this amorphous material as a precursor of apatite formation in the biomineralization process, especially considering that Nature often takes advantage of a transient precursor amorphous phase for crystals formation [121]. We have previously discussed ACP formation in simple aqueous solutions, reporting that the amorphous precursor to crystalline calcium phosphates can only form in sufficiently concentrated solutions of calcium and phosphate ions. In serum, these concentrations are lower than it would be necessary for triggering the precipitation of ACP [22,122]; nevertheless, the *in vivo* bone formation process is much more complicated than what simple thermodynamic considerations about mineral precipitation would predict. The biomineralization route is believed to involve the formation of the mineral phase in matrix vesicles rather than in extracellular skeletal fluid; these vesicles can be defined as small spherical bodies bounded by a lipid bilayer, often associated with small crystals of calcium phosphate mineral [80]. It is beyond the purpose of this work to delve into the fascinating details of bone formation and of the biomineralization process, but it is sufficient to point out that ACP can readily form under such compartmentalized conditions, as it was shown in studies with synthetic liposomes [82]; therefore, the possibility that ACP is involved in bone formation is not to be ruled-out, given its ability to form intracellularly in these vesicles [123]. In the last decade, some studies were published supporting the theory of bone mineral formation through ACP; even if these publications do not address specifically the human bone, the findings are of outmost importance to make some speculations of what may happen in our body. In 2006, Crane et al. studied early mineral deposits in mice calvaria by means of micro-Raman spectroscopy, showing that OCP is a precursor phase of bone apatite, and suggesting that ACP may form before OCP [124]. The theory of OCP as a precursor to bone mineral had been proposed in the past by Brown [125–127], and the report by Crane et al. is a significant step towards its demonstration. Despite some distinguished opinions considered this paper a strong evidence of the transient precursor strategy in vertebrates [128], others confuted the conclusions of the work, claiming that "care must be taken before pronouncing that detection of non-apatitic phosphates is the proof that OCP and/or ACP is the nucleating phase for in vivo vertebrate biological bone apatite" [129]. Few years later, Mahamid et al. showed that in the continuously forming fin rays of a zebrafish the newly formed bone contains large amounts of ACP [130]. Moreover, using synchrotron microbeam X-ray diffraction and small-angle scattering combined with cryo-scanning electron microscopy, they managed to demonstrate that the new mineral is delivered and deposited as packages of ACP nanospheres, which transform into platelets of crystalline apatite within the collagen matrix [131]. The mineral formation in larval zebrafish caudal fin bone was successively studied *in vivo* by Weiner and Addadi [132]: by means of fluorescence and cryo-SEM-microscopy, in combination with Raman and XRF spectroscopy, they detected the presence of intracellular mineral particles, which consist of a disordered calcium phosphate phase with characteristic features of OCP, located both between bones and away from the mineralized bone, in close association with blood vessels. These findings challenge the interpretation that mineral formation occurs in osteoblast cells juxtaposed to bone, and may shed light on bone mineralization processes in other vertebrates, including humans. The presence of large amounts of mineral particles bound to membranes in the mitochondria of osteoclasts and osteoblasts was detected by the same group in the rapidly forming embryonic chicken bone, suggesting new pathways of bone formation [133]. The templating effect of collagen fibrils on the growth on bone mineral phase, which is currently of great interest to the biomineralization research [134–136], will not be addressed here. We only point out that it was recently shown by TEM analysis that disordered collagen fibrils may play a role in stabilizing ACP and give rise to a mix of amorphous and crystalline bone mineral [137].

In conclusion, the presence and the role of the amorphous mineral phase at the nanoscale in bone has garnered much attention in biomineralization research community. It appears that ACP acts as the precursor for the formation of bone mineral phase, and some evidences in animal experiments suggest that it may be found as a component of mature bone; despite these indications, in 2016 Addadi et al. reported that "there is no direct evidence that crystals form *de novo* inside the collagen fibril from a saturated solution or from an amorphous precursor phase" [123]. Therefore, as the topic is highly controversial and is currently the subject of active research from many different groups, we believe that in the future new findings on the biomineralization process will probably reshape these statements, further clarifying the role of ACP in bone formation.

4.2. Tooth enamel

Enamel is the hardest and most mineralized tissue of our body, having a total inorganic component of 97% wt [1]. Together with Ca^{2+} and phosphate, it contains impurities of CO_3^{2-} (3.5% wt), Na^+ (0.5% wt) and Mg^{2+} (0.44% wt) [1]. The mineral matrix can be described as a dense array of needle-shaped carbonated apatite crystals (diameter ~50 nm and length of tens of μm), whose crystalline *c*-axes are aligned and form micrometric rods. These mineral rods, whose shape differs from the plate-like apatitic crystals of bone and dentin, form an intricate 3D network that constitutes the bulk of enamel [138]. This peculiar arrangement reduces cracks propagation, enhancing its mechanical strength and fatigue resistance [139]. Unlike bone and dentin, enamel is acellular and therefore does not resorb or remodel [140]. The organic phase does not contain collagen, being mainly composed by amelogenin (hydrophobic), ameloblastin (amphiphilic and acidic) and enamelin (hydrophilic and acidic), which are the proteins involved in the mineralization of enamel crystals [19,141]. Dental enamel formation (*i. e.* amelogenesis) is a complex process, which is the result of combined cellular and extracellular processes that control growth, shape, location and arrangement of the forming crystals [142,143]. The presence of transient mineral phases in developing enamel has been suggested in several studies starting from the eighties, as it was reviewed by Beniash et al. [138]; in 2009, it was proved that the mineral nascent enamel

consists of a transient ribbon-shaped ACP, which in time transforms into the final apatitic crystalline mineral [138]. The authors of this study hypothesize that the transformation may be triggered by proteolytic degradation of the enamel matrix proteins, which directly control the shape and organization of the mineral particles. The crucial role of amelogenin and enamelin in ACP stabilization was demonstrated in successive studies [144–146], as well as the importance of their self-assembly in the stabilization of pre-nucleation clusters [147]. For a detailed overview about this post-classical enamel biomineralization theory, which involves the amorphous precursor, the reader is referred to the review by Simmer et al. [148].

In addition to its role as a transient precursor of crystalline apatite, it was recently reported that a Mg-substituted amorphous calcium phosphate (Mg-ACP) is present in mature enamel [149,150]. It was first shown by atom probe tomography that in regular rodent enamel, the Mg^{2+} present (0.2–0.5% wt) segregates at grain boundaries; the analyses by means of X-ray absorption near-edge structure (XANES) and extended X-ray absorption fine structure (EXAFS) revealed that the environment of most Mg^{2+} in enamel exhibits short- to medium-range order, showing the same spectrum of Mg-ACP [149]. This enduring amorphous phase has a dramatic influence on the physico-chemical properties of enamel. In 2016, La Fontaine et al. reported a direct observation of an intergranular Mg-rich ACP phase between apatite nanowires in human mature enamel, by means of laser-assisted atom probe tomography [150]. In the same study, transmission electron microscopy investigations revealed that the amorphous layer is ~2 nm wide, and that it is homogeneously distributed along all sides of apatite nanowires. This Mg-ACP phase is more soluble than crystalline apatite, making thus enamel rod boundaries the most susceptible area to decay. As we described in paragraph 3.1, Mg^{2+} is known to stabilize the amorphous phase of ACP; therefore, the fact that this ion is concentrated along the grain boundaries of enamel rods is likely the responsible for the amorphous structure of that region.

4.3. Small intestine

The inclusion of small intestine as a location where amorphous calcium phosphates can be found in human body is probably unexpected for the reader; nevertheless, as we will discuss in this paragraph, it was recently reported that amorphous magnesium-calcium phosphate (AMCP) particles can form in the gut lumen and have a role in the immune surveillance of the organism [151,152]. It is known since a long time that Ca^{2+} and phosphate ions are actively secreted from the intestinal mucosa into the lumen (in particular, the former ion in the jejunum and the ileum, while the latter in the ileum) [153]. These secretions, known as “endogenous losses”, despite the little contribution to Ca^{2+} homeostasis in the organism, are maintained even under calcium and phosphorous-poor diets, suggesting that their biological function is of uppermost importance [151,153].

In 1967 Schedl et al., while studying calcium and phosphate concentration in dogs’ intestine, first suggested that a portion of these ions forms a precipitate [154], which comprises about one-third of the secreted Ca^{2+} [155]. The group by Powell, which pioneers the study of these endogenous particles, in 1999 showed that, in rats, this precipitate consists of particles < 2 μm, with a Ca:P ratio of ~5:3, similar to the one of hydroxyapatite [156]. The same group then hypothesized that these particles could bind lumen biomolecules (toxins and antigens) and then be scavenged by the M-cells-rich mucosa overlying intestinal lymphoid aggregates, thus promoting immune tolerance [153,157]. Without entering in biological details, it is important here to mention that M-cells are able to capture and transport microparticles and nanoparticles from one side of the cell and release them to the opposite site (transcytosis) [158]. Tolerance can be defined as the prevention of an immune response against a specific antigen; for instance, the immune system is tolerant of self-antigens, thus avoiding the attack of the body's own cells, tissues, and organs. However, when tolerance is lost, disorders like autoimmune diseases or food allergies may occur. The conclusive evidence of the existence and the role of these endogenous particles was given in 2015, when Powell et al. isolated and characterized them, showing their precise function in our body [151]. By collecting the particles from the distal small bowel contents of both humans and mice, the authors found out that the endogenous particles are: *(i)* constituted by calcium, magnesium and phosphate; *(ii)* porous; *(iii)* amorphous; *(iv)* able to incorporate molecules present in the gut lumen. The amorphous nature of AMCP particles in the intestinal juice is certainly favored by the presence of Mg^{2+} and by the relatively high pH of the ileum [159], and their properties are affected by the presence of biological macromolecules [160]. AMCPs are abundant in the gut (Powell and coworkers estimate the presence of ~2×10^{14} luminal particles/day) and they chaperone antigens and peptidoglycans from the lumen to the immune cells of the intestinal tissue (*i.e.* antigens presenting cells, APCs, located in the Peyer’s patches) *via* M-cells. This process induces the expression of programmed death-ligand 1 (PD-L1) on the surface of APCs, promoting immune tolerance. This mechanism (see Fig. 3), hypothesized by the same group, was demonstrated by means of specific investigations. First, mice fed with a diet low in Ca and P showed, in Peyer’s patches, phosphorous-deficient AMCPs (if compared to the ones found in mice fed with diets replete in Ca and P); this evidence supports a lumen-to-Peyer’s patch route for the particles. Then, the nanomineral was almost absent from the Peyer’s patches of mice lacking M-cells, proving their essential role for the transit of AMCPs from the lumen to the intestinal tissue. AMCPs were successively shown to have implications in pathological conditions, such as Crohn’s disease [161], and biological pathways, as the reduction of T-Helper cell responses to recall antigens [162]. The group of Powell also prepared synthetic analogs of AMCPs and reported that, *in vitro*, the particles have a marked capacity to trap macromolecules during formation and deliver them to APCs, without regulating any gene or modifying any gene regulation [163].

From a chemical perspective, many interesting issues arise from the features of these particles: for instance, is the amorphous nature necessary to achieve their biological function? Can crystallization processes occur *in vivo* and, if so, are the crystalline particles still able to incorporate macromolecules and transport them to APCs? Do dysfunctions in the pH of the ileum and/or Mg^{2+} concentration affect the formation and the stability of AMCPs? We believe that in the next future the characteristic and the role of these newly-discovered amorphous particles will be clarified.

4.4. Calciprotein particles in blood

The concentration of calcium and phosphate ions in serum is supersaturated with respect to apatite: if we simply consider the ion activity product of $[Ca^{2+}]$, $[PO_4^{3-}]$ and $[OH^-]$, together with the solubility product (K_{sp}) of hydroxyapatite, we obtain a degree of supersaturation ~12 for this mineral [164]. That would mean that any nucleation event (contusions, injections, fractures etc…) would result in a dramatic and catastrophic calcification of muscles, blood, skin and brain [164]. This does not happen because serum contains many substances, such as proteins, that are able to bind the cited ions and modulate biomineralization processes. In normal situations, CaP calcifications are restricted to bone and teeth; ageing and diseases (atherosclerosis, arthritis, diabetes, cancer…) can cause the alteration of regular pathways, resulting in ectopic crystal depositions (*i.e.* inappropriate biomineralization occurring in soft tissues [165]). Among serum proteins, albumin and fetuin-A (Fet-A, in humans known as α_2-Heremans Schmidt glycoprotein) are particularly relevant. Albumin is the most abundant blood protein in mammals and acts by binding free Ca^{2+} to its acidic residues, thus reducing its supersaturation in serum [166]; nevertheless, in spite of its low concentration, the most efficient protein in inhibiting serum calcifications is Fet-A. This liver-derived plasma protein, although circulating at around one-hundredth the concentration of albumin (~0.7 g/L vs ~46 g/L [167])

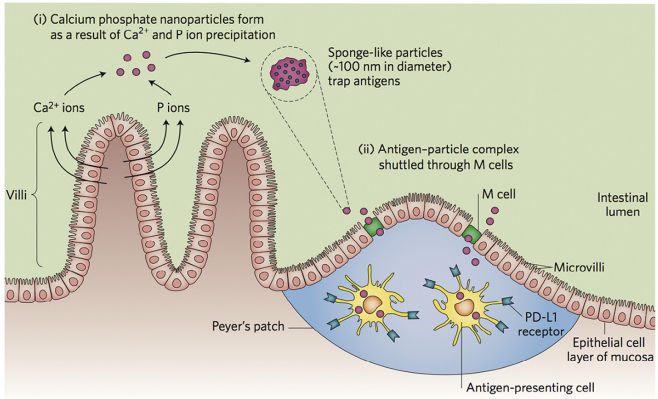

Fig. 3. Action mechanism of AMCPs: (i) formation of the nanoparticles, which trap antigens; (ii) AMCP-antigen complex is transported to APCs through M-cells (reproduced with permission from [152]).

is much more efficient in preventing ectopic calcifications. Rather than binding to Ca^{2+} single ions, like albumin does, Fet-A binds to nascent clusters of calcium and phosphate ions, forming the so-called calciproteins particles (CPPs) [168]. The formation of CPPs can thus be regarded as a defense mechanism against the precipitation of CaP in the blood, urine and soft tissues: in fact, mice lacking Fet-A suffer from severe ectopic calcifications [169]. These mineral-protein complexes were first detected in 2002 by Price et al. who observed, in the serum of rats treated with doses of the bone-active bisphosphonate etidronate (that inhibit normal bone mineralization), the formation of a complex constituted of 18% mineral, 80% fetuin, and 2% matrix Gla (γ-carboxyglutamic acid) protein [170]. Several studies from the group of Jahen-Dechent contributed to unravel the features of these mineral-organic complexes: using TEM and DLS (dynamic light scattering) they showed that CPPs have diameters of the order of 25–150 nm and are initially constituted of amorphous calcium phosphate [168]. The *in vitro* analysis of CPPs revealed that, in time, the initial CPPs transform into mature secondary CPPs, each consisting of a needle-shaped core of OCP covered by a shell of Fet-A [171,172]. These two stages of CPPs are often referred to as "CPP1" for the primary amorphous particles, and "CPP2" for the secondary crystalline CPPs [166,173]. In 2009, a time-resolved synchrotron SAXS (small angle x-ray scattering) study showed that Fet-A does not influence the formation of mineral nuclei, whereas it coats the surface of the initially-formed ACP particles, acting as a barrier that prevents further cluster aggregation (see Fig. 4A) [174]. Over time, however, the particles may aggregate and form crystalline CaP particles; all the factors that enhance ACP lifetime (alkaline pH, concentration of Fet-A, albumin, Mg^{2+}, pyrophosphate…) cause a delay in the conversion of CPP1 to CPP2 (see Fig. 4B). As this transition is associated with a change in shape and an increase in particles' diameter [175], a light scattering-based test was developed by Pasch et al. to measure the overall propensity for calcification in serum ("T_{50} test", see Fig. 4B) [176]. The conversion of CPPs from amorphous to crystalline, and the subsequent growth of the particles, will result in an enhancement of the scattered light. The lag time (T_{50}) measures the time taken for light scattering intensity to reach its half-maximum and reflects the time taken for 50% of CPP1 to convert to CPP2 [166]. T_{50}, measuring the maturation time of CPPs, can therefore give indications about the balance of pro- and anti-calcification factors in serum or, in other words, of its calcification propensity. This is of outmost importance, as a high serum calcification propensity (*i.e.* low T_{50}) is distinctive of patients suffering from arterial hypertension and/or chronic kidney disease (CKD) [177]. It was very recently proposed the use of T_{50} as biomarker for other pathologies, such as systemic lupus erythematosus disease activity [178].

The question that arises at this point is the following: are CPPs present in healthy individuals or their existence in serum is solely related to

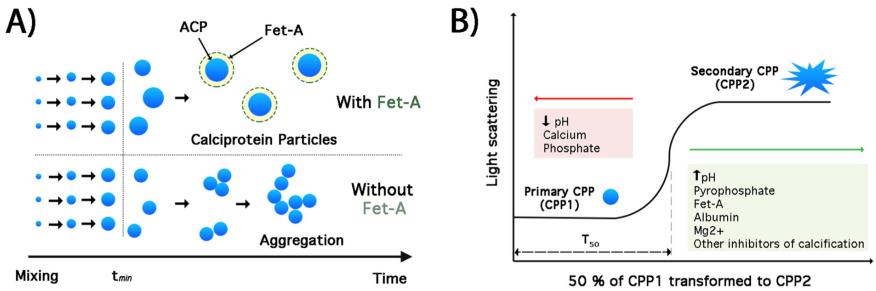

Fig. 4. (A) Role of Fet-A in the early stages of mineralization: without Fet-A, ACP forms large aggregates, while in the presence of the protein the primary particles are shielded and the aggregation is prevented (readapted with permission from [174]). (B) Conversion of CPP1 to CPP2 and the T50 test (reproduced from [166]).

pathological situations? Clinical studies have shown that CPPs are undetectable in healthy people, while they circulate in the blood of patients and animal models with CKD, increasingly with the pathology progression [179–182]. Interestingly, patients suffering from CKD often experience the so-called "calcification paradox", as they undergo an ectopic artery mineralization (and an increase in CPPs) accompanied by decreased bone mineral density or disturbed bone turnover [183,184]. CPPs were very recently also connected to diabetes in the study of Yamada et al., who found an increase in CPP levels in diabetic patients in postprandial state (the used method cannot distinguish between primary and secondary CPPs) [185]. Interestingly, in this study, the amount of serum CPPs was inversely correlated to magnesium levels; this observation is particularly relevant if we recall the stabilizing effect which this ion exerts on ACP lifetime. The formation of mineral nanoparticles described as CPPs and the simultaneous decrease in the concentration of Fet-A were shown to occur in human amniotic fluid and fetal membranes in cases of idiopathic preterm birth [186]. The possibility that CPPs could translocate from the blood to the renal tissue so to form kidney stones was also suggested [187]. From these observations about CPPs implications in pathological situations, we could infer that CPPs are pathogenic. However, at the beginning of this section, we learned that the complexation of Ca^{2+} and phosphate clusters by Fet-A prevents the formation of large CaP precipitates that would form because of the supersaturation of blood with respect to apatite. Two hypotheses can justify these apparently contradictory evidences: *(i)* the amount of CPPs is crucial for making them pathogenic; *(ii)* CPP1 have a different effect than CPP2. Smith et al. found that high levels of CPPs elicit a pro-inflammatory response from macrophage *in vitro*; they reported that this effect was not seen at low levels of CPPs, suggesting that "these potentially harmful effects are only likely to be encountered in extreme pathological states where CPP synthesis is very high, or where chronic exposure has overwhelmed clearance capacity" [172]. They also speculate that "low-level physiological CPP production (if any) might be protective, and unlikely to present a significant pro-inflammatory insult". On the other hand, the pathogenic effect of CPPs could be connected to the different cellular response to amorphous or crystalline CaP: this hypothesis is supported by the recent work of Aghagolzadeh et al., who reported that the exposure of vascular smooth muscle cells towards secondary CPP led to pronounced and concentration-dependent calcification, whereas exposure towards primary CPP did not [188]. According to the authors, the specific reason for the absence of an effect of CPP1 on calcification is unknown yet; the presence of ACP rather than crystalline CaP is one of the possible hypothesis, but the effect of other factors such as a lower Ca- and phosphate content, the protein content and/or protein composition, the mineral-to-protein ratio and/or the size of the particles are not to be ruled out.

4.5. Casein micelles in breast milk

Human breast milk contains all the nutrients necessary for the optimal infant growth and development. Milk is composed roughly of 87% water, 4% fat, 1% protein, and 7% lactose, though the exact nutrient balance changes according to the stages of nursing [189]. The 1% of milk proteins can be grouped into two different classes, namely caseins and whey proteins; the relative whey/casein ratio varies throughout lactation, and the frequently cited ratio of 60:40 approximates their average relation during the normal course of lactation. Recent studies found a whey/casein ratio ranging from 45:55 to 97:3, and increasing throughout the lactation period [190]. Despite the low amount of caseins being present in human milk, this class of proteins has a paramount importance in the complexation and subsequent transport to the infant of calcium and phosphate ions, at concentrations well beyond their solubility product. "Casein" refers to a family of phosphoproteins (*i.e.* proteins which are modified by the attachment of a phosphate group after their biosynthesis); according to the amino-acidic sequence and to the characteristics, they can be divided into 4 categories: α_{s1}-, α_{s2}-, β- and κ-casein. These 4 classes differ in the amount of phosphate groups and in the ability to interact with Ca^{2+} (α- and β-caseins are highly phosphorylated and bind a considerable amount of calcium, while κ-caseins do not) [191]. In human milk, β-casein is the most abundant, while α_{s2}-casein, present in bovine milk, is absent [190]. What makes this protein so peculiar (this is the reason why it is included in this paper) is its ability to form micelles that embed amorphous calcium phosphate clusters. Only bovine casein micelles have been studied in detail [192], but all milks (including human) contain these colloidal particles [193]. Despite their name, the structure of casein micelles differs from the one of the classical micelle that we are used to in colloid science. A typical casein micelle of 100 nm radius contains about 10^4 casein molecules and 800 nanoclusters of amorphous calcium phosphate [194]. Casein is thus not assembled in the "hydrophilic heads out, hydrophobic tails in" typical of the assembly of amphiphilic molecules in water solutions [195]; rather, the particles result from the aggregation of the α- and β-casein fractions with calcium phosphate nanoclusters and surface stabilization by κ-casein. The precise structure of these micelles has been deeply investigated in the literature, mainly by means of neutron and X-rays scattering, and it is still a subject of debate (a collection of all the proposed structural models is reviewed in [196]). The readers interested in the analysis of the casein micelles' structure are referred elsewhere [192,195,197–201]. Here, we briefly focus on the structure of ACP nanoclusters contained into them, rather than on the self-assembly of the protein component.

Why does casein interact with calcium phosphate? We previously mentioned that α- and β-caseins are heavily phosphorylated. This allows the interaction and strong binding of the protein with Ca^{2+} ions, that leads to the formation of CaP amorphous nanoclusters. κ-casein, not interacting with calcium, provides the stabilization of the micelles and prevents their agglomeration. Cryo-TEM investigation on casein micelles revealed that ACP nanoclusters are ~2.5 nm-sized and uniformly distributed in a homogeneous protein network [202]. Small angle scattering investigations reveal a similar cluster size (2 nm) and a correlation length of 0.35 nm^{-1}, which indicates that each ACP nanocluster is, on average, 18.6 nm apart from the other [196]. The binding action of casein slows down the rate of maturation of the amorphous state, and prevents its crystallization [193]. The amorphous nature of CaP facilitates the infant assimilation of calcium and phosphorous, which are essential elements for the formation and growth of its bone tissue.

According to Holt, the ability of casein to bind ACP nanoclusters has three-fold biological function: *(i)* the control of CaP precipitation in milk through ACP sequestration, *(ii)* the suppression of toxic amyloid fibril formation that casein would produce in the absence of ACP *(iii)* the nutrition of the neonate [192]. The first two functions are related to the mother and her ability to lactate: in fact, pathological calcifications or amyloidosis of the mammary gland would threaten the life of both the mother and the neonate but also, from an evolutionary point of view, her prospects for future reproductive success. The role of breast milk in the building of an effective immune system of the newborns has been deeply discussed. [203–205] Recalling that ACP-based nanostructures are involved in gut immune-surveillance mechanisms (see section 4.3), it was speculated that there is a connection between these two scenarios, particularly in the tolerance of the neonate towards the antigens present in the maternal milk [151]. This is indeed a fascinating hypothesis; nevertheless, the possibility that ACP nanoclusters embedded in casein micelles can survive the transit through the neonates' gastrointestinal tract is remote due to stomach's acidic conditions.

5. ACP-based biomaterials

In the previous sections, we learned that Nature takes advantage of amorphous calcium phosphates to build some essential components of our organism and to achieve specific functions. The first use of CaP-based materials for biomedical applications dates to 1920, when an aqueous slurry of "triple calcium phosphate" was used to stimulate bone

growth [206]. This study opened up a new field, which is the use of crystalline CaPs (mostly apatite-based) as materials for the preparation of biocompatible ceramics [207,208] and bone/dental cements [209–211]. The reason for the success of these materials follows the logic that repairing a damaged tissue with something with close resemblance might reduce problems due to chemical incompatibility [212]. Moreover, the idea that ACP-based biomaterials could have some advantages over their crystalline counterpart recently emerged.

5.1. Dentistry

In the field of dentistry, great attention has been devoted to ACP-based materials [25,213,214], and in particular to the system casein phosphopeptide-ACP (from here on, the abbreviation CasPP will be used for casein phosphopeptide; we will not use the acronym CPP, widely used in the literature, in order to avoid ambiguities with calciprotein particles discussed in section 4.4). Casein phosphopeptides are casein-derived compounds, obtained from the tryptic digestion of casein and containing the cluster sequence -Ser(P)-Ser(P)-Glu-Glu, which endows the molecule with the capacity of binding ACP nanoclusters and to stabilize them [215]. It is claimed that CasPP-ACP have beneficial effects in teeth remineralization and caries prevention; CasPP-ACP, *in vivo*, would act as calcium and phosphate reservoir, by releasing the two ions into the voids on enamel surface, thus contributing to remineralization [76,216]. Moreover, this complex acts synergistically with fluoride and enhances the remineralization efficiency [217]. The CasPP-ACP complex was patented by Reynolds from the University of Melbourne (Australia) and it was included in many commercial products, such as toothpastes, mouthwashes, chewing gums and mints (trademark: Recaldent™) [218,219]. Although the usefulness of CasPP-ACP-based treatments nowadays appears solid [215,218], some doubts on its efficiency were recently raised. In 2008, Azarpazhooh systemically reviewed 98 articles on the clinical efficacy of casein derivatives, concluding that there was insufficient evidence in clinical trials to draw any conclusion about the long-term effectiveness of CasPP-ACP [220]. An evaluation of 20 studies by Hani et al., in 2016, showed that no evidence could be provided to support the use of CasPP-ACP-based toothpastes. The authors advocated "high quality randomized clinical trials" before legitimately recommend these products for the prevention and treatment of early carious lesions [221]. The effectiveness of CasPP against the treatment of white spot lesions on teeth was assessed in 2018 by two independent studies, which obtained conflicting results: on the one hand, Rechmann et al. reported that the daily use of a CasPP-ACP-based toothpaste in combination with fluoride did not appear to significantly reduce white spot lesions incidence during fixed orthodontic treatment [222]. On the other hand, Mendes et al. found that at the end of the 90-day trial, the use of CasPP-ACP and fluoride showed comparable results in terms of remineralization, while the best white spot lesion remineralization was observed when CasPP-ACP and fluoride were combined [223]. The discrepancy between the results of these studies is possibly due to the difference in the adopted protocols, such as the age of the recruited patients and the length of the treatment. Further systematic studies are therefore required to assess the efficacy of these ACP-based formulations.

Together with CasPP-ACP, other systems containing ACP were proposed in oral science: for instance, at the end of the last century, Skrtic et al. developed a polymeric matrix derived from ambient polymerization of acrylic monomers which embeds ACP as bioactive filler, to be used as dental sealant and adhesive material [224,225]. The amorphous nature of calcium phosphate allows for a significant solubility, causing the gradual release of calcium and phosphate ions that enables the remineralization activity: *in vitro* experiments showed that tooth sections coated with a HA-filled composite experienced a fractional recovery of ~14% of the mineral initially lost during in vitro caries formation, whereas similarly treated sections coated with ACP-containing composites regained 71% [226]. However, in contrast with conventional glass composites, these ACP-based materials display poor mechanical properties, as ACP powders do not act as reinforcing fillers as in the case of the commonly used silanized glass; for this reason, the same group successively described the preparation of silica- and zirconia-modified ACP fillers for use in bioactive methacrylate composites [224,225].

Recently, the inclusion of ACP nanoparticles in products for dental remineralization was reported in the literature, for the remineralization of both enamel [227,228] and dentin [229]. Composites with antibacterial properties were also described [230,231]; carboxymethyl chitosan and lysozyme nanogels with encapsulated amorphous calcium phosphate were shown to increase the dentinal tubule occluding effectiveness [232].

Several products containing ACP are nowadays available on the market of dental healthcare: in addition to the already-cited products based on CasPP-ACP from Recaldent™, Nite White® ACP and Day White® ACP are whiteners which are claimed to combine the leading bleaching formulas with ACP, that should confer the added benefits of remineralization and sensitivity management. Enamel Pro®, containing ACP, was found to deliver significantly more fluoride to both intact and demineralized enamel than an analogous formulation containing TCP [233]. Aegis® Ortho a is light-cured orthodontic adhesive containing ACP; this product demonstrated a low but satisfactory bond strength for functioning as an orthodontic adhesive [234,235]. It is believed that the efficiency of these products relies on the fact that ACP rapidly hydrolyzes to form hydroxyapatite and, while precipitating on the surface and within the lumens of open dentinal tubules, it occludes them, resulting in reduced sensitivity. A more robust scientific evidence of this mechanism is nevertheless required.

5.2. Coatings

The importance of ACP as biomaterial is not limited to dentistry, as amorphous calcium phosphates display a great potential as hard tissue repair materials, in the form of coatings, cements or ceramics [4]. The strategy of coating an orthopedic or dental implant with CaP is quite common, as the mineral layer above the metallic or polymeric implant should provide bioactivity and osteoconductivity [236]. Typically, CaPs coatings obtained by means of plasma-spray techniques are never 100% crystalline, as they contain a variable amount of ACP [4]. The crystallinity of the coating has a deep impact on the stability and the biological response of the material, and the comprehension of the effect of this parameter on cells' behavior is challenging. Early reports suggest that amorphous coatings could be more effective in bone regeneration over their crystalline counterpart: de Bruijn et al. found that more bone was present on Ti substrates coated with amorphous apatite and tetracalcium phosphate, when compared to highly crystalline HA and magnesium whitlockite coatings [237]. It was also reported that polymeric implants coated with HA or ACP display different osteoconductivity and dissolution behavior, being the latter highly degradable and allowing for the rapid replacement by bone which achieves mechanical interlocking with the surface of the underlying material [238]. The work of Frayssinet et al. suggested an inhibition of cell proliferation onto highly crystalline HA coatings [239], while dos Santos et al. found a higher cellular spreading and a smaller number of cells on the surface of a Ti implant coated with an ACP layer rather than HA [240]. Yet, it is not possible to state that an amorphous coating provides a better osteogenic response of an implant than a crystalline one. A factor which should certainly be considered is the surface topography of the coating, which is different in the case of ACP and HA: this parameter affects cellular adhesion and cytoskeleton structure, making it difficult to evaluate the effect of the sole crystallinity [236]. In the attempt of solving this issue, Hu et al. synthesized nanoparticles of HA and ACP of the same size (~20 nm) and studied the adhesion, proliferation, and differentiation of bone marrow mesenchymal stem cells on films prepared with these particles [241]. Cell adhesion on nano-ACP, as well as proliferation and differentiation to osteoblasts, was lower compared to that on the nano-HA. Similarly, Brugge et al. reported that amorphous CaP coatings on Ti substrates inhibit the growth

and osteogenic differentiation of rat bone marrow cells, unlike crystalline and mixed amorphous/crystalline coatings of comparable roughness [242]. Moreover, Berube et al. also reported that osteoblast function on a crystalline HA surface was superior to that on amorphous and poorly crystalline surfaces [243]. The authors ascribed this behavior to the extensive dissolution that amorphous coatings encounter, as high calcium and phosphate ions in the surroundings may be detrimental to osteoblast attachment. It was suggested that the osteoinductive potential of the different crystalline forms of CaP in the presence of osteogenic supplements could be ranged as TCP>BCP (biphasic calcium phosphate) ≈ HA>ACP [244].

The results obtained on the effectiveness of ACP as a coating material for orthopedic implants are controversial likely because of the difficulty in isolating the effect of the crystallinity itself from other features that affect cellular response: morphology, roughness, wettability and surface energies influence the surface adhesion of the cells and their proliferation and differentiation [245–247]. The conclusive evidence of ACP primacy over HA would require the design of coatings differing only in crystallinity, which is a challenging but necessary task to fully understand the features of CaP-based materials and exploit their potentialities.

5.3. Cements

In the field of bone cements, some examples in the literature show that ACP-based precursors can be used to produce CaP cements with bone-like features. α-BSM ® (bone substitute material), commercialized in the past by Etex Corporation, was constituted by a mixture of DCPD (50% wt) and ACP (50% wt); when in contact with an aqueous medium, the rapid hydrolysis of ACP to apatite produced an injectable paste, which sets in 20 min at 37 °C [248]. After setting, slow hydrolysis of DCPD to apatite occurred; DCPD crystals acted as seeds to facilitate apatite nucleation and crystal growth. The paste had the peculiar characteristic of not being able to harden at room temperature, requiring body temperature for the setting reaction to begin and develop. The obtained final phase was a highly bioactive, fast resorbable CaP cement, close to bone mineral. The features of this ACP-based cement have been modified using additives; for instance, it was shown that the injectability and the setting time can be augmented by the addition of Na_2HPO_4 solution to the paste but reduced by the addition of PEG 200, glycerin, or citric acid [249]. α-BSM ® was also loaded with the growth factor rh-BMP-2 (a protein involved in the growth and regeneration of bone tissue) and it was shown to promote *in vivo* bone healing in animal models [250–252].

The compressive strength of ACP-based cements can be improved through the inclusion of poly(ethylenimine) or poly(allylamine hydrochloride) (six-fold increase) or bovine serum albumin (two-fold increase) [253]. The improvement in compressive strength was correlated with a reduction of crystallite dimensions, suggesting that polycation or protein adsorption inhibits crystal growth and possibly leads to a larger crystal aspect ratio. The inclusion of chitosan, sodium alginate or modified starch in the formulation can enhance the anti-washout ability [254]. ACP-based cements were also prepared with strontium ions [255,256] and beta-cyclodextrins [257]. Wang et al. prepared cements by mixing variable amounts of ACP, PCCP (partially crystallized calcium phosphate) and DCPA (dicalcium phosphate anhydrous); upon setting, the conversion to HA is observed [258]. The crystallinity and the degradation rate of the cements depend on the amount of ACP used. Brunner et al. studied the effect of the crystallinity of TCP in the preparation of bone cements, showing that the amorphous, nanoparticulate TCP powder shows the most adequate reaction time for a clinical application with respect to crystalline TCP [259]. The cells' response towards ACP-containing cements is again puzzling: while some authors suggest that the use of ACP instead of crystalline CaPs can lead to the formation of bone-like apatite, the study from Van den Vreken et al. reported a poor cell viability on the pure ACP cement, together with a decrease in the crystallinity of the end-product, the setting time and the mechanical properties (comparing to more crystalline formulations) [260]. Previously, Oreffo et al. showed an enhanced osteoblastic differentiation on a 70% carbonated apatite, whereas cell toxicity was observed on cells grown on amorphous calcium phosphate [261]. ACP-based cements can also be loaded with actives for a sustained release: the group of Uskoković recently described the preparation of CaP cements containing two different antibiotics and their release kinetic [262]. The samples were prepared using a variable amount of two different HA powders (HA1 and HA2), which differ in the duration of the preservation of the amorphous phase before the final transformation into crystalline HA; the authors found that the greater the content of HA2 (*i.e.* the sample which retains the amorphous nature for a longer time) in the cement, the slower the setting and the faster the drug release.

Some reports describe the doping of ACP with foreign ions, in the attempt of improving different features of the material; amorphous calcium carbonate phosphate doped with Mg^{2+}, Zn^{2+} and F^- ions was used to prepare cements, revealing that samples doped with F^- had shorter setting times, greater compressive strength and lower porosity than those prepared with Mg^{2+} or Zn^{2+} [263]. Furthermore, addition of doped ACP to the cement formulation did not affect osteoblastic morphology, viability and activity. In a recent study, Shahrezaee et al. prepared a bioceramic by adding Mg^{2+} to ACP, so to stabilize the amorphous phase and control the nucleation and growth of HA crystals formed upon incubation in a simulated body fluid [264]. Their biological investigation showed that Mg-doped ACP displayed higher biocompatibility than pure ACP.

Besides the cited applications, ACP was also exploited to prepare different kinds of biomaterials, such as composites with poly(lactic acid) nanofibers [265–268] or porous hollow microspheres for drug loading and sustained release [269]. This versatility reveals the potentialities of amorphous calcium phosphate as a biomaterial in several areas; however, one of the main issues that hampers the full exploitation of its features is the conclusive evaluation of the cellular response towards this material. New systematic studies are therefore essential to definitely assess and control the ACP interaction with cells and living organisms.

5.4. Antibacterial properties

Another attractive feature of ACP is the possibility of including it in antibacterial formulations. Early works combined ACP with Ag or other antibacterial agents to obtain a material able to remineralize and inhibit dental caries [270–274]. Very recently, Wu et al. demonstrated that, in the nanoparticle form, ACP itself has an intrinsic antimicrobial activity [275]: in particular, the study compared the effect of ACP and HA against Gram-positive and Gram-negative organisms. The results of the investigation demonstrated that ACP is more effective than HA against Gram-positive organisms, while the two forms of CaP have similar antibacterial activity against Gram-negative bacteria. Despite the mechanism of this antibacterial activity is not yet fully understood, the paper [275] paves the way towards the use of amorphous calcium phosphate as antimicrobial agent that in principle should not induce antibiotic-resistance phenomena in bacterial strains.

6. Conclusions

Amorphous calcium phosphate has been herein reviewed, with a particular emphasis on the relevance of ACP-based structures to the human body. Its formation kinetics and structure, also in the presence of different stabilizing agents, were first summarized; afterwards, the occurrence of this peculiar material in several districts of the body was presented, focusing on the characteristics and on the different biological functions fulfilled by this mineral. The research on this topic has been critically analyzed also considering the historical perspective: it was highlighted that the presence and the importance of ACP in bone formation has been known for a long time, while the role of amorphous calcium phosphate structures in other sites of our body, such as enamel

and intestine, was discovered only recently. The fact that the very same material has a role in diverse locations and processes is intriguing, and stimulates a continuous effort in the scientific and medical research, also in the attempt of including ACP in biomaterials, such as coatings and scaffolds for bone tissue engineering. Despite the huge amount of literature on ACP, several contradictory results have been reported and still need a full clarification. For these reasons, we believe that the research on amorphous calcium (and magnesium) phosphates is a vivid research topic, which is going to bring important innovations in the near future.

Acknowledgements

Fondazione CR Firenze (project 2017.0720), CSGI consortium and MIUR-Italy ("Progetto Dipartimenti di Eccellenza 2018–2022" allocated to Department of Chemistry "Ugo Schiff") are acknowledged for financial support.

References

[1] Dorozhkin SV. Calcium orthophosphates (CaPO4): occurrence and properties. Prog Biomater 2016;5:9–70. https://doi.org/10.1007/s40204-015-0045-z.
[2] Vallet-Regí M, González-Calbet JM. Calcium phosphates as substitution of bone tissues. Prog Solid State Chem 2004;32:1–31. https://doi.org/10.1016/j.progsolidstchem.2004.07.001.
[3] LeGeros RZ. Formation and transformation of calcium phosphates: relevance to vascular calcification. Z Für Kardiologie 2001;90:116–24. https://doi.org/10.1007/s003920170032.
[4] Combes C, Rey C. Amorphous calcium phosphates: synthesis, properties and uses in biomaterials. Acta Biomater 2010;6:3362–78. https://doi.org/10.1016/j.actbio.2010.02.017.
[5] Combes C, Cazalbou S, Rey C. Apatite biominerals. Minerals 2016;6:34. https://doi.org/10.3390/min6020034.
[6] Lowenstam HA, Weiner S. On biomineralization. Oxford, New York: Oxford University Press; 1989.
[7] Gower LB. Biomimetic model systems for investigating the amorphous precursor pathway and its role in biomineralization. Chem Rev 2008;108:4551–627. https://doi.org/10.1021/cr800443h.
[8] Weiss IM, Tuross N, Addadi L, Weiner S. Mollusc larval shell formation: amorphous calcium carbonate is a precursor phase for aragonite. J Exp Zool 2002;293:478–91. https://doi.org/10.1002/jez.90004.
[9] Politi Y, Arad T, Klein E, Weiner S, Addadi L. Sea urchin spine calcite forms via a transient amorphous calcium carbonate phase. Science 2004;306:1161–4. https://doi.org/10.1126/science.1102289.
[10] Addadi L, Raz S, Weiner S. Taking advantage of disorder: amorphous calcium carbonate and its roles in biomineralization. Adv Mater 2003;15:959–70. https://doi.org/10.1002/adma.200300381.
[11] Dorozhkin V, Amorphous S. Calcium Orthophosphates: nature, chemistry and biomedical applications. Int J Mater Chem 2012;2:19–46. https://doi.org/10.5923/j.ijmc.20120201.04.
[12] McNaught AD, Wilkinson A. IUPAC. compendium of chemical terminology, 2nd ed. (the "Gold Book"). Oxford: Blackwell Scientific Publications; 1997.
[13] Eanes ED. Amorphous calcium phosphate: thermodynamic and kinetic considerations. In: Amjad Z, editor. calcium phosphates biol. ind. syst. US: Springer; 1998. p. 21–39.
[14] Watson ML, Robinson RA. Collagen-crystal relationships in bone. II. Electron microscope study of basic calcium phosphate crystals. Am J Anat 1953;93:25–59. https://doi.org/10.1002/aja.1000930103.
[15] Wang L, Nancollas GH. Calcium orthophosphates: crystallization and dissolution. Chem Rev 2008;108:4628–69. https://doi.org/10.1021/cr0782574.
[16] Eanes ED, Gillessen IH, Posner AS. Intermediate states in the precipitation of hydroxyapatite. Nature 1965;208:365–7. https://doi.org/10.1038/208365a0.
[17] Cölfen H, Mann S. Higher-Order organization by mesoscale self-assembly and transformation of hybrid nanostructures. Angew Chem Int Ed 2003;42:2350–65. https://doi.org/10.1002/anie.200200562.
[18] De Yoreo JJ. Principles of crystal nucleation and growth. Rev Mineral Geochem 2003;54:57–93. https://doi.org/10.2113/0540057.
[19] Margolis HC, Kwak S-Y, Yamazaki H. Role of mineralization inhibitors in the regulation of hard tissue biomineralization: relevance to initial enamel formation and maturation. Front Physiol 2014;5. https://doi.org/10.3389/fphys.2014.00339.
[20] Johnsson MS-A, Nancollas GH. The Role of brushite and octacalcium phosphate in apatite formation. Crit Rev Oral Biol Med 1992;3:61–82. https://doi.org/10.1177/10454411920030010601.
[21] Boskey AL. Amorphous calcium phosphate: the contention of bone. J Dent Res 1997;76:1433–6. https://doi.org/10.1177/00220345970760080501.
[22] Boskey AL, Posner AS. Formation of hydroxyapatite at low supersaturation. J Phys Chem 1976;80:40–5. https://doi.org/10.1021/j100542a009.
[23] Betts F, Posner AS. An X-ray radial distribution study of amorphous calcium phosphate. Mater Res Bull 1974;9:353–60. https://doi.org/10.1016/0025-5408(74)90087-7.
[24] Kanzaki N, Treboux G, Onuma K, Tsutsumi S, Ito A. Calcium phosphate clusters. Biomaterials 2001;22:2921–9. https://doi.org/10.1016/S0142-9612(01)00039-4.
[25] Zhao J, Liu Y, Sun W, Yang X. First detection, characterization, and application of amorphous calcium phosphate in dentistry. J Dent Sci 2012;7:316–23. https://doi.org/10.1016/j.jds.2012.09.001.
[26] Mancardi G, Tamargo CEH, Tommaso DD, de Leeuw NH. Detection of Posner's clusters during calcium phosphate nucleation: a molecular dynamics study. J Mater Chem B 2017;5:7274–84. https://doi.org/10.1039/C7TB01199G.
[27] Habraken WJEM, Tao J, Brylka LJ, Friedrich H, Bertinetti L, Schenk AS, et al. Ion-association complexes unite classical and non-classical theories for the biomimetic nucleation of calcium phosphate. Nat Commun 2013;4:1507. https://doi.org/10.1038/ncomms2490.
[28] Gebauer D, Kellermeier M, Gale JD, Bergström L, Cölfen H. Pre-nucleation clusters as solute precursors in crystallisation. Chem Soc Rev 2014;43:2348–71. https://doi.org/10.1039/C3CS60451A.
[29] Posner AS, Betts F, Blumenthal NC. Formation and structure of synthetic and bone hydroxyapatites. Prog Cryst Growth Charact 1980;3:49–64. https://doi.org/10.1016/0146-3535(80)90011-8.
[30] Eanes ED, Meyer JL. The maturation of crystalline calcium phosphates in aqueous suspensions at physiologic pH. Calcif Tissue Res 1977;23:259–69. https://doi.org/10.1007/BF02012795.
[31] Boskey AL, Posner AS. Conversion of amorphous calcium phosphate to microcrystalline hydroxyapatite. A pH-dependent, solution-mediated, solid-solid conversion. J Phys Chem 1973;77:2313–7. https://doi.org/10.1021/j100638a011.
[32] Meyer JL, Weatherall CC. Amorphous to crystalline calcium phosphate phase transformation at elevated pH. J Colloid Interface Sci 1982;89:257–67. https://doi.org/10.1016/0021-9797(82)90139-4.
[33] Wang Y-W, Christenson HK, Meldrum FC. Confinement increases the lifetimes of hydroxyapatite precursors. Chem Mater 2014;26:5830–8. https://doi.org/10.1021/cm501770r.
[34] Rajasekharan AK, Andersson M. Role of nanoscale confinement on calcium phosphate formation at high supersaturation. Cryst Growth Des 2015;15:2775–80. https://doi.org/10.1021/acs.cgd.5b00139.
[35] Eanes ED. Amorphous calcium phosphate. In: Chow LC, Eanes ED, editors. Monogr. oral sci. octacalcium phosphate. Basel: Karger; 2001. p. 130–47.
[36] Bachra BN, Fischer HRA. The effect of some inhibitors on the nucleation and crystal growth of apatite. Calcif Tissue Res 1969;3:348–57. https://doi.org/10.1007/BF02058677.
[37] Boskey AL, Posner AS. Magnesium stabilization of amorphous calcium phosphate: a kinetic study. Mater Res Bull 1974;9:907–16. https://doi.org/10.1016/0025-5408(74)90169-X.
[38] Mitchell PCH, Parker SF, Simkiss J, Simmons J, Taylor MG. Hydrated sites in biogenic amorphous calcium phosphates: an infrared, Raman, and inelastic neutron scattering study. J Inorg Biochem 1996;62:183–97. https://doi.org/10.1016/0162-0134(95)00146-8.
[39] Harries JE, Hukins DWL, Holt C, Hasnain SS. Conversion of amorphous calcium phosphate into hydroxyapatite investigated by EXAFS spectroscopy. J Cryst Growth 1987;84:563–70. https://doi.org/10.1016/0022-0248(87)90046-7.
[40] Holt C, Van Kemenade MJJM, Nelson LS, Hukins DWL, Bailey RT, Harries JE, et al. Amorphous calcium phosphates prepared at pH 6.5 and 6.0. Mater Res Bull 1989;24:55–62. https://doi.org/10.1016/0025-5408(89)90008-1.
[41] Eanes ED, Posner AS. Intermediate phases in the basic solution preparation of alkaline earth phosphates. Calcif Tissue Res 1968;2:38–48. https://doi.org/10.1007/BF02279192.
[42] Kibalczyc W, Christoffersen J, Christoffersen MR, Zielenkiewicz A, Zielenkiewicz W. The effect of magnesium ions on the precipitation of calcium phosphates. J Cryst Growth 1990;106:355–66. https://doi.org/10.1016/0022-0248(90)90080-5.
[43] Blumenthal NC, Betts F, Posner AS. Stabilization of amorphous calcium phosphate by Mg and ATP. Calcif Tissue Res 1977;23:245–50. https://doi.org/10.1007/BF02012793.
[44] Posner AS, Betts F, Blumenthal NC. Role of ATP and Mg in the stabilization of biological and synthetic amorphous calcium phosphates. Calcif Tissue Res 1976;22:208–12. https://doi.org/10.1007/BF02064066.
[45] Abbona F, Baronnet A. A XRD and TEM study on the transformation of amorphous calcium phosphate in the presence of magnesium. J Cryst Growth 1996;165:98–105. https://doi.org/10.1016/0022-0248(96)00156-X.
[46] Christoffersen J, Christoffersen MR, Kibalczyc W, Andersen FA. A contribution to the understanding of the formation of calcium phosphates. J Cryst Growth 1989;94:767–77. https://doi.org/10.1016/0022-0248(89)90102-4.
[47] Ajibola VO, Thomas SA. Transformation of amorphous calcium phosphate hydroxyapatite in the presence of some ions. Bull Chem Soc Ethiop 1997;11:19–24.
[48] Amjad Z. Inhibition of the amorphous calcium phosphate phase transformation reaction by polymeric and non-polymeric inhibitors. Phosphorus Res Bull 1997;7:45–54. https://doi.org/10.3363/prb1992.7.0_45.
[49] Holt C, Van Kemenade M, Harries JE, Nelson LS, Bailey RT, Hukins DWL, et al. Preparation of amorphous calcium-magnesium phosphates at pH 7 and characterization by x-ray absorption and fourier transform infrared spectroscopy. J Cryst Growth 1988;92:239–52. https://doi.org/10.1016/0022-0248(88)90455-1.
[50] Salimi MH, Heughebaert JC, Nancollas GH. Crystal growth of calcium phosphates in the presence of magnesium ions. Langmuir 1985;1:119–22. https://doi.org/10.1021/la00061a019.
[51] Jahnen-Dechent W, Ketteler M. Magnesium basics. Clin Kidney J 2012;5:13–4. https://doi.org/10.1093/ndtplus/sfr163.
[52] Bertran O, del Valle LJ, Revilla-López G, Rivas M, Chaves G, Casas MT, et al. Synergistic approach to elucidate the incorporation of magnesium ions into hydroxyapatite. Chem A Eur J 2015;21:2537–46. https://doi.org/10.1002/chem.201405428.

[53] Yang X, Xie B, Wang L, Qin Y, Henneman ZJ, Nancollas GH. Influence of magnesium ions and amino acids on the nucleation and growth of hydroxyapatite. CrystEngComm 2011;13:1153–8. https://doi.org/10.1039/C0CE00470G.

[54] Ding H, Pan H, Xu X, Tang R. Toward a detailed understanding of magnesium ions on hydroxyapatite crystallization inhibition. Cryst Growth Des 2014;14:763–9. https://doi.org/10.1021/cg401619s.

[55] Liu Q, Chen Z, Pan H, Darvell BW, Matinlinna JP. Effect of magnesium on the solubility of hydroxyapatite. Eur J Inorg Chem 2016;2016:5623–9. https://doi.org/10.1002/ejic.201601056.

[56] Buljan Meić I, Kontrec J, Domazet Jurašin D, Njegić Džakula B, Štajner L, Lyons DM, et al. Comparative study of calcium carbonates and calcium phosphates precipitation in model systems mimicking the inorganic environment for biomineralization. Cryst Growth Des 2017;17:1103–17. https://doi.org/10.1021/acs.cgd.6b01501.

[57] Blumenthal NC, Cosma V, Levine S. Effect of gallium on the in vitro formation, growth, and solubility of hydroxyapatite. Calcif Tissue Int 1989;45:81–7. https://doi.org/10.1007/BF02561406.

[58] Blumenthal NC, Cosma V, Skyler D, LeGeros J, Walters M. The effect of cadmium on the formation and properties of hydroxyapatite *In vitro* and its relation to cadmium toxicity in the skeletal system. Calcif Tissue Int 1995;56:316–22. https://doi.org/10.1007/BF00318053.

[59] Root MJ. Inhibition of the amorphous calcium phosphate phase transformation reaction by polyphosphates and metal ions. Calcif Tissue Int 1990;47:112–6. https://doi.org/10.1007/BF02555994.

[60] Fuierer TA, LoRe M, Puckett SA, Nancollas GH. A mineralization adsorption and mobility study of hydroxyapatite surfaces in the presence of zinc and magnesium ions. Langmuir 1994;10:4721–5. https://doi.org/10.1021/la00024a054.

[61] LeGeros RZ, Bleiwas CB, Retino M, Rohanizadeh R, LeGeros JP. Zinc effect on the in vitro formation of calcium phosphates: relevance to clinical inhibition of calculus formation. Am J Dent 1999;12:65–71.

[62] LeGeros RZ, Mijares D, Park J, Chang X-F, Khairoun I, Kijkowska R, et al. Amorphous calcium phosphates (ACP): formation and stability. Key Eng Mater 2005;284–286:7–10. https://doi.org/10.4028/www.scientific.net/KEM.284-286.7.

[63] Eanes ED, Meyer JL. The influence of fluoride on apatite formation from unstable supersaturated solutions at pH 7.4. J Dent Res 1978;57:617–24. https://doi.org/10.1177/00220345780570041501.

[64] Termine JD, Peckauskas RA, Posner AS. Calcium phosphate formation in vitro. II. Effects of environment on amorphous-crystalline transformation. Arch Biochem Biophys 1970;140:318–25. https://doi.org/10.1016/0003-9861(70)90072-X.

[65] Fleisch H, Russell RGG, Bisaz S, Termine JD, Posner AS. Influence of pyrophosphate on the transformation of amorphous to crystalline calcium phosphate. Calcif Tissue Res 1968;2:49–59. https://doi.org/10.1007/BF02279193.

[66] Blumenthal NC, Betts F, Posner AS. Effect of carbonate and biological macromolecules on formation and properties of hydroxyapatite. Calcif Tissue Res 1975;18:81–90. https://doi.org/10.1007/BF02546228.

[67] Greenfield DJ, Eanes ED. Formation chemistry of amorphous calcium phosphates prepared from carbonate containing solutions. Calcif Tissue Res 1972;9:152–62. https://doi.org/10.1007/BF02061953.

[68] Hu Y-Y, Rawal A, Schmidt-Rohr K. Strongly bound citrate stabilizes the apatite nanocrystals in bone. Proc Natl Acad Sci 2010;107:22425–9. https://doi.org/10.1073/pnas.1009219107.

[69] Brecević L, Füredi-Milhofer H. Precipitation of calcium phosphates from electrolyte solutions. V. The influence of citrate ions. Calcif Tissue Int 1979;28:131–6. https://doi.org/10.1007/BF02441231.

[70] Chen Y, Gu W, Pan H, Jiang S, Tang R. Stabilizing amorphous calcium phosphate phase by citrate adsorption. CrystEngComm 2014;16:1864–7. https://doi.org/10.1039/C3CE42274G.

[71] Becker GL, Chen C-H, Greenawalt JW, Lehninger AL. Calcium phosphate granules in the hepatopancreas of the blue crab callinectes sapidus. J Cell Biol 1974;61:316–26. https://doi.org/10.1083/jcb.61.2.316.

[72] Betts F, Blumenthal NC, Posner AS, Becker GL, Lehninger AL. Atomic structure of intracellular amorphous calcium phosphate deposits. Proc Natl Acad Sci U S A 1975;72:2088–90.

[73] Wuthier RE, Rice GS, Wallace JEB, Weaver RL, LeGeros RZ, Eanes ED. In vitro precipitation of calcium phosphate under intracellular conditions: formation of brushite from an amorphous precursor in the absence of ATP. Calcif Tissue Int 1985;37:401–10. https://doi.org/10.1007/BF02553710.

[74] Blumenthal NC, Betts F, Posner AS. Nucleotide stabilization of amorphous calcium phosphate. Mater Res Bull 1975;10:1055–60. https://doi.org/10.1016/0025-5408(75)90214-7.

[75] Christoffersen MR, Christoffersen J. The inhibitory effects of ATP, ADP, and AMP on the rate of dissolution of calcium hydroxyapatite. Calcif Tissue Int 1984;36:659–61. https://doi.org/10.1007/BF02405386.

[76] Cross KJ, Reynolds NLH. EC. Casein phosphopeptides in oral health - chemistry and clinical applications. Curr Pharm Des 2007;13:793–800. https://doi.org/10.2174/138161207780363086.

[77] Cross KJ, Huq NL, Palamara JE, Perich JW, Reynolds EC. Physicochemical characterization of casein phosphopeptide-amorphous calcium phosphate nanocomplexes. J Biol Chem 2005;280:15362–9. https://doi.org/10.1074/jbc.M413504200.

[78] Blumenthal NC, Posner AS, Silverman LD, Rosenberg LC. Effect of proteoglycans on in vitro hydroxyapatite formation. Calcif Tissue Int 1979;27:75–82. https://doi.org/10.1007/BF02441164.

[79] Blumenthal NC. Mechanisms of inhibition of calcification. Clin Orthop 1989:279–89.

[80] Golub EE. Role of matrix vesicles in biomineralization. Biochim Biophys Acta 1790;2009:1592–8. https://doi.org/10.1016/j.bbagen.2009.09.006.

[81] Boskey AL, Posner AS. The role of synthetic and bone extracted Ca-phospholipid-PO4 complexes in hydroxyapatite formation. Calcif Tissue Res 1977;23:251–8. https://doi.org/10.1007/BF02012794.

[82] Eanes ED, Hailer AW, Costa JL. Calcium phosphate formation in aqueous suspensions of multilamellar liposomes. Calcif Tissue Int 1984;36:421–30. https://doi.org/10.1007/BF02405354.

[83] Wuthier RE, Eanes ED. Effect of phospholipids on the transformation of amorphous calcium phosphate to hydroxyapatite in vitro. Calcif Tissue Res 1975;19:197–210. https://doi.org/10.1007/BF02564004.

[84] Boskey AL, Dick BL. The effect of phosphatidylserine on in vitro hydroxyapatite growth and proliferation. Calcif Tissue Int 1991;49:193–6. https://doi.org/10.1007/BF02556117.

[85] Crowther RS, Soloway RD. Pigment gallstone pathogenesis: from man to molecules. Semin Liver Dis 1990;10:171–80. https://doi.org/10.1055/s-2008-1040471.

[86] Qiu SM, Wen G, Hirakawa N, Soloway RD, Hong NK, Crowther RS. Glycochenodeoxycholic acid inhibits calcium phosphate precipitation in vitro by preventing the transformation of amorphous calcium phosphate to calcium hydroxyapatite. J Clin Invest 1991;88:1265–71. https://doi.org/10.1172/JCI115430.

[87] Li Y, Weng W, Cheng K, Du P, Shen G, Wang J, et al. Preparation of amorphous calcium phosphate in the presence of poly(ethylene glycol). J Mater Sci Lett 2003;22:1015–6. https://doi.org/10.1023/A:1024741426069.

[88] Li Y, Weng W. In vitro synthesis and characterization of amorphous calcium phosphates with various Ca/P atomic ratios. J Mater Sci Mater Med 2007;18:2303–8. https://doi.org/10.1007/s10856-007-3132-4.

[89] Liu S, Weng W, Li Z, Pan L, Cheng K, Song C, et al. Effect of PEG amount in amorphous calcium phosphate on its crystallized products. J Mater Sci Mater Med 2009;20:359–63. https://doi.org/10.1007/s10856-008-3584-1.

[90] Li YB, Weng WJ, Cheng K, Du PY, Shen G, Han GR. Complexes of Ca(II) with polymers as precursors for preparation of amorphous calcium phosphate. Mater Sci Technol 2004;20:1075–8. https://doi.org/10.1179/026708304225019740.

[91] Luo J, Qiu S, Zhou X, Lai R, Dong P, Xie X. In situ grafting polyethylene glycol chains onto amorphous calcium phosphate nanoparticles to improve the storage stability and organic solvent redispersibility. Colloids Surf A Physicochem Eng Asp 2014;444:81–8. https://doi.org/10.1016/j.colsurfa.2013.12.041.

[92] Urch H, Vallet-Regi M, Ruiz L, Gonzalez-Calbet JM, Epple M. Calcium phosphate nanoparticles with adjustable dispersability and crystallinity. J Mater Chem 2009;19:2166–71. https://doi.org/10.1039/B810026H.

[93] Antonucci JM, Liu DW, Skrtic D. Amorphous calcium phosphate based composites: effect of surfactants and poly(ethylene oxide) on filler and composite properties. J Dispers Sci Technol 2007;28:819–24. https://doi.org/10.1080/01932690701346255.

[94] Selmani A, Coha I, Magdić K, Čolović B, Jokanović V, Šegota S, et al. Multiscale study of the influence of cationic surfactants on amorphous calcium phosphate precipitation. CrystEngComm 2015;17:8529–48. https://doi.org/10.1039/C5CE01516B.

[95] Wang J, Chen Y, Li L, Sun J, Gu X, Xu X, et al. Remineralization of dentin collagen by meta-stabilized amorphous calcium phosphate. CrystEngComm 2013;15:6151–8. https://doi.org/10.1039/C3CE40449H.

[96] Bar-Yosef Ofir P, Govrin-Lippman R, Garti N, Füredi-Milhofer H. The Influence of polyelectrolytes on the formation and phase transformation of amorphous calcium phosphate. Cryst Growth Des 2004;4:177–83. https://doi.org/10.1021/cg034148g.

[97] Olszta MJ, Cheng X, Jee SS, Kumar R, Kim Y-Y, Kaufman MJ, et al. Bone structure and formation: a new perspective. Mater Sci Eng R Rep 2007;58:77–116. https://doi.org/10.1016/j.mser.2007.05.001.

[98] Bigi A, Boanini E, Gazzano M, Kojdecki MA, Rubini K. Microstructural investigation of hydroxyapatite–polyelectrolyte composites. J Mater Chem 2004;14:274–9. https://doi.org/10.1039/B308687A.

[99] Burke EM, Guo Y, Colon L, Rahima M, Veis A, Nancollas GH. Influence of polyaspartic acid and phosphophoryn on octacalcium phosphate growth kinetics. Colloids Surf B Biointerfaces 2000;17:49–57. https://doi.org/10.1016/S0927-7765(99)00084-3.

[100] Furedi-Milhofer H, Moradian-Oldak J, Weiner S, Veis A, Mintz KP, Addadf L. Interactions of matrix proteins from mineralized tissues with octacalcium phosphate. Connect Tissue Res 1994;30:251–64. https://doi.org/10.3109/03008209409015041.

[101] Tsortos A, Nancollas GH. The Role of polycarboxylic acids in calcium phosphate mineralization. J Colloid Interface Sci 2002;250:159–67. https://doi.org/10.1006/jcis.2002.8323.

[102] Cantaert B, Beniash E. C. Meldrum F. The role of poly(aspartic acid) in the precipitation of calcium phosphate in confinement. J Mater Chem B 2013;1:6586–95. https://doi.org/10.1039/C3TB21296C.

[103] Ridi F, Meazzini I, Castroflorio B, Bonini M, Berti D, Baglioni P. Functional calcium phosphate composites in nanomedicine. Adv Colloid Interface Sci 2017;244:281–95. https://doi.org/10.1016/j.cis.2016.03.006.

[104] Schweizer S, Taubert A. Polymer-controlled, bio-inspired calcium phosphate mineralization from aqueous solution. Macromol Biosci 2007;7:1085–99. https://doi.org/10.1002/mabi.200600283.

[105] Bleek K, Taubert A. New developments in polymer-controlled, bioinspired calcium phosphate mineralization from aqueous solution. Acta Biomater 2013;9:6283–321. https://doi.org/10.1016/j.actbio.2012.12.027.

[106] Robinson RA, Watson ML. Crystal-collagen relationships in bone as observed in the electron microscope. III. Crystal and collagen morphology as a function of age. Ann N Y Acad Sci 1955;60:596–630. https://doi.org/10.1111/j.1749-6632.1955.tb40054.x.

[107] Harper RA, Posner AS. Measurement of non-crystalline calcium phosphate in bone mineral. Proc Soc Exp Biol Med Soc Exp Biol Med 1966;122:137–42. https://doi.org/10.3181/00379727-122-31073.

[108] Termine JD, Posner AS. Amorphous/crystalline interrelationships in bone mineral. Calcif Tissue Res 1967;1:8–23. https://doi.org/10.1007/BF02008070.

[109] Termine JD, Posner AS. Infrared analysis of rat bone: age dependency of amorphous and crystalline mineral fractions. Science 1966;153:1523–5.

[110] Posner AS, Betts F. Synthetic amorphous calcium phosphate and its relation to bone mineral structure. Acc Chem Res 1975;8:273–81. https://doi.org/10.1021/ar50092a003.

[111] Grynpas MD, Bonar LC, Glimcher MJ. Failure to detect an amorphous calcium-phosphate solid phase in bone mineral: a radial distribution function study. Calcif Tissue Int 1984;36:291–301. https://doi.org/10.1007/BF02405333.

[112] Burnell JM, Teubner EJ, Miller AG. Normal maturational changes in bone matrix, mineral, and crystal size in the rat. Calcif Tissue Int 1980;31:13–9. https://doi.org/10.1007/BF02407162.

[113] Matsushima N, Hikichi K. Age changes in the crystallinity of bone mineral and in the disorder of its crystal. Biochim Biophys Acta BBA - Gen Subj 1989;992:155–9. https://doi.org/10.1016/0304-4165(89)90004-4.

[114] Bonar LC, Roufosse AH, Sabine WK, Grynpas MD, Glimcher MJ. X-ray diffraction studies of the crystallinity of bone mineral in newly synthesized and density fractionated bone. Calcif Tissue Int 1983;35:202–9. https://doi.org/10.1007/BF02405032.

[115] Kiebzak GM. Age-related bone changes. Exp Gerontol 1991;26:171–87. https://doi.org/10.1016/0531-5565(91)90010-J.

[116] Molnar Z. Development of the parietal bone of young mice: 1. Crystals of bone mineral in frozen-dried preparations. J Ultrastruct Res 1959;3:39–45. https://doi.org/10.1016/S0022-5320(59)80012-5.

[117] Thyberg J. Electron microscopic studies on the initial phases of calcification in guinea pig epiphyseal cartilage. J Ultrastruct Res 1974;46:206–18. https://doi.org/10.1016/S0022-5320(74)80056-0.

[118] Gay CV. The ultrastructure of the extracellular phase of bone as observed in frozen thin sections. Calcif Tissue Res 1977;23:215–23. https://doi.org/10.1007/BF02012788.

[119] Eanes ED. The interaction of supersaturated calcium phosphate solutions with apatitic substrates. Calcif Tissue Res 1976;20:75–89. https://doi.org/10.1007/BF02546399.

[120] Wang Y, Von Euw S, Fernandes FM, Cassaignon S, Selmane M, Laurent G, et al. Water-mediated structuring of bone apatite. Nat Mater 2013;12:1144–53. https://doi.org/10.1038/nmat3787.

[121] Weiner S, Sagi I, Addadi L. Choosing the crystallization path less traveled. Science 2005;309:1027–8. https://doi.org/10.1126/science.1114920.

[122] Termine JD, Eanes ED. Calcium phosphate deposition from balanced salt solutions. Calcif Tissue Res 1974;15:81–4. https://doi.org/10.1007/BF02059046.

[123] Addadi L, Gal A, Faivre D, Scheffel A, Weiner S. Control of biogenic nanocrystal formation in biomineralization. Isr J Chem 2016;56:227–41. https://doi.org/10.1002/ijch.201500038.

[124] Crane NJ, Popescu V, Morris MD, Steenhuis P, Ignelzi MA. Raman spectroscopic evidence for octacalcium phosphate and other transient mineral species deposited during intramembranous mineralization. Bone 2006;39:434–42. https://doi.org/10.1016/j.bone.2006.02.059.

[125] Brown WE. Crystal growth of bone mineral. Clin Orthop 1966;44:205–20.

[126] Brown WE, Eidelman N, Tomazic B. Octacalcium phosphate as a precursor in biomineral formation. Adv Dent Res 1987;1:306–13. https://doi.org/10.1177/08959374870010022201.

[127] Brown WE, Chow LC. Chemical properties of bone mineral. Annu Rev Mater Sci 1976;6:213–36. https://doi.org/10.1146/annurev.ms.06.080176.001241.

[128] Weiner S. Transient precursor strategy in mineral formation of bone. Bone 2006;39:431–3. https://doi.org/10.1016/j.bone.2006.02.058.

[129] Grynpas MD, Omelon S. Transient precursor strategy or very small biological apatite crystals? Bone 2007;41:162–4. https://doi.org/10.1016/j.bone.2007.04.176.

[130] Mahamid J, Sharir A, Addadi L, Weiner S. Amorphous calcium phosphate is a major component of the forming fin bones of zebrafish: Indications for an amorphous precursor phase. Proc Natl Acad Sci U S A 2008;105:12748–53. https://doi.org/10.1073/pnas.0803354105.

[131] Mahamid J, Aichmayer B, Shimoni E, Ziblat R, Li C, Siegel S, et al. Mapping amorphous calcium phosphate transformation into crystalline mineral from the cell to the bone in zebrafish fin rays. Proc Natl Acad Sci 2010;107:6316–21. https://doi.org/10.1073/pnas.0914218107.

[132] Akiva A, Malkinson G, Masic A, Kerschnitzki M, Bennet M, Fratzl P, et al. On the pathway of mineral deposition in larval zebrafish caudal fin bone. Bone 2015;75:192–200. https://doi.org/10.1016/j.bone.2015.02.020.

[133] Kerschnitzki M, Akiva A, Ben Shoham A, Asscher Y, Wagermaier W, Fratzl P, et al. Bone mineralization pathways during the rapid growth of embryonic chicken long bones. J Struct Biol 2016;195:82–92. https://doi.org/10.1016/j.jsb.2016.04.011.

[134] Nudelman F, Pieterse K, George A, Bomans PHH, Friedrich H, Brylka LJ, et al. The role of collagen in bone apatite formation in the presence of hydroxyapatite nucleation inhibitors. Nat Mater 2010;9:1004–9. https://doi.org/10.1038/nmat2875.

[135] Wang Y, Azaïs T, Robin M, Vallée A, Catania C, Legriel P, et al. The predominant role of collagen in the nucleation, growth, structure and orientation of bone apatite. Nat Mater 2012;11:724–33. https://doi.org/10.1038/nmat3362.

[136] Alexander B, Daulton TL, Genin GM, Lipner J, Pasteris JD, Wopenka B, et al. The nanometre-scale physiology of bone: steric modelling and scanning transmission electron microscopy of collagen–mineral structure. J R Soc Interface 2012;9:1774–86. https://doi.org/10.1098/rsif.2011.0880.

[137] Tertuliano OA, Greer JR. The nanocomposite nature of bone drives its strength and damage resistance. Nat Mater 2016;15:1195–202. https://doi.org/10.1038/nmat4719.

[138] Beniash E, Metzler RA, Lam RSK, Gilbert PUPA. Transient amorphous calcium phosphate in forming enamel. J Struct Biol 2009;166:133–43. https://doi.org/10.1016/j.jsb.2009.02.001.

[139] Bechtle S, Habelitz S, Klocke A, Fett T, Schneider GA. The fracture behaviour of dental enamel. Biomaterials 2010;31:375–84. https://doi.org/10.1016/j.biomaterials.2009.09.050.

[140] Palmer LC, Newcomb CJ, Kaltz SR, Spoerke ED, Stupp SI. Biomimetic systems for hydroxyapatite mineralization inspired by bone and enamel. Chem Rev 2008;108:4754–83. https://doi.org/10.1021/cr8004422.

[141] Hu JC-C, Sun X, Zhang C, Simmer JP. A comparison of enamelin and amelogenin expression in developing mouse molars. Eur J Oral Sci 2001;109:125–32. https://doi.org/10.1034/j.1600-0722.2001.00998.x.

[142] Simmer JP, Papagerakis P, Smith CE, Fisher DC, Rountrey AN, Zheng L, et al. Regulation of Dental Enamel Shape and Hardness. J Dent Res 2010;89:1024–38. https://doi.org/10.1177/0022034510375829.

[143] Weiner S, Lowenstam H. Organization of Extracellularly Mineralized Tissues: A Comparative Study of Biological Crystal Growt. Crit Rev Biochem 1986;20:365–408. https://doi.org/10.3109/10409238609081998.

[144] Kwak S-Y, Wiedemann-Bidlack FB, Beniash E, Yamakoshi Y, Simmer JP, Litman A, et al. Role of 20-kDa amelogenin (P148) phosphorylation in calcium phosphate formation in vitro. J Biol Chem 2009;284:18972–9. https://doi.org/10.1074/jbc.M109.020370.

[145] Iijima M, Fan D, Bromley KM, Sun Z, Moradian-Oldak J. Tooth enamel proteins enamelin and amelogenin cooperate to regulate the growth morphology of octacalcium phosphate crystals. Cryst Growth Des 2010;10:4815–22. https://doi.org/10.1021/cg100696r.

[146] Yang X, Wang L, Qin Y, Sun Z, Henneman ZJ, Moradian-Oldak J, et al. How amelogenin orchestrates the organization of hierarchical elongated microstructures of apatite. J Phys Chem B 2010;114:2293–300. https://doi.org/10.1021/jp910219s.

[147] Fang P-A, Conway JF, Margolis HC, Simmer JP, Beniash E. Hierarchical self-assembly of amelogenin and the regulation of biomineralization at the nanoscale. Proc Natl Acad Sci U S A 2011;108:14097–102. https://doi.org/10.1073/pnas.1106228108.

[148] Simmer JP, Richardson AS, Hu Y-Y, Smith CE, Hu JC-C. A post-classical theory of enamel biomineralization… and why we need one. Int J Oral Sci 2012;4:129–34. https://doi.org/10.1038/ijos.2012.59.

[149] Gordon LM, Cohen MJ, MacRenaris KW, Pasteris JD, Seda T, Joester D. Amorphous intergranular phases control the properties of rodent tooth enamel. Science 2015;347:746–50. https://doi.org/10.1126/science.1258950.

[150] Fontaine AL, Zavgorodniy A, Liu H, Zheng R, Swain M, Cairney J. Atomic-scale compositional mapping reveals Mg-rich amorphous calcium phosphate in human dental enamel. Sci Adv 2016;2:e1601145. https://doi.org/10.1126/sciadv.1601145.

[151] Powell JJ, Thomas-McKay E, Thoree V, Robertson J, Hewitt RE, Skepper JN, et al. An endogenous nanomineral chaperones luminal antigen and peptidoglycan to intestinal immune cells. Nat Nanotechnol 2015;10:361–9. https://doi.org/10.1038/nnano.2015.19.

[152] Söderholm JD. Gut immunology: nanoparticles ferry gut antigens. Nat Nanotechnol 2015;10:298–9. https://doi.org/10.1038/nnano.2015.58.

[153] Lomer MCE, Thompson RPH, Powell JJ. Fine and ultrafine particles of the diet: influence on the mucosal immune response and association with Crohn's disease. Proc Nutr Soc 2002;61:123–30. https://doi.org/10.1079/PNS2001134.

[154] Schedl HP, Osbaldiston GW, Mills IH. Role of intraluminal precipitation in secretion of small intestinal calcium and phosphate in the dog. Nature 1967;215:198–9. https://doi.org/10.1038/215198b0.

[155] Schedl H, Osbaldiston G, Mills I. Absorption, secretion, and precipitation of calcium in the small intestine of the dog. Am J Physiol-Leg Content 1968;214:814–9. https://doi.org/10.1152/ajplegacy.1968.214.4.814.

[156] Powell JJ, Whitehead MW, Ainley CC, Kendall MD, Nicholson JK, Thompson RPH. Dietary minerals in the gastrointestinal tract: hydroxypolymerisation of aluminium is regulated by luminal mucins. J Inorg Biochem 1999;75:167–80. https://doi.org/10.1016/S0162-0134(99)00094-X.

[157] Powell JJ, Thoree V, Pele LC. Dietary microparticles and their impact on tolerance and immune responsiveness of the gastrointestinal tract. Br J Nutr 2007;98:S59–63. https://doi.org/10.1017/S0007114507832922.

[158] Powell JJ, Faria N, Thomas-McKay E, Pele LC. Origin and fate of dietary nanoparticles and microparticles in the gastrointestinal tract. J Autoimmun 2010;34:J226–33. https://doi.org/10.1016/j.jaut.2009.11.006.

[159] Gelli R, Scudero M, Gigli L, Severi M, Bonini M, Ridi F, et al. Effect of pH and Mg2+ on amorphous magnesium-calcium phosphate (AMCP) stability. J Colloid Interface Sci 2018. https://doi.org/10.1016/j.jcis.2018.07.102.

[160] Gelli R, Tempesti P, Ridi F, Baglioni P. Formation and properties of amorphous magnesium-calcium phosphate particles in a simulated intestinal fluid. J Colloid Interface Sci 2019;546:130–8. https://doi.org/10.1016/j.jcis.2019.03.060.

[161] Robertson J, Haas CT, Pele LC, Monie TP, Charalambos C, Parkes M, et al. Intestinal APCs of the endogenous nanomineral pathway fail to express PD-L1 in Crohn's disease. Sci Rep 2016;6. https://doi.org/10.1038/srep26747.

[162] Hewitt RE, Robertson J, Haas CT, Pele LC, Powell JJ. Reduction of T-Helper cell responses to recall antigen mediated by codelivery with peptidoglycan via the intestinal nanomineral–antigen pathway. Front Immunol 2017;8. https://doi.org/10.3389/fimmu.2017.00284.

[163] Pele LC, Haas CT, Hewitt RE, Robertson J, Skepper J, Brown A, et al. Synthetic mimetics of the endogenous gastrointestinal nanomineral: Silent constructs that

trap macromolecules for intracellular delivery. Nanomedicine Nanotechnol Biol Med 2017;13:619–30. https://doi.org/10.1016/j.nano.2016.07.008.
[164] Pan H, Zhao X, Darvell BW, Lu WW. Apatite-formation ability – Predictor of "bioactivity"? Acta Biomater 2010;6:4181–8. https://doi.org/10.1016/j.actbio.2010.05.013.
[165] Giachelli CM. Ectopic Calcification. Am J Pathol 1999;154:671–5. https://doi.org/10.1016/S0002-9440(10)65313-8.
[166] Cai MMX, Smith ER, Holt SG. The role of fetuin-A in mineral trafficking and deposition. BoneKEy Rep 2015;4:672. https://doi.org/10.1038/bonekey.2015.39.
[167] Ketteler M, Bongartz P, Westenfeld R, Wildberger JE, Mahnken AH, Böhm R, et al. Association of low fetuin-A (AHSG) concentrations in serum with cardiovascular mortality in patients on dialysis: a cross-sectional study. The Lancet 2003;361:827–33. https://doi.org/10.1016/S0140-6736(03)12710-9.
[168] Heiss A, DuChesne A, Denecke B, Grötzinger J, Yamamoto K, Renné T, et al. Structural basis of calcification inhibition by α2-HS Glycoprotein/Fetuin-A. Formation of colloidal calciprotein particles. J Biol Chem 2003;278:13333–41. https://doi.org/10.1074/jbc.M210868200.
[169] Schäfer C, Heiss A, Schwarz A, Westenfeld R, Ketteler M, Floege J, et al. The serum protein α2–Heremans-Schmid glycoprotein/fetuin-A is a systemically acting inhibitor of ectopic calcification. J Clin Invest 2003;112:357–66. https://doi.org/10.1172/JCI200317202.
[170] Price PA, Thomas GR, Pardini AW, Figueira WF, Caputo JM, Williamson MK. Discovery of a high molecular weight complex of calcium, phosphate, fetuin, and matrix γ-carboxyglutamic acid protein in the serum of etidronate-treated rats. J Biol Chem 2002;277:3926–34. https://doi.org/10.1074/jbc.M106366200.
[171] Heiss A, Jahnen-Dechent W, Endo H, Schwahn D. Structural dynamics of a colloidal protein-mineral complex bestowing on calcium phosphate a high solubility in biological fluids. Biointerphases 2007;2:16–20. https://doi.org/10.1116/1.2714924.
[172] Smith ER, Hanssen E, McMahon LP, Holt SG. Fetuin-A-containing calciprotein particles reduce mineral stress in the macrophage. PLoS One 2013;8:e60904. https://doi.org/10.1371/journal.pone.0060904.
[173] Holt SG, Smith ER. Fetuin-A-containing calciprotein particles in mineral trafficking and vascular disease. Nephrol Dial Transplant Off Publ Eur Dial Transpl Assoc - Eur Ren Assoc 2016;31:1583–7. https://doi.org/10.1093/ndt/gfw048.
[174] Rochette CN, Rosenfeldt S, Heiss A, Narayanan T, Ballauff M, Jahnen-Dechent W. A Shielding topology stabilizes the early stage protein–mineral complexes of fetuin-A and calcium phosphate: a time-resolved small-angle X-ray study. ChemBioChem 2009;10:735–40. https://doi.org/10.1002/cbic.200800719.
[175] Wald J, Wiese S, Eckert T, Jahnen-Dechent W, Richtering W, Heiss A. Formation and stability kinetics of calcium phosphate–fetuin-A colloidal particles probed by time-resolved dynamic light scattering. Soft Matter 2011;7:2869–74. https://doi.org/10.1039/C0SM01191F.
[176] Pasch A, Farese S, Gräber S, Wald J, Richtering W, Floege J, et al. Nanoparticle-Based test measures overall propensity for calcification in serum. J Am Soc Nephrol 2012;23:1744–52. https://doi.org/10.1681/ASN.2012030240.
[177] Pruijm M, Lu Y, Megdiche F, Piskunowicz M, Milani B, Stuber M, et al. Serum calcification propensity is associated with renal tissue oxygenation and resistive index in patients with arterial hypertension or chronic kidney disease. J Hypertens 2017;35:2044. https://doi.org/10.1097/HJH.0000000000001406.
[178] Dahdal S, Devetzis V, Chalikias G, Tziakas D, Chizzolini C, Ribi C, et al. Serum calcification propensity is independently associated with disease activity in systemic lupus erythematosus. PLoS One 2018;13:e0188695. https://doi.org/10.1371/journal.pone.0188695.
[179] Matsui I, Hamano T, Mikami S, Fujii N, Takabatake Y, Nagasawa Y, et al. Fully phosphorylated fetuin-A forms a mineral complex in the serum of rats with adenine-induced renal failure. Kidney Int 2009;75:915–28. https://doi.org/10.1038/ki.2008.700.
[180] Hamano T, Matsui I, Mikami S, Tomida K, Fujii N, Imai E, et al. Fetuin-Mineral complex reflects extraosseous calcification stress in CKD. J Am Soc Nephrol 2010;21:1998–2007. https://doi.org/10.1681/ASN.2009090944.
[181] Smith ER, Ford ML, Tomlinson LA, Rajkumar C, McMahon LP, Holt SG. Phosphorylated fetuin-A-containing calciprotein particles are associated with aortic stiffness and a procalcific milieu in patients with pre-dialysis CKD. Nephrol Dial Transplant 2012;27:1957–66. https://doi.org/10.1093/ndt/gfr609.
[182] Wong T-Y, Wu C-Y, Martel J, Lin C-W, Hsu F-Y, Ojcius DM, et al. Detection and characterization of mineralo-organic nanoparticles in human kidneys. Sci Rep 2015;5:15272. https://doi.org/10.1038/srep15272.
[183] Persy V, D'Haese P. Vascular calcification and bone disease: the calcification paradox. Trends Mol Med 2009;15:405–16. https://doi.org/10.1016/j.molmed.2009.07.001.
[184] Cai MMX, Smith ER, Tan S-J, Hewitson TD, Holt SG. The Role of Secondary Calciprotein Particles in the Mineralisation Paradox of Chronic Kidney Disease. Calcif Tissue Int 2017;101:570–80. https://doi.org/10.1007/s00223-017-0313-0.
[185] Yamada H, Kuro-o M, Ishikawa S, Funazaki S, Kusaka I, Kakei M, et al. Daily variability in serum levels of calciprotein particles and their association with mineral metabolism parameters: a cross-sectional pilot study. Nephrology 2018;23:226–30. https://doi.org/10.1111/nep.12994.
[186] Shook LL, Buhimschi CS, Dulay AT, McCarthy ME, Hardy JT, Buniak CMD, et al. Calciprotein particles as potential etiologic agents of idiopathic preterm birth. Sci Transl Med 2016;8:364ra154. https://doi.org/10.1126/scitranslmed.aah4707.
[187] Martel J, Wu C-Y, Peng H-H, Young JD. Mineralo-organic nanoparticles in health and disease: an overview of recent findings. Nanomed 2018. https://doi.org/10.2217/nnm-2018-0108.
[188] Aghagolzadeh P, Bachtler M, Bijarnia R, Jackson C, Smith ER, Odermatt A, et al. Calcification of vascular smooth muscle cells is induced by secondary calciprotein particles and enhanced by tumor necrosis factor-α. Atherosclerosis 2016;251:404–14. https://doi.org/10.1016/j.atherosclerosis.2016.05.044.
[189] Martin CR, Ling P-R, Blackburn GL. Review of Infant Feeding: Key Features of Breast Milk and Infant Formula. Nutrients 2016;8. https://doi.org/10.3390/nu8050279.
[190] Liao Y, Weber D, Xu W, Durbin-Johnson BP, Phinney BS, Lönnerdal B. Absolute quantification of human milk caseins and the whey/casein ratio during the first year of lactation. J Proteome Res 2017;16:4113–21. https://doi.org/10.1021/acs.jproteome.7b00486.
[191] Van Kemenade MJJM, de Bruyn PL. The influence of casein on the kinetics of hydroxyapatite precipitation. J Colloid Interface Sci 1989;129:1–14. https://doi.org/10.1016/0021-9797(89)90411-6.
[192] Holt C, Carver JA, Ecroyd H, Thorn DC. Invited review: caseins and the casein micelle: Their biological functions, structures, and behavior in foods. J Dairy Sci 2013;96:6127–46. https://doi.org/10.3168/jds.2013-6831.
[193] Lenton S, Nylander T, Teixeira SCM, Holt C. A review of the biology of calcium phosphate sequestration with special reference to milk. Dairy Sci Technol 2015;95:3–14. https://doi.org/10.1007/s13594-014-0177-2.
[194] Holt C. Unfolded phosphopolypeptides enable soft and hard tissues to coexist in the same organism with relative ease. Curr Opin Struct Biol 2013;23:420–5. https://doi.org/10.1016/j.sbi.2013.02.010.
[195] Dalgleish DG. On the structural models of bovine casein micelles—review and possible improvements. Soft Matter 2011;7:2265–72. https://doi.org/10.1039/C0SM00806K.
[196] de Kruif CG, Huppertz T, Urban VS, Petukhov AV. Casein micelles and their internal structure. Adv Colloid Interface Sci 2012;171–172:36–52. https://doi.org/10.1016/j.cis.2012.01.002.
[197] Horne DS. Casein structure, self-assembly and gelation. Curr Opin Colloid Interface Sci 2002;7:456–61. https://doi.org/10.1016/S1359-0294(02)00082-1.
[198] Kruif CGD, Holt C. Casein micelle structure, functions and interactions. Adv. dairy chem. proteins. Boston, MA: Springer; 2003. p. 233–76. https://doi.org/10.1007/978-1-4419-8602-3_5.
[199] Horne DS. Casein micelle structure: models and muddles. Curr Opin Colloid Interface Sci 2006;11:148–53. https://doi.org/10.1016/j.cocis.2005.11.004.
[200] Fox PF, Brodkorb A. The casein micelle: Historical aspects, current concepts and significance. Int Dairy J 2008;18:677–84. https://doi.org/10.1016/j.idairyj.2008.03.002.
[201] Kruif CGD. The structure of casein micelles: a review of small-angle scattering data. J Appl Cryst 2014;47:1479–89. https://doi.org/10.1107/S1600576714014563.
[202] Marchin S, Putaux J-L, Pignon F, Léonil J. Effects of the environmental factors on the casein micelle structure studied by cryo transmission electron microscopy and small-angle x-ray scattering/ultrasmall-angle x-ray scattering. J Chem Phys 2007;126:045101. https://doi.org/10.1063/1.2409933.
[203] Minniti F, Comberiati P, Munblit D, Piacentini GL, Antoniazzi E, Zanoni L, et al. Breast-milk characteristics protecting against allergy. Endocrine, metabolic & immune disorders-drug targets (formerly current drug targets-immune, endocrine & metabolic disorders), vol. 14. ; 2014. p. 9–15. https://doi.org/10.2174/1871530314666140121145045.
[204] Walker WA, Iyengar RS. Breast milk, microbiota, and intestinal immune homeostasis. Pediatr Res 2017;77:220–8. https://doi.org/10.1038/pr.2014.160.
[205] Mosconi E, Rekima A, Seitz-Polski B, Kanda A, Fleury S, Tissandie E, et al. Breast milk immune complexes are potent inducers of oral tolerance in neonates and prevent asthma development. Mucosal Immunol 2010;3:461–74. https://doi.org/10.1038/mi.2010.23.
[206] Albee FH. Studies in bone growth - triple calcium phosphate as a stimulus to osteogenesis. Ann Surg 1920;71(1):32–9.
[207] Dorozhkin SV. Calcium orthophosphate bioceramics. Ceram Int 2015;41:13913–66. https://doi.org/10.1016/j.ceramint.2015.08.004.
[208] Eliaz N, Metoki N. Calcium phosphate bioceramics: a review of their history, structure, properties, coating technologies and biomedical applications. Materials 2017;10. https://doi.org/10.3390/ma10040334.
[209] Dorozhkin SV. Self-Setting calcium orthophosphate formulations: cements, concretes, pastes and putties. Int J Mater Chem 2012;1:1–48. https://doi.org/10.5923/j.ijmc.20110101.01.
[210] Zhang J, Liu W, Schnitzler V, Tancret F, Bouler J-M. Calcium phosphate cements for bone substitution: chemistry, handling and mechanical properties. Acta Biomater 2014;10:1035–49. https://doi.org/10.1016/j.actbio.2013.11.001.
[211] Tempesti P, Nicotera GS, Bonini M, Fratini E, Baglioni P. Poly(N-isopropylacrylamide)-hydroxyapatite nanocomposites as thermoresponsive filling materials on dentinal surface and tubules. J Colloid Interface Sci 2018;509:123–31. https://doi.org/10.1016/j.jcis.2017.09.001.
[212] Habraken W, Habibovic P, Epple M, Bohner M. Calcium phosphates in biomedical applications: materials for the future? Mater Today 2016;19:69–87. https://doi.org/10.1016/j.mattod.2015.10.008.
[213] Tung M, Eichmiller F. Dental applications of amorphous calcium phosphates. J Clin Dent 1999;10:1–6.
[214] Zhao J, Liu Y, Sun W, Zhang H. Amorphous calcium phosphate and its application in dentistry. Chem Cent J 2011;5:40. https://doi.org/10.1186/1752-153X-5-40.
[215] Divyapriya GK, Yavagal PC, Veeresh DJ. Casein phosphopeptide-amorphous calcium phosphate in dentistry: An update. Int J Oral Health Sci 2016;6:18–25. https://doi.org/10.4103/2231-6027.186660.
[216] Reynolds EC. Remineralization of enamel subsurface lesions by casein phosphopeptide-stabilized calcium phosphate solutions. J Dent Res 1997;76:1587–95. https://doi.org/10.1177/00220345970760091101.
[217] Reynolds EC, Cai F, Cochrane NJ, Shen P, Walker GD, Morgan MV, et al. Fluoride and casein phosphopeptide-amorphous calcium phosphate. J Dent Res 2008;87:344–8. https://doi.org/10.1177/154405910808700420.

[218] Chhabra N, Chhabra A. Enhanced remineralisation of tooth enamel using casein phosphopeptide-amorphous calcium phosphate complex: a review. Int J Clin Prev Dent 2018;14:1–10. https://doi.org/10.15236/ijcpd.2018.14.1.1.

[219] Gurunathan D, Somasundaram S, Kumar S. Casein phosphopeptide-amorphous calcium phosphate: a remineralizing agent of enamel: CPP-ACP. Aust Dent J 2012;57: 404–8. https://doi.org/10.1111/adj.12006.

[220] Azarpazhooh A, Limeback H. Clinical Efficacy of casein derivatives. J Am Dent Assoc 2008;139:915–24. https://doi.org/10.14219/jada.archive.2008.0278.

[221] Hani TB, O'Connell AC, Duane B. Casein phosphopeptide-amorphous calcium phosphate products in caries prevention. Evid Based Dent 2016;17:46. https://doi.org/10.1038/sj.ebd.6401168.

[222] Rechmann P, Bekmezian S, Rechmann BMT, Chaffee BW, Featherstone JDB. MI Varnish and MI Paste Plus in a caries prevention and remineralization study: a randomized controlled trial. Clin Oral Investig 2018;22:2229–39. https://doi.org/10.1007/s00784-017-2314-9.

[223] Mendes AC, Restrepo M, Bussaneli D, Zuanon AC. Use of casein amorphous calcium phosphate (CPP-ACP) on white-spot lesions: randomised clinical trial. Oral Health Prev Dent 2018:27–31. https://doi.org/10.3290/j.ohpd.a39749.

[224] Skrtic D, Antonucci JM, Eanes ED. Improved properties of amorphous calcium phosphate fillers in remineralizing resin composites. Dent Mater 1996;12:295–301. https://doi.org/10.1016/S0109-5641(96)80037-6.

[225] Skrtic D, Antonucci JM, Eanes ED, Eichmiller FC, Schumacher GE. Physicochemical evaluation of bioactive polymeric composites based on hybrid amorphous calcium phosphates. J Biomed Mater Res 2000;53:381–91. https://doi.org/10.1002/1097-4636(2000)53:4<381::AID-JBM12>3.0.CO;2-H.

[226] Skrtic D, Hailer AW, Takagi S, Antonucci JM, Eanes ED. Quantitative assessment of the efficacy of amorphous calcium phosphate/methacrylate composites in remineralizing caries-like lesions artificially produced in bovine enamel. J Dent Res 1996;75:1679–86. https://doi.org/10.1177/00220345960750091001.

[227] Weir MD, Chow LC, Xu HHK. Remineralization of demineralized enamel via calcium phosphate nanocomposite. J Dent Res 2012;91:979–84. https://doi.org/10.1177/0022034512458288.

[228] Melo MAS, Weir MD, Rodrigues LKA, Xu HHK. Novel calcium phosphate nanocomposite with caries-inhibition in a human in situ model. Dent Mater 2013;29: 231–40. https://doi.org/10.1016/j.dental.2012.10.010.

[229] Weir MD, Ruan J, Zhang N, Chow LC, Zhang K, Chang X, et al. Effect of calcium phosphate nanocomposite on in vitro remineralization of human dentin lesions. Dent Mater 2017;33:1033–44. https://doi.org/10.1016/j.dental.2017.06.015.

[230] Liu Y, Zhang L, Niu L, Yu T, Xu HHK, Weir MD, et al. Antibacterial and remineralizing orthodontic adhesive containing quaternary ammonium resin monomer and amorphous calcium phosphate nanoparticles. J Dent 2018;72:53–63. https://doi.org/10.1016/j.jdent.2018.03.004.

[231] Al-Dulaijan YA, Cheng L, Weir MD, Melo MAS, Liu H, Oates TW, et al. Novel rechargeable calcium phosphate nanocomposite with antibacterial activity to suppress biofilm acids and dental caries. J Dent 2018;72:44–52. https://doi.org/10.1016/j.jdent.2018.03.003.

[232] Song J, Wang H, Yang Y, Xiao Z, Lin H, Jin L, et al. Nanogels of carboxymethyl chitosan and lysozyme encapsulated amorphous calcium phosphate to occlude dentinal tubules. J Mater Sci Mater Med 2018;29. https://doi.org/10.1007/s10856-018-6094-9.

[233] Schemehorn B, Wood G, McHale W, Winston A. Comparison of fluoride uptake into tooth enamel from two fluoride varnishes containing different calcium phosphate sources. J Clin Dent 2011;22:51–4.

[234] Foster JA, Berzins DW, Bradley TG. Bond strength of an amorphous calcium phosphate–containing orthodontic adhesive. Angle Orthod 2008;78:339–44. https://doi.org/10.2319/020807-60.

[235] Minick GT, Oesterle LJ, Newman SM, Shellhart WC. Bracket bond strengths of new adhesive systems. Am J Orthod Dentofacial Orthop 2009;135:771–6. https://doi.org/10.1016/j.ajodo.2007.06.021.

[236] Surmenev RA, Surmeneva MA, Ivanova AA. Significance of calcium phosphate coatings for the enhancement of new bone osteogenesis – a review. Acta Biomater 2014;10:557–79. https://doi.org/10.1016/j.actbio.2013.10.036.

[237] de Bruijn JD, Bovell YP, van Blitterswijk CA. Structural arrangements at the interface between plasma sprayed calcium phosphates and bone. Biomaterials 1994;15: 543–50. https://doi.org/10.1016/0142-9612(94)90021-3.

[238] Nagano M, Nakamura T, Kokubo T, Tanahashi M, Ogawa M. Differences of bone bonding ability and degradation behaviour in vivo between amorphous calcium phosphate and highly crystalline hydroxyapatite coating. Biomaterials 1996;17: 1771–7. https://doi.org/10.1016/0142-9612(95)00357-6.

[239] Frayssinet P, Tourenne F, Rouquet N, Conte P, Delga C, Bonel G. Comparative biological properties of HA plasma-sprayed coatings having different crystallinities. J Mater Sci Mater Med 1994;5:11–7. https://doi.org/10.1007/BF00121147.

[240] dos Santos EA, Moldovan S, Mateescu M, Faerber J, Acosta M, Pelletier H, et al. Physical–chemical and biological behavior of an amorphous calcium phosphate thin film produced by RF-magnetron sputtering. Mater Sci Eng C 2012;32: 2086–95. https://doi.org/10.1016/j.msec.2012.05.041.

[241] Hu Q, Tan Z, Liu Y, Tao J, Cai Y, Zhang M, et al. Effect of crystallinity of calcium phosphate nanoparticles on adhesion, proliferation, and differentiation of bone marrow mesenchymal stem cells. J Mater Chem 2007;17:4690–8. https://doi.org/10.1039/B710936A.

[242] Brugge PJT, Wolke JGC, Jansen JA. Effect of calcium phosphate coating composition and crystallinity on the response of osteogenic cells in vitro. Clin Oral Implants Res 2003;14:472–80. https://doi.org/10.1034/j.1600-0501.2003.00886.x.

[243] Berube P, Yang Y, Carnes DL, Stover RE, Boland EJ, Ong JL. The Effect of sputtered calcium phosphate coatings of different crystallinity on osteoblast differentiation. J Periodontol 2005;76:1697–709. https://doi.org/10.1902/jop.2005.76.10.1697.

[244] Samavedi S, Whittington AR, Goldstein AS. Calcium phosphate ceramics in bone tissue engineering: A review of properties and their influence on cell behavior. Acta Biomater 2013;9:8037–45. https://doi.org/10.1016/j.actbio.2013.06.014.

[245] Xu L-C, Siedlecki CA. Effects of surface wettability and contact time on protein adhesion to biomaterial surfaces. Biomaterials 2007;28:3273–83. https://doi.org/10.1016/j.biomaterials.2007.03.032.

[246] Gentleman MM, Gentleman E. The role of surface free energy in osteoblast–biomaterial interactions. Int Mater Rev 2017;59:417–29. https://doi.org/10.1179/1743280414Y.0000000038.

[247] Hallab NJ, Bundy KJ, O'Connor K, Clark R, Moses RL. Cell adhesion to biomaterials: correlations between surface charge, surface roughness, adsorbed protein, and cell morphology. J Long Term Eff Med Implants 1995;5:209–31.

[248] Tofighi A, Mounic S, Chakravarthy P, Rey C, Lee D. Setting reactions involved in injectable cements based on amorphous calcium phosphate. Key Eng Mater 2001;192–195:769–72. https://doi.org/10.4028/www.scientific.net/KEM.192-195.769.

[249] Wang X, Ye J, Wang H. Effects of additives on the rheological properties and injectability of a calcium phosphate bone substitute material. J Biomed Mater Res B Appl Biomater 2006;78:259–64. https://doi.org/10.1002/jbm.b.30481.

[250] Li RH, Bouxsein ML, Blake CA, D'Augusta D, Kim H, Li XJ, et al. rhBMP-2 injected in a calcium phosphate paste (alpha-BSM) accelerates healing in the rabbit ulnar osteotomy model. J Orthop Res Off Publ Orthop Res Soc 2003;21:997–1004. https://doi.org/10.1016/S0736-0266(03)00082-2.

[251] Miranda DAO, Blumenthal NM, Sorensen RG, Wozney JM, Wikesjö UME. Evaluation of recombinant human bone morphogenetic protein-2 on the repair of alveolar ridge defects in baboons. J Periodontol 2005;76:210–20. https://doi.org/10.1902/jop.2005.76.2.210.

[252] Seeherman HJ, Azari K, Bidic S, Rogers L, Li XJ, Hollinger JO, et al. rhBMP-2 delivered in a calcium phosphate cement accelerates bridging of critical-sized defects in rabbit radii. J Bone Joint Surg Am 2006;88:1553–65. https://doi.org/10.2106/JBJS.E.01006.

[253] Mickiewicz RA, Mayes AM, Knaack D. Polymer–calcium phosphate cement composites for bone substitutes. J Biomed Mater Res 2002;61:581–92. https://doi.org/10.1002/jbm.10222.

[254] Wang X, Chen L, Xiang H, Ye J. Influence of anti-washout agents on the rheological properties and injectability of a calcium phosphate cement. J Biomed Mater Res B Appl Biomater 2007;81:410–8. https://doi.org/10.1002/jbm.b.30678.

[255] Wang X, Ye J, Wang Y. Influence of a novel radiopacifier on the properties of an injectable calcium phosphate cement. Acta Biomater 2007;3:757–63. https://doi.org/10.1016/j.actbio.2007.01.004.

[256] Wang X, Ye J. Variation of crystal structure of hydroxyapatite in calcium phosphate cement by the substitution of strontium ions. J Mater Sci Mater Med 2008;19: 1183–6. https://doi.org/10.1007/s10856-007-3209-0.

[257] Yu T, Ye J, Wang Y. Synthesis and property of a novel calcium phosphate cement. J Biomed Mater Res B Appl Biomater 2009;90:745–51. https://doi.org/10.1002/jbm.b.31343.

[258] Wang X, Ye J, Wang Y, Wu X, Bai B. Control of crystallinity of hydrated products in a calcium phosphate bone cement. J Biomed Mater Res A 2007;81:781–90. https://doi.org/10.1002/jbm.a.31059.

[259] Brunner TJ, Grass RN, Bohner M, Stark WJ. Effect of particle size, crystal phase and crystallinity on the reactivity of tricalcium phosphate cements for bone reconstruction. J Mater Chem 2007;17:4072–8. https://doi.org/10.1039/B707171J.

[260] Van den Vreken NMF, Pieters IY, Declercq HA, Cornelissen MJ, Verbeeck RMH. Characterization of calcium phosphate cements modified by addition of amorphous calcium phosphate. Acta Biomater 2010;6:617–25. https://doi.org/10.1016/j.actbio.2009.07.038.

[261] Oreffo RO, Driessens FC, Planell JA, Triffitt JT. Growth and differentiation of human bone marrow osteoprogenitors on novel calcium phosphate cements. Biomaterials 1998;19:1845–54. https://doi.org/10.1016/S0142-9612(98)00084-2.

[262] Ghosh S, Wu V, Pernal S, Uskoković V. Self-Setting calcium phosphate cements with tunable antibiotic release rates for advanced antimicrobial applications. ACS Appl Mater Interfaces 2016;8:7691–708. https://doi.org/10.1021/acsami.6b01160.

[263] Julien M, Khairoun I, LeGeros RZ, Delplace S, Pilet P, Weiss P, et al. Physico-chemical–mechanical and in vitro biological properties of calcium phosphate cements with doped amorphous calcium phosphates. Biomaterials 2007;28:956–65. https://doi.org/10.1016/j.biomaterials.2006.10.018.

[264] Shahrezaee M, Raz M, Shishehbor S, Moztarzadeh F, Baghbani F, Sadeghi A, et al. Synthesis of magnesium doped amorphous calcium phosphate as a bioceramic for biomedical application: in vitro study. Silicon 2018;10:1171–9. https://doi.org/10.1007/s12633-017-9589-y.

[265] Huang X, Yang D, Yan W, Shi Z, Feng J, Gao Y, et al. Osteochondral repair using the combination of fibroblast growth factor and amorphous calcium phosphate/poly (L-lactic acid) hybrid materials. Biomaterials 2007;28:3091–100. https://doi.org/10.1016/j.biomaterials.2007.03.017.

[266] Ma Z, Chen F, Zhu Y-J, Cui T, Liu X-Y. Amorphous calcium phosphate/poly(d,l-lactic acid) composite nanofibers: electrospinning preparation and biomineralization. J Colloid Interface Sci 2011;359:371–9. https://doi.org/10.1016/j.jcis.2011.04.023.

[267] Zhang H, Fu Q-W, Sun T-W, Chen F, Qi C, Wu J, et al. Amorphous calcium phosphate, hydroxyapatite and poly (d , l -lactic acid) composite nanofibers: electrospinning preparation, mineralization and in vivo bone defect repair. Colloids Surf B Biointerfaces 2015;136:27–36. https://doi.org/10.1016/j.colsurfb.2015.08.015.

[268] Niu X, Liu Z, Tian F, Chen S, Lei L, Jiang T, et al. Sustained delivery of calcium and orthophosphate ions from amorphous calcium phosphate and poly(L-lactic acid)-based electrospinning nanofibrous scaffold. Sci Rep 2017;7:45655. https://doi.org/10.1038/srep45655.

[269] Ding G-J, Zhu Y-J, Qi C, Lu B-Q, Chen F, Wu J. Porous hollow microspheres of amorphous calcium phosphate: soybean lecithin templated microwave-assisted hydrothermal synthesis and application in drug delivery. J Mater Chem B 2015;3:1823–30. https://doi.org/10.1039/C4TB01862A.
[270] Cheng L, Weir MD, Xu HHK, Antonucci JM, Kraigsley AM, Lin NJ, et al. Antibacterial amorphous calcium phosphate nanocomposites with a quaternary ammonium dimethacrylate and silver nanoparticles. Dent Mater 2012;28:561–72. https://doi.org/10.1016/j.dental.2012.01.005.
[271] Cheng L, Weir MD, Xu HHK, Antonucci JM, Lin NJ, Lin-Gibson S, et al. Effect of amorphous calcium phosphate and silver nanocomposites on dental plaque microcosm biofilms. J Biomed Mater Res B Appl Biomater 2012;100B:1378–86. https://doi.org/10.1002/jbm.b.32709.
[272] Melo MAS, Cheng L, Zhang K, Weir MD, Rodrigues LKA, Xu HHK. Novel dental adhesives containing nanoparticles of silver and amorphous calcium phosphate. Dent Mater 2013;29:199–210. https://doi.org/10.1016/j.dental.2012.10.005.
[273] Chen C, Weir MD, Cheng L, Lin NJ, Lin-Gibson S, Chow LC, et al. Antibacterial activity and ion release of bonding agent containing amorphous calcium phosphate nanoparticles. Dent Mater 2014;30:891–901. https://doi.org/10.1016/j.dental.2014.05.025.
[274] Wu J, Weir MD, Melo MAS, Xu HHK. Development of novel self-healing and antibacterial dental composite containing calcium phosphate nanoparticles. J Dent 2015;43:317–26. https://doi.org/10.1016/j.jdent.2015.01.009.
[275] Wu VM, Tang S, Uskoković V. Calcium phosphate nanoparticles as intrinsic inorganic antimicrobials: the antibacterial effect. ACS Appl Mater Interfaces 2018;10:34013–28. https://doi.org/10.1021/acsami.8b12784.

Paper V

Materials Science & Engineering C 95 (2019) 248–255

Contents lists available at ScienceDirect

Materials Science & Engineering C

journal homepage: www.elsevier.com/locate/msec

Tuning the properties of magnesium phosphate-based bone cements: Effect of powder to liquid ratio and aqueous solution concentration

Rita Gelli, Laura Mati, Francesca Ridi*, Piero Baglioni

Department of Chemistry "Ugo Schiff" and CSGI, University of Florence, via della Lastruccia 3, Sesto Fiorentino, 50019 Florence, Italy

ARTICLE INFO

Keywords:
Magnesium phosphate cements
Bone cements
Struvite
Crystallinity
Mechanical properties
Microstructure

ABSTRACT

The use of magnesium phosphate-based cements (MPCs) in the biomedical field has recently come under investigation in the scientific community, as these materials display many intriguing properties in the replacement and/or integration of calcium phosphate-based bone cements; however, the diverse preparation conditions reported in the literature make it difficult to evaluate how the modification of a specific parameter in the preparation of the paste affects the final properties of the material. In this paper, we prepared and characterized MPCs by mixing a tri-magnesium phosphate powder with a solution of di-ammonium hydrogen phosphate, so to form struvite as a final setting product. The powder to liquid ratio and the concentration of the aqueous solution were systematically varied, and their effect on the properties of the final product was studied. The handling properties of the pastes were investigated, as well as the crystallinity and the microstructure; the porosity and compressive strength of the final materials were also assessed. The multi-technique approach allowed us to relate the amount of formed struvite with the properties of the material, and to identify the preparation conditions to be used to obtain a cement with desired features.

1. Introduction

The development of new materials for the treatment of bone defects and diseases is a topic that has recently attracted great attention [1–3]. While traditional approaches include the use of autografts, allografts or xenografts, the research is nowadays focusing on the development of synthetic bone substitutes, able to partially overcome the drawbacks associated to the previously mentioned approaches [4]. Among synthetic materials, bone cements hold an important position and are currently used in the field of minimally invasive surgery as fillers for bone voids, to stabilize fractures and for the treatment of osteoporosis [5]. Bone cements are obtained by a chemical reaction between a solid and a liquid phase; upon mixing of the two components, the formation of a viscous and moldable paste occurs. This undergoes a chemical dissolution/precipitation reaction, and the entanglement of crystals precipitating within the paste causes the setting and hardening of the cement [6]. Bone cements are typically classified into four main categories, namely polymethylmethacrylate, calcium silicate, calcium sulphate and calcium phosphate-based [7]. An ideal bone cement should be not only biocompatible and bioresorbable, but it should also be endowed with several additional features: after mixing, the paste should be easily shaped and/or injected into the defect area, so to adapt to the surrounding bone [8]; furthermore, it should set at physiological conditions within 15 min and form a solid micro and macroporous material whose mechanical properties are compatible with bone [9]. Calcium phosphate-based cements (CPCs) probably represent the most widely investigated category of bone cements, given the resemblance to bone inorganic phase. CPCs are divided into brushite- or apatite-forming and display a number of interesting properties, such as biocompatibility, moderate bioresorbability and injectability [9]; however, some drawbacks exist. On the one hand, brushite-based cements require an acidic pH for setting and display poor mechanical properties, despite their good resorbability and rapid setting [10]. On the other hand, apatite-based CPCs set and resorb very slowly *in vivo*, even if they can achieve optimal compressive strengths [11].

It has been recently proposed that magnesium phosphate-based cements (MPCs) could be used as an alternative to CPCs, since they display a more efficient combination of mechanical properties, resorption rate and setting time than CPCs [12,13]. In addition, it is reported that Mg plays a key role in bone metabolism [14–16] and the release of Mg^{2+} ions enhances the activity of osteoclasts and osteoblasts [17]. MPCs have been used in the past for waste remediation [18,19] and structural engineering applications [20–23], and nowadays their use in the biomedical field is an emerging research area [24–28]. The first report about MPCs in the biomedical field dates back to 1995, when Driessens *et al.* described the implantation of three CPCs and one

* Corresponding author.
E-mail address: francesca.ridi@unifi.it (F. Ridi).

https://doi.org/10.1016/j.msec.2018.10.083
Received 20 April 2018; Received in revised form 24 September 2018; Accepted 23 October 2018
Available online 26 October 2018
0928-4931/

Table 1
Composition of prepared samples.

Sample	P/L (g/mL)	DAHP concentration [mol/L]	TMP [mg]	DAHP solution [μL]	DAHP [mmol]	Ratio mol TMP/mol DAHP	DAHP solution[a] [g]	DAHP [g]	Water [g]
0.5M_P/L 1	1.0	0.5	500.45	500	0.25	7.6	0.53	0.03	0.49
2.0M_P/L 1	1.0	2.0	500.85	501	1.00	1.9	0.58	0.13	0.44
3.5M_P/L 1	1.0	3.5	500.89	501	1.75	1.1	0.60	0.23	0.36
0.5M_P/L 1.5	1.5	0.5	500.62	334	0.17	11.4	0.35	0.02	0.33
2.0M_P/L 1.5	1.5	2.0	500.42	333	0.67	2.9	0.38	0.09	0.29
3.5M_P/L 1.5	1.5	3.5	500.46	333	1.17	1.6	0.40	0.15	0.24
0.5M_P/L 2	2.0	0.5	500.31	250	0.13	15.2	0.26	0.02	0.25
2.0M_P/L 2	2.0	2.0	500.25	250	0.50	3.8	0.29	0.07	0.22
3.5M_P/L 2	2.0	3.5	500.05	250	0.88	2.2	0.30	0.12	0.18

[a] The densities of the solutions used in the calculation were: 1.05 g/mL for DAHP 0.5 M, 1.15 g/mL for DAHP 2.0 M, 1.19 g/mL for DAHP 3.5 M (data obtained by weighting a known volume of each DAHP solution).

MPC in rats [29]; nevertheless, the majority of MPC research in this field has been conducted in the last decade [12].

For the preparation of MPCs, MgO (magnesium oxide) or $Mg_3(PO_4)_2$ (tri-magnesium phosphate, TMP) are typically used as powder components, while a variety of soluble phosphate salt solutions have been employed as liquid phase [13]. As reaction product, struvite ($MgNH_4PO_4{\cdot}6H_2O$) is often formed; for a detailed overview of all the possible reactions and products formed, the reader is referred elsewhere [12]. Focusing our attention on TMP-based systems, which have been explored to a lesser extent than MgO, in the literature we can find very different preparation conditions. Ewald *et al.* and Grossardt *et al.* prepared MPCs by mixing the powder component (TMP and struvite, 1:2 ratio by weight) with a 3.5 M solution of di-ammonium hydrogen phosphate ($(NH_4)_2HPO_4$, DAHP), using a powder to liquid ratio (P/L) of 2 g/mL [30,31]. Kanter *et al.* employed as a liquid phase a solution containing both $(NH_4)_2HPO_4$ and $NH_4H_2PO_4$, and mixed it with TMP at P/L of 2.0 and 3.0 g/mL [26,27]. A similar liquid composition was used by Klammert *et al.*, who reported an application of MPCs for the 3D printing: TMP was blended with 20% of $(NH_4)_2HPO_4$ powder and a solution 0.75 M $(NH_4)_2HPO_4$ and 0.75 M $(NH_4)H_2PO_4$ was used as liquid binder [32]. Remaining in the 3D printing field, Vorndran *et al.* combined TMP with 20% H_3PO_4, K_2HPO_4 2 M or $(NH_4)_2HPO_4$ 0.5 M (P/L 2 g/mL); the samples were then post-hardened in 20% phosphoric acid, 2 M K_2HPO_4 or 3.5 M $(NH_4)_2HPO_4$ solution, respectively [33]. Kim *et al.* extruded a TMP paste prepared with hydroxypropyl methylcellulose and ethanol, which was then post-hardened in an aqueous solution of 3.5 M DAHP [28,34]. Ostrowski *et al.* described the preparation of MPCs using amorphous, semi-crystalline and crystalline TMP mixed with a pH 7, 3.0 M solution of $NH_4H_2PO_4$ and $(NH_4)_2HPO_4$, and explored a variety of P/L (1:1, 1:2, 2:3, 3:2, 2:5) [35]. The P/L ratio was also varied by Moeske *et al.*, who prepared MPCs at P/L ratios from 1.0 to 3.3 g/mL using TMP and solutions of pure $(NH_4)_2HPO_4$ or mixtures of $(NH_4)_2HPO_4$ and di-ammonium citrate, with a total salt concentration of 3.5 M [36]. Recently, the group of Gbureck showed that by following high-energy ball milling of pure TMP, a nanocrystalline material forms, which reacts with water to form a cementitious material, without the addition of further reactants (in this case, the final product is $Mg_3(PO_4)_2{\cdot}22H_2O$) [37]. In the literature, we can also find some reports where TMP-based cements were investigated in combination with CPCs [38–40]. Lee *et al.* took advantage of TMP hardening in the presence of DAHP solution to prepare a 3D magnesium phosphate-based scaffold [41], while as an alternative liquid component, the use of phytic acid was reported by Christel *et al.* [42].

As one can easily imagine by examining the body of data reported above, comparing the performances of different systems prepared in such diverse conditions is difficult. Moreover, the mechanism of formation of struvite, which is the main final product formed in this kind of formulations, is not entirely known [43].

The goal of this paper is to clarify the effect of the P/L ratio and of the DAHP concentration on the formation of struvite and on the final properties of MPCs obtained by reaction of TMP and DAHP. MPCs were prepared by systematically varying the P/L ratio (1.0, 1.5 and 2.0 g/mL) and the concentration of DAHP aqueous solution (0.5, 2.0 and 3.5 M). Both the pastes and the final cements were studied with multi-technique approach, aiming at understanding how the variation of these two parameters affects the most meaningful properties of the obtained materials.

2. Materials and methods

2.1. TMP synthesis

Tri-Magnesium Phosphate (TMP) powder was obtained by means of a calcination reaction, according to a method reported in the literature [36]. Briefly, 12 g of newberyite ($MgHPO_4{\cdot}3H_2O$, Sigma-Aldrich) and 2 g of $Mg(OH)_2$ (Fluka) were mixed (molar ratio 2:1) and heated in a muffle at 1000 °C for 5 h. The sintered cake was crushed with mortar and pestle and sieved (mesh size 150 μm).

2.2. Cements preparation

Cement pastes were produced by mixing 0.5 g of TMP with an aqueous solution of DAHP (Fluka). The amount and the concentration of the DAHP solutions were varied so to obtain samples with powder to liquid ratio (P/L) of 1.0, 1.5 and 2.0 g/mL and DAHP concentration of 0.5, 2.0 and 3.5 M. The composition, together with the sample nomenclature and other useful parameters, are reported in Table 1. After mixing, the pastes were poured into cylindrical polyethylene molds (diameter 1 cm) and stored at 37 °C, relative humidity > 90%, for some days.

2.3. Handling properties

The handling properties and the cohesion degree of the pastes at different P/L ratio and DAHP concentrations were evaluated as it follows: 0.5 g of TMP were mixed with the appropriate amount of aqueous solution (see Table 1) for 1 min and, after 2 v min from the beginning of mixing, the paste was poured onto a piece of millimeter graph paper. The cohesion degree was evaluated qualitatively according to the spreading of the paste. The compactness of the set cements was assessed after removing the cements from the mold after 5 days of setting at 37 °C.

2.4. Setting time

The initial (t_1) and final (t_2) setting times were measured using a Gillmore apparatus (Matest) and performing the test according to the ASTM 266 standard. About 0.5 g of TMP were mixed with the appropriate amount of DAHP solution for about 1 min, and poured in cylindrical molds (diameter 1 cm). The cements were set at 37 °C and

relative humidity > 90% [36] and, every 10 min, the measurement was performed.

2.5. X-rays diffraction

The crystallinity of the cements was investigated by means of powder X-Rays Diffraction (XRD), using an X-ray diffractometer D8 Advance with a DAVINCI design (Bruker). Diffraction data were collected in the 2θ range from 10° to 50°, with an increment of 0.03° and 0.3 s *per* step, using a 2-mm slit. Peaks were assigned using the Powder Diffraction Files (PDF) of the International Centre for Diffraction Data (PDF 25-1373 for farringtonite and 03-0240 for struvite).

We estimated the relative amount of the formed phases by means of the Rietveld method, using the software Topas (Bruker). The CIF (Crystallographic Information File) data used for the analysis were obtained from the American Mineralogist Crystal Structure Database (0011901 for farringtonite and 0009807 for struvite). The percentage error associated to the fitting is 10%.

2.6. Field emission scanning Electron microscopy

The morphology and the microstructure of the cements were investigated using Field Emission Scanning Electron Microscopy (FE-SEM). Fragments of the cements were fixed on aluminum stubs, using conductive tape, to visualize the internal fracture surfaces. The measurements were performed by means of a Zeiss ΣIGMA FE-SEM (Carl Zeiss Microscopy GmbH, Germany). The use of a Field Emission source, together with a low accelerating voltage (2.0 kV), the In-Lens detector and a reduced sample-detector distance (between 2 and 3 mm) allowed for the imaging of non-metallized samples.

2.7. Total porosity

The total porosity of the samples was evaluated by preparing cement samples with cylindrical shape, by mixing 1 g of TMP with the adequate amount of DAHP solution to achieve the desired composition. After setting in a mold (diameter 8 mm) at 37 °C and relative humidity > 90% for 7 days, each sample was weighted and measured, so to calculate density. This parameter was used to obtain the porosity of the samples, according to Eq. (1) [44]:

$$\text{Porosity} = \frac{\rho_{\text{fully dense material}} - \rho_{\text{cement}}}{\rho_{\text{fully dense material}}} \quad (1)$$

The density of the fully dense material was calculated considering the weight fraction of the two phases composing each sample (farringtonite and struvite), as obtained by means of the Rietveld method from the X-Rays Diffraction results (see paragraph 2.5); the density of farringtonite is 2.74 g/cm^3 [45] and struvite 1.70 g/cm^3 [46]. The porosity corresponding to the density of each cement specimen was calculated, and for each composition the average value ± the standard deviation was considered.

2.8. Specific surface area measurement

The specific surface area and the pore size distribution of the cements were assessed by means of gas sorption measurements. The experiments were conducted using a Coulter SA3100 (Beckman Coulter): nitrogen was used as adsorbate, while freespace was measured with helium. Prior to the measurement, samples were outgassed at 50 °C for 3 h. A low outgas temperature is required to prevent struvite transformation to dittmarite [47]. The specific surface area (SSA) was obtained using the Brunauer-Emmet-Teller (BET) method, while the pore size distribution was estimated using Barrett-Joyner-Halenda (BJH) analysis.

2.9. Compressive strength

The samples prepared for the porosity measurements were tested for their compressive strength, using a 50 kN load cell (Controls, Milan). The surface of the specimens was polished so to obtain an aspect ratio of about 2 (height/diameter) and to make the two surfaces of the cylinders as flat as possible. Four samples for each composition were tested.

3. Results and discussion

3.1. TMP characterization

We characterized the obtained TMP powder as described in paragraph 2.1. The XRD pattern shows that we obtained a crystalline material (see Fig. S1_a) in which the particle size is in the micrometric range (see Fig. S1_b). The grains have an irregular shape with a smooth surface, as it appears from SEM micrographs (Fig. S1_c); the specific surface area of the powder, as measured by means of nitrogen sorption, is 0.29 m^2/g.

3.2. Handling properties and setting time

The handling properties and the cohesion of the paste were evaluated as described in Section 2.3, and the results are shown in Fig. 1. When comparing the aspect and the consistency of the pastes (Fig. 1A), it is evident that the cohesion degree immediately after mixing increases while increasing the P/L ratio. This observation is consistent with data reported in the literature for CPCs [8,9], and it was expected, considering the amount of water in the samples (see Table 1): in fact, immediately after mixing, a high water content makes the paste less viscous and less compact. Interestingly, we also noticed that the initial cohesion of the samples increases with the decrease of DAHP concentration. This effect may be due to the high wettability of the TMP powder, which in the 0.5M_samples is in large excess with respect to

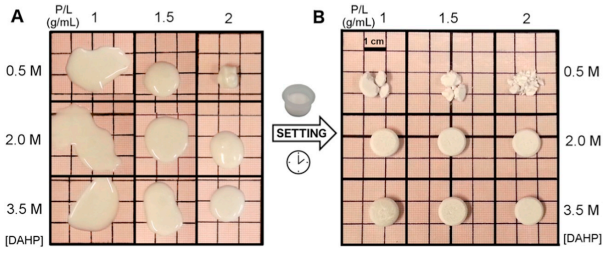

Fig. 1. Photos of the samples (A) after 2 min from the mixing and (B) after setting in the mold for 5 days. In both pictures, the P/L ratio increases horizontally from the left to the right, while the concentration of DAHP increases from the top to the bottom.

DAHP (see Table 1) [48]. We can hypothesize that, for a given P/L ratio, when the amount of TMP with respect to DAHP is large, during mixing an immediate reaction between the two components occurs, and the small amount of formed struvite covers the large TMP grains; this results in an apparently more compact paste, in which, the volume of the formed struvite network is limited. On the other hand, when more NH_4^+ and phosphate ions are available for the reaction (*i.e.* higher concentration of DAHP solution), a more homogeneous struvite precipitation occurs; consequently, the paste will appear more liquid-like, as DAHP can react with a larger amount of TMP and form a more interconnected and diffused struvite network which penetrates the whole sample in the early stages (after 2 min, Fig. 1A).

The setting time of the cements was measured by means of the Gillmore method (see Section 2.4), and the results are reported in Fig. S2. All the samples display both initial and final setting times well above the ideal values for clinical applications, which are $t_1 \sim 8$ min and $t_2 \sim 15$ min [12]. The t_2 cannot be measured for 0.5M_samples, as the cements' surface crumbles upon indentation. Some trends can be identified: at a given DAHP concentration, t_1 and t_2 decrease with the increase of the P/L ratio, while at a given P/L ratio, a higher DAHP concentration reduces setting time.

The compactness of the dried cements was assessed by observing the samples' aspect after 5 days of setting (Fig. 1B). The initial cohesion degree does not reflect on the compactness of the final cements: for example, the system which displays the highest cohesion degree after mixing (0.5M_P/L 2, top right in Fig. 1A), is the one that after setting crumbles the most and is not able to maintain the shape of the mold, as for all the 0.5M_samples. On the other hand, the samples prepared with DAHP solution 2.0 M and 3.5 M allow for the formation of compact and hard cements. This observation is consistent with a significant and diffused formation of struvite in the 2.0M_ and 3.5M_samples, which finally percolates and hardens the whole specimens.

3.3. Crystallinity and struvite content

According to the literature, TMP and DAHP react in a molar ratio 1:1 and form struvite ($MgNH_4PO_4{\cdot}6H_2O$) [36]. X-rays diffraction patterns of the final cements are reported in Fig. 2. In every analyzed sample, we observe the simultaneous presence of crystalline TMP (farringtonite) and struvite. The presence of unreacted TMP within the resulting cement structure is often observed in the literature [12]; it is worth stressing that in all the prepared samples TMP is in excess with respect to DAHP (see Table 1). When the ratio between TMP and DAHP is close to 1 (but again in a slight excess of TMP, sample 3.5M_P/L 1) we detect in its XRD pattern the signals characteristic of unreacted DAHP (see Fig. 2C, pattern on the bottom), despite the stoichiometry of the reaction would predict a complete consumption of the DAHP. This evidence indicates that it is not possible to entirely convert the reactants to the final product, suggesting that the formation of struvite occurs on the boundaries of the TMP grains and this mechanism prevents (or hinders) them from further reacting with DAHP.

Comparing the intensities of the diffraction peaks, it is evident that a different composition of reactants leads to a different amount of struvite and farringtonite in the cement, since the relative intensities of the diagnostic peaks of the two phases are markedly different. In the 0.5M_samples, struvite peaks are very weak, while farringtonite signals predominate. When we increase the concentration of DAHP, struvite's diffraction peaks become more intense compared to farringtonite ones. In order to estimate the conversion degree to struvite, we performed a quantitative Rietveld analysis on the recorded diffractograms. The amount of formed struvite is reported in Fig. 3A. Consistently with the qualitative observations of the intensities of the diffraction peaks, the amount of struvite in the cements increases with the increasing of the DAHP concentration and decreases as the P/L ratio raises. The obtained trend agrees with the theoretical conversion degree to struvite that we obtain by simply looking at the molar ratio between TMP and DAHP (see Table 1): as the powder/liquid ratio decreases, the composition gets closer to the stoichiometry of the reaction (1:1) and the conversion degree to struvite increases (we recall that all the investigated compositions display an excess of TMP with respect to struvite). This observation is straightforward if we observe the plot of the amount of formed struvite (found by Rietveld method) against the ratio between the moles of TMP and DAHP (Fig. 3B).

3.4. Morphology and microstructure

The morphology of the prepared MPCs was investigated by means of FE-SEM, and the micrographs are shown in Fig. 4. In the 0.5M_samples, we can clearly recognize two different kinds of structures, which are highlighted by the arrows in Fig. 4B. The smooth objects indicated by the outlined empty arrows are typical of TMP (see the morphology in Fig. S1_c for comparison), while the full arrows indicate the parallelepiped-like structures with a rough surface, characteristic of struvite [49].

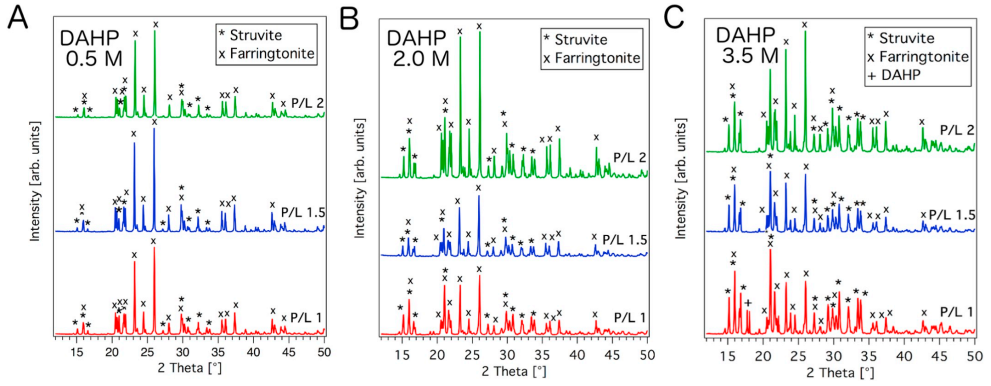

Fig. 2. XRD patterns of the investigated samples (the diffractograms are offset for display purpose): (A) DAHP 0.5 M, (B) DAHP 2.0 M, (C) DAHP 3.5 M. The powder diffraction files used for the assignment are: PDF 25-1373 for farringtonite (TMP) and PDF 03-0240 for struvite; the diffractogram for pure DAHP was acquired experimentally.

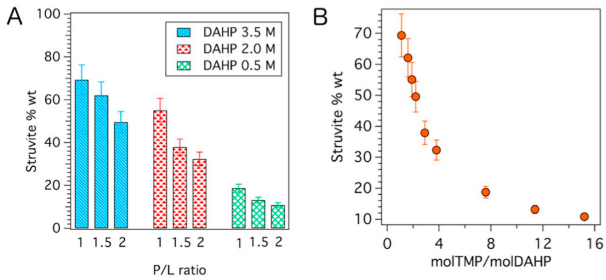

Fig. 3. (A) Histogram reporting the amount of struvite obtained by means of a Rietveld fitting on the recorded diffractograms. From the left: DAHP concentration of 3.5 M, 2.0 M and 0.5 M. For each set, the P/L ratio increases from the left to the right; (B) Plot of the amount of struvite (according to the Rietveld fitting) vs the ratio between the moles of TMP and DAHP, which reflects the theoretical conversion degree to struvite.

High magnification images of struvite crystals, shown in Fig. S3 in the Supplementary Material, reveal the very peculiar morphology of this mineral, which displays a typical hemimorphic character (*i.e.* the two ends of a crystallographic *c*-axis are not related by symmetry, see Fig. S3_a and S3_b) [50]. The crystals thus show both tabular planes and rough surfaces showing cracks with regular shapes that carry an intrinsic porosity (see Fig. S3_c and S3_d) [51]. It is interesting to observe that when we increase the concentration of DAHP in the formulations, the amount of struvite-like structures increases, and the number of TMP-rich domains diminishes (see Fig. 4). This observation agrees with the data obtained by means of XRD and discussed in Section 3.3, which revealed that the conversion degree to struvite increases with increasing the concentration of DAHP (and decreasing the P/L ratio). Furthermore, when DAHP 3.5 M is used, we observe a more compact and uniform morphology produced by the network of the formed struvite.

3.5. Porosity and surface area

Porosity is one of the parameters which should be taken into account in the design of a bone cement, as it affects both the biological activity and the mechanical properties of the material; cements should display a combination of micro and macroporosity, so to allow for the impregnation of biological fluids, for cell ingrowth and for the replacement by new bone [8]. The total porosity of our cements was calculated as described in Section 2.7, and the results are reported in Fig. 5A. The 0.5M_samples were not analyzed, as once the specimens were removed from the mold, they crumbled and we could not measure their height and diameter. All the obtained porosities are in the range of 0.1–0.4 (being 0 a non-porous sample), and this parameter is higher for

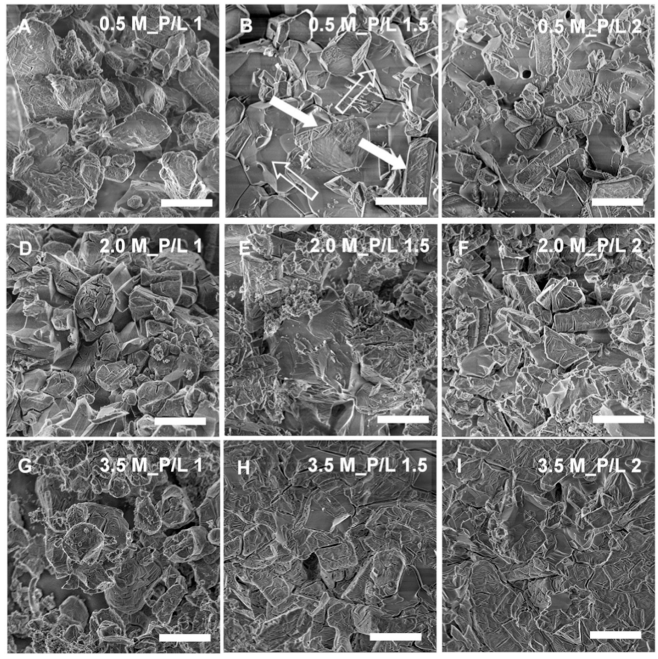

Fig. 4. FE-SEM micrographs of the investigated MPCs. The name of the samples is reported on each picture. Scale bar: 5 μm.

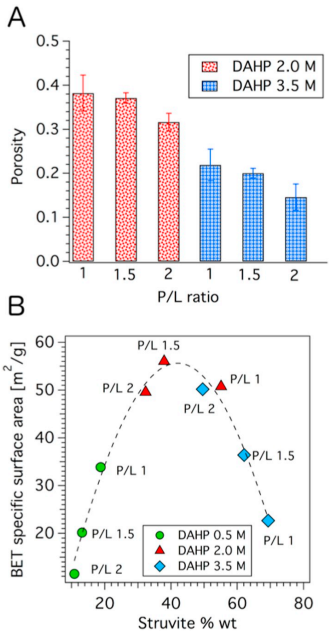

Fig. 5. (A) Total porosity of the investigated samples, calculated according to Eq. (1); (B) Plot of specific surface area vs % wt of struvite (from Rietveld analysis). DAHP 0.5 M (circles), DAHP 2.0 M (triangles), DAHP 3.5 M (diamonds). P/L ratio is reported on the graph. The dashed curve is a guide to the eyes, not a fitting of the experimental data.

the 2.0M_samples than for the 3.5M_samples; moreover, at a given DAHP concentration, the porosity decreases when the P/L ratio increases. The latter trend is probably ascribable to the larger amount of unreacted water that generates larger porosities while evaporating during setting [9]; furthermore, at fixed P/L ratio, the porosity is larger for the 2.0M_samples, consistently with the higher amount of water present (see Table 1).

We also investigated the specific surface area (SSA) and the pore size distribution of the prepared cements. All the investigated samples display a reversible type II isotherm with a multi-layer adsorption (a representative example is given in Fig. S4_a). The BJH analysis reveals that the cements possess a quite heterogeneous pore size distribution, with a small population of micropores and most pores with a diameter over 30 nm (see Fig. S4_b for a significant example). The SSA of the cements was calculated with the BET method. Given the fact that unreacted TMP is characterized by a smooth morphology while struvite is endowed with some intrinsic porosity on its surface, we plotted the SSA against the struvite content of each sample (see paragraph 3.3), to evaluate a possible connection between these two parameters (see Fig. 5B). Interestingly, we observe that, up to 40%wt of struvite, the SSA increases with the increase in struvite content; however, when the amount of struvite exceeds 40%wt, the trend inverses, and the SSA decreases as the quantity of struvite in the sample increases. We believe that this peculiar trend is strictly related to the morphology of the cements (see Fig. 4): samples prepared with DAHP 3.5 M display a very compact microstructure, which becomes more “dense” as struvite content increases (see Fig. 4G, H and I). This type of structure possibly decreases the overall surface area of the samples, leading to the observed effect. It is worth commenting that the SSA trend does not correspond to the total porosity of the cements previously discussed: in fact, nitrogen sorption technique gives access to porosities from few to hundreds of nm, while large macropores, which can increase the total porosity of the material, do not contribute to the BET specific surface area of the samples.

3.6. Mechanical properties

The compressive strength of the cements was assessed so to understand if different formulations lead to a diverse behavior in terms of load withstanding. The 0.5M_samples could not be analyzed, as they crumbled once removed from the mold and could not retain their shape. The measured compressive strengths for the other samples are reported in Fig. 6A. The cements display a compressive strength which ranges from about 10 to 30 MPa, in agreement with literature data for similar materials [12]. Moreover, considering the error bars, the measurements show that the compressive strengths increase with the P/L ratio and with the concentration of DAHP (at fixed P/L ratio). From these results, we can infer that the compressive strength is not directly correlated with the amount of struvite in the samples (see Section 3.3), which increases with the concentration of DAHP but decreases with the P/L ratio. Interestingly, the samples which display the highest compressive strength (3.5M_P/L 1.5 and 3.5M_P/L 2) are the ones whose morphology appears more compact and uniform. Since for CPCs the compressive strength is described to be dependent on the total porosity of the material [8], we calculated the porosity of the specimens, as described in paragraph 2.7. The plot of the compressive strength against the porosity is shown in Fig. 6B.

The porosity of the specimens increases as the P/L ratio decreases,

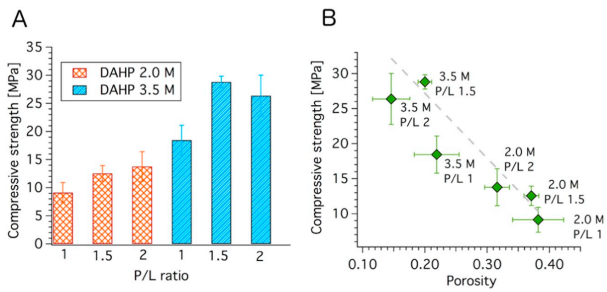

Fig. 6. (A) Compressive strength of the analyzed cements (average of 4 different measurements ± standard deviation); (B) Plot of compressive strength vs porosity of the cements. The dashed line represents a linear fitting of the experimental data.

probably due to the larger amount of unreacted water that generates larger porosities while evaporating during setting [9]; furthermore, at fixed P/L ratio, the porosity is larger for the 2.0M_samples, consistently with the higher amount of water present (see Table 1). The obtained plot of the compressive strength as a function of porosity shows that this mechanical property increases as the porosity decreases; this trend well matches the data reported in the literature for CPCs [8] and for calcium-magnesium mixed cements [40]. To sum up, we can state that there is not a direct correlation between the amount of struvite and the mechanical properties; in fact, if we plot the compressive strength vs the struvite percentage in each sample, we can clearly understand that an increase of the struvite content does not monotonically result in an improvement of the compressive strength (see Fig. S5). We can hypothesize that a specific conversion degree to struvite is necessary to obtain an interconnected network that binds together the unreacted TMP grains and to produce a very compact microstructure of the material.

4. Conclusions

This paper deals with the physico-chemical and mechanical properties of magnesium phosphate-based bone cements, prepared by mixing TMP with an aqueous solution of DAHP. We succeeded in understanding how the modification of the P/L ratio and the DAHP concentration affect the most meaningful properties of these materials, *i.e.* cohesion, crystallinity, morphology, porosity and compressive strength. All the final cements are constituted by variable amounts of struvite and unreacted TMP, as shown by XRD analysis. SEM micrographs reveal than when the amount of struvite is low, the morphology of the two components is detectable, whereas when the quantity of struvite increases, only its typical morphology can be observed, despite XRD measurements still indicate the presence of a significant amount of unreacted TMP. This suggests that the formation of struvite occurs on TMP grains, and that the network which is generated prevents a further reaction between TMP and DAHP. The use of DAHP solution 2.0 M and 3.5 M allows for the formation of compact and hard cements, whose compressive strengths significantly vary with the formulation: in particular, the compressive strength grows with the P/L ratio and with the concentration of DAHP solution, being inversely proportional to the total porosity of the material. The results presented in this work can be useful guidelines in the design and realization of this kind of bone cements, representing a step forward in the preparation and use of MPCs in the biomedical field.

Abbreviations

CPCs	Calcium Phosphate-based Cements
MPCs	Magnesium Phosphate-based Cements
TMP	Tri-Magnesium Phosphate
P/L	Powder to Liquid (ratio)
DAHP	Di-Ammonium Hydrogen Phosphate
XRD	X-Rays Diffraction
FE-SEM	Field Emission Scanning Electron Microscopy
BET	Brunauer-Emmet-Teller
BJH	Barrett-Joyner-Halenda
SSA	Specific Surface Area

Acknowledgements

Enzo Barlacchi and Leonardo Bucci from the “Laboratorio Prove Strutture e Materiali” of the Department of Civil and Environmental Engineering (DICEA), University of Florence, are gratefully acknowledged for the compressive strength measurements. CSGI is acknowledged for financial support.

Appendix A. Supplementary data

Supplementary data to this article can be found online at https://doi.org/10.1016/j.msec.2018.10.083.

References

[1] Z. Sheikh, S. Najeeb, Z. Khurshid, V. Verma, H. Rashid, M. Glogauer, Biodegradable materials for bone repair and tissue engineering applications, Materials 8 (2015) 5744–5794, https://doi.org/10.3390/ma8095273.
[2] S. Pina, J.M. Oliveira, R.L. Reis, Natural-based nanocomposites for bone tissue engineering and regenerative medicine: a review, Adv. Mater. 27 (2015) 1143–1169, https://doi.org/10.1002/adma.201403354.
[3] T. Gong, J. Xie, J. Liao, T. Zhang, S. Lin, Y. Lin, Nanomaterials and bone regeneration, Bone Res. 3 (2015), https://doi.org/10.1038/boneres.2015.29 boneres201529.
[4] A. Kolk, J. Handschel, W. Drescher, D. Rothamel, F. Kloss, M. Blessmann, M. Heiland, K.-D. Wolff, R. Smeets, Current trends and future perspectives of bone substitute materials – from space holders to innovative biomaterials, J. Cranio-Maxillofac. Surg. 40 (2012) 706–718, https://doi.org/10.1016/j.jcms.2012.01.002.
[5] Z. Chen, X. Zhang, L. Kang, F. Xu, Z. Wang, F.-Z. Cui, Z. Guo, Recent progress in injectable bone repair materials research, Front. Mater. Sci. 9 (2015) 332–345, https://doi.org/10.1007/s11706-015-0310-z.
[6] H.H. Xu, P. Wang, L. Wang, C. Bao, Q. Chen, M.D. Weir, L.C. Chow, L. Zhao, X. Zhou, M.A. Reynolds, Calcium phosphate cements for bone engineering and their biological properties, Bone Res. 5 (2017) 17056, , https://doi.org/10.1038/boneres.2017.56.
[7] Y.J. No, S. Roohani-Esfahani, H. Zreiqat, Nanomaterials: the next step in injectable bone cements, Nanomedicine 9 (2014) 1745–1764, https://doi.org/10.2217/nnm.14.109.
[8] J. Zhang, W. Liu, V. Schnitzler, F. Tancret, J.-M. Bouler, Calcium phosphate cements for bone substitution: chemistry, handling and mechanical properties, Acta Biomater. 10 (2014) 1035–1049, https://doi.org/10.1016/j.actbio.2013.11.001.
[9] S.V. Dorozhkin, Self-setting calcium orthophosphate formulations: cements, concretes, pastes and putties, Int. J. Mater. Chem. 1 (2012) 1–48, https://doi.org/10.5923/j.ijmc.20110101.01.
[10] S. Pina, J.M.F. Ferreira, Brushite-forming Mg-, Zn- and Sr-substituted bone cements for clinical applications, Materials 3 (2010) 519–535, https://doi.org/10.3390/ma3010519.
[11] M. Geffers, J. Groll, U. Gbureck, Reinforcement strategies for load-bearing calcium phosphate biocements, Materials 8 (2015) 2700–2717, https://doi.org/10.3390/ma8052700.
[12] N. Ostrowski, A. Roy, P.N. Kumta, Magnesium phosphate cement systems for hard tissue applications: a review, ACS Biomater Sci. Eng. 2 (2016) 1067–1083, https://doi.org/10.1021/acsbiomaterials.6b00056.
[13] M. Nabiyouni, T. Brückner, H. Zhou, U. Gbureck, S.B. Bhaduri, Magnesium-based bioceramics in orthopedic applications, Acta Biomater. 66 (2018) 23–43, https://doi.org/10.1016/j.actbio.2017.11.033.
[14] J. Cabrejos-Azama, M.H. Alkhraisat, C. Rueda, J. Torres, L. Blanco, E. López-Cabarcos, Magnesium substitution in brushite cements for enhanced bone tissue regeneration, Mater. Sci. Eng. C 43 (2014) 403–410, https://doi.org/10.1016/j.msec.2014.06.036.
[15] Z. Wang, Y. Ma, J. Wei, X. Chen, L. Cao, W. Weng, Q. Li, H. Guo, J. Su, Effects of sintering temperature on surface morphology/microstructure, in vitro degradability, mineralization and osteoblast response to magnesium phosphate as biomedical material, Sci. Rep. 7 (2017), https://doi.org/10.1038/s41598-017-00905-2.
[16] E. Babaie, B. Lin, S.B. Bhaduri, A new method to produce macroporous Mg-phosphate bone growth substitutes, Mater. Sci. Eng. C 75 (2017) 602–609, https://doi.org/10.1016/j.msec.2017.02.111.
[17] G. Mestres, M.-P. Ginebra, Novel magnesium phosphate cements with high early strength and antibacterial properties, Acta Biomater. 7 (2011) 1853–1861, https://doi.org/10.1016/j.actbio.2010.12.008.
[18] R.B. Kogbara, A. Al-Tabbaa, S.R. Iyengar, Utilisation of magnesium phosphate cements to facilitate biodegradation within a stabilised/solidified contaminated soil, Water Air Soil Pollut. 216 (2011) 411–427, https://doi.org/10.1007/s11270-010-0541-7.
[19] J.-S. Li, Q. Xue, P. Wang, T.-T. Zhang, Y. Zhao, Comparison of solidification/stabilization of lead contaminated soil between magnesia–phosphate cement and ordinary Portland cement under the same dosage, Environ. Prog. Sustain. Energy 35 (2016) 88–94, https://doi.org/10.1002/ep.12204.
[20] F. Qiao, C.K. Chau, Z. Li, Property evaluation of magnesium phosphate cement mortar as patch repair material, Constr. Build. Mater. 24 (2010) 695–700, https://doi.org/10.1016/j.conbuildmat.2009.10.039.
[21] N. Yang, C. Shi, J. Yang, Y. Chang, Research progresses in magnesium phosphate cement-based materials, J. Mater. Civ. Eng. 26 (2014), https://doi.org/10.1061/(ASCE)MT.1943-5533.0000971.
[22] J.W. Park, K.H. Kim, K.Y. Ann, Fundamental properties of magnesium phosphate cement mortar for rapid repair of concrete, Adv. Mater. Sci. Eng. 2016 (2016) e7179403, , https://doi.org/10.1155/2016/7179403.
[23] S.A. Walling, J.L. Provis, Magnesia-based cements: a journey of 150 years, and cements for the future? Chem. Rev. 116 (2016) 4170–4204, https://doi.org/10.1021/acs.chemrev.5b00463.
[24] F. Wu, J. Wei, H. Guo, F. Chen, H. Hong, C. Liu, Self-setting bioactive

calcium–magnesium phosphate cement with high strength and degradability for bone regeneration, Acta Biomater. 4 (2008) 1873–1884, https://doi.org/10.1016/j.actbio.2008.06.020.
[25] Y. Yu, J. Wang, C. Liu, B. Zhang, H. Chen, H. Guo, G. Zhong, W. Qu, S. Jiang, H. Huang, Evaluation of inherent toxicology and biocompatibility of magnesium phosphate bone cement, Colloids Surf. B: Biointerfaces 76 (2010) 496–504, https://doi.org/10.1016/j.colsurfb.2009.12.010.
[26] B. Kanter, M. Geffers, A. Ignatius, U. Gbureck, Control of in vivo mineral bone cement degradation, Acta Biomater. 10 (2014) 3279–3287, https://doi.org/10.1016/j.actbio.2014.04.020.
[27] B. Kanter, A. Vikman, T. Brückner, M. Schamel, U. Gbureck, A. Ignatius, Bone regeneration capacity of magnesium phosphate cements in a large animal model, Acta Biomater. 69 (2018) 352–361, https://doi.org/10.1016/j.actbio.2018.01.035.
[28] J.A. Kim, H. Yun, Y.-A. Choi, J.-E. Kim, S.-Y. Choi, T.-G. Kwon, Y.K. Kim, T.-Y. Kwon, M.A. Bae, N.J. Kim, Y.C. Bae, H.-I. Shin, E.K. Park, Magnesium phosphate ceramics incorporating a novel indene compound promote osteoblast differentiation in vitro and bone regeneration in vivo, Biomaterials 157 (2018) 51–61, https://doi.org/10.1016/j.biomaterials.2017.11.032.
[29] F.C.M. Driessens, M.G. Boltong, M.I. Zapatero, R.M.H. Verbeeck, W. Bonfield, O. Bérmúdez, E. Fernández, M.P. Ginebra, J.A. Planell, In vivo behaviour of three calcium phosphate cements and a magnesium phosphate cement, J. Mater. Sci. Mater. Med. 6 (1995) 272–278, https://doi.org/10.1007/BF00120270.
[30] A. Ewald, K. Helmschrott, G. Knebl, N. Mehrban, L.M. Grover, U. Gbureck, Effect of cold-setting calcium- and magnesium phosphate matrices on protein expression in osteoblastic cells, J Biomed Mater Res B Appl Biomater 96 (2011) 326–332, https://doi.org/10.1002/jbm.b.31771.
[31] C. Großardt, A. Ewald, L.M. Grover, J.E. Barralet, U. Gbureck, Passive and active in vitro resorption of calcium and magnesium phosphate cements by osteoclastic cells, Tissue Eng. Part A 16 (2010) 3687–3695, https://doi.org/10.1089/ten.tea.2010.0281.
[32] U. Klammert, E. Vorndran, T. Reuther, F.A. Müller, K. Zorn, U. Gbureck, Low temperature fabrication of magnesium phosphate cement scaffolds by 3D powder printing, J. Mater. Sci. Mater. Med. 21 (2010) 2947–2953, https://doi.org/10.1007/s10856-010-4148-8.
[33] E. Vorndran, K. Wunder, C. Moseke, I. Biermann, F.A. Müller, K. Zorn, U. Gbureck, Hydraulic setting $Mg_3(PO_4)_2$ powders for 3D printing technology, Adv. Appl. Ceram. 110 (2011) 476–481, https://doi.org/10.1179/1743676111Y.0000000030.
[34] J.-A. Kim, J. Lim, R. Naren, H. Yun, E.K. Park, Effect of the biodegradation rate controlled by pore structures in magnesium phosphate ceramic scaffolds on bone tissue regeneration in vivo, Acta Biomater. 44 (2016) 155–167, https://doi.org/10.1016/j.actbio.2016.08.039.
[35] N. Ostrowski, V. Sharma, A. Roy, P.N. Kumta, Systematic assessment of synthesized tri-magnesium phosphate powders (amorphous, semi-crystalline and crystalline) and cements for ceramic bone cement applications, J. Mater. Sci. Technol. 31 (2015) 437–444, https://doi.org/10.1016/j.jmst.2014.12.002.
[36] C. Moseke, V. Saratsis, U. Gbureck, Injectability and mechanical properties of magnesium phosphate cements, J. Mater. Sci. Mater. Med. 22 (2011) 2591–2598, https://doi.org/10.1007/s10856-011-4442-0.
[37] T. Brückner, K. Hurle, A. Stengele, J. Groll, U. Gbureck, Mechanical activation and cement formation of trimagnesium phosphate, J. Am. Ceram. Soc. 101 (2018) 1830–1834, https://doi.org/10.1111/jace.15397.
[38] F.C.M. Driessens, M.G. Boltong, R. Wenz, J. Meyer, Calcium phosphates as fillers in struvite cements, Key Eng. Mater. 284–286 (2005) 161–164, https://doi.org/10.4028/www.scientific.net/KEM.284-286.161.
[39] U. Klammert, T. Reuther, M. Blank, I. Reske, J.E. Barralet, L.M. Grover, A.C. Kübler, U. Gbureck, Phase composition, mechanical performance and in vitro biocompatibility of hydraulic setting calcium magnesium phosphate cement, Acta Biomater. 6 (2010) 1529–1535, https://doi.org/10.1016/j.actbio.2009.10.021.
[40] E. Vorndran, A. Ewald, F.A. Müller, K. Zorn, A. Kufner, U. Gbureck, Formation and properties of magnesium-ammonium-phosphate hexahydrate biocements in the Ca-Mg-PO4 system, J. Mater. Sci. Mater. Med. 22 (2011) 429–436, https://doi.org/10.1007/s10856-010-4220-4.
[41] J. Lee, M.M. Farag, E.K. Park, J. Lim, H. Yun, A simultaneous process of 3D magnesium phosphate scaffold fabrication and bioactive substance loading for hard tissue regeneration, Mater. Sci. Eng. C 36 (2014) 252–260, https://doi.org/10.1016/j.msec.2013.12.007.
[42] T. Christel, S. Christ, J.E. Barralet, J. Groll, U. Gbureck, Chelate bonding mechanism in a novel magnesium phosphate bone cement, J. Am. Ceram. Soc. 98 (2015) 694–697, https://doi.org/10.1111/jace.13491.
[43] M. Le Rouzic, T. Chaussadent, G. Platret, L. Stefan, Mechanisms of k-struvite formation in magnesium phosphate cements, Cem. Concr. Res. 91 (2017) 117–122, https://doi.org/10.1016/j.cemconres.2016.11.008.
[44] W. Liu, J. Zhang, P. Weiss, F. Tancret, J.-M. Bouler, The influence of different cellulose ethers on both the handling and mechanical properties of calcium phosphate cements for bone substitution, Acta Biomater. 9 (2013) 5740–5750, https://doi.org/10.1016/j.actbio.2012.11.020.
[45] Farringtonite Mineral Data, http://webmineral.com/data/Farringtonite.shtml#.WoG8zZM-eCf.
[46] Struvite Mineral Data, http://webmineral.com/data/Struvite.shtml#.WoG88pM-eCf.
[47] M.V. Ramlogan, A.A. Rouff, An investigation of the thermal behavior of magnesium ammonium phosphate hexahydrate, J. Therm. Anal. Calorim. 123 (2016) 145–152, https://doi.org/10.1007/s10973-015-4860-1.
[48] G. Buckton, Contact angle, adsorption and wettability — a review with respect to powders, Powder Technol. 61 (1990) 237–249, https://doi.org/10.1016/0032-5910(90)80090-L.
[49] H. Li, S.-H. Yu, Q.-Z. Yao, G.-T. Zhou, S.-Q. Fu, Chemical control of struvite scale by a green inhibitor polyaspartic acid, RSC Adv. 5 (2015) 91601–91608, https://doi.org/10.1039/C5RA17149K.
[50] J. Rakovan, Hemimorphism, Rocks Miner. 82 (2007) 329–337.
[51] F. Abbona, R. Boistelle, Growth morphology and crystal habit of struvite crystals (MgNH4PO4·6 H2O), J. Cryst. Growth 46 (1979) 339–354, https://doi.org/10.1016/0022-0248(79)90082-4.

Supplementary Material

Tuning the properties of magnesium phosphate-based bone cements: Effect of powder to liquid ratio and aqueous solution concentration

Rita Gelli, Laura Mati, Francesca Ridi, Piero Baglioni*

Department of Chemistry "Ugo Schiff" and CSGI, University of Florence, via della Lastruccia 3, Sesto Fiorentino, 50019 Florence, Italy

Corresponding author: Dr. Francesca Ridi
phone: +39 055 4573015
e-mail: francesca.ridi@unifi.it

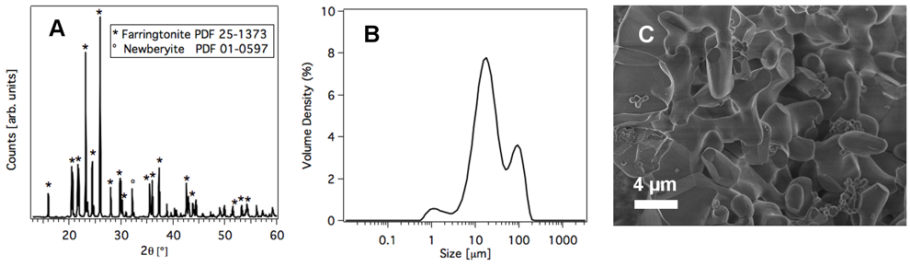

Fig. S1: (a) XRD pattern of the synthesized TMP powder; (b) Particle size distribution of TMP, measured using laser diffraction (Mastersizer 3000, Malvern Instruments); (c) FE-SEM micrograph of TMP powder.

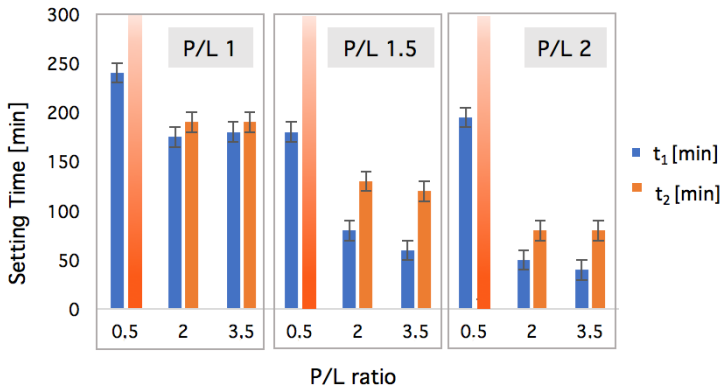

Fig. S2: initial (t1) and final (t2) setting times of the cements, as measured by means of the Gillmore method.

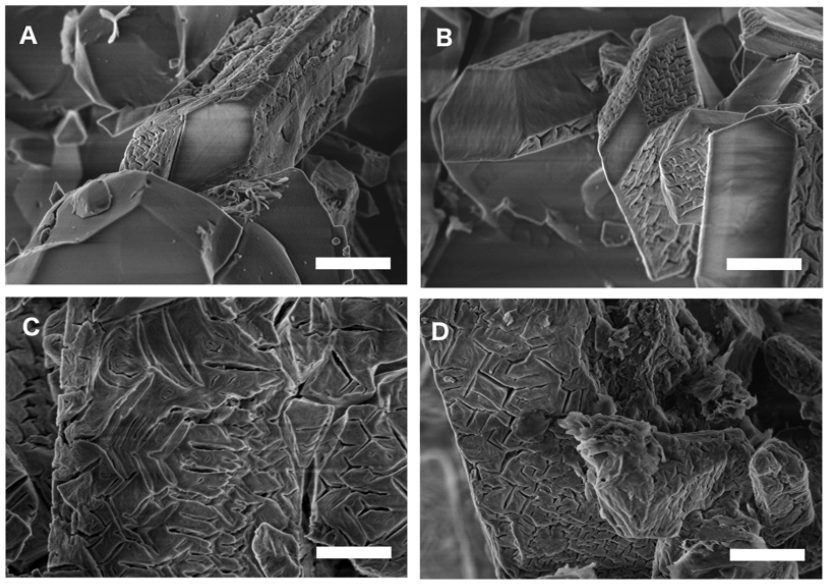

Fig. S3: High magnification FE-SEM micrographs of struvite crystals in MPCs samples. (a) and (b) refer to 0.5M P/L1.5, (c) to 3.5M P/L 1.5 and (d) to 0.5M P/L1. Scale bar: 2 µm.

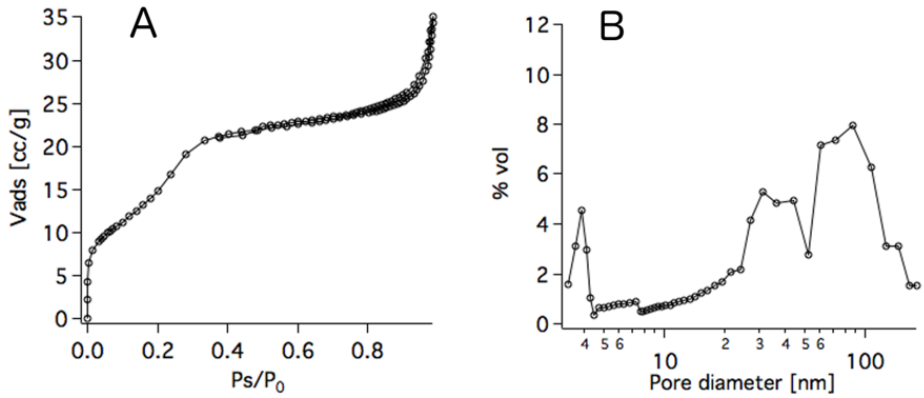

Fig. S4: Representative adsorption and desorption isotherm (a) and pore size distribution plot (b) of the investigated cements. The curves refer to the sample 2.0M_P/L1.5.

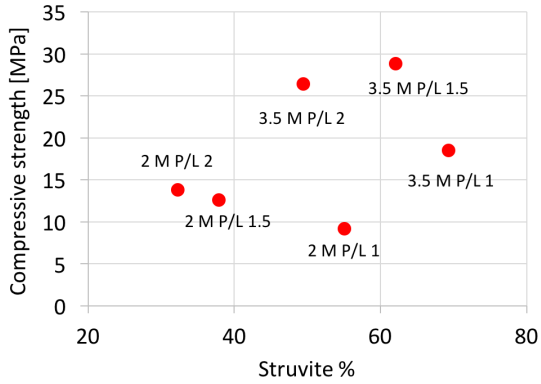

Fig. S5: Plot of the compressive strengths of the materials vs the % of struvite.

Paper VI

Colloids and Surfaces A 532 (2017) 18–25

Contents lists available at ScienceDirect

Colloids and Surfaces A

journal homepage: www.elsevier.com/locate/colsurfa

Multi-scale investigation of gelatin/poly(vinyl alcohol) interactions in water

Rita Gelli, Stefano Del Buffa, Paolo Tempesti, Massimo Bonini, Francesca Ridi, Piero Baglioni*

Department of Chemistry "Ugo Schiff" and CSGI, University of Florence, via della Lastruccia 3, Sesto Fiorentino, 50019 Florence, Italy

GRAPHICAL ABSTRACT

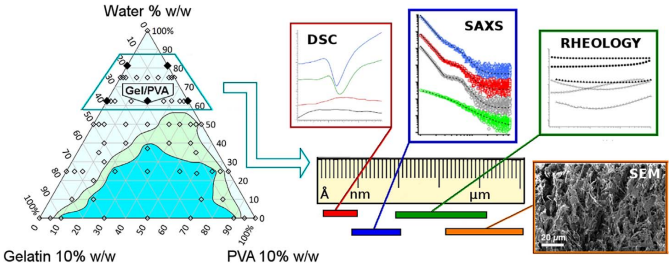

ARTICLE INFO

Keywords:
Gelatin
Poly(vinyl alcohol)
DSC
SAXS
Rheology
Ternary diagram

ABSTRACT

This paper reports on a physico-chemical investigation of gelatin and PVA hydrogels and aqueous solutions, aiming at clarifying the interactions between the two polymers in water. The stability of gelatin/PVA/water mixtures was investigated and a ternary phase diagram was evaluated. The morphology, thermal behaviour and structure of selected gelatin/PVA/water samples were studied using several techniques, including scanning electron microscopy, differential scanning calorimetry, small angle X-ray scattering and rheology. The obtained results indicate that gelatin and PVA interact weakly and the behaviour of the mixed system is mainly dictated by their different interaction with water.

1. Introduction

In the field of polymers, great attention has been recently devoted to biocompatible and biodegradable hydrogels and to their use in medical and pharmaceutical applications [1]. Hydrogels obtained from a single polymer have been widely investigated, as well as the modifications induced by the presence of cross-linkers [2] and/or inorganic fillers [3]. Nowadays, blends obtained using synthetic polymers and biopolymers are of particular significance [4]. Polymer blends have been a topic of major interest in the last five decades, both from an academic and a technological perspective, since the combination of two or more polymers leads to new materials whose properties may be modulated on purpose through compositional changes [5,6]. According to IUPAC, a polymer blend is defined as a macroscopically homogeneous mixture of two or more different species of polymer [7]. The same definition specifies that, in most cases, blends are homogeneous on a scale larger than the wavelengths of visible light, but no specific account is given on the miscibility or immiscibility of the constituent macromolecules. These materials have been mainly considered from an industrial and technological perspective, even if the physico-chemical study of the interactions taking place between the

* Corresponding author.
E-mail address: piero.baglioni@unifi.it (P. Baglioni).

http://dx.doi.org/10.1016/j.colsurfa.2017.07.049
Received 28 February 2017; Received in revised form 13 July 2017; Accepted 14 July 2017
Available online 17 July 2017

polymers composing the mixture probably represents the most intriguing aspect. In particular, the properties of polymer aqueous solutions are of outmost relevance, as they often dictate the structure of the final material [8].

Polymer blends can be potentially applied to the biomedical field [9], in which the biocompatibility of the used materials is an essential requirement [1]. Gelatin and poly(vinyl alcohol) (PVA) are two significant examples since they are biodegradable, chemically versatile, easily available, and already used in a variety of industrial and biomedical applications. Gelatin is a natural polymer, produced by partial hydrolysis of collagen, which is the main structural protein in the extracellular matrix of animals' connective tissues. At a temperature of about 40 °C, gelatin in water is in the sol state, while it forms physical thermo-reversible gels upon cooling. When gelling, gelatin chains locally refold, partially recovering the collagen triple-helix structure [10,11]. Given its resemblance with the organic component of bone, gelatin is of special interest in tissue engineering [12,13] and has already been blended with several polymers, such as silk, hyaluronic acid and poly(lactic-co-glycolic acid) [12]. PVA is a water soluble synthetic polymer bearing hydroxyl groups, produced by hydrolysis of poly (vinyl acetate) [14]. The hydrolysis degree, as well as the molecular weight, is largely responsible for the physico-chemical properties of the polymer in water (*e.g.*, solubility), due to the extent of hydrogen bonding interactions among polymer chains and solvent molecules. PVA is of great biomedical and pharmaceutical interest because of its biodegradability, filmability, bioadhesivity and high swelling degree. Furthermore, PVA has been combined with different natural and synthetic polymers in order to obtain blend hydrogels [15–17].

The combination of collagen/PVA and gelatin/PVA to obtain films was first studied in 1995 by Sarti and Scandola [18], who concluded that, "though thermodynamically immiscible with both native and denatured collagen, PVA forms mechanically compatible blends with collagen and gelatin." The ternary system gelatin/PVA/water was investigated in detail in 1998 by Tanaka *et al.* The authors proposed an interaction between PVA and gelatin through hydrogen bonding between −OH groups of PVA and $-COO^-$ and $-NH_3^+$ groups of gelatin, and claimed the formation of uniform particles by coacervation as the cause of the turbidity of gelatin/PVA mixed solutions [19,20].

Several strategies have been recently pursued to develop bare gelatin/PVA blend systems [21,22]. Nevertheless, in order to improve the properties of the final material, these systems are typically cross-linked. Sodium trimetaphosphate [23], genipin [24] and glutaraldehyde vapours [25,26] have been employed as chemical cross-linkers. Freeze-thaw cycles, which result in the growth of PVA microcrystallites, have also been used to physically cross-link the blend [27–31]. An alternative approach used to chemically connect gelatin and PVA is through an esterification reaction between −COOH groups of Asp and Glu amino acid residues of gelatin and −OH groups of PVA chains, under acid catalysis at 70 °C [32–34]. Gelatin/PVA systems have been used to prepare films [33,35–37], membranes [38,39], nanofibers [40], wound dressings [15,32] and porous sponges [26,41]. Gelatin/PVA blends have also been proposed as good candidates for tissue engineering [30,41], since the evaluation of their biocompatibility has shown promising results [26,28,42]. However, in the aforementioned works, the interactions between the polymers and their behaviour in presence of water are not fully clarified.

This work reports on the preparation and the physico-chemical characterisation of Gelatin and PVA hydrogels and polymeric aqueous solutions, in view of their potential applications in the biomedical field. With this purpose, our experiments were conducted at 37 and 20 °C, and at pH = 9. At this pH the degree of deprotonation of gelatin amine groups is increased, enhancing the reactivity towards chemical cross-linkers, such as biocompatible bis-epoxy reactants [43]. The stability of gelatin/PVA/water mixtures was studied by the preparation and observation of several samples to draw a ternary phase diagram. Then, selected gelatin/PVA/water samples were investigated by means of a multi-technique approach, including electron microscopy, differential scanning calorimetry, small angle X-ray scattering and rheology. The results were analysed and discussed in terms of the possible interactions between the two polymers and the solvent.

2. Materials and methods

2.1. Materials

Gelatin from porcine skin (Type A, 250 g Bloom) and Poly(vinyl alcohol) (PVA, M_w 31.000–50.000, 98–99% hydrolysed) were purchased from Sigma-Aldrich and used as received. MilliQ grade water (Millipore, resistivity 18.2 MΩ·cm at 25 °C) was used throughout the experiments. Sodium hydroxide (NaOH) and sodium azide (NaN_3) were obtained from Sigma-Aldrich.

2.2. Samples preparation

All samples were prepared using the following procedure: two stock aqueous solutions of gelatin and PVA were obtained by dissolving 3 g of PVA and 3 g of gelatin in 27 g of MilliQ water at pH = 9 under vigorous stirring at 80 °C, in order to obtain two 10% w/w solutions. Gelatin 10% w/w pH = 9, PVA 10% w/w pH = 9 and H_2O pH = 9 were heated at 60 °C and mixed to obtain homogeneous systems, using different ratios according to the desired composition. The amount of solutions used to prepare the samples that were investigated by all the techniques is reported in Table 1, while the composition of the other ones can be extracted from the phase diagram (Fig. 1). 1–2 mg of sodium azide (NaN_3) were added to samples containing gelatin in order to prevent microbial growth. This antibacterial is known to have no effect on gelatin helix formation [10].

Table 1
Composition and nomenclature of the prepared samples.

Sample	Polymeric concentration% w/w	Gelatin (g)	PVA (g)	Gelatin 10% w/w pH = 9 (g)	PVA 10% w/w pH = 9 (g)	H_2O pH = 9 (g)	Total weight (g)
Gel 3.75%	3.75%	0.2	/	2	/	3.333	5.333
PVA 3.75%	3.75%	/	0.2	/	2	3.333	5.333
Gel/PVA	3.75%	0.1	0.1	1	1	3.333	5.333
Gel 1.875%	1.875%	0.1	/	1	/	4.333	5.333
PVA 1.875%	1.875%	/	0.1	/	1	4.333	5.333

2.3. Stability ternary phase diagram

The samples for the stability ternary phase diagram were prepared as described in paragraph 2.2. After complete homogenization, all the samples were equilibrated in oven at 37 °C for 24 h, and then their macroscopic appearance was coded as single phase, hazy or two phases. The boundaries between the different phases were interpolated using the IgorPro software.

2.4. Field emission scanning electron microscopy (FE-SEM)

Field Emission Scanning Electron Microscopy (FE-SEM) was used to investigate the morphology of the xerogels obtained by freeze drying the corresponding hydrogels. Freeze drying was performed by plunging small pieces of hydrogels (volume around 1 cc) in liquid nitrogen during 10 min, followed by lyophilization at about 30 mTorr and −55 °C during 24 h. The obtained xerogels were cut with a blade and the internal surface was characterized by means of a Zeiss ΣIGMA FE-SEM (Carl Zeiss Microscopy GmbH, Germany). The use of a Field Emission source, together with the use of the In-Lens detector, a reduced sample-detector distance (2 mm) and the low accelerating voltage (0.50 kV), allowed for the imaging of non-metallized samples.

2.5. Differential scanning calorimetry (DSC)

DSC analyses were carried out on a Q2000 DSC (TA Instruments, New Castle, DE, USA). The samples were lodged in aluminium hermetic pans (TZero Aluminum Hermetic, TA Instruments) and heated at 5 °C/min in N_2 atmosphere (flow rate 50 mL/min). The samples were equilibrated at −5 °C, heated to 70 °C and cooled to −5 °C. The heating cycle was repeated twice, and the first heating cycle was commented in the Results and discussion section. For the low temperature experiments, samples were equilibrated at 5.00 °C, cooled at 0.50 °C/min to −80.00 °C and heated at 0.50 °C/min to 25.00 °C.

2.6. Small angle X-ray scattering (SAXS)

SAXS experiments were carried out with a S3-MICRO instrument (HECUS GmbH, Graz, Austria) equipped with a position-sensitive detector (OED 50 M) containing 1024 channels of width 54 μm. Cu Kα radiation (λ = 1.542 Å) was provided by a GeniX X-ray source (Xenocs, Grenoble, France), operating at a maximum power of 50 W (50 kV and 1 mA). Glass capillaries 1.5 mm in diameter were filled with the fluid samples, while a capillary filled with water was used for the background subtraction. The temperature was controlled at 20 and 37 °C by means of a Peltier TCCS-3 Hecus. The sample-detector distance was calibrated by measuring the scattering pattern of silver behenate. Scattering curves were obtained in the q-range between 0.09 and 5.4 nm^{-1}, where $q = (4\pi/\lambda)\cdot\sin\theta/2$ is the scattering vector and θ the scattering angle. The scattered radiation was collected in a scattering angle between 0° and 7°. All scattering curves were corrected for the empty capillary contribution considering the relative transmission factor.

2.7. Rheology

Rheological measurements were carried out on a Discovery HR-3 rheometer (TA Instruments, Newcastle, DE, USA) fitted with a stainless-steel plate and plate geometry (40 mm) and a Peltier plate temperature control. Gelled samples were characterized at 20 °C by means of oscillatory measurements. First, strain-sweep measurements were performed at a constant oscillation frequency of 1 Hz for strains ranging from 10^{-1}% to 10^{4}%. Then, frequency-sweep measurements were performed at a constant strain of 1% for frequencies ranging from 10^{-2} Hz to 10 Hz. In these dynamic measurements, the shear storage modulus G' and the shear loss modulus G" were obtained and plotted against strain % and frequency. In order to minimize water evaporation during measurements, silicone oil was placed at the free surface between the two plates. All rheology measurements were performed at least twice on duplicate samples.

3. Results and discussion

3.1. Stability ternary phase diagram

The gelatin/PVA/water stability ternary phase diagram at 37 °C is reported in Fig. 1. Pure gelatin and PVA solutions display a single phase for all the investigated concentrations. When mixing the two solutions, different situations occur, depending on the polymeric concentration with respect to water and on the weight ratio of the two polymers. Three distinct regions can be defined: two phases, hazy and single phase.

Macroscopic phase separation takes place when the total polymer concentration is above 6% w/w, as revealed by the formation of transparent PVA-rich upper phase and a pale yellow gelatin-rich bottom phase. The hazy region is shifted towards the PVA-rich samples, while when the system is diluted one single and transparent phase is observed. These observations are consistent with the phase diagram reported by Tanaka *et al.*, [19] even if the characterisation reported in the reference was performed in slightly different conditions (T = 30 °C, neutral pH and with PVA 99% hydrolysed with Mw ~88.000). When cooled down to 20 °C, pure gelatin and PVA samples are still transparent and a single phase is again observed, whereas mixed systems become turbid, especially when PVA concentration is higher than gelatin. To study the interaction between the two polymers in water, we selected 3.75% w/w gelatin/PVA 50/50 (referred to as Gel/PVA in the phase diagram) as a case study. This sample displays a reversible transition from transparent fluid at 37 °C to turbid hydrogel at 20 °C. The corresponding pure gelatin and PVA solutions were characterized too, in order to compare the behaviour of the single polymers with that of the mixture.

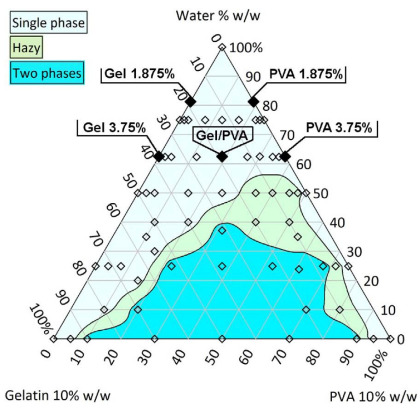

Fig. 1. Stability ternary phase diagram at 37 °C, pH = 9. Bottom left corner: weight of gelatin 10% w/w pH = 9 solution. Bottom right corner: weight of PVA 10% w/w pH = 9 solution. Top corner: weight of water pH = 9. The markers correspond to each investigated composition. Full markers indicate the fully characterized samples.

3.2. Scanning electron microscopy

SEM micrographs on xerogels were recorded to investigate the morphology of the samples at different length scales and to detect the possible effects of the interaction between gelatin and PVA on it.

It is important to stress here that the morphology of xerogels is not necessarily representative of the structure of the corresponding hydrogels, especially at the shorter length scales. Different methods have been developed to reliably image hydrogels by means of electron microscopy. Environmental scanning electron microscopy (ESEM) has been recently introduced as a valuable tool for the imaging of wet materials and hydrogels [44]; nevertheless, controlling the moisture at the sample level is a challenge, both in terms of stability and resolution [45].

Aiming at removing water without affecting the structure of hydrogels before their investigation by conventional SEM (*i.e.*, in high vacuum conditions), critical point drying, freeze etching and freeze drying are the most common methods. In the first one, water is first replaced by a polar organic solvent (typically acetone), which is then permeated with liquid CO_2 that is finally evaporated in supercritical conditions [46]. Unfortunately, this approach has been shown to produce several changes in the structure of the hydrogel, mostly related to modifications in the assembly of the polymer when the organic solvent replaces water [47,48]. Both freeze etching and freeze drying comprise the removal of water through a freezing step to form ice, followed by its sublimation. The critical step in both cases is the cooling rate and the freezing temperature: in fact, when the cooling rate is too slow (and/or the freezing temperature not low enough), water is able to form ice crystals, whose growth modifies the hydrogel structure. The controlled freezing and freeze drying has been recently exploited to intentionally modify the structure of hydrogels and, more generally, to produce porous and micro/nano-structured materials [14,49]. On the other hand, the direct plunging of hydrogel samples in liquid nitrogen (−196 °C) takes to the formation of amorphous ice and, when combined with the low temperature freeze drying, has been shown as a suitable method to preserve the native morphology of hydrogels [48]. Nevertheless, it has to be kept in mind that hydrogels typically consist of very hydrophilic polymers: *i.e.*, part of the water in the hydrogel does not behave as free water in terms of freezing, as it strongly interacts with the polymer. As a consequence, that water would not reach the solid state, eventually taking to the modification of the structure of the xerogel at the supra-molecular scale during the freeze drying process.

Fig. 2 displays the FE-SEM micrographs of the xerogel obtained by freeze drying the sample gelatin 3.75%. Results are consistent with what previously reported in the literature [50]: pores with dimensions in the order of few micrometers are clearly visible in Fig. 2a, while Fig. 2b highlights the presence of fibers on the pore walls, most reasonably consisting of non-denatured collagen.

The FE-SEM micrographs of the xerogel obtained through the freeze drying of the sample PVA 3.75% are given in Fig. 3. Results show the presence of micrometric pores aligned along a preferred orientation, together with inter-connecting pores, consistently with what previously reported in literature for PVA xerogels prepared by freeze etching [51].

The presence of both gelatin and PVA significantly affects the structure of the xerogels, as shown in Fig. 4. The most important evidence is that the whole sample consists of a single homogeneous phase. Compared to the microstructure observed in the pure components, the mixed sample displays a much less ordered architecture. The pores are present, but they are not arranged along a preferential direction, as it was the case with PVA. Furthermore, compared to what observed in pure gelatin, the shape of the pores is less defined and sub-micrometric irregularities are detected, suggesting that phase segregation takes place at the sub-micrometer scale. This behaviour could be the result of capillary forces [52], which are known to take to a phase separation when mixed polymer solutions (especially when their composition approaches the binodal curve) are confined in the proximity of surfaces

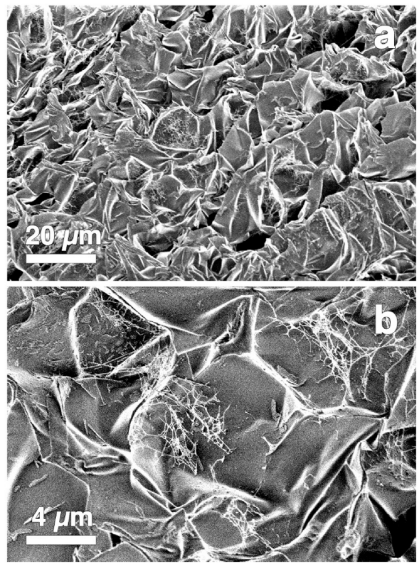

Fig. 2. FE-SEM micrographs at different magnifications of the xerogel obtained by freeze drying gelatin 3.75%.

[53,54]. Unfortunately, as the water-confining ability of both PVA and gelatin could hinder the fast freezing of water near the pore walls, xerogels' structure could significantly differ at the sub-micrometer scale

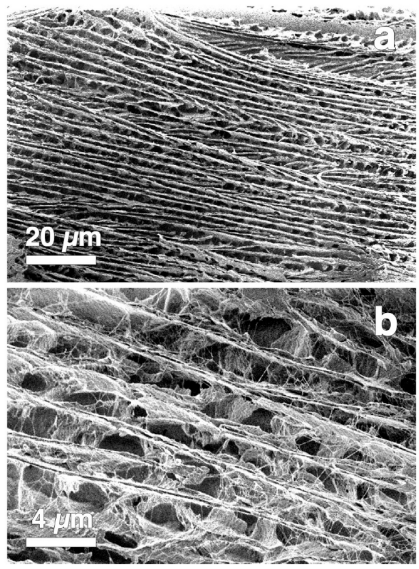

Fig. 3. FE-SEM micrographs at different magnifications of the xerogel obtained by freeze drying PVA 3.75%. The imaged surface was obtained by cutting the sample along the pore's direction.

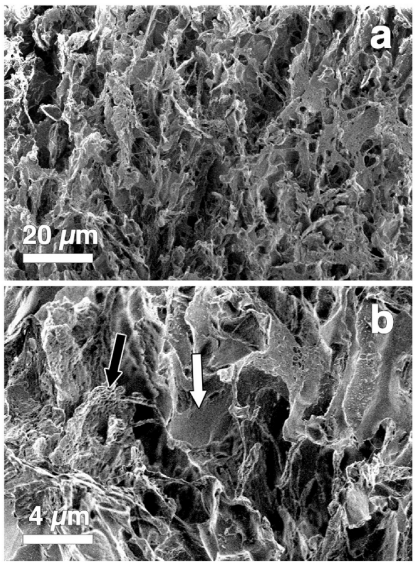

Fig. 4. FE-SEM micrographs at different magnifications of the xerogel obtained by freeze drying Gel/PVA. The arrows in Figure b indicate two regions with different morphologies, reminding that of pure gelatin (white) and pure PVA (black).

from their parent hydrogels. Furthermore, as the ice front reaches the proximity of the pore walls during the freezing process, capillary forces could play a key role, being another possible reason for structural differences.

We can therefore conclude that no macro- or micro-phase segregation is observed and that the co-presence of the two macromolecules takes to a homogeneous architecture (which is neither that of gelatin or PVA) at those length scales. The micrographs suggest a phase segregation at the sub-micrometric scale, but we cannot extend our discussion to shorter length scales: in fact, as we have already stressed before, the xerogels could significantly differ at the nanoscale from the corresponding hydrogels.

3.3. Differential scanning calorimetry

The thermal behaviour of gelatin, PVA, and their mixture was investigated by means of Differential Scanning Calorimetry (DSC). The thermograms registered on the samples are reported in Fig. 5. The heating scan of the Gel 3.75% sample shows the endothermic peak due to the gel-sol transition of the gelatin [55]. The same feature appears in the thermogram of the sample Gel/PVA, which contains 1.875% w/w of gelatin and 1.875% w/w of PVA, as it is reported in the Materials and methods section. It is interesting to note that samples of pure PVA (both 1.875% w/w and 3.75% w/w, the latter shown in Fig. 5) and the sample Gel 1.875% do not show any peak in the 0–70 °C temperature range. The results indicate that PVA has a higher ability to interact with water, thus increasing the effective concentration of gelatin, which exhibits the characteristic gel-sol transition (see Table 2). A similar effect has been observed, for instance, in the case of gelatin in the presence of sugars and polyols [56], resulting in the stabilization of the gel phase.

The PVA proficiency to interact with water is confirmed by measuring the freezable water in the 3.75% solutions. By slowly cooling

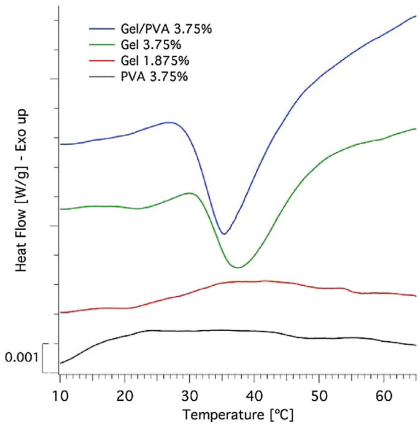

Fig. 5. DSC heating scan of the investigated samples. (For interpretation of the references to colour in this figure legend, the reader is referred to the web version of this article).

Table 2
Parameters obtained by DSC on the investigated samples.

	Gel-Sol transition		Water	
	Minimum (°C)	Enthalpy (J/g)	Freezing water (% wt on total H_2O)	Non-freezing water (% wt of polymer)
Gel 3.75%	37.9 ± 0.5	0.40 ± 0.02	99 ± 1	26.4
Gel/PVA	35.4 ± 0.5	0.53 ± 0.03	98 ± 1	41.6
PVA 3.75%	–	–	96 ± 1	95.5

down to −80 °C and heating to room temperature 3.75% solutions of Gel, PVA and Gel/PVA, the melting transition of the "free" water is detected and from the measurement of the area under the peak we obtain the enthalpy associated to the transition. Comparing this value to the standard melting enthalpy of water (333 J/g) we obtain the amount of water that underwent the melting transition. Considering the weight fraction of water in the sample, we can quantify the amount of freezable water and, by difference, that of the non-freezing water. This value, scaled for the amount (weight) of polymer in the sample, is reported in the last column of the table and indicates the proficiency of the polymers in hindering the freezing of water. However, it is important to stress that, as recently reported in the literature, the amount of non-freezing water cannot be used as a measure of strength of polymer-water interactions: in fact, non-freezing water exists because of the interplay between water crystallization and the glass transition temperature of the polymer [57]. A typical DSC scan is reported in Fig. S1. The data reported in Table 2 show that PVA has a much higher proficiency than gelatin to interact with the water, as it can constrain an amount of water almost equal to its dry weight.

3.4. Small angle X-rays scattering

SAXS experiments have been carried out to obtain information on the structural details of Gel 3.75%, PVA 1.875%, PVA 3.75%, and Gel/PVA samples at 20 (Fig. 6a) and 37 °C (Fig. S2 in the Supplementary Material). Samples containing PVA show a distinct peak centred at $q \sim 0.63\ nm^{-1}$, which corresponds to a distance of $d \sim 9.9$ nm. This value is in very good agreement with literature [58] and is known to represent the average distance between microcrystalline regions

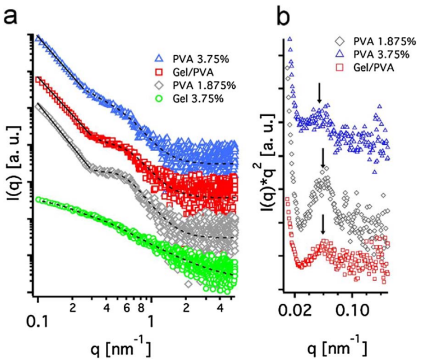

Fig. 6. a) SAXS curves of Gel 3.75% (green circles), PVA 1.875% (grey diamonds), Gel/PVA (red squares), and PVA 3.75% (blue triangles) at 20 °C. Dashed lines represent the fitting curves according to the Beaucage model, while solid lines represent power law fittings. b) Kratky plot of samples Gel/PVA (red squares), PVA 1.875% (grey diamonds), and PVA 3.75% (blue triangles) at 20 °C. Arrows indicate the peak-top position. (For interpretation of the references to colour in this figure legend, the reader is referred to the web version of this article).

generated from hydrogen bonding between PVA chains. The results in Fig. 6a and Fig. 6b show that the peak-top position of PVA 3.75% sample is slightly lower than that of PVA 1.875%, while it is not affected by the presence of Gel and the temperature change (see Fig. S2 in the Supplementary Material).

Gelatin scattering profiles and the mid- and high-q portions of samples containing PVA were fitted using a one-level Beaucage function [59].

$$I(q) = Bkg + Aexp\left(-\frac{q^2R_g^2}{3}\right) + B\frac{\left[\mathrm{erf}\left(\frac{qR_g}{\sqrt{6}}\right)\right]^{3P_1}}{q^{P_1}} \quad (1)$$

where A and B are the Guinier and Porod scaling factors, respectively, q is the scattering vector, R_g is the radius of gyration, P_1 is the Porod exponent, and Bkg takes into account for the background scattering.

The fitting results are reported in Table 3. The radii of gyration obtained for gelatin are consistent with the value of 11.2 nm reported in literature for a 6% w/w solution [60]. The obtained P_1 values are close to $P = -5/3$, in agreement with a fully swollen coil in solution [61].

In the samples containing PVA, the low-q regions ($q < 0.3\ nm^{-1}$) were fitted according to a power-law function:

$$I(q) = \frac{K}{q^{P_2}} \quad (2)$$

where K is a scale factor and P_2 is the power-law exponent.

The scattering profile of Gel/PVA arises from the contribution of both PVA and gelatin profiles; however, since the scattering intensity of PVA is much larger than gelatin, the former contribution is predominant. As a result, the radii of gyration of samples PVA 1.875%, Gel/PVA, and PVA 3.75% are similar within the experimental error at both 20 and 37 °C. As far as the exponent of the power-law is concerned, P_1 is close to the theoretical value of −4 for an infinite smooth surface, while in the low-q region P_2 is $4 < P_2 < 3$, which is characteristic of surface fractals with fractal dimensions $D_s = 6\text{-}|P_2|$. Typically, D_s is 2 for smooth surfaces, and increases towards 3 as the roughness increases [62]. From the results in Table 3 it is evident that, while the radii of gyration remain constant, D_s values are strongly dependent on samples composition. In particular, D_s is close to 2 for PVA 1.875%, while it increases for PVA 3.75% and even more for Gel/PVA. The same trend can be observed at both 20 and 37 °C. The analysis of the parameters obtained from SAXS measurements and fittings suggest that only the fractal dimension is affected by the presence of gelatin, while the average distance between the scattering centres (PVA microcrystallites) remains constant. This fact indicates that, in the dimensional range probed by SAXS, PVA–PVA interactions are preferred with respect to gelatin-PVA. Hence, no segregation phenomena are detected at the nanoscale.

3.5. Rheology

The dynamic viscoelastic behaviour of gelatin and gelatin/PVA hydrogels was assessed by means of strain and frequency sweeps. The results of the strain sweep measurement for gelatin and Gel/PVA hydrogels are shown in Fig. 7a.

Up to a critical strain, both samples show a linear viscoelastic region in which G' and G" are independent of the applied strain. Then, when the applied strain is further increased, G' and G" start to decrease as a consequence of the rupture of gel networks, and both samples show a predominant liquid-like behaviour (*i.e.*, G" > G'). As reported in the literature, gelatin displays an overshoot of G′ and G″ with strain, which is related to its typical strain-hardening behaviour [63]. The presence of PVA causes a significant lowering of the storage modulus of the gel, and a reduction of the linear viscoelastic region (approximately by a factor of 5), similar to what happens in the half-concentrated sample (Gel 1.875%). Actually, the curve of Gel 1.875% is essentially the same of the mixed sample in terms of critical strain (*i.e.*, the strain at which G' equals G") and of the behaviour of the gel at higher strain, but Gel/PVA displays a higher storage modulus. The trends of the storage (G') and loss modulus (G") as a function of frequency (measured at a constant strain of 1%, within the linear viscoelastic region) are also reported in Fig. 7b. The curves show a typical behaviour of gel networks with a predominant solid-like character, since G' is significantly larger than G" (approximately by two order of magnitude) and nearly independent of the frequency in the 0.01–10 Hz range [64]. The plateau value of G' for the Gel/PVA sample is lower than that of Gel 3.75%, but higher than that of diluted gelatin sample, reflecting the same situation observed by means of strain sweep measurements. Interestingly, the trend of G" against frequency for the Gel/PVA sample shows a peculiar behaviour (see also the tanδ *vs* frequency curve in the Supplementary Material): in fact, the minimum in the loss modulus curve [65], betraying the presence of a low-frequency relaxation mechanism, is shifted toward lower frequencies as to indicate additional dampening mechanisms of the gelatin network due to gelatin-PVA interactions [66]. Together with the invoked dilution effect, these interactions have an additional

Table 3
Parameters obtained from the fitting of SAXS curves in Fig. 6a according to Eq.(1) and Eq. (2).

	20 °C				37 °C			
Sample	Rg (nm)	P_1	P_2	D_s	Rg (nm)	P_1	P_2	D_s
Gel 3.75%	11.4 ± 0.7	−1.64 ± 0.04			10.8 ± 0.5	−1.76 ± 0.04		
Gel/PVA	6.1 ± 0.6	−3.95 ± 0.82	−3.24 ± 0.05	2.76	6.3 ± 0.6	−3.84 ± 1.04	−3.34 ± 0.03	2.66
PVA 3.75%	6.4 ± 0.6	−3.77 ± 0.22	−3.33 ± 0.03	2.63	7.0 ± 0.6	−4.01 ± 0.18	−3.61 ± 0.03	2.39
PVA 1.875%	6.2 ± 0.6	−4.08 ± 0.81	−3.58 ± 0.08	2.42	6.4 ± 0.6	−4.05 ± 0.22	−3.82 ± 0.05	2.18

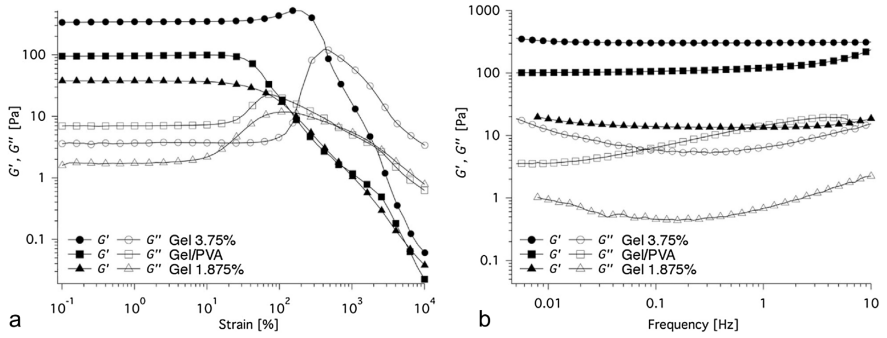

Fig. 7. Storage modulus and loss modulus as a function of strain (a) and oscillation frequency (b) for gelatin (3.75% and 1.875%) and Gel/PVA gels. All measurements were performed at 20 °C.

detrimental effect on the formation of the gelatin helical network and in the subsequent development of the gel.

4. Conclusions

We investigated the interactions taking place between gelatin and PVA using a multi-technique approach that provided information at different length-scales. From the macro to the micro scale, FE-SEM analysis revealed that the morphology of Gel/PVA xerogel at the investigated concentration is homogeneous. At higher magnifications, sub-micrometric domains were observed, suggesting phase segregation at this length scale. This hypothesis was confirmed by DSC and SAXS results, both accounting for the organisation of the polymers at the supra-molecular level. DSC measurements provided information about the gelatin component in the mixture: in fact, only the signal related to the gelatin gel-sol thermal transition was observed. Results demonstrated that the gelatin–gelatin interactions are not affected by the presence of PVA. The effect of PVA in the mixture is to constrain a significant amount of water (as demonstrated by the free water evaluation), resulting in a “concentrating” effect on gelatin. SAXS experiments proved that PVA structural features are not altered by the presence of gelatin, thus indicating that PVA–PVA interactions are preferred with respect to gelatin-PVA. The rheological behaviour of the mixed system in terms of viscoelastic properties is mostly dictated by the interaction of the two polymers with water. Nevertheless, frequency sweep curves provide evidences of additional dampening mechanisms due to gelatin-PVA interactions, consistent with a reduced extension of the gelatin network.

In summary, the experimental results do not provide evidence of strong interactions between gelatin and PVA. Interestingly, the behaviour of the mixed system is rather ascribable to a different interaction of the two polymers with water.

Acknowledgment

CSGI is acknowledged for financial support. The referees of the paper are acknowledged for the helpful comments that improved the quality of the work.

Appendix A. Supplementary data

Supplementary data associated with this article can be found, in the online version, at http://dx.doi.org/10.1016/j.colsurfa.2017.07.049.

References

[1] A.S. Hoffman, Hydrogels for biomedical applications, Adv. Drug Deliv. Rev. 64 (2012) 18–23, http://dx.doi.org/10.1016/j.addr.2012.09.010 (Supplement).
[2] W.E. Hennink, C.F. van Nostrum, Novel crosslinking methods to design hydrogels, Adv. Drug Deliv. Rev. 54 (2002) 13–36, http://dx.doi.org/10.1016/S0169-409X(01)00240-Xs.
[3] S. Utech, A.R. Boccaccini, A review of hydrogel-based composites for biomedical applications: enhancement of hydrogel properties by addition of rigid inorganic fillers, J. Mater. Sci. 51 (2016) 271–310, http://dx.doi.org/10.1007/s10853-015-9382-5.
[4] J.G. Lyons, L.M. Geever, M.J.D. Nugent, J.E. Kennedy, C.L. Higginbotham, Development and characterisation of an agar-polyvinyl alcohol blend hydrogel, J. Mech. Behav. Biomed. Mater. 2 (2009) 485–493, http://dx.doi.org/10.1016/j.jmbbm.2008.12.003.
[5] L. Robeson, Historical perspective of advances in the science and technology of polymer blends, Polymers 6 (2014) 1251–1265, http://dx.doi.org/10.3390/polym6051251.
[6] Z. Horák, I. Fortelný, J. Kolařík, D. Hlavatá, A. Sikora, Polymer blends, Encycl. Polym. Sci. Technol. John Wiley & Sons, Inc., 2002, http://dx.doi.org/10.1002/0471440264.pst276.
[7] W.J. Work, K. Horie, M. Hess, R.F.T. Stepto, Definition of terms related to polymer blends, composites, and multiphase polymeric materials (IUPAC Recommendations), Pure Appl. Chem. 76 (2009) (2004) 1985–2007, http://dx.doi.org/10.1351/pac200476111985.
[8] T. Kato, S. Aoshima, H. Kikuchi, Special issue: self-Assembled materials, Polym. J. 44 (2012) 451, http://dx.doi.org/10.1038/pj.2012.62 (451).
[9] S.T. Lin, L. Kimble, D. Bhattacharyya, Polymer blends and composites for biomedical applications, in: Q. Li, Y.-W. Mai (Eds.), Biomater. Implants Scaffolds, Springer Berlin, Heidelberg, 2017, pp. 195–235, http://dx.doi.org/10.1007/978-3-662-53574-5_7.
[10] E. Terentjev, J.L. Gornall, Helix-coil transition of gelatin: helical morphology and stability, Soft Matter 4 (2008) 544–549, http://dx.doi.org/10.1039/B713075A.
[11] A. Bigi, G. Cojazzi, S. Panzavolta, K. Rubini, N. Roveri, Mechanical and thermal properties of gelatin films at different degrees of glutaraldehyde crosslinking, Biomaterials 22 (2001) 763–768, http://dx.doi.org/10.1016/S0142-9612(00)00236-2.
[12] K. Su, C. Wang, Recent advances in the use of gelatin in biomedical research, Biotechnol. Lett. 37 (2015) 2139–2145, http://dx.doi.org/10.1007/s10529-015-1907-0.
[13] K.Y. Lee, D.J. Mooney, Hydrogels for tissue engineering, Chem. Rev. 101 (2001) 1869–1880, http://dx.doi.org/10.1021/cr000108x.
[14] C.M. Hassan, N.A. Peppas, Structure and applications of poly(vinyl alcohol) hydrogels produced by conventional crosslinking or by Freezing/Thawing methods, Biopolym PVA Hydrogels, Anionic Polym. Nanocomposites, Springer Berlin, Heidelberg, 2000, pp. 37–65, http://dx.doi.org/10.1007/3-540-46414-X_2.
[15] E.A. Kamoun, X. Chen, M.S. Mohy Eldin, E.-R.S. Kenawy, Crosslinked poly(vinyl alcohol) hydrogels for wound dressing applications: a review of remarkably blended polymers, Arab. J. Chem. 8 (2015) 1–14, http://dx.doi.org/10.1016/j.arabjc.2014.07.005.
[16] A. Kumar, S.S. Han, PVA-based hydrogels for tissue engineering: a review, Int. J. Polym. Mater. Polym. Biomater. 66 (2017) 159–182, http://dx.doi.org/10.1080/00914037.2016.1190930.
[17] Y.-F. Tang, Y.-M. Du, X.-W. Hu, X.-W. Shi, J.F. Kennedy, Rheological characterisation of a novel thermosensitive chitosan/poly(vinyl alcohol) blend hydrogel, Carbohydr. Polym. 67 (2007) 491–499, http://dx.doi.org/10.1016/j.carbpol.2006.06.015.
[18] B. Sarti, M. Scandola, Viscoelastic and thermal properties of collagen/poly(vinyl alcohol) blends, Biomaterials 16 (1995) 785–792, http://dx.doi.org/10.1016/0142-

9612(95)99641-X.
[19] T. Tanaka, T. Tanigami, K. Yamaura, Phase separation structure in poly(vinyl alcohol)/silk fibroin blend films, Polym. Int. 45 (1998) 175–184, http://dx.doi.org/10.1002/(SICI)1097-0126(199802)45:2<175:AID-PI883>3.0 (CO;2-K.).
[20] T. Tanaka, S. Ohnishi, K. Yamaura, Phase separation in poly(vinyl alcohol)/gelatin blend systems, Polym. Int. 48 (1999) 811–818, http://dx.doi.org/10.1002/(SICI)1097-0126(199909)48:9<811:AID-PI221>3.0 (CO;2-V.).
[21] P.J. do A. Sobral, R.A. de Carvalho, I.C.F. Moraes, Bittante A.M.Q.B, E.S. Monterrey-Quintero, Phase transitions in biodegradable films based on blends of gelatin and poly (vinyl alcohol), Food Sci Technol. Camp 31 (2011) 372–379, http://dx.doi.org/10.1590/S0101-20612011000200015.
[22] S.M. Pawde, K. Deshmukh, S. Parab, Preparation and characterisation of poly(vinyl alcohol) and gelatin blend films, J. Appl. Polym. Sci. 109 (2008) 1328–1337, http://dx.doi.org/10.1002/app.28096.
[23] J.M. Ino, E. Sju, V. Ollivier, E.K.F. Yim, D. Letourneur, C. Le Visage, Evaluation of hemocompatibility and endothelialization of hybrid poly(vinyl alcohol) (PVA)/gelatin polymer films, J. Biomed. Mater. Res. B Appl. Biomater. 101 (2013) 1549–1559, http://dx.doi.org/10.1002/jbm.b.32977.
[24] T.-H. Nguyen, R. Ventura, Y.-K. Min, B.-T. Lee, Genipin cross-Linked polyvinyl alcohol-Gelatin hydrogel for bone regeneration, J. Biomed. Sci. Eng. 9 (2016) 419, http://dx.doi.org/10.4236/jbise.2016.99037.
[25] M.G. Cascone, Dynamic–mechanical properties of bioartificial polymeric materials, Polym. Int. 43 (1997) 55–69, http://dx.doi.org/10.1002/(SICI)1097-0126(199705)43:1<55:AID-PI762>3.0 (CO;2-#.).
[26] S. Moscato, L. Mattii, D. D'Alessandro, M.G. Cascone, L. Lazzeri, L.P. Serino, A. Dolfi, N. Bernardini, Interaction of human gingival fibroblasts with PVA/gelatine sponges, Micron 39 (2008) 569–579, http://dx.doi.org/10.1016/j.micron.2007.06.016.
[27] Y. Liu, N.E. Vrana, P.A. Cahill, G.B. McGuinness, Physically crosslinked composite hydrogels of PVA with natural macromolecules: structure, mechanical properties, and endothelial cell compatibility, J. Biomed. Mater. Res. B Appl. Biomater. 90 B (2009) 492–502, http://dx.doi.org/10.1002/jbm.b.31310.
[28] A. Bajpai, R. Saini, Preparation and characterisation of biocompatible spongy cryogels of poly(vinyl alcohol)-gelatin and study of water sorption behaviour, Polym. Int. 54 (2005) 1233–1242, http://dx.doi.org/10.1002/pi.1813.
[29] E.-E. Hago, X. Li, Interpenetrating polymer network hydrogels based on gelatin and PVA by biocompatible approaches: synthesis and characterisation, Adv. Mater. Sci. Eng. (2013) e328763, http://dx.doi.org/10.1155/2013/328763.
[30] M.G. Cascone, L. Lazzeri, E. Sparvoli, M. Scatena, L.P. Serino, S. Danti, Morphological evaluation of bioartificial hydrogels as potential tissue engineering scaffolds, J. Mater. Sci. Mater. Med. 15 (2004) 1309–1313, http://dx.doi.org/10.1007/s10856-004-5739-z.
[31] S. Nkhwa, K.F. Lauriaga, E. Kemal, S. Deb, Poly(vinyl alcohol): physical approaches to designing biomaterials for biomedical applications, Conf. Pap. Sci. 2014 (2014) 1–7, http://dx.doi.org/10.1155/2014/403472.
[32] K. Pal, A.K. Banthia, D.K. Majumdar, Biomedical evaluation of polyvinyl alcohol–gelatin esterified hydrogel for wound dressing, J. Mater. Sci. Mater. Med. 18 (2007) 1889–1894, http://dx.doi.org/10.1007/s10856-007-3061-2.
[33] S.M. Pawde, K. Deshmukh, Characterisation of polyvinyl alcohol/gelatin blend hydrogel films for biomedical applications, J. Appl. Polym. Sci. 109 (2008) 3431–3437, http://dx.doi.org/10.1002/app.28454.
[34] A. Porcaro, M.L. Ottone, J.A. Deiber, Microstructure characterisation through mechanical, electrokinetic and spectroscopic methods of polyampholyte gelatin hydrogels crosslinked with poly(vinyl alcohol), Polymer 54 (2013) 2706–2716, http://dx.doi.org/10.1016/j.polymer.2013.03.045.
[35] E. Chiellini, P. Cinelli, V.I. Ilieva, A. Ceccanti, P. Alexy, D. Bakos, Biodegradable hybrid polymer films based on poly(vinyl alcohol) and collagen hydrolyzate, Macromol. Symp. 197 (2003) 125–132, http://dx.doi.org/10.1002/masy.200350712.
[36] X. Gao, K. Tang, J. Liu, X. Zheng, Y. Zhang, Compatibility and properties of biodegradable blend films with gelatin and poly(vinyl alcohol), J. Wuhan Univ Technol.-Mater Sci Ed. 29 (2014) 351–356, http://dx.doi.org/10.1007/s11595-014-0920-9.
[37] O. Mendieta-Taboada, P.J. do, A. Sobral, R.A. Carvalho, A.M.B.Q. Habitante, Thermomechanical properties of biodegradable films based on blends of gelatin and poly(vinyl alcohol), Food Hydrocoll. 22 (2008) 1485–1492, http://dx.doi.org/10.1016/j.foodhyd.2007.10.001.
[38] K. Pal, A.K. Banthia, D.K. Majumdar, Preparation and characterisation of polyvinyl alcohol-gelatin hydrogel membranes for biomedical applications, Aaps Pharmscitech. 8 (2007) E142–E146, http://dx.doi.org/10.1208/pt080121.
[39] H. Liao, K. Shi, J. Peng, Y. Qu, J. Liao, Z. Qian, Preparation and properties of nano-Hydroxyapatite/Gelatin/Poly(vinyl alcohol) composite membrane, J. Nanosci. Nanotechnol. 15 (2015) 4188–4192, http://dx.doi.org/10.1166/jnn.2015.9722.
[40] D. Yang, Y. Li, J. Nie, Preparation of gelatin/PVA nanofibers and their potential application in controlled release of drugs, Carbohydr. Polym. 69 (2007) 538–543, http://dx.doi.org/10.1016/j.carbpol.2007.01.008.
[41] S.M. Choi, D. Singh, A. Kumar, T.H. Oh, Y.W. Cho, S.S. Han, Porous three-Dimensional PVA/Gelatin sponge for skin tissue engineering, Int. J. Polym. Mater. Polym. Biomater. 62 (2013) 384–389, http://dx.doi.org/10.1080/00914037.2012.710862.
[42] M. Wang, Y. Li, J. Wu, F. Xu, Y. Zuo, A. Jansen, In vitro and in vivo study to the biocompatibility and biodegradation of hydroxyapatite/poly(vinyl alcohol)/gelatin composite, J. Biomed. Mater. Res. A 85A (2008) 418–426, http://dx.doi.org/10.1002/jbm.a.31585.
[43] G. Vargas, J.L. Acevedo, J. López, J. Romero, Study of cross-linking of gelatin by ethylene glycol diglycidyl ether, Mater. Lett. 62 (2008) 3656–3658, http://dx.doi.org/10.1016/j.matlet.2008.04.020.
[44] A.M. Donald, The use of environmental scanning electron microscopy for imaging wet and insulating materials, Nat. Mater. 2 (2003) 511–516, http://dx.doi.org/10.1038/nmat898.
[45] L.-M. Joubert, Visualization of hydrogels with variable-Pressure SEM, Microsc. Microanal. 15 (2009) 1308–1309, http://dx.doi.org/10.1017/S1431927609096263.
[46] D. Bray, Critical point drying of biological specimens for scanning electron microscopy, in: J. Williams, A. Clifford (Eds.), Supercrit. Fluid Methods Protoc. Humana Press, 2000, pp. 235–243, http://dx.doi.org/10.1385/1-59259-030-6:235.
[47] B.G. Nordestgaard, J. Rostgaard, Critical-point drying versus freeze drying for scanning electron microscopy: a quantitative and qualitative study on isolated hepatocytes, J. Microsc. 137 (1985) 189–207, http://dx.doi.org/10.1111/j 1365-2818. tb02577. x.
[48] S.M. Paterson, Y.S. Casadio, D.H. Brown, J.A. Shaw, T.V. Chirila, M.V. Baker, Laser scanning confocal microscopy versus scanning electron microscopy for characterisation of polymer morphology: sample preparation drastically distorts morphologies of poly(2-hydroxyethyl methacrylate)-based hydrogels, J. Appl. Polym. Sci. 127 (2013) 4296–4304, http://dx.doi.org/10.1002/app.38034.
[49] L. Qian, H. Zhang, Controlled freezing and freeze drying: a versatile route for porous and micro-/nano-structured materials, J. Chem. Technol. Biotechnol. 86 (2011) 172–184, http://dx.doi.org/10.1002/jctb.2495.
[50] D. Tatini, P. Tempesti, F. Ridi, E. Fratini, M. Bonini, P. Baglioni, Pluronic/gelatin composites for controlled release of actives, Colloids Surf. B Biointerfaces 135 (2015) 400–407, http://dx.doi.org/10.1016/j.colsurfb.2015.08.002.
[51] H.H. Trieu, S. Qutubuddin, Polyvinyl alcohol hydrogels I. Microscopic structure by freeze-etching and critical point drying techniques, Colloid. Polym. Sci. 272 (1994) 301–309, http://dx.doi.org/10.1007/BF00655501.
[52] R. von Klitzing, E. Thormann, T. Nylander, D. Langevin, C. Stubenrauch, Confinement of linear polymers, surfactants, and particles between interfaces, Adv. Colloid Interface Sci. 155 (2010) 19–31, http://dx.doi.org/10.1016/j.cis.2010.02.003.
[53] M. Olsson, P. Linse, L. Piculell, Capillary-Induced phase separation in binary and quasi-Binary polymer solutions a mean-Field lattice study, Langmuir 20 (2004) 1611–1619, http://dx.doi.org/10.1021/la035931d.
[54] F. Joabsson, P. Linse, Capillary-Induced phase separation in mixed polymer solutions a lattice mean-Field calculation study, J. Phys. Chem. B. 106 (2002) 3827–3834, http://dx.doi.org/10.1021/jp013199q.
[55] S.E.B. Petrie, R. Becker, Thermal behavior of aqueous gelatin solutions, in: R.S. Porter, J.F. Johnson (Eds.), Anal. Calorim. Springer, US, 1970, pp. 225–238, http://dx.doi.org/10.1007/978-1-4615-8621-0_20.
[56] D. Oakenfull, A. Scott, Stabilization of gelatin gels by sugars and polyols, Food Hydrocoll. 1 (1986) 163–175, http://dx.doi.org/10.1016/S0268-005X(86)80018-2.
[57] V. Kocherbitov, The nature of nonfreezing water in carbohydrate polymers, Carbohydr. Polym. 150 (2016) 353–358, http://dx.doi.org/10.1016/j.carbpol.2016.04.119.
[58] E. Otsuka, S. Komiya, S. Sasaki, J. Xing, Y. Bando, Y. Hirashima, M. Sugiyama, A. Suzuki, Effects of preparation temperature on swelling and mechanical properties of PVA cast gels, Soft Matter. 8 (2012) 8129–8136, http://dx.doi.org/10.1039/c2sm25513h.
[59] B. Hammouda, Analysis of the Beaucage model, J. Appl. Crystallogr. 43 (2010) 1474–1478, http://dx.doi.org/10.1107/S0021889810033856.
[60] M. Helminger, B. Wu, T. Kollmann, D. Benke, D. Schwahn, V. Pipich, D. Faivre, D. Zahn, H. Cölfen, Synthesis and characterisation of gelatin-Based magnetic hydrogels, Adv. Funct. Mater. 24 (2014) 3187–3196, http://dx.doi.org/10.1002/adfm.201303547.
[61] B. Hammouda, Probing Nanoscale Structures – The SANS Toolbox, (2012).
[62] D.W. Schaefer, Fractal models and the structure of materials, MRS Bull. 13 (1988) 22–27, http://dx.doi.org/10.1557/S088376940006632X.
[63] K. Hyun, M. Wilhelm, C.O. Klein, K.S. Cho, J.G. Nam, K.H. Ahn, S.J. Lee, R.H. Ewoldt, G.H. McKinley, A review of nonlinear oscillatory shear tests: analysis and application of large amplitude oscillatory shear (LAOS), Prog. Polym. Sci. 36 (12) (2011) 1697–1753, http://dx.doi.org/10.1016/j.progpolymsci.2011.02.002.
[64] Z. Yang, Y. Hemar, L. Hilliou, E.P. Gilbert, D.J. McGillivray, M.A.K. Williams, S. Chaieb, Nonlinear behavior of gelatin networks reveals a hierarchical structure, Biomacromolecules 17 (2016) 590–600, http://dx.doi.org/10.1021/acs.biomac.5b01538.
[65] K. Te Nijenhuis, Thermoreversible networks – viscoelastic properties and structure of gels, Adv. Polym. Sci. 130 (1997), http://dx.doi.org/10.1007/BFb0008699.
[66] R.K. Richardson, G. Robinson, S.B. Ross-Murphy, S. Todd, Mechanical spectroscopy of filled gelatin gels, Polym. Bull. 4 (1981) 541–546, http://dx.doi.org/10.1007/BF00284067.

Supplementary Material

Multi-scale investigation of gelatin/poly(vinyl alcohol) interactions in water

Rita Gelli[a], Stefano Del Buffa[a], Paolo Tempesti[a], Massimo Bonini[a], Francesca Ridi[a], Piero Baglioni[a]*

[a] Department of Chemistry "Ugo Schiff" and CSGI, University of Florence, via della Lastruccia 3, Sesto Fiorentino, 50019 Florence, Italy

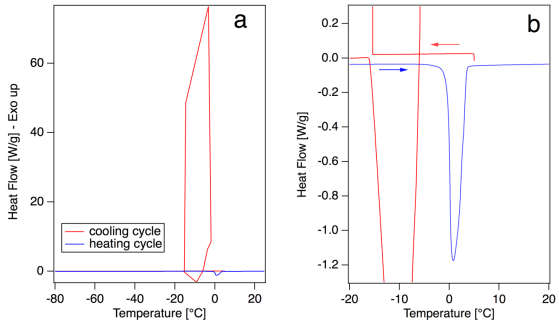

Figure S1:(a) DSC scan of Gel 3.75%. Cooling ramp is red, while heating ramp is blue. (b) zoom of water melting peak, which was used to calculate the amount of freezing and non-freezing water.

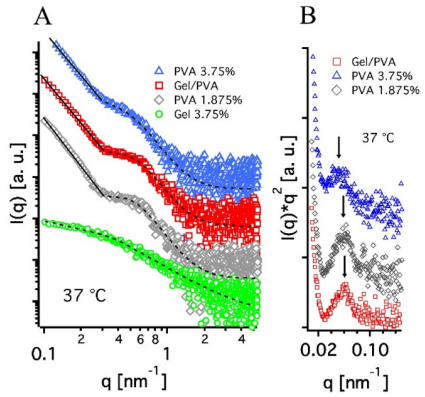

Figure S2: A) SAXS curves of Gel (green circles), PVA 1.875% (grey diamonds), Gel/PVA (red squares), and PVA (blue triangles) at 37 °C. Dashed lines represent the fitting curves according to the Beaucage model, while solid lines represent power law fittings. B) b) Kratky plot of samples Gel/PVA (red squares), PVA 1.875% (grey diamonds), and PVA (blue triangles) at 20 °C. Arrows indicate the peak-top position.

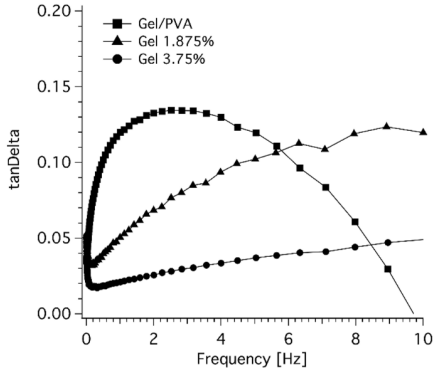

Figure S3: Tan Delta (G''/G') vs Frequency of Gel 3.75%, Gel 1.875% and Gel/PVA samples.

Paper VII

Journal of Colloid and Interface Science 511 (2018) 145–154

Contents lists available at ScienceDirect

Journal of Colloid and Interface Science

journal homepage: www.elsevier.com/locate/jcis

Regular Article

Enhanced formation of hydroxyapatites in gelatin/imogolite macroporous hydrogels

Rita Gelli, Stefano Del Buffa, Paolo Tempesti, Massimo Bonini, Francesca Ridi *, Piero Baglioni *

Department of Chemistry "Ugo Schiff" and CSGI, University of Florence, via della Lastruccia 3, Sesto Fiorentino, 50019 Florence, Italy

GRAPHICAL ABSTRACT

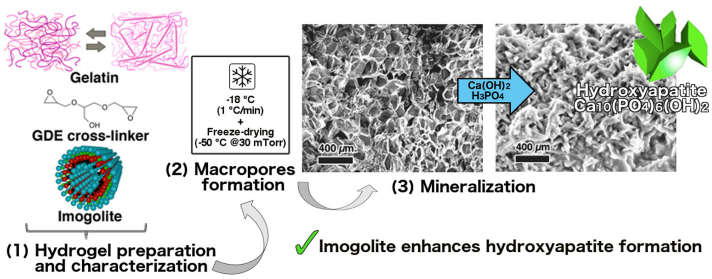

ARTICLE INFO

Article history:
Received 2 August 2017
Revised 25 September 2017
Accepted 26 September 2017
Available online 28 September 2017

Keywords:
Gelatin
Macroporous hydrogel
Imogolite
Nanoclay
Calcium phosphates
Mineralization
Electron microscopy
Differential scanning calorimetry
Small angle X-rays scattering
Rheology

ABSTRACT

Hypothesis: Gelatin is widely investigated for the fabrication of synthetic scaffolds in bone tissue engineering. Practical limitations to its use are mainly due to the fast dissolution rate in physiological conditions and to the lack of pores with suitable dimensions for cell permeation. The aim of this work is to exploit imogolite clays as nucleation sites for the growth of calcium phosphates in gelatin-based hydrogels and to take advantage of a cryogenic treatment to obtain pores of ~100 μm.

Experiments: We evaluated the effect of imogolites and a biocompatible cross-linker on the gelatin network in terms of morphology, thermal and rheological behavior. The hydrogels were cryogenically-treated and characterized to investigate the modification of the polymer network, both at the micro- and nano-scale. The samples were mineralized to investigate the effect of imogolites on the formation of calcium phosphates.

Findings: The interaction between gelatin, imogolite and cross-linker leads to the modification of the hydrogel structure at the micro-scale, while minor effects are detected at the nano-scale. The cryogenic procedure is successful in generating pores with the desired size, while the presence of imogolites in the hydrogel promotes hydroxyapatites formation. These results demonstrate that imogolites can be effectively employed as functional fillers in polymer-based scaffolds.

Abbreviations: HA, hydroxyapatite; CHA, carbonated hydroxyapatite; Gel, gelatin; Imo, imogolite; GDE, glycerol diglycidyl ether; EGDE, ethylene glycol diglycidyl ether; EDC, 1-ethyl-3-(3-dimethylaminopropyl)carbodiimide; CaP, calcium phosphates; TEOS, tetraethyl orthosilicate; ASB, aluminum-tri-sec-butoxide; FT-IR, Fourier transform infrared spectroscopy; XRD, X-rays diffraction; FE-SEM, field emission scanning electron microscopy; DSC, differential scanning calorimetry; TGA, thermogravimetric analysis; SAXS, small angle X-rays scattering; SSA, specific surface area; PDF, powder diffraction file.

* Corresponding authors.

E-mail addresses: gelli@csgi.unifi.it (R. Gelli), delbuffa@csgi.unifi.it (S. Del Buffa), tempesti@csgi.unifi.it (P. Tempesti), massimo.bonini@unifi.it (M. Bonini), francesca.ridi@unifi.it (F. Ridi), piero.baglioni@unifi.it (P. Baglioni).

https://doi.org/10.1016/j.jcis.2017.09.094
0021-9797/

1. Introduction

Hydroxyapatite, $Ca_{10}(PO_4)_6(OH)_2$ (HA), composes the main mineral fraction of human bones and teeth [1]. In bones, it is found as a nano-sized, non-stoichiometric calcium-deficient apatite containing carbonate and impurities such as sodium and magnesium ions [2,3]. The presence of these inclusions, especially carbonate, contributes to the unique features of bone in terms of mechanical and biological properties [4]. Great efforts have been recently devoted to rationalize HA formation and crystallization in organic matrices in the attempt to unravel the process of bone tissue formation and remodeling [5]. This is of particular interest in the fields of bone and dental tissue engineering where synthetic scaffolds are designed to support and promote the growth of new tissue, including HA crystals with tunable composition and structural properties [6,7].

One of the most investigated matrices suitable to this purpose are hydrogels [8] and, among hydrogel forming polymers, gelatin (Gel) is one of the most interesting materials having the same chemical composition of bone organic matrix. Gelatin is produced by partial hydrolysis of collagen, which partially loses its characteristic triple-helix structure. Unfortunately, the application of gelatin is practically limited by the fast dissolution rate in physiological conditions, making it necessary to increase the stability of gelatin-based materials by means of chemical and physical methods [9,10]. Covalent cross-linking sites can be obtained by using high-energy radiations (*e.g.*, electrons or gamma rays) [11], by fabricating composite materials [12], or by employing chemical cross-linking agents, such as glutaraldehyde [13], 1-ethyl-3-(3-dimethy laminopropyl)carbodiimide (EDC) [14] and genipin [15]. Bis-epoxy molecules, such as glycerol diglycidyl ether (GDE) and ethylene glycol diglycidyl ether (EGDE), have also been reported to enhance the stability of gelatin hydrogels [16]. Such molecules display a lower toxicity compared to glutaraldehyde and EDC, representing a better alternative to typical gelatin cross-linking agents when the toxicity of unreacted cross-linker molecules represents an issue, as in biomedical applications [17].

Unquestionably, biocompatibility and bioactivity are crucial prerequisites for the *in vitro* and *in vivo* application of biomaterials [18,19], but there are still many structural and physico-chemical factors to be considered. For instance, the presence of interconnected pores with micrometer size (at least 100 μm) is especially recommended to allow for cell permeation and adequate diffusion of nutrients into the material [20]. Cryogenic formation is typically used to generate pores in hydrogels [21]. The polymeric material is frozen and the water inside the matrix crystallizes producing porosities whose dimensions depend on cooling rate and polymer concentration.

In the field of biomaterials considerable attention has been recently devoted to the development of multifunctional nanocomposites, in the attempt of integrating different physico-chemical features and mimicking natural biological systems [22,23]. Imogolite (Imo) is a naturally occurring hydrous aluminosilicate with empirical formula $(OH)_3Al_2O_3SiOH$, displaying a nano-tubular structure consisting of a single-walled nanotube made of gibbsite ($Al(OH)_3$) where the inner hydroxyl groups are replaced by O_3SiOH groups [24]. The different reactivity of the inner and outer surfaces allows, in principle, for selective functionalization reactions [25], while the presence of the nano-sized cavity can be exploited for multiple purposes, such as gas storage [26] and trapping of small molecules [27]. Thanks to its composition and unique structural properties, Imo has also emerged as a promising material for the fabrication of bio-nanocomposites (*e.g.*, hybrid hydrogels with DNA and enzymes [28,29], photo-crosslinkable gelatin-based nanocomposites [30]). Imo nanotubes present mild, if any, toxic responses in a variety of cell models and tests [31] and its presence has been demonstrated to enhance osteoblastic proliferation and differentiation [32].

In the present work, we envisaged the use of Imo in gelatin-based hydrogels as nucleation site for the formation of calcium phosphates (CaP). The combined action of chemical cross-linking (GDE) and cryogenic treatment allows for the fabrication of a hybrid gelatin hydrogel with increased stability against dissolution at physiological temperature, and with a μm-sized porosity matching the proper dimensions for the permeation of cells. The obtained hydrogels were characterized with a multi-technique approach and then subjected to a mineralization experiment which demonstrated that the material was able to support the formation of calcium apatite phases. We also found, for the first time, that Imo effectively acts as a nucleation site for the formation of CaP and for this reason it enhances the formation of both HA and carbonated HA (CHA), thus producing a material with suitable properties for applications in bone tissue engineering.

2. Materials and Methods

2.1. Materials

Tetraethyl orthosilicate (TEOS) was obtained from Fluka (Milan, Italy) and aluminum-tri-sec-butoxide (ASB, purity 97%) was purchased from Sigma Aldrich (Milan, Italy). Perchloric acid (70%) was obtained from Merck (Milan, Italy). Calcium hydroxide was purchased from Acros (Geel, Belgium) and phosphoric acid (85%) from Carlo Erba (Milan, Italy). Gelatin from porcine skin, 250 Bloom, was obtained from Fluka and glycerol diglycidyl ether (GDE) was purchased from Sigma Aldrich.

2.2. Imogolite synthesis

Tetraethyl orthosilicate (TEOS, 840 μL) and aluminum-tri-sec-butoxide (ASB, 1.90 g) were added to a $HClO_4$ solution (150 mL, 0.025 M) pre-heated at 70 °C so to reach a Si:Al:$HClO_4$ molar ratio of 1:2:1. The dispersion was kept at 70 °C during 5 h under continuous stirring, and then refluxed at 100 °C during 10 days. The reaction mixture was then cooled down, dialyzed with a cellulose membrane (Sigma Aldrich D9777, M_w cut-off = 14.4 kDa) against de-ionized MilliQ water (resistivity > 18.2 MΩ cm) to remove unreacted reagents and small nanostructures, concentrated into a gel by centrifugation at 1000 g during 1 h (the supernatant was discarded), and finally freeze-dried (−50 °C, $3 \cdot 10^{-2}$ mmHg). FT-IR and XRD results are consistent with the presence of proto-imogolites, together with imogolite nanotubes. A detailed characterization of the obtained imogolites is reported elsewhere [33].

2.3. Samples preparation

2.3.1. Hydrogels

Gelatin hydrogels were prepared using the following procedure: the amount of gelatin necessary to reach the concentration of 5% wt was dissolved in MilliQ water (0.5 g of gelatin in 9.5 g of water) and heated at 50 °C under magnetic stirring. After complete dissolution, imogolite and/or GDE was added to the gelatin solution, which was stirred for about 10 min, obtaining the samples Gel+GDE, Gel+Imo and Gel+GDE+Imo. In each sample, the amount of GDE is 5% wt with respect to gelatin's weight, while Imo is 10% wt with respect to organic content (gelatin or gelatin + GDE). The nomenclature and exact composition of the prepared hydrogels is reported in Table 1. After homogenization, the hot dispersions were poured in polyethylene cylindrical molds (diam-

Table 1
Nomenclature and composition of the prepared hydrogels.

Sample	Gelatin [g]	Water [g]	GDE [g]	Imo [g]	GDE% wt[a]	Imo% wt[b]
Gel	0.5	9.5	/	/	/	/
Gel+GDE	0.5	9.5	0.025	/	5	/
Gel+Imo	0.5	9.5	/	0.0500	/	10
Gel+GDE+Imo	0.5	9.5	0.025	0.0525	5	10

[a] % wt with respect to gelatin.
[b] % wt with respect to organic content (gelatin + GDE).

eter 1 cm, height 1 cm) and were allowed to gel at room temperature.

2.3.2. Cryogenic pore formation

The formation of macropores in the four hydrogels was obtained by a cryogenic formation procedure: the hydrogels were cooled overnight in a freezer to −18 °C (cooling rate 1 °C/min) and then freeze-dried at −50 °C and 30 mTorr for two days. The obtained macroporous samples investigated in the present paper are: Cryo_Gel, Cryo_Gel+GDE, Cryo_Gel+Imo, Cryo_Gel+GDE+Imo.

2.3.3. Mineralization

The synthesis of calcium phosphates (CaP) inside the gels was performed using a method reported in the literature for the synthesis of hydroxyapatite nanocrystals [34]. A portion of the Cryo_Gel+GDE and Cryo_Gel+GDE+Imo samples was cut and each portion was soaked in a $Ca(OH)_2$ suspension (2.5 mL, 0.5 M at 37 °C). H_3PO_4 solution (2.5 mL, 0.3 M) was added in aliquots of 105 μl every 5 min. The slow addition of H_3PO_4 enables obtaining crystalline HA with nanometric size (∼50 nm), according to the literature [34]. At the end of the experiment, gels were recovered and dried in air.

2.4. Characterization

2.4.1. Electron microscopy

Field Emission Scanning Electron Microscopy (FE-SEM) was used to study the morphology of the xerogels obtained by freeze-drying the corresponding hydrogels. Freeze-drying was performed by plunging small pieces of hydrogels (volume ∼1 cc) in liquid nitrogen during 10 min, followed by lyophilization at 30 mTorr and -55 °C during 24 h. The obtained xerogels were cut with a blade and the internal surface was characterized by means of a Zeiss ΣIGMA FE-SEM (Carl Zeiss Microscopy GmbH, Germany). The use of a Field Emission source, together with a low accelerating voltage (0.50 kV), the In-Lens detector and a reduced sample-detector distance (2 mm) allowed for the imaging of non-metallized samples.

2.4.2. Thermal analysis

Differential Scanning Calorimetry (DSC) analyses were carried out on a Q2000 DSC (TA Instruments, New Castle, DE, USA). The samples were lodged in aluminum hermetic pans (Tzero Aluminum Hermetic, TA Instruments) and heated/cooled at 5 °C/min in N_2 atmosphere (flow rate 50 mL/min). The samples were equilibrated at −5 °C, heated to 70 °C and cooled to −5 °C (cycle 1). The sequence was repeated and cycle 2 was obtained. Thermogravimetric analysis (TGA) was performed with a SDT Q600 from TA Instruments to evaluate the affinity between gelatin and imogolites, both in the presence or not of GDE. Measurements were conducted in N_2 atmosphere (flow rate 100 mL/min) from room temperature to 1000 °C, at 10 °C/min. The samples analyzed with this technique were obtained as it follows: 2 g of Gel, Gel+GDE, Gel+Imo and Gel+GDE+Imo hydrogels were separately soaked in 5 mL of water for 12 h at 37 °C. Samples not containing Imo were added with 10 mg of Imo and mixed for 4 h at 37 °C. All the samples were then centrifuged (1 h at 37 °C at 6000 g) and the supernatant was discarded. The precipitates were freeze-dried and then analyzed.

2.4.3. Rheology

Rheological measurements were performed by means of a Paar Physica UDS 200 (Moline, IL, USA) rheometer fitted with a stainless-steel plate-plate geometry (40 mm) and a Peltier temperature controller. Samples were characterized at 20 °C by means of oscillatory measurements. First, strain-sweep measurements were performed at a constant oscillation frequency of 1 Hz for strains ranging from 10^{-1}% to 10^{4}% to determine the linear viscoelastic regime. Then, frequency-sweep measurements were performed at a constant strain of 1% for frequencies ranging from 10^{-2} Hz to 100 Hz. The shear storage modulus G' and the shear loss modulus G" were thus obtained, and plotted against frequency. Silicone oil was placed at the free surface between the two plates to minimize water evaporation during measurements. All rheology measurements were performed at least twice on duplicate samples.

2.4.4. Small Angle X-rays Scattering

The hydrogels' structure at the nano-scale was investigated by Small Angle X-rays Scattering (SAXS). Measurements were carried out with a HECUS SWAX camera (Kratky) equipped with a position-sensitive detector (OED 50 M) containing 1024 channels of width 54 μm. Cu Kα radiation of wavelength λ = 1.542 Å was provided by a Seifert ID-3003 X-rays generator (sealed-tube type), operating at a maximum power of 2 kW (50 kV and 1 mA). A 10 μm-thick Ni filter was used to remove the Cu Kβ radiation. The sample-to-detector distance was 275 mm. The volume between the sample and the detector was kept under vacuum during the measurements to minimize scattering from the air. The Kratky camera was calibrated in the small angle region using silver behenate (d = 58.38 Å). Scattering curves were obtained in the q-range between 0.009 and 0.544 $Å^{-1}$, $q = (4\pi/\lambda)\sin(\theta/2)$ being the scattering vector, and θ the scattering angle. A thin slice of each sample was sealed in a cell between two Kapton windows. Cryogenically-treated xerogels were put in MilliQ-grade water to rehydrate for 3 days before being analyzed. Standard measurement conditions were 50 kV, 40 mA, and 3 h (acquisition time) at 25 °C. SAXS curves reported in this work have been compared with those obtained on a very short time scale and no differences were detected between the two sets of measurements, confirming the absence of relevant radiation damage to the hydrogel structures during the measurements. All scattering curves were corrected for the water/empty cell contribution considering the relative transmission factor. SAXS curves were iteratively desmeared using the procedure reported by Lake [35] and were fitted using the Ornstein-Zernike function describing polymers in a semi-dilute regime:

$$I(q) = \frac{I_0}{1 + \xi^2 q^2} \quad (1)$$

where I_0 is a scaling factor, and ξ is the correlation length of the polymer.

Additional fittings were performed with power law functions to obtain information about the fractal nature of the scattering objects:

$$I(q) \propto q^{-p} \quad (2)$$

where p is the fractal dimension (D_m), that is 1 for 1D objects and 3 for full solid materials [36]. For $3 \leq p \leq 4$ one can obtain the surface fractal dimension (D_s) from the equation:

$$D_S = 6 - p \quad (3)$$

Typically, D_s is 2 for smooth surfaces, and goes toward 3 as the roughness increases [36].

2.4.5. X-rays Diffraction

The crystallinity of the mineralized samples was investigated using X-rays Diffraction (XRD). The diffractograms were collected with a D8 Advance with DAVINCI design (Bruker, Milan, Italy), using Cu Kα radiation (λ = 1.54 Å), a range of 2θ of 5°–70°, a step size of 0.03°, and a time/step of 0.5 s. Peaks were assigned using the Powder Diffraction File (PDF) of the ICDD database (International Centre for Diffraction Data). Quantitative phase analysis was carried out according to the Rietveld method, using the software Topas (Bruker). The % error associated to the obtained value is ±5%.

3. Results and discussion

3.1. Hydrogels

The morphology of the hydrogels was investigated by looking at their parent xerogels (prepared as described in Section 2) by means of FE-SEM. It is worth stressing that the morphology of xerogels at high magnifications should be discussed only at a qualitative level, as the xerogels' morphology could significantly differ from their parent hydrogels at the nano-scale. In fact, the direct plunging of hydrogel samples in liquid nitrogen (−196 °C) typically leads to the formation of amorphous ice and, in combination with the low temperature freeze-drying, it represents a suitable method to preserve the native morphology of hydrogels [37]. However, since hydrogels typically consist of very hydrophilic polymers, part of the water in the hydrogel does not behave as free water in terms of freezing, as it strongly interacts with the polymer's chains. Therefore, that water would not reach the solid state eventually taking to the modification of the structure of the xerogel at the supra-molecular scale during the freeze-drying process.

The structure formed by gelatin is shown in Fig. 1a, highlighting the presence of pores in the size range between 1 and 10 μm. The pore wall thickness was also evaluated: the average of different measurements taken from images at high magnification (a representative example is reported in Fig. S1 in the Supplementary Material) has shown that the wall thickness is quite homogeneous over the whole sample and resulted in a value of 80 ± 20 nm.

The introduction of GDE does not produce a significant change in the pore size, but causes a decrease of order in the structure (see Fig. 1b): disordered regions (one example is highlighted with an arrow) are observed together with regions very similar to those observed in gelatin. This suggests that the GDE effect does not take place homogeneously over the entire hydrogel structure. The pore walls were evaluated both in terms of morphology and thickness (an example is given in Fig. S1), showing that the walls are smooth and their thickness is quite homogeneous over the whole sample, resulting in a value (90 ± 15 nm) nearly identical to pure gelatin.

Fig. 1c reports a representative micrograph of the sample Gel+Imo. The introduction of imogolites in the hydrogel does not dramatically change the overall structure of the system, even though the presence of regions where the concentration of clays is higher (see the white arrow) results in a decrease of the homogeneity of the sample at the micro-scale. Nevertheless, no regions entirely made of clays are detected, suggesting that imogolites are able to interact with gelatin without significantly changing the average pore size and the thickness (89 ± 12 nm) of the pore walls (see Fig. S1).

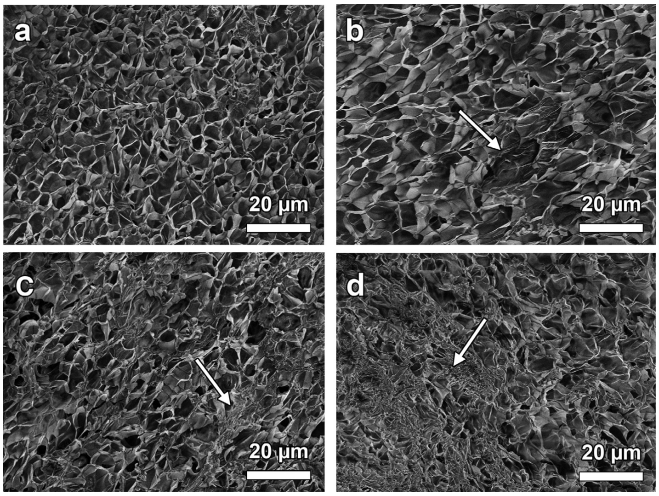

Fig. 1. FE-SEM micrographs of samples (a) Gel, (b) Gel+GDE, (c) Gel+Imo, and (d) Gel+GDE+Imo.

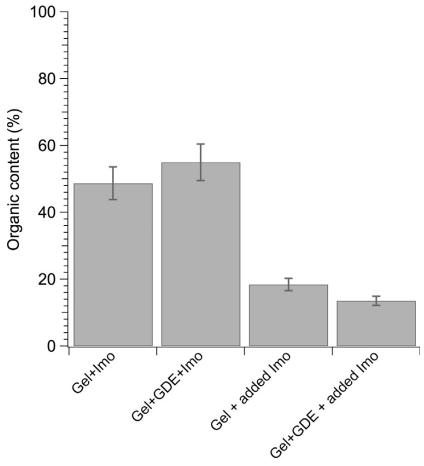

Fig. 2. Percentage of organic material physisorbed on Imo.

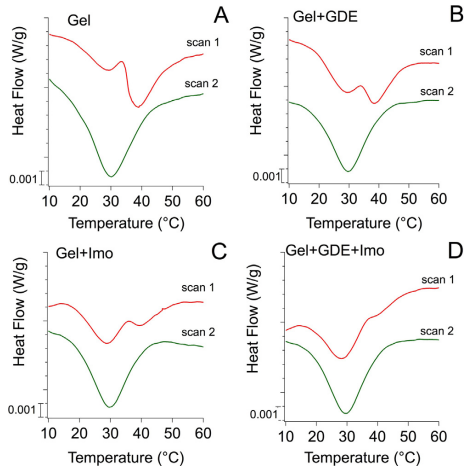

Fig. 3. Heating thermograms registered on hydrogel samples: (A) Gel; (B) Gel+GDE; (C) Gel+Imo; (D) Gel+GDE+Imo. Each graph shows both the first heating (scan 1) and the second heating (scan 2) curves. The curves have been offset for clarity.

When both GDE and imogolites are introduced, the size of the inhomogeneous regions significantly increases (the arrow in Fig. 1d points toward one of these regions), suggesting a preferential interaction between GDE and imogolites. Furthermore, the pore wall morphology and the thickness in the inhomogeneous regions is very variable (as shown in Fig. S1).

In order to evaluate the interactions between imogolites and gelatin (either in the presence or not of GDE), Gel and Gel+GDE hydrogels were dissolved in water in the presence of imogolites, as described in Section 2, and the precipitates were characterized by means of thermogravimetry. The amount of organic material physisorbed on imogolite clays was calculated from the residual weight at 1000 °C (see Fig. 2), corrected for the weight loss of pure imogolites (the thermograms are reported in Fig. S2, in the Supplementary Material). Since gelatin completely degrades at 1000 °C and displays a residual weight of 0%, the weights % of the samples at 1000 °C are due only to the imogolite component (which loses only ~30% of its weight when heated, see Fig. S2). Given the fact that all the samples display a weight % at 1000 °C lower than pure imogolite, we can state that before heating some gelatin was physisorbed on imogolite, and it was completely degraded during the experiment. By knowing the weight loss of pure Imo we can calculate, from the weight % at 1000 °C of the samples, the amount of gelatin physisorbed on imogolite clays before the experiment. Results on Gel+Imo and Gel+GDE +Imo highlight the affinity of gelatin for Imo: in fact, about 50% wt of the precipitate consists of organic material and the presence of GDE has no significant effect. We performed an additional experiment by adding Imo to already dissolved hydrogels (see Section 2), showing that the organic content in the precipitate is still relevant (~20% wt), even though significantly lower. Since samples with added Imo have not been cooled below the gel-sol transition temperature of gelatin, we demonstrate that the presence of Imo during the formation of the hydrogel takes to an increased interaction between the inorganic filler and the organic matrix.

Aiming at further understanding the interactions between the components, samples were characterized by DSC. In the temperature range from 10 °C to 50 °C the thermograms show the endothermic feature typical of the gel-sol transition of gelatin (see Fig. 3), which is due to the unfolding of the residual triple helices to reach a completely molten state of the polymeric chains. The double peak visible in the first heating scan (red curves in Fig. 3) accounts for the thermal history of gelatin samples producing two species of "junction zones" with different thermal stability [38]: some of these junctions are less stable and melt around 30 °C, while the others are thermally more stable and require more energy to melt (peak at ~40 °C). The intensity of these two peaks reflects the aging time because the system slowly reorganizes itself increasing the stable junctions at the expenses of the less stable ones.

The comparison of the first heating scan registered on the four samples, aged for the same time after their preparation (24 h), provides information about the reorganization capacity of the gels, which is indirectly related to the degree of "perturbation" on the gelatin network introduced by GDE and/or Imo. To quantify this effect, the two peaks have been fitted with Exponentially Modified Gaussian functions:

$$f(T) = \sqrt{\frac{\pi}{2}}\frac{hw}{|s|}\exp\left(\frac{T_0 - T}{s} + \frac{1}{2}\left(\frac{w}{s}\right)^2\right)\cdot erf\left(\frac{\frac{1}{2}(T_0 - T)}{w + \frac{w}{|s|}}\right) \quad (4)$$

where h is the height, T_0 the center, w the width, and s is the distortion factor (shape) of the peak. This equation is commonly used to account for asymmetric DSC peaks that can be due to the presence of impurities [39,40] or to the complexity of polymeric systems [12]. The results of the fitting are shown in Fig. S3 in the Supplementary Material. The shape of the four thermograms and the relative weight of the two peaks resulting from the fitting (see Table 2) clearly indicate that the presence of GDE or Imo enhances the formation of poorly stable junctions with respect to the pure gelatin sample, the most relevant effect being associated to the presence of Imo. When GDE and Imo are both present they produce a sort of synergetic effect and the destabilization of the network is maximized, confirming the considerations extracted from the analysis of SEM micrographs.

Table 2
Parameters obtained with DSC and SAXS fittings. The second and third columns refer to the relative weight of the areas of the two peaks in the first heating scan (calculated with respect to the total area). In the fourth column, the enthalpies measured by integration of the peak in the second heating scan are reported. The last column lists the correlation lengths obtained from the fitting according to Eq. (1).

	DSC			SAXS
	1st heating cycle		2nd heating cycle	Correlation length (Å)
Sample	% high T peak	% low T peak	ΔH (J/g) ± 2%	
Gel	69	31	1.25 ± 0.03	27 ± 6
Gel+GDE	46	54	0.88 ± 0.02	28 ± 6
Gel+Imo	28	72	0.87 ± 0.02	30 ± 6
Gel+GDE+Imo	11	89	0.90 ± 0.02	32 ± 6

We also investigated the behavior of the samples when their thermal memory is reset: *i.e.*, after the first heating scan. In the second heating scan the thermograms (green[1] lines in Fig. 3) show only one peak, centered at ~30 °C, due to the melting of the junctions formed between polymeric chains during the cooling segment of the first scan. The area obtained by integrating this peak is reported in Table 2. The evident decrease in the enthalpy of the transition in the samples containing GDE and/or Imo is a further indication that both are able to hinder or, at least, to slow down the ability of gelatin to self-interact.

The effect of Imo and GDE on the structural properties of the gelatin network is further confirmed by rheology. Oscillatory measurements were performed on hydrogels at 20 °C, well below the sol-gel transition of gelatin. At this temperature, all samples display the typical feature of viscoelastic materials with a predominant solid-like character, *i.e.* G' is significantly larger than G" (approximately by two orders of magnitude) and nearly frequency-independent in an extended frequency range (see Fig. S4). However, when GDE and/or Imo are present, the storage modulus of the gel is significantly lowered (the effect of Imo is slightly larger) indicating a less ordered organization of polymer chains with respect to pristine gelatin, which leads to a limited extension of the "solid-like" 3D network. The non-homogeneous distribution of imogolite clays inside the matrix (see Fig. 1c) and the moderate reactivity of GDE toward gelatin likely represent the main reasons for the observed weakening of hybrid gels in terms of mechanical properties.

In order to evaluate the influence of both GDE and Imo on the nanostructure of the gels, SAXS curves for Gel, Gel+GDE, Gel+Imo and Gel+GDE+Imo have been collected (see Fig. 4). The curves are almost superimposable in the mid-to-high q range ($0.03 \leq q \leq 0.5$ Å^{-1}). The correlation lengths obtained from the fitting according to Eq. (1) are reported in Table 2. Results indicate that the main contribution to the scattering profiles in this region is due to the Gel matrix and that the modification of GDE and/or Imo to the network are negligible. The increase in the scattered intensity in the low q region ($0.009 \leq q \leq 0.03$ Å^{-1}) in Gel+Imo and Gel+GDE+Imo is a consequence of the presence of Imo in the gel, as it is not present in the other profiles. Fitting according to Eq. (2) results in a mass fractal dimension of 1.6 and 1.7 for Gel+Imo and Gel+GDE+Imo respectively, that is typical of aggregated rod-like structures [41].

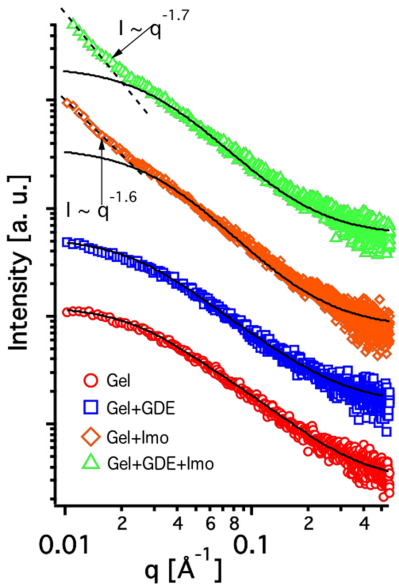

Fig. 4. SAXS curves of Gel (circles), Gel+GDE (squares), Gel+Imo (diamonds), and Gel+GDE+Imo (triangles). The curves are offset for display purposes. Full solid lines represent the curve fittings according to the Ornstein-Zernike function, while the dotted lines delineate the power law fittings.

3.2. Cryogenically-modified hydrogels

Hydrogels were modified by a cryogenic treatment (controlled freezing followed by lyophilization, see Section 2) to obtain pores in the 100–250 μm, as required in materials for the regeneration of bone tissues [42]. SEM micrographs (Fig. 5) clearly show that the procedure was successful, providing also useful insights into GDE and Imo effect on the gelatin matrix and on the pore enlargement process. The enlargement process takes place quite homogeneously in pure gelatin (Fig. 5a). When GDE is present (Fig. 5b), regions with large pores are alternated to regions where the cryogenic treatment has been much less effective (one example is highlighted by the arrow), most reasonably because of the reinforcing effect of the cross-linker in those regions, eventually hindering the growth of ice crystals. These results are consistent with an inhomogeneous distribution of GDE over the hydrogel structure, as already introduced when analyzing the results on hydrogels before the cryogenic treatment. The introduction of imogolites affects to a minor extent the ability of the hydrogel to form large pores. The presence of the nanoclays could be pointed out by the slightly smaller size of the pores and, more evidently, by the rough morphology of the pore walls (see Fig. 5c). When GDE and Imo are introduced together, both effects are visible (see Fig. 5d): the pore walls' morphology is rough and regions where the cryogenic treatment had a minor effect are visible.

[1] For interpretation of color in Fig. 3, the reader is referred to the web version of this article.

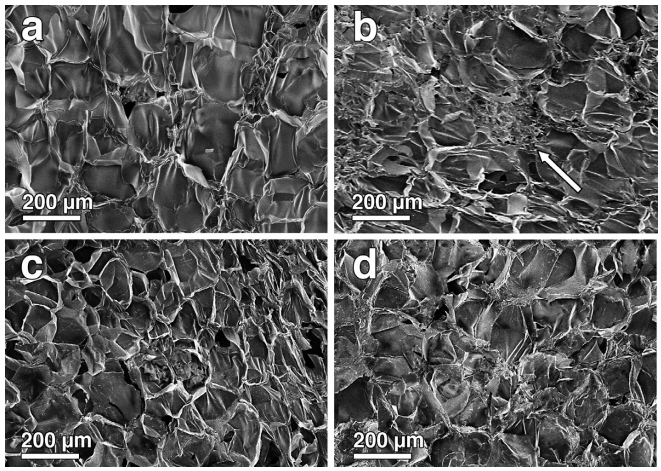

Fig. 5. FE-SEM micrographs of samples obtained by cryo-poration of (a) Cryo_Gel, (b) Cryo_Gel+GDE, (c) Cryo_Gel+Imo, and (d) Cryo_Gel+GDE+Imo.

Summarizing, SEM results clearly demonstrate that the cryogenic treatment of all our samples successfully produces architectures suitable for bone tissue engineering, at least in terms of porosity. The average size of the pores after the cryo-modification is increased by a factor of about 25 (from ~5 μm to ~125 μm), while the pore walls are about ten times thicker (see Fig. S5). These results indicate that the process takes place through the formation of Mullins-Sekerka instabilities, as previously reported for similar systems [37], resulting in the formation of sub-millimetric and highly interconnected pores with thick pore walls.

It is worth mentioning here that, together with chemical and physical cross-linkers (GDE and Imo, respectively), increasing the pore size and the pore wall thickness could be also effective in extending the dissolution of the scaffolds over time. In particular, the ice growth during the cryogenic process results in the merging of many smaller pores into few bigger pores with the collapsing of thinner pore walls into thicker ones. The overall effect is a significant decrease in the total surface area. Considering that the Specific Surface Area (SSA) of a porous system is inversely proportional to the pore size, and that the dissolution rate is directly proportional to SSA, it results that increasing the pore size of a hydrogel is an effective strategy when aiming at decreasing the dissolution rate. This hypothesis can be easily verified by checking the amount of time needed by a small piece of hydrogel to completely dissolve in a water excess. We observed that Gel sample dissolves at 37 °C within 30 min, while Cryo_Gel takes about two hours. The presence of Imo and GDE further increases the time required for the dissolution to occur (around 3 days for Gel+GDE+Imo).

The effect of the cryogenic pore formation on the nanostructure of the hydrogels was also investigated by means of SAXS experiments (see Fig. 6). The samples have been rehydrated (as reported in Section 2) before being analyzed. SAXS curve of sample Cryo_Gel +Imo is not reported as it showed a scattering profile superimposable to that of Cryo_Gel+GDE+Imo. The analysis of the polymer correlation length in the high q region provided very small values, comparable to the instrumental resolution, not allowing for further discussion. In the region between 0.01 and 0.05 $Å^{-1}$ all samples exhibit linear trends. This behavior (not found in the untreated

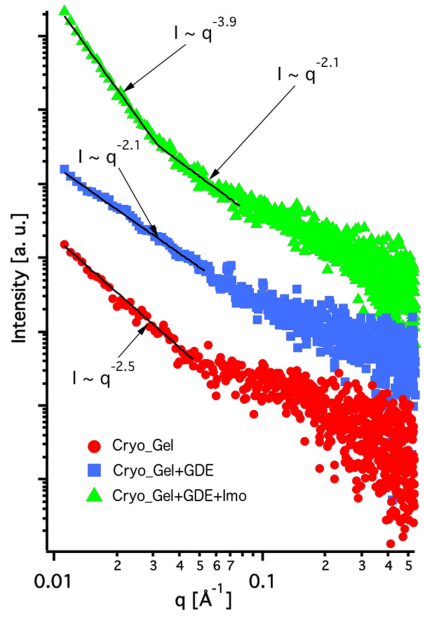

Fig. 6. SAXS curves of Cryo_Gel (full circles), Cryo_Gel+GDE (full squares), and Cryo_ Gel+GDE+Imo (full triangles). The curves are offset for display purposes. The dotted lines delineate the power law fittings. The SAXS profile of sample Cryo_Gel +Imo is superimposable to that of Cryo_Gel+GDE+Imo and, therefore, not reported.

hydrogels) is typically observed in the presence of fractal domains, in this case probably originated from the extreme reduction of the volume occupied by the polymer molecules and Imo during the

cryogenic treatment. For all samples a region with a p between 2.1 and 2.5 is found, with Cryo_Gel showing the highest exponent. This means that the hydrogels containing GDE show a D_m lower than that of pure gelatin, suggesting that the presence of the cross-linker leads to the disorganization of the polymer chains. In addition, Cryo_Gel+GDE+Imo shows a second linear region in the low q-range with $p = 3.9$. By using Eq. (3) a D_s of 2.1 was obtained, meaning that the scattering profile of the sample is that of a full solid material with a very smooth surface. This is probably due to the Imo clays and the polymer network collapsing together into a compact structure during the cryogenic treatment.

3.3. Mineralization

The obtained Cryo_Gel+GDE+Imo macroporous xerogel is endowed with some features that make it suitable as a scaffold for bone remineralization: the single components of the material are biocompatible and the porosity obtained by means of the cryo-formation process is appropriate for cell adhesion and growth. In addition, we hypothesize that imogolite clays can act as nucleation sites for the formation of mineral phases inside the gel matrix. To validate this hypothesis, we used this sample to perform an experiment of hydroxyapatite mineralization, following the protocol described in Section 2. As a reference, we carried out the same experiment on the sample Cryo_Gel+GDE to evaluate the effect of Imo on the formation of the inorganic phases. Fig. 7a and b report FE-SEM micrographs of the mineralized Cryo_Gel+GDE+Imo and Cryo_Gel+GDE xerogels, which from now on will be referred to as Cryo_Gel+GDE+Imo_CaP and Cryo_Gel+GDE_CaP, respectively. It is evident that, in both cases, the gel phase is homogeneously filled with sub-micrometric particles and the gelatin matrix is no longer visible. The micrographs evidence that the morphology of the Imo-containing mineralized sample (see Fig. 7a) does not show the well-defined platelets typical of HA that are instead visible in Cryo_Gel+GDE_CaP (Fig. 7b). This suggests that Imo can template the growth of HA particles, being effective in modifying the shape of the formed crystals.

The crystallinity of the inorganic phases obtained by means of X-rays Diffraction shows that for both samples most of the peaks can be attributed to hydroxyapatite and carbonated hydroxyapatite (see Fig. 7c). In order to quantify the amount of these two phases, the diffractograms were analyzed according to the Rietveld method. We found that the presence of Imo promotes the carbonation of hydroxyapatite, since CHA is 34% in Cryo_Gel+GDE_CaP vs 65% in Cryo_Gel+GDE+Imo_CaP (see Figs. S6 and S7); a small amount of calcite (4%) is also observed in the Imo-containing sample. These results are of outmost importance considering the beneficial effect of carbonate on both the mechanical and osteoconductive/osteoinductive properties of bones. The superior characteristics of CHA with respect to HA are indeed well documented in literature [43].

To understand if the presence of Imo is also able to enhance the formation of HA, the amount of mineral phase was evaluated by means of TGA (Fig. 7d). Data were first normalized to 100% at 130 °C to consider their different water content and then corrected to take into account the weight loss associated to pure HA and Imo. Very interestingly, it was found that the inorganic fraction (after mineralization) is 10.4% wt in the Cryo_Gel+GDE_CaP sample, while it increases up to 21.3% wt in Cryo_Gel+GDE+Imo_CaP. This result shows that Imo significantly promotes the mineralization of the scaffold (the amount of inorganic phase formed is twofold with respect to the gel without Imo) and acts as nucleation center.

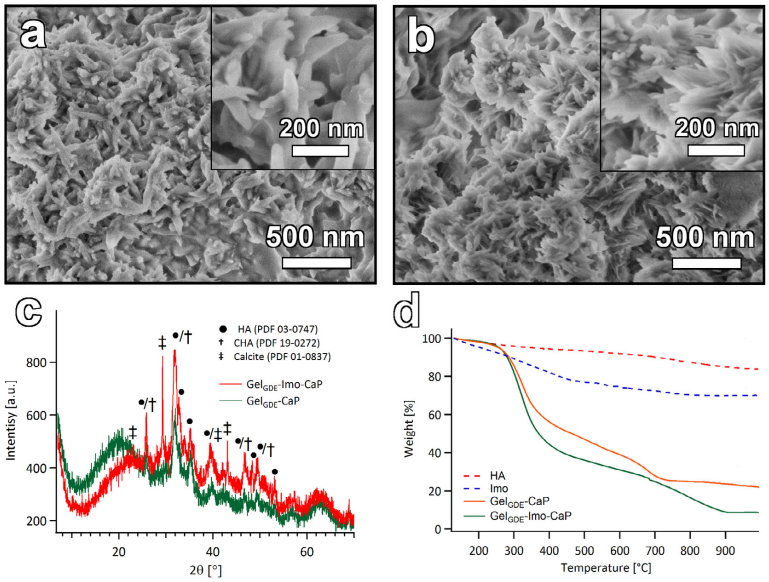

Fig. 7. FE-SEM micrographs of (a) Cryo_Gel+GDE+Imo_CaP, (b) Cryo_Gel+GDE_CaP. In the insets, an image at higher magnification of the same sample is shown. (c) XRD patterns of Cryo_Gel+GDE+Imo_CaP and Cryo_Gel+GDE_CaP, together with the peak assignments according to HA (PDF 03-0747), carbonated HA (PDF 19-0272) and calcite (PDF 01-0837); (d) TGA profiles of Cryo_Gel+GDE_CaP and Cryo_Gel+GDE+Imo_CaP, together with pure HA and Imo.

4. Conclusions

In this manuscript, we investigated the possibility to combine nanotubular clays and gelatin to obtain a composite material with composition, porosity, and mineralization properties suitable as a synthetic scaffold in bone tissue engineering. While gelatin has been largely investigated in the past, practical limitations (primarily, fast dissolution rate in physiological conditions, lack of pores with suitable dimensions for cell permeation and limited mineralization ability) still hamper its application [9,10].

Our results demonstrate that imogolite nanotubes (Imo) and a biocompatible chemical cross-linker (GDE) could be effectively employed to modify the structural, thermal and rheological properties of gelatin-based hydrogels, especially affecting the triple helices-forming ability of pure gelatin. The inclusion of Imo and GDE affects the structure of the network, but it does not hinder the possibility to modify its porosity through a cryogenic treatment, allowing for the tuning of pore size in the range required for bone cell permeation (in the order of 100 μm). We also found that the presence of Imo strongly enhances the mineralizing properties of the scaffold toward the formation of hydroxyapatite and carbonated hydroxyapatite (twofold increase with respect to pristine gelatin).

The integration of 1D inorganic and organic fillers in gelatin, as well as the mineralization properties of the resulting scaffolds, has been already investigated in the literature [44–47]. However, to the best of our knowledge, the effect of imogolite nanoclays on the mineralization properties of gelatin scaffolds has never been reported.

Given the biocompatible composition, the proper porosity and the effectiveness in promoting the formation of hydroxyapatites, we believe that the material described in this paper represents a promising scaffold for bone tissue engineering. Its properties in biologically relevant fluids remain to be investigated, especially in terms of the composition and crystallinity of the formed mineral phases. As it has been recently discovered [48], calcium phosphates are not only relevant in bone tissues, but are also crucially involved in many biological processes, including the immunological surveillance. In this context, the possibility of controlling the kinetics of formation and the crystalline evolution of the calcium phosphates could make our material interesting to biotechnologically relevant applications other than scaffolds for bone tissue regeneration.

Acknowledgments

CSGI is acknowledged for financial support.

Appendix A. Supplementary material

Supplementary data associated with this article can be found, in the online version, at https://doi.org/10.1016/j.jcis.2017.09.094.

References

[1] V. Uskoković, D.P. Uskoković, Nanosized hydroxyapatite and other calcium phosphates: chemistry of formation and application as drug and gene delivery agents, J. Biomed. Mater. Res. B Appl. Biomater. 96B (2011) 152–191, https://doi.org/10.1002/jbm.b.31746.
[2] M.J. Olszta, X. Cheng, S.S. Jee, R. Kumar, Y.-Y. Kim, M.J. Kaufman, E.P. Douglas, L. B. Gower, Bone structure and formation: a new perspective, Mater. Sci. Eng. R Rep. 58 (2007) 77–116, https://doi.org/10.1016/j.mser.2007.05.001.
[3] S.V. Dorozhkin, Calcium orthophosphates (CaPO4): occurrence and properties, Prog. Biomater. 5 (2016) 9–70, https://doi.org/10.1007/s40204-015-0045-z.
[4] J.-Y. Rho, L. Kuhn-Spearing, P. Zioupos, Mechanical properties and the hierarchical structure of bone, Med. Eng. Phys. 20 (1998) 92–102, https://doi.org/10.1016/S1350-4533(98)00007-1.
[5] F. Ridi, I. Meazzini, B. Castroflorio, M. Bonini, D. Berti, P. Baglioni, Functional calcium phosphate composites in nanomedicine, Adv. Colloid Interface Sci. (2016), https://doi.org/10.1016/j.cis.2016.03.006.
[6] T.G. Kim, H. Shin, D.W. Lim, Biomimetic scaffolds for tissue engineering, Adv. Funct. Mater. 22 (2012) 2446–2468, https://doi.org/10.1002/adfm.201103083.
[7] E.K. Moioli, P.A. Clark, X. Xin, S. Lal, J.J. Mao, Matrices and scaffolds for drug delivery in dental, oral and craniofacial tissue engineering, Adv. Drug Deliv. Rev. 59 (2007) 308–324, https://doi.org/10.1016/j.addr.2007.03.019.
[8] S. Van Vlierberghe, P. Dubruel, E. Schacht, Biopolymer-based hydrogels as scaffolds for tissue engineering applications: a review, Biomacromolecules 12 (2011) 1387–1408, https://doi.org/10.1021/bm200083n.
[9] S.J. Buwalda, K.W.M. Boere, P.J. Dijkstra, J. Feijen, T. Vermonden, W.E. Hennink, Hydrogels in a historical perspective: from simple networks to smart materials, J. Controll. Release 190 (2014) 254–273, https://doi.org/10.1016/j.jconrel.2014.03.052.
[10] M. Santoro, A.M. Tatara, A.G. Mikos, Gelatin carriers for drug and cell delivery in tissue engineering, J. Controll. Release 190 (2014) 210–218, https://doi.org/10.1016/j.jconrel.2014.04.014.
[11] E.I. Wisotzki, P. Tempesti, E. Fratini, S.G. Mayr, Influence of high energy electron irradiation on the network structure of gelatin hydrogels as investigated by small-angle X-ray scattering (SAXS), Phys. Chem. Chem. Phys. PCCP 19 (2017) 12064–12074, https://doi.org/10.1039/c7cp00195a.
[12] D. Tatini, P. Tempesti, F. Ridi, E. Fratini, M. Bonini, P. Baglioni, Pluronic/gelatin composites for controlled release of actives, Colloids Surf. B Biointerfaces 135 (2015) 400–407, https://doi.org/10.1016/j.colsurfb.2015.08.002.
[13] A. Bigi, G. Cojazzi, S. Panzavolta, K. Rubini, N. Roveri, Mechanical and thermal properties of gelatin films at different degrees of glutaraldehyde crosslinking, Biomaterials 22 (2001) 763–768, https://doi.org/10.1016/S0142-9612(00)00236-2.
[14] K. Ulubayram, E. Aksu, S.I.D. Gurhan, K. Serbetci, N. Hasirci, Cytotoxicity evaluation of gelatin sponges prepared with different cross-linking agents, J. Biomater. Sci. Polym. Ed. 13 (2002) 1203–1219, https://doi.org/10.1163/156856202320892966.
[15] A. Bigi, G. Cojazzi, S. Panzavolta, N. Roveri, K. Rubini, Stabilization of gelatin films by crosslinking with genipin, Biomaterials 23 (2002) 4827–4832, https://doi.org/10.1016/S0142-9612(02)00235-1.
[16] G. Vargas, J.L. Acevedo, J. López, J. Romero, Study of cross-linking of gelatin by ethylene glycol diglycidyl ether, Mater. Lett. 62 (2008) 3656–3658, https://doi.org/10.1016/j.matlet.2008.04.020.
[17] C. Nishi, N. Nakajima, Y. Ikada, In vitro evaluation of cytotoxicity of diepoxy compounds used for biomaterial modification, J. Biomed. Mater. Res. 29 (1995) 829–834, https://doi.org/10.1002/jbm.820290707.
[18] F.J. O'Brien, Biomaterials & scaffolds for tissue engineering, Mater. Today 14 (2011) 88–95, https://doi.org/10.1016/S1369-7021(11)70058-X.
[19] T. Albrektsson, C. Johansson, Osteoinduction, osteoconduction and osseointegration, Eur. Spine J. 10 (2001) S96–S101, https://doi.org/10.1007/s005860100282.
[20] V. Karageorgiou, D. Kaplan, Porosity of 3D biomaterial scaffolds and osteogenesis, Biomaterials 26 (2005) 5474–5491, https://doi.org/10.1016/j.biomaterials.2005.02.002.
[21] S. Van Vlierberghe, V. Cnudde, P. Dubruel, B. Masschaele, A. Cosijns, I. De Paepe, P.J.S. Jacobs, L. Van Hoorebeke, J.P. Remon, E. Schacht, Porous gelatin hydrogels: 1 cryogenic formation and structure analysis, Biomacromolecules 8 (2007) 331–337, https://doi.org/10.1021/bm060684o.
[22] U.G.K. Wegst, H. Bai, E. Saiz, A.P. Tomsia, R.O. Ritchie, Bioinspired structural materials, Nat. Mater. 14 (2015) 23–36, https://doi.org/10.1038/nmat4089.
[23] M. Darder, P. Aranda, E. Ruiz-Hitzky, Bionanocomposites: a new concept of ecological, bioinspired, and functional hybrid materials, Adv. Mater. 19 (2007) 1309–1319, https://doi.org/10.1002/adma.200602328.
[24] P.D.G. Cradwick, V.C. Farmer, J.D. Russell, C.R. Masson, K. Wada, N. Yoshinaga, Imogolite, a hydrated aluminium silicate of tubular structure, Nature 240 (1972) 187–189, https://doi.org/10.1038/10.1038/physci240187a0.
[25] D.-Y. Kang, J. Zang, C.W. Jones, S. Nair, Single-walled aluminosilicate nanotubes with organic-modified interiors, J. Phys. Chem. C 115 (2011) 7676–7685, https://doi.org/10.1021/jp2010919.
[26] I. Bottero, B. Bonelli, S.E. Ashbrook, P.A. Wright, W. Zhou, M. Tagliabue, M. Armandi, E. Garrone, Synthesis and characterization of hybrid organic/inorganic nanotubes of the imogolite type and their behaviour towards methane adsorption, Phys. Chem. Chem. Phys. 13 (2011) 744–750, https://doi.org/10.1039/c0cp00438c.
[27] M.S. Amara, E. Paineau, S. Rouzière, B. Guiose, M.-E.M. Krapf, O. Taché, P. Launois, A. Thill, Hybrid, tunable-diameter, metal oxide nanotubes for trapping of organic molecules, Chem. Mater. 27 (2015) 1488–1494, https://doi.org/10.1021/cm503428q.
[28] N. Jiravanichanun, K. Yamamoto, K. Kato, J. Kim, S. Horiuchi, W.-O. Yah, H. Otsuka, A. Takahara, Preparation and characterization of imogolite/DNA hybrid hydrogels, Biomacromolecules 13 (2012) 276–281, https://doi.org/10.1021/bm201616m.
[29] N. Inoue, H. Otsuka, S.-I. Wada, A. Takahara, (Inorganic nanofiber/enzyme) hybrid hydrogel: preparation, characterization, and enzymatic activity of imogolite/pepsin conjugate, Chem. Lett. 35 (2006) 194–195, https://doi.org/10.1246/cl.2006.194.
[30] N. Teramoto, A. Hayashi, K. Yamanaka, A. Sakiyama, A. Nakano, M. Shibata, Preparation and mechanical properties of photo-crosslinked fish gelatin/imogolite nanofiber composite hydrogel, Materials 5 (2012) 2573–2585, https://doi.org/10.3390/ma5122573.

[31] B.M. Rotoli, P. Guidi, B. Bonelli, M. Bernardeschi, M.G. Bianchi, S. Esposito, G. Frenzilli, P. Lucchesi, M. Nigro, V. Scarcelli, M. Tomatis, P.P. Zanello, B. Fubini, O. Bussolati, E. Bergamaschi, Imogolite: an aluminosilicate nanotube endowed with low cytotoxicity and genotoxicity, Chem. Res. Toxicol. 27 (2014) 1142–1154, https://doi.org/10.1021/tx500002d.

[32] K. Ishikawa, T. Akasaka, S. Abe, Y. Yawaka, M. Suzuki, F. Watari, Application of imogolite, almino-silicate nanotube, as scaffold for the mineralization of osteoblasts, Bioceram. Dev. Appl. 1 (2010) 1–3, https://doi.org/10.4303/bda/D110133.

[33] M. Bonini, A. Gabbani, S. Del Buffa, F. Ridi, P. Baglioni, R. Bordes, K. Holmberg, Adsorption of amino acids and glutamic acid-based surfactants on imogolite clays, Langmuir 33 (2017) 2411–2419, https://doi.org/10.1021/acs.langmuir.6b04414.

[34] E. Bouyer, F. Gitzhofer, M.I. Boulos, Morphological study of hydroxyapatite nanocrystal suspension, J. Mater. Sci. Mater. Med. 11 (2000) 523–531, https://doi.org/10.1023/A:1008918110156.

[35] J.A. Lake, An iterative method of slit-correcting small angle X-ray data, Acta Crystallogr. 23 (1967) 191–194, https://doi.org/10.1107/S0365110X67002440.

[36] D.W. Schaefer, Fractal models and the structure of materials, MRS Bull. 13 (1988) 22–27, https://doi.org/10.1557/S088376940006632X.

[37] L. Qian, H. Zhang, Controlled freezing and freeze drying: a versatile route for porous and micro-/nano-structured materials, J. Chem. Technol. Biotechnol. 86 (2011) 172–184, https://doi.org/10.1002/jctb.2495.

[38] C. Michon, G. Cuvelier, P. Relkin, B. Launay, Influence of thermal history on the stability of gelatin gels, Int. J. Biol. Macromol. 20 (1997) 259–264, https://doi.org/10.1016/S0141-8130(97)00024-X.

[39] M. Elsabee, R.J. Prankerd, Solid-state properties of drugs. II. Peak shape analysis and deconvolution of overlapping endotherms in differential scanning calorimetry of chiral mixtures, Int. J. Pharm. 86 (1992) 211–219, https://doi.org/10.1016/0378-5173(92)90199-C.

[40] E.M. Anghel, A. Georgiev, S. Petrescu, R. Popov, M. Constantinescu, Thermo-physical characterization of some paraffins used as phase change materials for thermal energy storage, J. Therm. Anal. Calorim. 117 (2014) 557–566, https://doi.org/10.1007/s10973-014-3775-6.

[41] H. Wang, W. Zhou, D.L. Ho, K.I. Winey, J.E. Fischer, C.J. Glinka, E.K. Hobbie, Dispersing single-walled carbon nanotubes with surfactants: a small angle neutron scattering study, Nano Lett. 4 (2004) 1789–1793, https://doi.org/10.1021/nl048969z.

[42] K. Whang, C.H. Thomas, K.E. Healy, G. Nuber, A novel method to fabricate bioabsorbable scaffolds, Polymer 36 (1995) 837–842, https://doi.org/10.1016/0032-3861(95)93115-3.

[43] E.F. Morgan, D.N. Yetkinler, B.R. Constantz, R.H. Dauskardt, Mechanical properties of carbonated apatite bone mineral substitute: strength, fracture and fatigue behaviour, J. Mater. Sci. Mater. Med. 8 (1997) 559–570, https://doi.org/10.1023/A:1018550831834.

[44] L. Ji, W. Qiao, Y. Zhang, H. Wu, S. Miao, Z. Cheng, Q. Gong, J. Liang, A. Zhu, A gelatin composite scaffold strengthened by drug-loaded halloysite nanotubes, Mater. Sci. Eng. C 78 (2017) 362–369, https://doi.org/10.1016/j.msec.2017.04.070.

[45] I.-K. Yoon, J.-Y. Hwang, J. Seo, W.-C. Jang, H.-W. Kim, U.S. Shin, Carbon nanotube-gelatin-hydroxyapatite nanohybrids with multilayer core–shell structure for mimicking natural bone, Carbon 77 (2014) 379–389, https://doi.org/10.1016/j.carbon.2014.05.041.

[46] Y. Zuo, X. Liu, D. Wei, J. Sun, W. Xiao, H. Zhao, L. Guo, Q. Wei, H. Fan, X. Zhang, Photo-cross-linkable methacrylated gelatin and hydroxyapatite hybrid hydrogel for modularly engineering biomimetic osteon, ACS Appl. Mater. Interfaces 7 (2015) 10386–10394, https://doi.org/10.1021/acsami.5b01433.

[47] H. Wang, C. Chu, R. Cai, S. Jiang, L. Zhai, J. Lu, X. Li, S. Jiang, Synthesis and bioactivity of gelatin/multiwalled carbon nanotubes/hydroxyapatite nanofibrous scaffolds towards bone tissue engineering, RSC Adv. 5 (2015) 53550–53558, https://doi.org/10.1039/C5RA07806G.

[48] J.J. Powell, E. Thomas-McKay, V. Thoree, J. Robertson, R.E. Hewitt, J.N. Skepper, A. Brown, J.C. Hernandez-Garrido, P.A. Midgley, I. Gomez-Morilla, G.W. Grime, K.J. Kirkby, N.A. Mabbott, D.S. Donaldson, I.R. Williams, D. Rios, S.E. Girardin, C. T. Haas, S.F.A. Bruggraber, J.D. Laman, Y. Tanriver, G. Lombardi, R. Lechler, R.P. H. Thompson, L.C. Pele, An endogenous nanomineral chaperones luminal antigen and peptidoglycan to intestinal immune cells, Nat. Nanotechnol. 10 (2015) 361–369, https://doi.org/10.1038/nnano.2015.19.

Supplementary Material

Enhanced formation of hydroxyapatites in gelatin/imogolite macroporous hydrogels

Rita Gelli, Stefano Del Buffa, Paolo Tempesti, Massimo Bonini, Francesca Ridi, Piero Baglioni**

Department of Chemistry "Ugo Schiff" and CSGI, University of Florence, via della Lastruccia 3, Sesto Fiorentino, 50019 Florence, Italy

*Corresponding authors. E-mail: piero.baglioni@unifi.it; francesca.ridi@unifi.it

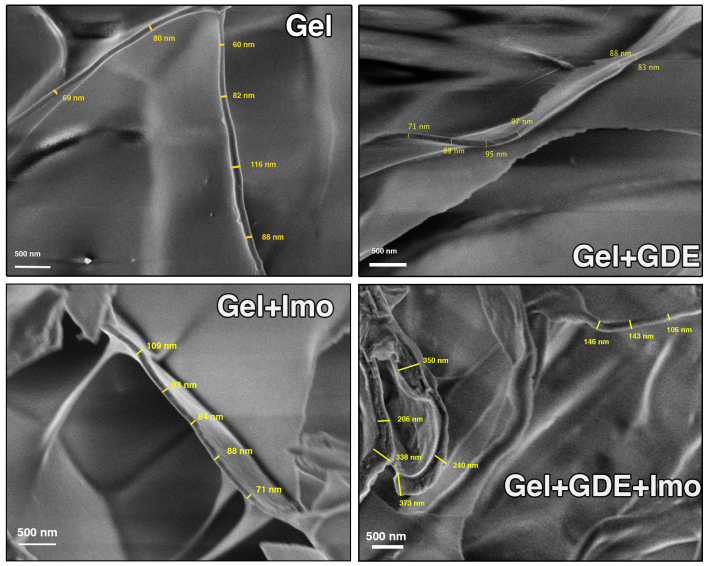

Figure S1: FE-SEM micrographs of samples (a) Gel, (b) Gel+GDE, (c) Gel+Imo, and (d) Gel+GDE+Imo.

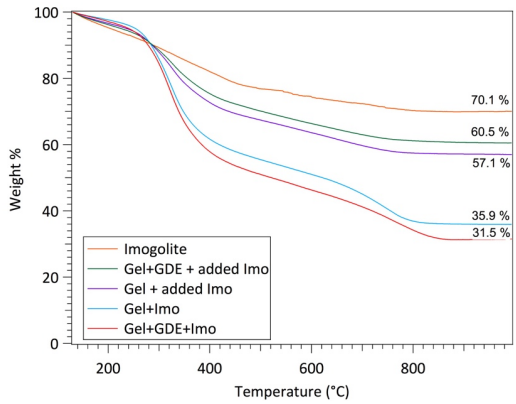

Figure S2: Thermogravimetry of the samples recovered after dissolution, centrifugation and freeze-drying.

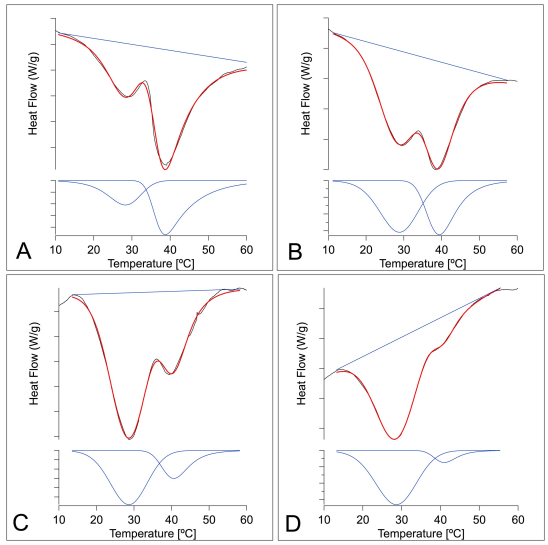

Figure S3: Deconvolution of the double peak in the first heating scan for the samples A) Gel; B) Gel+GDE; C) Gel+Imo; D) Gel+GDE+Imo.

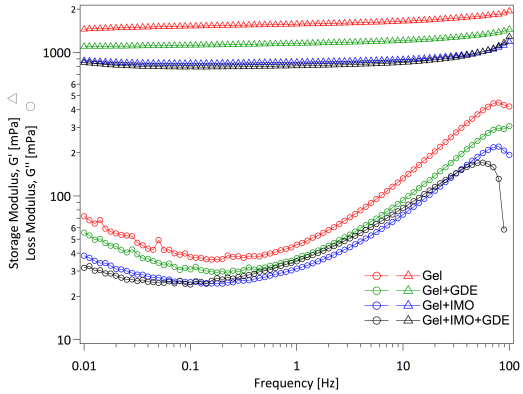

Figure S4: Storage modulus and loss modulus as a function of frequency for Gel, Gel+GDE, Gel+Imo and Gel+GDE+Imo samples.

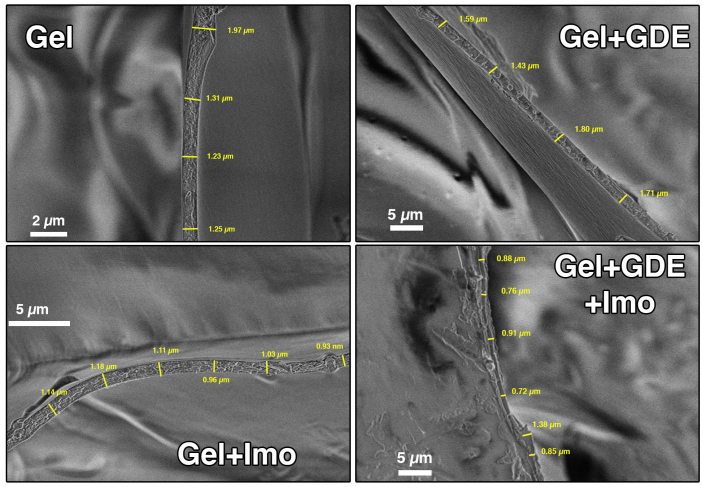

Figure S5: FE-SEM micrographs of samples obtained by cryo-poration of (a) Cryo_Gel, (b) Cryo_Gel+GDE, (c) Cryo_Gel+Imo, and (d) Cryo_Gel+GDE+Imo.

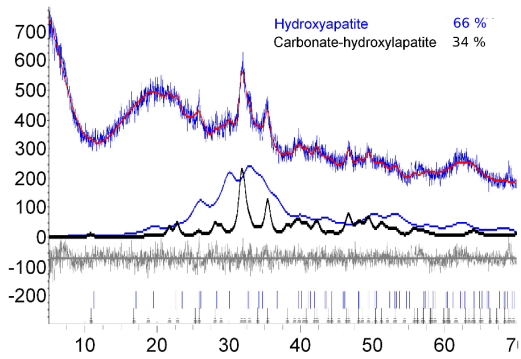

Figure S6: Rietveld fitting of Cryo_Gel+GDE_CaP.

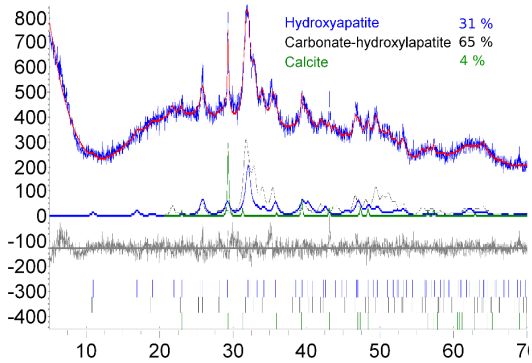

Figure S7: Rietveld fitting of Cryo_Gel+GDE+Imo_CaP.

Appendix III

Manuscripts in preparation

Effect of mucins on the formation of endogenous-like amorphous magnesium-calcium phosphate nanoparticles

Rita Gelli, Francesca Ridi, Piero Baglioni

Department of Chemistry "Ugo Schiff" and CSGI, University of Florence, via della Lastruccia 3-13, 50019 Sesto Fiorentino (FI), Italy

Abstract

The formation of amorphous magnesium-calcium phosphate nanoparticles (AMCPs) in the small intestine is a recently-discovered phenomenon that present many interesting outcomes from a physico-chemical perspective: the study of the effect of macromolecules that the particles could encounter during their formation is particularly relevant, as it could give important insights in the biogenic formation process. In this paper, we investigate the formation and features of synthetic analogs of AMCPs prepared in the presence of mucins, large glycoproteins which are the main component of the intestinal mucus layer. Particles were synthesized in the presence of different mucin concentrations, and characterized in terms of chemical nature, crystallinity, morphology and microstructure. The existence of a specific interaction between the amorphous particles and mucins was also inspected.

Formation and crystallization of amorphous magnesium-calcium phosphate nanoparticles in the presence of proteins from *Moringa Oleifera* seeds

Rita Gelli[a], Monica Tonelli[a], Francesca Ridi[a], Adrian Rennie[b], Piero Baglioni[a]

[a]*Department of Chemistry "Ugo Schiff" and CSGI, University of Florence, via della Lastruccia 3-13, 50019 Sesto Fiorentino (FI), Italy*
[b]*Materials Physics, Department of Physics and Astronomy, Ångström Laboratory, Uppsala University, Box 516, 751 20, Uppsala, Sweden*

Abstract

The development of nanocarriers for the loading of drugs or food products is an open challenge, as it allows to improve their bioavailability and to protect valuable nutraceuticals at food processing or digestion. In this contribution, we explore the possibility of using amorphous magnesium-calcium phosphate nanoparticles (AMCPs) for the loading of proteins extracted from the seeds of *Moringa Oleifera*, a tree which has an impressive range of medicinal uses and high nutritional values, and which is commonly taken as supplement. AMCPs consistently form in mammalians' small intestine, and their amorphous nature allows for the effective incorporation of organic molecules within its structure. Endogenous-like AMCPs were prepared in the presence of dispersions of the protein, and characterized by means of a multi-technique approach; moreover, the effect of the protein on the lifetime of the amorphous phase was also explored. The obtained results clearly highlight that proteins extracted from *Moringa Oleifera* have an effect in shaping the stability and the crystallization pathway of AMCP. These macromolecules can also be loaded within AMCP in a concentration-dependent fashion, paving the way for a potential application of this material in nutraceutics and drug delivery.

Development of magnesium phosphate-based bone cements containing citrate

Rita Gelli[a], Gemma di Pompo[b], Gabriela Graziani[b], Sofia Avnet[b], Nicola Baldini[b], Francesca Ridi[a], Piero Baglioni[a]

[a]*Department of Chemistry "Ugo Schiff" and CSGI, University of Florence, via della Lastruccia 3-13, 50019 Sesto Fiorentino (FI), Italy*
[b]*Laboratory for Orthopedic Pathophysiology and Regenerative Medicine, IRCCS Istituto Ortopedico Rizzoli, via di Barbiano 1/10, 40136 Bologna, Italy*

Abstract

Magnesium phosphate-based bone cements (MPCs) represent a new category of biomaterials towards which the interest of the scientific community recently emerged, given their interesting features which make them good candidates for orthopedic applications. As it was demonstrated that the inclusion of citrate in a biomaterial presents several beneficial effects in bone healing process, we aimed at preparing and characterizing the features of MPCs able to release citrate. Formulations containing different amounts of this ion were prepared, and its effect on the most meaningful properties of both the pastes and the set cements was assessed. Cements were then incubated in aqueous-based media, and the pH of the solution and the release profile of citrate were evaluated. The biocompatibility of the systems was assessed, and results show that only cements which release an amount of citrate < 10 mM result in a good cells' viability, while maintaining promising physico-chemical properties.

Ringraziamenti

La conclusione di questo dottorato rappresenta per me un momento fondamentale della mia esperienza di crescita professionale e personale, e sono molte le persone che, a vario titolo, hanno contribuito a rendere questi tre anni così speciali e che voglio quindi ringraziare.
Il mio ringraziamento più grande va indubbiamente alla mia tutor, la Dr. Francesca Ridi, che è stata per me un punto di riferimento sotto ogni aspetto: grazie per avermi dato questa opportunità e per aver sempre creduto nelle mie capacità.
Un altro enorme grazie va al Prof. Massimo Bonini, per i continui confronti e scambi di idee, al Prof. Piero Baglioni ed a tutti i membri del CSGI.
Ringrazio i colleghi che mi hanno accompagnato in questi anni per i bei momenti passati insieme sia dentro che fuori il laboratorio, in particolare Monica, Stefano, Paolo e Claudio. Voglio anche ringraziare gli (ex) laureandi che ho avuto il piacere di accompagnare nella realizzazione dei loro lavori di tesi (Lucia, Laura, Serena e Alberto), a cui auguro un brillante futuro.
Desidero ringraziare i ricercatori dell'Istituto Ortopedico Rizzoli di Bologna, in particolare il Prof. Nicola Baldini, la Dr. Gemma di Pompo, la Dr. Gabriela Graziani e la Dr. Sofia Avnet, con l'augurio che questa stimolante collaborazione possa portare in futuro nuovi frutti.
Ringrazio anche il Dr. Samuele Ciattini e la Dr. Laura Chelazzi del Centro di Cristallografia Strutturale dell'Università di Firenze, per l'aiuto nelle numerose misure di diffrazione di raggi X effettuate in questi tre anni, e il Dr. Enzo Barlacchi e il Dr. Leonardo Bucci del Laboratorio Prove Strutture e Materiali del Dipartimento di Ingegneria Civile e Ambientale dell'Università di Firenze, per le misure di proprietà meccaniche.
Ringrazio infine la mia famiglia, Ale ed i miei amici di sempre, per non avermi mai fatto mancare il loro supporto.